A scientist counts calories to make sense of human evolution p. 710

Ordinary bilayer graphene is superconducting pp. 719 & 774

New insights on the peopling of the Americas p. 727

Science

$15
18 FEBRUARY 2022
science.org

AAAS

QUICK RELEASE

How lizards rapidly shed their tails to escape predators pp. 721 & 770

Rutgers Congratulates Our Newest AAAS Fellows

"I applaud Rutgers' newest fellows of the American Association for the Advancement of Science—12 eminent scientists who exemplify the excellence of Rutgers faculty and whose scholarly achievements, as recognized by their peers, fulfill the AAAS mission to advance science, engineering, and innovation throughout the world for the benefit of all people."

—Jonathan Holloway, Rutgers President and University Professor

Emanuel M. DiCicco-Bloom
Professor of Neuroscience and Cell Biology, Robert Wood Johnson Medical School ♦ **Distinguished contributions to understanding growth factor regulation of neurogenesis during mammalian brain development, focusing on human neurodevelopmental disorders**

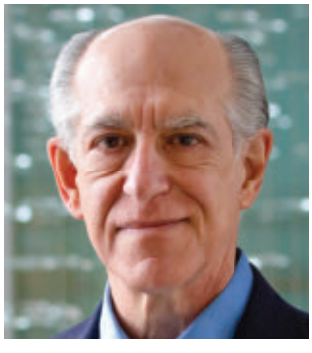

Cecile Arlene Feldman
Dean and Professor, Rutgers School of Dental Medicine ♦ **Outstanding contributions to dentistry and distinguished leadership and advocacy in addressing contemporary issues facing dental education, research, and delivery of oral health care**

Ying Fan Reinfelder
Professor of Earth and Planetary Sciences, School of Arts and Sciences ♦ **Advancing understanding of continental-scale hydrology, particularly groundwater and near-surface systems interactions, including vegetation and surface water**

Patricia Fitzgerald-Bocarsly
Provost, Rutgers Biomedical and Health Sciences–Newark; Professor of Pathology and Laboratory Medicine, New Jersey Medical School ♦ **Distinguished science leadership and contributions to the field of biology, especially innate immune responses to human viral infections**

William C. Gause

Director, Center for Immunity and Inflammation; Senior Associate Dean for Research, New Jersey Medical School ♦ **Advancing understanding of molecular and translational immunology, especially the initiation and function of type 2 immunity during infectious disease**

Margaret Marsh

University Professor of History, Rutgers University–Camden and Institute for Health, Health Care Policy, and Aging Research ♦ **Distinguished contributions to the social sciences, particularly the history of medicine, academic leadership, and communicating and interpreting science to the public**

Alan S. Goldman

Distinguished Professor of Chemistry and Chemical Biology, School of Arts and Sciences ♦ **Distinguished contributions to catalysis by transition-metal complexes, particularly elucidation of reaction mechanisms and development of catalysts for hydrocarbon functionalization**

Tara C. Matise

Chair and Professor of Genetics, School of Arts and Sciences ♦ **Distinguished contributions to developing human genetic maps and for critical efforts to bring genetics to diverse human populations**

Max M. Häggblom

Chair and Distinguished Professor of Biochemistry and Microbiology, School of Environmental and Biological Sciences ♦ **Advancing understanding of fundamental and application components of microbial biotransformations of pollutants**

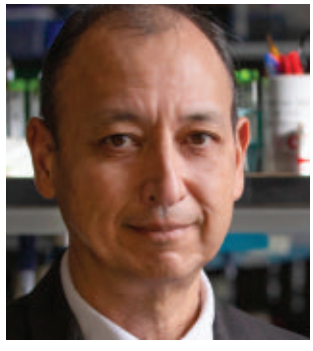

Andrew Singson

Professor of Genetics, School of Arts and Sciences and Waksman Institute of Microbiology ♦ **Innovations in the field of fertilization, particularly discovery and characterization of genes required for fertilization in *Caenorhabditis elegans***

Julie L. Lockwood

Chair and Professor of Ecology, Evolution, and Natural Resources, School of Environmental and Biological Sciences ♦ **Furthering knowledge of ecology and conservation biology, particularly biological invasions and causes of biotic homogenization**

Renping Zhou

William and Myrle Garbe Chair in Cancer and Leukemia Research, Ernest Mario School of Pharmacy ♦ **Advancing knowledge of molecular signaling in organizing biological structures and function, particularly protein interactions regulating growth of neuronal processes**

Rutgers is a leading national research university and New Jersey's preeminent public institution of higher education. Established in 1766, Rutgers is the nation's eighth-oldest higher education institution.

RUTGERS
THE STATE UNIVERSITY OF NEW JERSEY

This is what **Excellence** *looks like*

excellence.rutgers.edu

CONTENTS

18 FEBRUARY 2022
VOLUME 375
ISSUE 6582

710

NEWS

IN BRIEF

IN DEPTH

FEATURES

INSIGHTS

PERSPECTIVES

POLICY FORUM

PHOTO: JUSTIN COOK

ON THE COVER

Although its tail aids in fast and stable locomotion, a lizard species (*Hemidactylus flaviviridis*) from the Gekkonidae family will quickly detach this appendage when attacked by a predator. A biomimetic model elucidates the hierarchical micro- and nanoscale structures required to enable predetermined fracture planes that balance attachment and detachment, enabling the "just right" connection to maximize the animal's chance of survival. See pages 721 and 770. *Photo: Shiji Ulleri/Wise Monkeys Photography*

SCIENCE (ISSN 0036-8075) is published weekly on Friday, except last week in December, by the American Association for the Advancement of Science, 1200 New York Avenue, NW, Washington, DC 20005. Periodicals mail postage (publication No. 484460) paid at Washington, DC, and additional mailing offices.

Domestic individual membership, including subscription (12 months): $165 ($74 allocated to subscription). Domestic institutional subscription (51 issues): $2212; Foreign postage extra: Air assist delivery: $98. First class, airmail, student, and emeritus rates on request. Canadian rates with GST available upon request, GST #125488122. Publications Mail Agreement Number 1069624. **Printed in the U.S.A.**
Change of address: Allow 4 weeks, giving old and new addresses and 8-digit account number. **Postmaster:** Send change of address to AAAS, P.O. Box 96178, Washington, DC 20090–6178. **Single-copy sales:** $15 each plus shipping and handling available from backissues.science.org; bulk rate on request. **Authorization to reproduce** material for internal or personal use under circumstances not falling within the fair use provisions of the Copyright Act can be obtained through the Copyright Clearance Center (CCC), www.copyright.com. The identification code for *Science* is 0036-8075. *Science* is indexed in the *Reader's Guide to Periodical Literature* and in several specialized indexes.

Science AAAS

Editor-in-Chief Holden Thorp, hthorp@aaas.org

Executive Editor Monica M. Bradford

Editors, Research Valda Vinson, Jake S. Yeston **Editor, Insights** Lisa D. Chong

DEPUTY EDITORS Stella M. Hurtley (UK), Phillip D. Szuromi, Sacha Vignieri **SR. EDITORIAL FELLOW** Andrew M. Sugden (UK) **SR. EDITORS** Gemma Alderton (UK), Caroline Ash (UK), Brent Grocholski, Pamela J. Hines, Di Jiang, Priscilla N. Kelly, Marc S. Lavine (Canada), Yevgeniya Nusinovich, Ian S. Osborne (UK), Beverly A. Purnell, L. Bryan Ray, H. Jesse Smith, Keith T. Smith (UK), Jelena Stajic, Peter Stern (UK), Valerie B. Thompson, Brad Wible, Yuen Yiu, Laura M. Zahn **ASSOCIATE EDITORS** Michael A. Funk, Bianca Lopez, Seth Thomas Scanlon (UK), Yury V. Suleymanov **LETTERS EDITOR** Jennifer Sills **LEAD CONTENT PRODUCTION EDITORS** Harry Jach, Lauren Kmec **CONTENT PRODUCTION EDITORS** Amelia Beyna, Jeffrey E. Cook, Chris Filiatreau, Julia Haber-Katris, Nida Masiulis, Abigail Shashikanth, Suzanne M. White **SR. EDITORIAL COORDINATORS** Carolyn Kyle, Beverly Shields **EDITORIAL COORDINATORS** Aneera Dobbins, Joi S. Granger, Jeffrey Hearn, Lisa Johnson, Maryrose Madrid, Ope Martins, Shannon McMahon, Jerry Richardson, Hilary Stewart (UK), Alice Whaley (UK), Anita Wynn **PUBLICATIONS ASSISTANTS** Alexander Kief, Ronmel Navas, Isabel Schnaidt, Brian White **EXECUTIVE ASSISTANT** Jessica Slater **ASI DIRECTOR, OPERATIONS** Janet Clements (UK) **ASI SR. OFFICE ADMINISTRATOR** Jessica Waldock (UK)

News Editor Tim Appenzeller

NEWS MANAGING EDITOR John Travis **INTERNATIONAL EDITOR** Martin Enserink **DEPUTY NEWS EDITORS** Elizabeth Culotta, Lila Guterman, David Grimm, Eric Hand (Europe), David Malakoff **SR. CORRESPONDENTS** Daniel Clery (UK), Jon Cohen, Jeffrey Mervis, Elizabeth Pennisi **ASSOCIATE EDITORS** Jeffrey Brainard, Kelly Servick, Catherine Matacic **NEWS REPORTERS** Adrian Cho, Jennifer Couzin-Frankel, Jocelyn Kaiser, Rodrigo Pérez Ortega (Mexico City), Robert F. Service, Erik Stokstad, Paul Voosen, Meredith Wadman **INTERN** Tess Joose **CONTRIBUTING CORRESPONDENTS** Warren Cornwall, Andrew Curry (Berlin), Ann Gibbons, Sam Kean, Eli Kintisch, Kai Kupferschmidt (Berlin), Andrew Lawler, Mitch Leslie, Eliot Marshall, Virginia Morell, Dennis Normile (Tokyo), Elisabeth Pain (Careers), Charles Piller, Gabriel Popkin, Michael Price, Joshua Sokol, Richard Stone, Emily Underwood, Gretchen Vogel (Berlin), Lizzie Wade (Mexico City) **CAREERS** Rachel Bernstein (Editor), Katie Langin (Associate Editor) **COPY EDITORS** Julia Cole (Senior Copy Editor), Morgan Everett, Cyra Master (Copy Chief) **ADMINISTRATIVE SUPPORT** Meagan Weiland

Creative Director Beth Rakouskas

DESIGN MANAGING EDITOR Marcy Atarod **GRAPHICS MANAGING EDITOR** Chris Bickel **PHOTOGRAPHY MANAGING EDITOR** William Douthitt **WEB STRATEGY MANAGER** Kara Estelle-Powers **MULTIMEDIA MANAGING PRODUCER** Joel Goldberg **DESIGN EDITOR** Chrystal Smith **DESIGNER** Christina Aycock **GRAPHICS EDITOR** Nirja Desai **INTERACTIVE GRAPHICS EDITOR** Kelly Franklin **SENIOR GRAPHICS SPECIALISTS** Holly Bishop, Nathalie Cary **SENIOR SCIENTIFIC ILLUSTRATOR** Valerie Altounian **SCIENTIFIC ILLUSTRATOR** Ashley Mastin **SENIOR PHOTO EDITOR** Emily Petersen **PHOTO EDITOR** Kaitlyn Dolan **SOCIAL MEDIA STRATEGIST** Jessica Hubbard **SOCIAL MEDIA PRODUCER** Sabrina Jenkins **WEB DESIGNER** Jennie Pajerowski **SENIOR PODCAST PRODUCER** Sarah Crespi **VIDEO PRODUCER** Meagan Cantwell

Chief Executive Officer and Executive Publisher Sudip Parikh

Publisher, Science Family of Journals Bill Moran

DIRECTOR, BUSINESS SYSTEMS AND FINANCIAL ANALYSIS Randy Yi **DIRECTOR, BUSINESS OPERATIONS & ANALYSIS** Eric Knott **DIRECTOR OF ANALYTICS** Enrique Gonzales **MANAGER, BUSINESS OPERATIONS** Jessica Tierney **MANAGER, BUSINESS ANALYSIS** Cory Lipman **BUSINESS ANALYST** Kurt Ennis **FINANCIAL ANALYST** Isacco Fusi **ADVERTISING SYSTEM ADMINISTRATOR** Tina Burks **DIGITAL/PRINT STRATEGY MANAGER** Jason Hillman **SENIOR MANAGER, PUBLISHING AND CONTENT SYSTEMS** Marcus Spiegler **ASSISTANT MANAGER DIGITAL/PRINT** Rebecca Doshi **SENIOR CONTENT AND PUBLISHING SYSTEMS SPECIALIST** Jacob Hedrick **SENIOR CONTENT SPECIALISTS** Steve Forrester, Lori Murphy **PRODUCTION SPECIALIST** Kristin Wowk **DIGITAL PRODUCTION MANAGER** Lisa Stanford **CONTENT SPECIALIST** Kimberley Oster **ADVERTISING PRODUCTION OPERATIONS MANAGER** Deborah Tompkins **DESIGNER, CUSTOM PUBLISHING** Jeremy Huntsinger **SR. TRAFFIC ASSOCIATE** Christine Hall **SPECIAL PROJECTS ASSOCIATE** Sarah Dhere

ASSOCIATE DIRECTOR, BUSINESS DEVELOPMENT Justin Sawyers **GLOBAL MARKETING MANAGER** Allison Pritchard **DIGITAL MARKETING MANAGER** Aimee Aponte **JOURNALS MARKETING MANAGER** Shawana Arnold **MARKETING ASSOCIATES** Ashley Hylton, Mike Romano, Tori Velasquez, Jenna Voris, Justin Wood **SENIOR DESIGNER** Kim Huynh

DIRECTOR AND SENIOR EDITOR, CUSTOM PUBLISHING Sean Sanders **ASSISTANT EDITOR, CUSTOM PUBLISHING** Jackie Oberst

DIRECTOR, PRODUCT & PUBLISHING DEVELOPMENT Chris Reid **DIRECTOR, BUSINESS STRATEGY AND PORTFOLIO MANAGEMENT** Sarah Whalen **ASSOCIATE DIRECTOR, PRODUCT MANAGMENT** Kris Bishop **PRODUCT DEVELOPMENT MANAGER** Scott Chernoff **PUBLISHING TECHNOLOGY MANAGER** Michael Di Natale **SR. PRODUCT ASSOCIATE** Robert Koepke **PRODUCT ASSOCIATE** Caroline Breul, Anne Mason **SPJ ASSOCIATE MANAGER** Samantha Bruno Fuller **SPJ ASSOCIATE** Casey Buchta

MARKETING MANAGER Kess Knight **BUSINESS DEVELOPMENT MANAGER** Rasmus Andersen **SENIOR INSTITUTIONAL LICENSING MANAGER** Ryan Rexroth **INSTITUTIONAL LICENSING MANAGER** Marco Castellan, Claudia Paulsen-Young **SENIOR MANAGER, INSTITUTIONAL LICENSING OPERATIONS** Judy Lillibridge **SENIOR OPERATIONS ANALYST** Lana Guz

DIRECTOR, GLOBAL SALES Tracy Holmes **US EAST COAST AND MID WEST SALES** Stephanie O'Connor **US MID WEST, MID ATLANTIC AND SOUTH EAST SALES** Chris Hoag **US WEST COAST SALES** Lynne Stickrod **ASSOCIATE DIRECTOR, ROW** Roger Goncalves **SALES REP, ROW** Sarah Lelarge **SALES ADMIN ASSISTANT, ROW** Victoria Glasbey **DIRECTOR OF GLOBAL COLLABORATION AND ACADEMIC PUBLISHING RELATIONS, ASIA** Xiaoying Chu **ASSOCIATE DIRECTOR, INTERNATIONAL COLLABORATION** Grace Yao **SALES MANAGER** Danny Zhao **MARKETING MANAGER** Kilo Lan **ASCA CORPORATION, JAPAN** Yoshimi Toda (Tokyo), Miyuki Tani (Osaka)

DIRECTOR, COPYRIGHT, LICENSING AND SPECIAL PROJECTS Emilie David **RIGHTS AND PERMISSIONS ASSOCIATE** Elizabeth Sandler **LICENSING ASSOCIATE** Virginia Warren

MAIN HEADQUARTERS
Science/AAAS
1200 New York Ave. NW
Washington, DC 20005

SCIENCE INTERNATIONAL
Clarendon House
Clarendon Road
Cambridge, CB2 8FH, UK

SCIENCE CHINA
Room 1004, Culture Square
No. 59 Zhongguancun St.
Haidian District, Beijing, 100872

SCIENCE JAPAN
ASCA Corporation
Sibaura TY Bldg. 4F, 1-14-5
Shibaura Minato-ku
Tokyo, 108-0073 Japan

EDITORIAL
science_editors@aaas.org

NEWS
science_news@aaas.org

INFORMATION FOR AUTHORS
science.org/authors/
science-information-authors

REPRINTS AND PERMISSIONS
science.org/help/
reprints-and-permissions

MEDIA CONTACTS
scipak@aaas.org

MULTIMEDIA CONTACTS
SciencePodcast@aaas.org
ScienceVideo@aaas.org

INSTITUTIONAL SALES AND SITE LICENSES
science.org/librarian

PRODUCT ADVERTISING & CUSTOM PUBLISHING
advertising.science.org/
products-services
science_advertising@aaas.org

CLASSIFIED ADVERTISING
advertising.science.org/
science-careers
advertise@sciencecareers.org

JOB POSTING CUSTOMER SERVICE
employers.sciencecareers.org
support@sciencecareers.org

MEMBERSHIP AND INDIVIDUAL SUBSCRIPTIONS
science.org/subscriptions

MEMBER BENEFITS
aaas.org/membership/benefits

Science serves as a forum for discussion of important issues related to the advancement of science by publishing material on which a consensus has been reached as well as including the presentation of minority or conflicting points of view. Accordingly, all articles published in *Science*—including editorials, news and comment, and book reviews—are signed and reflect the individual views of the authors and not official points of view adopted by AAAS or the institutions with which the authors are affiliated.

EDITORIAL

Empower with evidence

This week (17 to 20 February), the virtual annual meeting of the American Association for the Advancement of Science (AAAS, the publisher of *Science*) will address the challenges of building the public's trust and understanding of science by illuminating both great science and innovative initiatives in advocacy, education, and policy. The theme, "Empower with Evidence," speaks to the critical importance of decision-making, policy-making, and interventions that are grounded in knowledge and facts, not opinions—or worse, misinformation.

The ability of science to transform the world is increasingly threatened by misinformation that is jeopardizing trust in science. As highlighted in *Science* last week, the world's information ecosystem is rapidly changing, and online environments have become a powerful open marketplace of facts, ideas, and opinions—where the meaningfulness of science is easily drowned out by the noise.

Solutions to this dilemma include training students and professional scientists to more effectively translate their work to the public, harnessing insights from the behavioral and social sciences to better engage with the public, and working with social media platforms to improve information delivery to a broader audience. These are important efforts, but do they get to the root of the problem?

> "...misinformation... is jeopardizing trust in science."

Science has long been touted as the solver of all problems, and during crises like the COVID-19 pandemic, the public craves certainty. But science is dynamic, and when knowledge changes—and technology is now enabling rapid changes—the public can become confused and even doubtful when shifts in understanding are framed the wrong way. Scientists and educators must do a better job of explaining how science works to the public, as well as to policy-makers and leaders. Science continually challenges and improves on the current state of knowledge. This is how the world progresses. It is the job of the scientific community to explain new findings in this context. Without this framing, the dynamic nature of science may be misunderstood as a weakness rather than a strength, and new findings may be misrepresented to the public. The COVID-19 pandemic exposed this vulnerability, with dire consequences. One need only look at the hundreds of thousands of needless deaths resulting from vaccine misinformation.

Part of making the scientific process less mysterious and questionable for everyone is providing greater transparency. Science advances through positive and negative results, and better ways are needed to report or share this information and present the full picture of studies. There also must be a means through which all fields of study commit to rigorously assessing the reproducibility of their findings. These are efforts that bolster, not diminish, confidence in science, both within and outside the scientific community. Collaborative and open science efforts have spurred the rapid growth of open-source platforms, data sharing, common methodology, and computational tools that enhance both scientific rigor and the generalizability of findings. Well-validated data are essential for the further development of new inventions and innovations. In parallel, the scientific enterprise still must provide opportunities for exploratory research, hypothesis-generating studies, and high risk–high reward endeavors, again affirming to the public that such pursuits can lead to deeper understanding as well as breakthrough discoveries.

As science progresses, society must be ever aware of the consequences. It can be challenging for advances that generate change to gain widespread acceptance. Sadly, there are examples throughout history in which scientific advances were implemented without careful thought about their long-term impacts on the environment or society. This breeds distrust in science. For example, the failure to consider subgroups in population-level research has sometimes led to social and economic disparities in human health. Conversely, stratification of subgroups in clinical trials—such as Black patients with congestive heart failure, for example—has led to improved therapies that might otherwise have been missed. Building greater diversity in the scientific workforce may also lead to a more equitable impact of new advances and improve the ability to communicate science to wider communities.

Public perception of science depends on an appreciation that the scientific process is nuanced and cannot be reduced to overstated conclusions, and worse, premature implications for use by society. Without this understanding, failures to predict outcomes or revisions of earlier findings may reinforce, in some quarters, a belief that science cannot be trusted. Let this be science's overriding message: As new discoveries inevitably alter our understanding, the methods of science push us ever closer to the truth.

–Susan G. Amara

PHOTO: DELANY TORRES-SALAZAR

Susan G. Amara
is president of the American Association for the Advancement of Science, Washington, DC, USA.
susan.amara@nih.gov

10.1126/science.abo5963

NEWS

> "I just wish when people say 'Follow the science,' it's ... followed by 'and here's the evidence.'"
>
> **Princeton University science historian Michael Gordin**, in *The Washington Post*, about the phrase's use and misuse by policymakers and others in public discussions of COVID-19.

IN BRIEF

Edited by **Jeffrey Brainard**

ECOLOGY

Dry heat fuels increase in nighttime wildfires

In 2017, a wildfire burned some 20,000 hectares in Oregon near the Columbia River Gorge.

Rising nighttime temperatures around the globe are helping fuel more intense and long-lasting wildfires, researchers report. Wildfire fighters have often relied on cooler temperatures and higher humidity at night to help calm blazes. But detailed satellite observations of fires stretching back 2 decades, paired with 4 decades of hour-by-hour weather data, have revealed a change. In fire-prone ecosystems around the world, the number of nights during which atmospheric conditions would encourage fires to keep burning has increased by 15% since 1979. That added five more nights per year on average when blazes are unlikely to be snuffed by cooler, more humid weather. In some regions, the effect was greater: In the western United States, the increase was 45% since 1979—the equivalent of 11 additional fire-friendly nights. The research team said the changes may be associated with climate change but did not document a causal link. But, "The 'night brakes' on fires are failing," they write in this week's issue of *Nature*.

FDA chief confirmed in close vote

LEADERSHIP | For the first time in more than 1 year, the U.S. Food and Drug Administration (FDA) is set to have a permanent head. On 15 February, the Senate confirmed Robert Califf, a cardiologist with close ties to the drug industry, as commissioner. The 50-46 vote was unusually close, with four Democrats and independent Senator Bernie Sanders (VT) opposing Califf, whom President Joe Biden nominated in November 2021. The vote returns Califf—a longtime clinical research leader at Duke University who has recently been senior adviser for Google Health—to a job he held under former President Barack Obama in 2016 and early 2017. Dissenting Democrats protested Califf's ties to drugmakers and FDA's approval of five new prescription opioids during that tenure. Abortion opponents protested Califf's role in FDA's easing of access to medical abortion pills in 2016. Six Republicans voted in favor of Califf, assuring his confirmation.

Omicron treatment wins U.S. nod

COVID-19 | The U.S. Food and Drug Administration (FDA) last week gave emergency use authorization to a monoclonal antibody that in test-tube studies neutralizes the SARS-CoV-2 Omicron variant and

PHOTO: TRISTAN FORTSCH/KATU-TV VIA AP

its "subvariant" BA.2. The monoclonal, bebtelovimab, made by Eli Lilly and Company, can be used in people at least 12 years old who have mild to moderate COVID-19 and are at high risk of progressing to severe disease. In January, FDA revoked emergency use authorizations for two other monoclonal treatments—one made by Eli Lilly, the other by Regeneron Pharmaceuticals—that did not neutralize Omicron. Sotrovimab, another monoclonal authorized before Omicron appeared, appears to have "sufficient" activity against it and BA.2, according to studies briefly described in press releases by its makers, Vir Biotechnology and GlaxoSmithKline. But a preprint report, posted on bioRxiv on 9 February, suggested BA.2 had "marked resistance" to sotrovimab in lab studies. In addition to the monoclonals, three antiviral drugs widely used for months to treat COVID-19 are also effective against Omicron, their makers say.

French co-discoverer of HIV dies

VIROLOGY | Luc Montagnier, who won the Nobel Prize in Physiology or Medicine for his role in discovering HIV, died last week at age 89. After receiving the award, he later lost the respect of many colleagues for embracing unscientific theories about cofactors he claimed were needed for the virus to cause AIDS, water's ability to hold memory, and the dangers of COVID-19 vaccines. In a landmark *Science* paper in 1983, Montagnier's Pasteur Institute lab reported the first isolation of a novel retrovirus from an AIDS patient. But it wasn't until 1 year later that Robert Gallo's group at the U.S. National Cancer Institute conclusively proved the virus caused the disease. This led to a blood test and a prolonged, impassioned, high-profile patent battle between Montagnier, Gallo, and the French and U.S. governments. A 1987 settlement described the two scientists as "co-discoverers" of the virus, but Gallo did not share the Nobel, awarded in 2008.

Stormy skies for satellite swarm

ASTRONOMY | SpaceX's Starlink project to ring the globe with thousands of internet satellites was buffeted this month by natural and institutional forces. A 3 February launch that put 49 satellites into orbit (joining 1800 already lofted Starlinks) suffered a blow the next day when a blast of particles from a solar storm swelled Earth's atmosphere, dragging as many as 40 of the satellites to a fiery death on reentry. Then last week, NASA and the U.S. National Science Foundation (NSF) sent letters to the Federal Communications Commission about SpaceX's proposal to expand its approved constellation of 12,000 Starlinks by another 30,000. NASA cited concerns about collision hazards, interference with Earth-observation satellites and space telescopes, and a reduced number of launch windows for rockets. NASA does not oppose the expanded fleet but says coordination will be required to protect assets from damage. NSF noted the work SpaceX has already done to lessen impacts on radio and optical observatories but says such efforts will be "even more critical" for larger constellations.

PHOTO: JUERGEN & CHRISTINE SOHNS/MINDEN PICTURES

CONSERVATION

Koalas declared endangered as wolves get reprieve

The iconic koala is now endangered in parts of Australia, the government announced last week. The status of the marsupial was changed from threatened, on the advice of an expert panel that blamed dwindling numbers on habitat loss from land clearing and bush fires, droughts and heat waves, and disease. Koala populations have declined by 50% to 60% in eastern Australia since 2001, environmental organizations estimate. The endangered listing triggers greater protection of habitats, and the government promised to adopt a national recovery plan. Last month, it announced it will spend $36 million over 4 years to support conservation. Scientists say saving the koala will depend on quickly implementing these and other countermeasures. Meanwhile, a federal court in the United States last week struck down a decision by former President Donald Trump's administration to remove gray wolves from the endangered species list in much of the country outside of the Rockies and Yellowstone National Park. The ruling restores protection from hunting.

Judge blocks higher carbon cost

CLIMATE POLICY | A federal judge last week prevented President Joe Biden's administration from increasing its estimate of how much carbon pollution costs

society. Federal agencies use that number to evaluate the costs and benefits of new regulations, particularly in the energy sector; the figure is called the social cost of carbon because it factors in costs, such as declines in health outcomes and agricultural productivity, that are not reflected in market prices. The administration plans to raise the estimate of this cost from about $7 per ton of carbon dioxide emissions to $51 per ton. But U.S. District Judge James Cain of the Western District of Louisiana sided with Republican attorneys general in ruling that the higher cost would harm states that produce fossil fuels, and that the administration had overstepped its authority. Environmental advocates say the ruling, if upheld, would make it harder to tighten limits on greenhouse gas emissions.

Webb space telescope takes selfie

ASTRONOMY | NASA last week released the first images taken by its flagship James Webb Space Telescope. Although

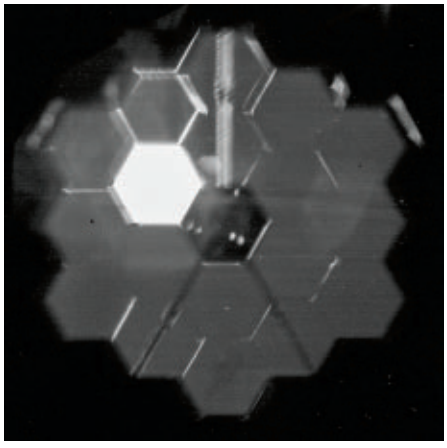

The Webb telescope's camera snapped a selfie of its mirror, with one segment reflecting starlight.

unspectacular, they mark an initial step in tuning the instrument's segmented mirror to observe the earliest galaxies and nearby exoplanets. One composite image showed 18 blurry dots—all the same star—taken by each of the mirror's 18 segments. In the coming weeks, engineers will adjust the alignment and curvature of the segments to create a single reflecting surface and focus those scattered dots into a single pinpoint of light.

U.S. steps in to help porpoise

CONSERVATION | The U.S. Trade Representative's Office filed a complaint against Mexico last week for failing to protect the vaquita, a critically endangered porpoise. It is the first complaint under the trade agreement between the two countries and Canada that took effect in 2020; the pact includes stronger environmental regulations than its predecessor. If the dispute is not resolved, the United States could impose trade sanctions. Until July 2021, the Mexican government had prohibited fishing in a part of the Gulf of California that harbors the roughly 10 vaquitas that are the last survivors of their species. But that month, Mexico changed its policies to allow up to 60 boats to fish there at once. The vaquita population has dropped drastically because of entanglements in illegal fishing nets used to catch an endangered fish, the totoaba, whose swim bladder is considered a delicacy and is used medicinally in China.

Depression in poor rarely treated

MENTAL HEALTH | Few people worldwide receive treatment for major depressive disorder, particularly in low and lower middle income countries, a meta-analysis shows. Only 8% of patients living in poorer countries were treated, versus 33% in wealthy countries, researchers report this week in *PLOS Medicine*. Their analysis covered 149 studies conducted in 84 countries. Major depressive disorder is defined as a persistent loss of pleasure or interest in activities for 2 weeks or longer; symptoms can range from mild to severe. Globally, about 5% of adults suffer from it, with an associated economic loss estimated at $1 trillion per year, according to a report by *The Lancet*–World Psychiatric Association Commission on Depression published this week. "There is arguably no other health condition which is as common, as burdensome, as universal, or as treatable as depression, yet it receives little policy attention and resources," said commission Co-Chair Christian Kieling of the Federal University of Rio Grande do Sul. The commission's recommendations include folding treatment for depression into routine health care.

Oshkosh Defense has developed a hybrid electric version of the Joint Light Tactical Vehicle, a successor to the U.S. Army's Humvee.

POLICY

U.S. Army takes on climate change

The U.S. Army wants to step up its attack on a pervasive, global adversary: climate change. The military branch's first ever climate strategy, released last week, outlines an ambitious plan for reducing greenhouse gas emissions from one of the world's largest energy users, while also preparing to fight on battlefields transformed by global warming. Goals include starting a large-scale shift to electric vehicles in 2027, achieving net-zero emissions from Army installations by 2045, and boosting the number of soldiers and civilian employees with advanced credentials on climate change topics. The plan also calls for incorporating the latest climate science into decisions such as where to build bases and position forces. The Army put no price tag on its plan, but said setting clear goals is a necessary first step toward realizing them.

SCIENCE.ORG/NEWS
Read more news from *Science* online.

PHOTOS: (TOP TO BOTTOM) NASA; OSHKOSH DEFENSE

Like many locales recently, Barcelona, Spain, has lifted pandemic restrictions on indoor gatherings.

PHOTO: DAVIDE BONALDO/SIPA USA/NEWSCOM

COVID-19

Scientists call 'endemic' message premature

As pandemic restrictions lift, virus tracking and preparation for next variant may suffer

By **Kelly Servick**

As surges of COVID-19 cases driven by the highly infectious Omicron variant recede, parts of the United States, Canada, and Europe are moving swiftly to lift constraints on a pandemic-fatigued public. Sweden, Denmark, and Norway have abolished nearly all COVID-19–related restrictions in recent weeks, and the United Kingdom announced it would do the same this month, dropping even the legal requirement that people quarantine after testing positive for SARS-CoV-2. In the United States, despite persistently high numbers of COVID-19–related deaths and busy hospitals, 10 governors, many known for being cautious in their pandemic response, last week announced immediate or impending ends to their states' indoor or school mask mandates.

Some of those moves came with assertions that it's time to "live with the disease" and treat the coronavirus as endemic—a stable, enduring figure in the panoply of human pathogens, alongside cold viruses and influenza. That suggestion troubles many scientists, who warn it is eroding governments' commitment to tracking and responding to the pandemic—which could leave countries flying blind and unprepared for any new variant.

"Endemic delusion is probably what captures it the best," says Kristian Andersen, an infectious disease researcher at Scripps Research who has been especially critical of recent moves by his home country of Denmark, which include an announcement that as of this month COVID-19 would no longer be categorized as a "socially critical disease" even though related death and hospitalization rates were still climbing there.

Still, many scientists acknowledge the challenges of steering public restrictions during the reign of the more infectious but generally less severe Omicron variant, when some of the metrics that previously guided policy have become less informative. For example, how meaningful are case counts as mild and asymptomatic infections increase and unreported at-home tests become ubiquitous? How much do incidental findings of COVID-19 in patients hospitalized for other conditions pollute the official numbers?

"The challenge for each and every health authority is to figure out, well, what should we track?" says Michael Bang Petersen, a political scientist at Aarhus University.

Denmark's recent moves are a case in point. Petersen, a pandemic adviser to the Danish government, supports its decision to lift measures such as limits on nightlife hours, caps on attendance at indoor public events, and mandatory face masks or proof of vaccination for indoor venues. He argues the government could no longer justify the economic, social, and constitutional tradeoffs of those restrictions amid promising signs, such as numbers of intensive care unit (ICU) patients that remain stable and below the health system's capacity.

Andersen, however, calls keeping hospitals from overflowing "a pretty low bar." Bringing down overall cases, and thereby reducing transmission, remains key, he argues, to minimizing risks of Long Covid and protecting the elderly and immunocompromised from infection.

In the United States, governors cited various metrics to justify recent decisions to lift or let expire indoor mask mandates. California Governor Gavin Newsom noted stable hospitalization rates and a 65% reduction in cases since Omicron's peak in announcing the state's mandate would end this week. But leaders also face political and economic pressures. States' moves may be driven largely by the public's impatience with restrictions, says epidemiologist Dustin Duncan of Columbia University.

"Even people who recognize the importance of masking, social distancing, all that stuff, may be more amenable to take more risk," he says. "At the same time, to me, go-

ing maskless just seems egregious." Indeed, the U.S. Centers for Disease Control and Prevention has held firm in recommending masks for indoor public spaces in areas of high transmission—which is nearly all of the country.

"I do feel it is on the early side" to lift indoor mask requirements in most states, says Emory University epidemiologist Jodie Guest—though recommendations may be a better option than requirements as case numbers plummet, she adds.

Still, with the United States logging more than 2000 daily deaths last week, "We cannot say we are at a level that's tolerable to live with this virus," Guest says. Her team has been developing rough guidelines for when a true endemic stage of COVID-19 has been reached: daily case rates below 30 per 100,000, ICUs below 80% of capacity, vaccination rates of at least 75%, and fewer than 100 COVID-19 deaths a day nationwide.

Deciding when to end mask requirements in schools is especially difficult, in part because of continued (but hard to prove) concerns the coverings impede learning and social development. "If you ask a bunch of scientists, 'Should kids wear face masks in school?' you're probably going to get a lot of disagreement," Andersen notes, "and I don't know who is right."

Guest says she doesn't have as clear a sense of the numerical thresholds that could determine when schools should stop mandating masks. "I would be hesitant [to remove requirements] right now," she says, adding the step could soon be justified in parts of the country.

Data to inform such debates may become less available or reliable if governments pivot too soon to an endemic view of the coronavirus, scientists say. As pandemic restrictions in Denmark relax, "people are becoming less motivated to get tested and we are beginning to downscale our test system," Petersen says.

Some governments are limiting efforts to find and report cases. Sweden, long an outlier among European countries for its laissez-faire approach to the pandemic, ended widespread testing at mobile centers as cases declined from their Omicron peak. The United Kingdom is reportedly weighing ending free public testing for the virus in the coming weeks. Meanwhile, the Canadian province of Saskatchewan last week switched from providing daily to weekly reports of COVID-19 cases. And Tennessee last month joined several states already reporting case counts weekly. "Daily case counts matter," Guest says. "Every time I lose the ability to have a number, it makes me nervous."

Official counts are already becoming less meaningful as the reliance on at-home test increases, making other surveillance approaches all the more important. Last week, researchers took to Twitter in outrage after a U.K. news report claimed the United Kingdom might not continue to fund a long-running study in which the Office for National Statistics (ONS) conducts repeated antibody surveys and SARS-CoV-2 testing of more than 100,000 randomly selected households. "What that's meant is that you've had a way of seeing the prevalence in your population that does not depend on people accessing testing," says Christina Pagel, a health services researcher at University College London.

Discontinuing the ONS study would also obscure data on asymptomatic cases, differences in disease burden between different ethnic and occupational groups, and the impact of Long Covid, Pagel says. She suspects the outcry will sway the U.K. government, which responded in the news report by saying no funding decision had been made and it "obviously" wanted to "maintain our world-leading surveillance capacity" for COVID-19.

> **"More alarming to me is that our public health system doesn't seem to have any plan for dealing with the next surge."**
>
> **KJ Seung**, Partners In Health

But in the growing number of "back to normal" messages, Pagel sees leaders ignoring obvious next steps to protect public safety. Even researchers who aren't speaking up to defend specific restrictions are urging governments to step up their COVID-19 fight, rather than scale it back. They want aggressive new pushes to reach the unvaccinated, distribute rapid tests, and make COVID-19 treatments much more accessible, for example. "Frankly, I don't really think that 2 to 3 weeks more of a mask mandate is going to make much difference in the long run," says KJ Seung, a health policy adviser at Partners In Health. "More alarming to me is that our public health system doesn't seem to have any plan for dealing with the next surge."

"I don't particularly want to be in a future where I get COVID twice a year," Pagel adds. Averting that future may mean adaptations such as technologies to improve indoor air quality and strong virus surveillance that can be ramped up at the first sign of another surge. "Why would we not make that effort?" she wonders. "It's almost like having that conversation is considered a failure." ■

ECOLOGY

Transgenic fish invades Brazilian streams

Fluorescent aquarium curiosity has escaped from fish farms and may threaten local biodiversity

By **Sofia Moutinho**

Fish genetically engineered to glow blue, green, or red under blacklight have been a big hit among aquarium lovers for years. But the fluorescent pet is not restricted to glass displays anymore. The red- and green-glowing versions, more vivid than normal zebrafish even in natural light, have escaped fish farms in southeastern Brazil and are multiplying in creeks in the Atlantic Forest, a new study shows. It is a rare example of a transgenic animal accidentally becoming established in nature, and a concern for biologists, who worry the engineered exotic fish could threaten the local fauna in one of the most biodiverse spots on the planet.

"This is serious," says ecologist Jean Vitule at the Federal University of Paraná, Curitiba. Vitule, who was not part of the research, says the ecological impacts are unpredictable. He worries, for example, that the fluorescence-endowing genes from the escapees could end up being introduced in native fish with detrimental effects, perhaps making them more visible to predators. "It's like a shot in the dark," he says.

The unwelcome visitors are well known to scientists who have used zebrafish (*Danio rerio*) for developmental and genetic studies for decades. Native to Southeast Asia, the match-size freshwater fish were engineered to glow for research purposes in the late 1990s by endowing them with genes from fluorescent jellyfish (for blue and green colors) and coral (for red). In the 2000s, companies saw the potential of the neon fish as pets. Trademarked as Glofish, they became the world's first genetically engineered species to be commercially available.

Now, they are one of the first to escape and thrive in nature. Early on, environmentalists worried about the possibility, and Glofish sales were banned in some U.S. states such as California and several countries—including Brazil. In 2014, a single Glofish was spotted in canals near ornamental fish farms in the Tampa Bay region of Florida. But it had not multiplied, probably because native predators such as the eastern mosquitofish (*Gambusia holbrooki*) and the largemouth bass (*Micropterus salmoides*) ate the interloper, says the biologist who spotted the transgenic animal, Quenton Tuckett of the University of Florida.

Brazil is proving more hospitable. André Magalhães, a biologist at the Federal University of São João del-Rei's main campus, first spotted groups of the engineered zebrafish swimming in the Paraíba do Sul River Basin in 2015, in slow-moving creeks. The waters border the largest ornamental aquaculture center of Latin America, in Muriaé, and Magalhães says the fish probably escaped some of the center's 4500 ponds, which release water into the streams.

Unlike Florida, the Brazilian creeks don't have any local predators for zebrafish, and Magalhães believes they are now thriving. In 2017 he and colleagues began to survey five creeks in three municipalities, finding transgenic zebrafish in all of them. Every 2 months over 1 year, they collected and measured the animals and their eggs and analyzed their stomach content to see what they were eating.

The fish are reproducing all year round, with a peak during the rainy season—just as native zebrafish do in Asia. But the transgenic fish seem to achieve sexual maturity earlier than their forebears, which allows them to reproduce more and spread faster. The invaders are also eating well: a diversified diet of native insects, algae, and zooplankton, the researchers reported last week in *Studies on Neotropical Fauna and Environment*.

"They are in the first stages of invasion with potential to keep going," Magalhães says. Before long, he says, the fish could become plentiful enough to directly affect local species by competing for food or preying on them.

Despite Brazil's ban on sales of the fish, local farms keep breeding them, and stores all over the country sell them as pets. They may soon colonize other parts of the country: Isolated Glofish individuals were spotted in ponds and streams in south and northeast Brazil in 2020.

Tuckett, whose lab in Florida is close to U.S. farms that grow hundreds of thousands of glowing fish, says the Brazilian detection "should be a wake-up call" for fish producers and natural resource managers in Brazil. But he is not terribly worried about impacts. He suspects the transgenic fish will encounter predators as they move to larger bodies of water. And the animals' bright colors will make them vulnerable.

For now, the glowing fish "could be considered little weeds growing up out of the concrete," Tuckett says. Magalhães likes the metaphor, but points out that even little weeds can grow to cause a lot of damage. ■

Sofia Moutinho is a journalist based in Rio de Janeiro.

PHOTO: PAULO DE OLIVEIRA/MINDEN PICTURES

Genetically modified zebrafish (*Danio rerio*) are sold in fluorescent red, blue, and green.

CHEMISTRY

Machine builds druglike molecules in a snap

Automated assembly of 3D molecules could revolutionize drug discovery

By **Robert F. Service**

Organic chemistry, one of science's most grueling disciplines, is poised to get a whole lot easier. Six years ago, a team of chemists created a robotic system that could construct a wide variety of organic molecules including potential pharmaceuticals, dyes, and perfumes. But the setup had limited abilities: It could only build flat molecules—chains or 2D rings. It couldn't make anything 3D, which many medicines and materials require.

Now, 3D has arrived. The team reported last week in *Nature* that it has reworked its design to enable automated setups to build the majority of molecules now painstakingly assembled by organic chemists in the lab. "It's a landmark achievement," says Timothy Cernak, a medicinal chemist at the University of Michigan, Ann Arbor, who was not involved with the work. "This has been a holy grail for chemistry for a long time."

Robots have previously revolutionized making DNA, RNA, and short proteins, all of which are built from a relatively small number of building blocks that can be linked with the same kind of chemical bond. In contrast, small organic molecules—those needed for medicines and many other applications—use an array of reaction conditions, catalysts, reagents, and so on to connect different atoms, with bonds at various angles or orientations. The process resembles making fine furniture, securing irregularly shaped pieces of wood together using many different joinery techniques. It takes years of experience to master the craft.

"We're trying to change that," says Martin Burke, a chemist at the University of Illinois, Urbana-Champaign. He and colleagues started in 2015 by creating a machine ca-

pable of synthesizing a vast array of organic compounds. Their chemical building blocks had different shapes but all contained two chemical linkers, one called a MIDA that's attached to one carbon atom, the other called a boronate that's attached to a different carbon.

The machine piped in reactants sequentially so that the MIDA on the first building block came together with the boronate on the second, joining their carbon atoms. Then the second building block's MIDA hooked up with boronate on the third, and so on, until the desired molecule was complete. The MIDA and boronate linkers wash away in the process.

The setup allowed the creation of many druglike organic compounds. By now, more than 250 academic and industrial labs have used MIDA-boronate chemistry to synthesize new molecules, Burke says.

But the process almost always creates an "sp^2-sp^2" bond, which links two carbon atoms and the atoms attached to them into a single plane. "Nature is not flat," Cernak says. "It lives in 3D." Innumerable organic molecules, from antibiotics to perfumes, include sp^3 bonds, in which some of the two carbons' attachments jut out of the plane.

Burke and his colleagues tried to use MIDA-boronate connectors to forge sp^3 bonds. But doing so required harsher reagents, which wound up ripping MIDA off the building blocks, causing a cascade of uncontrolled chemical reactions that created a broad mix of byproducts.

The team has now solved this problem by discovering a MIDA relative, known as TIDA. TIDA linkers are up to 1000 times more stable than MIDA linkers, which allows them to withstand the harsher reagents needed to construct sp^3 bonds. TIDA-boronate linkers in hand, the team used its molecular synthesizer to create two complex natural products, an antibiotic called ieodomycin C and an antifungal compound called sch725674. Both contain what are known as chiral centers, in which elements are arranged in just one of two distinct mirror-image orientations. Such chiral centers are key to the function of many drugs and other organic compounds.

Burke is now working to commercialize the new setup and come up with libraries of building blocks that contain TIDA and boronate linkers so that chemists can assemble molecules at will. He says he's also working with colleagues to create artificial intelligence software to dream up novel organic compounds as potential new medicines. "We want nonspecialists to be able to make molecules at the push of the button," he says. "If it becomes child's play to make new molecules, the bottleneck becomes imagination." ■

COVID-19

COVID-19 boosts risk of heart disease 1 year later

Giant study shows even mild cases can take a long-term toll on heart and blood vessels

By **Meredith Wadman**

From very early in the pandemic, it was clear SARS-CoV-2 can damage the heart and blood vessels while people are acutely ill. Patients developed clots, heart inflammation, arrhythmias, and heart failure.

Now, the first large study to assess cardiovascular outcomes 1 year after SARS-CoV-2 infection has demonstrated the virus' impact is often lasting. In an analysis of more than 11 million U.S. veterans' health records, researchers found the risk of 20 different heart and vessel maladies was substantially increased in veterans who had COVID-19 1 year earlier, compared with those who didn't. The risks rose significantly with severity of initial disease and extended to every outcome the team examined, including heart attacks, arrhythmias, strokes, cardiac arrest, and more. But even people who never went to the hospital had more cardiovascular disease than those who were never infected.

The results are "stunning … worse than I expected, for sure," says Eric Topol, a cardiologist at Scripps Research. "All of these are very serious disorders. … If anybody ever thought that COVID was like the flu this should be one of the most powerful data sets to point out it's not." He adds that the new study "may be the most impressive Long Covid paper we have seen to date."

Others agree the results of the study, published in *Nature Medicine* on 7 February, are powerful. "In the post-COVID era, COVID might become the highest risk factor for cardiovascular outcomes," greater than well-documented risks such as smoking and obesity, says Larisa Tereshchenko, a cardiologist and biostatistician at the Cleveland Clinic. She cautions that the new study will need to be replicated and that it was retrospective. "It looked back. We have to do prospective studies to calculate accurate [risk] estimates."

Nor do researchers know how the virus orchestrates this long-term damage. But they think the cardiovascular risks and the constellation of symptoms collectively known as Long Covid (which in addition to heart symptoms includes brain fog, fatigue, and loss of smell) could have common roots. "This is clearly evidence of long-term heart and vascular damage. Similar things could be happening in the brain and other organs resulting in symptoms characteristic of Long Covid," says senior author Ziyad Al-Aly, a clinical epidemiologist at Washington University in St. Louis and chief of research at the VA St. Louis Health Care system. In a parallel study, out this week, his team found higher risks of neuropsychiatric effects, including brain fog, 1 year after COVID-19 infection (see sidebar, p. 707).

Myriad other studies have suggested COVID-19 prompts lingering damage. For example, a preprint on 320,000 health records from Estonia, posted on 7 February by *The Lancet*, found all-cause mortality over the 12 months after infection was more than three times higher than in uninfected people. But most published studies examining long-term outcomes of COVID-19 have followed patients for just a few months and focused on far fewer outcomes; many lacked controls.

In the new study, the team drew on the largest set of electronic health records in the United States, at the Department of Veterans Affairs (VA). They analyzed data from nearly 154,000 people who contracted COVID-19 between 1 March 2020 and 15 January 2021, and who survived at least 30 days after becoming infected. They identified two control groups: 5.6 million people who sought VA care during the pandemic but were not diagnosed with COVID-19, and 5.9 million people who went to the VA in 2017.

The authors analyzed data from a period before vaccines were widely available: 99.7% of infected veterans were unvaccinated when they got COVID-19. (The paper doesn't address what might happen after breakthrough infections in already vaccinated people, although the authors have a paper in review on that question.) In addition, the study demographics were skewed: About 90% of participants were men and 71% to 76% were white. Patients were in their early 60s, on average.

The researchers controlled for the possibility that the people who contracted COVID-19 were already more prone to de-

veloping cardiovascular disease. They found "COVID is an equal opportunity offender," Al-Aly says. "We found an increased risk of cardiovascular problems in old people and in young people, in people with diabetes and without diabetes, in people with obesity and people without obesity, in people who smoked and who never smoked."

COVID-19 boosted the risk of all 20 cardiovascular ailments studied, including heart attacks, arrhythmias, strokes, heart failure, cardiac arrest, pulmonary embolism, and deep vein thrombosis.

For example, veterans who had COVID-19 faced a 72% higher risk of heart failure after 12 months than their pandemic-era peers who didn't test positive. That translated to nearly 12 more infected people per 1000 developing heart failure than controls. Overall, infection raised the risk of developing any of the 20 conditions by 63%, compared with pandemic-era controls. But Miriam Merad, an immunologist at the Icahn School of Medicine at Mount Sinai, notes the researchers also found "a clear correlation between the severity of the [post–COVID-19] symptoms and the severity of the initial disease." The long-term risks grew markedly from outpatients to hospitalized patients to those in the intensive care unit.

The team used statistical tools to try to correct for the scarcity of women and people of color, and their results are likely to be relevant for those groups, too, says Elizabeth Ofili, a preventive cardiologist at Morehouse School of Medicine. "The correction for gender and race goes a long way."

One possible mechanism for long-term damage is inflammation of the endothelial cells that line the heart and blood vessels, Al-Aly says; the virus is known to directly attack such cells. But the researchers also include a list of other potential mechanisms, including a greater tendency of the blood to clot, persistent virus in some sites, and elevated levels of proinflammatory chemical messengers called cytokines. "The putative mechanistic pathways are still in the realm of speculation," Al-Aly says.

The authors say their findings suggest millions of COVID-19 survivors could suffer long-term consequences, straining health care delivery for years. "Governments and health systems around the world should be prepared to deal with the likely significant contribution of the COVID-19 pandemic to a rise in the burden of cardiovascular diseases," they write.

Al-Aly adds: "Some of these conditions are chronic [and] will literally scar people for a lifetime. It's not like you wake up tomorrow and suddenly no longer have heart failure." ■

The heartbreak of COVID-19

One year later, veterans infected with COVID-19 faced higher risk of cardiovascular ailments, with risk rising with the severity of initial disease and translating into many more affected people per thousand than in controls.

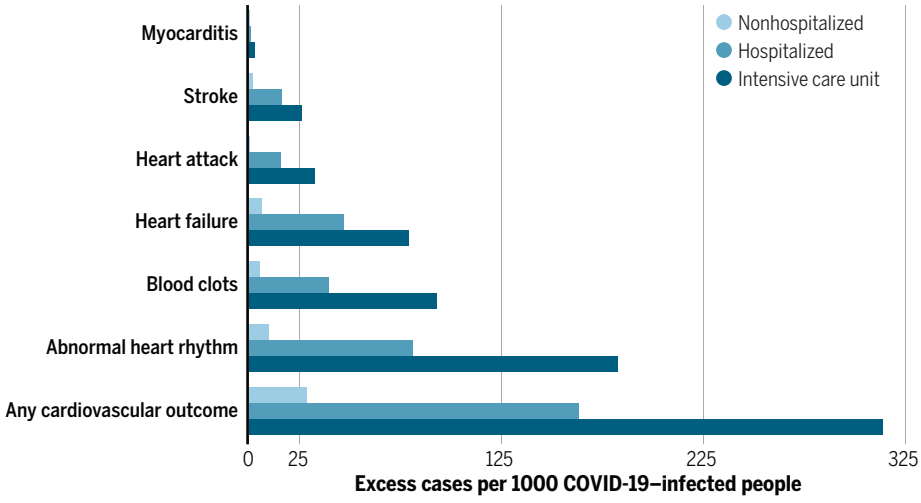

CREDITS: (GRAPHIC) K. FRANKLIN/*SCIENCE*; (DATA) Y. XIE *ET AL.*, *NAT MED* (2022). DOI: 10.1038/S41591-022-01689-3376659

Lasting impact of infection extends to the brain

The team that last week found elevated long-term risks of cardiovascular ailments among U.S. veterans who got COVID-19 (see main story, p. 706) is reporting more bad news. According to a huge analysis published this week in *The BMJ*, 1 year later the veterans also faced higher risks of neuropsychiatric ailments, including brain fog, than their uninfected peers.

"Most of us experienced some sort of mental distress during the pandemic, but this shows that people with COVID-19 had a much higher risk of mental health disorders than their contemporaries," says senior author Ziyad Al-Aly, a clinical epidemiologist at Washington University in St. Louis and chief of research at the VA St. Louis Health Care system. "It's a wake-up call."

Many papers have used health records to examine post–COVID-19 psychiatric outcomes, but "The scale of … this study sets [it] apart, as well as the quality of the statistical methods used," says Alex Charney, a neuroscientist and psychiatrist at the Mount Sinai Health System.

Al-Aly and colleagues analyzed the electronic health records of nearly 154,000 infected veterans (almost all unvaccinated at the time) and 5.8 million uninfected controls who used Affairs health system in the first 10.5 months of the U.S. pandemic.

One year later, survivors of COVID-19 were 46% more likely than controls to have been diagnosed with any of 14 neuropsychiatric disorders. These included depression, suicidal thoughts, anxiety, sleep disturbance, opioid use disorder, and neurocognitive decline or "brain fog." The risk of brain fog was 80% higher than in controls, which translates to 10.75 more people in every 1000 experiencing the condition. People hospitalized with coronavirus infections had the highest risk of developing any of the disorders—343% more than controls. Outpatients faced 40% higher risk.

The study has limitations, including that its population was 71% to 76% white, 90% male, and on average 63 years old. "This is a Veterans Affairs cohort and not generalizable," says Sung-Min Cho, a neurointensivist and physician-scientist at Johns Hopkins University's School of Medicine.

Neuroimmunologist Cecilie Bay-Richter of Aarhus University adds that just how infection could damage mental health is unclear. She says animal studies will be needed "to be able to truly disentangle the direct, biological causes from the indirect causes" of long-term neuropsychiatric conditions. —*M.W.*

Bisphenol A is often used in the plastic linings of steel and aluminum cans that hold food and drink.

PHOTO: PHILIPPE DESMAZES/AFP/GETTYIMAGES

CHEMICAL REGULATION

Europe proposes drastic cut of endocrine disruptor in plastic

Food safety agency adopts cautious approach in calling for 100,000-fold cut in allowable exposure to bisphenol A

By **Erik Stokstad**

In a move that could signal a new approach to regulating potentially hazardous compounds, European health experts are recommending a drastic cut in the allowable human consumption of a common chemical in food. The European Food Safety Authority (EFSA) has proposed reducing by a factor of 100,000 the tolerable daily intake of bisphenol A (BPA), an endocrine disruptor that interferes with hormone systems and has been linked to disease.

The huge reduction could lead to a de facto ban on the cheap and durable material in food-related uses, such as lining metal cans. And it could mark a shift in how European regulators use research findings in setting exposure limits. Traditionally, those limits have been shaped by large studies directly linking a chemical to an increased risk of disease. In this case, however, risk assessors put greater weight on smaller studies showing low levels of BPA can cause subtle changes that could lead to future health problems. This approach, if adopted widely, could justify much lower exposure limits for other chemicals.

"It's a big deal," says Laura Vandenberg, an endocrinologist at the University of Massachusetts, Amherst, who calls the proposed limit "a gravestone for BPA in Europe." Environmental and public health advocates are praising the proposal, which is open for comment until 22 February.

Industry groups, however, are dismayed. Plastics Europe argues EFSA ignored relevant, older studies in setting the standard. "If the entire scientific evidence had been evaluated … we are convinced that the conclusions would have been different," says Jasmin Bird, a spokesperson for the group. Jennifer Garfinkel, a spokesperson for the industry-backed American Chemistry Council, calls EFSA's proposal "unprecedented," noting that the U.S. Food and Drug Administration (FDA) has concluded that BPA is safe at current exposures.

Bisphenol A is used in many plastics, including thermal paper for receipts, but most people are exposed through food. BPA leaches out of polycarbonates used to make bottles and food containers, for example, as well as the epoxy liners used to protect steel and aluminum cans from acidic food and beverages.

In 2014, after reviewing recent studies, an expert panel assembled by EFSA recommended temporarily lowering the tolerable daily intake from 50 to 4 micrograms per kilogram of body weight per day. The panel was especially intrigued by studies suggesting BPA altered the immune systems of rats. Before making a firmer recommendation, however, the EFSA panel wanted to see the results of a $30 million research program funded by the U.S. government.

This program, which ran from 2014 to 2018, compared academic research studies with a large study of rats exposed to BPA—the kind of standardized animal study that industry and FDA typically rely on to assess health risks. The rat study supported FDA's recommended daily limit of 5 micrograms. But the academic studies, which included analyses of how low doses affected mammary glands in lab animals, produced results that EFSA experts considered worrisome.

To set an intake limit, the EFSA panel looked at the study in which the lowest dose produced a biological effect. That research, conducted at Anhui Medical University in China, showed that as BPA exposure rose in mice, so did the numbers of immune cells that are key players in inflammatory and autoimmune diseases. Based on that finding, the panel recommended cutting the BPA limit 100,000-fold, to 0.04 nanograms.

Although EFSA says it did not change its basic approach in re-evaluating BPA, scientists say risk assessors are giving increasing weight to smaller research studies that agency experts have traditionally discounted. "It's a tremendous change," says Ángel Nadal, a physiologist at the Miguel Hernández University of Elche. EFSA unveiled its analysis and proposed limit in December 2021. BPA exposure was "a health concern … for all age groups," the expert panel wrote. And it noted that most people consume far more BPA than allowed under the proposed limit.

EFSA is now pushing to finalize the new standard by December. EU legislators would then use it to establish legally binding limits on how much BPA is allowed to leach from packaging into food.

"If we are logical, there should be some action very quickly on BPA," says Robert Barouki, a toxicologist at the University of Paris.

In the United States, a number of groups recently urged FDA to follow EFSA's lead and consider new limits on BPA. Others note that people are often exposed to BPA in combination with other chemicals, which could increase the risk from low doses. For example, children of Swedish women exposed to BPA and other endocrine disrupters early in pregnancy have a higher risk of language delays, according to a study in *Science* this week (pp. 720 and 735).

Even if Europe adopts the new standard, public health advocates worry manufacturers will replace BPA with very similar chemicals, such as bisphenol S, that have also been linked to health effects. To avoid that problem, many advocates have called for regulators around the world to set limits for whole classes of related compounds, rather than consider them one by one. For now, Vandenberg says, regulators are simply playing "chemical whack-a-mole." ■

BIOMEDICINE

Microbiome data dominated by wealthy countries

Skew could hamper development of targeted therapies

By **Rodrigo Pérez Ortega**

Thousands of studies have linked the trillions of microbes living in and on our bodies to conditions from cancer to autism to depression. But most microbiome samples come from wealthy countries in North America and Europe, a new analysis finds, distorting our understanding of human-microbe interactions.

"There are many ethnic groups and geographical locations that are dramatically underrepresented," says Rob Knight, a microbiologist at the University of California, San Diego, who was not part of the study. The distribution of samples "speaks to deep inequities in how research is funded and conducted." A fuller picture of how different microbiomes impact health could aid the development of diagnostics and therapies for specific populations, says Knight, who is working to make microbiome sampling more equitable.

Unlike the human genome, which only varies slightly among individuals, the human microbiome differs radically. Diet, exercise, socioeconomic status, antibiotic use, and even pollution can influence its makeup, with some studies suggesting geography is one of the strongest variables.

Research comparing the gut microbiomes of people from the Amazonas state in rural Venezuela, rural Malawi, and U.S. metropolitan areas shows microbiomes in less industrialized environments are more diverse. Studies have also found that compared with microbiomes in urban populations, those of hunter-gatherers in Tanzania are very dynamic, changing with the seasonal availability of foods.

To see how well microbiome research captures these global variations, Ran Blekhman, Elizabeth Adamowicz, and Richard Abdill of the University of Minnesota, Twin Cities, compiled geographic information for more than 440,000 publicly available microbial DNA sequences from the past 11 years. They found more than 40% of the samples were from the United States—almost five times as many as from any other country, the scientists report this week in *PLOS Biology*.

The researchers then compared the number of samples with each region's population. They found Europe and North America provided more than 71% of samples even though they hold about 15% of the world's population, whereas central and southern Asia contributed 1.5% of samples from almost 26% of the world's population. "It is clear that our understanding of the 'human' microbiome does not include most humans," Abdill says. "Our study is a step towards quantifying this disparity."

Clement Adebamowo, an epidemiologist at the University of Maryland, Baltimore, agrees. "[The authors] have done a great service to the field by highlighting the scope of the problem," he says.

The sparse representation of developing countries reflects low levels of research funding, lack of state-of-the-art technology, and few people trained to analyze samples, says Adebamowo, who has a joint appointment at the Institute of Human Virology, Nigeria. Countries may also focus research efforts on more urgent needs, such as malaria, he says.

The cost of equipment to identify bacteria is a major barrier. "[We] have a very difficult time having access to those technologies," says Pablo Jarrín Valladares, a biologist at the National Institute of Biodiversity in Quito, Ecuador, who leads the Ecuadorian Microbiome Project. Bureaucracy can also delay the permits required for sampling. "The issue for us in catching up is reducing the bumps."

A lack of specialists to analyze data is another obstacle in developing countries, says Victor Pylro, a molecular microbial ecologist at the Federal University of Lavras and coordinator of the Brazilian Microbiome Project. He, Jarrín Valladares, and other researchers hope to attract funding from the private sector and foreign institutions by forming local networks. With funding from Thermo Fisher Scientific, Pylro's team is already working to evaluate how the microbiome changes when people have COVID-19.

Blekhman, Knight, and others point to the Human Heredity and Health in Africa (H3Africa) consortium, which has boosted genomic science in the region, as an example of local groups improving sampling and data sharing. Adebamowo, who leads H3Africa's African Collaborative Center for Microbiome and Genomics Research (ACCME), says the consortium has helped African researchers build infrastructure and expertise, and is now taking on microbial diversity in health and disease. At ACCME, Adebamowo and colleagues are working to find biomarkers linking variations in the vaginal microbiome with persistent high-risk human papillomavirus infections in African women.

For María Gloria Domínguez Bello, a microbiome researcher at Rutgers University, New Brunswick, having samples from populations across the world is essential to understanding not just disease, but also human history and diversity. "Our microbiomes are coevolved entities," she says. "These are genomes that belong to us in the sense that we can't live without them, and they can't live without us." She, Knight, and others have launched a Microbiota Vault in Basel, Switzerland, a storage project akin to the "doomsday" crop seed vault, aiming to preserve microbiome samples from all over the world.

"With the way the field is growing, the best time to course correct was 5 years ago," Abdill says. "But the second best time is now." ■

Missing microbes

To understand how microbes that live on and in us affect health, researchers sequence their DNA. But most of the world's people are underrepresented in the data.

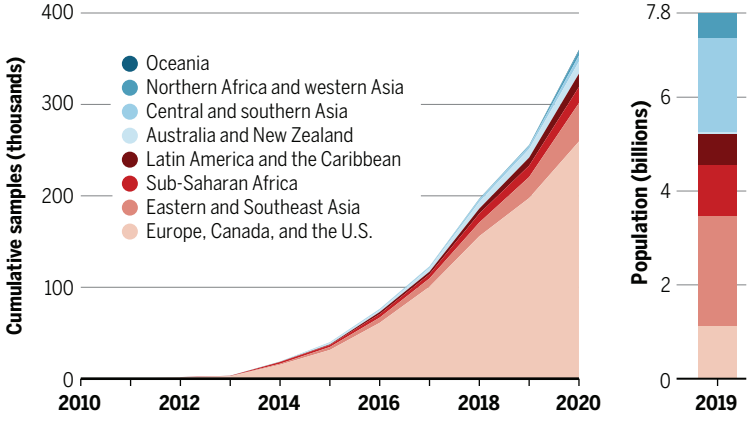

CREDITS: (GRAPHIC) C. BICKEL/*SCIENCE*; (DATA) U.S. NATIONAL LIBRARY OF MEDICINE/NATIONAL CENTER FOR BIOTECHNOLOGY INFORMATION; U.N. DEPARTMENT OF ECONOMIC AND SOCIAL AFFAIRS/POPULATION DIVISION (2019), *WORLD POPULATION PROSPECTS 2019*, ONLINE EDITION. REV.1; R.J. ABDILL, E.M. ADAMOWICZ, R. BLEKHMAN/UNIVERSITY OF MINNESOTA

THE CALORIE COUNTER

Evolutionary anthropologist Herman Pontzer busts myths about how humans burn calories—and why

By **Ann Gibbons**, *in Durham, North Carolina;*
Photograph by **Justin Cook**

On a warm Wednesday morning in October, Herman Pontzer puts on a wrinkled lab coat, adjusts his mask, and heads into his lab at Duke University, hoping to stress out a student. An undergraduate named Christina is resting on a lab table with her head in a clear plastic hood. Pontzer greets her formally and launches into a time-honored method to boost her blood pressure: He gives her an oral math test.

"Start off with number 1022 and subtract 13 until you get to zero," he says, speaking at full volume to be heard over a clanking air conditioner. "If you make a mistake, we'll start over again. You ready to go?"

"1009, 997," Christina says.

"Start over," Pontzer barks.

Christina, who has signed up for a "stress test," laughs nervously. She tries again and gets to 889, only to have Pontzer stop her. This happens again and again. Then Pontzer asks her to multiply 505 by 117, out loud. By this point, she is clenching her sock-clad toes.

Postdoc Zane Swanson and undergrad Gabrielle Butler monitor her heart rate and how much carbon dioxide (CO_2) she exhales into the hood. Then Pontzer asks a set of questions designed to boost a student's stress levels: What's her dream job, and what exactly is she going to do after graduation?

It's another day in the Pontzer lab, where he and his students measure how much energy people expend when they are stressed, exercising, or mounting an immune response to a vaccine, among other states. By measuring the CO_2 in Christina's breath, he is finding out how much energy she has burned while coping with math anxiety.

At 44, Pontzer's life's work as a biological anthropologist is counting calories. It's not to lose weight—at 1.85 meters tall and about 75 kilograms (6 feet 1 inch and 165 pounds), with a passion for running and rock climbing, he is "a skinny to normal size dude," in the words of an online reviewer of Pontzer's 2021 book *Burn: New Research Blows the Lid Off How We Really Burn Calories, Lose Weight, and Stay Healthy*.

Pontzer is happy to expound on weight loss on *The Dr. Oz Show* and NPR, but his real mission is to understand how, alone among great apes, humans manage to have it all, energetically speaking: We have big brains, lengthy childhoods, many children, and long lives. The energy budget needed to support those traits involves trade-offs he's trying to unravel, between energy spent on exercise, reproduction, stress, illness, and vital functions.

By borrowing a method developed by physiologists studying obesity, Pontzer and colleagues systematically measure the total energy used per day by animals and people in various walks of life. The answers coming from their data are often surprising: Exercise doesn't help you burn more energy on average; active hunter-gatherers in Africa don't expend more energy daily than sedentary office workers in Illinois; pregnant women don't burn more calories per day than other adults, after adjusting for body mass.

Pontzer's skill as a popularizer can rankle some of his colleagues. His message that exercise won't help you lose weight "lacks nuance," says exercise physiologist John Thyfault of the University of Kansas Medical Center, who says it may nudge dieters into less healthy habits.

But others say besides busting myths about human energy expenditure, Pontzer's work offers a new lens for understanding human physiology and evolution. As he wrote in *Burn*, "In the economics of life, calories are the currency."

"His work is revolutionary," says paleoanthropologist Leslie Aiello, past president of the Wenner-Gren Foundation, which has funded Pontzer's work. "We now have data … that has given us a completely new framework for how we think about how humans adapted to energetic limits."

Metabolism over the life span

Adjusted for body mass, toddlers burn the most calories per day. Total energy expenditure (TEE) declines after age 60, although individuals show some variation (gray dots).

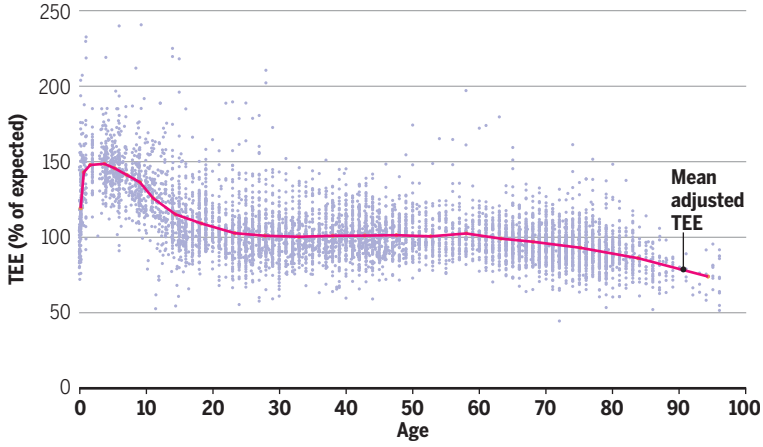

THE SON OF TWO high school English teachers, Pontzer grew up on 40 hectares of woods in the Appalachian hills near the small town of Kersey, Pennsylvania. His dad, who helped build their house, taught Pontzer to be curious about how things worked and to fix them. "No one ever called plumbers or electricians," Pontzer recalls.

Those lessons in self-sufficiency and an outgoing nature helped him cope when his dad died when Pontzer was just 15. An older cousin also took him climbing, which taught him to be both brave and organized—skills he says later helped him take intellectual risks and challenge established ideas. "When you have a bad experience and life plucks you off your track, it's scary," Pontzer says. "You have to move forward, though, and that teaches you not to be scared of new things."

Pontzer applied to a single college—Pennsylvania State University, whose football games were a highlight of his childhood. "I assumed I'd be my dad—go to Penn State, get my teaching degree, and stay in Kersey," he says. But once at Penn State, he worked with the late, renowned paleoanthropologist Alan Walker and found himself considering grad school in biological anthropology.

After learning his promising student was choosing schools based on their proximity to mountains, Walker was blunt: He told Pontzer he was an idiot if he didn't apply to Harvard University—and, once Pontzer was accepted, he'd be an idiot if he didn't go.

Pontzer went. In the early 2000s, scientists knew little about humans' total energy expenditure (TEE)—the number of kilocalories (the "calories" on food labels) a person's 37 trillion cells burn in 24 hours. Researchers had measured the rate at which our bodies burn energy while at rest—the basal metabolic rate (BMR), which includes energy used for breathing, circulation, and other vital functions. They knew BMR was roughly the same among larger mammals, when adjusted for body size. So although BMR only captures 50% to 70% of total energy use, researchers figured that, kilo for kilo, humans burn energy at roughly the same rate as other apes.

But humans have an added energy expense: our big brains, which account for 20% of our energy use per day. Aiello had proposed that our ancestors had compensated for those expensive brains by evolving smaller guts and other organs (*Science*,

Herman Pontzer in the hood and metabolic chamber he uses to measure carbon dioxide, a gauge of how fast the body burns calories.

CREDITS: (GRAPHIC) N. DESAI/*SCIENCE*; (DATA) H. PONTZER *ET AL.*, *SCIENCE*, 373, 6556 (2021)

15 June 2007, p. 1560). Others thought humans had saved energy by evolving to walk and run more efficiently.

At Harvard, Pontzer wanted to test those ideas. But he realized there weren't enough data to do so: No one knew how much total energy primates use when they move, much less how differences in anatomy or trade-offs in organ size impact energy use. "We talked about locomotor adaptations in hominins, we talked about efficiency, power, and strength, but it [was] all sort of made up," Pontzer says.

He realized he had to go back to basics, measuring the calories expended by humans and animals walking and running on treadmills. Mammals use oxygen to convert sugars from food into energy, with CO_2 as a byproduct. The more CO_2 a mammal exhales, the more oxygen—and calories—it has burned.

For his Ph.D. thesis, Pontzer measured how much CO_2 dogs and goats exhaled while running and walking. He found, for example, that dogs with long legs used less energy to run than corgis, as he reported in 2007, soon after he got his first job at Washington University in St. Louis. Over time, he says, "What started as an innocent project measuring the cost of walking and running in humans, dogs, and goats grew into a sort of professional obsession with measuring energy expenditures."

Pontzer still measures exhaled CO_2 to get at calories burned in a particular activity, as he did with Christina's stress test. But he found that physiologists had developed a better way to measure TEE over a day: the doubly labeled water method, which measures TEE without asking a subject to breathe into a hood all day.

Physiologist Dale Schoeller, now at the University of Wisconsin, Madison, had adapted the method, first used in mice, to humans. People drink a harmless cocktail of labeled water, in which distinct isotopes of hydrogen and oxygen replace the common forms. Then researchers sample their urine several times over 1 week. The labeled hydrogen passes through the body into urine, sweat, and other fluids, but as a person burns calories, some of the labeled oxygen is exhaled as CO_2. The ratio of labeled oxygen to labeled hydrogen in the urine thus serves as a measure of how much oxygen a person's cells used on average in a day and therefore how many calories were burned. The method is the gold standard for total energy use, but it costs $600 per test and was out of reach for most evolutionary biologists.

Pontzer's first of many breakthroughs with the method came in 2008 when, with $20,000 from the Wenner-Gren Foundation, he got the chance to collect urine samples at what was then the Great Ape Trust, a sanctuary and research center in Iowa. There, primatologist Rob Shumaker poured isotope-laced sugar-free iced tea into the mouths of four orangutans. Pontzer worried about collecting the urine from a full-grown ape, but Shumaker reassured him the orangs were trained to pee in a cup.

Later that fall, when Pontzer got the urine results, he didn't believe them: The orangutans burned one-third of the energy expected for a mammal their size. A retest returned the same results: Azy, a 113-kilogram adult male, for example, burned 2050 kilocalories per day, much less than the 3300 a 113-kilogram man typically burns. "I was in total disbelief," Pontzer says. Orangs were perhaps the "sloths in the ape family tree," he thought, because they suffered prolonged food scarcity in their past and had evolved to survive on fewer calories per day.

Subsequent doubly labeled water studies of apes in captivity and in sanctuaries shattered the consensus view that mammals all have similar metabolic rates when adjusted for body mass. Among great apes, humans are the outlier. When adjusted for body mass, we burn 20% more energy per day than chimps and bonobos, 40% more than gorillas, and 60% more than orangutans, Pontzer and colleagues reported in *Nature* in 2016 (see graphic, left).

Pontzer says the difference in body fat is just as shocking: Male humans pack on twice as much fat as other male apes and women three times as much as other female apes. He thinks our hefty body fat evolved in tandem with our faster metabolic rate: Fat burns less energy than lean tissue and provides a fuel reserve. "Our metabolic engines were not crafted by millions of years of evolution to guarantee a beach-ready bikini body," Pontzer writes in *Burn*.

Our ability to convert food and fat stores into energy faster than other apes has important payoffs, however: It gives us more energy every day so we can fuel our big brains as well as feed and protect offspring with long, energetically costly childhoods.

Pontzer thinks characteristically human traits in behavior and anatomy help us maintain amped-up metabolisms. For example, humans routinely share more food with other adults than do other apes. Sharing food is more efficient for the group, and would have given early humans an energy safety net. And our big brains created a positive feedback loop. They demanded more energy but also gave early humans the smarts to invent better tools, control fire, cook, and adapt in other ways to get or save more energy.

PONTZER GOT A LESSON in the value of food sharing in 2010, when he traveled to Tanzania to study the energy budgets of the Hadza hunter-gatherers. One of the first things he noticed was how often the Hadza used the word "za," which means "to give." It's the magic word all Hadza learn as children to get someone to share berries, honey, or other foods with them. Such sharing helps all the Hadza be active: As they hunt and forage, Hadza women walk about 8 kilometers daily; men, 14 kilometers—more than a typical American walks in 1 week.

To learn about their energy expenditure, Pontzer asked the Hadza whether they'd drink his tasteless water cocktail and give urine samples. They agreed. He almost couldn't get funding for the study, because other researchers assumed the answer was

The high-energy ape

Humans burn far more energy daily—and also store much more energy as fat—than other apes. Our total energy expenditure (TEE) includes our basal metabolic rate (BMR) plus other activities including exercise.

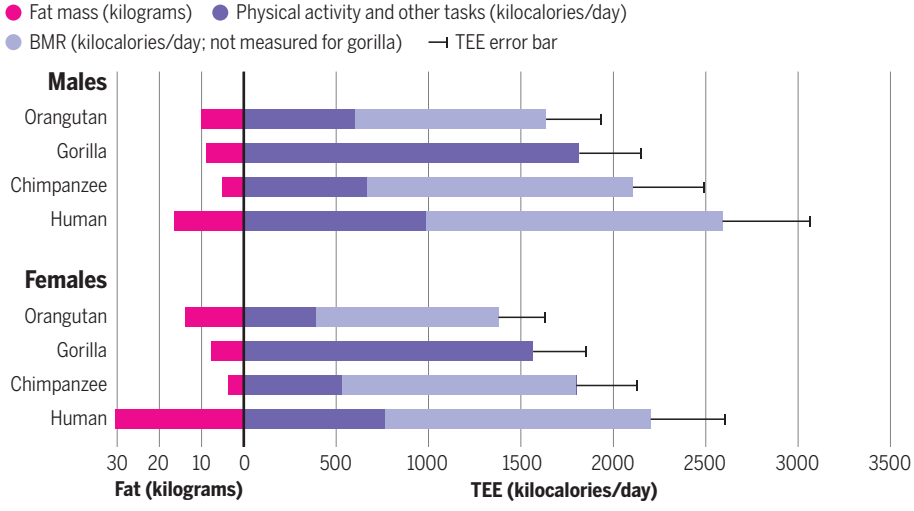

CREDITS: (GRAPHIC) N. DESAI/*SCIENCE*; (DATA) H. PONTZER *ET AL.*, *NATURE*, 533, 390 (2016)

obvious. "Everyone knew the Hadza had exceptionally high energy expenditures because they were so physically active," he recalls. "Except they didn't."

Individual Hadza had days of more and less activity, and some burned 10% more or less calories than average. But when adjusted for nonfat body mass, Hadza men and women burned the same amount of energy per day on average as men and women in the United States, as well as those in Europe, Russia, and Japan, he reported in *PLOS ONE* in 2012. "It's surprising when you consider the differences in physical activity," Schoeller says.

One person who wasn't surprised was epidemiologist Amy Luke at Loyola University Chicago. She'd already gotten a similar result with doubly labeled water studies, showing female farmers in western Africa used the same amount of energy daily when adjusted for fat-free body mass as women in Chicago—about 2400 kilocalories for a 75-kilogram woman. Luke says her work was not well known—until Pontzer's paper made a splash. The two have collaborated ever since.

Pontzer is "very good at selling big ideas," whether on social media or writing for general audiences, says his former postdoc, Sam Urlacher of Baylor University. "That ruffles some feathers, but he's not afraid of being proven wrong."

Studies of other hunter-gatherer and forager groups have confirmed the Hadza are not an anomaly. Pontzer thinks hunter-gatherers' bodies adjust for more activity by spending fewer calories on other unseen tasks, such as inflammation and stress responses. "Instead of increasing the calories burned per day, the Hadza's physical activity was changing the way they spend their calories," he says.

He backed this up with a new analysis of data from another team's study of sedentary women trained to run half marathons: After weeks of training, they barely burned more energy per day when they were running 40 kilometers per week than before they started to train. In another study of marathoners who ran 42.6 kilometers daily 6 days per week for 140 days in the Race Across the USA, Pontzer and his colleagues found the runners burned gradually less energy over time—4900 calories per day at the end of the race compared with 6200 calories at the start.

As the athletes' ran more and more over weeks or months, their metabolic engines cut back elsewhere to make room for the extra exercise costs, Pontzer says. Conversely, if you're a couch potato, you might still spend almost as many calories daily, leaving more energy for your body to spend on internal processes such as a stress response.

This is Pontzer's "most controversial and interesting idea," says Harvard paleoanthropologist Daniel Lieberman, who was Pontzer's thesis adviser. "This morning I ran about 5 miles; I spent about 500 calories running. In a very simplistic model that would mean my TEE would be 500 calories higher. … According to Herman, humans who are more active don't have that much higher TEE as you'd predict … but we still don't know why or how that occurs."

Pontzer's findings have a discouraging implication for people wanting to lose weight. "You can't exercise your way out of obesity," says evolutionary physiologist John Speakman of the Chinese Academy of Sciences. "It's one of those zombie ideas that refuses to die." Already the research is influencing dietary guidelines for nutrition and weight loss. The U.K. National Food Strategy, for example, notes that "you can't outrun a bad diet."

> **"Our metabolic engines were not crafted by millions of years of evolution to guarantee a beach-ready bikini body."**
>
> **Herman Pontzer**, Duke University

But Thyfault warns that message may do more harm than good. People who exercise are less likely to gain weight in the first place, and those who exercise while they diet tend to keep weight off better, he says. Exercise also can impact where fat is stored on the body and the risk of diabetes and heart disease, he says.

Pontzer agrees that exercise is essential for good health: The Hadza, who are active and fit into their 70s and 80s, don't get diabetes and heart disease. And, he adds, "If exercise is tamping down the stress response, that compensation is a good thing." But he says it's not fair to mislead dieters: "Exercise prevents you from getting sick, but diet is your best tool for weight management."

Meanwhile, Pontzer was laying the groundwork for other surprises. Last year, he and Speakman co-led an effort to assemble a remarkable new resource, the International Atomic Energy Agency Doubly Labelled Water Database. This includes existing doubly labeled water studies of almost 6800 people between the ages of 8 days and 95 years.

They used the database to do the first comprehensive study of human energy use over the life span. Again a popular assumption was at stake: that teenagers and pregnant women have higher metabolisms. But Pontzer found it was toddlers who are the dynamos. Newborns have the same metabolic rate as their pregnant mothers, which is no different from other women when adjusted for body size. But between the ages of 9 and 15 months, babies expend 50% more energy in a day than do adults, when adjusted for body size and fat (see graphic, p. 711). That's likely to fuel their growing brain and, perhaps, developing immune systems. The findings, reported in *Science*, help explain why malnourished infants may show stunted growth.

Children's metabolisms stay high, when adjusted for body size, until about age 5, when they begin a slow decline until age 20, and stabilize in adulthood. Humans begin to use less energy at age 60, and by age 90, elders use 26% less than middle-aged adults.

Pontzer is now probing a mystery that emerged from his studies of athletes: There seems to be a hard limit on how many calories our bodies can burn per day, set by how fast we can digest food and turn it into energy. He calculates that the ceiling for an 85-kilogram man would be about 4650 calories per day.

Speakman thinks that limit is too low, noting that cyclists in the Tour de France in the 1980s and '90s exceeded it. But they were injecting fat and glucose directly into their bloodstreams, a practice Pontzer thinks might have helped them bypass the physiological limits on converting food into energy. Elite athletes can push the limits for several months, as the study of marathoners showed, but can't sustain it indefinitely, Pontzer says.

To understand how the body can fuel intense exercise or fight off disease without busting energy limits, Pontzer and his students are exploring how the body tamps down other activities. "I think we're going to find these adjustments lower inflammation, lower our stress reaction. We do it to make the energy books balance."

That's why he wanted to know how much energy Christina burned while he grilled her in the lab. After the test, Christina said she "definitely was stressed." As it went on her heart rate rose from 75 to 80 beats per minute to 115. And her energy use rose from 1.2 kilocalories per minute to as much as 1.7 kilocalories per minute.

"She burned 40% more energy per minute in the math test and 30% in the interview," Pontzer says. "Think about any other process that boosts your energy by about 40%."

He hopes data points like hers will help reveal the hidden cost of mental stress. Measuring how stress and immune reactions amp up energy use could help reveal how these invisible activities add up and are traded off in our daily energy budgets. Pontzer knows he's got his work cut out for him. "Until we can show how the levers get pulled to make these adjustments in energy use, people will always be skeptical. It's on us to do the next generation of experiments." ■

INSIGHTS

PERSPECTIVES

ENERGY

Optimizing Amazonian dams for nature

Algorithms assess opportunities, forgone benefits, and environmental trade-offs

By **Gordon W. Holtgrieve**[1] *and* **Mauricio E. Arias**[2]

Large river systems, particularly those shared by developing nations in the tropics, exemplify the interconnected and thorny challenges of achieving sustainability with respect to food, energy, and water (*1*). Numerous countries in South America, Africa, and Asia have committed to hydropower as a means to supply affordable energy with net-zero emissions by 2050 (*2*). The placement, size, and number of dams within each river basin network have enormous consequences for not only the ability to produce electricity (*3*) but also how they affect people whose livelihoods depend on the local river systems (*4*). On page 753 of this issue, Flecker *et al.* (*5*) present a way to assess a rich set of environmental parameters for an optimization analysis to efficiently sort through an enormous number of possible combinations for dam placements and help find the combination(s) that can achieve energy production targets while minimizing environmental costs in the Amazon basin.

To sustainably develop river systems that maximally and equitably benefit society, decision-making must start with considering the optimal number and geographic configuration of dams. Currently, there are approximately 38,000 dams taller than 15 m

PHOTO: FEDERICO RIOS ESCOBAR/THE NEW YORK TIMES/REDUX

The geographic configuration of dams—such as the Coca Codo Sinclair Dam in Ecuador—throughout a river network determines the overall environmental impact for a given amount of energy produced.

worldwide (*6*) and around 3500 dams greater than 50 MW planned or under construction (*7*). Identifying the number and placement of dams to achieve energy targets, while minimizing negative impacts, is challenging because of the volume of information necessary to spatially represent impacts and the sheer number of ways in which the network of potential dams could be spatially configured.

Flecker *et al*. have provided new tools to assist with this challenge, and the lessons learned are a powerful demonstration of lost opportunities with previous poor dam placement, the importance of transboundary cooperation, and inevitable trade-offs among competing objectives. The relatively small number of dams currently in the Amazon have already set an environmentally inefficient trajectory, especially in terms of threatened fish diversity, and maximum energy benefits with minimal environmental costs can only be realized if countries are willing to cooperate in sharing both those benefits and the costs. Equally if not more challenging, Flecker *et al*. artfully demonstrate that stark trade-offs exist among their five environmental metrics of river flow, river connectivity, sediment transport, fish diversity, and greenhouse gas emissions, and that no dam configuration is optimal for all five aspects. Although the most favorable solutions from the analysis represent minimum environmental costs for a given energy target, it is clear that those costs will not be minimal. Nonetheless, this research suggests that there are still ample opportunities to improve the future path of hydropower development in the Amazon Basin to minimize the environmental impacts, particularly for river flow regulation, sediment trapping, and greenhouse gas emissions.

Power production and environmental impacts are two of many complex factors that inform decisions around dams. Sustainability science is fundamentally transdisciplinary (*8, 9*). If assessments like that of Flecker *et al*. are to be most useful, they must also include more direct socioeconomic metrics of dam construction impacts, ranging from distribution of economic benefits to human food security and population displacement and resettlement. Furthermore, although the broad concept of ecosystem services—economic, cultural, spiritual, and health benefits derived from well-functioning ecosystems (*10*)—is scientifically mainstream and widely understood, it is not clear how specific metrics like fish diversity, riverine connectivity, and flow regulation considered in this study relate to human well-being. These connections need to be better integrated into the regulatory, permitting, and development sectors, which have a more direct influence on where and how many hydropower projects are built.

These points are not lost on the diverse research team of the Flecker *et al*. study, whose members come from a wide array of academic and nongovernmental institutions in the US, Europe, and South America. Included with their research products is a graphical interface of the results aimed directly at transmitting the new knowledge from this highly sophisticated study to the relevant sectors at the appropriate level. These efforts are rarely, if ever, rewarded academically or with funding but are nonetheless essential to bring such research into practice.

The indeterminate nature of scientific research is not an excuse for ignoring what is currently known. Although dam placement on the basis of an existing set of criteria may be inefficient for another yet unquantified criterion, Flecker *et al*. highlight that using tools such as this to quickly and objectively screen the most environmentally harmful dam configurations narrows the potential number of options when considering other, less well quantified criteria. Science alone cannot provide an answer to whether expanding hydropower is the best way to sustainably support the sharply increasing global energy demand. It can, however, provide tools like the one presented by Flecker *et al*. that make the best of the information and technology available to identify trade-offs, highlight options, and facilitate policy discussions that are critically needed not only in the Amazon but also in river basins around the world facing similar sustainable development dilemmas. ■

REFERENCES AND NOTES

1. N. L. Poff, J. D. Olden, *Science* **358**, 1252 (2017).
2. C. Zarfl *et al*., *Sci. Rep*. **9**, 18531 (2019).
3. G. F. White, *Law Contemp. Probl*. **22**, 157 (1957).
4. K. O. Winemiller *et al*., *Science* **351**, 128 (2016).
5. A. S. Flecker *et al*., *Science* **375**, 753 (2022).
6. M. Mulligan, A. van Soesbergen, L. Sáenz, *Sci. Data* **7**, 31 (2020).
7. C. Zarfl, A. E. Lumsdon, J. Berlekamp, L. Tydecks, K. Tockner, *Aquat. Sci*. **77**, 161 (2015).
8. X. N. Fang, B. B. Zhou, X. Y. Tu, Q. Ma, J. G. Wu, *Sustainability* **10**, 16 (2018).
9. R. W. Kates, *Proc. Natl. Acad. Sci. U.S.A*. **108**, 19449 (2011).
10. Millennium Ecosystem Assessment, *Ecosystems and Human Well-being: Synthesis* (Island Press, 2005).

ACKNOWLEDGMENTS

G.W.H. is supported by US National Science Foundation EAR 1740042.

10.1126/science.abn8311

[1]School of Aquatic and Fishery Sciences, University of Washington, Seattle, WA, USA. [2]Department of Civil and Environmental Engineering, University of South Florida, Tampa, FL, USA. Email: gholt@uw.edu

BIOMEDICINE

Repairing the blood-brain barrier

Engineered Wnt ligands specifically target blood-brain barrier function

By **Andrew P. McMahon** *and* **Justin K. Ichida**

Specialized vasculature within the brain forms a blood-brain barrier (BBB) that excludes cellular and soluble plasma contents from the inner workings of the central nervous system (CNS) (*1*). Stroke, neurodegenerative disease, and brain tumors result in a loss of BBB properties, which contributes to pathology, arguing for therapeutic approaches to restore BBB functions. Conversely, the BBB poses a problem for drug accessibility. Modulating barrier function can enhance and broaden the effectiveness of therapeutic agents on the CNS (*2*). Development and maintenance of the BBB is regulated by two Wnt ligands, Wnt7a and Wnt7b (*3*). On page 737 of this issue, Martin *et al*. (*4*) describe an elegant molecular dissection of Wnt7 signaling, demonstrating that a single amino acid change in Wnt7a markedly increases its specificity for vascular endothelial cells, resulting in improved outcomes in zebrafish and mouse models of disrupted BBB in tumor growth and stroke.

Cell-cell interactions mediated by Wnt signals regulate an enormous diversity of cellular processes. Similarly, disrupted Wnt signaling has been ascribed to a broad spectrum of disease (*5*). For example, vascular breakdown in ischemic stroke compromises the BBB, disrupting tight junctions between endothelial cells and leading to damage of the underlying nervous systems by infiltrating immune cells and serum factors (*6*). In glioblastoma, tumor growth disrupts the BBB, creating a hypoxic, acidic microenvironment that fuels tumor growth. Vascular normalization improves survival of glioblastoma patients (*7*).

In CNS development, neural progenitor–derived Wnt7 ligands (Wnt7a and Wnt7b),

Department of Stem Cell Biology and Regenerative Medicine, Keck School of Medicine of the University of Southern California, CA, USA. Email: amcmahon@med.usc.edu

Engineering Wnt7a for blood-brain barrier–specific activity

A K190A (Lys[190]→Ala) point mutation in Wnt7a restricts Wnt7a signaling to cells with the co-receptor complex GPR124 (G protein–coupled receptor 124) and RECK (reversion-inducing cysteine-rich protein with Kazal motifs), activating Wnt signaling specifically in endothelial cells of the central nervous system (CNS). When introduced into mouse brains, Wnt7a-K190A regulates blood-brain barrier (BBB) functions and limits the pathogenesis of brain tumors and stroke.

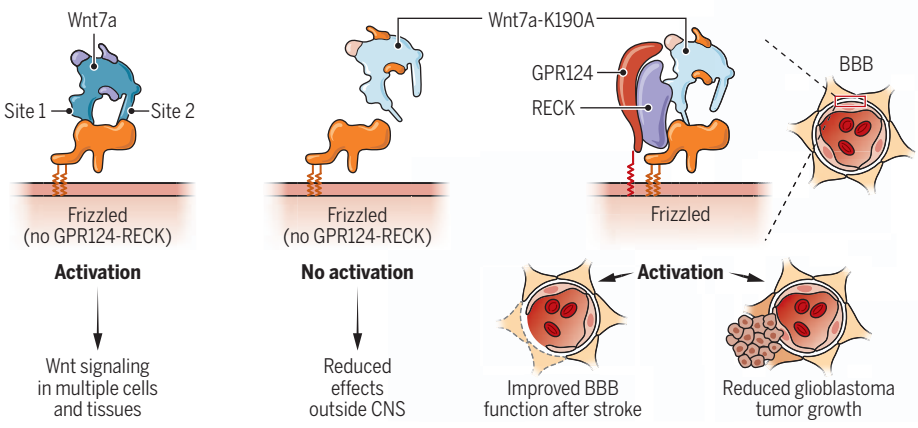

regulate vascular invasion and initiate BBB formation (*2*). In the adult brain, astrocyte, neuron, and oligodendrocyte progenitor cell–derived Wnt7 signaling maintains the BBB through canonical, Frizzled (Fz) receptor– and β-catenin–dependent, signaling (*8*). In addition, vascular endothelial signaling uses a distinct Wnt7 co-receptor complex comprising G protein–coupled receptor 124 (GPR124) and the glycosylphosphatidylinositol (GPI)–anchored surface protein RECK (reversion-inducing cysteine-rich protein with Kazal motifs) (*9*–*10*). Localized RECK-GPR124-Wnt7 complex activity in brain endothelial cells stimulates Wnt7 signaling through Fz receptors.

Crystallographic and biochemical evidence has identified two regions in Wnt ligands, one toward the amino terminus (site 1), the other toward the carboxyl terminus and associated also with selective Fz interactions (site 2) (see the figure) (*11*). A distinct linker domain on Wnt7 ligands is thought to mediate Wnt7 association with the RECK-GPR124 complex, binding to RECK (*12*). Martin *et al.* showed that amino-terminal Wnt7a, with the linker domain, was sufficient to activate Fz signaling but only when RECK-GPR124 were present, suggesting a strategy for restricted Wnt pathway activation.

Screening identified 25-point mutations in Wnt7a that confer similar RECK-GPR124 selectivity. One of these, K190A (Lys[190]→Ala) was singled out for further study. Wnt7a-K190A is a sensitive agonist of RECK-GPR124-Fz5/8 signaling with limited off-target activity when only the Fz receptors are present. This selective outcome is critical for therapeutic utility, given the potential for wide-ranging pathology from activation of broadly distributed Fz receptors. Although the molecular explanation for selectivity is unclear, the authors suggest that decreased stability of the mutant form may affect interactions with Fz receptor complexes.

To address the in vivo actions of Wnt7a-K190A, the authors used gene editing in zebrafish to demonstrate that Wnt7aa activity is required for early vascular ingrowth and activation of the glucose transporter, Glut1, indicating initiation of BBB formation. Introduction of Wnt7a-K190A rescued Wnt7aa mutant phenotypes in a transgenic model. Comparison of the sites of Wnt7a-K190A production in relation to the observed rescue suggests long-range activity, which is potentially at odds with the reduced stability and short-range signaling interpretation from in vitro cell culture studies. Further analysis in a zebrafish stroke model showed reduced bleeding and leakage in wild-type zebrafish ectopically expressing Wnt7a-K190A, which is consistent with improved BBB activity.

"Restoration of Wnt-signaling and [blood-brain barrier] properties reduced tumor size..."

Moving to mouse models of BBB breakdown—brain tumors and stroke—the authors delivered Wnt7a-K190A through adeno-associated virus (AAV) injection into the circulation, demonstrating broad infectivity of endothelial and nonendothelial associated cell types in the brain. Wnt7a-K190A showed no off-target (nonvascular endothelial) activation of Wnt signaling in the brain. Implantation of glioblastoma tumor cells resulted in a breakdown of BBB properties and vascular leakage. The accompanying reduction in Wnt7-target gene expression in vascular endothelium was ameliorated by infection with AAV encoding Wnt7a-K190A. Restoration of Wnt-signaling and BBB properties reduced tumor size, whereas inhibiting canonical Wnt signaling, with the secreted Wnt-inhibitor Dickkopf-1 (DKK1), enhanced tumor growth. Wnt7a-K190A also showed beneficial effects in a cerebral artery occlusion model of stroke. The infarct volume was reduced, and post-stroke reperfusion injury, which is linked to vascular leakage, was limited, pointing to improved BBB function, which is consistent with studies transiently stabilizing β-catenin (*9*).

Whether these beneficial effects reflect a direct action of Wnt7a-K190A on the BBB was not addressed. The mechanism is important given previous reports suggesting that Wnt responses in the BBB were not altered by stroke (*13*). It will be interesting to determine whether modified Wnt ligands could be effective for other indications in which BBB dysfunction has a causal or early role in pathogenesis. For example, biomarkers of BBB breakdown showed better correlation with the emergence of cognitive impairment in Alzheimer's disease patients than did amyloid-β or tau pathology (*14*). Overall, Martin *et al.* make a strong case for modified Wnt ligands as potential pharmacological agents that could stimulate specific Wnt receptor–mediated cellular outcomes in selected cell types. ■

REFERENCES AND NOTES

1. M. D. Sweeney, Z. Zhao, A. Montagne, A. R. Nelson, B. V. Zlokovic, *Physiol. Rev.* **99**, 21 (2019).
2. R. Whelan, G. C. Hargaden, A. J. S. Knox, *Pharmaceutics* **13**, 1980 (2021).
3. J. M. Stenman *et al.*, *Science* **322**, 1247 (2008).
4. M. Martin *et al.*, *Science* **375**, eabm4459 (2022).
5. R. Nusse, H. Clevers, *Cell* **169**, 985 (2017).
6. Z. Nadareishvili, A. N. Simpkins, E. Hitomi, D. Reyes, R. Leigh, *Cerebrovasc. Dis.* **47**, 135 (2019).
7. C. D. Arvantis *et al.*, *Nat. Rev. Cancer* **20**, 26 (2020).
8. S. Liebner *et al.*, *J. Cell Biol.* **183**, 409 (2008).
9. B. Vanhollebeke *et al.*, *eLife* **4**, e06489 (2015).
10. C. Cho, P. M. Smallwood, J. Nathans, *Neuron* **95**, 1056 (2017).
11. C. Y. Janda, D. Waghray, A. M. Levin, C. Thomas, K. C. Garcia, *Science* **337**, 59 (2012).
12. M. Eubelen *et al.*, *Science* **361**, eaat1178 (2018).
13. R. N. Munji *et al.*, *Nat. Neurosci.* **22**, 1892 (2019).
14. D. A. Nation *et al.*, *Nat. Med.* **25**, 270 (2019).

ACKNOWLEDGMENTS

A.P.M. is supported by grants from the National Institute of Diabetes and Digestive and Kidney Diseases (UC2DK126024, DK054364, DK121409, and DK126925). A.P.M. declares no conflicts of interest. J.K.I. is a cofounder of AcuraStem and Modulo Bio and serves on the scientific advisory board of Spinogenix.

10.1126/science.abn7921

GRAPHIC: KELLIE HOLOSKI/*SCIENCE*

Global growth of earthquake early warning

Public-private partnerships provide a method for vastly expanding sensor networks

By **Richard M. Allen**[1,2] *and* **Marc Stogaitis**[2]

Observations of physical Earth processes used to be the exclusive domain of governmental agencies. In the United States, NASA satellites observe surface changes, National Oceanic and Atmospheric Administration buoys monitor the ocean and the atmosphere, and US Geological Survey (USGS) seismometers detect earthquakes, allowing scientists to tackle questions that were unimaginable before these observational networks were built. Today, much larger observational networks exist in the private sector that could also be harnessed to study Earth processes and reduce the impact of natural hazards. The development of public-private partnerships is therefore increasingly key for Earth scientists to use the complete observational dataset needed to answer fundamental scientific questions and solve societal challenges.

The recent rapid growth of earthquake early warning (EEW) globally (see the first figure) is one example of such a public-private partnership and how a massive observational network in the private sector can be applied to accelerate the implementation of a life-saving technology.

EEW uses seismic sensors close to an earthquake epicenter to rapidly detect an earthquake and then deliver an alert to those in harm's way ahead of the shaking. Warnings are typically a few seconds, but can be up to a minute for larger earthquakes, and are used by individuals and institutions to reduce the shaking hazard (*1*). The idea behind EEW dates back to the 1906 San Francisco earthquake, with the first implementation in Japan in the 1960s. The first public alerting system did not arrive until 1991, when an array of seismometers along the subduction zone coast of Mexico was used to start providing alerts to Mexico City.

This slow development was due to the substantial scientific and technical challenges to operating an EEW system. An array of seismic sensors has to be operating in the earthquake source region continuously. Algorithms to characterize the earthquake source must process large volumes of data in real-time to determine when and where an alert should be issued. Then, the alert must be delivered to the affected area. This process must all happen within a few seconds if the alerts are to be useful. These challenges slowed the implementation of EEW globally.

After the implementation in Mexico City, it took 16 years before the next public system was implemented in Japan in 2007. Another decade passed until the Taiwan and South Korea systems were implemented, bringing the total population with access to alerts to just over 210 million by 2018. Next came the 2019 public launch of ShakeAlert, providing EEW to the 40 million occupants of California. The state also adopted the MyShake smartphone app that both delivers alerts and records earthquake shaking (*2*). ShakeAlert extended into Oregon and Washington in early 2021, bringing the total global population with access to EEW to 260 million people (see the second figure). All of these systems use traditional seismic networks that are mostly operated by governmental and academic institutions with fixed and dedicated sensors. The accelerating expansion of these systems continues, with testing underway for a public system across much of China and Israel. The alerting algorithms used are often the product of international seismological collaboration [for example, (*3*–*6*)].

In 2020, Google launched the Android Earthquake Alerts system. Initially, in a public-private partnership with the USGS, it delivered ShakeAlert messages to all Android phones in California. Then in 2021, it started delivering alerts to New Zealand and Greece. Later in the year, Turkey, the Philippines and central Asia were added. Building on the MyShake model (*7*, *8*), alerts in these countries are made possible by using the accelerometers in private Android phones to detect the earthquakes and to deliver alerts. The addition of the Android system has added another 150 million early-warning users in the first year of operation. More than 400

Global distribution of earthquake shaking and early warning systems

Earthquake early warning (EEW) systems are important for regions likely to have damaging earthquakes. Each circle shows the approximate shaking regions for magnitude 6.5 and larger earthquakes. The pink regions are where shaking is felt, and the red regions are where shaking causes damage. The current geographic distribution of EEW are highlighted in blue and green, with green areas entirely depending on Android Earthquake Alerts. Japan, Mexico, South Korea, and Taiwan have systems that use permanent seismic networks. The western US states have ShakeAlert, which initially sent alerts using wireless emergency alerts, MyShake, and other apps, but they now also have alerts delivered through Android Earthquake Alerts.

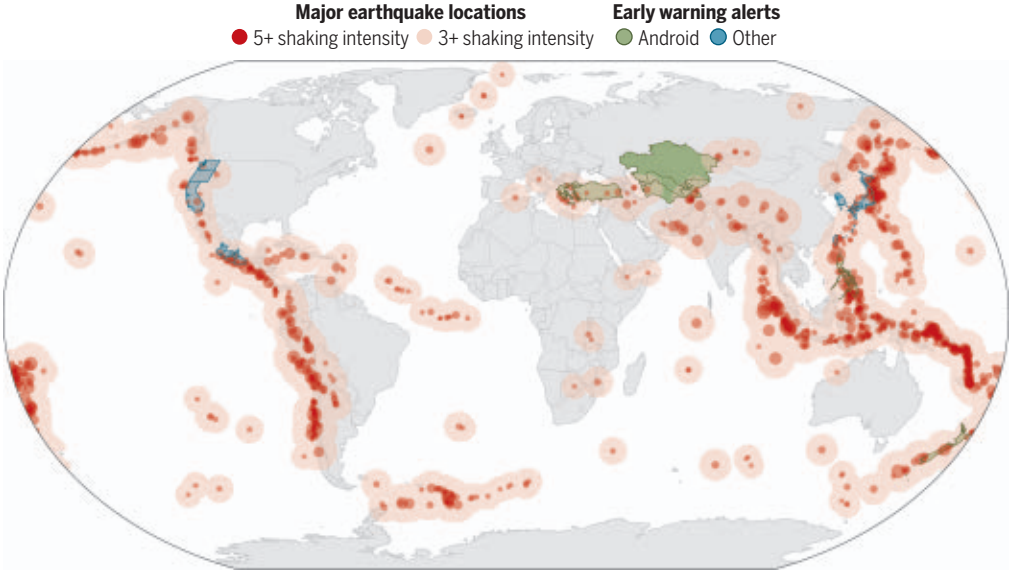

GRAPHIC: K. FRANKLIN/*SCIENCE*

million people have access to EEW today. Google has also stated its goal to make the Android Earthquake Alerts system available globally (*9*), which is possible because there are now, for the most part, phones wherever there are people.

The rapid expansion of an early-warning service could potentially save lives. But ongoing human and technical challenges remain: The public must be engaged in effective use of the alerts. Typically, the first time a user becomes aware of the system is when they get their first alert. In that moment, users are overwhelmingly enthusiastic about this technology as they feel the shaking a few seconds later. The challenge is in translating that enthusiasm into appropriate protective actions (*10*). This not only includes individual actions for personal safety but also integration of the alert technology into the infrastructure of our lives. Trains already slow and stop, and self-driving cars could be programmed to do so as well. Our increasingly automated homes and offices could also react to reduce risk.

On the technical side, the challenge remains to ensure the best performance of the warnings, getting the fastest possible alerts to the most accurate estimate of the shaking region. The metamorphosis of research-oriented seismic networks into public-safety infrastructure has expanded the available datasets. On the US West Coast, the number of observatory-quality seismic stations will have almost tripled thanks to the implementation of ShakeAlert. Similar seismic networks are being installed in other earthquake-prone countries, such as China and Israel. The release of MyShake demonstrated the use of personal smartphone accelerometers to record earthquake shaking, increasing the number of sensors from thousands to more than a million (although not all sensors are recording all the time). With the integration of this capability into Android, more than a billion sensors are now in use. This proliferation of sensors is providing a more detailed picture of earthquake shaking and the factors that affect amplifications and variability in motions.

The progress we outlined, and the ability to meet the challenges ahead, are dependent on interdisciplinary, interinstitutional, and intersector partnerships. EEW came out of a research project that worked with public safety and emergency response agencies to deliver alerts. Seismologists partnered with social scientists to identify the intersection of what is physically possible with humanly useful. Emergency management agencies are currently funding dual-use scientific-grade sensor networks that provide the data for alerts and for research into earthquakes and other physical Earth processes that will inevitably lead to new strategies for hazard reduction.

Including the private sector into these partnerships—to leverage the massive sensor networks they operate for a variety of purposes—is leading to a paradigm shift. In the case of EEW, it is the adaptation of personal smartphone sensors and the scalability that comes from integration with Android that is enabling alerts globally. Other disciplines may also benefit from similar sorts of partnerships. Smartphone sensors include pressure, magnetic field, and infrasound. Pressure data can be used to improve weather forecasts (*11*). The magnetometer could be used to detect severe geomagnetic storms (*12*), and infrasound could be used to detect natural and human-made hazards, including eruptions, landslides, and explosions.

Beyond smartphones, Raspberry Shake, Weather Underground, and Purple Air crowdsource privately owned sensor networks of accelerometers, infrasound, pressure, temperature, and air particulate content to provide ground motion, weather, and air quality data. The National Lightning Detection Network operates in the private sector but provides data for atmospheric research and wildfire response. Multiple private constellations of satellites now collect radar images of the Earth's surface, repeating observations every few days. The resulting InSAR images reveal millimeter-scale deformation of Earth's surface that could be used to study surface deformation such as landslides and subsurface fluid flow of water and magma. Transoceanic communications cables can be used to detect earthquakes (*13*), as can dark fiber beneath our cities (*14*).

Various questions arise about the longevity of these networks and their products and about the motivations of the for-profit companies that operate them. Even in the case of entirely public networks, their longevity and continued funding require demonstrating value, whether that is in terms of risk mitigation or in the development of private-sector products such as weather information networks. In the private sector, some amount of value must be delivered back to the owners in exchange for the data collected. Respecting user privacy is paramount. Data can be anonymized in various ways, including through the use of differential privacy, aggregated sensor data, and with licensing agreements. But with the right partnership, these networks can provide by orders of magnitude more observations than were available a few years ago, and they can be leveraged for research and societal good. Such public-private partnerships not only provide the data to understand physical Earth processes, they also provide networks that could speed the development and delivery of solutions. ■

Global growth of EEW

Mexico implemented an EEW system in 1991. Japan followed with their own more than a decade later, with Taiwan, South Korea, and finally the United States adding warning capabilities. However, adding Earthquake Alerts to Android phones almost doubled the number of people with access to early warning in a very short time frame.

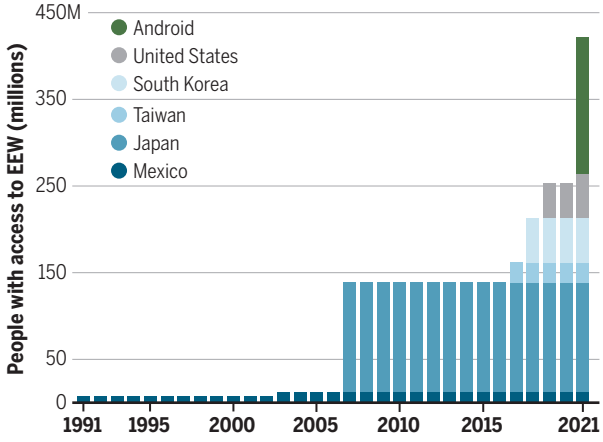

GRAPHIC: K. FRANKLIN/*SCIENCE*

[1]Seismological Laboratory, University of California, Berkeley; Berkeley, CA, USA. [2]Google LLC; Mountain View, CA, USA. Email: rallen@berkeley.edu

REFERENCES AND NOTES

1. R. M. Allen, D. Melgar, *Annu. Rev. Earth Planet. Sci.* **47**, 361 (2019).
2. J. A. Strauss *et al.*, *Front. Commun.* (Lausanne) **5**, 32 (2020).
3. H. Peng *et al.*, *Seismol. Res. Lett.* **82**, 394 (2011).
4. R. N. Nof, R. M. Allen, *Bull. Seismol. Soc. Am.* **106**, 2332 (2016).
5. D. Sheen *et al.*, *Seismol. Res. Lett.* **88**, 1491 (2017).
6. D. Kilb *et al.*, *J. Geophys. Res. Solid Earth* **126**, e2020JB021053 (2021).
7. Q. Kong, R. M. Allen, L. Schreier, Y.-W. Kwon, *Sci. Adv.* **2**, e1501055 (2016).
8. A. Barski, M. Stogaitis, S. Malkos, R. Bosch, "Earthquake Early Warning System", Technical Disclosure Commons (30 October 2018); www.tdcommons.org/dpubs_series/1620.
9. F. Lee, "6 new features on Android this summer," Google Keyword post (15 June 2021); https://blog.google/products/android/new-features-summer-2021.
10. S. K. McBride *et al.*, *Geophysics* **87**, WA77 (2022).
11. C. McNicholas, C. Mass, *Weather Forecast.* **36**, 1867 (2021).
12. S. Odenwald, *IEEE Access* **6**, 43460 (2018).
13. Z. Zhan *et al.*, *Science* **371**, 931 (2021).
14. N. Lindsey, E. R. Martin, *Annu. Rev. Earth Planet. Sci.* **49**, 309 (2021).

ACKNOWLEDGMENTS

R.A. is an inventor on the MyShake smartphone EEW patent held by the University of California, Berkeley and licensed to Google (US10887748B2).

10.1126/science.abl5435

SUPERCONDUCTIVITY

Surprising superconductivity of graphene

An ordinary graphene bilayer exhibits extraordinary superconductivity

By **Tero T. Heikkilä**

Graphene-based materials are an interesting platform for studying exotic electronic states (*1*, *2*) such as superconductivity, where the electrical resistivity of the material becomes zero. Although superconductivity has been observed in graphene, earlier observations were of samples with unstable physical structures, hampering a consistent explanation for the phenomenon. On page 774 of this issue, Zhou *et al.* (*3*) report how a graphene bilayer becomes superconducting in the presence of suitably arranged electric and magnetic fields. Their experiments indicate a rarely found exotic state for the electrons, where superconductivity is particularly robust against large magnetic fields that usually destroy the effect. The discovery of superconductivity in as relatively simple a structure as a graphene bilayer opens an avenue for better understanding the phenomenon. Such understanding can facilitate the search for superconducting materials with more-practical operating conditions.

Graphene is a single-atom-thick layer of carbon atoms arranged in a hexagonal lattice. Ordinary bilayer graphene is composed of two layers of graphene. One layer is on top of the other so that the atoms in both layers find their minimum-energy positions (see the figure), in contrast to the unstable twisted bilayer graphene (*1*). This discovery of superconductivity in bilayer graphene is surprising because bilayer graphene has already been thoroughly studied for its potential to replace silicon in building smaller and faster electronic devices. A single layer of graphene lacks a bandgap, which is a problem for its use in digital electronics. Namely, without a gap between the valence and conduction bands for electrons, the ratio of conductivities in the on and off states is too small to be practical for logical operations. One solution to the problem is to place a bilayer graphene between two metallic electrodes, as was demonstrated in 2009 (*4*). Doing so opens a tunable bandgap in the bilayer because of the electrical potential difference between the two electrodes. The combined device—a transistor—can then be controlled by the common electrode potential. When the common potential is zero, the transistor is in the off state. Increasing or decreasing the common potential injects electrons into the conduction band or removes them from the valence band. As a result, the transistor goes to the on state.

Zhou *et al.* found that near the onset of the on state, electronic interactions deform the electronic band structure at low temperatures and break some of its symmetries. To begin, they studied how the resistance of the bilayer graphene oscillates as a function of the magnetic field in its nonsuperconducting state. Using such a measurement, the authors uncovered different types of electronic states with spontaneously broken spin or valley symmetries as signatures of a phase transition to a magnetic state. Spin is a fundamental quantum property inherent to electrons, whereas the valley describes the shape of the band structure, which in turn determines the range of energy that electrons can have when moving inside a specific material. Then, the bilayer graphene device was cooled to temperatures below 30 mK, where the material becomes superconducting for certain values of the electric and magnetic fields.

The superconducting transition is formally described as the build-up of coherent pairing between electrons. In conventional superconductors, the electron pairs contain opposite spins. This pairing is known as a spin-singlet state and is governed by a quantum-mechanical principle known as Pauli exclusion, which constrains the types of pairs that can be formed. The singlet state is vulnerable to a magnetic field in that the field provides different energies to the electrons of opposite spins and eventually destroys superconductivity. The other possibility for electron pairing is the spin-triplet state, where spins in the pair point in the same direction and are not affected by magnetic fields. Such states are interesting because they may be useful in quantum computing (*5*). Before graphene, spin triplets have been observed only in materials composed of heavy elements. Therefore, it is particularly notable that the superconducting graphene of Zhou *et al.* required applying a magnetic field. This along with the resistance remaining at zero up to very large fields indicates the possibility of a spin-triplet superconducting state. Here, the presence of the valleys in graphene may help to satisfy the Pauli exclusion principle.

The discovery made by Zhou *et al.* lines up with the other recent findings of the superconducting state in few-layer graphene systems (*1*), especially in bi- and trilayer

Recipe for superconductivity in bilayer graphene

Take two layers of graphene and place them at a staggered fashion into their most stable arrangement. Apply a perpendicular electric and an in-plane magnetic field. Measure while cold to find superconductivity.

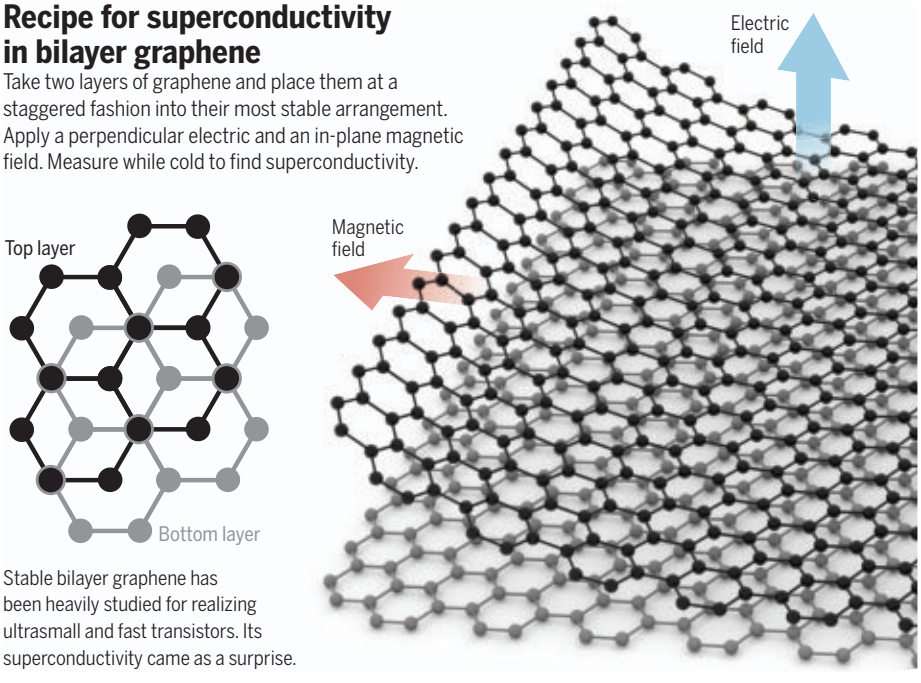

Stable bilayer graphene has been heavily studied for realizing ultrasmall and fast transistors. Its superconductivity came as a surprise.

GRAPHIC: V. ALTOUNIAN/*SCIENCE*

Nanoscience Center and Department of Physics, University of Jyväskylä, Jyväskylä, Finland. Email: tero.t.heikkila@jyu.fi

systems, where the layers are rotated as they are stacked, and with the trilayer rhombohedral graphene (*2*). Some of those showed similar robustness of superconductivity to magnetic fields (*2*, *6*). However, the bilayer graphene of Zhou *et al.* is arguably the simplest graphene system where superconductivity has been observed. Hence, it works as an ideal candidate for further experimenting with graphene superconductivity.

One remaining question is the underlying mechanism for electron pairing in graphene. A common idea is that extraordinary superconductivity requires an extraordinary pairing mechanism (*7*). However, it may be possible to explain the phenomenon with a conventional mechanism, where electron pairing is mediated by lattice vibrations (*8*–*11*). In this case, the exotic nature of the superconductivity of graphene seems to originate from its special band structure. Other open questions are related to the interplay of magnetism and superconductivity, competition of the spin-singlet and spin-triplet forms of superconductivity, and the precise nature of excitations in the triplet state. The experimental challenge comes from optimizing the conditions for superconductivity with a maximal operating temperature.

Before the gold rush of superconductivity studies on graphene, there were claims of superconductivity in graphite (*12*). Those findings reported much higher critical temperatures than those measured in few-layer graphene (*1*, *2*, *6*), but they were not widely accepted by the field because of strong sample-to-sample variations and difficulty reproducing the results. However, based on the findings of Zhou *et al.*, superconductivity of graphene-based systems seems more commonplace than what was previously thought. This may open new possibilities for graphene-based, ultrasmall electronics. Perhaps in the future, ordinary graphene will be used for extraordinary applications. ■

REFERENCES AND NOTES

1. Y. Cao *et al.*, *Nature* **556**, 43 (2018).
2. H. Zhou, T. Xie, T. Taniguchi, K. Watanabe, A. F. Young, *Nature* **598**, 434 (2021).
3. H. Zhou *et al.*, *Science* **375**, 774 (2022).
4. Y. Zhang *et al.*, *Nature* **459**, 820 (2009).
5. Y.-T. Hsu, *Nature* **595**, 495 (2021).
6. J. M. Park, Y. Cao, K. Watanabe, T. Taniguchi, P. Jarillo-Herrero, *Nature* **590**, 249 (2021).
7. A. Ghazaryan, T. Holder, M. Serbyn, E. Berg, *Phys. Rev. Lett.* **127**, 247001 (2021).
8. R. Ojajärvi, T. Hyart, M. A. Silaev, T. T. Heikkilä, *Phys. Rev. B* **98**, 054515 (2018).
9. T. J. Peltonen, R. Ojajärvi, T. T. Heikkilä, *Phys. Rev. B* **98**, 220504 (2018).
10. Y.-Z. Chou, F. Wu, J. D. Sau, S. Das Sarma, *Phys. Rev. Lett.* **127**, 187001 (2021).
11. Y.-Z. Chou, F. Wu, J. D. Sau, S. Das Sarma, https://arxiv.org/abs/2110.12303 (2021).
12. P. Esquinazi, *Pap. Phys.* **5**, 050007 (2013).

ACKNOWLEDGMENTS

I thank R. Ojajärvi, Y. Lu, and T. Hyart for illuminating discussions.

10.1126/science.abn9631

ENVIRONMENTAL HEALTH

Human health effects of chemical mixtures

Child neurodevelopment can be adversely affected by endocrine-disrupting chemicals

By **Zeyan Liew**[1,2] *and* **Pengfei Guo**[1,2]

Human populations are exposed to a large and diverse set of endocrine-disrupting chemicals (EDCs), exogenous chemicals that can interfere with hormone activity and the endocrine system (*1*). Toxicological and epidemiological studies have relied on a one-chemical-at-a-time approach to investigate possible human health effects of EDC exposure. It has been suggested that this approach provides inadequate protection against human exposure to EDCs because it fails to consider the mixture effects of exposure to multiple chemicals simultaneously. Indeed, adverse health effects from EDC exposure arise at regulation-compliant concentrations, raising the possibility that mixtures manifest additive effects at lower doses than the regulatory thresholds for single chemicals. A robust and evidence-based approach for regulating exposure to chemical mixtures has been lacking. On page 735 of this issue, Caporale *et al.* (*2*) demonstrate a mixture-centered risk assessment strategy and identify a prenatal EDC-mixture concentration that could increase risks of child language delay.

Humans are exposed to multiple classes of EDCs through their encounters with polluted air, water, food, and consumer products. Caporale *et al.* investigated simultaneous exposure to three classes of synthetic compounds widely used in commercial applications, including perfluoroalkyl substances (PFASs), phthalates, and phenols. PFASs are extremely persistent, with a biological half-life of up to 4 to 8 years in the human body (*3*). Phthalates and phenols are less persistent, but humans are repeatedly and constantly exposed to them, for example, from personal care products. Exposure to these EDCs has been linked to several major health conditions (*4*, *5*) (see the figure).

To what extent long-term developmental consequences can be caused by these widespread EDCs is not fully understood. The fetus or infant is exposed to various EDCs through placental and lactational transfer from the mother (*6*). Fetal and infant development are sensitive periods that can be adversely affected by EDCs. For example, disruption of central nervous system devel-

Early life exposure to endocrine-disrupting chemicals

Endocrine-disrupting chemicals (EDCs) are widespread and can migrate into the air, water, and food. Maternal exposure to EDCs can transfer them to the fetus through the placenta and to infants through breastfeeding, potentially leading to a range of neurodevelopmental disorders in offspring.

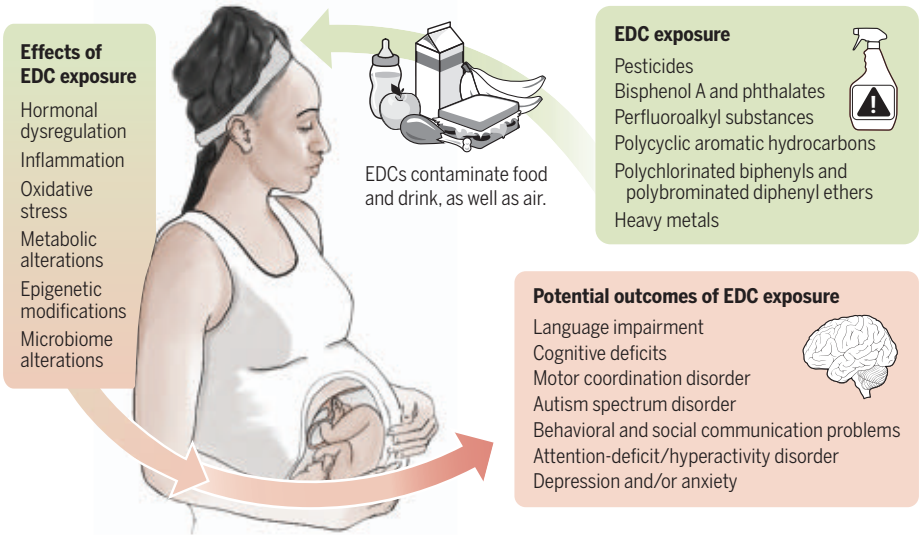

GRAPHIC: N. CARY/*SCIENCE*

opment could lead to permanent damage to neurological function (*5*). The biological mechanisms of how EDCs influence human fetal brain development are difficult to study, partly because the tools to effectively monitor brain development in utero are lacking (*7*).

Standard chemical risk assessment consists of several steps, including quantification of chemical exposure for a given population (exposure assessment), determination of safe concentrations for chemicals (hazard identification and characterization), and estimation of the health risks associated with exposures (risk characterization) (*8*). Over the past 60 years, chemical risk assessments for thousands of individual environmental substances have been performed. Regulatory agencies have now started to develop guidelines to assess chemical mixtures (*9*).

Caporale *et al.* used a population-based cohort of 1874 mother-child pairs enrolled from Sweden during 2007–2010 with measured concentrations of PFASs, phthalates, bisphenol A, and triclosan in serum or urine from mothers in the 10th week of pregnancy. They estimated an EDC mixture that was associated with subsequent delayed language development in children using biostatistical modeling. About 10% of children in the cohort had language delay, defined as the use of fewer than 50 words at the age of 30 months old. Six varying concentrations of the EDC mixture identified from this cohort analysis were tested in multiple experimental models, including human cerebral organoids, *Xenopus laevis* tadpoles, and zebrafish larvae. The authors identified gene networks altered by the EDC mixture in human cerebral organoids, and validated thyroid, estrogen, and peroxisome proliferator-activated receptor (PPAR) endocrine pathways as major convergent targets in vivo. Based on these empirical data, the authors estimated that ~54% of the children in the cohort had been prenatally exposed to EDC mixture concentrations that could induce biological effects, including language development.

The traditional risk assessment approach depends on testing single chemicals across dosage concentrations in animal models, but uncertainty remains about directly applying these toxicological outputs to guide policy. This is especially true when testing a combination of chemicals; there are multitudinous combinations (in terms of relative proportions and concentrations) between and within different classes of chemicals to consider. Caporale *et al.* showed that the existing human epidemiological cohort data can be used to guide and determine typical human-relevant mixtures and subsequently test their biologic and molecular effects in relevant in vitro and in vivo models. This integrated approach strengthens the causality of the exposure-outcome associations observed in human cohorts and improves the generalizability of experimental data.

The success of this approach, however, is highly dependent on the mixture analysis from the cohort study to be valid. Methodological challenges in environmental epidemiological research—such as errors in measuring exposures or health outcomes, uncontrolled confounding or selection bias, and incorrect statistical models—could threaten the validity of findings. Multiple experiments were conducted by Caporale *et al.*, but drawing conclusions might have become difficult if the results from each did not collaborate. The extent to which and how many such experiments are needed to generate reliable data for mixture risk assessment is unclear.

The study of Caporale *et al.* focused on three classes of EDCs, but this is not an exhaustive list of chemicals of concern. For example, it has been reported that more than 4000 PFASs have been applied in commercial products, whereas, at present, no human studies can accurately detect and quantify the concentrations for all possible PFASs (*6*). Technological advancement and cost-effective methods are needed to generate exposure profiles accurately and comprehensively. Setting up a longitudinal cohort study is costly and time consuming. A continuing investment to support ongoing cohorts (to assess cumulative exposure and long-term health impacts) as well as setting up new cohorts (to capture contemporary exposure profiles) is essential to keep up with assessing and mitigating human exposure to harmful chemical mixtures. A framework is also needed for mixture risk assessment to test new chemicals (including the replacement of recently banned chemicals) that are rapidly introduced in the global environment. ■

REFERENCES AND NOTES

1. M. A. La Merrill *et al.*, *Nat. Rev. Endocrinol.* **16**, 45 (2020).
2. N. Caporale *et al.*, *Science* **375**, eabe8244 (2022).
3. G. W. Olsen *et al.*, *Environ. Health Perspect.* **115**, 1298 (2007).
4. L. G. Kahn *et al.*, *Lancet Diabetes Endocrinol.* **8**, 703 (2020).
5. T. Colborn *et al.*, *Our Stolen Future: Are We Threatening Our Fertility, Intelligence, and Survival? A Scientific Detective Story* (Plume, 1996).
6. E. M. Sunderland *et al.*, *J. Expo. Sci. Environ. Epidemiol.* **29**, 131 (2019).
7. L. Konkel, *Environ. Health Perspect.* **126**, 112001 (2018).
8. R. Eisler, *Handbook of Chemical Risk Assessment: Health Hazards to Humans, Plants, and Animals* (CRC Press, 2000).
9. E. S. Committee *et al.*, *EFSA J.* **17**, e05634 (2019).

ACKNOWLEDGMENTS

Z.L. is supported by the National Institutes of Health–National Institute of Environmental Health Sciences Pathway to Independence Award (R00ES026729).

10.1126/science.abn9080

[1]Department of Environmental Health Sciences, Yale School of Public Health, Yale University, New Haven, CT, USA. [2]Yale Center for Perinatal, Pediatric, and Environmental Epidemiology, Yale School of Public Health, New Haven, CT, USA. Email: zeyan.liew@yale.edu

BIOPHYSICS

How does a lizard shed its tail?

Hierarchical microstructures help a lizard self-amputate its tail when needed

By **Animangsu Ghatak**

Among many escape strategies that animals have evolved to evade capture by their predators, autotomy is a prominent one, whereby an animal self-amputates a body part, such as a leg or a tail (see the photo), just to elude its attacker. The ease with which animals can shed their body parts depends on the anatomy of the joint that connects the said body part to their body (*1*). How does the animal ensure that a limb does not shed off during its regular activity yet easily and quickly detaches when it struggles to escape the grasp of a predator? On page 770 of this issue, Baban *et al.* (*2*) show that for lizards that self-amputate their tail when under threat, the hierarchical microstructure of the tail plays an important role in this balancing act.

The lizard tail consists of segments separated by distinct fracture planes that are weak zones. Experiments with three different lizard species—*Hemidactylus flaviviridis*, *Cyrtopodion scabrum*, and *Acanthodactylus schmidti*—show that these planes are not smooth but instead consist of microscopic structural features with sizes spanning from hundreds of micrometers down to tens of nanometers. On the larger side, the tail consists of a wedge-shaped tissue assembly, the proximal and distal parts of which form a "plug and socket" type of arrangement. Going down to the submillimeter scale, the tissue surface contains microscopic pillars in the shape of mushrooms. Zooming in even further, the "mushroom heads" themselves are decorated with nanoscopic pores and, in some cases, nanoscopic beads. Proteomic studies and scanning electron microscopy of the fractured planes show that the mushrooms that compose the cleaved surface of the tail do not get into mechanical interlocking or covalent

Department of Chemical Engineering, Indian Institute of Technology Kanpur, Kanpur, Uttar Pradesh, India. Email: aghatak@iitk.ac.in

Researchers have shown that caudal autotomy in lizards, such as that seen in the Japanese five-lined skink (*Eumeces japonicus*) pictured here, is mediated by the hierarchical microstructures at the fracture plane of their tails.

bonding with the main body of the animal but rather form physical bonds through adhesive forces.

Baban *et al.* show that this adhesion is strong enough that the tail does not break away during regular activities. Indeed, straight pulling of the tail does not result in any failure at all. On the contrary, when a supposed predator grabs the tail a small distance down a fracture plane, a slight act of bending of the tail initiates a crack from one side, which propagates catastrophically and leads to complete separation of the portion of the tail that is under siege. It seems that hierarchy in microstructure helps the tail by providing flexibility to the mushroom-shaped structures present on the fractured surface of the severed limb. This flexibility allows these structures to remain in intimate contact with the complementary surface of the animal's body. The mushrooms help distribute the pulling load throughout the area of contact. As a result, the magnitude of stresses at the interface hardly gets large enough to cause a separation. Structural hierarchy also generates spatial modulation in topography as well as variation in deformability, features that help to trap and deflect a crack. A trapped crack loses all its energy to propagate forward and gets reinitiated only when the interface is sufficiently stretched again at the location of the crack tip. In wet conditions, liquid nanobridges between the contacting surfaces increase adhesion further through capillary forces.

The findings of Baban *et al.* are relevant to similar hierarchical features that are present on the feet of many wall-climbing animals (*3*–*6*). Geckos, insects, and frogs have all drawn the attention of scientists for their exceptional ability to walk or dart on a variety of surfaces in their habitat, often when situated on a vertical surface or even completely upside down. The strong, yet reversible, adhesion at their feet is derived from hierarchical microstructures that divide into finer and finer hairs, which terminate as spatula- or mushroom-shaped caps (*7*). Billions of these hairs or bristles not only allow these animals to follow the contours of the nano- to microscopic roughness of the surface that they hold on to but also help in debonding and reattaching through multiple crack arrests and reinitiation at the edge of each of these caps (*8*).

Subsurface effects, like tunable pressure within sacs filled with liquid or air (*4*, *9*) and hysteretic adhesion at the internal walls of subsurface vessels, further amplify the effect of crack arrest (*10*, *11*) and the consequent dissipation of energy. In some cases, a liquid emerges from tiny holes on the bristles to form a capillary bridge with the adherent surface, resulting in both strong and switchable adhesion. (*12*, *13*). When the animal's foot is pulled off perpendicular to the surface, hundreds and thousands of minuscule attachments distribute the load and help resist separation. By contrast, during bending or peeling from one edge of the contact, the pulling stress gets sufficiently concentrated at the peeling front so that the crack can overcome the resistance to fracture, similar to the mechanism of autotomy of the lizard tail.

The findings of Baban *et al.* are quite notable in that a phenomenon such as self-amputation, which was previously believed to occur through a cohesive fracture, is shown to be the result of adhesive failure mediated by physical principles linked to the structural hierarchy of the adherent surfaces. It is worth noting that not only lizards, but also salamanders, crustaceans, spiders, mice, and worms, use autotomy as a defense strategy, and it will be interesting to determine whether these animals use adhesion as the dominant mechanism for keeping their expendable limb connected to the main torso.

Autotomy is but one strategy that organisms have evolved to escape capture by their predators. However, it starkly contrasts other survival skills that work either on the principle of camouflage or on the ploy of a preemptive strike, such as spraying hot and toxic chemicals or oozing out a bad odor (*14*). Yet a large variety of species in the animal kingdom and even some plant species use autotomy to survive. For example, plants like sourgrass resort to autotomy (*15*) for defending themselves from being completely uprooted when pulled by herbivores. A notch present at the base of the stalk of the leaves of these plants acts as a weak link that ensures that only the leaf gets torn away, thereby saving the whole plant. Thus, autotomy proves to be a successful survival tool in the natural world, and its prevalence in both plants and animals gives confidence that it may be useful for scientific and engineering applications. Particularly in robotics, stealth technology, and prosthetics and for the safe operation of many critical installations, an optimized link similar to the one present at the lizard tail can go a long way in protecting an expensive component or a device from an unforeseen accident or mishap. ■

REFERENCES AND NOTES

1. I. Fernández-Rodríguez, F. Braña, *J. Exp. Zool. A Ecol. Integr. Physiol*. 10.1002/jez.2562 (2021).
2. N. S. Baban, A. Orozaliev, S. Kirchhof, C. J. Stubbs, Y.-A. Song, *Science* **375**, 770 (2022).
3. K. Autumn *et al.*, *Proc. Natl. Acad. Sci. U.S.A.* **99**, 12252 (2002).
4. S. Gorb, Y. Jiao, M. Scherge, *J. Comp. Physiol. A* **186**, 821 (2000).
5. E. Arzt, S. Gorb, R. Spolenak, *Proc. Natl. Acad. Sci. U.S.A.* **100**, 10603 (2003).
6. M. Kappl, F. Kaveh, W. J. P. Barnes, *Bioinspir. Biomim.* **11**, 035003 (2016).
7. M. Micciché, E. Arzt, E. Kroner, *ACS Appl. Mater. Interfaces* **6**, 7076 (2014).
8. A. Ghatak, L. Mahadevan, J. Y. Chung, M. K. Chaudhury, V. Shenoy, *Proc. R. Soc. London Ser. A* **460**, 2725 (2004).
9. J. D. Gilett, V. B. Wigglesworth, *Proc. R. Soc. London Ser. B* **111**, 364 (1932).
10. E. P. Arul, A. Ghatak, *Langmuir* **25**, 611 (2009).
11. E. P. Arul, A. Ghatak, *J. Mater. Sci.* **46**, 832 (2011).
12. M. J. Vogel, P. H. Steen, *Proc. Natl. Acad. Sci. U.S.A.* **107**, 3377 (2010).
13. T. Eisner, D. J. Aneshansley, *Proc. Natl. Acad. Sci. U.S.A.* **97**, 6568 (2000).
14. T. Eisner, *For Love of Insects* (Harvard Univ. Press, 2003).
15. I. Shtein, A. Koyfman, A. Eshel, B. Bar-On, *J. R. Soc. Interface* **16**, 20180737 (2019).

10.1126/science.abn4949

PHOTO: RYU UCHIYAMA/MINDEN PICTURES

RETROSPECTIVE

Richard Leakey (1944–2022)

Renowned conservationist and advocate for African scientists

By **Paula Kahumbu**

Richard Leakey, renowned paleoanthropologist, wildlife conservationist, and pro-democracy activist, died on 2 January. He was 77. Forthright and courageous, Richard nurtured the emergence of a new generation of scientists in postcolonial Africa. He faced frequent threats to his life with a fierce determination that at times bordered on recklessness. His achievements defied his treatment as an outsider by mainstream academics.

Richard was born in Nairobi on 19 December 1944, when Kenya was still a British colony. The second son of archaeologists Louis and Mary Leakey, he left school without qualifications and found himself drawn, unwillingly at first, toward his parents' profession. In 1967, he observed fossil-rich sedimentary rocks on the shore of Lake Turkana in northern Kenya. Over the next 20 years, his expeditions to the area uncovered hundreds of human fossil remains, including several intact skulls that called into question established ideas about human evolution. This research culminated in the discovery, in 1975, of "Turkana Boy," the almost complete skeleton of an early hominid who died 1.6 million years ago.

In 1963, Richard became a citizen of newly independent Kenya. He carried out his groundbreaking paleoanthropology work not from a university but in his role as director of the National Museums of Kenya. Richard took the job in 1968 at age 23 and held the post for 20 years, during which time he transformed the organization into one of Africa's leading scientific research institutions.

Unlike many white Kenyans of his generation, Richard spoke fluent Kiswahili. He moved effortlessly between the white scientists who still dominated wildlife conservation organizations, the emerging Black ruling class, and young up-and-coming Black scientists and community leaders. Richard rarely talked publicly about race, but racism and gender inequality infuriated him. The diversity of the people closest to him was a reflection of his inclusive nature.

I first knew Richard as a knowledgeable and patient neighbor who helped me care for small animals that my siblings and I caught in the gardens. He encouraged my interest in the natural world and, when I finished high school, found me an internship at one of many research groups he had set up at the National Museums of Kenya. I was just one of many young Kenyans he mentored. Possibly mindful of his own problems in getting accepted by academia, he urged his protégés, many of whom are now prominent scientists and conservationists, to obtain a doctorate (master's degrees were "a waste of time").

In 1989, Kenya's president made Richard director of the Kenya Wildlife Service and charged him with ending the rampant ivory poaching that was decimating the country's elephant population. Richard acted decisively, dismissing corrupt officials, creating armed antipoaching units that were authorized to shoot on sight, and publicly burning Kenya's ivory stockpiles. This high-profile demonstration of African opposition to the ivory trade was a pivotal moment for global conservation; it influenced the decision by the Convention on International Trade in Endangered Species to ban all international trade in ivory and shaped discourse on elephant conservation for decades to come.

PHOTO: MARION KAPLAN/ALAMY STOCK PHOTO

Richard's uncompromising approach made him many enemies. He left the Kenya Wildlife Service in 1994, shortly after losing both legs in an airplane crash that was, he was convinced, the result of sabotage. Characteristically, he returned immediately to the fray by founding Africa's first avowedly multiracial political party—Safina, meaning "Noah's ark" in Kiswahili—to oppose the vested interests that he saw as the principal obstacle to Africa's development. Elected to parliament, he distinguished himself as an advocate for the rights of disabled people before being recalled to government service in 1998. As head of the Kenyan Civil Service, he was tasked with rooting out government corruption, which was putting support from the World Bank and other donor agencies at risk. Once again, his measures, although effective, proved politically unacceptable, and he resigned in 2002 after the Kenyan parliament voted to outlaw his anti-corruption reforms.

I worked for Richard at the National Museums of Kenya; at the Kenya Wildlife Service; and in his latest initiative, WildlifeDirect, an environmental nongovernmental organization linking donors directly to conservation projects through blog posts from the front line. This innovative use of technology reflected Richard's understanding of the power of storytelling. A master storyteller in his lectures and books, he saw the internet as an opportunity to give voice to African conservationists and to raise money to support their work. Richard tirelessly promoted WildlifeDirect's television series, *Wildlife Warriors*, which tells the stories of Africa's frontline conservation heroes. He came to believe that television was "the most powerful force for conservation in Africa."

In his final years, Richard's passion for storytelling and his enduring love for Turkana came together in an ambitious project to create a "Museum of Humankind" in Kenya's Rift Valley. Never one to do things halfway, he commissioned the architect of the World Trade Center site in New York City to design a futuristic building inspired by the shape of ancient stone axes. The museum's ambitious twin goals of presenting "more than 2 million years of human history and the origins of our universe" were inspired by Richard's belief that "by showing people the amazing journey of humanity, we can shift paradigms and change the world."

Richard's impact on me and so many others was incalculable. As a mentor, he opened doors, made introductions, and challenged my preconceptions. As a friend, he was the go-to person for advice on everything: an eye operation, relationships, university choices, or business deals. He had an extraordinary capacity to singularly focus on the issue or person at hand while juggling many ideas and projects, as well as an incredible memory and a need for intellectual discourse. So vast was his network that many in his close circle of friends had never met each other. His legacy lives on in the hundreds of people who had the privilege of calling him a mentor. ■

WildlifeDirect, Nairobi, Kenya. Email: pkahumbu@gmail.com

10.1126/science.abo2200

POLICY FORUM

GLOBAL HEALTH

Sovereignty, sanctions, and data sharing under international law

Pathogen samples and scientific data are bargaining chips in a global argument about who gets what in a pandemic

By **Michelle Rourke[1,2], Mark Eccleston-Turner[3], Stephanie Switzer[4]**

In September 2021, after inaugurating the Berlin-based World Health Organization (WHO) Hub for Pandemic and Epidemic Intelligence, German Health Minister Jens Spahn indicated that sanctions might be an appropriate tool to deal with WHO member states that do not cooperate on data sharing during disease outbreaks. Tedros Adhanom Ghebreyesus, director general of the WHO, affirmed this, stating that "exploring the [idea of] sanctions may be important" in cases where collaboration fails (*1*). Such comments indicate that the WHO Hub has been designed without much consideration of data sovereignty and "access and benefit sharing" (ABS) debates occurring across multiple United Nations (UN) bodies, including the WHO. Threats of sanctions do little to promote the ideals of equity and solidarity often touted as foundational to global health governance. They entrench the idea that pathogen samples and associated data are "bargaining chips" rather than vital inputs to public health research and pandemic response.

ACCESS AND BENEFIT SHARING

The informal sharing of scientific samples and associated data between researchers is largely over, due in part to developments in international law in the early 1990s that saw genetic resources change status from the common heritage of humankind (essentially public domain resources) to sovereign resources of the country of origin. Under the UN's 1992 Convention on Biological Diversity (CBD), states have sovereign rights over their genetic resources and can regulate access to them in accordance with their domestic laws and policies. Under the CBD and its associated Nagoya Protocol, the use of sovereign genetic resources requires the prior informed consent of the originating state. Then the provider and user must come to mutually agreed terms, which can include the sharing of benefits associated with the use of the genetic resources in research and development, but can also include conditions about sample collection, storage, and destruction, for example.

The ABS transactional mechanism was designed to generate benefits for countries providing samples so as to incentivize their conservation of biological diversity and the sustainable use of its components. At the very heart of ABS lie questions of power differentials between nations of the Global North and South, and the fair and equitable sharing of the benefits of scientific research and development. Unfortunately, despite laudable principles, ABS has in practice failed to generate the quantum of benefits required to make an impact on biodiversity conservation, as the world continues to deal with an unprecedented ecological crisis and species loss. Furthermore, every nation can implement ABS rules in their domestic laws, so the process of obtaining prior informed consent and coming to mutually agreed terms is different in every country and has resulted in onerous bureaucratic processes for scientists engaging in research on genetic resources from around the globe. Nevertheless, despite such challenges, the ABS concept now applies to other areas of international law, including global health security.

On the issue of pathogenic genetic resources, the ABS debate has largely centered around the WHO's Pandemic Influenza Preparedness (PIP) Framework (2011), a nonbinding instrument that asks WHO member states to share influenza virus samples of human pandemic potential with the WHO. The WHO can then provide those samples to pharmaceutical companies that use them to make influenza vaccines. The pharmaceutical companies are asked to share associated benefits (including vaccine doses) with the WHO for distribution to countries in need during an influenza pandemic. This is an example of the ABS transaction in action: sharing samples in exchange for vaccines, or other future benefits. Notably, the PIP Framework is not underpinned by the threat of sanctions but rather was designed to place sample sharing on an "equal footing" with the sharing of benefits such as vaccines.

The PIP Framework applies only to influenza viruses with human pandemic potential, not seasonal influenza viruses. But the PIP Framework as a piece of WHO policy is built around the Global Influenza Surveillance and Response System: infrastructure that exists to constantly monitor seasonal influenza and update the virus strains used to develop a new seasonal influenza vaccine each year. The PIP Framework's ability to generate and deliver pandemic influenza vaccine doses has not yet been tested in an actual influenza pandemic.

Furthermore, it has a substantial blind spot: genetic sequence data (GSD). The PIP Framework encourages (but does not require) the sharing of GSD on publicly accessible sequence repositories like GenBank. Increasingly, synthetic genetic resources, created using open-access GSD and sourced from commercial providers, are sufficient for some research and development that previously required physical virus samples. This approach might thus avoid the requirement to share the benefits associated with the use of physical virus samples sourced through the PIP Framework. Countries from the Global South that depend on the benefits promised through the PIP Framework for their national influenza pandemic preparedness plans are concerned that the increasing use of synthetic biology techniques will lead to the PIP Framework's obsolescence, cutting them out of any benefit sharing and minimizing the incentives to share virus samples in the first place (*2*).

Similar discussions about the ability of synthetic biology to undercut the ABS transactional mechanism are taking place under the placeholder term "Digital Sequence Information" (DSI) at the CBD, the UN's Food and Agriculture Organization (FAO), and in negotiations for the new international legally binding instrument under the UN Convention on the Law of the Seas (UNCLOS). The contention of some, particularly nations of the Global South, is that the use of DSI for research and development is equivalent to the use of physical genetic resources for the purposes of ABS. This potentially represents a major regulatory burden for

[1]Law Futures Centre, Griffith University, Brisbane, Australia. [2]CSIRO Synthetic Biology Future Science Platform, Brisbane, Australia. [3]King's College London, London, UK. [4]Strathclyde Law School, University of Strathclyde, Glasgow, Scotland. Email: m.rourke@griffith.edu.au

nations of the Global North who have grown accustomed to open-access DSI. Negotiations to resolve this issue are ongoing, focusing on the CBD as the main international ABS convention covering most genetic resources, including pathogens.

This is the international legal context that was either missed or dismissed during the announcement of the new WHO Hub. Supported in part by the German Government, the WHO Hub will collate epidemiological, social, and environmental data from both formal and informal sources, analyze that data for insights into disease detection and response strategies, and have a strong focus on global collaboration and data sharing (*3*). However, there was no discussion of benefit sharing at the WHO Hub's announcement. Although an accompanying strategy paper mentions benefit sharing, it was linked to sharing the benefits of data insights rather than more holistic notions of benefit sharing embraced by other UN institutions. Benefit sharing was instead presented in the strategy paper in the same sentence as the notion of participation, underlying the clear expectation that WHO member states would share their data "for the common good" (*4*) and seemingly, based upon the comments at the Hub's inauguration, if such lofty cosmopolitan ideals were ineffective, member states would share under threat of sanction.

SANCTIONS

This is not the first time that the WHO has floated the idea of sanctions on nation states that fail to live up to their international public health obligations, including data sharing. The closest thing to an existing international legal obligation to share pathogen sequence data is found in the WHO's 2005 International Health Regulations (IHR). Member states are required to notify the WHO of all events within a state's territory that may constitute a public health emergency of international concern, together with provision of all relevant public health information. The term "public health information" has been interpreted by some to mean pathogen sequence data, but this is not specified in the IHR, and it clearly does not include pathogen samples.

In 2011, the Review Committee on the Functioning of the IHR during the 2009 H1N1 influenza pandemic lamented the "lack of enforceable sanctions" as the "most important structural shortcoming of the IHR" (*5*). Similarly, the report of the Ebola Interim Assessment Panel requested the IHR Review Committee to "examine options for sanctions for inappropriate and unjustified actions under the Regulations" (*6*). Although the subsequent IHR Review Committee on Ebola did not ultimately recommend a sanctions regime, more recently, in the midst of the COVID-19 pandemic, the Report of the Review Committee on the Functioning of the IHR during the COVID-19 response listed "sanctions for non-compliance" as part of the "[p]ossible contents of a future global convention on pandemic preparedness and response" (*7*).

In floating the idea of sanctions at the announcement of the WHO Hub, Minister Spahn stated that the WHO should look to the World Trade Organization (WTO), a non-UN agency, as an example of how the WHO could impose state sanctions. The WTO has 164 members, and its Dispute Settlement Body can authorize trade sanctions—so-called suspension of concessions or other obligations—if a WTO member is found in breach of its multilateral trade obligations or has nullified or impaired the trading situation of another WTO member.

The problem with sanctions in the context of global public health is that the WHO is not a policing or enforcement body (*8*) and it is not, nor should it be anything like, the WTO. Indeed, using the WTO as a potential model for the imposition of sanctions within the global health arena represents a fundamental misunderstanding of how WTO sanctions work. The WTO as an institution does not itself have the authority or capacity to impose sanctions. It has "no enforcement power to speak of… [it] cannot force compliance; it cannot punish violators" (*9*). Rather, sanctions—or suspension of concessions or other obligations, to use WTO parlance—may only be instituted by an individual member of the WTO following a successful dispute before its dispute settlement system.

Although the WTO Dispute Settlement Body may grant the authorization, it is individual members that actually institute the sanctions. "Collective" sanctions are not permitted and because sanctions reduce trade and hence are economically harmful (in that they involve the erection of trade barriers to, in theory at least, "rebalance" trade relations between the disputing members), smaller countries have tended to avoid imposing them as they generally lack the economic capacity to retaliate. It is also of note that the WTO dispute settlement system is not at present functioning as intended, owing to the refusal by the United States to agree to the appointment of new members to the WTO's Appellate Body, which hears appeals from first-instance WTO dispute settlement panels.

THE PANDEMIC TREATY

It is difficult, if not impossible, to see how the imposition of sanctions could effectively work in the global health arena, particularly a system modeled on the multilateral trade regime. It would require, at the bare minimum, an adversarial system of dispute settlement to be introduced, with compliance tied to specific legal obligations that do not yet exist. Perhaps such obligatory norms might be introduced through a Pandemic Treaty, first touted by the European Union (EU) Council President Charles Michel in November 2020 at the Paris Peace Forum. The idea for a Pandemic Treaty gained further support from a range of actors, including the public endorsement by 26 world leaders and Tedros, with the current tools for pandemic preparedness noted as being insufficient to such a degree that "a treaty is the best thing that we can do that can bring the political commitment of member states" (*10*). On 1 December 2021, a special session of the World Health Assembly, the decision-making body of the WHO, adopted a consensus decision to start the negotiation process for

ILLUSTRATION: IMAGEFLOW/SHUTTERSTOCK

a "convention, agreement, or other international instrument" on pandemic prevention, preparedness, and response (*11*).

There are legitimate concerns that the proposed pandemic instrument merely represents another example of rich nations imposing their will on the poorest nations, including by disregarding their sovereign rights over pathogens and associated data. Indeed, the limited substantive content available has focused mainly on the sharing of data and samples, health system strengthening, and One Health (integration of human, animal, and environmental health), with only limited reference to concerns regarding vaccine nationalism, and equitable access to vaccines (*12*). The fact that the pandemic instrument is being proposed by the very nations that engaged so proactively in rampant vaccine nationalism during COVID-19 raises questions about the extent to which these nations are actually willing to solve problems in equitable access to vaccine through a pandemic instrument, particularly when the current situation works so well for these wealthy states (*13*).

To bolster this concern, the WHO has not only proposed the pandemic instrument and inaugurated the WHO Hub in Berlin that is focused on information sharing, but also launched a new (and separate) "WHO BioHub Facility" focused on pathogen sample sharing. Announced in May 2021 by the Swiss Confederation and the WHO, the WHO BioHub Facility is based in Spiez, Switzerland, and is intended as an "international exchange system for [samples of] SARS-CoV-2 and other emerging pathogens" (*14*). These initiatives have been announced in quick succession and without much by way of member state consultation.

Through initiatives such as the Hub in Germany, the BioHub in Switzerland, and wider initiatives at the WHO, there is a growing sense that rich countries are building a global pandemic infrastructure that prioritizes their access to information and samples over developing nations' access to vaccines and other countermeasures. These initiatives not only bypass formal modes of governance within the WHO but also result in the further "decentraliz[ation]" of the WHO, all "paid by and in favour of rich countries" [comments by M. Voss in (*15*)]. In addition, the comments from Tedros and Minister Spahn imply that what are at present voluntary initiatives in respect of information and pathogen sharing might not stay voluntary for long.

Clearly, the introduction of an international legal obligation—backed by sanctions—to share pathogen samples and associated sequence data would change the legal and normative underpinnings of global health research and governance, but for whose benefit? Such a model would see sanctions for those nations that do not share their samples and data, but would there be sanctions for countries that fail to share associated benefits such as vaccines and other medical countermeasures during a pandemic? And if so, would the ability to sanction be out of reach for smaller countries, as it often is at the WTO, given the limited capacity of smaller economies to retaliate? Even if the WHO were capable of imposing sanctions, private entities like pharmaceutical companies would be out of their jurisdictional reach. The WHO would only be able to rule to sanction member states. And how would a punitive system secure the much-needed trust required to make global health governance function? Can solidarity and equity, mentioned countless times in discussions on the Pandemic Treaty, be achieved by a one-sided system that seemingly privileges concerns of richer countries?

"If rich countries want samples and data from developing nations, they need to start treating those nations as equals..."

International sharing of pathogen samples and scientific data is essential to epidemic and pandemic response, but the adoption of ABS terms for the sharing of pandemic influenza samples through the WHO's PIP Framework in 2011 cemented the legal status of pathogens as resources that poorer countries can trade for much needed medical countermeasures. The ABS transaction, previously embraced by the WHO, cannot now be ignored by deciding that pathogen samples and GSD or DSI should be shared by nations out of some lofty commitment to the common good, while the benefits generated from research and development on those very resources remain private goods to be sold to the highest bidders (*13*).

Countries that have been denied adequate access to COVID-19 vaccines during this pandemic are highly unlikely to give up one of their few bargaining chips and agree to share pathogen samples and associated data without some meaningful guarantees that they will receive vaccines and other benefits in return during the next pandemic, as per their rights under the CBD and Nagoya Protocol. The threat of sanctions is only going to entrench this transactional attitude further. If rich countries want samples and data from developing nations, they need to start treating those nations as equals—partners in a joint scientific endeavor. And that means not leaving them to fend for themselves while the developed world sets up its own early warning system, complete with sanctions to threaten and punish the noncompliant poor. ■

REFERENCES AND NOTES

1. WHO, WHO Hub for Pandemic and Epidemic Intelligence, Press conference of the inauguration of the WHO Hub for Pandemic and Epidemic Intelligence (2021); www.who.int/initiatives/who-hub-for-pandemic-and-epidemic-intelligence.
2. M. Rourke, M. Eccleston-Turner, *North. Irel. Leg. Q.* **72**, 411 (2021).
3. WHO, News Release: WHO, Germany open Hub for Pandemic and Epidemic Intelligence in Berlin (2021); www.who.int/news/item/01-09-2021-who-germany-open-hub-for-pandemic-and-epidemic-intelligence-in-berlin.
4. WHO Health Emergencies Programme, "WHO Hub for Pandemic and Epidemic Intelligence. Better Data. Better Analytics. Better Decisions," WHO Strategy Paper (2021); https://cdn.who.int/media/docs/default-source/2021-dha-docs/who_hub.pdf?sfvrsn=8dc28ab6_5, p. 2.
5. WHO, Sixty-fourth World Health Assembly, Report of the Review Committee on the Functioning of the International Health Regulations, (2005) in relation to Pandemic (H1N1) 2009, (A64/10) (2011); https://apps.who.int/gb/ebwha/pdf_files/WHA64/A64_10-en.pdf.
6. WHO, "Report of the Ebola Interim Assessment Panel" (2016); www.who.int/csr/resources/publications/ebola/report-by-panel.pdf.
7. WHO, Seventy-Fourth World Health Assembly, Review Committee on the Functioning of the International Health Regulations, (2005) during the COVID-19 Response (A74/9 Add.1) (2021); https://apps.who.int/gb/ebwha/pdf_files/WHA74/A74_9Add1-en.pdf.
8. L. O. Gostin, R. Katz, *Milbank Q.* **94**, 264 (2016).
9. P. Busch, "Dispute Settlement in the WTO" in The Oxford Handbook of the Political Economy of International Trade, L. L. Martin, Ed. (Oxford Univ. Press, 2014), pp. 1–19.
10. Reuters, "WHO Chief Welcomes EU Council Proposal for Pandemic Preparedness Treaty" (2021); www.reuters.com/business/healthcare-pharmaceuticals/who-chief-welcomes-eu-council-proposal-pandemic-preparedness-treaty-2021-01-20/.
11. WHO, "World Health Assembly agrees to launch process to develop historic global accord on pandemic prevention, preparedness and response" (2021); www.who.int/news/item/01-12-2021-world-health-assembly-agrees-to-launch-process-to-develop-historic-global-accord-on-pandemic-prevention-preparedness-and-response.
12. WHO, "Report of the Member States Working Group on Strengthening WHO Preparedness and Response to Health Emergencies to the special session of the World Health Assembly" (2021); https://apps.who.int/gb/ebwha/pdf_files/WHASSA2/SSA2_3-en.pdf.
13. M. Eccleston-Turner, H. Upton, *Milbank Q.* **99**, 426 (2021).
14. WHO, News Release: "WHO and Switzerland launch global BioHub for pathogen storage, sharing and analysis" (2021); www.who.int/news/item/24-05-2021-who-and-switzerland-launch-global-biohub-for-pathogen-storage-sharing-and-analysis.
15. V. S. Balakrishnan, *Lancet Microbe* **2**, E290 (2021).

ACKNOWLEDGMENTS

The authors thank C. Lawson for helpful feedback on earlier versions of this article.

10.1126/science.abn5400

BOOKS *et al.*

Alaska's Bering Land Bridge National Preserve, shown here, encompasses a portion of the land bridge that once connected Asia and North America.

PHOTO: JIM WILSON/THE NEW YORK TIMES/REDUX

ANTHROPOLOGY

Genomes in motion

Ancient DNA sheds light on the peopling of the Americas

By **Anne C. Stone**

The story of humankind's journey out of Africa and across the globe is epic and intricate. In *Origin: A Genetic History of the Americas*, anthropological geneticist Jennifer Raff offers a sometimes personal account of how scientists have tried to reconstruct the portion of this story that deals with the first peopling of the Americas, revealing the successes and failures that have accompanied our efforts to understand this phenomenon along with some questions that still remain.

Raff's book is divided into three parts that give insight into the complexities of both science and human history. In the first section, she discusses the history of attempts by European colonists and early scientists to understand how people came to be in the Americas and reveals why these often-racist perspectives have understandably left many Native Americans hesitant to participate in scientific research today. Here, she also clearly summarizes how we know what we know about early people in the Americas, reporting some of the relevant archaeological, linguistic, and morphological findings and describing results from some of the first genetic studies that have brought new insights to debates over the timing and number of migrations, as well as the routes of entry into the Americas.

People first entered the Americas during the Late Pleistocene via Beringia, a region that includes part of northeastern Siberia and Alaska and the (now submerged) land bridge connecting them. Raff discusses how they may have moved farther into North America, either by navigating through the massive Laurentide and Cordilleran ice sheets via an "ice-free corridor" that opened ~14,000 years ago or by traveling around the ice sheets using watercraft on a coastal "kelp highway" (as well as some other fringe ideas).

Raff also outlines the debate surrounding the "Clovis First" hypothesis, a once widely accepted theory positing that the first Americans were large-game hunters who arrived after the glaciers receded. (Spear points used by the group were first identified near Clovis, New Mexico.) Clovis First adherents were highly critical of any archaeological evidence that supported earlier occupations and only began to let go of this theory when indisputable data emerged, including archaeological findings at the Monte Verde site in Chile, which indicated that humans were in the Americas at least 1300 years earlier than previously thought.

In the second section of the book, Raff gives an overview of how ancient DNA analyses are done and the questions that they can be used to address. Here, she uses a clever analogy, comparing the process of entering the successive chambers of the sacred cave Actun Tunichil Muknal in Belize to the rituals she performs to maintain sterility while carrying out her research. This research uses genetics to answer questions about the initial peopling of the Americas and the subsequent population history of this region, with a focus on understanding the diversity and interactions among Inuit and Aleut-speaking groups and their ancestors.

In this section, Raff also highlights the importance of working with, and being respectful of, descendant communities. Such efforts are critical to repairing relationships between those who study ancient humans and groups with special ties to ancient people.

In the book's final section, Raff describes what recent ancient DNA research has brought to scientific debates about the peopling of the Americas. She explains, for example, how ancient genomes reveal links between ancient East Asians and northern Siberians and modern Indigenous Americans. She also summarizes how recent ancient genome research in the Arctic and the Caribbean has illuminated our understanding of population expansions, interactions, and turnovers. In the Arctic, for example, we now know that Paleo-Inuit (Dorset) and later Neo-Inuit (Thule) populations interacted in some areas while Paleo-Inuit were replaced in others.

Origin: A Genetic History of the Americas
Jennifer Raff
Twelve, 2022. 368 pp.

Raff does not shy away from discussing Indigenous critiques and unease surrounding ancient DNA studies, describing how genome data can be used or perceived in ways that result in social, legal, and political consequences for individuals and communities. DNA testing might result in questions about tribal membership, for example, or in challenges to a community's land claims. She argues persuasively that ethical paleogenomic research should privilege Indigenous concerns and be collaborative. ■

The reviewer is at the School of Human Evolution and Social Change, Institute of Human Origins, Arizona State University, Tempe, AZ, USA. Email: acstone@asu.edu

10.1126/science.abn7262

HEALTH POLICY

Making progress on mental illness

A former NIH leader advocates more holistic approaches to mental health care

By **Benjamin F. Miller**

The United States' failings concerning mental illness are well documented. Despite decades of grim data, meaningful change to this aspect of human health has, as yet, failed to materialize. Somewhat paradoxically, this lack of progress has occurred during a period in which the science that has helped shape our understanding of mental illness has increased drastically. As Thomas Insel writes in his book, *Healing: Our Path from Mental Illness to Mental Health*, we are stuck.

Insel is well positioned to describe the pervasive mental health problems plaguing our nation. He has held several relevant leadership positions, serving, for example, for 13 years as the director of the National Institute of Mental Health, and his commitment to advancing scientific research drives much of his thinking. In this book, Insel looks back at the evolution of our understanding of mental illness and forward to the next chapter in this story.

Mental health care must be better integrated into health care structures, argues Thomas Insel.

The book's first section, "A Crisis of Care," documents how the United States has traditionally approached mental health care. Here, Insel outlines both the structures and foundations on which we continue to build and reform mental health.

From care delivery systems that separate mental and physical health to siloed payment models, the fractured treatment of mental illness—and frequently comorbid conditions such as substance abuse and addiction—has been all but codified in US policy. Adding to this complexity is a lack of attention to community factors and to prevention, both of which seem to have been an afterthought in the creation of the system. Insel returns frequently to this theme throughout the book—and for good reason: You cannot improve mental health outcomes if you do not address the underlying factors that cause and exacerbate mental illness.

At times, the reader can feel Insel's frustration in the anecdotes and stories he relays and in the phrasing he uses. The movement to "deinstitutionalize" the mentally ill, he notes, for example, might be more accurately described as "transinstitutionalization," because "policies that limited hospital access for people with mental illness created an on-ramp to the criminal justice system." These recollections give depth and provide a human face to the problems he articulates and offer hints at possible solutions.

"Overcoming the Barriers to Change," the book's second section, elaborates on the themes explored in the first but views them through more contemporary lenses. Major topics here include reimagining crisis care, addressing gaps in quality, and moving beyond stigma.

Healing: Our Path from Mental Illness to Mental Health
Thomas Insel
Penguin, 2022. 336 pp.

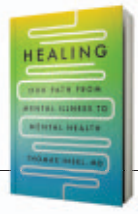

Like a good doctor, Insel identifies symptoms and prescribes solutions to the problems that plague the country's mental health infrastructure, but he maintains that holistic strategies are needed. "I argue that we need a medical approach to define the problem, but social and relational approaches to solve it," he writes.

For mental health, Insel posits, our traditional approaches usually come too late in the process; they are applied infrequently enough that improvement is not guaranteed; and in some cases, our solutions are focused on the wrong problems. Greater attention must be paid to "people, place, and purpose" as the keys to recovery, he writes.

Insel makes his most forceful arguments in the book's third section, which sketches potential paths forward. Here, the reader perceives most acutely a tension that underlies the rest of the book: Medical treatments and traditional care delivery are important, but they are wholly insufficient for addressing the size and scale of the mental health crisis. Without a more thoughtful approach that better integrates mental health into health care structures and communities, we perpetuate the same flawed silos that have kept us stymied for decades.

"At the beginning of my journey, I already recognized that none of these massive social challenges would be solved without fixing the mental health crisis," Insel notes. "By the end of my journey, I was convinced that the mental health crisis could be solved, but not without taking on these social challenges."

In the book's final section, titled "The Way Forward," Insel maintains that "mental health has become a measure of the soul of our nation." If this is true, then our country's soul is in a decidedly bad place. *Healing* suggests a path toward a better one. ■

The reviewer is president of Well Being Trust, Oakland, CA 94612, USA. Email: ben@wellbeingtrust.org

10.1126/science.abn8143

PHOTO: LEXEY SWALL/*THE NEW YORK TIMES*/REDUX

Edited by **Jennifer Sills**

Editorial Expression of Concern

On 22 August 2014, *Science* published the Research Article "Chemically mediated behavior of recruiting corals and fishes: A tipping point that may limit reef recovery" by D. L. Dixson *et al.* (*1*). *Science* has been made aware of data manipulation accusations pertaining to this paper. We are publishing this Editorial Expression of Concern to make readers aware of these accusations while the lead author's current and postdoctoral institutions investigate the claims.

H. Holden Thorp
Editor-in-Chief

REFERENCES AND NOTES

1. D. L. Dixson, D. Abrego, M. E. Hay, *Science* **345**, 892 (2014).

10.1126/science.abo1771

Arctic change reduces risk of cold extremes

In their Report "Linking Arctic variability and change with extreme winter weather in the United States" (3 September 2021, p. 1116), J. Cohen *et al.* explain how the combination of amplified Arctic warming and increased high-latitude snow cover disrupts the stratospheric polar vortex, which in turn drives severe winter weather in mid-latitudes. They infer that through this mechanism, Arctic change has caused an increase in cold extremes over the United States. However, this inferred connection is not confirmed by their analyses, and the increase in extreme cold is contradicted by past work.

Cohen *et al.*'s Report lacks analysis of the observed trends in winter cold extremes that have coincided with recent rapid Arctic warming. Studies have shown that winter cold extremes over the United States are becoming less frequent and less severe (*1*–*6*). These cold extremes are warming faster than the average temperature as day-to-day temperature variability decreases (*5*–*7*). Climate model experiments robustly show that Arctic warming contributes to this reduction in variability and cold extremes because when Arctic air spills into lower latitudes, this air is not as cold as it used to be (*6*, *8*–*11*). These results suggest that any short-lived cooling effect from disruptions of the polar vortex is not sufficiently large to cause long-term cooling trends over the United States; instead, warming trends are seen in observations and models.

Although we must investigate all possible consequences of climate change, even those that may seem counterintuitive, context is important. Observations and models strongly suggest that Arctic change is reducing, not increasing, the risk of winter cold extremes over the United States. The mechanism proposed by Cohen *et al.* may be relevant for year-to-year variability, but the evidence does not support a long-term increase in severe winter weather.

Russell Blackport[1]*, John C. Fyfe[1], James A. Screen[2]
[1]Canadian Centre for Climate Modelling and Analysis, Environment and Climate Change Canada, Victoria, BC, Canada. [2]College of Engineering, Mathematics, and Physical Sciences, University of Exeter, Exeter, UK.
*Corresponding author.
Email: russell.blackport@ec.gc.ca

REFERENCES AND NOTES

1. R. S. Vose, D. R. Easterling, K. E. Kunkel, A. N. LeGrande, M. F. Wehner, in "Climate science special report: Fourth National Climate Assessment, Volume I" (US Global Change Research Program, Washington, DC, 2017), pp. 185–206.
2. G. J. van Oldenborgh *et al.*, *Environ. Res. Lett.* **14**, 114004 (2019).
3. G. J. van Oldenborgh, R. Haarsma, H. D. Vries, M. R. Allen, *Bull. Am. Meteorol. Soc.* **96**, 707 (2015).
4. E. T. Smith, S. C. Sheridan, *Geophys. Res. Lett.* **47**, e2020GL086983 (2020).
5. A. Rhines, K. A. McKinnon, M. P. Tingley, P. Huybers, *J. Climate*. **30**, 1139 (2017).
6. T. W. Collow, W. Wang, A. Kumar, *J. Climate*. **32**, 5021 (2019).
7. R. Blackport, J. C. Fyfe, J. A. Screen, *Nat. Geosci.* **14**, 719 (2021).
8. J. A. Screen, C. Deser, L. Sun, *Bull. Am. Meteorol. Soc*. **96**, 1489 (2015).
9. L. Sun, J. Perlwitz, M. Hoerling, *Geophys. Res. Lett*. **43**, 5345 (2016).
10. T. Schneider, T. Bischoff, H. Płotka, *J. Climate*. **28**, 2312 (2015).
11. S. Chripko *et al.*, *J. Climate*. **34**, 5847 (2021).

10.1126/science.abn2414

PHOTO: REUTERS/MIKE SEGAR

Polar vortices can cause severe winter weather, such as this February 2021 snowstorm in New York City.

Response

We agree with Blackport *et al.* that the overall influence of global warming is to decrease the occurrence of cold extremes. However, global climate models consistently predict winter temperatures that are colder than those observed in the Arctic and warmer than those observed in Northern Hemisphere mid-latitudes (*1*, *2*). Our Report was not meant to suggest that cold extremes in the United States are increasing in frequency overall, although a

OUTSIDE THE TOWER

Empowering Afro-Indigenous girls

At 5:15 am on a clear morning in Cali, Colombia, Karen, a bright, curious, and passionate Indigenous 13-year-old girl from a humble suburban neighborhood, stepped onto our university-bound bus. She was excited for a second day of science activities, during which she would conclude experiments she began a week before. We had selected Karen and 12 other girls of Indigenous and African heritage to participate in our outreach program, a science, technology, engineering, and mathematics (STEM) experience grounded in ancestral knowledge.

Karen and the other girls, all of whom expressed interest in transforming their community by pursuing careers in science, were eager to build on their own knowledge and see how their traditions intersect with science. They could all explain how small-scale coffee and cocoa production involved wrapping beans in banana leaves to ferment, and they had many questions about commercial coffee and cocoa industrial processes. They also learned how biochemistry can alter the flavor and texture of the drinks.

Call for submissions
Outside the Tower is an occasional feature highlighting scientists' advocacy experiences. Submit your advocacy story at http://cts.sciencemag.org.

A week before, the girls had pressed their fingers into a petri dish. Now, they analyzed the microbes that had grown by looking through a microscope. Their traditions emphasize caring for the environment, a strategy that has been emphasized as a way to prevent pandemics. After months of isolation during the COVID-19 pandemic, they were fascinated to learn about the role of bacteria in health and disease.

Women are underrepresented in STEM, a fact that we both observed and studied during our scientific training. We developed the Biochemical Engineering Community Assistance Project to empower women in biochemistry fields. The program provides each participant with a science kit, including scientific gear and experimental materials. Feedback from the students indicated that owning scientific materials and conducting studies helped them to identify as scientists. We hope that by introducing scientific concepts that are relevant to the girls' life experiences, we can inspire them to pursue scientific opportunities.

Carolina Orozco Donneys,[1]* Jose Dario Perea[2]
[1]Departamento Ingeniería Bioquímica, Universidad Icesi, Cali, Colombia.
[2]Department of Chemistry, University of Toronto, Toronto, ON, Canada.
*Corresponding author. Email: corozco@icesi.edu.co

10.1126/science.abo4155

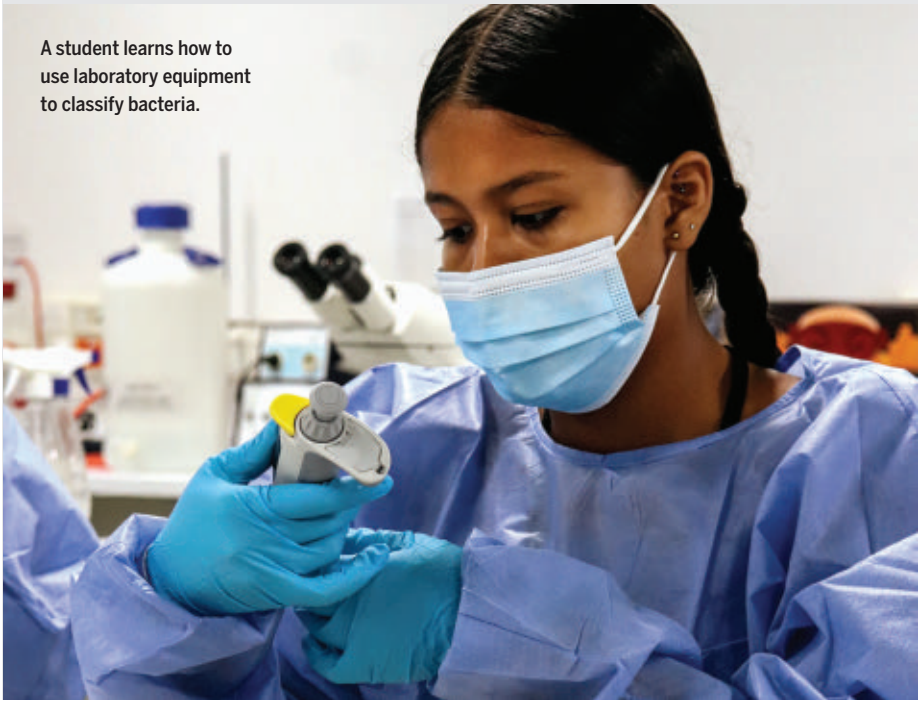

A student learns how to use laboratory equipment to classify bacteria.

PHOTO: JOSE DARIO PEREA

mid-winter cooling trend is observed over the period of Arctic amplification. Rather, we argued that an increasing trend in polar vortex disruptions related to Arctic amplification could resolve discrepancies between the observations and models.

Our analysis showed that across central North America, the winter warming trend is damped relative to the warming trend across the rest of the Northern Hemisphere and winter temperature anomalies are consistently colder than those predicted by global climate models. Both discrepancies can be explained by an increase in stretched polar vortices, for which the impact of the stretched polar vortex of February 2021 on weather can serve as a paradigm. If the number of stretched polar vortex days is increasing, it follows that the overall warming trend in the colder months across the United States will be dampened.

In addition to our observational analysis, we perturbed a global climate model with observed fall Arctic trends including increasing snow cover across Asia and less Arctic sea ice. The simulated response to these trends was both an increase in stretched polar vortex events and relatively colder surface temperatures across the United States that were regionally statistically significant.

Blackport *et al.* argue that in analyzing the mid-latitude cold extremes caused by polar vortices, we ignored studies showing that Arctic warming can also contribute to a decrease in both cold extremes and overall temperature variability. However, previous studies, including those cited by Blackport *et al.*, did not consider the influence of stretched polar vortices. In addition, the overwhelming number of studies on Arctic amplification are consistent with the conclusion that Arctic amplification can contribute to the occurrence of severe winter weather across the Northern Hemisphere midlatitudes (*1*).

Judah Cohen[1,2]*, Laurie Agel[3], Mathew Barlow[3], Chaim I. Garfinkel[4], Ian White[4]
[1]Atmospheric and Environmental Research, Inc., Lexington, MA 02421, USA. [2]Department of Civil and Environmental Engineering, Massachusetts Institute of Technology, Cambridge, MA 02139, USA. [3]Department of Environmental, Earth, and Atmospheric Sciences, University of Massachusetts Lowell, Lowell, MA 01854, USA. [4]Institute of Earth Sciences, The Hebrew University of Jerusalem, Edmond J. Safra Campus, Jerusalem, Israel.
*Corresponding author. Email: jcohen@aer.com

REFERENCES AND NOTES

1. J. Cohen *et al.*, *Nat. Clim. Change* **10**, 20 (2020).
2. C. I. Garfinkel, S-W. Son, K. Song, V. Aquila, L. D. Oman, *Geophys. Res. Lett.* **44**, 374 (2017).

10.1126/science.abn8954

RESEARCH

IN *SCIENCE* JOURNALS

Edited by **Michael Funk**

Bald eagles scavenging on carcasses contaminated with lead ammunition is a major exposure route, leading to both acute and chronic poisoning and reduced population growth.

PHOTO: RICHARD MITTLEMAN/GON2FOTO/ALAMY STOCK PHOTO

ECOTOXICOLOGY

A persistent lead problem

Although lead occurs naturally, its levels increased during the industrial revolution and have posed serious problems for humans and animals. Since the mid-1900s, efforts have been made to limit anthropogenic sources of lead in the environment, and these were largely considered successful. Despite this headway, anthropogenic lead remains an underappreciated threat to wildlife. Slabe *et al*. looked at lead levels in samples collected from bald and golden eagles across the United States. They found that almost half of all animals sampled had chronic, toxic levels of lead. Demographic modeling suggested that these levels are high enough to suppress population growth in both species. —SNV

Science, abj3068, this issue p. 779

ELECTROCHEMISTRY

Charging up terpene synthesis

A recent strategy for forming carbon–carbon bonds involves the reaction of a redox-active ester with an organometallic coupling partner. This approach suffers from the sensitivity of various functional groups in addition to the ester to the organometallic. Harwood *et al*. report a versatile electrochemical approach, paired with nickel catalysis, that avoids the organometallic. Modification of the electrode with silver nanoparticles proved key to the method's broad applicability, which the authors showcased across a range of total and formal terpene natural product syntheses. —JSY

Science, abn1395, this issue p. 745

BATTERIES

SAM to the rescue

During cycling of lithium metal batteries, the formation of dendrites on the electrodes can cause failure of the battery over time. Liu *et al*. were able to enhance lithium stripping and plating using self-assembled monolayers (SAMs) containing carboxylic groups. The SAMs are deposited on the aluminum oxide–coated polypropylene separator and promote the formation of a lithium fluoride–rich solid electrolyte interphase that shows greater overall stability and enhanced lithium ion transport. —MSL

Science, abn1818, this issue p. 739

CORONAVIRUS

Antibody-evading Omicron keeps function

The Omicron variant of severe acute respiratory syndrome coronavirus 2 (SARS-CoV-2) was reported in November 2021 and was quickly identified as a variant of concern because of its rapid spread. Relative to the original Wuhan-Hu-1 strain, this variant has 37 mutations in the spike protein that is responsible for binding and entry into host cells. Fifteen mutations are in the receptor-binding domain, which binds the host angiotensin-converting enzyme 2 (ACE2) receptor and is also the target of many neutralizing antibodies. Mannar *et al*. report a structure of the Omicron variant spike protein bound to human ACE2. The structure rationalizes the evasion of antibodies elicited by previous vaccination or infection

and shows how mutations that weaken ACE2 binding are compensated for by mutations that make new interactions. —VV

Science, abn7760, this issue p. 760

CORONAVIRUS

Beta variant antibody responses

Several severe acute respiratory syndrome coronavirus 2 (SARS-CoV-2) variants of concern that either enhance infectivity or resist neutralization by sera from vaccinated or convalescent individuals have emerged. The variants Beta and Omicron in particular no longer bind many neutralizing antibodies that target the receptor-binding domain (RBD) of the SARS-CoV-2 spike protein. Reincke *et al*. isolated antibodies from Beta-infected patients and showed that although some bound both the Beta and the wild-type RBD, others were specific for Beta. Some of the Beta antibodies had genetic characteristics similar to wild-type antibodies that were sensitive to the Beta mutations. Whereas some antibodies appeared to use a noncanonical binding mode, others accommodated Beta mutations into known binding modes. This work provides insights for the design of next-generation vaccines and antibody therapeutics. —VV

Science, abm5835, this issue p. 782

2D MATERIALS

Hiding in plain sight

Superconductivity observed in "twisted" bilayers of the two-dimensional (2D) material graphene requires the layers to be carefully stacked on top of each other at a very precise angle. Zhou *et al*. found superconductivity in the most common form of bilayer graphene, called Bernal, which does not require such precise manipulation (see the Perspective by Heikkilä). The researchers subjected the samples to an external electric field, but superconductivity emerged only after they also turned on an in-plane magnetic field. This unusual effect of a magnetic field, which normally acts to suppress superconductivity, is suggestive of exotic, spin-triplet pairing in Bernal-stacked bilayer graphene. —JS

Science, abm8386, this issue p. 774
see also abn9631, p. 719

TRANSPLANTATION

Expanding the lung transplantation donor pool

A major challenge in lung transplantation is the need for ABO blood group matching. Wang *et al*. used two enzymes, an *N*-acetylgalactosamine deacetylase and a galactosaminidase, to convert blood group A lungs to blood group O lungs during ex vivo lung perfusion. The authors demonstrated successful removal of blood group A antigen with no overt changes in lung health. In an ex vivo simulation of transplantation, the authors showed reduced antibody and complement deposition, suggesting that this technique may reduce antibody-mediated injury in vivo. —CSM

Sci. Transl. Med. **14**, eabm7190 (2022)

CULTURAL HERITAGE

Ecological methods for cultural history

Much of the narrative literature from the European Middle Ages has been lost because of manuscript physical degradation and destruction, including library fires. Kestemont *et al*. show that established methods from ecology for estimating the numbers of unseen species can be applied to abundance data representing cultural artifacts to estimate the losses that ancient cultural domains have sustained over the centuries. The authors obtained estimates that not only corroborate existing hypotheses from book history, but also reveal unexpected geographic differences that have thus far gone unnoticed. For example, insular literatures, such as those from Iceland and Ireland, combine a surprisingly strong cultural persistence with an elevated distributional evenness. —AMS

Science, abl7655, this issue p. 765.

IN OTHER JOURNALS

Edited by **Caroline Ash** *and* **Jesse Smith**

Streaks caused by SpaceX's Starlink satellites mar an image of the night sky in Utah.

OSTEOPOROSIS

Improved healing of rare fractures

Bisphosphonate (BP) therapy reduces the risk of fractures associated with osteoporosis. However, long-term BP use is linked to the development of a rare type of thigh fracture called atypical femoral fracture (AFF). Surgery is often required for AFF, but delayed healing can lead to further complications. Zheng *et al*. undertook molecular analysis of AFF healing stages and developed a rat model of long-term BP therapy with features of human AFF. Supplementation with the neuropeptide calcitonin gene-related peptide (CGRP) improved fracture repair by reducing the amount of extracellular matrix deposited by fibroblasts at the fracture site. Fracture healing was also improved by using a biodegradable magnesium-based implant that stimulated CGRP synthesis and release. —PNK

Mater. Today 10.1016/j.mattod.2021.11.028 (2022).

SOCIAL SCIENCES

Remnants of historical redlining

The long reach of racial inequities, as reflected by disparities in education and job advancement, are beginning to be recognized. In the 1930s, some US cities were mapped based on investment potential. Colors indicated neighborhoods that were considered hazardous (red), deteriorating (yellow), or desirable (blue/green). These zones largely corresponded to the racial makeup for these regions as Black, "foreigners," or White, respectively. Huang *et al*. found corresponding variations in levels of services, such as loans and insurance, provided to different colored regions in Baltimore. This practice, called "redlining," which was instituted almost 100 years ago, even today affects health and mortality. Life expectancy from red and yellow areas of Baltimore is about 5 years shorter than in those categorized as green or blue. —BAP

PLoS ONE **17**, e0261028 (2022).

PHOTO: ROBERT MCKENDRICK

LIGHT POLLUTION

Starlink contaminates astronomical survey

Several satellite "megaconstellations" are planned or are being deployed, increasing the number of artificial objects in the low Earth orbit by orders of magnitude. These satellites reflect sunlight, thus polluting astronomical observations, particularly surveys performed during twilight (such as those used to search for potentially hazardous asteroids). Mróz *et al.* examined images from the Zwicky Transient Facility twilight survey, searching for streaks caused by SpaceX's Starlink satellites. The rate of contamination increased from 0.5% in November 2019 to 18% in August 2021, as 1667 Starlink satellites were placed into orbit. The authors calculate that when the 12,000-satellite Starlink constellation is complete, "essentially all" twilight images will contain satellite trails. —KTS *Astrophys. J.* **924**, L30 (2022).

METABOLISM

Suppressing alcohol dependence

High alcohol consumption in humans is associated with variation in the genes encoding fibroblast growth factor 21 (FGF21) and its coreceptor β-klotho. FGF21 is a hormone that is produced from the liver in response to chronic and binge alcohol consumption, which can cross the blood–brain barrier and reduce alcohol preference in mice. Flippo *et al*. showed that a long-acting analog of FGF21 called PF-05231023 reduced alcohol consumption in mice and vervet monkeys, which will otherwise consume alcohol to intoxication. In mice, FGF21 induces excitation of β-klotho–expressing neurons in the basolateral amygdala, which are associated with consumption and reward-seeking behavior. Activation of the FGF21 axis might be a viable target to treat alcohol dependence in humans. —GKA

Cell Metab. **34**, 317 (2022).

DOMESTICATION

How sheep made it to the hearth

Aşıklı Höyük is a site in Anatolia showing exceptional preservation of 1000 years of Neolithic human history. The bone middens at this site offer a glimpse into one route for the domestication of goats and sheep. Stiner *et al.* discovered that the first stages of domestication (about 10,400 years ago) involved catching wild kids and lambs for fattening at the settlement. This is a form of meat storage without spoilage for hunter-gatherers that evolved into small-scale breeding of animals at the homestead and culminated in larger-scale herding. Herding allowed selective breeding, removal of males, milk harvesting, and consumption of adult meat. At Aşıklı Höyük, these developments were associated with social evolution involving organization of labor, settlement layout, and a not inconsiderable waste problem (maybe the dog's ancestors were useful in reducing the bone piles?). —CA

Proc. Natl. Acad. Sci. U.S.A. **119**, e2110930119 (2022).

The bone middens found at Aşıklı Höyük, an archeological site in Turkey, reveal an unique history of sheep and goat domestication.

PHOTO: KVAESTAD/WIKIMEDIA COMMONS

ORGANIC CHEMISTRY

Versatile allylation

Organic chemists often spend substantial amounts of time optimizing a catalyst to control the configuration of a single carbon center. Tunable control over all four configurations of two adjacent carbons is more challenging and has been realized in comparatively few cases. Chen *et al.* showcase how a structure-based regression technique, molecular field analysis, can help to achieve this aim in an allylation reaction. Specifically, they optimized chiral phosphoramidite ligands on iridium that, when paired with a second boron catalyst, can transform allyl esters into branched α-allyl acids with tunable configurations at both the α- and β-carbons. —JSY

Cell Rep. Phys. Sci. **2**, 100679 (2021).

GLYCOSYLATION

A sweet panel of enzymes

Many potent plant natural products come attached to sugars that help to solubilize and stabilize those compounds until they are needed by the plant, often as a defense mechanism against herbivores or parasites. Zhang *et al.* analyzed a large family of glycosyltransferases, uncovering patterns of reactivity and selectivity. The authors identified a particularly promiscuous group of enzymes that may be a valuable resource for the engineering of plant natural product biosynthetic pathways and for biocatalysis. —MAF

ACS Synth. Biol. 10.1021/acssynbio.1c00489 (2022).

ALSO IN *SCIENCE* JOURNALS

Edited by **Michael Funk**

ECOLOGY

Animal tracking in a big-data world

So-called "big-data" approaches have revolutionized fields of research from astronomy to genetics. Such approaches are not limited to fields that seem inherently technical, because the combination of rapid data collection and advanced analytical techniques could be applied to almost any scientific question. Nathan *et al*. reviewed how these modern approaches are being applied to the very old field of animal tracking and monitoring. Large-scale data collection can reveal details about how animals use their environment and interact with each other that were impossible to explore previously. Such methodological shifts will open new avenues of research—and conservation—across species. —SNV

Science, abg1780, this issue p. 734

ENVIRONMENTAL TOXINS

Mixed chemicals' potential risks

Exposure to endocrine-disrupting chemicals in the environment can cause a variety of health problems in human patients. Such exposures are not isolated, however, and environmental safety regulations that only consider doses of individual chemicals do not take multisubstance exposures into account. Caporale *et al*. examined chemical exposure data in a large cohort of human mother-child pairs and identified a set of common endocrine-disrupting chemicals (see the Perspective by Liew and Guo). The authors then showed that a mixture of these substances could cause abnormalities in two model organisms and may also be associated with language delay in humans. These findings suggest a need for further research into the effects of chemical mixtures and regulations that take such combinatorial effects into account. —YN

Science, abe8244, this issue p. 735; see also abn9080, p. 720

BLOOD–BRAIN BARRIER

Endothelial-targeted BBB therapeutics

The brain is protected not only by the skull, but also by the blood-brain barrier (BBB), which restricts transmission of substances from the blood into the central nervous system (CNS) extracellular fluid. If the BBB is breached, neurological disorders result. Therefore, it is desirable to develop intervention strategies that correct BBB deficits by restoring its function. Wnt signaling proteins have been shown to regulate the BBB, and Martin *et al*. developed a large, single-residue mutational screen covering more than half of the exposed surface of Wnt7a (see the Perspective by McMahon and Ichida). The authors identified a class of variants that exhibit strict specificity for the BBB's Gpr124/Reck Wnt signaling module. Gpr124/Reck agonists display "on-target" neurovascular protective properties in stroke and glioblastoma models in mice without "off-target" Wnt activation in other tissues, thereby defining a strategy to alleviate CNS disorders by repairing the BBB. —BAP

Science, abm4459, this issue p. 737; see also abn7921, p. 715

CELL BIOLOGY

Cystine as lysosomal fasting signal

Communication between the lysosome and mitochondria appears to help maintain control of metabolism in fruit flies deprived of food for prolonged periods. When food is limited, the target of rapamycin complex 1 (TORC1) protein kinase complex is inhibited, which promotes catabolism and autophagy to provide nutrients. Newly supplied amino acids could reactivate TORC1, but Jouandin *et al*. implicated cystine released from lysosomes in allowing continued catabolism during prolonged fasting. Cystine, when reduced to two molecules of cysteine, may promote the transient storage of remobilized amino acids in the form of tricarboxylic acid cycle intermediates in the mitochondria, thus limiting TORC1 reactivation during a prolonged fast. —LBR

Science, abc4203, this issue p. 736

IMMUNOLOGY

T cell proliferation with Themis

The T cell–specific protein Themis has been implicated in the homeostasis and activation of mature T cells. Liu *et al*. demonstrated that Themis is required for cytokine-dependent $CD8^+$ T cell homeostasis in mice and for T cell proliferation driven by the cytokines interleukin-2 (IL-2) and IL-15 in vitro. Themis stimulated cytokine signaling by reducing the activity of the phosphatase Shp1 and promoted cytokine-induced changes in gene expression and metabolic pathways that enabled T cell proliferation. These results identify Themis as an important determinant of T cell proliferation. —AMV

Sci. Signal. **15**, eabi9983 (2022).

INFLAMMATION

Stress leads to IL-24 danger

It is unclear how proteasome dysfunction leads to inflammation in patients with proteasome-associated autoinflammatory syndrome (PRAAS). Davidson *et al*. used multiple knockout cell lines, knockout mice, and primary PRAAS patient samples to show that protein kinase R (PKR) activation drives elevated innate immune responses. Activation of PKR was induced by the cytoplasmic accumulation of misfolded interleukin-24 (IL-24), acting as a danger-associated molecular pattern. Inhibiting PKR with a targeted inhibitor ameliorated the inflammation seen in PRAAS primary cells. Thus, IL-24–driven PKR activation induces innate inflammation in the context of PRAAS, and its inhibition may present a therapeutic route for these patients. —DAE

Sci. Immunol. **7**, eabi6763 (2022).

STRUCTURAL BIOLOGY

Clearing up roles of nebulin

Thin and thick actomyosin filaments are the key components of muscle. In skeletal muscle, the protein nebulin is essential for the length and strength of the thin filaments, with mutations of nebulin often leading to muscle diseases called nemaline myopathies. Wang *et al*. used cryo–electron tomography to identify nebulin integrated within the thin filament of native skeletal muscles. The authors determined a near-atomic in situ structure of nebulin and showed how it stabilizes thin filaments and functions as a "molecular ruler." The structure of nebulin along thin filaments is key to understanding the pathogenicity of nemaline myopathies. —SMH

Science, abn1934, this issue p. 738

RIVER ECOLOGY

Planning for Amazonian hydropower

Hydropower projects are proliferating in many parts of the world, but the benefits they bring in electricity supply are often offset by environmental costs. In an international collaboration, Flecker *et al*. present a study that aims to optimize the retention of ecosystem services in the face of hydropower expansion in the Amazon basin (see the

Perspective by Holtgrieve and Arias). The authors found that simultaneous consideration of multiple criteria (sediment transport, river connectivity, flow regulation, fish biodiversity, and greenhouse gas emissions) is necessary for optimizing the size and location of dams, and that the geographical scale of planning is also key (benefits from a smaller-scale plan may be detrimental at the basin scale). Their computational method allows the evaluation of each trade-off individually or all trade-offs simultaneously and is broadly applicable in other basin settings. —AMS

Science, abj4017, this issue p. 753; see also abn8311, p. 714

BIOMECHANICS

Engineered for a quick escape

When under attack, lizards will shed their tails as a way of escaping the predator while leaving behind a wiggling decoy to distract the enemy. The tail needs to be firmly attached most of the time, but it must also have a quick-release mechanism that won't engage during normal activities. Baban *et al*. devised a multiscale hierarchical model for lizard tail attachment (see the Perspective by Ghatak). Microscopy data of the broken surfaces of the tail showed that the fracture plane consists of mushroom-shaped pillars with nanopores at their tops. These pillars allow for enhanced adhesion of the tail in tension and peeling modes but enable fracture during oscillatory bending. The authors confirmed their hypothesis using polymer micropillars and computational fracture modeling. —MSL

Science, abh1614, this issue p. 770; see also abn4949, p. 721

REVIEW SUMMARY

ECOLOGY

Big-data approaches lead to an increased understanding of the ecology of animal movement

Ran Nathan*, Christopher T. Monk, Robert Arlinghaus, Timo Adam, Josep Alós, Michael Assaf, Henrik Baktoft, Christine E. Beardsworth, Michael G. Bertram, Allert I. Bijleveld, Tomas Brodin, Jill L. Brooks, Andrea Campos-Candela, Steven J. Cooke, Karl Ø. Gjelland, Pratik R. Gupte, Roi Harel, Gustav Hellström, Florian Jeltsch, Shaun S. Killen, Thomas Klefoth, Roland Langrock, Robert J. Lennox, Emmanuel Lourie, Joah R. Madden, Yotam Orchan, Ine S. Pauwels, Milan Říha, Manuel Roeleke, Ulrike E. Schlägel, David Shohami, Johannes Signer, Sivan Toledo, Ohad Vilk, Samuel Westrelin, Mark A. Whiteside, Ivan Jarić

BACKGROUND: Movement is ubiquitous across the natural world. All organisms move, actively or passively, regularly or during specific life stages, as a result of varied proximate drivers including energetic demands, social interactions, competition or predation. Movement closely interacts with individual fitness, affects a myriad of ecological processes, and is crucial for animals' ability to cope with human-induced rapid environmental changes. Driven by advances in analytical methods and technologies for tracking mammals, birds, fish, and other free-ranging vertebrates (hereafter, wildlife), movement ecology is rapidly transforming into a data-rich discipline, following previous developments in fields such as genomics and environmental monitoring. This ongoing revolution is facilitated by cost-effective automated high-throughput wildlife tracking systems that generate massive high-resolution datasets across scales relevant to the ecological context in which animals perceive, interact with, and respond to their environment.

ADVANCES: Modern tracking technologies efficiently generate copious, accurate information on the movements of multiple individual animals in the wild. Reverse-GPS technologies, which primarily use acoustic signals under water and radio signals over land, are automated high-throughput systems that are highly cost- and power-effective and capable of simultaneous tracking of multiple small animals (e.g., 20-g birds) at high spatiotemporal resolution (e.g., 1-s interval, a few meters) for months, but they require system installation and are usually limited to regional scales (≤100 km wide). GPS-based systems are, by contrast, readily available, longer term, and cover nearly global scales, but are similarly spatially accurate and periodically capable of high-resolution tracking at regional scales. However, they are more cost- and power-demanding, limited to larger animals, and cannot be applied under water. Two other tracking technologies, radar and computer vision, permit high-resolution snapshots of the movement of multiple individuals and can noninvasively track nontagged animals, but are less cost-effective, usually limited to smaller scales, and make individual identification challenging. Combined, these high-throughput technologies enable groundbreaking research in animal behavior, cognitive sciences, evolution, and ecology, facilitating previously infeasible investigation of animal movement ecology. Big movement data can help link interindividual variation in movement to individual behavior, traits, cognition and physiology; divulge fine-scale interactions within or among species; improve evidence-based management of human-wildlife interactions; and elucidate behavioral changes across spatiotemporal scales.

OUTLOOK: High-throughput wildlife tracking technologies are opening new research frontiers in biology and ecology. Their advantages, however, come with typical big-data costs such as computational load, intensive data management and processing, and challenging statistical analyses. Enlisting fields with a longer history of big data offers new prospects to address these challenges. Progress will arise from combining observational and experimental movement ecology and data-rich studies revealing behavioral shifts across individuals, species, scales, ecosystems, and life stages. High-resolution wildlife tracking is currently infeasible at large to global scales, a key limitation that can be addressed by combining low- and high-rate sampling, increasing interoperability between technologies, standardizing and sharing data, and promoting multidisciplinary international collaboration. Coupling movement and environmental big data could help determine impacts of major environmental and climate changes on animal–environment interactions, whereas real-time movement data could uniquely inform biodiversity conservation and ecosystem management. ■

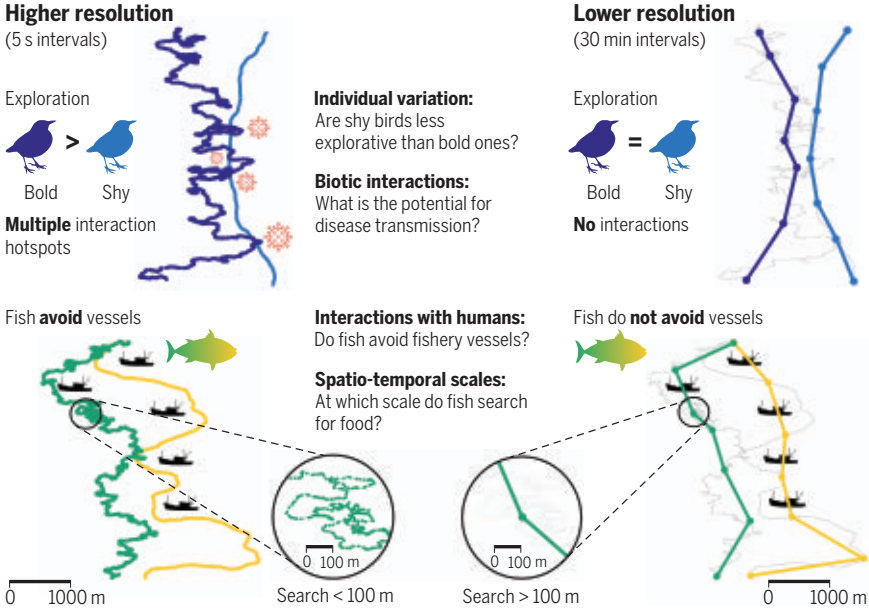

Why do high-throughput movement data matter? Big movement data are essential for addressing key ecological questions, as conclusions based on traditional lower-resolution data could differ markedly from the correct conclusions. We illustrate several examples for contrasting conclusions derived from lower- versus higher-resolution data of the same tracks from the same number of animals. Higher-resolution data can reveal that bolder birds visit more sites across the landscape and that bird tracks frequently cross each other, suggesting high potential for disease transmission, and that fish avoid fisheries and frequently search locally within small patches. None of these conclusions, however, could have been drawn from lower-resolution data. See also movies S1 to S5.

The list of author affiliations is available in the full article online.
*Corresponding author. Email: ran.nathan@mail.huji.ac.il
Cite this article as R. Nathan *et al.*, *Science* **375**, eabg1780 (2022). DOI: 10.1126/science.abg1780

READ THE FULL ARTICLE AT
https://doi.org/10.1126/science.abg1780

REVIEW

ECOLOGY

Big-data approaches lead to an increased understanding of the ecology of animal movement

Ran Nathan[1,2]*, Christopher T. Monk[3,4,5], Robert Arlinghaus[5,6], Timo Adam[7], Josep Alós[8], Michael Assaf[9], Henrik Baktoft[10], Christine E. Beardsworth[11,12], Michael G. Bertram[13], Allert I. Bijleveld[11], Tomas Brodin[13], Jill L. Brooks[14], Andrea Campos-Candela[5,8], Steven J. Cooke[14], Karl Ø. Gjelland[15], Pratik R. Gupte[11,16], Roi Harel[1,2], Gustav Hellström[13], Florian Jeltsch[17,18], Shaun S. Killen[19], Thomas Klefoth[20], Roland Langrock[21], Robert J. Lennox[22], Emmanuel Lourie[1,2], Joah R. Madden[12], Yotam Orchan[1,2], Ine S. Pauwels[23], Milan Říha[24], Manuel Roeleke[17], Ulrike E. Schlägel[17], David Shohami[1,2], Johannes Signer[25], Sivan Toledo[2,26], Ohad Vilk[1,2,9], Samuel Westrelin[27], Mark A. Whiteside[12,28], Ivan Jarić[24,29]

Understanding animal movement is essential to elucidate how animals interact, survive, and thrive in a changing world. Recent technological advances in data collection and management have transformed our understanding of animal "movement ecology" (the integrated study of organismal movement), creating a big-data discipline that benefits from rapid, cost-effective generation of large amounts of data on movements of animals in the wild. These high-throughput wildlife tracking systems now allow more thorough investigation of variation among individuals and species across space and time, the nature of biological interactions, and behavioral responses to the environment. Movement ecology is rapidly expanding scientific frontiers through large interdisciplinary and collaborative frameworks, providing improved opportunities for conservation and insights into the movements of wild animals, and their causes and consequences.

Movement characterizes life. It occurs in all organisms, affects individual fitness, determines evolutionary pathways, and shapes ecological processes, including responses to anthropogenic change. Consequently, studies of animal movement have long been central in ecology, animal behavior, and evolutionary and environmental biology. More recently, movement research has experienced a major upsurge with the introduction of a unifying theoretical framework termed "movement ecology" (*1*) in addition to the rapid development of new technologies and data processing tools (*1*–*3*). Specifically, recent advances in wildlife tracking techniques have revolutionized our capacity to obtain detailed movement information in space and time across species (*4*, *5*) (Fig. 1). With prolific data acquisition and ongoing advances in the processing of big data, movement ecology is rapidly shifting from a data-poor to a data-rich discipline, similar to previous high-throughput revolutions in diverse fields such as genomics, bioinformatics, nanoscience, biotechnology, cell biology, drug discovery, computer science, and environmental monitoring (*6*–*8*). High-throughput technologies break new ground in addressing long-standing basic science questions, such as the existence of cognitive maps in wild animals (*9*, *10*) and the extreme flight performance of soaring birds (*11*, *12*). Furthermore, high-resolution wildlife tracking data uniquely permit direct assessment of how individual animals respond to environmental and anthropogenic change (*13*, *14*).

The engines of the big-data revolution in movement ecology: Which technologies can finely track animals on the move?

Data on animal movement consist of time series of location estimates (*1*) and movement-related covariates (e.g., animal-borne sensor data and auxiliary environmental data). To assess which wildlife tracking techniques can generate big data for movement ecology research, we adjusted four major criteria used to define high-throughput data collection systems in other scientific fields (*7*, *15*). These systems are primarily defined by their ability to collect large amounts of data at a high sampling rate (temporal resolution in the context of movement ecology) as well as long tracking duration, high concurrency (simultaneous tracking of multiple individuals), and high cost-effectiveness (total number of localizations per amount of money, effort, or time invested). Thus, on the basis of these four defining criteria, high-throughput technologies in movement ecology are defined as "wildlife tracking systems that provide numerous data on the simultaneous movements of multiple animals, collected at high resolution over relatively long durations in a cost-effective manner." In addition to these four defining criteria, movement ecology studies typically consider other features of wildlife tracking technologies regardless of their ability to generate big data, particularly the following five key features: spatial scale (range covered by the system), spatial resolution (accuracy and precision), individual and species identification, invasiveness (disruption to tracked animals), and applicability (range of taxa and contexts).

According to the Nyquist-Shannon sampling theorem (*16*), sampling at time interval δt is sufficient to correctly characterize signals (e.g., behaviors and interactions) that typically last 2 δt or longer. In some of our examples, the temporal resolution is ~1 Hz (δt = 1 s), which enables characterization of behaviors and interactions lasting just a few seconds. Unfortunately, the phrase "high-resolution movement data" has been used in movement

[1]Movement Ecology Lab, A. Silberman Institute of Life Sciences, Edmond J. Safra Campus, The Hebrew University of Jerusalem, Jerusalem, Israel. [2]Minerva Center for Movement Ecology, The Hebrew University of Jerusalem, Jerusalem, Israel. [3]Institute of Marine Research, His, Norway. [4]Centre for Coastal Research (CCR), Department of Natural Sciences, University of Agder, Kristiansand, Norway. [5]Department of Fish Biology, Fisheries and Aquaculture, Leibniz Institute of Freshwater Ecology and Inland Fisheries, Berlin, Germany. [6]Division of Integrative Fisheries Management, Faculty of Life Sciences and Integrative Research Institute on Transformations of Human-Environment Systems (IRI THESys), Humboldt-Universität zu Berlin, Berlin, Germany. [7]Centre for Research into Ecological and Environmental Modelling, School of Mathematics and Statistics, University of St Andrews, St Andrews, UK. [8]Instituto Mediterráneo de Estudios Avanzados, IMEDEA (CSIC–UIB), Esporles, Spain. [9]Racah Institute of Physics, Edmond J. Safra Campus, The Hebrew University of Jerusalem, Jerusalem, Israel. [10]National Institute of Aquatic Resources, Section for Freshwater Fisheries and Ecology, Technical University of Denmark, Silkeborg, Denmark. [11]NIOZ Royal Netherlands Institute for Sea Research, Department of Coastal Systems, Den Burg, The Netherlands. [12]Centre for Research in Animal Behaviour, Psychology, University of Exeter, Exeter, UK. [13]Department of Wildlife, Fish, and Environmental Studies, Swedish University of Agricultural Sciences, Umeå, Sweden. [14]Fish Ecology and Conservation Physiology Laboratory, Department of Biology, Carleton University, Ottawa, ON, Canada. [15]Norwegian Institute for Nature Research, Tromsø, Norway. [16]Groningen Institute for Evolutionary Life Sciences, University of Groningen, Groningen, The Netherlands. [17]Plant Ecology and Nature Conservation, Institute of Biochemistry and Biology, University of Potsdam, Potsdam, Germany. [18]Berlin-Brandenburg Institute of Advanced Biodiversity Research (BBIB), Berlin, Germany. [19]Institute of Biodiversity, Animal Health and Comparative Medicine, University of Glasgow, Glasgow UK. [20]Ecology and Conservation, Faculty of Nature and Engineering, Hochschule Bremen, City University of Applied Sciences, Bremen, Germany. [21]Department of Business Administration and Economics, Bielefeld University, Bielefeld, Germany. [22]NORCE Norwegian Research Centre, Laboratory for Freshwater Ecology and Inland Fisheries, Bergen, Norway. [23]Research Institute for Nature and Forest (INBO), Brussels, Belgium. [24]Biology Centre of the Czech Academy of Sciences, Institute of Hydrobiology, České Budějovice, Czech Republic. [25]Wildlife Sciences, Faculty of Forest Sciences and Forest Ecology, University of Goettingen, Göttingen, Germany. [26]Blavatnik School of Computer Science, Tel-Aviv University, Tel-Aviv, Israel. [27]INRAE, Aix Marseille Univ, Pôle R&D ECLA, RECOVER, Aix-en-Provence, France. [28]School of Biological and Marine Sciences, University of Plymouth, Drake Circus, Plymouth, UK. [29]University of South Bohemia, Faculty of Science, Department of Ecosystem Biology, České Budějovice, Czech Republic.
*Corresponding author. Email: ran.nathan@mail.huji.ac.il

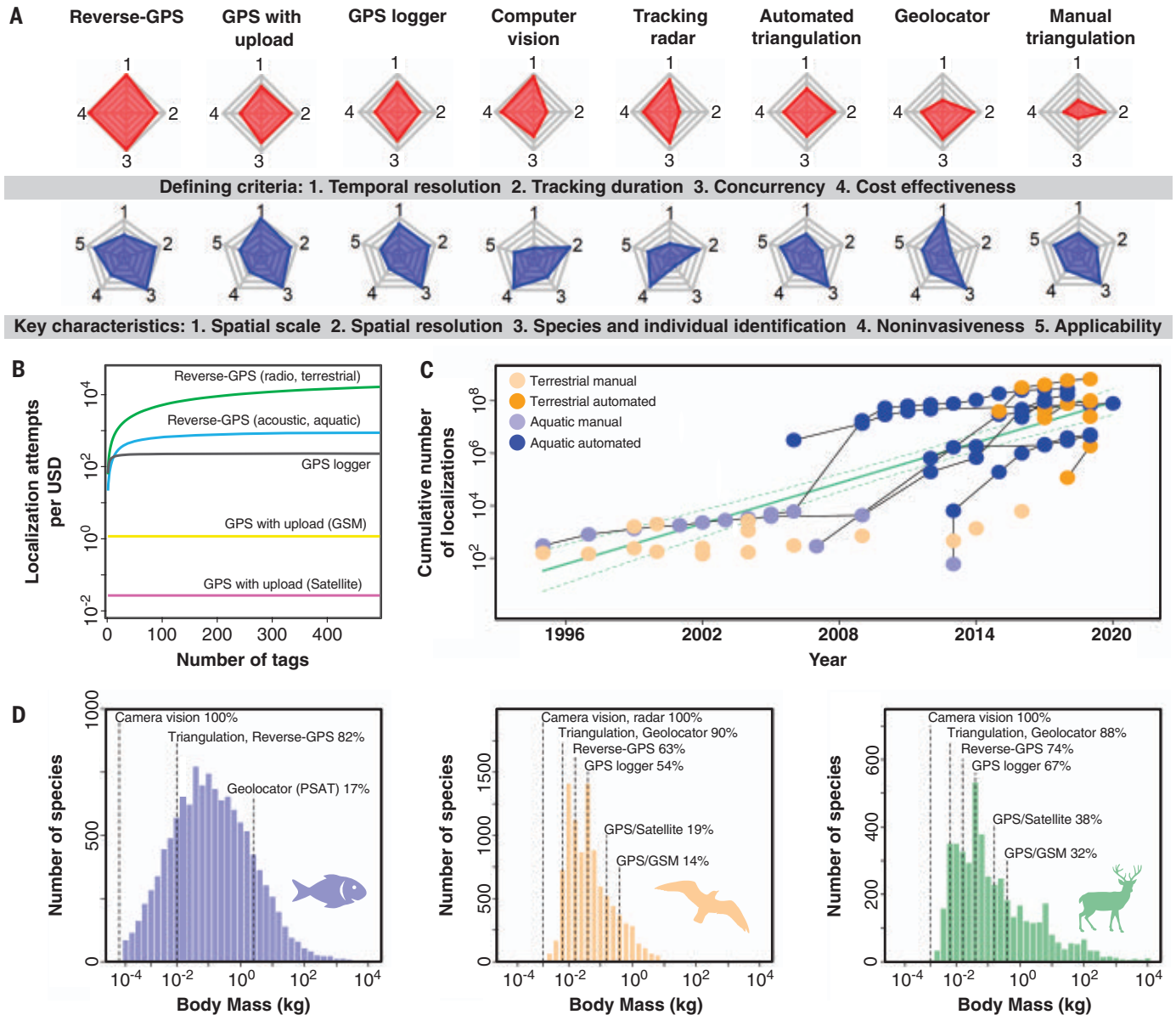

Fig. 1. High-throughput tracking technologies and trends. (**A**) Qualitative evaluation of the four defining criteria (red) and five key characteristics (blue) of eight major wildlife tracking technologies (ordered according to their high-throughput capacity), as estimated by 23 experts in animal tracking. Higher scores represent more favorable high-throughput performance. (**B**) Cost-effectiveness was quantitatively estimated as the number of localization attempts per investment (1 US dollar) for five tag-based tracking systems. (**C**) Pronounced increase (six orders of magnitude) in data yields over the past 15 years, marking a shift from manual triangulation to automated reverse-GPS systems in both fish and birds. Each symbol represents a single study system in a certain year, with those linked by black lines representing yields from the same system across years; the mean trend is shown in green with 95% CIs. (**D**) Proportion of species that can be tracked by the smallest tags currently used to track fish (tag mass <2% of body mass), birds, and mammals (<3% of body mass for both). For details on estimation procedures and data sources, see supplementary materials (*101*). GSM, global system for mobile communications (global standard for cellular networks); PSAT, pop-up satellite archival tags.

ecology literature for a wide range of temporal resolutions, with δt spanning seven orders of magnitude from tenths of a second to several hours and even days. In this Review, we deliberately narrowed this range down to encompass a much smaller variation (mostly δt = 1 to 10 s) and report δt for each example. This flexible approach avoids the pitfalls of attempting to find a general standard; rather, research programs in movement ecology should set thresholds for this and the other defining criteria and key characteristics according to the research goals and key features of the study system (*3*). Beyond the general trend of increased information loss at lower resolution implied by the Nyquist-Shannon criterion, general best-practice guidelines for selecting δt include, for example, substantial underestimation of total travel distance (and thereby underestimation of the apparent speed) at relatively low resolution typically applied in movement ecology studies (e.g., $\delta t \geq 30$ min) with stronger bias for more tortuous and faster paths (*17*, *18*) (see movie S1). However, the combination of high temporal and low spatial resolution tends toward the opposite bias especially when movement is slow with many stops, owing to accumulation of errors (*18*, *19*). To alleviate these biases, advanced machine learning methods can be combined

with mechanistic agent-based models to capture the relevant resolution and scale of the study system, as we further discuss in the "Data processing and analysis" section.

A rich variety of technologies have been used to gather information on animal movement in the wild (*3*, *20*). Over the past two decades, technological advances (Fig. 1A) have yielded much larger datasets than what was formerly possible (Fig. 1, B and C), and tag miniaturization has increased the proportion of species that can be tracked (Fig. 1D). However, wildlife tracking technologies vary in how they tackle the basic trade-offs between the four criteria and other key characteristics. We qualitatively assessed eight common tracking technologies on the basis of our four defining criteria and their main limitations and strengths (Fig. 1A), and we quantified their cost-effectiveness as the total number of localizations (the product of the first three criteria that can be generated on the basis of the same investment (Fig. 1B). These comparisons revealed three fairly distinct groups of high-throughput technologies (see "Data collection" for details): (i) Reverse-GPS systems, including acoustic trilateration of aquatic animals (*21*–*30*) and radio trilateration of terrestrial animals (*10*, *20*, *31*–*35*), regularly meet most criteria, and their main constraints are relatively limited spatial scale and installation costs. (ii) GPS with upload (*11*, *12*, *36*–*42*) and GPS loggers (*9*, *43*–*45*), also meet most criteria under certain circumstances and can track terrestrial (and some aquatic) animals at large to global scales; however, these are usually less cost-effective and less applicable (expensive tags, cannot be applied under water and are limited to relatively large animals or to study systems where animals, including small ones, can be recaptured to retrieve data). (iii) Tracking radars (*46*) and computer vision (*47*–*51*) also meet most criteria under certain circumstances and are usually noninvasive but are less cost-effective and much more restricted in their applicability, spatial range, and tracking duration; further, specific individuals (and often species) can seldom be identified. Three other technologies—manual triangulation, automated triangulation, and geolocators—have relatively low resolutions and do not generate big data, and therefore do not qualify as high-throughput tracking systems.

New big-data frontiers in movement ecology

Ecology, behavior, ontogeny, and fitness of individuals

Research under ecologically realistic conditions is imperative for understanding how variation among individual animals shapes ecological, behavioral, and evolutionary processes (*52*). Recent research is harnessing high-throughput technologies to quantify behavioral variability in free-ranging individuals, allowing exploration of the causes and consequences of variation among individuals in movement, internal state (e.g., energy status), ontogeny (e.g., maturation and experience), behavioral traits (e.g., personality), or cognitive skills (e.g., spatial memory), as well as trait covariation patterns and individual fitness (Fig. 2).

Practical difficulties in measuring individual states, traits, and behaviors have restricted researchers to conducting studies under controlled, often captive, conditions. However, reliance on captive animals poses problems of ecological validity (*53*). Wildlife tracking enables greater realism, but behavioral patterns can be missed by traditional low-throughput methods (e.g., movie S1). Some recent studies have successfully combined extensive yet relatively low-resolution GPS datasets and modeling approaches to infer behavioral variation among individual caribou (*Rangifer tarandus*; δt = 1 to 4 hours) (*54*) and white storks (*Ciconia ciconia*; δt = 5 min to 12 hours) (*55*). Further, an experimental field approach was successfully applied to roe deer (*Capreolus capreolus;* δt = 1 hour) (*56*). Despite the relatively low-resolution data, they all met the Nyquist-Shannon criterion such that the applied temporal resolution successfully captured the mechanisms investigated. High-throughput tracking systems can further transform this line of research by providing detailed, fine-scale data from a large number of individuals with known attributes moving simultaneously in their natural landscapes. For example, ATLAS (Advanced Tracking and Localization of Animals in real-life Systems) data (δt = 1 to 8 s) from free-ranging animals revealed evidence for cognitive maps in Egyptian fruit bats (*Rousettus aegyptiacus*) (*9*, *10*) and associations between cognitive traits and movement in pheasants (*Phasianus colchicus*) (*32*) (Fig. 2A). Data from high-throughput systems also improves estimates of individual fitness in wild animals, for instance by enabling accurate detection of the location, timing, and probable cause of mortality events, even when carcasses are moved by predators (Fig. 2A).

High-throughput technologies also enable new opportunities for investigating how ecological factors may impose physiological challenges on individuals during energy-demanding activities such as foraging, migration, predator-prey interactions, or parental care (*25*). For example, acoustic trilateration (δt = 9 s) revealed that more active northern pike (*Esox lucius*) were more vulnerable to angling (*30*) (Fig. 2B). Understanding the drivers and consequences of movement and space use may require tracking individuals over long time periods or across different life stages (*57*), hence a somewhat lower temporal resolution. For instance, long-term (11 years) GPS tracking (δt = 1 to 3 min) of northern gannets (*Morus bassanus*) revealed sex-related variation in foraging timing and duration and habitat selection in some years but not others (*44*).

Biotic interactions

High-throughput systems provide the means to detect social and other intraspecific interactions among individuals in natural environments through simultaneous tracking of most or all group members (*37*, *41*); such interactions have previously been difficult to assess (*52*) (see also movie S2). For example, in whole flocks of vulturine guineafowl (*Acryllium vulturinum*) tracked by GPS tags (δt = 1 s every fourth day), both dominant and subordinate birds were found to lead group foraging movements, depending on the resource type being exploited (*41*). Having more detailed data on the movement of the same number of individuals can also illuminate the true nature of interspecific interactions (see summary figure), ideally augmented by simultaneous tracking of most or all animals engaged in such interactions (e.g., competitors, predators, or prey). This highly challenging need (see "Data collection") has been acknowledged, for example, in studies of interactions among multiple host, vector, and reservoir populations involved in disease transmission (*58*) as well as in the context of predator-prey interactions (*59*).

Classic concepts in ecology and animal behavior (e.g., optimal foraging and ideal free distribution), are based on simplifying assumptions such as context-independent decisions and complete information transfer among individuals, which are often violated in real-life settings (*60*). High-throughput systems enable a more realistic perspective on biotic interactions both within and among species, revisiting existing concepts and permitting new insights on space use strategies in competitive or predator-prey relationships (*61*). For example, high-resolution ATLAS data (δt = 8 s) revealed robust spatial partitioning among two adjacent bat colonies that cannot be explained by commonly hypothesized competition, but could emerge from memory and information transfer (*34*). High-resolution GPS tracking (δt = 0.2 s) enabled the assessment of how individual pigeons within coordinated flying groups responded to a robotic predator, providing evidence that refutes the well-established selfish herd hypothesis (*45*). High-resolution data are generally necessary for analyzing interactions with a strong dynamic perspective because encounters (or avoidance) may be cryptic, occasional, or ephemeral (*62*). For example, the number of potential predation events (when a predator is in close proximity to its prey) decline exponentially with increasing sampling interval (original δt = 1 min), implying that the true nature of predator-prey dynamics among fish cannot be detected by lower resolution data of the same sample size (Fig. 3).

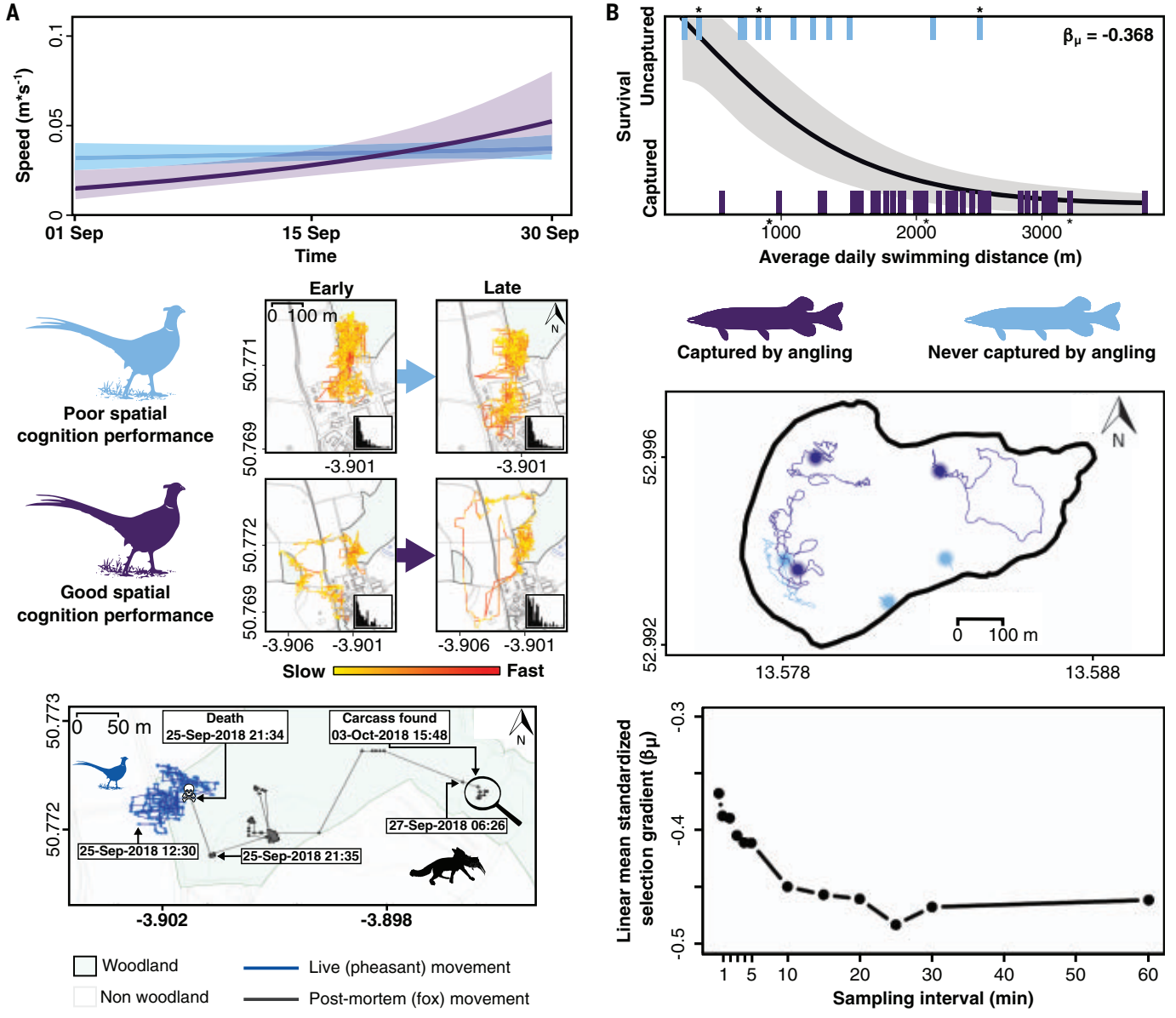

Fig. 2. Inference on patterns of variation in movement, behavior, and fitness among individuals and their potential drivers. (**A**) ATLAS-tracked (δt = 4 s) young pheasants (*P. colchicus*) that performed better in spatial cognitive tasks in captivity made slower transitory movements during early stages of exploration in the wild, but their speed increased with experience in the environment; poor cognitive performers moved faster during early exploration but did not differ in their speed later on (*32*) (top plot). This general trend is illustrated for two representative ATLAS-tracked individuals (middle plots). Histograms show the number of fast steps (>1 m/s). The bottom map shows the track of a pheasant (blue lines) that was killed and carried away (with the ATLAS tag intact) by an untagged fox (*Vulpes vulpes*) (black lines). ATLAS informed the exact timing and location of such mortality events, whereas in situ observations (skull and crossbones, magnifying glass) would place the mortality location 400 m away with an 8-day uncertainty about its timing in this example. (**B**) More active northern pike (*E. lucius*) tracked in the wild using acoustic trilateration (δt = 9 s) were more likely to be captured by angling (purple) (top plot), suggesting that angling pressure results in shyer, less active pike populations (blue) (*30*). Variation in activity between captured and noncaptured pike is illustrated in the map by six representative tracks (marked by asterisks in the top plot), with dotted lines representing data gaps (δt > 60 s). The strength of harvest selection on fish behavior, represented by the mean-standardized linear selection gradient (β_μ), is rapidly overestimated (more negative values) as temporal resolution decreases (longer sampling intervals) (bottom plot).

Interactions with natural and anthropogenic environments

Coupled with fine-scale environmental monitoring, high-throughput tracking systems reveal how animals respond to environmental stimuli (Fig. 4 and movies S3 to S5), providing critical information for developing effective management and restoration actions (*13*, *14*). For example, high-resolution GPS data (δt = 1 s) combined with triaxial accelerometry and atmospheric modeling were necessary to reveal differential responses of adult and juvenile griffon vultures (*Gyps fulvus*) to challenging soaring conditions (*38*) (Fig. 4A and movie S3). Further, whole-lake acoustic trilateration (δt = 9 s) revealed interaction between a non-native wels catfish (*Silurus glanis*) and physical features (e.g., water temperature) of a novel environment (*27*).

High-throughput tracking data, coupled with mapping of relevant human activities,

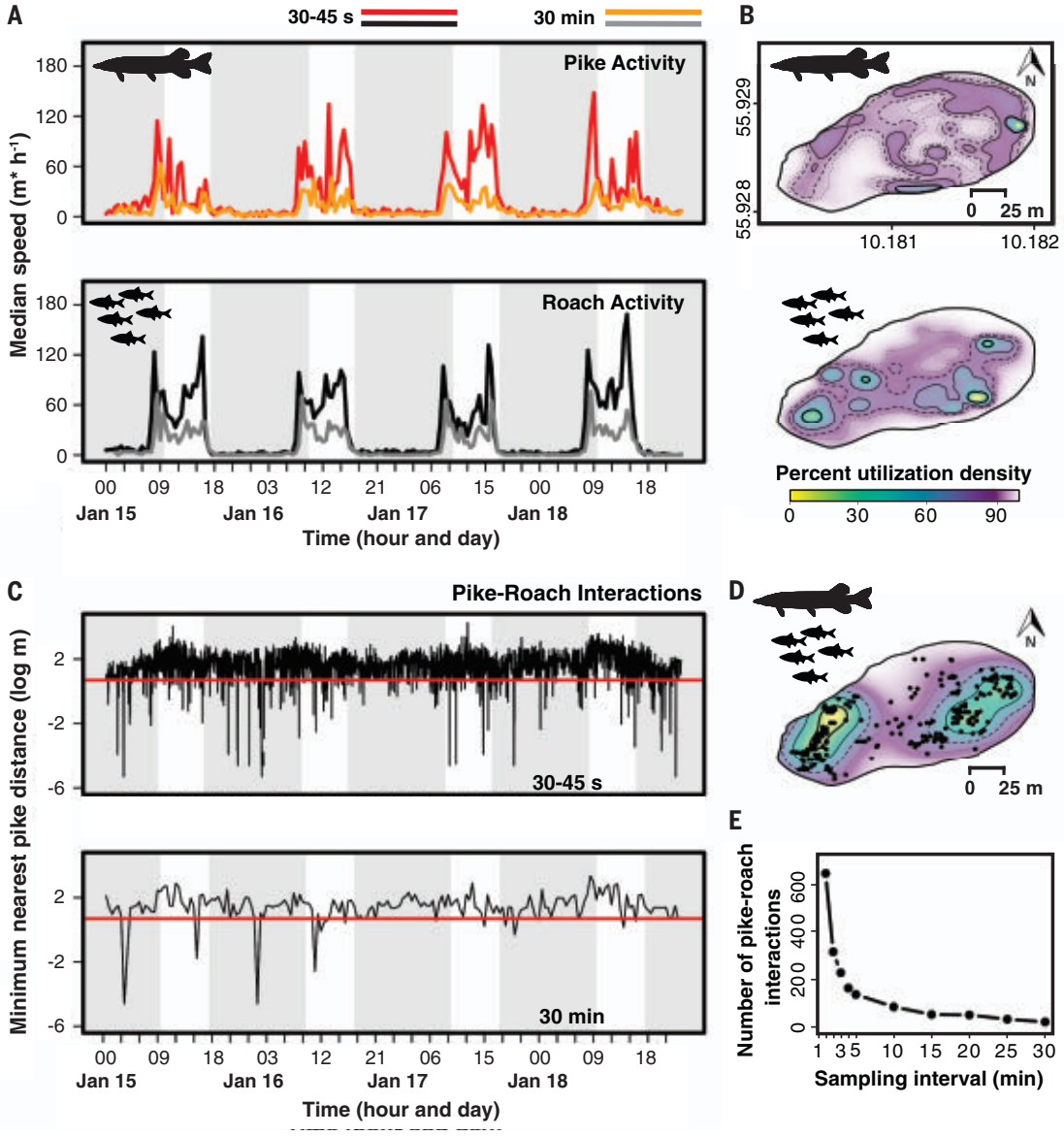

Fig. 3. The nature of biotic interactions. Prey fish (roach, *Rutilus rutilus*, black lines) were tracked using acoustic trilateration (δt = 9 s) simultaneously with predators (northern pike, *E. lucius*, red lines). Predators and prey were similar in their diurnal cycles (**A**) but differed in their spatial activity patterns (**B**). Short-range (>2 m) predator-prey encounters occurred throughout all times but more during the night (**C**), and at two large predation hotspots (**D**) that only partially overlapped with the main activity area of the predators. The number of potential predator-prey encounters (**E**) was rapidly underestimated as temporal resolution decreased (longer sampling intervals).

enable evidence-based conservation and management across diverse ecosystems (*28*). For example, endangered European eels (*Anguilla anguilla*) tracked during downstream migration by acoustic trilateration (δt = 1 s) showed rapid behavioral shifts upon encountering rapid experimentally induced fluctuations in flow velocity near dams (*23*), which cannot be detected when tracks are sampled at even slightly longer intervals (Fig. 4B; see another example in movie S4). This technology (δt = 5 s) also illuminated ecosystem-based effects of recreational activities such as anglers adding feed resources to lakes (*26*). Furthermore, emerging technologies enable rapid, nearly real-time, fine-scale data collection and have recently been used as early alert systems, revolutionizing how resources are managed (*63*). For instance, high-resolution GPS tracking of albatrosses (δt = 1 min) and condors (δt = 30 s) can autonomously and immediately reveal the location of illegal vessels in the ocean (*42*) and of potential collisions with wind turbines (*36*) (see also movie S5), respectively.

Patterns and mechanisms across spatiotemporal scales

Quantifying how movement patterns and drivers change across scales is a major challenge in movement ecology (*1*, *64*, *65*). In controlled settings, high-throughput methods allowed inference on multiscale behavior of zebrafish (*Danio rerio*) (*66*) and anomalous diffusion in small invertebrates (*48*). Scale-dependent behaviors have also been studied in free-ranging terrestrial and marine animals (*49*, *64*), but the relatively low-resolution data used in these studies cannot detect behavior at the fine resolution and scale at which animals typically sense and respond to their environment (*49*, *67*).

Black-winged kites (*Elanus caeruleus*) tracked using ATLAS (δt = 4 s), for example, showed substantial variation in movement phases at local scales, which remains undetectable even

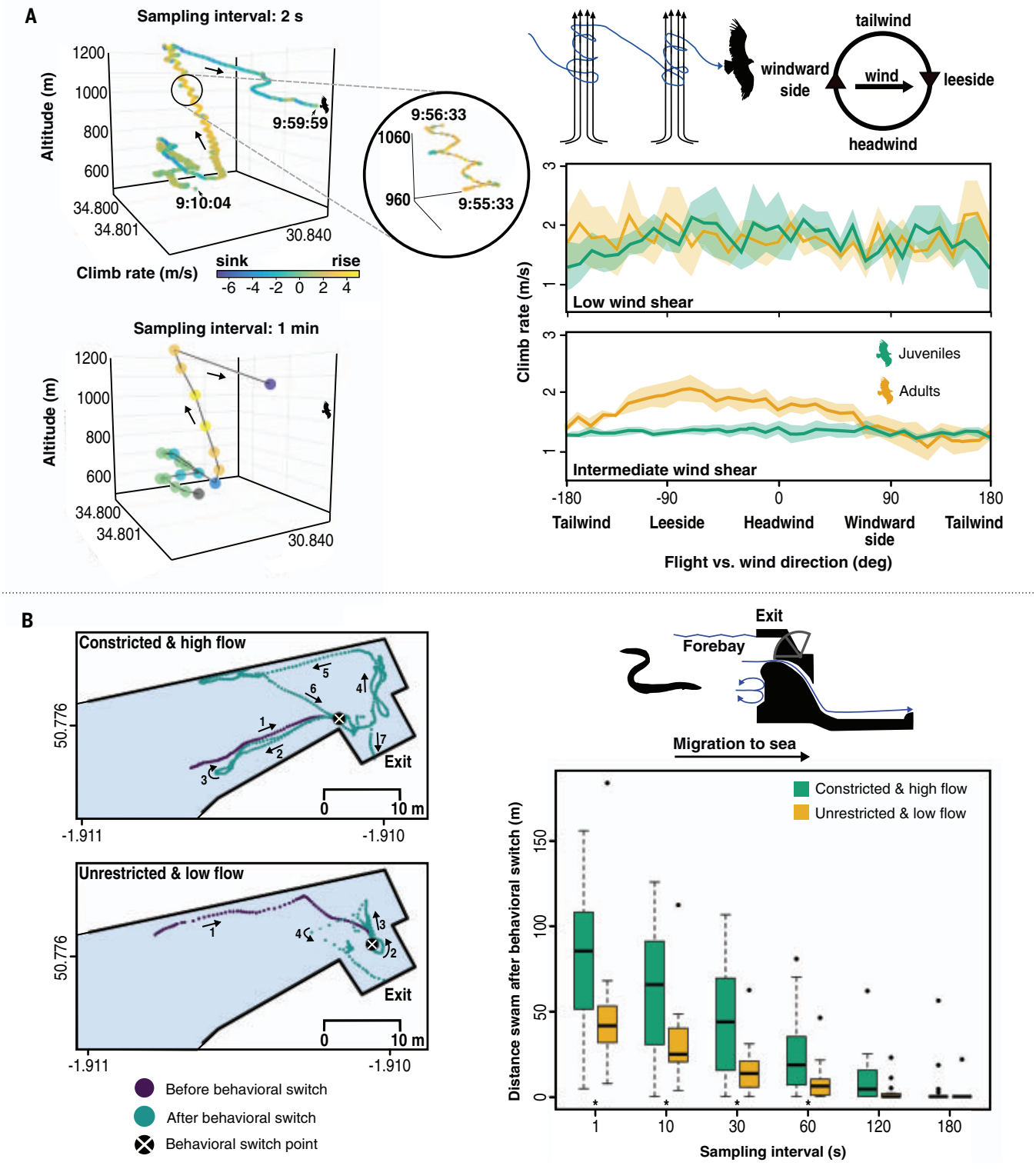

Fig. 4. Insights into the responses of wild animals to their abiotic environment and to human-induced environmental changes. (**A**) High-resolution (δt = 2 s) GPS tracking of griffon vultures (*G. fulvus*) revealed that under more challenging soaring conditions (intermediate wind shear), juveniles climbed more slowly in rising-air thermals because of their lower efficiency in circling around wind-drifted thermals compared with adults (*38*). Vulture thermal circling is clearly evident in the high-resolution data but cannot be recognized even at slightly lower resolution data (δt = 1 min). According to the Nyquist-Shannon criterion, a typical circling duration of ~15 s (~4 circles min^{-1}; zoomed-in section) requires $\delta t \leq 7.5$ s. (**B**) Acoustic trilateration (δt = 1 s) revealed that downstream-migrating endangered European eels (*A. anguilla*) shift their behavior from semipassive downstream swimming to either upstream escape or local search upon encountering experimentally varied flow regime near the exit of a hydropower facility (*23*). A constricted high flow regime generally elicits longer upstream escape (top map), whereas unrestricted low flow leads to shorter, spatially confined searches for the nearby exit. This difference in behavioral response becomes undetectable and insignificant as sampling interval increases, indicating that relatively high-resolution tracking is required to infer fish response to anthropogenic structures.

at slightly lower temporal resolution (Fig. 5). This shows that notions of universal foraging behavior and scale-free movement (*68*) should be replaced by case- and scale-specific behavior and movement, and that high-resolution data are needed to detect differences among these patterns. Furthermore, high-resolution data enabled researchers to distinguish ergodic from nonergodic processes, a key question in studies of dynamical systems and stochastic processes that has been overlooked in many disciplines (*69*), including movement ecology. In ergodic systems, different segments are equally representative of the whole; hence, averaging reveals a typical behavior. However averaging could be misleading in nonergodic systems, which lack a typical behavior. Assessment of ergodicity is therefore crucial in movement ecology, dictating whether one can infer by ensemble-averaging over multiple movement segments. For foraging raptors, ATLAS revealed a substantial distinction between the ergodic, superdiffusive (faster than diffusive) nature of commuting and the nonergodic, subdiffusive (slower than diffusive) nature of local movement, implying a limited number of ways to commute between distant patches but many ways to hunt or stop within a local patch (Fig. 5) (*35*).

The basic steps in high-throughput movement ecology research

Study design

Movement ecology studies are often based on the field observational approach, documenting the full complexity of natural movement but with limited capacity to discern and isolate the factors shaping movement variation. The alternative experimental approach is typically applied in controlled laboratory settings and is less prevalent in studies of animals in the wild. Although field experiments have been conducted with relatively low-resolution movement data (e.g., δt = 1 hour) (*56*), high-resolution data are necessary for field experiments involving short-term behaviors, fine-scale encounters, or multiple interacting individuals or species. High-throughput tracking systems can therefore broaden the scope of experimental movement ecology, creating new opportunities to develop a "laboratories-in-the-wild" experimental approach (*22*, *28*, *29*).

The two approaches can be combined to address key questions in movement ecology through high-resolution tracking of both manipulated and nonmanipulated free-ranging individuals. For example, 149 nonmanipulated ATLAS-tracked (δt = 1 to 8 s) Egyptian fruit bats undertook straight shortcuts during their foraging flights, and 23 additional manipulated (transferred to the periphery of their foraging range) bats returned directly to their preferred fruit tree, complementing evidence for a cognitive map (Fig. 6A) (*10*). Similarly, an individual's movement before, during, and after an experimental trigger can be compared (*23*) (Fig. 4B). Additionally, individuals with known

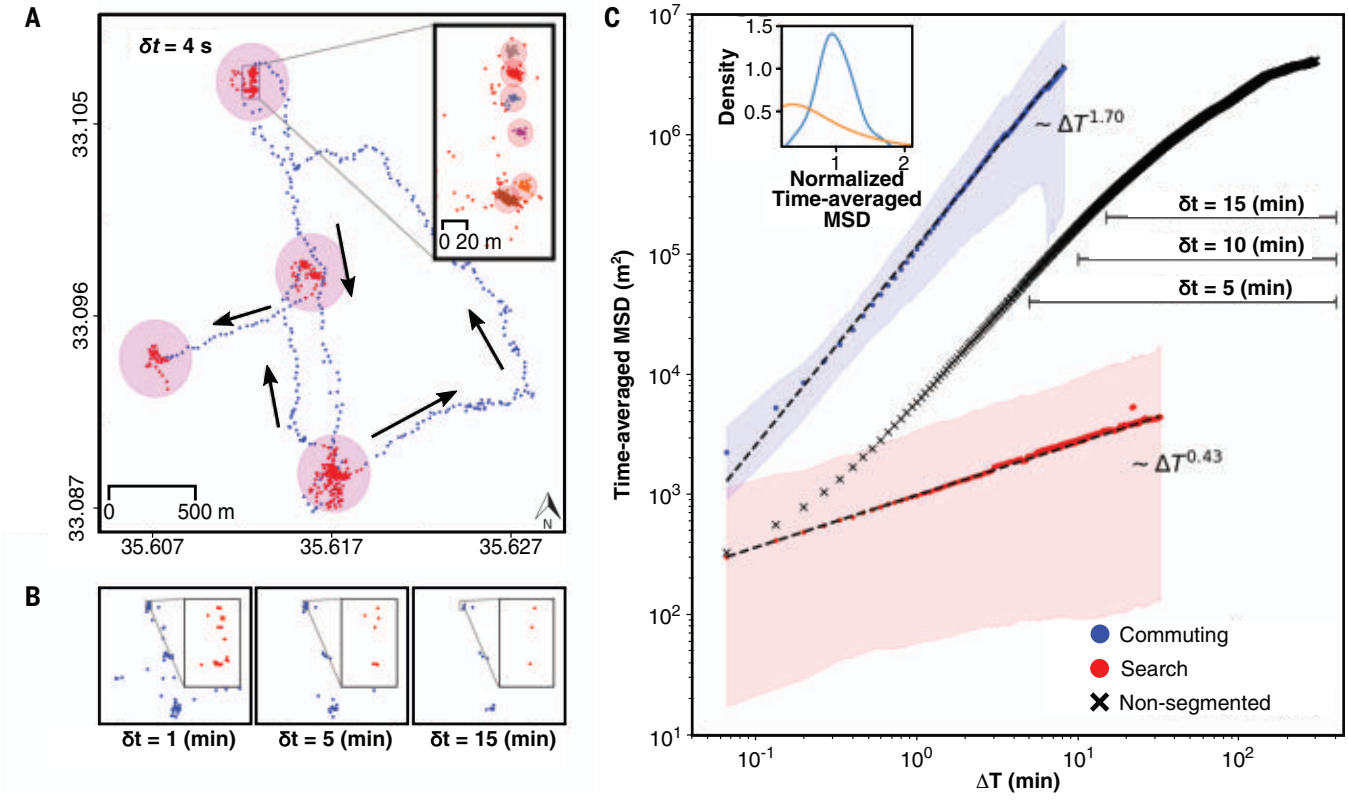

Fig. 5. Detecting commonalities and differences in animal movement and behavior across multiple spatiotemporal scales. Segmentation of a 3.6-hour track of a single black-winged kite (*E. caeruleus*) randomly selected from 155 days of high-resolution (>10^6 localizations) ATLAS tracking (δt = 4 s) revealing (**A**) four segments of area-restricted search (ARS, red dots within purple circles) connected by commuting flights (blue dots with black arrows showing direction). Zooming into one ARS (inset) reveals six local clusters (orange circles), which cannot be detected using lower-resolution data (**B**) that entail insufficient information (only 34, 7, and 3 ARS localizations for δt = 1, 5, and 15 min, respectively), compared with the high-resolution data (δt = 4 s; 491 localizations). (**C**) Time-averaged mean square displacement (MSD) of nonsegmented daily tracks recorded across 155 days (black crosses), which is not well fitted to a single power-law exponent across all temporal scales, but has a steeper slope indicating superdiffusive motion at ΔT < 100 min and a shallower slope indicating subdiffusive motion ΔT > 100 min. Segmenting the track to commuting and ARS (blue and red shaded areas, representing 90% of the trajectories), a clear distinction emerges between superdiffusive ergodic commuting (blue) and subdiffusive nonergodic ARS (red) (*35*). For the ARS, the distribution of the measured time-averaged MSD around the mean is large and skewed, indicating nonergodicity (inset, orange line), in contrast to the commuting (inset, blue line). Lower sampling frequencies are insufficient to detect such trends, as they hold information on a notably more limited temporal range, as indicated by the bars for δt = 5, 10, and 15 min.

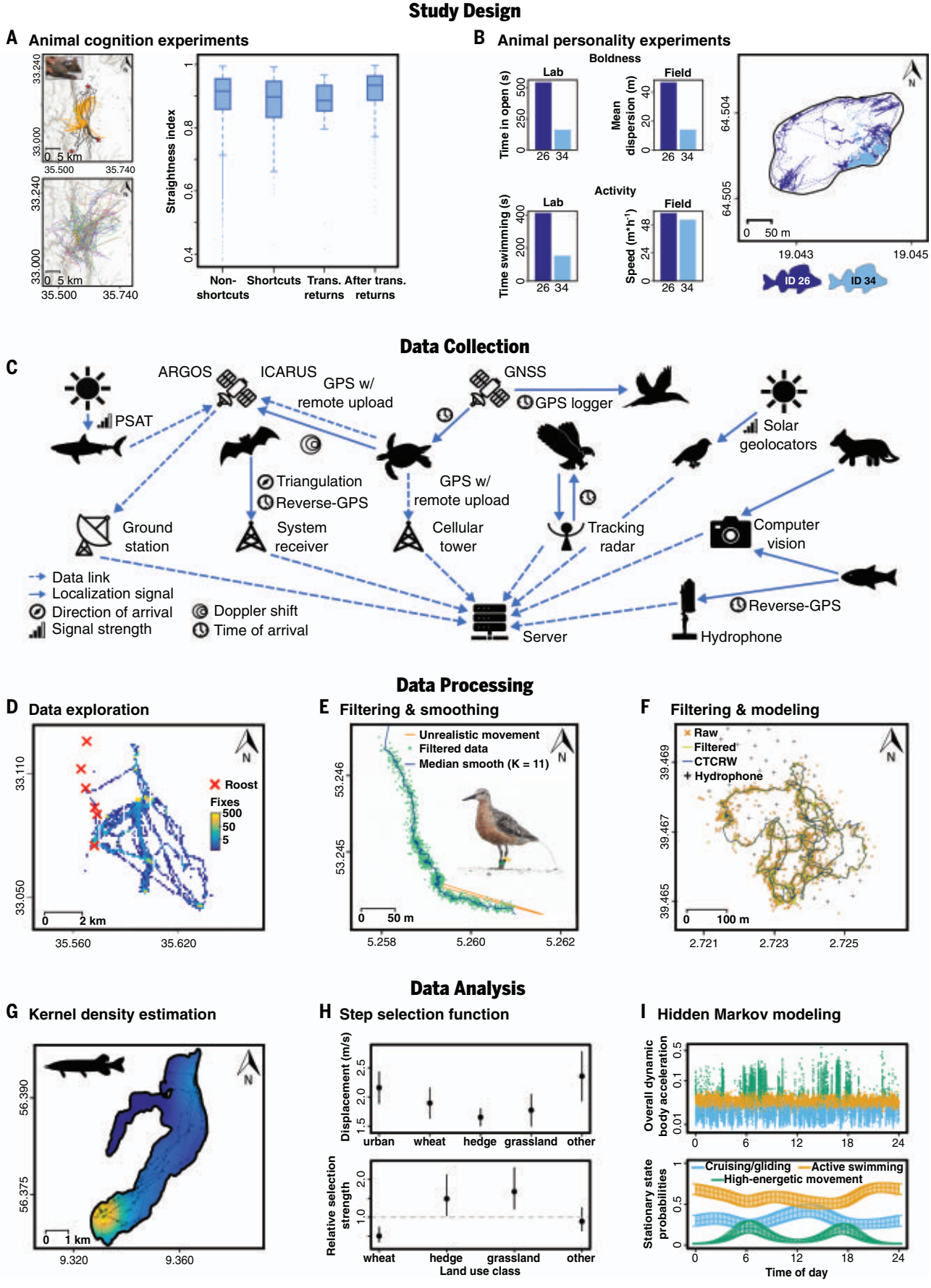
Study Design
A Animal cognition experiments
Straightness index
Non-shortcuts
Shortcuts
Trans. returns
After trans. returns
B Animal personality experiments
Boldness
Lab
Field
Time in open (s)
Mean dispersion (m)
Activity
Time swimming (s)
Speed (m*h-1)
ID 26
ID 34
Data Collection
C
ARGOS
ICARUS
GPS w/ remote upload
GNSS
GPS logger
PSAT
Solar geolocators
Triangulation
Reverse-GPS
GPS w/ remote upload
Ground station
System receiver
Cellular tower
Tracking radar
Computer vision
Data link
Localization signal
Direction of arrival
Signal strength
Doppler shift
Time of arrival
Server
Reverse-GPS
Hydrophone
Data Processing
D Data exploration
Roost
Fixes
E Filtering & smoothing
Unrealistic movement
Filtered data
Median smooth (K = 11)
F Filtering & modeling
Raw
Filtered
CTCRW
Hydrophone
Data Analysis
G Kernel density estimation
H Step selection function
Displacement (m/s)
urban
wheat
hedge
grassland
other
Relative selection strength
Land use class
I Hidden Markov modeling
Overall dynamic body acceleration
Cruising/gliding
Active swimming
High-energetic movement
Stationary state probabilities
Time of day

Fig. 6. Key steps in high-throughput movement ecology research. (**A**) ATLAS-tracked (δt = 1 to 8 s) Egyptian fruit bats (*R. aegyptiacus*), after being translocated to the periphery of their foraging range, returned to their specific foraging tree along straight trajectories (black lines), similar to nonmanipulated individuals taking shortcuts, altogether complementing field evidence for the existence of a cognitive map (*10*). (**B**) Evidence for consistent differences between bolder and more active (purple) versus shy and less active (blue) European perch (*Perca fluviatilis*) as observed in lab trials and after release to the wild. (**C**) An overview of primary wildlife tracking technologies. Referring to the animal icons from left to right and from top to bottom, the illustration shows (shark) popup PSAT tags that report Doppler, solar, or temperature geolocation through a satellite data link; (bat) automatic radio triangulation or reverse-GPS tags; (sea turtle) Doppler ARGOS tags and GPS tags that upload location through a satellite or cellular link; (eagle) radar tracking; (gannet) GPS logger; (small bird) solar geolocators; (fox) computer vision tracking; and (fish) computer vision tracking or ultrasonic aquatic reverse-GPS. Raw datasets are often subject to (**D**) exploratory data analysis, such as initial assessment of space use by ATLAS-tracked Egyptian fruit bats in relation to roosts and fruit trees, filtered to remove unrealistic movements and further processed and smoothed as illustrated for (**E**) ATLAS-tracked (δt = 9 s) red knots (*Calidris canutus*) and (**F**) acoustic trilateration tracking (δt = 2 to 10 s) of a rough ray (*Raja radula*) (*28*). In the following data analysis step, researchers can apply various statistical methods to extract information from high-throughput data to investigate, for example, (**G**) space use by a pike (*E. lucius*) using kernel density smoothing and residence patch analysis; (**H**) habitat selection assessed by applying integrated step-selection functions to ATLAS data (δt = 8 s) of yellowhammers (*Emberiza citrinella*), revealing that birds move faster in land-use classes that they avoid relative to urban areas; and (**I**) diel changes in the behavior of an oceanic whitetip shark (*Carcharhinus longimanus*) inferred from acceleration data using a hidden Markov model.

traits can be introduced to novel wild environments, to test predictions on trait-movement associations. For example, ATLAS-tracked (δt = 4 s) juvenile pheasants that exhibited higher spatial cognition under controlled conditions were slower to explore their landscape shortly after release into the wild but showed notable improvement after a few weeks (*32*) (Fig. 2A). Although behavioral and cognitive traits measured in confined controlled versus wild conditions might be similar (e.g., Fig. 6B), trait expression, variability, and among-trait correlations are extremely context-dependent, and hence can differ between laboratory and wild conditions (*70*). Finally, individual states can be manipulated and the outcome in the wild can be monitored to examine long-term consequences of short-term environmental stress. For example, acoustic trilateration (δt = 1 min) of largemouth bass (*Micropterus salmoides*) in a lake revealed both a short-term (first few days) response to experimentally induced stress of increased activity, and unexpected long-term (multiple months) carry-over effects rendering stressed fish vulnerable to hypoxia in winter (*21*).

Data collection

Wild animals are tracked using four fundamental methodologies (*20*): Two of these use an electronic animal-borne tag that either transmits a signal (transmitter localization) or receives or senses a signal (receiver-sensor localization), whereas the other two use animals or tags that reflect either an ambient signal (passive reflection) or a signal emitted by the tracking system (active reflection) (Fig. 6C). These systems can use radio, acoustic, or visual signals, as well as temperature, pressure, and other environmental cues. Transmitter localization systems require animal capture and tagging, whereas reflection systems can noninvasively track nontagged animals. In receiver-sensor localization systems, data are collected on the tag and must be retrieved by remote upload or animal recapture (*9*).

The five primary high-throughput wildlife tracking technologies (Fig. 1) differ in their compliance with high-throughput criteria. Reverse-GPS systems are transmitter localization systems that track transmitting tags through an array of receivers by time-of-arrival estimation (trilateration). The term "reverse-GPS" emphasizes that, similar to GPS, these are accurate trilateration-based systems, but unlike GPS, raw data and localizations are collected by the system and not on the tag. Reverse-GPS systems use small, energy-efficient, and inexpensive tags, which can be used to track multiple animals simultaneously at high spatiotemporal resolution (typically δt = 1 to 10 s, 1 to 5 m median spatial error) and hence regularly provide high-throughput data. These systems include acoustic trilateration of aquatic animals (*21*–*30*) and radio trilateration of terrestrial animals (e.g., ATLAS) (*10*, *20*, *31*–*35*). Historically, reverse-GPS techniques were applied to track wildlife >50 years ago (*71*, *72*) but did not reach high-throughput capacity until after automation during the past decade and even more recently for terrestrial systems (Fig. 1C). Their main limitations are relatively restricted range (≤100 km) and installation costs.

GPS and GPS-like systems are receiver localization systems that track tags by trilateration using a satellite constellation. GPS systems with upload capability retrieve data from tags through a satellite or cellular link, allowing global coverage at low-resolution mode (typically δt = 15 min to 1 day) and regional coverage (a few hundred kilometers) at high-resolution mode (*11*, *12*, *36*, *37*–*40*). However, GPS tags are expensive and relatively heavy as satellite and cellular links and onboard localization calculations impose energy costs, limiting these heavier tags to larger animals (though less so with solar charging), thus reducing cost-effectiveness. GPS loggers lacking remote upload facilitate collection of high-resolution data (δ = 0.1 to 1 s) from additional sensors (e.g., accelerometers), which are useful for estimating energy expenditure, identifying behaviors (*73*) and neighbors (*43*), and further refining path resolution through dead reckoning (*74*). However, they require animal recapture or tag recollection (*9*), which further limits spatial coverage and applicability.

Tracking radars use active reflection of radio signals and are capable of collecting extensive movement data of many nontagged animals simultaneously at high spatiotemporal resolution [e.g., δt = 1 s (*46*)]. However, they rely on expensive and highly specialized radio transceivers, have limited ability to identify species or individuals, and are usually limited to local or regional scales. Computer-vision algorithms based on modern machine learning approaches, such as convolutional neural networks, can be applied to noninvasively (i.e., without trapping and tagging) track wild birds (*47*) and fish (*49*, *50*, *51*) in their natural habitats at very high spatiotemporal resolution (e.g., δt = 0.03 s). However, camera tracking in the wild is typically limited to short ranges, an individual's identity cannot be maintained across videos without natural or artificial marking, tracking multiple individuals is still computationally demanding and time-consuming, and the tracking period is usually short (often ≤30 min) or intermittent.

Data processing and analysis

As in other fields, managing, processing, and analyzing massive datasets in a timely manner present major challenges (*75*). The computing infrastructure needed to store and analyze data is expensive and generates a large carbon footprint (*33*, *76*). Solutions may be inspired from other big-data fields, such as genomics (*6*), remote sensing (*77*), and human mobility (*75*), including robust exploratory data analysis and automated reproducible data-processing pipelines (*6*). Big-data exploration can be facilitated by spatial heatmaps of localizations (Fig. 6D) or by plotting individual tracks and distributions of key movement metrics such as speed. These first steps are crucial to identify patterns in the ecological processes observed, as well as location errors such as outliers (Fig. 6, D and E).

Preprocessing pipelines can then prepare the full dataset for statistical analyses by filtering unrealistic movement (*33*, *76*), after

which animal paths can be approximated from raw localizations using smoothing methods (*33*) (Fig. 6E), or by fitting a movement model such as a continuous-time correlated random walk (*28*) (Fig. 6F). Even after removal of technology-induced outliers, accounting for positioning error is critical, and effective error calibration and emerging methods for modeling data error structure can be used to improve positioning estimates of animal movement (*78*). Although position data from high-throughput technologies are generally more accurate than data from low-throughput ones (*17*), the high sampling frequency implies that location errors are autocorrelated, motivating further upgrades of calibration models (*78*), movement metrics (*18*), and space use estimates (*79*). Similar pipelines can be built for movement-associated data such as 3D acceleration (*80*) (Fig. 6G).

Practically, commercial GPS devices nearly always employ on-board data filtering and smoothing algorithms. Similarly, raw data from acoustic trilateration tags are typically processed by proprietary software to obtain position estimates, rendering these procedures a "black-box" for data users. The development and ownership of new high-throughput technologies by movement ecologists themselves, such as Yet-Another-Positioning-Solver (YAPS) (*24*) and ATLAS (*10*), could help the development of transparent and well-documented raw-data processing pipelines. Pipeline reproducibility can be improved by adopting computational science best practices, such as unit testing components for correct data handling, version control, and continuous integration testing (*6*, *81*). Increasing pipeline efficiency can allow massive datasets—which currently range between 10^6 and 10^9 data points per study for basic movement data alone (Fig. 1C)—to be processed on conventional computing hardware. Use of compiled languages for pipeline backends and parallel computing can reduce computational times (*6*, *77*).

Big data reinforce a trade-off between complex models that aim to adequately mimic individual decision-making in a rich physical or social environment but are challenging to work with, and simpler approaches that are easier to implement but may oversimplify the biological process or suffer from statistical shortcomings such as a lack of uncertainty propagation or inadequate modeling of the autocorrelation structure (*82*). Analytical approaches for movement data include home range analyses (*79*) (Fig. 6G), social network analyses (*37*, *41*), and time-varying integrated step-selection functions (*83*, *84*) (Fig. 6H). More complex individual-level or group-dynamic movement models such as stochastic differential equations or (hierarchical) hidden Markov models (Fig. 6I) have been developed over the past decade, with user-friendly software packages to aid implementation (*2*, *82*). Further methodological advancements allow identification of how individual foraging attempts are driven by highly dynamic local environments (*85*), as well as relating individual movement to that of nearby conspecifics (*86*). Individual behaviors can be classified from high-resolution GPS and acceleration data using machine learning algorithms (*39*, *40*, *73*, *87*) and identified behaviors can then be related to individual attributes and/or environmental features (*53*, *55*, *88*). However, elucidating the drivers of individual movement variation remains challenging (*53*).

One promising approach, recently proposed for related challenges in geographical, social, and computer sciences, combines computationally demanding agent-based models and data demanding deep learning methods to decode hidden mechanisms from high-throughput data (*89*, *90*). Agent-based models can reveal the emergence of system-level patterns from local-level behaviors and interactions of system components (*91*). Using genetic algorithms, initial candidate rulesets for individual decision-making can evolve into a robust ruleset that is able to reproduce the unique range and quality of spatial and temporal patterns in high-throughput data ("reinforcement learning" (*89*)]. Such patterns can be revealed by applying machine learning methods, including neural networks and deep learning (*90*). The combination of multiple patterns in high-throughput datasets at different hierarchical levels and scales leads to unprecedented model robustness, optimized model complexity, and reduced uncertainty (*91*). In this pattern-driven process, model specification, calibration, and validation steps are all implemented dynamically and iteratively during the model runtime, thus enabling "learning on the go" (*89*). Overall, the increased availability of high-throughput data will continue to motivate the uptake, refinement, and development of novel methods for both data processing and analysis (*3*, *84*, *86*, *87*, *92*).

Collaborative networks

By permitting comparisons of animal movement across sites, times, and species, high-throughput technologies can motivate large collaborative networks to address questions on animal adaptations and plastic responses to climate and other environmental changes. Notable examples include the Ocean Tracking Network (*93*), the European Tracking Network (*94*), and the Arctic Animal Movement Archive (*95*). Such collaborative networks and platforms guide the process of establishment and maintenance of tracking infrastructure, facilitate efficient exchange of data, knowledge, analytical tools, software packages, and preprocessing pipelines, and offer valuable opportunities for scaling up study areas, addressing broader ecological questions, training, outreach, and funding acquisition (*75*, *96*). Enhanced cooperation among traditionally separate disciplines such as ecology, computer science, engineering, bioinformatics, statistical physics, epidemiology, geography, and social sciences is crucial for advancing movement ecology research and facilitating efficient education and outreach.

Major challenges and future directions

Key high-throughput technologies provide the means to characterize, in fine resolution, what individual animals do in their natural ecological context. Although low-resolution data might potentially provide equivalent information by increasing sample size (e.g., tracking many more individuals), acquiring sufficiently large sample sizes is often impractical, and sample size should be kept as low as possible, not only for cost considerations but also for ethical reasons. However, despite their very broad scope, high-throughput technologies cannot by themselves cover all aspects of movement ecology research, mostly because they are practically and naturally limited to studies at local and regional spatial scales (currently ≤100 km) and/or intermediate durations (days to a few years). Although advances in tag technologies (miniaturization, energy harvesting, data storage, and communication) predict better high-throughput performance (e.g., higher temporal resolution and/or longer periods), spatial scale may remain limited for at least the near future. Projects focusing on larger spatiotemporal scales (*11*, *55*, *67*) are inherently confined to low-throughput tracking, with data collected at much lower frequencies or at much higher costs per tracked individual though they may still yield large datasets. These include automatic triangulation systems such as MOTUS (*97*), Doppler-based receiver localization systems (*98*), the new satellite-based ICARUS system, and geolocators (*99*). We thus see high- and low-throughput technologies as complementary rather than competing alternatives and advocate for their integration (*1*, *65*). We also call for better integration among high-throughput technologies, especially between reverse-GPS systems and computer vision, to provide detailed information on both tagged and nontagged interacting animals and their environments. Challenges in integrating contemporary tracking technologies—which hinder progress in addressing both small- and large-scale and single- and cross-taxa questions in addition to attempts to scale up from individual-based information to populations and communities (*100*)—could be addressed through better cooperation and coordination between manufacturers and users (*29*, *96*). Extending tracking duration and range, ideally to span the lifetime of tracked animals, is important for elucidating how behavior, cognition, and physiology develop

across spatial and temporal scales and in relation to environmental changes. Accomplishing this goal also requires further technological developments and greater integration of contextual environmental data with high-throughput movement data, linking movement ecology with studies of climate and environmental change.

REFERENCES AND NOTES

1. R. Nathan *et al*., A movement ecology paradigm for unifying organismal movement research. *Proc. Natl. Acad. Sci. U.S.A.* **105**, 19052–19059 (2008). doi: 10.1073/pnas.0800375105; pmid: 19060196
2. R. Joo *et al*., Navigating through the R packages for movement. *J. Anim. Ecol.* **89**, 248–267 (2020). doi: 10.1111/1365-2656.13116; pmid: 31587257
3. H. J. Williams *et al*., Optimizing the use of biologgers for movement ecology research. *J. Anim. Ecol.* **89**, 186–206 (2020). doi: 10.1111/1365-2656.13094; pmid: 31424571
4. N. E. Hussey *et al*., Aquatic animal telemetry: A panoramic window into the underwater world. *Science* **348**, 1255642 (2015). doi: 10.1126/science.1255642; pmid: 26068859
5. R. Kays, M. C. Crofoot, W. Jetz, M. Wikelski, Terrestrial animal tracking as an eye on life and planet. *Science* **348**, aaa2478 (2015). doi: 10.1126/science.aaa2478; pmid: 26068858
6. E. E. Schadt, M. D. Linderman, J. Sorenson, L. Lee, G. P. Nolan, Computational solutions to large-scale data management and analysis. *Nat. Rev. Genet.* **11**, 647–657 (2010). doi: 10.1038/nrg2857; pmid: 20717155
7. J. A. Reuter, D. V. Spacek, M. P. Snyder, High-throughput sequencing technologies. *Mol. Cell* **58**, 586–597 (2015). doi: 10.1016/j.molcel.2015.05.004; pmid: 26000844
8. C. J. Butts-Wilmsmeyer, S. Rapp, B. Guthrie, The technological advancements that enabled the age of big data in the environmental sciences: A history and future directions. *Curr. Opin. Environ. Sci. Health* **18**, 63–69 (2020). doi: 10.1016/j.coesh.2020.07.006
9. L. Harten, A. Katz, A. Goldshtein, M. Handel, Y. Yovel, The ontogeny of a mammalian cognitive map in the real world. *Science* **369**, 194–197 (2020). doi: 10.1126/science.aay3354; pmid: 32647001
10. S. Toledo *et al*., Cognitive map-based navigation in wild bats revealed by a new high-throughput tracking system. *Science* **369**, 188–193 (2020). doi: 10.1126/science.aax6904; pmid: 32647000
11. H. Weimerskirch, C. Bishop, T. Jeanniard-du-Dot, A. Prudor, G. Sachs, Frigate birds track atmospheric conditions over months-long transoceanic flights. *Science* **353**, 74–78 (2016). doi: 10.1126/science.aaf4374; pmid: 27365448
12. H. J. Williams *et al*., Physical limits of flight performance in the heaviest soaring bird. *Proc. Natl. Acad. Sci. U.S.A.* **117**, 17884–17890 (2020). doi: 10.1073/pnas.1907360117; pmid: 32661147
13. M. A. Tucker *et al*., Moving in the Anthropocene: Global reductions in terrestrial mammalian movements. *Science* **359**, 466–469 (2018). doi: 10.1126/science.aam9712; pmid: 29371471
14. M. A. Hindell *et al*., Tracking of marine predators to protect Southern Ocean ecosystems. *Nature* **580**, 87–92 (2020). doi: 10.1038/s41586-020-2126-y; pmid: 32238927
15. R. Macarron *et al*., Impact of high-throughput screening in biomedical research. *Nat. Rev. Drug Discov.* **10**, 188–195 (2011). doi: 10.1038/nrd3368; pmid: 21358738
16. C. E. Shannon, Communication in the presence of noise, *Proc. IRE* **37**, 10–21 (1949). doi: 10.1109/JRPROC.1949.232969
17. J. M. Rowcliffe, C. Carbone, R. Kays, B. Kranstauber, P. A. Jansen, Bias in estimating animal travel distance: The effect of sampling frequency. *Methods Ecol. Evol.* **3**, 653 (2012). doi: 10.1111/j.2041-210X.2012.00197.x
18. M. J. Noonan *et al*., Scale-insensitive estimation of speed and distance traveled from animal tracking data. *Mov. Ecol.* **7**, 35 (2019). doi: 10.1186/s40462-019-0177-1; pmid: 31788314
19. P. G. Ryan, S. L. Petersen, G. Peters, D. Grémillet, GPS tracking a marine predator: The effects of precision, resolution and sampling rate on foraging tracks of African Penguins. *Mar. Biol.* **145**, 215–223 (2004). doi: 10.1007/s00227-004-1328-4
20. S. Toledo, *Location Estimation from the Ground Up* (SIAM, 2020).
21. C. M. O'Connor *et al*., Seasonal carryover effects following the administration of cortisol to a wild teleost fish. *Physiol. Biochem. Zool.* **83**, 950–957 (2010). doi: 10.1086/656286; pmid: 20932160
22. H. Baktoft *et al*., Performance assessment of two whole-lake acoustic positional telemetry systems—Is reality mining of free-ranging aquatic animals technologically possible? *PLOS ONE* **10**, e0126534 (2015). doi: 10.1371/journal.pone.0126534; pmid: 26000459
23. A. T. Piper *et al*., Response of seaward-migrating European eel (*Anguilla anguilla*) to manipulated flow fields. *Proc. Biol. Sci.* **282**, 20151098 (2015). doi: 10.1098/rspb.2015.1098; pmid: 26136454
24. H. Baktoft, K. Ø. Gjelland, F. Økland, U. H. Thygesen, Positioning of aquatic animals based on time-of-arrival and random walk models using YAPS (Yet Another Positioning Solver). *Sci. Rep.* **7**, 14294 (2017). doi: 10.1038/s41598-017-14278-z; pmid: 29084968
25. J. W. Brownscombe *et al*., Ecology of exercise in wild fish: Integrating concepts of individual physiological capacity, behavior, and fitness through diverse case studies. *Integr. Comp. Biol.* **57**, 281–292 (2017). doi: 10.1093/icb/icx012; pmid: 28859404
26. T. Mehner *et al*., Whole-lake experimental addition of angler's ground bait strongly affects omnivorous fish despite low contribution to lake carbon budget. *Ecosystems* **22**, 346–362 (2019). doi: 10.1007/s10021-018-0273-x
27. C. T. Monk *et al*., Behavioural and fitness effects of translocation to a novel environment: Whole-lake experiments in two aquatic top predators. *J. Anim. Ecol.* **89**, 2325–2344 (2020). doi: 10.1111/1365-2656.13298; pmid: 32654123
28. E. Aspillaga *et al*., Performance of a novel system for high-resolution tracking of marine fish societies. *Anim. Biotelem.* **9**, 1 (2021). doi: 10.1186/s40317-020-00224-w
29. R. J. Lennox *et al*., A role for lakes in revealing the nature of animal movement using high dimensional telemetry systems. *Mov. Ecol.* **9**, 40 (2021). doi: 10.1186/s40462-021-00244-y; pmid: 34321114
30. C. T. Monk *et al*., The battle between harvest and natural selection creates small and shy fish. *Proc. Natl. Acad. Sci. U.S.A.* **118**, e2009451118 (2021). doi: 10.1073/pnas.2009451118; pmid: 33619086
31. C. E. Beardsworth *et al*., Is habitat selection in the wild shaped by individual-level cognitive biases in orientation strategy? *Ecol. Lett.* **24**, 751–760 (2021). doi: 10.1111/ele.13694; pmid: 33616308
32. C. E. Beardsworth *et al*., Spatial cognitive ability is associated with transitory movement speed but not straightness during the early stages of exploration. *R. Soc. Open Sci.* **8**, 201758 (2021). doi: 10.1098/rsos.201758; pmid: 33959338
33. P. R. Gupte, C. E. Beardsworth, O. Spiegel, E. Lourie, S. Toledo, R. Nathan, A. I. Bijleveld, A guide to pre-processing high-throughput animal tracking data. *J. Anim. Ecol.* **91**, 287–307 (2022). doi: 10.1111/1365-2656.13610; pmid: 34657296
34. E. Lourie, I. Schiffner, S. Toledo, R. Nathan, Memory and conformity, but not competition, explain spatial partitioning between two neighboring fruit bat colonies. *Front. Ecol. Evol.* **9**, 732514 (2021). doi: 10.3389/fevo.2021.732514
35. O. Vilk, Y. Orchan, M. Charter, N. Ganot, S. Toledo, R. Nathan, M. Assaf, Ergodicity breaking in area-restricted search of avian predators. arXiv:2101.11527 [q-bio.PE] (2021).
36. J. K. Sheppard, A. McGann, M. Lanzone, R. R. Swaisgood, An autonomous GPS geofence alert system to curtail avian fatalities at wind farms. *Anim. Biotelem.* **3**, 43 (2015). doi: 10.1186/s40317-015-0087-y
37. A. Strandburg-Peshkin, D. R. Farine, I. D. Couzin, M. C. Crofoot, Shared decision-making drives collective movement in wild baboons. *Science* **348**, 1358–1361 (2015). doi: 10.1126/science.aaa5099; pmid: 26089514
38. R. Harel, N. Horvitz, R. Nathan, Adult vultures outperform juveniles in challenging thermal soaring conditions. *Sci. Rep.* **6**, 27865 (2016). doi: 10.1038/srep27865; pmid: 27291590
39. E. Browning *et al*., Predicting animal behaviour using deep learning: GPS data alone accurately predict diving in seabirds. *Methods Ecol. Evol.* **9**, 681–692 (2018). doi: 10.1111/2041-210X.12926
40. T. Maekawa *et al*., Deep learning-assisted comparative analysis of animal trajectories with DeepHL. *Nat. Commun.* **11**, 5316 (2020). doi: 10.1038/s41467-020-19105-0; pmid: 33082335
41. D. Papageorgiou, D. R. Farine, Shared decision-making allows subordinates to lead when dominants monopolize resources. *Sci. Adv.* **6**, eaba5881 (2020). doi: 10.1126/sciadv.aba5881; pmid: 33239284
42. H. Weimerskirch *et al*., Ocean sentinel albatrosses locate illegal vessels and provide the first estimate of the extent of nondeclared fishing. *Proc. Natl. Acad. Sci. U.S.A.* **117**, 3006–3014 (2020). doi: 10.1073/pnas.1915499117; pmid: 31988130
43. S. Greif, Y. Yovel, Using on-board sound recordings to infer behaviour of free-moving wild animals. *J. Exp. Biol.* **222** (suppl 1.), jeb184689 (2019). doi: 10.1242/jeb.184689; pmid: 30728226
44. B. L. Clark *et al*., Sexual segregation of gannet foraging over 11 years: Movements vary but isotopic differences remain stable. *Mar. Ecol. Prog. Ser.* **661**, 1–16 (2021). doi: 10.3354/meps13636
45. D. W. Sankey *et al*., Absence of "selfish herd" dynamics in bird flocks under threat. *Curr. Biol.* **31**, 3192–3198 (2021). doi: 10.1016/j.cub.2021.05.009
46. N. Horvitz *et al*., The gliding speed of migrating birds: Slow and safe or fast and risky? *Ecol. Lett.* **17**, 670–679 (2014). doi: 10.1111/ele.12268; pmid: 24641086
47. M. Ballerini *et al*., Interaction ruling animal collective behavior depends on topological rather than metric distance: Evidence from a field study. *Proc. Natl. Acad. Sci. U.S.A.* **105**, 1232–1237 (2008). doi: 10.1073/pnas.0711437105; pmid: 18227508
48. L. Seuront, H. E. Stanley, Anomalous diffusion and multifractality enhance mating encounters in the ocean. *Proc. Natl. Acad. Sci. U.S.A.* **111**, 2206–2211 (2014). doi: 10.1073/pnas.1322363111; pmid: 24469823
49. V. Raoult, L. Tosetto, J. E. Williamson, Drone-based high-resolution tracking of aquatic vertebrates. *Drones (Basel)* **2**, 37 (2018). doi: 10.3390/drones2040037
50. F. A. Francisco, P. Nührenberg, A. Jordan, High-resolution, non-invasive animal tracking and reconstruction of local environment in aquatic ecosystems. *Mov. Ecol.* **8**, 27 (2020). doi: 10.1186/s40462-020-00214-w; pmid: 32582448
51. A. Engel *et al*., In situ three-dimensional video tracking of tagged individuals within site-attached social groups of coral-reef fish. *Limnol. Oceanogr. Meth.* **19**, 579–588 (2021). doi: 10.1002/lom3.10444
52. A. K. Shaw, Causes and consequences of individual variation in animal movement. *Mov. Ecol.* **8**, 12 (2020). doi: 10.1186/s40462-020-0197-x; pmid: 32099656
53. O. Spiegel, S. T. Leu, C. M. Bull, A. Sih, What's your move? Movement as a link between personality and spatial dynamics in animal populations. *Ecol. Lett.* **20**, 3–18 (2017). doi: 10.1111/ele.12708; pmid: 28000433
54. Q. M. R. Webber *et al*., The ecology of individual differences empirically applied to space-use and movement tactics. *Am. Nat.* **196**, E1–E15 (2020). doi: 10.1086/708721; pmid: 32552106
55. S. Rotics *et al*., Early-life behaviour predicts first-year survival in a long-distance avian migrant. *Proc. Biol. Sci.* **288**, 20202670 (2021). doi: 10.1098/rspb.2020.2670; pmid: 33434462
56. N. Ranc, P. R. Moorcroft, F. Ossi, F. Cagnacci, Experimental evidence of memory-based foraging decisions in a large wild mammal. *Proc. Natl. Acad. Sci. U.S.A.* **118**, e2014856118 (2021). doi: 10.1073/pnas.2014856118; pmid: 33837149
57. D. Cabrera, J. R. Nilsson, B. D. Griffen, The development of animal personality across ontogeny: A cross-species review. *Anim. Behav.* **173**, 137–144 (2021). doi: 10.1016/j.anbehav.2021.01.003
58. D. R. Daversa, A. Fenton, A. I. Dell, T. W. J. Garner, A. Manica, Infections on the move: How transient phases of host movement influence disease spread. *Proc. Biol. Sci.* **284**, 20171807 (2017). doi: 10.1098/rspb.2017.1807; pmid: 29263283
59. S. Creel, J. A. Winnie Jr., D. Christianson, Underestimating the frequency, strength and cost of antipredator responses with data from GPS collars: An example with wolves and elk. *Ecol. Evol.* **3**, 5189–5200 (2013). doi: 10.1002/ece3.896; pmid: 24455148
60. T. Tregenza, Building on the Ideal Free Distribution. *Adv. Ecol. Res.* **26**, 253–307 (1995). doi: 10.1016/S0065-2504(08)60067-7
61. P. Amarasekare, Competitive coexistence in spatially structured environments: A synthesis. *Ecol. Lett.* **6**, 1109–1122 (2003). doi: 10.1046/j.1461-0248.2003.00530.x
62. A. I. Bijleveld, E. O. Folmer, T. Piersma, Experimental evidence for cryptic interference among socially foraging shorebirds. *Behav. Ecol.* **23**, 806–814 (2012). doi: 10.1093/beheco/ars034
63. J. Wall, G. Wittemyer, B. Klinkenberg, I. Douglas-Hamilton, Novel opportunities for wildlife conservation and research with real-time monitoring. *Ecol. Appl.* **24**, 593–601 (2014). doi: 10.1890/13-1971.1; pmid: 24988762

64. J. M. Fryxell *et al*., Multiple movement modes by large herbivores at multiple spatiotemporal scales. *Proc. Natl. Acad. Sci. U.S.A.* **105**, 19114–19119 (2008). doi: 10.1073/pnas.0801737105; pmid: 19060190
65. S. Benhamou, Of scales and stationarity in animal movements. *Ecol. Lett.* **17**, 261–272 (2014). doi: 10.1111/ele.12225; pmid: 24350897
66. A. Soleymani *et al*., Integrating cross-scale analysis in the spatial and temporal domains for classification of behavioral movement. *J. Spat. Inf. Sci.* **8**, 1–25 (2014). doi: 10.5311/josis.2014.8.162
67. C. J. Torney, J. G. C. Hopcraft, T. A. Morrison, I. D. Couzin, S. A. Levin, From single steps to mass migration: The problem of scale in the movement ecology of the Serengeti wildebeest. *Philos. Trans. R. Soc. B.* **373**, 20170012 (2018). doi: 10.1098/rstb.2017.0012; pmid: 29581397
68. G. M. Viswanathan *et al*., Optimizing the success of random searches. *Nature* **401**, 911–914 (1999). doi: 10.1038/44831; pmid: 10553906
69. M. Mangalam, D. G. Kelty-Stephen, Point estimates, Simpson's paradox, and nonergodicity in biological sciences. *Neurosci. Biobehav. Rev.* **125**, 98–107 (2021). doi: 10.1016/j.neubiorev.2021.02.017; pmid: 33621638
70. S. J. Cooke *et al*., Remote bioenergetics measurements in wild fish: Opportunities and challenges. *Comp. Biochem. Physiol. A Mol. Integr. Physiol.* **202**, 23–37 (2016). doi: 10.1016/j.cbpa.2016.03.022; pmid: 27063208
71. J. J. Craighead, F. C. Craighead Jr., J. R. Varney, C. E. Cote, Satellite Monitoring of Black Bear. *Bioscience* **21**, 1206–1212 (1971). doi: 10.2307/1296018
72. A. D. Hawkins, D. N. MacLennan, G. G. Urquhart, C. Robb, Tracking cod *Gadus morhua* L. in a Scottish sea loch. *J. Fish Biol.* **6**, 225–236 (1974). doi: 10.1111/j.1095-8649.1974.tb04541.x
73. R. Nathan *et al*., Using tri-axial acceleration data to identify behavioral modes of free-ranging animals: General concepts and tools illustrated for griffon vultures. *J. Exp. Biol.* **215**, 986–996 (2012). doi: 10.1242/jeb.058602; pmid: 22357592
74. O. R. Bidder *et al*., Step by step: Reconstruction of terrestrial animal movement paths by dead-reckoning. *Mov. Ecol.* **3**, 23 (2015). doi: 10.1186/s40462-015-0055-4; pmid: 26380711
75. M. Thums *et al*., How big data fast tracked human mobility research and the lessons for animal movement ecology. *Front. Mar. Sci.* **5**, 21 (2018). doi: 10.3389/fmars.2018.00021
76. K. Bjørneraas, B. Van Moorter, C. M. Rolandsen, I. Herfindal, Screening global positioning system location data for errors using animal movement characteristics. *J. Wildl. Manage.* **74**, 1361–1366 (2010). doi: 10.1111/j.1937-2817.2010.tb01258.x
77. N. Gorelick *et al*., Google Earth Engine: Planetary-scale geospatial analysis for everyone. *Remote Sens. Environ.* **202**, 18–27 (2017). doi: 10.1016/j.rse.2017.06.031
78. C. H. Fleming *et al*., A comprehensive framework for handling location error in animal tracking data. *bioRxiv* 2020.06.12.130195 [Preprint] (2021); doi: 10.1101/2020.06.12.130195
79. M. J. Noonan *et al*., A comprehensive analysis of autocorrelation and bias in home range estimation. *Ecol. Monogr.* **89**, e01344 (2019). doi: 10.1002/ecm.1344
80. R. P. Wilson *et al*., Estimates for energy expenditure in free-living animals using acceleration proxies: A reappraisal. *J. Anim. Ecol.* **89**, 161–172 (2020). doi: 10.1111/1365-2656.13040; pmid: 31173339
81. H. Wickham, *R Packages: Organize, Test, Document, and Share Your Code* (O'Reilly Media, 2015).
82. T. A. Patterson *et al*., Statistical modelling of individual animal movement: An overview of key methods and a discussion of practical challenges. *AStA Adv. Stat. Anal.* **101**, 399–438 (2017). doi: 10.1007/s10182-017-0302-7
83. T. Avgar, J. R. Potts, M. A. Lewis, M. S. Boyce, Integrated step selection analysis: Bridging the gap between resource selection and animal movement. *Methods Ecol. Evol.* **7**, 619–630 (2016). doi: 10.1111/2041-210X.12528
84. R. Munden *et al*., Why did the animal turn? Time-varying step selection analysis for inference between observed turning-points in high frequency data. *Methods Ecol. Evol.* **12**, 921–932 (2021). doi: 10.1111/2041-210X.13574
85. L. Lieber, R. Langrock, W. A. M. Nimmo-Smith, A bird's-eye view on turbulence: Seabird foraging associations with evolving surface flow features. *Proc. Biol. Sci.* **288**, 20210592 (2021). doi: 10.1098/rspb.2021.0592; pmid: 33906396
86. U. E. Schlägel *et al*., Estimating interactions between individuals from concurrent animal movements. *Methods Ecol. Evol.* **10**, 1234–1245 (2019). doi: 10.1111/2041-210X.13235
87. H. Yu *et al*., An evaluation of machine learning classifiers for next-generation, continuous-ethogram smart trackers. *Mov. Ecol.* **9**, 15 (2021). doi: 10.1186/s40462-021-00245-x
88. A. G. Hertel, P. T. Niemelä, N. J. Dingemanse, T. Mueller, A guide for studying among-individual behavioral variation from movement data in the wild. *Mov. Ecol.* **8**, 30 (2020). doi: 10.1186/s40462-020-00216-8; pmid: 32612837
89. D. B. Fuller, E. F. de Arruda, V. J. M. Ferreira Filho, *Learning-agent*-based simulation for queue network systems. *J. Oper. Res. Soc.* **71**, 1723–1739 (2020). doi: 10.1080/01605682.2019.1633232
90. A. Heppenstall *et al*., Future developments in geographical agent-based models: Challenges and opportunities. *Geogr. Anal.* **53**, 76–91 (2021). doi: 10.1111/gean.12267; pmid: 33678813
91. V. Grimm *et al*., Pattern-oriented modeling of agent-based complex systems: Lessons from ecology. *Science* **310**, 987–991 (2005). doi: 10.1126/science.1116681; pmid: 16284171
92. R. Munden *et al*., Making sense of ultrahigh-resolution movement data: A new algorithm for inferring sites of interest. *Ecol. Evol.* **9**, 265–274 (2018). doi: 10.1002/ece3.4721; pmid: 30680112
93. S. J. Iverson *et al*., The Ocean Tracking Network: Advancing frontiers in aquatic science and management. *Can. J. Fish. Aquat. Sci.* **76**, 1041–1051 (2019). doi: 10.1139/cjfas-2018-0481
94. D. Abecasis *et al*., A review of acoustic telemetry in Europe and the need for a regional aquatic telemetry network. *Anim. Biotelem.* **6**, 12 (2018). doi: 10.1186/s40317-018-0156-0
95. S. C. Davidson *et al*., Ecological insights from three decades of animal movement tracking across a changing Arctic. *Science* **370**, 712–715 (2020). doi: 10.1126/science.abb7080; pmid: 33154141
96. A. M. M. Sequeira *et al*., A standardisation framework for bio-logging data to advance ecological research and conservation. *Methods Ecol. Evol.* **12**, 996–1007 (2021). doi: 10.1111/2041-210X.13593
97. P. Taylor *et al*., The Motus Wildlife Tracking System: A collaborative research network to enhance the understanding of wildlife movement. *Avian Conserv. Ecol.* **12**, art8 (2017). doi: 10.5751/ACE-00953-120108
98. T. E. Strikwerda, H. D. Black, N. Levanon, P. W. Howey, The bird-borne transmitter. *Johns Hopkins APL Tech. Dig.* **6**, 60 (1985).
99. E. S. Bridge *et al*., Advances in tracking small migratory birds: A technical review of light-level geolocation. *J. Field Ornithol.* **84**, 121–137 (2013). doi: 10.1111/jofo.12011
100. U. E. Schlägel *et al*., Movement-mediated community assembly and coexistence. *Biol. Rev. Camb. Philos. Soc.* **95**, 1073–1096 (2020). doi: 10.1111/brv.12600; pmid: 32627362
101. See supplementary materials.

ACKNOWLEDGMENTS

We thank V. Děd, H. Hansen, F. Hölker, K. Ribeiro de Moraes, J. Radinger, M. Šmejkal, and A.T. Souza for helpful comments and discussions on this topic; Y. Bartan, R. Shaish, and A. Levi for help in obtaining data for Fig. 5; and A. Piper for sharing the data for Fig. 4B. **Funding:** This work was supported by the Minerva Center for Movement Ecology, the Minerva Foundation, grants ISF-3277/21, ISF-1272/21, ISF-965/15, ISF-1259/09, ISF-1316/05, MOST 3-17405, JNF/KKL 60-01-221-18, GIF 1316/15, and the Adelina and Massimo Della Pergola Chair of Life Sciences to R.N.; the Marine Science programme within the Research Council of Norway, grant 294926 (CODSIZE) to C.T.M.; the German Ministry of Education and Research (projects Besatzfisch) and Leibniz Community (project BType) to R.A.; the Danish Rod and Net Fishing License Funds to H.B.; DFG-GRK Biomove 2118/1 to F.J, ISF-1919/19 and ISF-965/15 to S.T.; and SCHL 2259/1-1 to U.E.S. We also acknowledge support from the project "Multi-Lake Research of Fish Ecology and Management using High-Resolution 3D Telemetry Systems", funded by ALTER-Net within the Multi Site Research (MSR) initiative to I.J. **Author contributions:** R.N. conceived, conceptualized and coordinated the study; R.N. wrote the manuscript with text input from D.S., R.A., M.A., T.B., S.J.C., F.J., R.L., U.E.S., S.T., and O.V. and edits from M.G.B., P.R.G., I.J., S.S.K., J.R.M., M.A.W., and all other coauthors; C.T.M., H.B., R.N., T.A., J.A., R.A., C.E.B., A.I.B., T.B., P.R.G., R.H., G.H., R.L., E.L., J.R.M., M.Ř., M.R., U.E.S., J.S., S.T., O.V., and M.A.W. designed the figures and movies. **Competing interests:** The authors declare no competing interests. **Data and materials availability:** All unpublished data presented in figures will be made available on Dryad upon acceptance.

SUPPLEMENTARY MATERIALS

science.org/doi/10.1126/science.abg1780
Supplementary Text
References (*102*–*120*)
MDAR Reproducibility Checklist
Movies S1 to S5

10.1126/science.abg1780

RESEARCH ARTICLE SUMMARY

ENVIRONMENTAL TOXINS

From cohorts to molecules: Adverse impacts of endocrine disrupting mixtures

Nicolò Caporale†, Michelle Leemans†, Lina Birgersson†, Pierre-Luc Germain†, Cristina Cheroni†, Gábor Borbély, Elin Engdahl, Christian Lindh, Raul Bardini Bressan, Francesca Cavallo, Nadav Even Chorev, Giuseppe Alessandro D'Agostino, Steven M. Pollard, Marco Tullio Rigoli, Erika Tenderini, Alejandro Lopez Tobon, Sebastiano Trattaro, Flavia Troglio, Matteo Zanella, Åke Bergman, Pauliina Damdimopoulou, Maria Jönsson, Wieland Kiess, Efthymia Kitraki, Hannu Kiviranta, Eewa Nånberg, Mattias Öberg, Panu Rantakokko, Christina Rudén, Olle Söder, Carl-Gustaf Bornehag*‡, Barbara Demeneix*‡, Jean-Baptiste Fini‡, Chris Gennings‡, Joëlle Rüegg*‡, Joachim Sturve‡, Giuseppe Testa*‡

INTRODUCTION: Endocrine disrupting chemicals (EDCs) are compounds that interfere with physiological hormonal regulation. Humans are pervasively exposed to many different EDCs, and a growing body of evidence indicates that early life exposure to such EDC mixtures can induce changes in the human organism that underlie increased susceptibility to diseases throughout the life span, including neurodevelopmental disorders. Chemical regulation is, however, entirely based on the risk assessment of individual compounds, leaving the real-life impact of chemical mixtures unexamined and unregulated. This is relevant insofar as cumulative exposure to multiple compounds may be associated with adverse health outcomes even when the concentrations of individual chemicals fall below the regulatory dose.

RATIONALE: We set out to make the epidemiological associations between exposure to mixtures and health outcomes experimentally tractable, defining molecular pathways and dose responses that could be translated back to actual human exposures and thereby refine current risk assessment practices. As opposed to previous studies that focused on single compounds, we identified and tested an EDC mixture associated with adverse neurodevelopmental outcomes in the Swedish Environmental Longitudinal, Mother and child, Asthma and allergy (SELMA) pregnancy cohort (MIX N) by integrating epidemiological data with experimental toxicology and characterized real life–relevant exposure.

RESULTS: We used weighted quantile sum (WQS) regression to identify chemicals associated with language delay in children and included those chemicals in MIX N. MIX N was synthesized following the relative proportions and total concentrations found in the SELMA cohort. It was then tested in both in vitro and in vivo models. In human fetal primary neural stem cells and three-dimensional cortical brain organoids differentiated from human pluripotent stem cells, transcriptomic analysis showed that MIX N interferes with hormonal pathways and dysregulates expression of genes and biological pathways that are causally linked to autism spectrum disorders. Data from experiments in *Xenopus leavis* and *Danio rerio*, in vivo models validated by the Organisation for Economic Co-operation and Development (OECD), confirmed thyroid function as one of the key and unifying points of vulnerability to MIX N and linked thyroid disruption to neurodevelopmental effects measured as alterations in locomotor activity. The resulting dose-response relationships were then used to estimate a point of departure (POD), which is the toxicological measure to estimate no-effect concentration. This enabled us to apply a similar mixture approach (SMACH) where we (i) identified individuals in the SELMA study who were sufficiently similarly exposed compared with the experimental mixtures and (ii) determined the proportion of the SELMA children with exposure ranges of concern using the POD as reference.

CONCLUSION: Integrating experimental and epidemiological evidence, we established mechanistic and correlative evidence for neurodevelopmental adversities of an EDC mixture associated with language delay. Using the generated experimental data in a risk assessment concept, we found increased odds of language delay in offspring of up to 54% of pregnant women. These results emphasize the need to take mixtures into account during chemical testing and risk assessment and provide an integrative framework to guide risk assessment strategies. ■

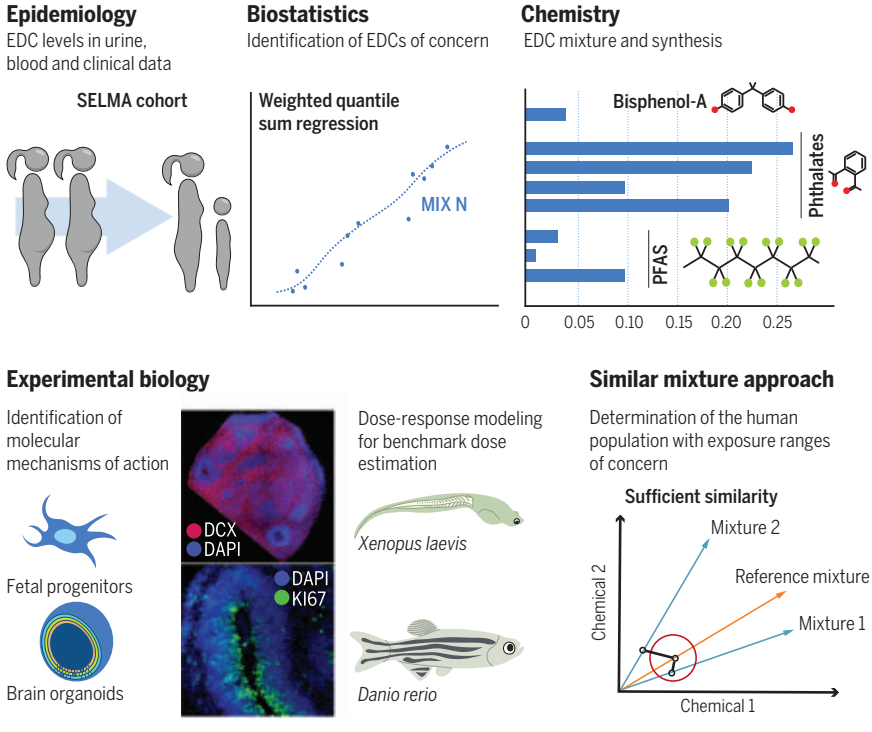

Diagram showing the integrative framework of the study. A mixture of EDCs was associated with adverse neurodevelopmental outcomes in the SELMA pregnancy cohort and was tested in human in vitro and in in vivo models to elucidate the molecular and functional impact of exposure. Experimental data were finally referred back to the cohort for risk assessment by a similar mixture approach. PFAS, perfluoroalkyl substance.

The list of author affiliations is available in the full article online.
*Corresponding author. Email: carl-gustaf.bornehag@kau.se (C.-G.B.); barbara.demeneix@mnhn.fr (B.D.); joelle.ruegg@ebc.uu.se (J.R.); giuseppe.testa@ieo.it (G.T.)
†These authors contributed equally to this work.
‡These authors contributed equally to this work.
Cite this article as N. Caporale *et al.*, *Science* 375, eabe8244 (2022). DOI: 10.1126/science.abe8244

READ THE FULL ARTICLE AT
https://doi.org/10.1126/science.abe8244

RESEARCH ARTICLE

ENVIRONMENTAL TOXINS

From cohorts to molecules: Adverse impacts of endocrine disrupting mixtures

Nicolò Caporale[1,2,3]†, Michelle Leemans[4]†‡, Lina Birgersson[5]†, Pierre-Luc Germain[1]†§, Cristina Cheroni[1,2,3]†, Gábor Borbély[6]¶, Elin Engdahl[6,7]¶, Christian Lindh[8], Raul Bardini Bressan[9], Francesca Cavallo[1], Nadav Even Chorev[1], Giuseppe Alessandro D'Agostino[1]#, Steven M. Pollard[9], Marco Tullio Rigoli[1,2], Erika Tenderini[1], Alejandro Lopez Tobon[1], Sebastiano Trattaro[1,2], Flavia Troglio[1], Matteo Zanella[1]**, Åke Bergman[6,10,11]¶, Pauliina Damdimopoulou[6,12]¶, Maria Jönsson[7], Wieland Kiess[13], Efthymia Kitraki[14], Hannu Kiviranta[15], Eewa Nånberg[16], Mattias Öberg[6,17]¶, Panu Rantakokko[15], Christina Rudén[10], Olle Söder[18], Carl-Gustaf Bornehag[19,20]*††, Barbara Demeneix[4]*††, Jean-Baptiste Fini[4]††, Chris Gennings[20]††, Joëlle Rüegg[6,7]*¶††, Joachim Sturve[5]††, Giuseppe Testa[1,2,3]*††

Convergent evidence associates exposure to endocrine disrupting chemicals (EDCs) with major human diseases, even at regulation-compliant concentrations. This might be because humans are exposed to EDC mixtures, whereas chemical regulation is based on a risk assessment of individual compounds. Here, we developed a mixture-centered risk assessment strategy that integrates epidemiological and experimental evidence. We identified that exposure to an EDC mixture in early pregnancy is associated with language delay in offspring. At human-relevant concentrations, this mixture disrupted hormone-regulated and disease-relevant regulatory networks in human brain organoids and in the model organisms *Xenopus leavis* and *Danio rerio*, as well as behavioral responses. Reinterrogating epidemiological data, we found that up to 54% of the children had prenatal exposures above experimentally derived levels of concern, reaching, for the upper decile compared with the lowest decile of exposure, a 3.3 times higher risk of language delay.

Human populations are exposed to a large number of chemicals with known or suspected endocrine-disrupting properties [endocrine-disrupting chemicals (EDCs)] (*1*). Whereas real life entails simultaneous exposure to multiple EDCs in mixtures, with additive effects manifesting at lower doses than experimental effect thresholds for single compounds (*2*), regulation has so far operated on a single-chemical basis. Because exposure to single EDCs has been repeatedly associated with major diseases and impaired development (*3*), including neurodevelopmental disorders (*4*), assessing the health impact of real-life mixtures is a crucial unmet challenge. However, experimental evidence with mixtures is, at present, limited to combinations within the same chemical class or to observational measurements for more complex mixtures and thus lacks the mechanistic weight to link actual population-based exposures with adverse health outcomes in humans.

In the context of chemical regulatory affairs, most authorities, including the Organisation for Economic Co-operation and Development (OECD), recommend integrated approaches for testing and assessment that incorporate results from multiple methodologies. Emphasis is placed on molecular initiating events and key events that lead to physiologically measurable adverse outcomes. The regulatory framework is, however, still entirely predicated on the assessment of individual chemicals, leaving the impact of simultaneous exposure to multiple compounds, even at modest concentrations, unexamined. Here, leveraging the Swedish Environmental Longitudinal, Mother and child, Asthma and allergy (SELMA) epidemiological study, we focused on language delay as a test case for a prototypical adverse outcome in the neurodevelopmental domain and tested whether a mixture-based approach was epidemiologically and experimentally viable in orienting a more realistic risk assessment. Speech and language development was chosen as an epidemiological end point because language delay is an early marker for intellectual functioning deficits in children and is routinely used for further assessment that might lead to habilitation and support. Several studies have reported that language developmental milestones in early childhood have predictive validity for intellectual functioning later in childhood (*5*, *6*) and even in adulthood (*7*). Indeed, in the SELMA study, language delay at 30 months was strongly associated with cognitive function at 7 years of age (*8*). Finally, in terms of the general applicability of this measure, its prevalence (10% in the SELMA cohort) was also similar across contexts; we found a language delay prevalence of 10% in the US The Infant Development and the Environment Study (TIDES) (*9*), and another Swedish study found a prevalence of 6% (*10*)

In terms of composition, to define the feasibility of a mixture-centered approach for EDC risk assessment, we focused on 15 chemicals that belong to the three chemical groups of phthalates, alkyl phenols, and perfluoroalkyl substances (PFAS). The rationale for

[1]High Definition Disease Modelling Lab, Stem Cell and Organoid Epigenetics, IEO, European Institute of Oncology, IRCCS, 20141 Milan, Italy. [2]Department of Oncology and Hemato-oncology, University of Milan, 20122 Milan, Italy. [3]Human Technopole, V.le Rita Levi-Montalcini, 1, 20157 Milan, Italy. [4]UMR 7221, Phyma, CNRS–Muséum National d'Histoire Naturelle, Sorbonne Université, 75005 Paris, France. [5]Department of Biological and Environmental Sciences, University of Gothenburg, 41463 Gothenburg, Sweden. [6]Swedish Toxicology Sciences Research Center (SWETOX), Södertälje, Sweden. [7]Department of Organismal Biology, Environmental Toxicology, Uppsala University, SE-752 36 Uppsala, Sweden. [8]Division of Occupational and Environmental Medicine, Department of Laboratory Medicine, Lund University, SE-221 85 Lund, Sweden. [9]Medical Research Council Centre for Regenerative Medicine and Edinburgh Cancer Research UK Centre, University of Edinburgh, Edinburgh, UK. [10]Department of Environmental Science, Stockholm University, SE-10691 Stockholm, Sweden. [11]School of Science and Technology, Örebro University, SE-70182 Örebro, Sweden. [12]Division of Obstetrics and Gynecology, Department of Clinical Science, Intervention and Technology, Karolinska Institutet and Karolinska University Hospital, 141 86 Stockholm, Sweden. [13]Hospital for Children and Adolescents, Department of Women and Child Health, University Hospital, University of Leipzig, 04103 Leipzig, Germany. [14]Lab of Basic Sciences, Faculty of Dentistry, National and Kapodistrian University of Athens, 152 72 Athens, Greece. [15]Department of Health Security, Finnish Institute for Health and Welfare (THL), Kuopio 70210, Finland. [16]School of Health Sciences, Örebro University, SE-70182 Örebro, Sweden. [17]Institute of Environmental Medicine, Karolinska Institutet, SE-17177 Stockholm, Sweden. [18]Department of Women's and Children's Health, Pediatric Endocrinology Division, Karolinska Institutet and University Hospital, SE-17176 Stockholm, Sweden. [19]Faculty of Health, Science and Technology, Department of Health Sciences, Karlstad University, SE- 651 88 Karlstad, Sweden. [20]Icahn School of Medicine at Mount Sinai, New York, NY 10029, USA.

***Corresponding author. Email: carl-gustaf.bornehag@kau.se (C.-G.B.); barbara.demeneix@mnhn.fr (B.D.); joelle.ruegg@ebc.uu.se (J.R.); giuseppe.testa@fht.org (G.T.)**

†These authors contributed equally to this work.

‡Present address: Université Paris -Est Créteil, INSERM, IMRB, Team CEpiA, F-94010 Créteil, France.

§Present address: D-HEST Institute for Neurosciences, ETH Zürich and Lab of Statistical Bioinformatics, University of Zürich, Zürich, Switzerland.

¶SWETOX was closed at the end of 2018.

#Present address: Lee Kong Chian School of Medicine, Nanyang Technological University, Singapore, Singapore.

**Present address: Evotec SE, Hamburg, Germany.

††These authors contributed equally to this work.

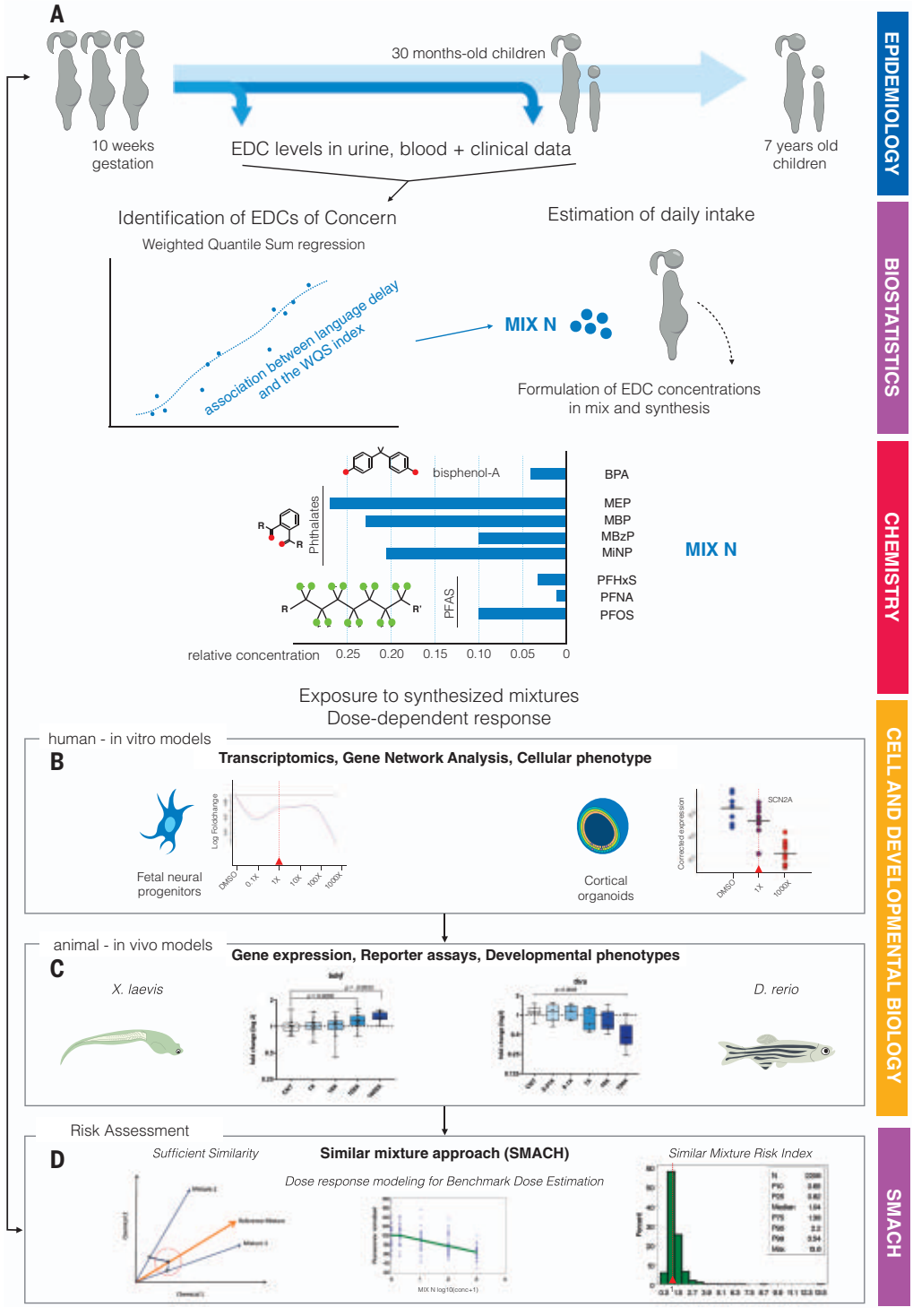

Fig. 1. Overview of the study.
(**A**) Identification of an EDC mixture associated with adverse health outcomes in neurodevelopment. In the SELMA pregnancy study, 20 analytes from 15 EDCs were measured in the urine or serum of women around pregnancy week 10. Associations between these exposures and language delay of the children at 2.5 years of age were established using WQS regression. This resulted in the identification, within the mixture, of sEDCs that contributed to the association with the adverse health outcome (language delay). Based on the ratios found in SELMA mothers, the identified sEDCs were mixed to compose MIX N for subsequent use in the experimental systems in concentrations corresponding to 0.01X, 0.1X, 1X, 10X, 100X, and 1000X the serum concentrations in SELMA mothers. MEP, mono-ethyl phthalate; MBP, mono-*n*-butyl phthalate; MBzP, monobenzyl phthalate; MiNP, Mono-isononyl phthalate; PFHxS, perfluorohexane sulfonate; PFNA, perfluorononanoic acid; PFOS, perfluorooctane sulfonate.
(**B**) Identification of gene regulatory networks and cellular responses dysregulated by MIX N, along with their dose-response relationships. Transcriptome analyses were carried out in HFPNSCs and COs upon treatment with 0.1X to 1000X MIX N at several model-relevant time points. Examples of dose-response patterns are shown across models. Significant (FDR < 0.05) transcriptional changes were already detected at 1X concentrations (red dotted line). Down-regulation by MIX N of the bona fide ASD-causing gene *SCN2A* in COs. The horizontal black bars represent the mean expression value for each exposure condition.
(**C**) Validation of key pathways affected by MIX N and their physiological impact in in vivo models. Effects on key genes and pathways identified in the cellular models were assessed in *X. laevis* and *D. rerio* larvae upon short-term treatment (48 to 72 hours), exemplified by brain-derived neurotrophic factor (*bdnf*) expression in *Xenopus* (left) and thyroid hormone receptor α (*thra*) expression in zebrafish (right) upon MIX N exposure, quantified using RT-qPCR. In the box plots, boxes and whiskers represent the interquartile range and minimum and maximum values, respectively. (**D**) Referring experimental in vivo evidence back to the SELMA cohort for risk assessment by SMACH. In the first step of SMACH, sufficient similarity was tested between prenatal exposures and the reference MIX N mixture. In the second step, a SMRI was calculated, which is based on the BMDL established in (C). Of the SELMA women, 54% had a SMRI higher than 1, indicating that their children are at risk of adverse neurodevelopmental outcomes. In the SMRI graph, the red dotted line indicates the median, N indicates the number of women in the analysis, and P10 to P99 indicate the different percentiles.

this selection was based on the following: (i) established evidence, within each group of compounds, for both their endocrine interfering properties and their association to neurodevelopment [from single-compound studies, as in the case of bisphenol A (BPA) (*11*)]; and (ii) our previous demonstration, with a single-compound approach, that prenatal exposure for three of the chemicals—diethyl phthalate (DEP), dibutyl phthalate (DBP), and benzyl butyl phthalate (BBzP)—was associated with language delay in children at 30 months of age (*9*).

Based on these choices of end point and compounds, we determined a chemical mixture associated with language delay in children

Table 1. Single-compound concentrations in prenatal urine and serum of SELMA women. Distribution of phthalate and phenol metabolites in urine and perfluorinated compounds (PFAS) in serum analyzed during the first trimester of 1874 pregnant women in the SELMA study. CI, confidence interval; GM, geometric mean; MEP, mono-ethyl phthalate; MBP, mono-*n*-butyl phthalate; MBzP, monobenzyl phthalate; DEHP, di(2-ethylhexyl) phthalate; MEHP, mono-(2-ethylhexyl) phthalate; MEHHP, mono-(2-ethyl-5-hydroxylhexyl); MEOHP, mono-(2-ethyl-5-oxohexyl) phthalate; MECPP, mono-(2-ethyl-5-carboxypentyl) phthalate; DiNP, diisononyl phthalate; MHiNP, mono-hydroxy-iso-nonyl phthalate; MOiNP, mono-, oxo-iso-nonyl phthalate; MCiOP, mono-carboxy-iso-octyl phthalate; PFOA, perfluorooctanoic acid; PFOS, perfluorooctane sulfonate; PFNA, perfluorononanoic acid; PFDA, perfluorodecanoic acid; PFUnDA, perfluoroundecanoic acid; PFDoDA, perfluorododecanoic acid; PFHxS, perfluorohexane sulfonate; PFHpA, perfluoroheptanoic acid.

Compound	Metabolite	Median	95% percentile	GM (95% CI)
Phthalate and metabolites in urine (ng/ml)				
DEP	MEP	62.6	507.7	68.7 (65.3–72.3)
DBP	MBP	71.9	233.1	69.0 (66.5–71.5)
BBzP	MBzP	16.8	99.4	16.6 (15.8–17.4)
DEHP	MEHP	3.8	15.6	3.8 (3.6–3.9)
	MEHHP	16.6	66.6	16.3 (15.7–17.0)
	MEOHP	11.2	45.0	11.1 (10.7–11.6)
	MECPP	15.7	62.7	15.8 (15.2–16.4)
DiNP	MHiNP	5.9	54.6	6.2 (5.9–6.6)
	MOiNP	2.7	19.2	2.9 (2.8–3.0)
	MCiOP	8.7	74.9	9.8 (9.3–10.2)
BPA		1.5	6.2	1.5 (1.4–1.6)
Triclosan		0.8	351.4	1.3 (1.2–1.5)
Perfluorinated compounds (PFAS) in serum (ng/ml)				
PFOA		1.60	3.96	1.60 (1.56–1.64)
PFOS		5.35	12.29	5.30 (5.18–5.43)
PFNA		0.53	1.29	0.54 (0.53–0.55)
PFDA		0.25	0.59	0.26 (0.25–0.27)
PFUnDA		0.23	0.54	0.21 (0.21–0.22)
PFDoDA		0.03	0.08	0.03 (0.03–0.03)
PFHxS		1.23	3.71	1.32 (1.29–1.36)
PFHpA		0.02	0.09	0.02 (0.02–0.02)

and then established molecular and cellular key events of the mixture experimentally, in both in vitro and in vivo models, making EDC mixtures experimentally tractable as the "real-life" relevant unit of human exposure. This finally allowed us to identify the population at risk from empirically derived EDC mixture concentrations.

Results

An integrated epidemiological-experimental design assessing the impact of EDC mixtures on human health and development

To enable risk assessment of real-life exposure to EDC mixtures, we harnessed (i) a prospective population-based mother-child pregnancy cohort (SELMA) to measure prenatal EDC exposures combined with biostatistical tools to infer the EDC mixture associated with child neurodevelopment (Fig. 1A); (ii) complementary assays in in vitro human cellular systems to define molecular mechanisms linking EDC-mixture exposure to adverse outcomes (Fig. 1B); (iii) in vivo models to determine the physiological impact and dose-response of key affected pathways (Fig. 1C); and (iv) a combination of in vivo evidence of effects from this EDC mixture and exposure information from the pregnancy cohort to assess risks associated with the mixture using a similar mixture approach (SMACH) (Fig. 1D).

Definition and establishment of the EDC mixture that affects human neurodevelopment

Humans are exposed to several classes of EDCs, such as phthalates, phenols, and perfluorinated alkyl acids (*12*). We focused on prenatal exposures to mixtures of 15 parent compounds (comprising 20 analytes and metabolites) measured in the SELMA study, a population-based pregnancy cohort that recruited more than 2300 women in the first trimester from prenatal clinics in Värmland County, Sweden, from November 2007 to March 2010 (*13*). Chemicals were selected based on an evaluation matrix that ranked their (i) known or suspected endocrine-disrupting properties based on scientific literature; (ii) inclusion in the European Chemical Agency (ECHA) list of very-high-concern substances (*14*); (iii) prevalence of empirically measured exposure in the SELMA pregnancy cohort; (iv) established knowledge on the most likely routes of exposure; (v) experimental tractability in terms of multiplex chemical analysis in complex mixtures; and (vi) available evidence on health outcomes of very serious concern. Although obviously not comprehensive, this served as a representative selection to spearhead the evaluation of the effects of mixture exposures.

As a marker of adverse outcomes in child neurodevelopment, we focused on language delay at 30 months of age. Delays in language development in early childhood, as assessed by validated tests, have been shown to be predictive of later academic achievement and the need for special education (*15*). SELMA data confirm that language delay at 30 months of age is significantly (P = 0.001) associated with lower cognitive function [Wechsler Intelligence Scale for Children (WISC-IQ)] at 7 years of age when adjusted for covariates (*8*). Thus, language delay in early childhood serves as a marker for more general neurodevelopmental processes rather than reflecting language development only (*5*, *6*).

The current analyses included 1874 pregnant women, who were assessed for their urinary or serum EDC concentrations at the 10th week (median) of gestation (Table 1 and table S1). Specifically, we profiled urine concentrations of 10 metabolites of five phthalates, BPA, and triclosan, as well as serum concentrations of eight PFAS.

A specific mixture (in terms of both composition and concentration) was found to be associated with language delay in a three-step procedure (Fig. 1A). First, we identified the prenatal exposures to EDCs that were associated with language delay in 594 children (prevalence of 10%) by using weighted quantile sum (WQS) regression (*16*), a strategy for estimating empirical weights for a weighted sum of concentrations that are most associated with the health outcomes. EDCs included in these exposures are hereafter referred to as sEDCs (selected EDCs based on WQS regression weights). Second, we estimated the equivalent daily intake of sEDCs measured in urine (phthalates and alkyl phenols) and estimated serum concentrations from the daily intake for these urinary measurement–based compounds. Finally, we used the geometric means, on a molar basis, for either the measured or estimated serum concentrations of the sEDCs in 1874 women to establish mixing proportions for the reference mixture used for experimental validation (MIX N, where N stands for neurodevelopment), (Fig. 1A and tables S2 and S3). The mixture was tested across concentrations (0.01X, 0.1X, 1X, 10X, 100X, and 1000X) corresponding to human exposure, where 1X denotes the geometric

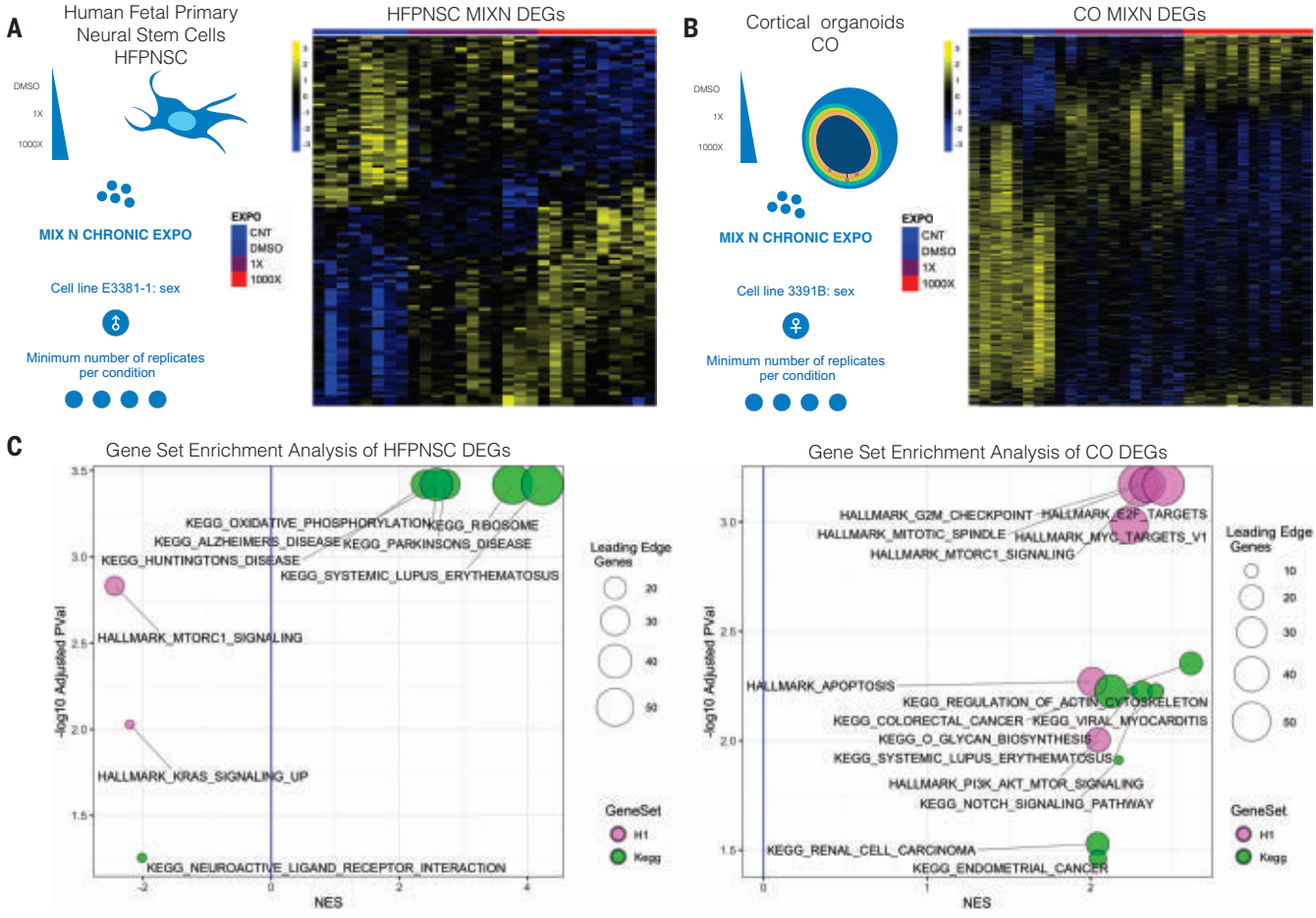

Fig. 2. MIX N chronic exposure of human cellular models. (**A**) Schematic representation of the experimental design for chronic (15 days) MIX N treatment of HFPNSCs and a heatmap showing the relative gene abundance [*z*-scores of surrogate variable analysis (SVA)–corrected values] of the DEGs (FDR < 0.05, logFC > 0.5, logCPM > 0) identified through differential expression analysis of MIX N dilutions versus negative control. CNT, unexposed samples; DMSO, samples exposed to 0.1% DMSO; 1X, samples exposed to 1X MIX N; 1000X, samples exposed to 1000X MIX N. (**B**) Schematic representation of the experimental design for chronic (50 days) MIX N treatment of human COs and a heatmap showing the relative gene abundance (*z*-scores of SVA-corrected values) of the DEGs (FDR < 0.05, logFC > 0.5, logCPM > 0) identified through differential expression analysis of MIX N dilutions versus negative control. (**C**) Gene sets significantly (adjusted *P* < 0.1) associated with MIX N exposure by GSEA in HFPNSCs and COs, respectively; results are presented as −log10 adjusted *P* values and normalized enrichment score (NES).

mean of serum concentrations in SELMA pregnant women. The tested dose range was adjusted to the experimental models to accommodate their differential responsiveness.

Acute MIX N exposure disrupts human neurodevelopmental pathways

To define the molecular impact of MIX N, we started off with primary neural stem cells sourced from the cortex of human fetuses at 11 and 19 weeks of gestational age [henceforth human fetal primary neural stem cells (HFPNSCs) in the figures and fetal progenitors in the text]. Given the potentially nonlinear and nonmonotonic dose-response patterns associated with EDC mixtures (*17*, *18*), the experimental design included five doses of MIX N, ranging in concentration from 0.1X to 1000X, and a global assessment of the early impact on gene expression to define the proximal targets (fig. S1A). To this end, RNA sequencing (RNA-seq) was performed after 48 hours of MIX N exposure, and patterns of EDC dose-dependent transcriptional responses were determined using an analysis that considers MIX N dilutions as distinct categories. By not assuming any particular response pattern (linearity or monotonicity), this approach allowed us to define a core list of 16 differentially expressed genes (DEGs) {false discovery rate (FDR) < 0.05; absolute log–fold change [abs(logFC)] > 0.2 (henceforth logFC); log–counts per million (logCPM) > 0} that follow similar dose responses in the two fetal cortical lines (fig. S1, B to E). This core set includes the genes *EPHB2* and *CLSTN2*, an ephrin receptor and a transmembrane protein of the cadherin superfamily, respectively. These two genes are particularly relevant to the phenotype scored in the SELMA cohort (language delay) because their down-regulation by MIX N (fig. S1F) is consistent with their autism spectrum disorder (ASD)–causative role by haploinsufficiency that was initially defined in the Simons Simplex Collection of 2700 families and later validated in additional cohorts (*19*–*25*).

Chronic MIX N exposure uncovers convergence with genetic causes of ASD

The observation that even acute exposure to MIX N triggered the dysregulation of a core set of phenotypically relevant genes in two genetically independent fetal cortex samples, sourced at different developmental stages, motivated us to investigate the molecular impact of MIX N exposure in a setting that more closely recapitulates human in utero exposure. To this end, we selected two anchor doses, 1X and 1000X MIX N, and tested them in two experimental models with a minimum of four replicates per condition: (i) the same 19-weeks-of-gestational-age fetal progenitor line that was already subjected to acute exposure, now exposed for 2 weeks to mimic the

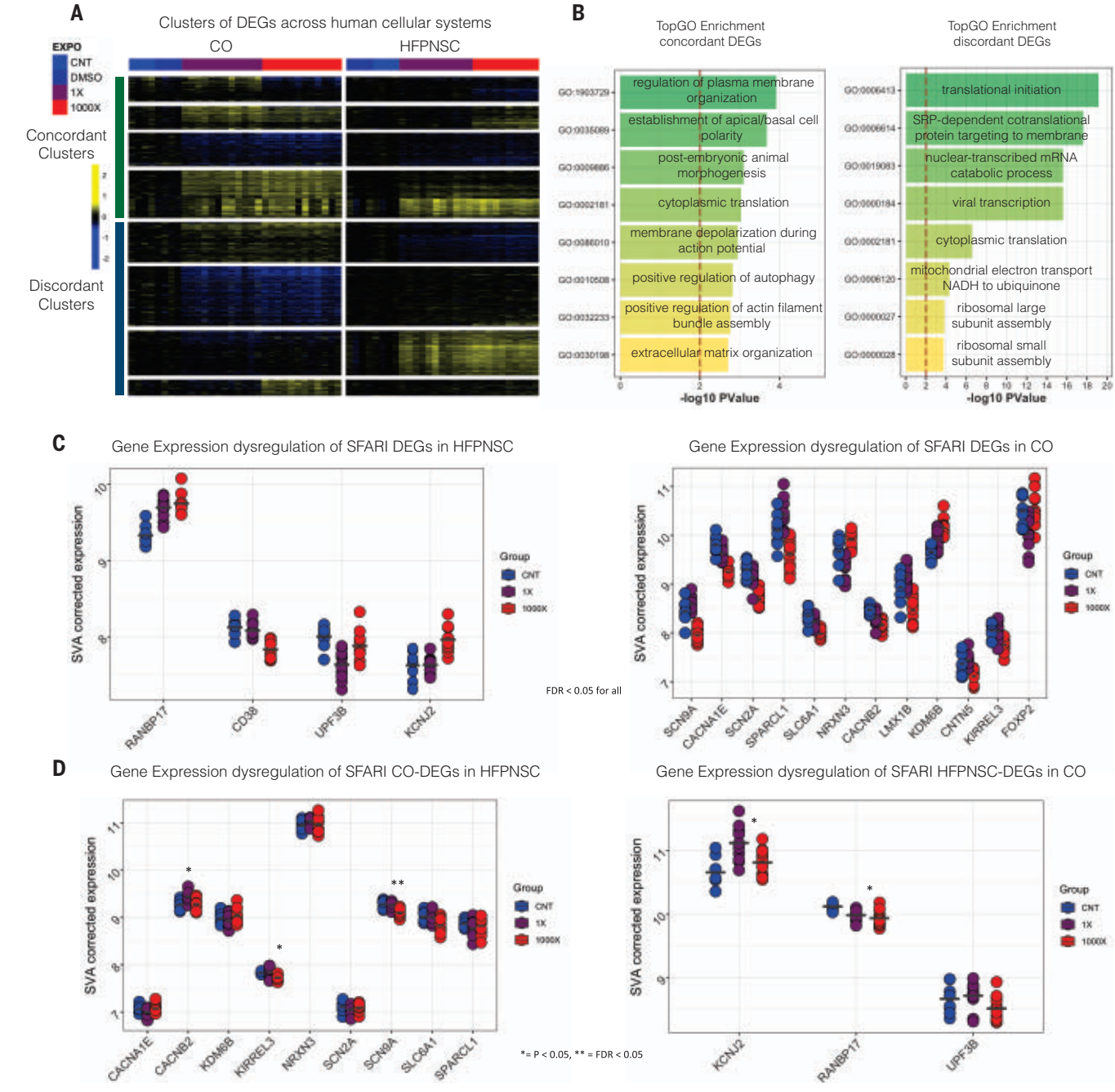

Fig. 3. Pathophysiological relevance of MIX N effects on human cellular models. (**A**) Heatmap showing the relative gene abundance (*z*-scores of SVA-corrected values) of the DEGs that are consistently and discordantly dysregulated upon exposure of HFPNSCs and COs to MIX N. (The rows across the heatmaps refer to the same genes plotted in the two experimental systems, with vertical white spaces visually defining gene clusters and experimental systems.) (**B**) Results of GO enrichment analysis performed on the DEGs that are consistently or discordantly dysregulated in HFPNSCs and COs. Bar plots depict the *P* values for the top eight biological process GO terms. (**C**) Plots of gene expression levels (SVA-corrected values) across exposure conditions for the DEGs that overlap with the list of SFARI genes in HFPNSCs and COs, respectively. (**D**) Gene expression levels (SVA-corrected values) across exposure conditions for the DEGs that overlap with the list of SFARI genes in COs plotted for HFPNSCs, and vice versa. (*P* values and FDR are calculated through differential expression analysis for each experimental model.) In (C) and (D), gray bars indicate the mean expression value for each gene in each exposure condition.

continuous exposure that occurs in vivo during progenitor expansion (*26*); and (ii) three-dimensional (3D) cortical brain organoids (henceforth COs in the figures and organoids in the text) differentiated from induced pluripotent stem cells (iPSCs), a neurodevelopmental model that recapitulates salient features of human corticogenesis, including, as we previously showed (*27*), the emergence of outer radial glia cells, which is a cell population with a central role in multiple human-specific brain diseases (*28*–*31*). Organoids present two key advantages that warrant their comparison with fetal progenitors. First, they derive from highly standardized, self-renewing sources (iPSCs), which overcomes the inherent limitations, technical and ethical alike, of fetal progenitor procurement. Second, organoids are a developing system, which allows

exposure to be extended from pluripotency through an intermediate stage of corticogenesis (day 50), a stage that features a particularly relevant representation of progenitor cells, early neurons, and developmental trajectories that match, at the transcriptomic level, the gestation time when SELMA women were profiled (fig. S2A).

Differential expression analysis showed, as expected, a much broader impact than that in the acute setting and included three genes (*DHRS3*, *LGI4*, and *NEFL*) that were dysregulated upon both acute and chronic exposure (fig. S2B). The effect of MIX N chronic exposure on gene expression highlighted a high degree of concordance between the two doses for both experimental systems (Fig. 2, A and B, and fig. S2C) and revealed a major impact of MIX N exposure (132 DEGs for fetal progenitors and 599 DEGs for organoids; FDR < 0.05, logFC > 0.5, logCPM > 0). In both fetal progenitors and organoids, genes down-regulated upon MIX N exposure were enriched for gene ontology (GO) terms related to extracellular compartment regulation, such as extracellular matrix organization in fetal progenitors and collagen fibril organization in organoids, whereas up-regulated genes were enriched for categories related to cellular differentiation, such as post-embryonic animal organ development in fetal progenitors and neuronal fate specification in organoids (fig. S2D). Moreover, gene set enrichment analysis (GSEA) revealed significant (adjusted $P < 0.1$ and normalized enrichment score > 2) enrichment for disease-relevant genes, such as genes associated with neurodegenerative diseases (*32*), cell proliferation, and several types of cancer (*33*) (Fig. 2C).

We next complemented the analysis with a more comprehensive approach by surveying, in both experimental systems, the transcriptional changes of genes modulated in at least one of the examined conditions and applying a clustering approach to identify the genes that were concordantly dysregulated, as well as the ones that have an opposite response in organoids and fetal progenitors (Fig. 3A). This showed that concordantly regulated genes are enriched for GO categories related to the plasma membrane, cell polarity, and extracellular matrix organization, whereas genes with opposite regulation are enriched for categories related to the regulation of translation and RNA metabolism (Fig. 3B).

Finally, given the founding epidemiological evidence associating MIX N exposure to language delay, we tested whether the genes significantly (FDR < 0.05) altered by MIX N in fetal progenitors or organoids were enriched for genes underlying neurodevelopmental disability, harnessing the best-established databases of causative gene annotations for neurodevelopmental disorders (NDDs), including ASD (*19*, *34*–*42*). As shown in Fig. 3, C and D, and fig. S2E, we found not only that MIX N DEGs had significant ($P < 0.05$) overlaps with the NDD genetic burden but also that, of particular note, for some cases in which the genetic cause is known to be a copy number gain or loss, the direction of MIX N induced dysregulation was concordant with the genetic lesion (table S4). This is exemplified by the down-regulation by MIX N of the following bona fide ASD-causing genes, annotated with the highest score genes in the Simons Foundation Autism Research Initiative (SFARI) database: (i) in organoids, the subunit alpha 2 of sodium voltage-gated channel *SCN2A*, which is essential for the generation and propagation of action potentials and whose disruptive mutations impair channel function and cause ASD; and (ii) in fetal progenitors, the transmembrane glycoprotein *CD38*, for which genetic mutations and knock-out mouse models have shown a causative role for ASD (*21*, *43*–*47*) (Fig. 3, C and D). These results indicate that EDC exposure converges on the interference of the same gene targets and biological pathways of ASD (*48*, *49*).

To validate mixture-specific effects, both with regard to the current regulatory practice (single compound at a time) and in light of the complexity of molecular events triggered by endocrine disruption, our experimental design included a panel of additional exposures performed on the same human in vitro systems. Specifically, in addition to 0.1% dimethyl sulfoxide (DMSO) as a negative control, we also tested 5 nM triiodothyronine (T3) exposure to define the baseline of the effect of thyroid hormone (TH) modulation, given its essential role in brain development (*50*, *51*); indeed, previous epidemiological (*52*, *53*) and experimental (*54*) evidence had identified the main chemical classes of the tested mixture as TH disruptors (*55*). We thus exposed the human neurodevelopmental models to T3 and identified, as expected, a major transcriptional impact (391 DEGs for fetal progenitors and 2272 DEGs for organoids; FDR < 0.05, logFC > 0.5, logCPM > 0) and observed different patterns of dysregulation relative to MIX N (fig. S3, A to G). Moreover, in organoids, T3 and MIX N exposures showed an opposite effect for a sizable portion of the genes modulated by both treatments; in particular, cell proliferation-related genes (*CDC20B* and histone-related genes) as well as *NEUROG1*, which was shown to act as a negative regulator of neocortical neurogenesis (*56*), were significantly (FDR < 0.05) up-regulated by MIX N and down-regulated by T3 (fig. S3G).

Furthermore, because BPA has been reported to affect human brain development and behavior by epidemiological, in vitro, and in vivo evidence (*57*–*60*), we also probed its impact as a single compound at the same concentration at which it is present in 1X MIX N. For both fetal progenitors and organoids (fig. S3, H and I), the effect of MIX N, although showing an expected partial overlap, extended well beyond that of BPA alone (which determined 49 DEGs for fetal progenitors and 871 DEGs for organoids; FDR < 0.05, logFC > 0.5, logCPM > 0).

In addition to the molecular dissection of the MIX N effects, the same organoids that were profiled at the transcriptomic level after chronic exposure were also subjected to immunofluorescence analysis to score the cellular phenotypes and to investigate the MIX N impact on the developmental processes of neuronal differentiation. In particular, we stained for KI67, which marks proliferating progenitors, and DCX, a protein involved in neuronal migration that marks early neurons. The results showed a significant ($P < 0.05$) increase of KI67-positive cells for MIX N–exposed organoids coupled with a decrease of DCX-expressing cells ($P < 0.05$) for 1000X MIX N exposure, thus suggesting an effect favoring neural progenitor proliferation while hindering neuronal differentiation (fig. S4, A to D), which is in line with recent observations that hormonal exposure affects the same developmental processes that regulate neuronal progenitor proliferation and neuronal maturation of genetic mutations, increasing ASD vulnerability (*61*). This result was corroborated at the level of gene expression, which showed that a subset of genes related to neural differentiation (*DCX*, *SYP*, *MAP2*, and *RBFOX3*) were down-regulated ($P < 0.05$ for *SYP* and *RBFOX3*), whereas cell proliferation genes (*MKI67*, *CCNB1*, *CDC20*, and *HMGB2*) were up-regulated by MIX N (fig. S4, E and F; $P < 0.05$ for *MKI67*). This result is also in line with the observation that gene sets related to cell proliferation were among the top positively enriched sets in GSEA ("mitotic spindle," "G2M transition"; Fig. 2C). When the cellular phenotypic analysis was applied to T3-treated samples, it displayed the opposite effect of MIX N, both for proliferation and maturation, whereas BPA partially recapitulated MIX N effects only for progenitor proliferation. For T3 and BPA, the transcriptomics data were also in agreement with the immunostaining results (fig. S4).

MIX N alters hormonal pathways

Next, we set out to identify the key regulators that are responsible for the transcriptomic phenotypes as an inroad to the molecular pathways leading to the cellular and clinical adverse effects. To this end, we performed a master regulator analysis starting from the dysregulation observed in the chronic MIX N exposure setting, using recently released data from the PsychENCODE consortium (*62*) integrated into a human brain–specific gene regulatory network across genomic, transcriptomic, and epigenomic layers. We leveraged

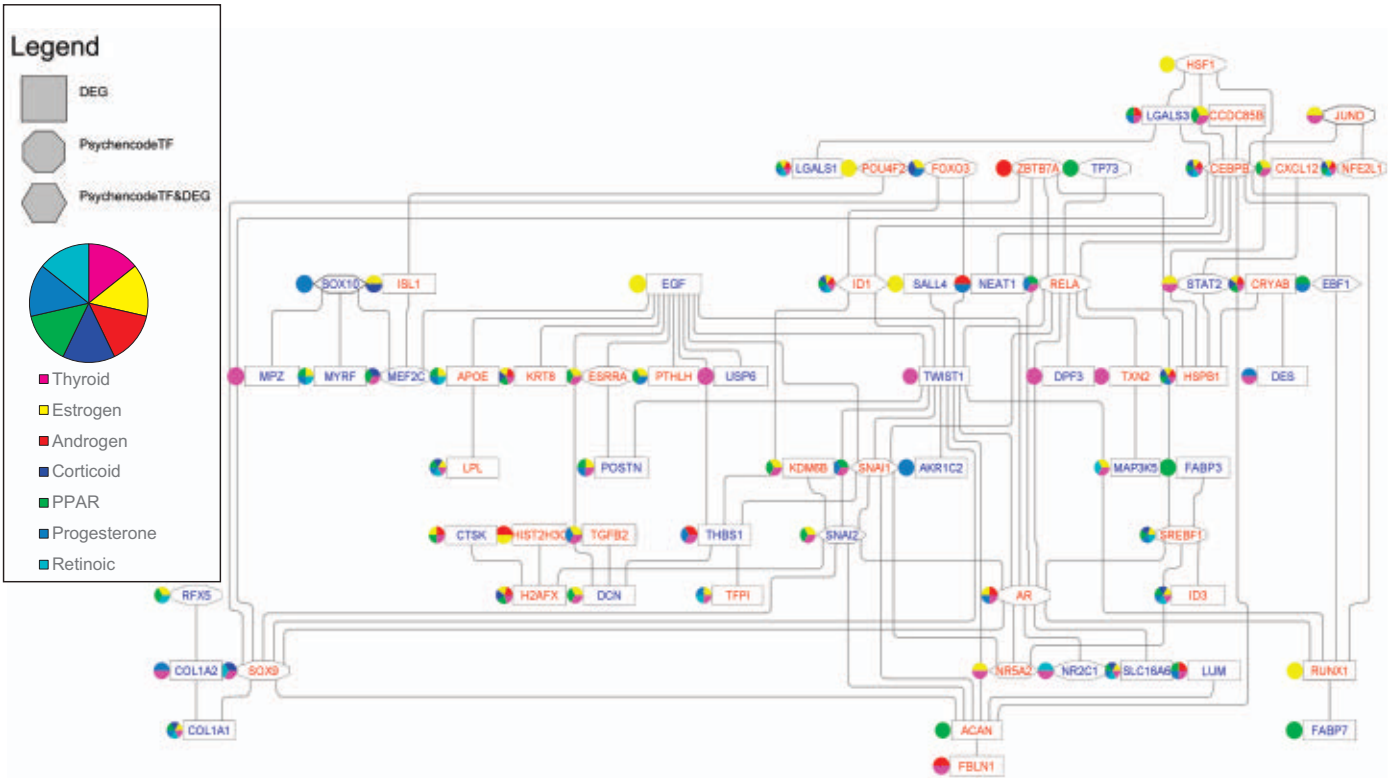

Fig. 4. DEGs and TFs identified in HFPNSCs and COs after MIX N exposure are linked to multiple endocrine pathways. Regulatory pathways were generated by the Genomatix GePS program that connects differentially expressed genes. Box sizes indicate absolute fold change, with red lettering showing up-regulation and blue showing down-regulation in organoids. Within this network, of the multiple endocrine pathways investigated, we found the following order of hormonal targets in the network: thyroid > estrogen > PPAR > progesterone > androgen > corticoid > retinoic, reflecting the overall number of DEGs identified.

this network to infer the transcription factors (TFs) whose altered activity (inferred from their downstream output and hence aggregating both their transcriptional or post-transcriptional regulation) was most likely mediating the impact of MIX N. The 92 regulators pinpointed by this analysis include up-regulation of *SOX9*, which is known to control neurogenesis and astrogenesis during development (*63*–*66*); down-regulation of *MEF2C*, which regulates multiple neurodevelopmental processes and whose haploinsufficiency is causatively linked to ASD (*67*–*69*), and down-regulation of the TH–dependent factor *KLF9*, which plays a key role in neurogenesis (*70*, *71*) (fig. S5, A and B).

To further characterize how different endocrine pathways were affected by MIX N, we intersected both the DEGs (FDR < 0.05) and the master regulator TFs with genes related to specific hormonal pathways, selected on the basis of their relevance in the context of neurodevelopment and endocrine disruption (*33*, *72*–*75*). Among the positive enrichment results, estrogen and thyroid-related genes were the most enriched at the level of DEGs and TFs, respectively (fig. S5, C and D). Moreover, plotting the expression of all the endocrine-relevant DEGs and TFs showed MIX N–dependent patterns of modulation for both (fig. S5, E and F). Finally, within this landscape of endocrine-related transcriptional dysregulation, the Genomatix Pathway System (GePS) program was used to identify critical hubs of disruption (Fig. 4 and table S5). From the MIX N targets (both DEGs and upstream TFs), 65 were found to interact with each other using the expert level within GePS as the minimum evidence level, with most DEGs within the network found to be related to TH (*43*), estrogen (*40*), and peroxisome proliferator-activated receptor (PPAR) (*36*), in line with the PsychENCODE network–based analysis showing the thyroid and estrogen pathways as the most enriched ones.

MIX N disrupts TH signaling in developmental in vivo models

Having determined the impact of MIX N in pathophysiologically relevant human models in vitro, we extended our analysis in vivo to define the impact of the mixture in regulatory toxicology-relevant whole-organism models (Fig. 5, A to H). We focused on the TH axis as an example of convergent EDC-mediated dysregulation, given our in vitro findings, its essential roles in brain development, and previous epidemiological and experimental evidence identifying the main chemical classes present in the mixture as TH disruptors (*76*).

The TH-disrupting capacity of the mixture was investigated using the *Xenopus* eleutheroembryonic thyroid assay (XETA), an assay that probes TH disruption at multiple levels (synthesis, transport, and metabolism) on the basis of TH sensitivity and metabolic competence of early-stage *Xenopus laevis* embryos. One-week-old transgenic tadpoles, harboring a green fluorescent protein (GFP) thyroid-responsive element reporter, were exposed for 72 hours to T3 (5 nM) and MIX N (Fig. 5A and fig. S6A). MIX N altered TH activity in the head, resulting in a significant (10X: $P = 0.0210$; 100X: $P < 0.0001$; 1000X: $P < 0.0001$) reduction in fluorescence at concentrations 10X, 100X, and 1000X (Fig. 5, B and C). Next, we investigated neural gene expression in tadpoles exposed to MIX N for 3 days by reverse transcription quantitative polymerase chain reaction (RT-qPCR) and found that, in line with in vitro results, MIX N had already decreased expression of the TH-dependent TF *klf9* at 1X concentration, whereas it decreased expression of the TH transporter *oatp1c1* at 10X and increased the expression of the TH transporter *mct8* at 1000X. In the high-dose range (100X and 1000X), mRNA concentrations of brain-derived neurotrophic factor (*bdnf*), a factor vital for synaptogenesis, were also significantly up-regulated by MIX N

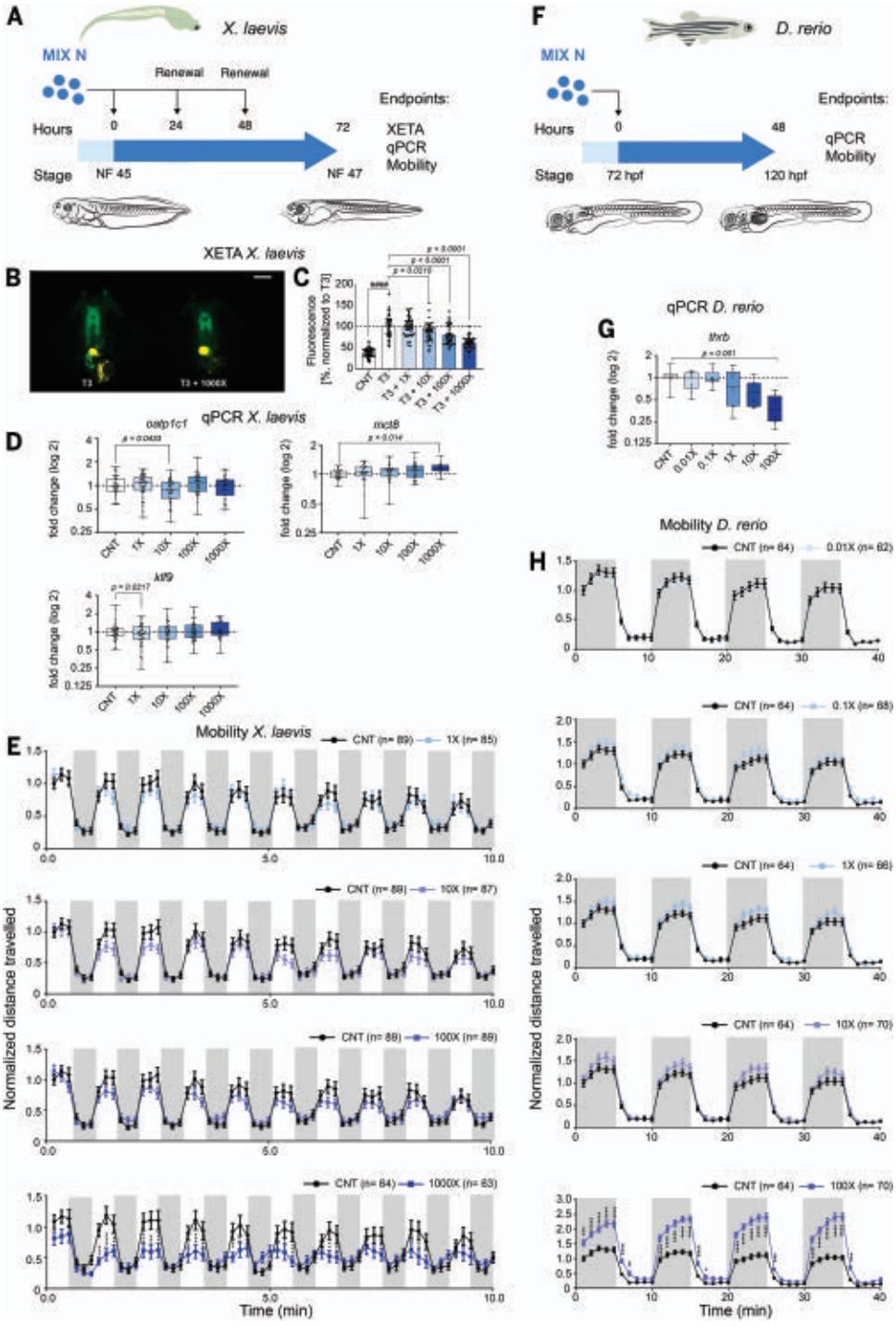

Fig. 5. MIX N exposure disrupts TH signaling and behavior both in *X. laevis* and *D. rerio*. (**A**) The experimental setup for *X. laevis*. (**B**) Thyroid-disrupting effects were assessed using XETA. Representative images of tadpoles exposed to T3 or T3 and 1000X MIX N are shown. Scale bar is 500 μm. (**C**) Specific fluorescence in tadpole heads was quantified as relative fluorescence units normalized against T3. A pool of three independent experiments with >11 tadpoles per concentration per experiment (mean ± SEM) was analyzed. #### indicates $P < 0.0001$ for T3 versus control using Student's *t* test. (**D**) RT-qPCR after brain dissection for TH early-response target genes (*oatp1c1*, *klf9*, and *mct8*) in wild-type tadpoles exposed to the protocol shown in (A). Shown is a pool of three to nine independent experiments (mean ± mininum or maximum response with two to five replicates per concentration per experiment; for *oatp1c1* and *klf9*, a pool of nine experiments for the concentrations 1X, 10X, and 100X and a pool of six experiments for 1000X, with each exposure compared with the appropriate control; for *mct8*, a pool of six experiments for 1X, 10X, and 100X and a pool of three experiments for 1000X, with each exposure compared with the appropriate control). (**E**) Mobility of exposed tadpoles was measured for 10 min in alternating 30-s light and 30-s dark cycles. Distance traveled was analyzed over time. A pool of five to seven independent experiments is shown (mean ± SEM, 9 to 14 tadpoles per concentration per experiment, with a pool of seven experiments for 1X, 10X, and 100X and a pool of five experiments for 1000X). (**F**) The experimental setup for *D. rerio*. (**G**) *D. rerio* embryos were exposed to MIX N [protocol shown in (F)], and RT-qPCR was performed on pooled whole larvae for genes that included thyroid receptor (*thrb*). Shown is a pool of three independent experiments (three replicates per concentration per experiment). (**H**) The mobility of exposed zebrafish embryos was measured for 40 min at 120 hours postfertilization in alternating 5-min dark and 5-min light cycles. Distance traveled was analyzed over time. Shown is a pool of three independent experiments as mean ± SEM, with six to eight larvae per concentration per plate and three plates per experiment. For box plots in (D) and (G), boxes and whiskers represent the interquartile range and minimum and maximum values, respectively.

exposure (100X: $P = 0.0006$; 1000X: $P = 0.0033$) (Figs. 1C and 5D and table S6).

To confirm the impact of the mixture on the thyroid system in an additional toxicology-relevant in vivo model, we assessed the expression of TH-related genes in zebrafish larvae (*Danio rerio*). Zebrafish embryos were exposed to MIX N (0.01X to 100X) for 48 hours (Fig. 5F), and gene expression was determined by RT-qPCR. Exposure to the mix led to significantly decreased expression of the thyroid hormone receptors *thra* ($P = 0.0006$) and *thrb* ($P = 0.0010$) at 100X concentration (Figs. 1C and 5G and table S6). To investigate whether endocrine systems other than the thyroid (estrogen, androgen, and glucocorticoid) were affected by the mixture in vivo, we probed a panel of candidate genes (table S6) and found them to be unaffected.

By analogy with the in vitro models, single-compound exposure to BPA was performed in the in vivo systems (fig. S6, A to H). In *Xenopus* embryos, the XETA test showed a stronger effect with MIX N versus BPA (10X versus 1000X,

respectively) (fig. S6, B and C). In line with this observation, although MIX N and BPA shared *bdnf* as a common dysregulated target (Fig. 1C and fig. S6D), no other MIX N target was modulated by BPA, showing that the dysregulation by MIX N cannot be primarily ascribed to BPA (table S6). In zebrafish larvae, BPA did not affect the genes that were affected by MIX N at the tested concentrations (Fig. 5G, fig. S6G, and table S6).

Taken together, the results across species demonstrate TH-disrupting effects of MIX N at molecular and physiological levels. These effects are not comparable with the effects of BPA alone, both at the concentrations measured and at concentrations associated with adverse outcomes in humans.

MIX N disrupts locomotion in developmental in vivo models

Finally, to establish the organismal-level impact of the mixture, we used locomotor assays. Locomotion is a well-established target of neurodevelopmental alterations, including, most prominently, those caused by TH disruption, given the role of TH in the maturation of the central and peripheral nervous systems (*77*–*79*). We analyzed light-induced locomotion in *Xenopus* tadpoles after 72 hours of MIX N exposure. Mobility was significantly ($P < 0.0001$ at certain time points) decreased after exposure to MIX N at 1000X and followed a dose-dependent decreasing pattern (Fig. 5E and fig. S9), whereas no effects were observed after BPA exposure (fig. S6E).

In zebrafish larvae, in which activity increases in darkness and abates in light, behavioral effects were assessed after 48 hours of exposure to MIX N, revealing significantly increased mobility during dark periods, which followed a dose-dependent increasing pattern ($P < 0.00011$), and at certain time points during light cycles ($P < 0.05$) after exposure to 100X MIX N (Fig. 5H and fig. S9). No effects were observed after exposure to BPA (fig. S6H). Together, these results demonstrate that MIX N affects animal behavior at concentrations associated with adverse outcomes in humans.

Integrating epidemiological and experimental evidence for risk assessment using SMACH

Finally, we combined the epidemiological and experimental evidence of adverse neurodevelopmental effects associated with prenatal exposure to the EDCs in a mixture-based risk assessment setting. To this end we used SMACH, which is a two-tiered strategy aimed at (i) assessing what percentage of a study population has a mixture exposure sufficiently similar to a reference mixture (*80*), in this case, MIX N that was epidemiologically defined and experimentally tested; and (ii) calculating a similar mixture risk indicator [SMRI (*80*)] for study participants that were determined to have sufficiently similar mixtures to the reference mixture. The SMRI relates the human exposure range to experimentally determined points of departure [in this case a benchmark dose (BMD) lower confidence limit (BMDL)], similar to a hazard quotient for single chemicals. The SMRI was further evaluated as a metric of risk assessment with an odds ratio relating low and high deciles of SMRI with language delay in the children.

Using equivalence testing methodology in SMACH, we linked experimental evidence of adverse effects in zebrafish and *Xenopus* that were attributed to MIX N with concentrations of EDCs in pregnant women in the SELMA study. First, we built on the analytical framework by Marshall *et al.* (*80*) and defined a similarity region as follows. For the XETA, according to OECD guidelines (*81*), the threshold for a response is set at a 12% decrease from the reference control; thus, a benchmark response (BMR) was set at 88% of the reference control. The similarity regions for the BMD were thus defined by adding a further 12% change in response from the BMR to define the radius of the similarity region, represented by the change in total dose of the mixture between a 12 and 24% response. For the zebrafish, a one–standard deviation (SD) change from control defined the BMR, and an additional one-SD change from the BMR defined the radius of the similarity region (fig. S7 and table S7). Using those similarity regions, the mixture for each SELMA pregnant woman was tested for similarity to MIX N. Based on the results of, respectively, of the XETA and zebrafish studies, 96 and 91% of the pregnant women were determined to have sufficiently similar exposures to the reference mixture (table S8).

In the second step, a SMRI was constructed for subjects that were determined to have been exposed to mixtures sufficiently similar to the reference mixture, such that a higher index indicates a higher exposure. Children with maternal prenatal concentrations sufficiently similar to MIX N with the highest decile values of SMRI were 3.3 times more likely (odds ratio) to have language delay at 2.5 years of age than the children with SMRI values in the lowest decile ($P = 0.043$ using zebrafish results, and $P = 0.031$ using XETA results).

Further, the index is similar to a hazard quotient for single chemicals but instead uses the specific reference mixture in units of total concentrations for each subject divided by the BMDL from experimental evidence of toxicity. The lowest BMDL, in terms of SELMA concentrations, was 8X in XETA compared with 44X in zebrafish (table S8). The XETA BMR is defined by OECD guidelines, and it resulted in the most sensitive test. Thus, we used it to calculate the percentage of women with SMRI values that exceed 1 and found that 54% women had values above levels of concern.

Discussion

The current vision for improving regulatory decision-making, in public health and health care alike, relies on the transforming potential of high-throughput and high-content data to elucidate and quantify the molecular, cellular, and organismal responses to genetic vulnerabilities and environmental insults (*82*, *83*). This work, through complementary experimental methodologies, uncovered the gene networks that were specifically altered by an EDC mixture that is epidemiologically associated with language delay, identifying thyroid, estrogen, and PPAR pathways as major convergent targets. This empirical evidence allowed us to determine the proportion of a human population with exposure ranges of concern, thereby providing an integrative framework for mixture-based risk assessment strategies (Fig. 6) whose key features can be summarized as follows, alongside the attending limitations.

First, the chemicals profiled in this study, selected for the strong rationale presented in the introduction, clearly only represent a portion of all chemicals that humans are exposed to at present. In terms of exposure to short-lived pollutants (BPA and phthalates), we measured metabolites in urine, whose concentrations can vary during pregnancy and can thus be most reliably evaluated with reference to the specific day or week (*84*, *85*). Our exposure assessment for these chemicals may thus only reflect concentrations near week 10 of pregnancy, and our results may not be necessarily comparable to studies that collected samples at time points later in pregnancy. However, prior research in Swedish populations has demonstrated that phthalate and BPA concentrations were correlated with many lifestyle and household characteristics (*86*, *87*), whose relative stability plausibly results in pseudo-persistent exposure to shorter-lived compounds (*88*). We also standardized urine collection by using only first-morning voids, which may be more reliable than spot sampling (*89*, *90*). Further, exposure misclassification should be arguably nondifferential with respect to the outcome, so we expect the bias to be toward the null.

In terms of statistical methods, based on the hypotheses of interest, the range of options included Bayesian kernel machine regression for detection of interactions (*91*, *92*), WQS regression for estimating a mixture effect, and latent class models for profile classifications. We used WQS regression as a strategy agnostic to chemical interactions for studying the association between prenatal mixture

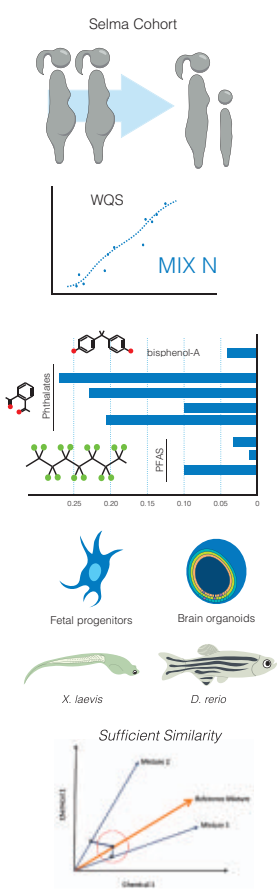

Motivation: Epidemiological data and human biomonitoring should guide experimental toxicology to include the concentrations of chemical mixtures relevant for real-life exposure and for which there is evidence of associations between exposures and health outcomes of concern. — EPIDEMIOLOGY

Step 1: Biostatistical methods for characterizing environmental mixtures such as weighted quantile sum (WQS) regression should be used to identify combinations of chemicals that are associated with health outcomes in humans. The selection of chemicals should be both sensitive (identifying chemicals of concern) and specific (identifying chemicals that are not of concern). — BIOSTATISTICS

Step 2: One or more human-relevant typical mixtures (relative proportions and total concentrations) should be identified, synthesized and experimentally tested. — CHEMISTRY

Step 3: Experimental evidence should identify the molecular mechanisms of action of the mixtures associated with adverse outcomes and dose-response experiments should be performed for estimation of a Point of Departure (POD), through the integration of:

- human experimental systems, especially induced pluripotent stem cell (iPSC) derived organoids that recapitulate the tissue-level complexity and developmental timings of human exposure
- in vivo models validated by the OECD

— EXPERIMENTAL BIOLOGY

Step 4: similar mixture approach (SMACH) should be applied to compare human exposure (determined to be sufficiently similar to the experimental mixture(s)) to experimental evidence of the mixture POD using the similar mixture risk index (SMRI) and determine the proportion of the human population with exposure ranges of concern (SMRI>1). — SMACH

Conclusion: Based on the integration of evidence from Step 1 through 4 standard single chemical risk assessment strategies should be benchmarked against the backdrop of relevant exposure to chemical mixtures of concern. — EDCMixRisk

Fig. 6. Strategic guidelines for chemical mixtures risk assessment.

exposure and language delay in children, on the basis of the original hypothesis on the direction of the outcome associated with prenatal EDC mixture exposure (delay rather than enhancement of language development). The focus of WQS regression is not on individual components where hypothesis testing and effect sizes are generally of interest. Instead, its aim is to detect components of interest (sEDCs) through non-negligible weights, particularly when the components have complex correlation patterns. The effect size of the mixture is measured in terms of a mixture effect of a weighted index of deciled components. So, a unit increase in the weighted index has an effect size of β. In a logistic model with a binary outcome such as language delay, the effect size is exp(β) as an odds ratio. For language delay, the odds ratio was roughly 1.4 across multiple WQS analyses. WQS regression was then adjusted to control for the following relevant potential confounders (though there may conceivably be residual confounding from variables that we were unable to collect): sex of the child, smoking status for the mother, parity, fish consumption, maternal education, and creatinine concentrations (for urinary metabolite concentrations). Adjustment by these potential confounders increased the odds ratio from 1.2 to 1.4. As in all regression models, WQS regression suffers from the impact of unmeasured confounders.

For the experimental identification of the genes dysregulated by MIX N exposure, our complimentary analysis in fetal progenitors and brain organoids demonstrated the feasibility of translating epidemiological evidence into mechanistic readouts in pathophysiologically relevant human models. This allowed us to draw the following conclusions and challenges ahead.

First, whereas the two models shared concordant clusters of MIX N dysregulated genes, they also captured different and, at times, opposing aspects of MIX N–induced dysregulation, underscoring the importance of endophenotype-based analysis across human models and longitudinal alignment between high-resolution clinical and molecular data (*93*). Thus, whereas the enrichment of categories related to protein translation was mainly driven by genes that were dysregulated only in fetal progenitors, organoids uncovered dysregulation of specific neuronal functions such as axonogenesis and synaptic control (fig. S8). This functional partitioning is consistent with the inherent difference between models (self-renewal of progenitors in fetal progenitors versus actual development in organoids) and indicates that MIX N alters neurodevelopment by affecting both translational control in progenitors and more mature aspects of neuronal cell biology at later stages.

Second, organoids were more sensitive to EDC exposure, showing more DEGs upon MIX N exposure and more significant ($P < 0.05$) overlaps with NDD causative genes. Together with the above observation on stage-specific dysregulation in organoids versus fetal progenitors, this underscores the complementarity of the two systems in capturing different temporal windows of neurodevelopmental vulnerability. Thus, although fetal progenitors may have been considered a gold standard for developmental biology and toxicology because they are directly derived from primary tissue, our results show that brain organoids are not simply a more viable alternative (because of the inherent procurement issues associated with fetal material) but also a more sensitive and pathophysiologically relevant model.

Third, the integration of MIX N DEGs with comprehensive lists of NDD-causative genes allowed us to pinpoint two classes of molecular

targets: (i) those for which evidence of haploinsufficiency as disease mechanism was concordant with the down-regulation of the same genes by MIX N and which can be therefore prioritized for further investigations to confirm them as causative relays of EDC neurodevelopmental outcomes; and (ii) those for which the direction of dysregulation was different either across doses (1X and 1000X) or across models. Given the increasing number of loci that can cause NDD by both loss or gain of function (through either copy number variations or mutations) (*94*), we suggest a precautionary approach for this class of targets and consider both up- and down-regulation as potentially adverse, depending on specific times and concentrations of exposure.

In vivo, MIX N altered TH activity in *Xenopus* heads, where the observed reduction in TH activity acquires human relevance when placed in the context of epidemiological results, because slight changes in maternal TH concentrations during early pregnancy result in IQ loss and modified brain structure in offspring (*95*). The TH disruptive activity of MIX N was corroborated in zebrafish, where we observed a decrease in the expression of thyroid receptors α and β. A master regulator and Genomatix analysis of DEGs revealed TH and estrogen signaling as the main endocrine axes affected by MIX N, in line with the close link between estrogen and TH signaling in the brain, where many genes are coregulated by both hormones (*96*, *97*). Finally, MIX N affected locomotion in both animal models, providing direct evidence for the impact of EDC mixtures on organismal behavior, which is of long-established value in toxicology. Interestingly, the differential impact on the two organisms echoes the differences in species-specific outcomes that was also previously observed with single chemicals, highlighting how the diversity of species-specific behaviors (exemplified, for zebrafish and *Xenopus*, in their differential light-dark cycle locomotion) may affect the manner in which they respond to toxic exposures, with relevant implications, in terms of probing mechanisms, for both specific chemicals and mixtures in multiple models (*98*).

Our work translates the framework of regulatory methods for risk assessment—namely, combining evidence of human exposure ranges with experimental evidence of links to adverse health effects—from single chemicals to complex mixtures. Based on our results, we can thus recommend (as summarized in Fig. 6) a risk assessment pipeline attuned to the real-life impact of chemicals through mixture-centered biostatistics and experimental biology, alongside other complementary approaches to mixture assessment. For any given outcome of concern, as long as reliable mixture-effect estimates are available alongside relevant experimental models, we anticipate our approach to be broadly applicable across health domains. To maximize feasibility, given its greater costs over standard single chemical–based approaches, we suggest a three-pronged approach entailing (i) a broad benchmarking effort through which public and private stakeholders should prioritize together, for each health domain, the adverse outcomes for which mixture-based approaches are likely to enable the greatest strides in public health protection; (ii) a focused effort on these selected outcomes and mixtures in diverse populations through interdisciplinary research consortia; and (iii) a parallel, finer-grained community effort, in which the same interdisciplinary approach can be translated to smaller, more local settings where experimental and epidemiological teams are also systematically integrated from the outset on simpler mixtures and phenotypes.

Materials and methods summary

Exposure assessment

Using data from the SELMA pregnancy cohort (*13*), mixtures of prenatal EDC exposures of relevance for health outcomes in children were identified. Exposure was measured in urine and serum taken in weeks 3 to 27 of pregnancy (median week 10, and 96% of the samples were taken before week 13). First morning void urine samples were analyzed for 10 phthalate metabolites [mono-ethyl phthalate (MEP), metabolite of DEP; mono-*n*-butyl phthalate (MnBP), metabolite of DBP; monobenzyl phthalate (MBzP), metabolite of BBzP; mono-(2-ethylhexyl) phthalate (MEHP), mono-(2-ethyl-5-hydroxylhexyl) phthalate (MEHHP), mono-(2-ethyl-5-oxohexyl) phthalate (MEOHP), and mono-(2-ethyl-5-carboxypentyl) phthalate (MECPP), metabolites of DEHP; mono-hydroxy-iso-nonyl phthalate (MHiNP), mono-, oxo-iso-nonyl phthalate (MOiNP), and mono-carboxy-iso-octyl phthalate (MCiOP), metabolites of DiNP)]; and alkyl phenols, including BPA and triclosan. Serum samples were analyzed for eight perfluorinated alkyl acids [perfluoroheptanoic acid (PFHpA), perfluorooctanoic acid (PFOA), perfluorononanoic acid (PFNA), perfluorodecanoic acid (PFDA), perfluoroundecanoic acid (PFUnDA), perfluorododecanoic acid (PFDoDA), perfluorohexane sulfonate (PFHxS), and perfluorooctane sulfonate (PFOS)] as described in the supplementary materials and publications therein.

Health examinations

For a measure of neurodevelopment, we used data from a routinely made language screening of the children when they were 30 months old. Language development was assessed by nurse's evaluation and parental questionnaire, including the number of words the child used (<25, 25 to 50, and >50). The main study outcome was the use of fewer than 50 words, termed language delay corresponding to a prevalence of 10%.

Biostatistical analyses

WQS regression (*16*) adjusted for covariates was used to establish associations between mixture exposures and language delay in children (see statistical method in the supplementary materials). WQS regression is a strategy for estimating empirical weights for a weighted sum of quantiled concentrations (i.e., deciles) most associated with the health outcome. The results are a β coefficient associated with the weighted sum (estimate, standard error, and *P* value) and the empirical weights (which are the average weights, constrained to sum to 1, from an ensemble step—here, 100 bootstrap samples). The components most associated with the health outcomes have non-negligible weights and were treated as sEDCs when the estimated weight exceeds the equi-weight case.

Next, we estimated the equivalent daily intake of sEDCs measured in the urine (phthalates and alkyl phenols) and estimated serum concentrations from the daily intake for these urinary measurement-based compounds. Finally, we used the geometric means, on a molar basis, for either the measured (PFAS) or estimated serum concentrations (phthalates and alkyl phenols) and established mixing proportions to prepare the mixture associated with language delay (MIX N). This mixture was used in the experimental studies.

Composition of the mixtures

The chemicals needed for the mixture were obtained from commercial custom synthesis laboratories or vendors. BPA, DMSO, MBzP, PFHxS, PFNA, and PFOS were obtained from Sigma-Aldrich Inc. MEP and MiNP were obtained from Toronto Research Chemicals. MBP was purchased from TCI, Tokyo Chemical Industry Co., Ltd. For MIX N, 1 M solutions in DMSO were prepared using MEP, MBP, MBzP, MiNP, BPA, PFHxS, PFNA, and PFOS. Thereafter, the 1 M solutions were mixed in proportions as described in table S3.

Human cellular models

Human iPSCs have been previously validated in G.T.'s laboratory (*99*). HFPNSCs were derived and maintained as previously described (*100*). HFPNSCs were obtained after elective termination with no evidence of developmental abnormalities. For the differentiation of cortical brain organoids, we used the protocol set up by (*101*), with minor modifications to improve its efficiency as shown previously by us in (*27*). Detailed information on culture condition, experimental procedures, and quality control are available in the supplementary materials.

EDC exposure

For EDC chemical exposure of fetal progenitors, cells were seeded in six-well plates. When 70 to 80% confluency was reached, 0.1% DMSO or the other compounds diluted in DMSO, namely the five different concentrations of MIX N (from 0.1X to 1000X), 0.04 nM BPA, and 5 nM T3 were added to the culture medium and used to culture cells for 48 hours or for 15 days (in the chronic setting), adding the chemical every time media change was performed (every other day). After the exposure cells were collected for RNA extraction.

For EDC chemical exposure of organoids, 0.1% DMSO, or the other compounds diluted in DMSO, MIX N in the two different concentrations used (1X and 1000X), 0.04 nM BPA, or 5 nM T3 was added to the culture media and used to culture cells from days 0 to 50. The concentration we used for T3 is higher than the physiological dose of T3 in the developing human brain (*102*, *103*) in order to have a reference transcriptional impact on TH targets. After exposure, organoids were collected for both RNA extraction and fixed for immunofluorescence analysis.

Immunohistochemistry for neuronal systems

Protocols and antibodies used for immunohistochemistry are described in the supplementary materials.

RNA sequencing

Total RNA was isolated with the RNeasy Micro Kit (Qiagen) according to the manufacturer's instructions. RNA was quantified with Nanodrop, and then the integrity was evaluated with Agilent 2100 Bioanalyzer (only if the quality ratios were not optimal after Nanodrop analysis). TruSeq Stranded Total RNA LT Sample Prep Kit (Illumina) was used to run the library for each sample. Sequencing was performed with the Illumina HiSeq 2000 platform, sequencing on average 10 million 50–base pair paired-end reads per sample.

RNA-seq data analysis

All the data and the bioinformatic analyses to reproduce the results presented have been organized in a repository publicly available at Zenodo (*104*). This includes both Rmd files for bioinformaticians to reproduce the analysis and html interactive reports for noncomputational scientists to explore, in detail, all the analytical steps. A description of the bioinformatic analyses performed for alignment, filtering, normalization, batch correction, differential expressions analysis, GO, and GSEA and the master regulator analysis are included in the supplementary materials.

Gene network analyses

For connection analysis, Genomatix software was used. Cytoscape was used to visualize the network (https://cytoscape.org/). More detailed information on the gene network analysis is available in the supplementary materials.

X. laevis rearing and strains

Xenopus laevis strains were maintained in accordance with institutional and European guidelines (2010/63/UE Directive 2010). Heterozygous *X. laevis* tadpoles used for the XETA were obtained by crossing adult homozygous Tg(thibz:eGFP) adults with wild-type animals (*105*). Wild-type tadpoles were obtained by crossing wild-type adults. More detailed information on the *X. laevis* husbandry and breeding routine is available in the supplementary materials.

Chemical exposure protocol for *X. laevis*

T3 (Sigma-Aldrich) was prepared in 70% milliQ Water, 30% NaOH, at 0.01 M, aliquoted in volumes of 100 µl in 1.5 ml low-binding Eppendorf (100% polypropylene) tubes, and stored at −20°C until use. For XETA, mobility, and qPCR analyses, 15 tadpoles per well (stage Nieuwkoop and Faber 45) were incubated in a six-well plate (TPP). Each well contained 8 ml of exposure solution prepared in water (Evian) or T3 5 nM (prepared in Evian) and DMSO (either containing or not containing mixtures or BPA at different concentrations). All exposure solutions were extemporaneously prepared in Greiner polypropylene tubes (50 ml tubes) and transferred in the wells of the six-well plate with a final 0.01% DMSO concentration in all groups. MIX N and BPA screenings were done in the presence of T3 5 nM for XETA. BPA was tested at the actual concentration as described in the mixture. Furthermore, a total mixture concentration 0.1 µM was tested as well as 1 µM for BPA. The exposure time was 72 hours in the dark at 23°C with 24-hour renewal. After 72 hours of exposure, tadpoles were rinsed and tested for mobility or anesthetized with 0.01% tricaine methanesulfonate (MS222, Sigma-Aldrich) either for fluorescent screening (XETA) or euthanasia in 0.1% MS-222 for brain gene expression analysis.

XETA

After 72 hours of exposure, tadpoles were anesthetized with 0.01% MS-222 and placed dorsally, one per well, in a black, conic-based 96-well plate (Greiner). All images were acquired as described in (*54*). Quantifications were carried out on whole pictures, and data were expressed in relative units of fluorescence. GraphPad Prism 7 software was used for statistical analysis. All values were normalized (100%) to T3 when mixtures were tested in coexposure. Results are expressed as scatter dot plots with mean ± SEM. A d'Agostino and Pearson normality test was carried out to determine the distribution of values in each of the exposure groups. For all groups, normal distribution was found, and a one-way analysis of variance (ANOVA) and Dunnett's post test was applied.

RNA extraction and qPCR analysis in *X. laevis*

Pooled brains of *X. laevis* embryos were used for the collection of RNA using a TissueLyser (Qiagen) for homogenization and RNAqueous Micro kit (AMBION) for isolation of RNA. After quantification with NanoDrop, complementary DNA (cDNA) was synthesized with a High Capacity cDNA RT kit (Applied BioSystem), and qPCR was carried out with Power SyBR mix (Applied BioSystem). Primers and genes tested are listed in table S6. More detailed information about the protocols used, as well as for the analysis for gene expression in *Xenopus* is provided in the supplementary materials.

X. laevis mobility

The mobility of *Xenopus* embryos was recorded by the DanioVision behavior analysis system (Noldus). Embryos were transferred to individual wells in a 12-well plate and a protocol of alternating light-dark cycles (30 sec–30sec) was used to induce locomotion. Distance traveled was recorded for a total of 10 min and analyzed with the EthoVision software (11.5, Noldus). Further information on the mobility assay and analysis is available in the supplementary materials.

D. rerio husbandry

Adult AB-strain zebrafish were maintained in a recirculating system and bred to obtain embryos. After breeding, embryos were collected and kept in zebrafish embryo medium until the exposure was initiated. The fish were treated in accordance with Swedish ethical guidelines with the ethical permit (Dnr 5.2.18-4777/16) granted by the Swedish Board of Agriculture. More detailed information on the zebrafish husbandry and breeding routine is available in the supplementary materials.

Exposure of *D. rerio*

For exposure of zebrafish, randomly selected embryos from a minimum of three different breeding pairs were used. Exposure solutions in zebrafish embryo medium, including five different MIX N concentrations (0.01-100X), DMSO, or BPA (at concentrations corresponding to those present in MIX N at 1X to 100X as well as at 0.1 µM and 10 µM), were prepared by serial dilution with a final DMSO concentration of 0.01% in all treatments. Embryos were exposed for 48 hours (72 to 120 hours postfertilization) at 28°C with a 14:10 hour light-dark cycle. Three replicates with 20 to 25 embryos per concentration were used, and each experiment was independently repeated three times. After exposure, the embryos were

used for the larval mobility assay or collected for gene expression analysis.

RNA extraction and qPCR analysis in D. rerio

Pooled zebrafish larvae were used for collection of RNA using a TissueLyser (Qiagen) for homogenization and the RNeasy Plus Mini Kit (Qiagen) for isolation of RNA. After quantification with NanoDrop, cDNA was synthesized with an iScript cDNA synthesis kit (BioRad) and RT-qPCR was carried out with the SsoAdvanced Universal SYBR-Green Supermix (BioRad). The primers and genes that were tested are listed in table S6. More detailed information about the protocols used, as well as for the analysis of gene expression in zebrafish, is provided in the the supplementary materials.

D. rerio larvae mobility

Mobility of larval zebrafish was recorded with the ViewPoint automatic behavior tracking system (ViewPoint Life Science) and an infrared camera. Larvae were transferred to individual wells in 48-well plates, and a protocol of alternating dark-light cycles (5 min–5 min) was used to induce locomotion (*106*). Distance traveled was recorded for a total of 40 min and analyzed with the ViewPoint Zebralab software (ViewPoint Life Science). Three independent experiments with three technical replicates each (n = 6 to 8 per replicate) were performed, and results are presented as a pool of the three experiments. Further information on the mobility assay and analysis is available in the supplementary materials.

SMACH

We conducted SMACH using the SELMA pregnancy cohort linking human exposures with estimates of adverse outcomes in zebrafish and *Xenopus*. In short, we modeled the total distance each zebrafish swam using four connected 10-min flexible curves fit using truncated power cubic splines (fig. S7A). Characteristics of these curves were evaluated across zebrafish as a function of exposure concentrations. Herein, the average maximum distance across the four cycles was modeled to reflect the change in swimming patterns due to exposure to MIX N. We used a piecewise nonlinear model to approximate the concentration-response relationship splines (fig. S7B). For the XETA, results from three individual experiments were combined with the T3 condition as control. The read out was a normalized level of fluorescence (where the control mean is 100%). A piecewise model was used to approximate the concentration-response relationship (fig. S7C).

The SMACH was conducted by first testing whether the concentrations in SELMA pregnant women were sufficiently similar to the domain-specific reference mixture (*80*). For those determined to be sufficiently similar, the SMRI was calculated (the sum of concentrations relative to the estimated BMDL from experimental studies). The BMR was based on either established guideline values (XETA) or a one-SD decrease from the control mean (zebrafish average maximum distance). The percentages of women with and SMRI exceeding 1 were tabulated to provide a level of concern. Finally, adjusted models were used to determine if children associated with the highest and lowest decile of SMRI were significantly ($P < 0.05$) different in language delay for MIX N.

Ethics issues

The EDC-MixRisk project maintains both external and internal reviews of the ethically relevant aspects of the project. Each partner is subjected to H2020 self-assessment processes and to reviews by an internal ethics advisory board (EAB). The EAB is composed of two leading scholars with expertise in bioethics and research policy. The project as a whole and each of the participating partners comply with Horizon 2020 ethics policies as well as with national legislations. Each partner follows internal guidelines concerning the collection, handling, and securing of informed consent; health-related information and data in the epidemiological studies; human biological samples in the epidemiological studies; data processing, dissemination, and privacy; risk to research subjects; and human embryonic stem cells and human fetal tissues. In addition, depending on the various national legislations and the mandates of the local institutions, local institutional review boards (IRBs) from the various partners were also involved in the relevant aspects of the project. Finally, the project has also allocated one team member to the coordination of ethics issues.

Regarding human embryonic stem cells, following the regulation establishing Horizon 2020 (*107*) and the Horizon 2020 ethics self-assessment guide (*108*), only established cell lines registered on either the European (*109*) or National Institutes of Health (NIH) (*110*) registries have been used. The use of stem cell lines is also subject to the laws of the countries of the participating partners: Italy, France, and Sweden. The procurement and use of fetal tissues upon informed consent from women undergoing elective abortions was approved by the relevant local ethics committee (University of Edinburgh) and, where necessary, subjected to additional review by the EAB and approval by relevant commission officers. Procurement of human samples followed informed consent in all cases, and samples were codified (pseudo-anonymized).

REFERENCES AND NOTES

1. A. C. Gore *et al.*, EDC-2: The Endocrine Society's Second Scientific Statement on endocrine-disrupting chemicals. *Endocr. Rev.* **36**, E1–E150 (2015). doi: 10.1210/er.2015-1010; pmid: 26544531
2. A. Kortenkamp, Low dose mixture effects of endocrine disrupters and their implications for regulatory thresholds in chemical risk assessment. *Curr. Opin. Pharmacol.* **19**, 105–111 (2014). doi: 10.1016/j.coph.2014.08.006; pmid: 25244397
3. Å. Bergman, J. J. Heindel, S. Jobling, K. A. Kidd, R. T. Zoeller, Eds., "State of the science of endocrine disrupting chemicals - 2012" (Technical Report, World Health Organization, 2013).
4. C. Cheroni, N. Caporale, G. Testa, Autism spectrum disorder at the crossroad between genes and environment: Contributions, convergences, and interactions in ASD developmental pathophysiology. *Mol. Autism* **11**, 69 (2020). doi: 10.1186/s13229-020-00370-1; pmid: 32912338
5. H. Peyre, M.-L. Charkaluk, A. Forhan, B. Heude, F. Ramus, EDEN Mother–Child Cohort Study Group, Do developmental milestones at 4, 8, 12 and 24 months predict IQ at 5-6 years old? Results of the EDEN mother-child cohort. *Eur. J. Paediatr. Neurol.* **21**, 272–279 (2017). doi: 10.1016/j.ejpn.2016.11.001; pmid: 27889381
6. E. Vlasblom *et al.*, Predictive validity of developmental milestones for detecting limited intellectual functioning. *PLOS ONE* **14**, e0214475 (2019). doi: 10.1371/journal.pone.0214475; pmid: 30921424
7. T. Flensborg-Madsen, E. L. Mortensen, Associations of early developmental milestones with adult intelligence. *Child Dev.* **89**, 638–648 (2018). doi: 10.1111/cdev.12760; pmid: 28198006
8. M. Marinopoulou, E. Billstedt, P.-I. Lin, M. Hallerbäck, C.-G. Bornehag, Number of words at age 2.5 years is associated with intellectual functioning at age 7 years in the SELMA study. *Acta Paediatr.* **110**, 2134–2141 (2021). doi: 10.1111/apa.15835; pmid: 33686710
9. C.-G. Bornehag *et al.*, Association of prenatal phthalate exposure with language development in early childhood. *JAMA Pediatr.* **172**, 1169–1176 (2018). doi: 10.1001/jamapediatrics.2018.3115; pmid: 30383084
10. M. Westerlund, C. Sundelin, Screening for developmental language disability in 3-year-old children. Experiences from a field study in a Swedish municipality. *Child Care Health Dev.* **26**, 91–110 (2000). doi: 10.1046/j.1365-2214.2000.00171.x; pmid: 10759750
11. J. R. Rochester, Bisphenol A and human health: A review of the literature. *Reprod. Toxicol.* **42**, 132–155 (2013). doi: 10.1016/j.reprotox.2013.08.008; pmid: 23994667
12. A. C. Gore *et al.*, EDC-2: The Endocrine Society's second Scientific Statement on endocrine-disrupting chemicals. *Endocr. Rev.* **36**, E1–E150 (2015). doi: 10.1210/er.2015-1010; pmid: 26544531
13. C.-G. Bornehag *et al.*, The SELMA study: A birth cohort study in Sweden following more than 2000 mother-child pairs. *Paediatr. Perinat. Epidemiol.* **26**, 456–467 (2012). doi: 10.1111/j.1365-3016.2012.01314.x; pmid: 22882790
14. European Chemicals Agency (ECHA), Candidate List of substances of very high concern for authorisation; www.echa.europa.eu/en/web/guest/candidate-list-table.
15. L. L. McIntyre, W. E. Pelham III, M. H. Kim, T. J. Dishion, D. S. Shaw, M. N. Wilson, A Brief Measure of Language Skills at 3 Years of Age and Special Education Use in Middle Childhood. *J. Pediatr.* **181**, 189–194 (2017). doi: 10.1016/j.jpeds.2016.10.035; pmid: 27908645
16. C. Carrico, C. Gennings, D. C. Wheeler, P. Factor-Litvak, Characterization of weighted quantile sum regression for highly correlated data in a risk analysis setting. *J. Agric. Biol. Environ. Stat.* **20**, 100–120 (2015). doi: 10.1007/s13253-014-0180-3; pmid: 30505142
17. O. S. Anderson *et al.*, Epigenetic responses following maternal dietary exposure to physiologically relevant levels of bisphenol A. *Environ. Mol. Mutagen.* **53**, 334–342 (2012). doi: 10.1002/em.21692; pmid: 22467340
18. L. N. Vandenberg, T. Colborn, T. B. Hayes, J. J. Heindel, D. R. Jacobs Jr., D.-H. Lee *et al.*, Hormones and endocrine-disrupting chemicals: Low-dose effects and nonmonotonic dose responses. *Endocr. Rev.* **33**, 378–455 (2012). doi: 10.1210/er.2011-1050; pmid: 22419778
19. B. S. Abrahams *et al.*, SFARI Gene 2.0: A community-driven knowledgebase for the autism spectrum disorders (ASDs). *Mol. Autism* **4**, 36 (2013). doi: 10.1186/2040-2392-4-36; pmid: 24090431
20. T. Wang *et al.*, De novo genic mutations among a Chinese autism spectrum disorder cohort. *Nat. Commun.* **7**, 13316 (2016). doi: 10.1038/ncomms13316; pmid: 27824329
21. S. J. Sanders *et al.*, De novo mutations revealed by whole-exome sequencing are strongly associated with autism. *Nature* **485**, 237–241 (2012). doi: 10.1038/nature10945; pmid: 22495306

22. H. Guo *et al*., Inherited and multiple de novo mutations in autism/developmental delay risk genes suggest a multifactorial model. *Mol. Autism* **9**, 64 (2018). doi: 10.1186/s13229-018-0247-z; pmid: 30564305
23. L. Y. AlAyadhi *et al*., High-resolution SNP genotyping platform identified recurrent and novel CNVs in autism multiplex families. *Neuroscience* **339**, 561–570 (2016). doi: 10.1016/j.neuroscience.2016.10.030; pmid: 27771533
24. S. V. Ranneva, V. F. Maksimov, I. M. Korostyshevskaja, T. V. Lipina, Lack of synaptic protein, calsyntenin-2, impairs morphology of synaptic complexes in mice. *Synapse* **74**, e22132 (2020). doi: 10.1002/syn.22132; pmid: 31529526
25. S. V. Ranneva, K. S. Pavlov, A. V. Gromova, T. G. Amstislavskaya, T. V. Lipina, Features of emotional and social behavioral phenotypes of calsyntenin2 knockout mice. *Behav. Brain Res.* **332**, 343–354 (2017). doi: 10.1016/j.bbr.2017.06.029; pmid: 28647593
26. J. C. Silbereis, S. Pochareddy, Y. Zhu, M. Li, N. Sestan, The cellular and molecular landscapes of the developing human central nervous system. *Neuron* **89**, 248–268 (2016). doi: 10.1016/j.neuron.2015.12.008; pmid: 26796689
27. A. López-Tobón *et al*., Human cortical organoids expose a differential function of GSK3 on cortical neurogenesis. *Stem Cell Reports* **13**, 847–861 (2019). doi: 10.1016/j.stemcr.2019.09.005; pmid: 31607568
28. T. J. Nowakowski *et al*., Spatiotemporal gene expression trajectories reveal developmental hierarchies of the human cortex. *Science* **358**, 1318–1323 (2017). doi: 10.1126/science.aap8809; pmid: 29217575
29. A. A. Pollen *et al*., Molecular identity of human outer radial glia during cortical development. *Cell* **163**, 55–67 (2015). doi: 10.1016/j.cell.2015.09.004; pmid: 26406371
30. M. Florio *et al*., Human-specific gene *ARHGAP11B* promotes basal progenitor amplification and neocortex expansion. *Science* **347**, 1465–1470 (2015). doi: 10.1126/science.aaa1975; pmid: 25721503
31. B. E. L. Ostrem, J. H. Lui, C. C. Gertz, A. R. Kriegstein, Control of outer radial glial stem cell mitosis in the human brain. *Cell Rep.* **8**, 656–664 (2014). doi: 10.1016/j.celrep.2014.06.058; pmid: 25088420
32. M. Kanehisa, S. Goto, KEGG: Kyoto encyclopedia of genes and genomes. *Nucleic Acids Res.* **28**, 27–30 (2000). doi: 10.1093/nar/28.1.27; pmid: 10592173
33. A. Liberzon *et al*., The Molecular Signatures Database hallmark gene set collection. *Cell Syst.* **1**, 417–425 (2015). doi: 10.1016/j.cels.2015.12.004; pmid: 26771021
34. Deciphering Developmental Disorders Study, Prevalence and architecture of de novo mutations in developmental disorders. *Nature* **542**, 433–438 (2017). doi: 10.1038/nature21062; pmid: 28135719
35. R. K. C. Yuen *et al*., Whole genome sequencing resource identifies 18 new candidate genes for autism spectrum disorder. *Nat. Neurosci.* **20**, 602–611 (2017). doi: 10.1038/nn.4524; pmid: 28263302
36. H. Guo *et al*., Genome sequencing identifies multiple deleterious variants in autism patients with more severe phenotypes. *Genet. Med.* **21**, 1611–1620 (2019). doi: 10.1038/s41436-018-0380-2; pmid: 30504930
37. H. A. F. Stessman *et al*., Targeted sequencing identifies 91 neurodevelopmental-disorder risk genes with autism and developmental-disability biases. *Nat. Genet.* **49**, 515–526 (2017). doi: 10.1038/ng.3792; pmid: 28191889
38. Online Mendelian Inheritance in Man (OMIM), About OMIM; www.omim.org/about.
39. D. Velmeshev *et al*., Single-cell genomics identifies cell type-specific molecular changes in autism. *Science* **364**, 685–689 (2019). doi: 10.1126/science.aav8130; pmid: 31097668
40. F. K. Satterstrom *et al*., Large-Scale Exome Sequencing Study Implicates Both Developmental and Functional Changes in the Neurobiology of Autism. *Cell* **180**, 568–584.e23 (2020). doi: 10.1016/j.cell.2019.12.036; pmid: 31981491
41. C. Yang *et al*., AutismKB 2.0: A knowledgebase for the genetic evidence of autism spectrum disorder. *Database* **2018** bay106 (2018). doi: 10.1093/database/bay106
42. M. J. Gandal *et al*., Transcriptome-wide isoform-level dysregulation in ASD, schizophrenia, and bipolar disorder. *Science* **362**, eaat8127 (2018). doi: 10.1126/science.aat8127; pmid: 30545856
43. L. A. Weiss *et al*., Sodium channels *SCN1A*, *SCN2A* and *SCN3A* in familial autism. *Mol. Psychiatry* **8**, 186–194 (2003). doi: 10.1038/sj.mp.4001241; pmid: 12610651
44. S. De Rubeis *et al*., Synaptic, transcriptional and chromatin genes disrupted in autism. *Nature* **515**, 209–215 (2014). doi: 10.1038/nature13772; pmid: 25363760
45. R. Ben-Shalom *et al*., Opposing effects on $Na_V1.2$ function underlie differences between *SCN2A* variants observed in individuals with autism spectrum disorder or infantile seizures. *Biol. Psychiatry* **82**, 224–232 (2017). doi: 10.1016/j.biopsych.2017.01.009; pmid: 28256214
46. T. Munesue *et al*., Two genetic variants of *CD38* in subjects with autism spectrum disorder and controls. *Neurosci. Res.* **67**, 181–191 (2010). doi: 10.1016/j.neures.2010.03.004; pmid: 20435366
47. L. L. Martucci *et al*., A multiscale analysis in $CD38^{-/-}$ mice unveils major prefrontal cortex dysfunctions. *FASEB J.* **33**, 5823–5835 (2019). doi: 10.1096/fj.201800489R; pmid: 30844310
48. E. K. Ruzzo *et al*., Inherited and de novo genetic risk for autism impacts shared networks. *Cell* **178**, 850–866.e26 (2019). doi: 10.1016/j.cell.2019.07.015; pmid: 31398340
49. D. H. Geschwind, Genetics of autism spectrum disorders. *Trends Cogn. Sci.* **15**, 409–416 (2011). doi: 10.1016/j.tics.2011.07.003; pmid: 21855394
50. G. R. Williams, Neurodevelopmental and neurophysiological actions of thyroid hormone. *J. Neuroendocrinol.* **20**, 784–794 (2008). doi: 10.1111/j.1365-2826.2008.01733.x; pmid: 18601701
51. P. Berbel *et al*., Delayed neurobehavioral development in children born to pregnant women with mild hypothyroxinemia during the first month of gestation: The importance of early iodine supplementation. *Thyroid* **19**, 511–519 (2009). doi: 10.1089/thy.2008.0341; pmid: 19348584
52. R. Morgenstern *et al*., Phthalates and thyroid function in preschool age children: Sex specific associations. *Environ. Int.* **106**, 11–18 (2017). doi: 10.1016/j.envint.2017.05.007; pmid: 28554096
53. S. Lignell *et al*., Maternal body burdens of PCDD/Fs and PBDEs are associated with maternal serum levels of thyroid hormones in early pregnancy: A cross-sectional study. *Environ. Health* **15**, 55 (2016). doi: 10.1186/s12940-016-0139-7; pmid: 27114094
54. J.-B. Fini *et al*., Human amniotic fluid contaminants alter thyroid hormone signalling and early brain development in *Xenopus* embryos. *Sci. Rep.* **7**, 43786 (2017). doi: 10.1038/srep43786; pmid: 28266608
55. M. Boas, U. Feldt-Rasmussen, K. M. Main, Thyroid effects of endocrine disrupting chemicals. *Mol. Cell. Endocrinol.* **355**, 240–248 (2012). doi: 10.1016/j.mce.2011.09.005; pmid: 21939731
56. S. Han *et al*., A non-canonical role for the proneural gene *Neurog1* as a negative regulator of neocortical neurogenesis. *Development* **145**, dev.157719 (2018). doi: 10.1242/dev.157719; pmid: 30201687
57. J. R. Rochester, A. L. Bolden, C. F. Kwiatkowski, Prenatal exposure to bisphenol A and hyperactivity in children: A systematic review and meta-analysis. *Environ. Int.* **114**, 343–356 (2018). doi: 10.1016/j.envint.2017.12.028; pmid: 29525285
58. M. N. Grohs *et al*., Prenatal maternal and childhood bisphenol a exposure and brain structure and behavior of young children. *Environ. Health* **18**, 85 (2019). doi: 10.1186/s12940-019-0528-9; pmid: 31615514
59. S. K. Witchey, J. Fuchs, H. B. Patisaul, Perinatal bisphenol A (BPA) exposure alters brain oxytocin receptor (OTR) expression in a sex- and region- specific manner: A CLARITY-BPA consortium follow-up study. *Neurotoxicology* **74**, 139–148 (2019). doi: 10.1016/j.neuro.2019.06.007; pmid: 31251963
60. V. Mustieles *et al*., Bisphenol A and its analogues: A comprehensive review to identify and prioritize effect biomarkers for human biomonitoring. *Environ. Int.* **144**, 105811 (2020). doi: 10.1016/j.envint.2020.105811; pmid: 32866736
61. H. R. Willsey *et al*., Parallel in vivo analysis of large-effect autism genes implicates cortical neurogenesis and estrogen in risk and resilience. *Neuron* **109**, 788–804.e8 (2021). doi: 10.1016/j.neuron.2021.01.002; pmid: 33497602
62. S. Akbarian *et al*., The PsychENCODE project. *Nat. Neurosci.* **18**, 1707–1712 (2015). doi: 10.1038/nn.4156; pmid: 26605881
63. A. Jo *et al*., The versatile functions of Sox9 in development, stem cells, and human diseases. *Genes Dis.* **1**, 149–161 (2014). doi: 10.1016/j.gendis.2014.09.004; pmid: 25685828
64. K. I. Vong, C. K. Y. Leung, R. R. Behringer, K. M. Kwan, Sox9 is critical for suppression of neurogenesis but not initiation of gliogenesis in the cerebellum. *Mol. Brain* **8**, 25 (2015). doi: 10.1186/s13041-015-0115-0; pmid: 25888505
65. W. Sun *et al*., SOX9 is an astrocyte-specific nuclear marker in the adult brain outside the neurogenic regions. *J. Neurosci.* **37**, 4493–4507 (2017). doi: 10.1523/JNEUROSCI.3199-16.2017; pmid: 28336567
66. P. Selvaraj *et al*., Neurotrophic factor-α1: A key Wnt-β-catenin dependent anti-proliferation factor and ERK-Sox9 activated inducer of embryonic neural stem cell differentiation to astrocytes in neurodevelopment. *Stem Cells* **35**, 557–571 (2017). doi: 10.1002/stem.2511; pmid: 27709799
67. N. N. Parikshak *et al*., Integrative functional genomic analyses implicate specific molecular pathways and circuits in autism. *Cell* **155**, 1008–1021 (2013). doi: 10.1016/j.cell.2013.10.031; pmid: 24267887
68. C. Gilissen *et al*., Genome sequencing identifies major causes of severe intellectual disability. *Nature* **511**, 344–347 (2014). doi: 10.1038/nature13394; pmid: 24896178
69. S. Tu *et al*., NitroSynapsin therapy for a mouse MEF2C haploinsufficiency model of human autism. *Nat. Commun.* **8**, 1488 (2017). doi: 10.1038/s41467-017-01563-8; pmid: 29133852
70. R. J. Denver, K. E. Williamson, Identification of a thyroid hormone response element in the mouse Kruppel-like factor 9 gene to explain its postnatal expression in the brain. *Endocrinology* **150**, 3935–3943 (2009). doi: 10.1210/en.2009-0050; pmid: 19359381
71. F. Hu, J. R. Knoedler, R. J. Denver, A mechanism to enhance cellular responsivity to hormone action: Krüppel-Like factor 9 promotes thyroid hormone receptor-β autoinduction during postembryonic brain development. *Endocrinology* **157**, 1683–1693 (2016). doi: 10.1210/en.2015-1980; pmid: 26886257
72. M. Maekawa *et al*., Polyunsaturated fatty acid deficiency during neurodevelopment in mice models the prodromal state of schizophrenia through epigenetic changes in nuclear receptor genes. *Transl. Psychiatry* **7**, e1229 (2017). doi: 10.1038/tp.2017.182; pmid: 28872641
73. O. Baud, N. Berkane, Hormonal changes associated with intra-uterine growth restriction: Impact on the developing brain and future neurodevelopment. *Front. Endocrinol. (Lausanne)* **10**, 179 (2019). doi: 10.3389/fendo.2019.00179; pmid: 30972026
74. T. Colborn, Neurodevelopment and endocrine disruption. *Environ. Health Perspect.* **112**, 944–949 (2004). doi: 10.1289/ehp.6601; pmid: 15198913
75. The Signaling Pathways Project; www.signalingpathways.org/index.jsf.
76. A. Ghassabian, L. Trasande, Disruption in thyroid signaling pathway: A mechanism for the effect of endocrine-disrupting chemicals on child neurodevelopment. *Front. Endocrinol.* **9**, 204 (2018). doi: 10.3389/fendo.2018.00204; pmid: 29760680
77. R. M. Basnet, D. Zizioli, S. Taweedet, D. Finazzi, M. Memo, Zebrafish larvae as a behavioral model in neuropharmacology. *Biomedicines* **7**, 23 (2019). doi: 10.3390/biomedicines7010023; pmid: 30917585
78. K. G. Pratt, A. S. Khakhalin, Modeling human neurodevelopmental disorders in the *Xenopus* tadpole: From mechanisms to therapeutic targets. *Dis. Model. Mech.* **6**, 1057–1065 (2013). doi: 10.1242/dmm.012138; pmid: 23929939
79. J. F. Rovet, The role of thyroid hormones for brain development and cognitive function. *Endocr. Dev.* **26**, 26–43 (2014). doi: 10.1159/000363153; pmid: 25231442
80. S. Marshall *et al*., An empirical approach to sufficient similarity: Combining exposure data and mixtures toxicology data. *Risk Anal.* **33**, 1582–1595 (2013). doi: 10.1111/risa.12015; pmid: 23398277
81. OECD iLibrary, Test no. 248: *Xenopus* eleutheroembryonic thyroid assay (XETA); www.oecd-ilibrary.org/environment/tg-248-xenopus-eleutheroembryonic-thyroid-assay-xeta_a13f80ee-en.
82. R. M. Califf *et al*., Transforming evidence generation to support health and health care decisions. *N. Engl. J. Med.* **375**, 2395–2400 (2016). doi: 10.1056/NEJMsb1610128; pmid: 27974039
83. A. Peters, T. S. Nawrot, A. A. Baccarelli, Hallmarks of environmental insults. *Cell* **184**, 1455–1468 (2021). doi: 10.1016/j.cell.2021.01.043; pmid: 33657411
84. M. Fisher *et al*., Bisphenol A and phthalate metabolite urinary concentrations: Daily and across pregnancy variability. *J. Expo. Sci. Environ. Epidemiol.* **25**, 231–239 (2015). doi: 10.1038/jes.2014.65; pmid: 25248937
85. L. E. Johns, G. S. Cooper, A. Galizia, J. D. Meeker, Exposure assessment issues in epidemiology studies of phthalates.

Environ. Int. **85**, 27–39 (2015). doi: 10.1016/j.envint.2015.08.005; pmid: 26313703
86. K. Larsson *et al.*, Exposure determinants of phthalates, parabens, bisphenol A and triclosan in Swedish mothers and their children. *Environ. Int.* **73**, 323–333 (2014). doi: 10.1016/j.envint.2014.08.014; pmid: 25216151
87. K. Larsson *et al.*, Phthalates, non-phthalate plasticizers and bisphenols in Swedish preschool dust in relation to children's exposure. *Environ. Int.* **102**, 114–124 (2017). doi: 10.1016/j.envint.2017.02.006; pmid: 28274486
88. C. G. Daughton, Cradle-to-cradle stewardship of drugs for minimizing their environmental disposition while promoting human health. I. Rationale for and avenues toward a green pharmacy. *Environ. Health Perspect.* **111**, 757–774 (2003). doi: 10.1289/ehp.5947; pmid: 12727606
89. J. L. Preau Jr., L.-Y. Wong, M. J. Silva, L. L. Needham, A. M. Calafat, Variability over 1 week in the urinary concentrations of metabolites of diethyl phthalate and di(2-ethylhexyl) phthalate among eight adults: An observational study. *Environ. Health Perspect.* **118**, 1748–1754 (2010). doi: 10.1289/ehp.1002231; pmid: 20797930
90. M. K. Townsend, A. A. Franke, X. Li, F. B. Hu, A. H. Eliassen, Within-person reproducibility of urinary bisphenol A and phthalate metabolites over a 1 to 3 year period among women in the Nurses' Health Studies: A prospective cohort study. *Environ. Health* **12**, 80 (2013). doi: 10.1186/1476-069X-12-80; pmid: 24034517
91. J. M. Braun, C. Gennings, R. Hauser, T. F. Webster, What can epidemiological studies tell us about the impact of chemical mixtures on human health? *Environ. Health Perspect.* **124**, A6–A9 (2016). doi: 10.1289/ehp.1510569; pmid: 26720830
92. J. F. Bobb *et al.*, Bayesian kernel machine regression for estimating the health effects of multi-pollutant mixtures. *Biostatistics* **16**, 493–508 (2015). doi: 10.1093/biostatistics/kxu058; pmid: 25532525
93. N. Rajewsky *et al.*, LifeTime and improving European healthcare through cell-based interceptive medicine. *Nature* **587**, 377–386 (2020). doi: 10.1038/s41586-020-2715-9; pmid: 32894860
94. A. Deshpande, L. A. Weiss, Recurrent reciprocal copy number variants: Roles and rules in neurodevelopmental disorders. *Dev. Neurobiol.* **78**, 519–530 (2018). doi: 10.1002/dneu.22587; pmid: 29575775
95. T. I. M. Korevaar *et al.*, Association of maternal thyroid function during early pregnancy with offspring IQ and brain morphology in childhood: A population-based prospective cohort study. *Lancet Diabetes Endocrinol.* **4**, 35–43 (2016). doi: 10.1016/S2213-8587(15)00327-7; pmid: 26497402
96. N. Vasudevan, S. Ogawa, D. Pfaff, Estrogen and thyroid hormone receptor interactions: Physiological flexibility by molecular specificity. *Physiol. Rev.* **82**, 923–944 (2002). doi: 10.1152/physrev.00014.2002; pmid: 12270948
97. A. Zsarnovszky *et al.*, Thyroid hormone- and estrogen receptor interactions with natural ligands and endocrine disruptors in the cerebellum. *Front. Neuroendocrinol.* **48**, 23–36 (2018). doi: 10.1016/j.yfrne.2017.10.001 pmid: 28987779
98. A. Hussain *et al.*, Multiple screening of pesticides toxicity in zebrafish and daphnia based on locomotor activity alterations. *Biomolecules* **10**, 1224 (2020). doi: 10.3390/biom10091224; pmid: 32842481
99. A. Adamo *et al.*, 7q11.23 dosage-dependent dysregulation in human pluripotent stem cells affects transcriptional programs in disease-relevant lineages. *Nat. Genet.* **47**, 132–141 (2015). doi: 10.1038/ng.3169; pmid: 25501393
100. R. B. Bressan *et al.*, Regional identity of human neural stem cells determines oncogenic responses to histone H3.3 mutants. *Cell Stem Cell* **28**, 877–893.e9 (2021). doi: 10.1016/j.stem.2021.01.016; pmid: 33631116
101. A. M. Paşca *et al.*, Functional cortical neurons and astrocytes from human pluripotent stem cells in 3D culture. *Nat. Methods* **12**, 671–678 (2015). doi: 10.1038/nmeth.3415; pmid: 26005811
102. M. H. A. Kester *et al.*, Iodothyronine levels in the human developing brain: Major regulatory roles of iodothyronine deiodinases in different areas. *J. Clin. Endocrinol. Metab.* **89**, 3117–3128 (2004). doi: 10.1210/jc.2003-031832; pmid: 15240580
103. R. M. Calvo, J. M. Roda, M. J. Obregón, G. Morreale de Escobar, Thyroid hormones in human tumoral and normal nervous tissues. *Brain Res.* **801**, 150–157 (1998). doi: 10.1016/S0006-8993(98)00576-9; pmid: 9729351
104. P.-L. Germain, N. Caporale, C. Cheroni, G. Testa, GiuseppeTestaLab/EDCMixRisk: version 1.0.0. Zenodo (2021); .doi: 10.5281/zenodo.5599212
105. J.-B. Fini *et al.*, An in vivo multiwell-based fluorescent screen for monitoring vertebrate thyroid hormone disruption. *Environ. Sci. Technol.* **41**, 5908–5914 (2007). doi: 10.1021/es0704129; pmid: 17874805
106. G. Ašmonaitė, S. Boyer, K. B. de Souza, B. Wassmur, J. Sturve, Behavioural toxicity assessment of silver ions and nanoparticles on zebrafish using a locomotion profiling approach. *Aquat. Toxicol.* **173**, 143–153 (2016). doi: 10.1016/j.aquatox.2016.01.013; pmid: 26867187
107. European Commission, Regulation (EU) No 1291/2013 of the European parliament and of the council of 11 December 2013 establishing Horizon 2020 - the Framework Programme for Research and Innovation (2014-2020) and repealing decision no. 1982/2006/EC. Brussels (2013); https://eur-lex.europa.eu/legal-content/EN/TXT/?uri=CELEX%3A32013D0743.
108. European Commission, "How to complete your ethics Self-Assessment, version 1.0. Brussels: DG Research and Innovation" (2014); https://ec.europa.eu/research/participants/data/ref/h2020/grants_manual/hi/ethics/h2020_hi_ethics-self-assess_en.pdf.
109. S. Seltmann *et al.*, hPSCreg—The human pluripotent stem cell registry. *Nucleic Acids Res.* **44**, D757–D763 (2016). doi: 10.1093/nar/gkv963; pmid: 26400179
110. National Institutes of Health, NIH Human Embryonic Stem Cell Registry; http://grants.nih.gov/stem_cells/registry/current.htm [accessed 18 May 2013].
111. R. Edgar, M. Domrachev, A. E. Lash, Gene Expression Omnibus: NCBI gene expression and hybridization array data repository. *Nucleic Acids Res.* **30**, 207–210 (2002). doi: 10.1093/nar/30.1.207; pmid: 11752295

ACKNOWLEDGMENTS

The authors wish to dedicate this work to the memory of Bo A. G. Jönsson (1960–2016), whose dedication and knowledge was instrumental to this project. **Funding:** This work received funding from the European Union's Horizon 2020 research and innovation program under grant agreement no. 634880, EDC-MixRisk (Å.B., J.R., C.-G.B., C.G., E.N., C.R., M.J., B.D., W.K., J.S., E.K., H.K., and G.T.); the European Research Council (ERC) (DISEASEAVATARS 616441 to G.T.); the EPIGEN Flagship Project of the Italian National Research Council (CNR) (G.T.); the ERANET-Neuron grant from the Italian Ministry of Health (AUTSYN) (P.-L.G.); the Umberto Veronesi Foundation (P.-L.G.); the Italian Ministry of Health (Ricerca Corrente Grant to G.T.); ENDpoiNTs, European Union's Horizon 2020 research and innovation program (grant no. 825759 to G.T.); Science Without Borders Program (CAPES, Brazil) (R.B.B.); the Swedish Research Council Formas (G.B. and J.R.); Centre National de la Recherche Scientifique (CNRS) (J.-B.F. and B.D.); and the Muséum National d'Histoire Naturelle (MNHN) (B.D. and J.-B.F.).
Author contributions: C.-G.B. is principal investigator for the SELMA study and was responsible for the biostatistical modeling together with C.G. N.C. carried out all the experiments with human neurodevelopmental systems, with the help of M.T.R.; P.-L.G. and C.C. designed the analytical strategy of transcriptomic data; C.C., P.-L.G., and N.C. performed bioinformatic analysis; A.L.T., S.T., and N.C. set up the cortical organoids protocol; R.B.B. and S.M.P. provided human fetal primary stem cells; N.C., M.T.R., and F.C. performed the staining of organoids; E.T. and F.T. helped with cortical organoid maintenance and library preparation; G.A.D. helped with the graphical representation of the figures; L.B. carried out all the experiments with *D. rerio*, including EDC exposure, RT-qPCR, and the mobility assay; L.B. and J.S. analyzed the *D. rerio* data; M.L. carried out all the experiments with *X. laevis*, including EDC exposure, XETA, RT-qPCR, and the mobility assay; B.D., J.-B.F., and M.L. analyzed the *Xenopus* data; M.L. and B.D. made the Genomatix figure; N.E.C. and G.T. attended to the bioethical issues of the project; C.L. contributed the chemical analysis and preparation of the mix; Å.B., P.D., M.J., W.K., E.K., J.-B.F., H.K., M.Ö., P.R., C.R., E.E., E.N., G.B., M.Z., and O.S. contributed to the study design, discussions, and critical reading of the manuscript; C.-G.B., C.G., N.C., C.C., B.D., P.-L.G., M.L., L.B., J.R., J.S., and G.T. wrote the paper; and C.-G.B., B.D., J.-B.F., C.G., J.R., J.S., and G.T. conceived, designed, and supervised the study. **Competing interests:** B.D. holds a patent under the name "Transgenic clawed frog embryos and use thereof as detectors of endocrine disruptors in the environment," filed in 2002 (number FR020669) and extended by a Patent Cooperation Treaty filed in 2003 (patent number 8476484). All other authors declare no competing interests. **Data and materials availability:** All transcriptomic data have been made publicly available on the National Center for Biotechnology Information's Gene Expression Omnibus (GEO) repository (*111*) and are accessible through GEO series accession number GSE171566 (www.ncbi.nlm.nih.gov/geo/query/acc.cgi?acc=GSE171566). All other data are available in the main text and supplementary materials. All the bioinformatic analyses and the code to reproduce the figures are available in a GitHub repository that is publicly accessible to ensure complete reproducibility and to help the reader to consult, understand, and reuse our data and analytical pipelines [available at GitHub at https://giuseppetestalab.github.io/EDCMixRisk/ and Zenodo (*104*)]. Materials are available from the corresponding authors upon request

SUPPLEMENTARY MATERIALS

15 November 2020; accepted 20 December 2021
10.1126/science.abe8244

AAAS.ORG/COMMUNITY

AAAS' Member Community is a one-stop destination for scientists and STEM enthusiasts alike. It's "Where Science Gets Social": a community where facts matter, ideas are big and there's always a reason to come hang out, share, discuss and explore.

Member COMMUNITY
AAAS

AMERICAN ASSOCIATION FOR THE ADVANCEMENT OF SCIENCE

RESEARCH ARTICLE SUMMARY

CELL BIOLOGY

Lysosomal cystine mobilization shapes the response of TORC1 and tissue growth to fasting

Patrick Jouandin*†, Zvonimir Marelja†, Yung-Hsin Shih, Andrey A. Parkhitko, Miriam Dambowsky, John M. Asara, Ivan Nemazanyy, Christian C. Dibble, Matias Simons*‡, Norbert Perrimon*‡

INTRODUCTION: Adaptation to changes in diet involves a complex cellular response controlled by interacting metabolic and signaling pathways. During fasting periods, this response remobilizes nutrients from internal stores through catabolic programs. In *Drosophila*, the fat body, an organ analogous to the liver and adipose tissue in mammals, functions as the organism's main energy reserve, integrating nutrient status with energy expenditure. How the fat body sustains its own needs and balances remobilization of nutrients over the course of a starvation period during developmental growth is unclear.

RATIONALE: The target of rapamycin complex 1 (TORC1) signaling pathway is a master regulator of growth and metabolism. Activated when nutrients are replete, TORC1 promotes biosynthesis and represses catabolic processes such as autophagy. In the fat body of fasting animals, however, TORC1 activity is dynamic. Activated to a maximum in feeding animals, TORC1 is acutely down-regulated at the onset of fasting, followed by partial and progressive reactivation through the amino acids generated by proteolysis during autophagy. This reactivation hints at a model in which TORC1 reaches a specific activity threshold allowing for minimal anabolism to occur concomitantly with catabolism, such as autophagy. To analyze how TORC1 dynamics is achieved, we used screening approaches, combined metabolomics with genetics, and developed specific heavy isotope–tracing methods in intact animals.

RESULTS: A screen to test the role of amino acids on animal fitness when starved on a low-protein diet identified cysteine as a potent suppressor of growth. During fasting, cysteine concentration was elevated through lysosomal cystine export through dCTNS, the mammalian ortholog of which, cystinosin, is responsible for the lysosomal storage disease cystinosis. dCTNS depletion and overexpression, respectively, lowered and elevated cysteine concentration in fasted animals, providing us with a genetic means with which to manipulate cysteine levels in vivo. Parallel metabolomics profiling of fasting animals revealed an increased concentration of tricarboxylic acid (TCA) cycle intermediates during fasting. Moreover, heavy isotope cysteine tracing demonstrated cysteine metabolism to coenzyme A (CoA) and further to acetyl-CoA, a process that was coupled to lipid catabolism in the fat body during fasting. Acetyl-CoA appeared to facilitate incorporation of additional substrates in the TCA cycle, with dCTNS overexpression increasing the entry of a heavy isotope alanine tracer in the TCA cycle. The elevation of TCA cycle intermediates by cysteine metabolism could be linked to the reactivation of TORC1. dCTNS overexpression dampened the reactivation of TORC1 during fasting, and it was sufficient to suppress TORC1 activity and cause ectopic autophagy in the fat body of fed animals. By contrast, dCTNS deletion did not affect TORC1 activity nor autophagy in fed animals but elevated the reactivation of TORC1 above a threshold suitable to halt autophagy during fasting. Finally, we show that cysteine metabolism regulates anaplerotic carbon flow in the TCA cycle and the level of amino acids, in particular aspartate. Combinatorial amino acid treatments rescued TORC1 activity upon fasting when cysteine levels were high. This suggests that the balance between cysteine metabolism and amino acid synthesis by the TCA cycle ultimately controls TORC1 reactivation, and thereby autophagy, during fasting. As a consequence, dCTNS depletion shortened life span during fasting, which could be restored by dietary cysteine, highlighting the central role of cysteine in the metabolism of fasted animals.

CONCLUSION: We found that in developing animals, adipose cells control biosynthesis during fasting by channeling nutrients between the lysosome and the mitochondria. After autophagy induction, amino acids are released from the lysosome, and some serve as substrates for the TCA cycle to replenish carbons in the mitochondria. Nutrients appear to be transiently stored in the form of TCA cycle intermediates and then extracted for the synthesis of amino acids that promote the reactivation of TORC1. We uncovered a new regulatory role for the metabolism of cysteine to acetyl-CoA during this process. By facilitating the incorporation of carbons into the TCA cycle and limiting amino acid synthesis, cysteine appears to regulate the partitioning of carbons in the TCA cycle. We propose that cysteine acts in a negative metabolic feedback loop that antagonizes TORC1 reactivation upon fasting above a threshold that would compromise metabolic homeostasis and animal fitness. ■

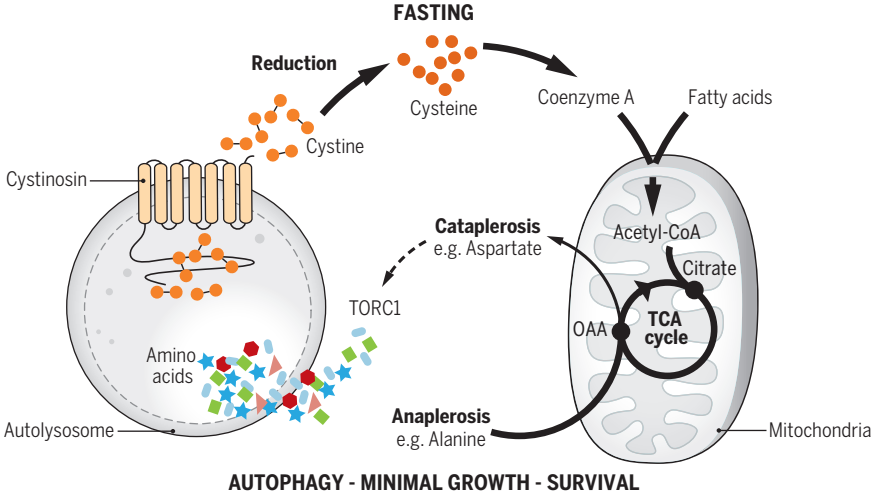

Cysteine metabolism acts in a negative feedback loop to maintain autophagy during fasting. The lysosomal transporter Cystinosin exports cystine, which is further reduced to cysteine in the cytosol. Cysteine is metabolized to coenzyme A (CoA) and fuels acetyl-CoA metabolism. Cysteine metabolism drives anaplerotic substrates into the TCA cycle and limits biosynthesis from oxaloacetate (OAA). This process is particularly important during fasting to regulate the reactivation of TORC1 and control autophagy.

The list of author affiliations is available in the full article online.
*Corresponding author. Email: Patrick_Jouandin@hms.harvard.edu (P.J.); matias.simons@med.uni-heidelberg.de (M.S.); perrimon@receptor.med.harvard.edu (N.P.)
†These authors contributed equally to this work.
‡These authors contributed equally to this work.
Cite this article as P. Jouandin *et al.*, *Science* 375, eabc4203 (2022). DOI: 10.1126/science.abc4203

READ THE FULL ARTICLE AT
https://doi.org/10.1126/science.abc4203

RESEARCH ARTICLE

CELL BIOLOGY

Lysosomal cystine mobilization shapes the response of TORC1 and tissue growth to fasting

Patrick Jouandin[1]*†, Zvonimir Marelja[2,3]†, Yung-Hsin Shih[3], Andrey A. Parkhitko[1], Miriam Dambowsky[2], John M. Asara[4,5], Ivan Nemazanyy[6], Christian C. Dibble[7,8], Matias Simons[2,3]*‡, Norbert Perrimon[1,9]*‡

Adaptation to nutrient scarcity involves an orchestrated response of metabolic and signaling pathways to maintain homeostasis. We find that in the fat body of fasting *Drosophila*, lysosomal export of cystine coordinates remobilization of internal nutrient stores with reactivation of the growth regulator target of rapamycin complex 1 (TORC1). Mechanistically, cystine was reduced to cysteine and metabolized to acetyl-coenzyme A (acetyl-CoA) by promoting CoA metabolism. In turn, acetyl-CoA retained carbons from alternative amino acids in the form of tricarboxylic acid cycle intermediates and restricted the availability of building blocks required for growth. This process limited TORC1 reactivation to maintain autophagy and allowed animals to cope with starvation periods. We propose that cysteine metabolism mediates a communication between lysosomes and mitochondria, highlighting how changes in diet divert the fate of an amino acid into a growth suppressive program.

Organisms cope with variations in diet by adjusting their metabolism. Specific organs integrate the availability of nutrients and respond to maintain systemic homeostasis. In fasting animals, the liver remobilizes nutrients through gluconeogenesis and β-oxidation of fatty acids to support peripheral tissue function (*1*, *2*). Variation in nutrient availability induces parallel changes in activity of signaling pathways, which resets intracellular metabolic turnover. The target of rapamycin complex 1 (TORC1) signaling pathway integrates sensing of amino acids and other nutrients with signals from hormones and growth factors to promote growth and anabolism (*3*). Nutrient scarcity inhibits TORC1 to limit growth and promote catabolic programs, including autophagy, which recycles internal nutrient stores to promote survival (*4*). Autophagy sequesters cytosolic material into autophagosomes that fuse with lysosomes for cargo degradation and recycling. The lysosomal surface is also the site where nutrient and growth factor–sensing pathways converge to activate TORC1. Degradation within autolysosomes generates new amino acids that in turn fuel metabolic pathways, including the tricarboxylic acid (TCA) cycle and gluconeogenesis, and reactivate TORC1, altogether maintaining minimal anabolism and growth (*5*–*8*). However, how organisms regulate the limited pools of remobilized nutrients and balance homeostatic metabolism with anabolic TORC1 activity over the course of starvation is poorly understood.

[1]Department of Genetics, Blavatnik Institute, Harvard Medical School, Boston, MA 02115, USA. [2]Université de Paris, INSERM, IHU *Imagine* – Institut des maladies génétiques, Laboratory of Epithelial Biology and Disease, 75015 Paris, France. [3]Institute of Human Genetics, University Hospital Heidelberg, 69120 Heidelberg, Germany. [4]Division of Signal Transduction, Beth Israel Deaconess Medical Center, Boston, MA 02115, USA. [5]Department of Medicine, Harvard Medical School, Boston, MA 02175, USA. [6]Platform for Metabolic Analyses, Structure Fédérative de Recherche Necker, INSERM US24/CNRS UMS 3633, Paris 75015, France. [7]Department of Pathology and Cancer Center, Beth Israel Deaconess Medical Center, Boston, MA 02115, USA. [8]Department of Pathology, Harvard Medical School, Boston, MA 02115, USA. [9]Howard Hughes Medical Institute, Harvard Medical School, Boston, MA 02115, USA.
***Corresponding author. Email: Patrick_Jouandin@hms.harvard.edu (P.J.); matias.simons@med.uni-heidelberg.de (M.S.); perrimon@receptor.med.harvard.edu (N.P.)**
†These authors contributed equally to this work.
‡These authors contributed equally to this work.

Results

TORC1 signaling is reactivated in vivo during prolonged fasting

To study the regulation of metabolism and TORC1 signaling in vivo, we used the *Drosophila* larval fat body, an organ analogous to the liver and adipose tissue in mammals. The fat body responds to variations in nutrient availability through TORC1 signaling, which in turn regulates systemic larval growth rate by the secretion of growth factors from distant organs (*9*, *10*). When larvae were fasted, i.e., completely deprived of their food source but kept otherwise hydrated, TORC1 signaling in the fat body was acutely decreased at the onset of fasting. However, prolonged fasting led to partial and progressive reactivation of TORC1 over time, as measured by phosphorylation of the specific TORC1 substrate S6K (Fig. 1A). This process was dependent on autophagy induction (fig. S1, A and B), consistent with autophagy facilitating amino acid recycling and TORC1 reactivation in mammalian cells (*6*, *8*). To understand how changes in nutrients and metabolites intersect with TORC1 signaling during this fasting response, we used two complementary, unbiased approaches: (i) a targeted mass spectrometry–based screen for polar metabolites altered during fasting and (ii) a larval growth screen to test the effects of individual amino acids in animals fed a low-protein diet.

Interplay between TORC1 signaling and the TCA cycle during fasting

In the first screen, metabolic profiling of whole animals revealed depletion of most metabolites over the course of fasting (Fig. 1B). By contrast, multiple TCA cycle intermediates accumulated over time, in particular citrate and isocitrate. This appeared not to result from defective TCA cycle activity upon fasting because U-$^{13}C_6$-glucose oxidation in the TCA cycle was functional and the ratios between NADH and NAD^+ were comparable between fed and fasting conditions (fig. S2, A and B). Similar metabolomic profiles were observed in fat bodies from fed and fasted animals (Fig. 1B), indicating that TORC1 reactivation in the fat body correlates with accumulation of TCA cycle intermediates, in particular citrate and isocitrate. Next, we tested whether TORC1 activity affects the accumulation of TCA cycle intermediates during fasting. For this, we measured the concentrations of TCA cycle intermediates in fed and fasted larvae of GATOR1 (*nrpl2*$^{-/-}$) and GATOR2 (*mio*$^{-/-}$) mutants, which exhibit constitutive activation or suppression of TORC1 signaling, respectively (*11*, *12*) (fig. S3A). Activation of TORC1 in GATOR1 mutants blunted the elevation of the concentration of TCA cycle intermediates normally observed during fasting. Conversely, inhibition of TORC1 in GATOR2 mutants raised the concentration of TCA cycle intermediates in fed animals, suggesting that the accumulation of TCA cycle intermediates during fasting requires TORC1 inhibition. We also tested whether changes in the TCA cycle during fasting affects TORC1 reactivation by targeting pyruvate carboxylase (PC). PC serves an anaplerotic function by replenishing oxaloacetate (OAA) and hence other TCA cycle intermediates (Fig. 1C), a process that regulates gluconeogenesis and regeneration of amino acids (*1*). Depletion of PC (*pcb/CG1516*) in the larval fat body increased the concentration of the PC substrate alanine in the fat body (fig. S3B) (*1*). Consistent with impaired TCA cycle activity, depletion of PC elevated the level of OAA and the ratio between NAD(P) and NAD(P)H while decreasing the levels of other TCA cycle intermediates as well as cataplerotic products such as asparagine, intermediates of the urea cycle, carbamoyl aspartate, and inosine 5′-monophosphate (IMP)

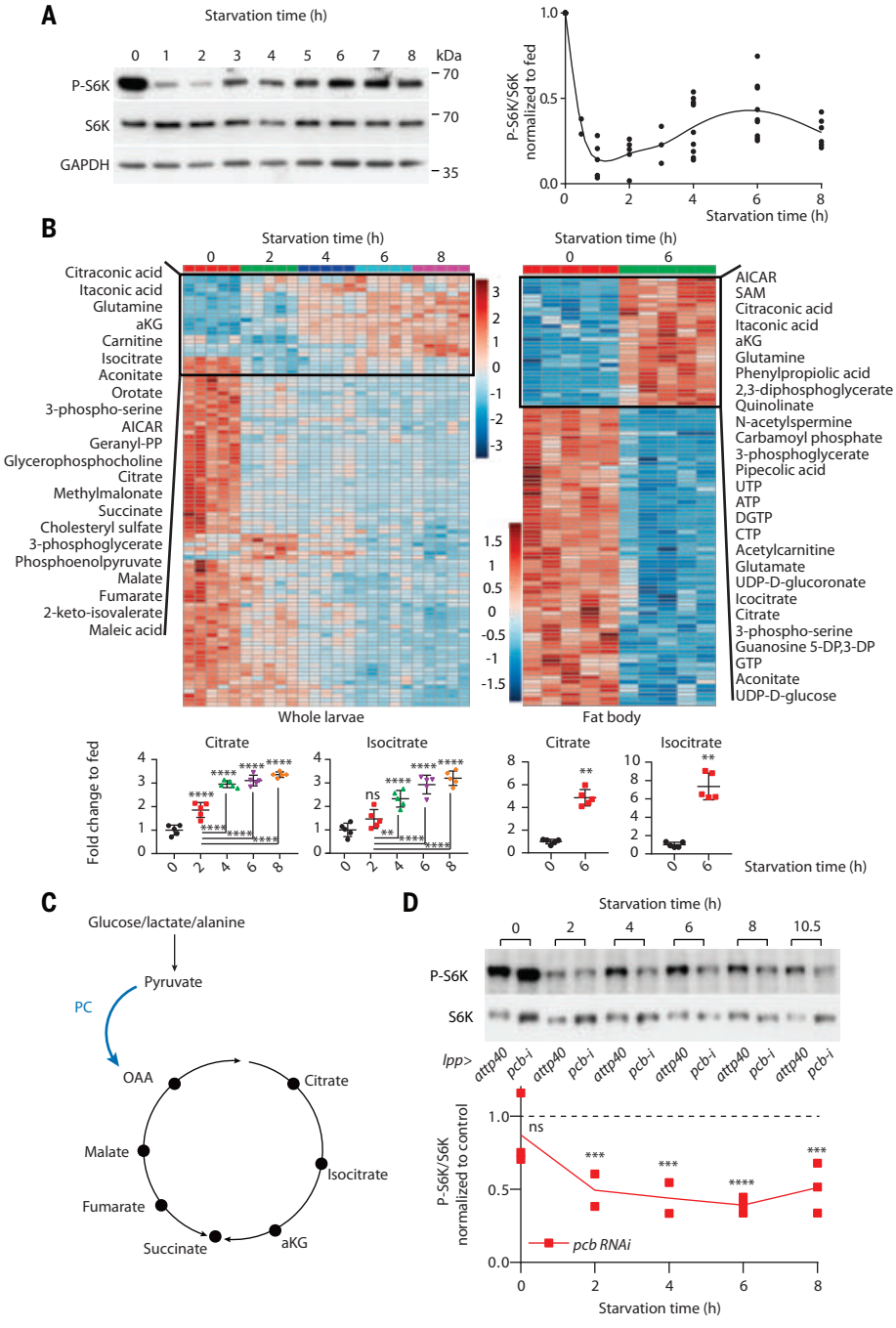

Fig. 1. TORC1 reactivation upon prolonged fasting correlates with increase of TCA cycle intermediates. (**A**) Prolonged fasting leads to TORC1 reactivation. Phosphorylation levels of the direct TORC1 target S6K in dissected fat bodies from fasting larvae (i.e., placed on a tissue soaked in PBS). (**B**) Heatmap metabolite levels (LC-MS/MS) from whole mid-third-instar larvae (left) or dissected fat bodies (right), fed (0h) and fasted. Lower panels are individual plots from the same dataset. (**C**) Schematic of anaplerosis through PC. (**D**) Knockdown of *pcb*/PC suppresses mTORC1 reactivation upon prolonged fasting. For (B) and (D), data are shown as mean ± SD. ns, $P \geq 0.05$; $^{**}P \leq 0.01$; $^{***}P \leq 0.005$; $^{****}P \leq 0.0001$ (see the materials and methods for details).

(fig. S3B). Depletion of PC also suppressed TORC1 reactivation during fasting (Fig. 1D), supporting the functional link between the TCA cycle and TORC1 signaling. These data suggest that at the onset of fasting, TORC1 inhibition appears necessary to raise the concentration of TCA cycle intermediates, which in turn affect TORC1 reactivation, possibly through the synthesis of building blocks downstream of PC, i.e., cataplerosis.

Cysteine suppresses growth in a TORC1-dependent manner

In the second screen, we tested the effects of supplementation with single amino acids on growth of larvae fed a low-protein diet (see the supplementary materials) (Fig. 2A). Fasting and a low-protein diet may trigger distinct metabolic states with intrinsic differences, but both protocols trigger a starvation response. Supplementation of food with cysteine suppressed growth in larvae to a distinctly greater extent than any other amino acid, and this phenotype was accentuated in a low-protein diet (see the supplementary text S1 and fig. S4, A to D). The inhibition of growth by cysteine was interdependent with TORC1 signaling, because cysteine treatment partially inhibited TORC1 activity in fat bodies and constitutive activation of TORC1 in GATOR1-null (*nprl2*$^{-/-}$) mutants (*12*) and partially restored growth under cysteine supplementation (fig. S5, A to E). Conversely, cysteine supplementation did not further suppress growth in mutants with constitutive suppression of TORC1 activity caused by either loss of GATOR2 (*mio*$^{-/-}$) or overexpression of TSC complex subunits (*lpp>UAS-TSC1, UAS-TSC2*) in the fat body (fig. S5, E and F). Altogether, these data suggest that cysteine has a specific inhibitory effect on growth and TORC1 signaling in larvae fed a low-protein diet, and that this growth suppression requires suppression of TORC1 signaling.

Lysosomal cystine transporter dCTNS regulates cysteine level during fasting

The results of our two screens led us to explore the relationship among cysteine metabolism, the TCA cycle, and TORC1 during fasting. Cysteine concentrations increased during fasting (Fig. 2B and fig. S6A) (*13*), and cysteine treatment increased the concentration of TCA cycle intermediates, particularly for animals fed a low-protein diet (fig. S6B). To further understand this effect of cysteine, we searched for its intracellular source during fasting. Abolishing autophagy in the fat body decreased cysteine levels upon fasting (fig. S7A), suggesting that autolysosomal function regulates cysteine balance. Thus, we focused on the role of the lysosomal cystine transporter cystinosin in recycling cysteine during fasting. Cystinosin, which is encoded by *CTNS* in mammals, is mutated in the lysosomal storage disorder cystinosis and has been implicated in the regulation of TORC1 signaling and autophagy (*14*–*16*). Endogenous tagging of the *Drosophila* ortholog *CG17119* (hereafter referred to as *dCTNS*) confirmed its specific lysosomal localization in cells of the fat body (fig. S7, B and C). *dCTNS*$^{-/-}$ larvae showed accumulation of cystine (fig. S7D), consistent with a role for cystinosin in lysosomal cystine transport (Fig. 2C). In fed conditions, control and *dCTNS*$^{-/-}$

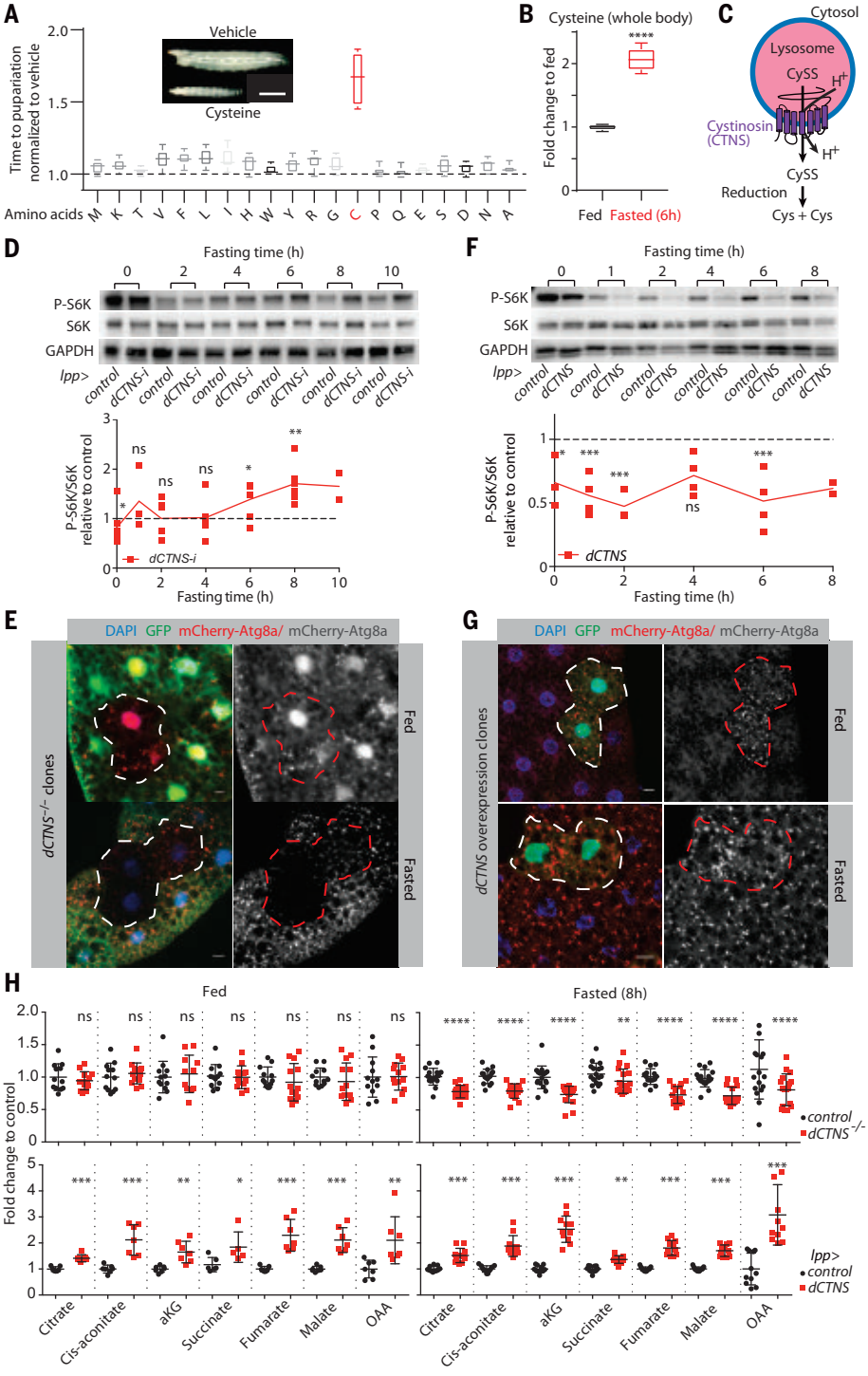

Fig. 2. Lysosome-derived cysteine promotes elevation of TCA cycle intermediates and antagonizes TORC1 reactivation. (**A**) Amino acid screen reveals cysteine as a growth suppressor. Time to pupariation for larvae fed a low-protein diet supplemented with the indicated amino acids all along development (see supplementary materials and methods for concentrations; the cysteine concentration is 5 mM). Scale bar, 1 mm. (**B**) Cysteine levels in whole control larvae (*lpp>attp40*) ($N = 5$). (**C**) Schematic of lysosomal cystine (CySS) efflux through cystinosin/*CTNS*. (**D**) Loss of *Drosophila* cystinosin in the fat body (*lpp>dCTNS RNAi, dCTNS-i)* leads to higher TORC1 reactivation upon prolonged fasting. *P*-S6K levels in dissected fat bodies from larvae fasted for the indicated time. *lpp>white RNAi*, control background. (**E**) dCTNS maintains autophagy during fasting. *dCTNS*$^{-/-}$ clones (non-GFP, outlined) in 80-hour AEL larvae expressing mCherry-Atg8a fasted for 8 hours. Scale bar, 10 μm. (**F**) *dCTNS* overexpression suppresses TORC1 activity. *P*-S6K levels in dissected fat bodies from larvae fasted for the indicated time. *Lpp>GFP RNAi (GFP-i)*, control background. (**G**) *dCTNS* overexpression induces autophagy. *dCTNS* overexpression clones (GFP marked, outlined) in 80-hour AEL larvae. Scale bar, 10 μm. (**H**) dCTNS regulates TCA cycle intermediate levels upon fasting. Relative metabolites levels measured by LC-MS/MS in 80-hour AEL larvae fed or fasted for 8 hours. Controls are dCTNS$^{+/-}$ (upper graphs) or GFP-i (lower graphs). For (B), (D), (F), and (H), data are shown as mean ± SD. ns, $P \geq 0.05$; *$P \leq 0.05$; **$P \leq 0.01$; ***$P \leq 0.005$; ****$P \leq 0.0001$ (see the materials and methods for details).

larvae showed similar abundance of cysteine, likely reflecting dietary intake as the main source of cysteine. By contrast, in fasting animals, cysteine concentration dropped in *dCTNS*$^{-/-}$ larvae (fig. S7E). Conversely, *dCTNS* overexpression increased cysteine levels, which caused a developmental delay similar to cysteine treatment (fig. S7, F and G). In sum, our results indicate that dCTNS recycles cysteine from the lysosome during fasting.

Cytosolic cysteine synthesis compensates for defective lysosomal cystine export

To evaluate the contribution of cytosolic cysteine synthesis during fasting, we also analyzed the trans-sulfuration pathway, a process that requires cystathionine β-synthase (Cbs) (fig. S8A) (*17*, *18*). Depletion of *cbs* in the fat body reduced cysteine levels upon fasting, but this was not the case in fed animals. Cbs and dCTNS showed additive roles in maintaining cysteine concentration in fasted animals (fig. S8B), suggesting that the phenotypic effects of *dCTNS* deficiency are partially masked by the trans-sulfuration pathway. Because the trans-sulfuration pathway involves the breakdown of methionine, we found that *dCTNS* overexpression increased the concentration of the intermediates of the trans-sulfuration pathway, particularly methionine (fig. S8C). By contrast, methionine was depleted in

fasted *dCTNS* mutant animals (fig. S8C), suggesting that cysteine from lysosomal origin limits the activity of the trans-sulfuration pathway. Methionine is an essential amino acid, and dCTNS appears to limit its depletion upon fasting, a process possibly reminiscent of the methionine-sparing effect of dietary cystine previously observed in humans (*19*, *20*).

dCTNS affects TORC1 reactivation and the TCA cycle during fasting

Next, we analyzed the effect of cysteine recycling by dCTNS on TORC1 reactivation and the TCA cycle. Although *dCTNS* depletion in the larval fat body did not affect TORC1 inhibition at the onset of fasting, it slightly increased TORC1 reactivation upon prolonged fasting, as indicated by increased S6K phosphorylation (Fig. 2D) and cytosolic accumulation of Mitf/TFEB (fig. S9A). Analysis of *dCTNS*$^{-/-}$ fat body clones showed that increased TORC1 signaling was cell autonomous and sufficient to compromise maintenance of autophagy during fasting (Fig. 2E and fig. S9B). Accordingly, treatment with the TORC1 inhibitor rapamycin restored autophagy in *dCTNS*-deficient cells (fig. S9C). Conversely, *dCTNS* overexpression caused down-regulation of TORC1 in fed and fasting animals and induced ectopic autophagy in fed animals (Fig. 2, F and G). Metabolic profiling of *dCTNS*$^{-/-}$ animals showed a depletion of TCA cycle intermediates specifically during fasting, whereas they accumulated after overexpression of *dCTNS* in fed and fasted animals (Fig. 2H).

dCTNS is required for animal fitness during starvation

We also examined the role of *dCTNS* on starvation resistance. In normally fed animals, *dCTNS* deficiency delayed larval development but appeared to have no effect on the life span of adult flies (Fig. 3, A and B). However, *dCTNS*-deficient animals had an increased developmental delay when raised in a low-protein diet, and adults died more quickly from starvation (Fig. 3, B and C). Depletion of *dCTNS* specifically in the fat body did not affect development in fed animals but caused a developmental delay on a low-protein diet, consistent with the importance of dCTNS function in the fat body during fasting (Fig. 3B). The starvation sensitivity of *dCTNS*-deficient animals was decreased by low concentrations of rapamycin (that did not elevate cysteine concentration), indicating a possible role for altered TORC1 signaling and autophagy in mediating *dCTNS* growth phenotypes (Fig. 3D, fig. S9D; see supplementary text S2). The role of *dCTNS* during starvation was dependent on its cystine transport function as treatment with either cysteamine [which facilitates cystine export out of the lysosome independently of cystinosin (*21*)]

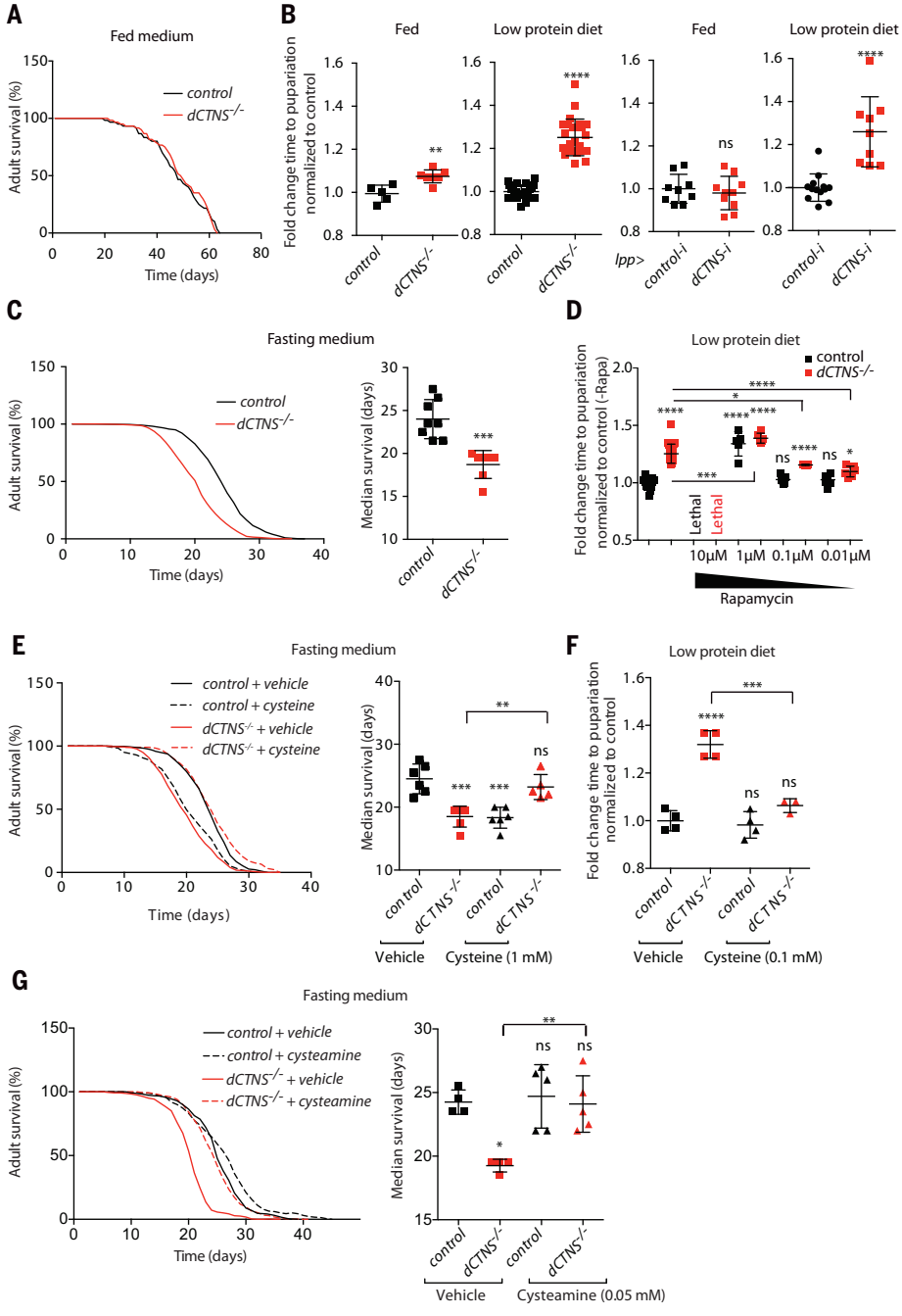

Fig. 3. *dCTNS* controls resistance to starvation through cysteine efflux and TORC1. (**A**) dCTNS does not affect life span in the fed condition. Life span of control (w^{1118}) and *dCTNS*$^{-/-}$ animals fed a standard diet (N = 2). (**B**) dCTNS in the fat body controls starvation resistance during development. Shown is the fold change time to pupariation for larvae of indicated genotype grown on control (fed) or low-protein diet. Controls are dCTNS$^{+/-}$ (left panel) or white RNAi (control-i, right panel). (**C**) dCTNS controls starvation resistance of adult animals. Survival of control (w^{1118}) and *dCTNS*$^{-/-}$ animals fed a chemically defined starved diet composed only of physiologically relevant ions, including biometals (see the materials and methods). (**D** to **F**) Low dose of rapamycin and cysteine treatments rescues starvation sensitivity of *dCTNS*$^{-/-}$ animals. Shown is the developmental time of larvae raised on a low-protein diet supplemented with the indicated concentration of rapamycin (D) or 0.1 mM cysteine (F) and survival of adult flies on chemically defined starved diet with or without 1 mM cysteine (E). Controls are *dCTNS*$^{+/-}$ [(D) and (F)] and w^{1118} (E). (**G**) Cysteamine treatment restores starvation resistance of *dCTNS*$^{-/-}$ animals. Shown is the life span of control (w^{1118}) and *dCTNS*$^{-/-}$ animals fed a chemically defined starved diet supplemented with 0.5 mM cysteamine or vehicle. For (B) to (G), data are shown as mean ± SEM. ns, $P \geq 0.05$; *$P \leq 0.05$; **$P \leq 0.01$; ***$P \leq 0.005$; ****$P \leq 0.0001$ (see the materials and methods for statistics details).

or low concentrations of cysteine (which did not affect development of control animals) decreased the starvation sensitivity of *dCTNS*$^{-/-}$ animals (Fig. 3, E to G). Altogether, we demonstrate the physiological importance of cysteine recycling from the lysosome through dCTNS during fasting, which supports the accumulation of TCA cycle intermediates and antagonizes TORC1 reactivation to maintain autophagy.

dCTNS connects with the TCA cycle through acetyl-CoA metabolism

To search for a mechanistic link between cysteine metabolism and the TCA cycle, we performed heavy isotope-labeled cysteine tracing experiments by feeding larvae either U-^{13}C-cysteine or $^{13}C_3$ $^{15}N_1$-cysteine. Consistent with cysteine metabolism in mammals, this revealed three major metabolic fates for cysteine: glutathione (GSH), taurine, and coenzyme A (CoA) (Fig. 4, A and B). CoA derived from labeled cysteine was subsequently used to form acetyl-CoA in the fat body of larvae fed a control and low-protein diet (Fig. 4, A and B, and fig. S10, A and B). We found that the starvation sensitivity of *dCTNS*$^{-/-}$ animals was partially suppressed by dietary treatment with pantethine, a disulfide intermediate of the CoA biosynthetic pathway downstream of cysteine incorporation (fig. S11, A and C), but not with pantothenic acid, the vitamin precursor upstream of cysteine incorporation during CoA synthesis (fig. S11B). This suggests that deficiencies in CoA synthesis caused by limiting cysteine availability contribute to the *dCTNS* phenotypes. To analyze how this affects the TCA cycle, we further focused on the direct flow of carbons from cysteine into acetyl-CoA. Upon feeding, the pyruvate dehydrogenase complex (PDHc) harvests the acetyl moiety from pyruvate and transfers it to CoA to generate acetyl-CoA (*22*) (fig. S12A). Upon fasting, PDHc activity decreases, draining pyruvate toward PC to support biosynthesis, whereas β-oxidation of fatty acids may provide the acetyl moiety for acetyl-CoA synthesis (*23*) (Fig. 5A and fig. S12A). In fed larvae overexpressing *dCTNS* in the fat body, depletion of the PDHc activator pyruvate dehydrogenase phosphatase (*pdp*) (*24*) normalized growth, TORC1 activity, and the concentration of TCA cycle intermediates (fig. S12, B to D). By contrast, when *dCTNS*-overexpressing larvae were fed a low-protein diet or fasted, PDHc inhibition failed to restore development or fully restore TORC1 activity, respectively, presumably reflecting the use of substrates other than pyruvate for acetyl-CoA synthesis under these conditions, such as acetate and fatty acids (fig. S12, B and C). In turn, depletion of CPT1/*whd*, the acylcarnitine transferase required for β-oxidation of fatty acids, restored growth of dCTNS-overexpressing larvae to a larger extent on a fed diet than on a low-protein diet, suggesting that increased cysteine metabolism is sufficient to promote β-oxidation upon feeding (fig. S12F). Accordingly, *dCTNS* overexpression increased the abundance of acetyl-CoA and decreased the abundance of acyl-carnitines and fatty acids in both fed and fasted animals. By contrast, in *dCTNS*$^{-/-}$ animals, acetyl-CoA levels were decreased, whereas acylcarnitines and fatty acids showed higher levels, specifically during fasting, which could be normalized by cysteamine treatment (Fig. 5,

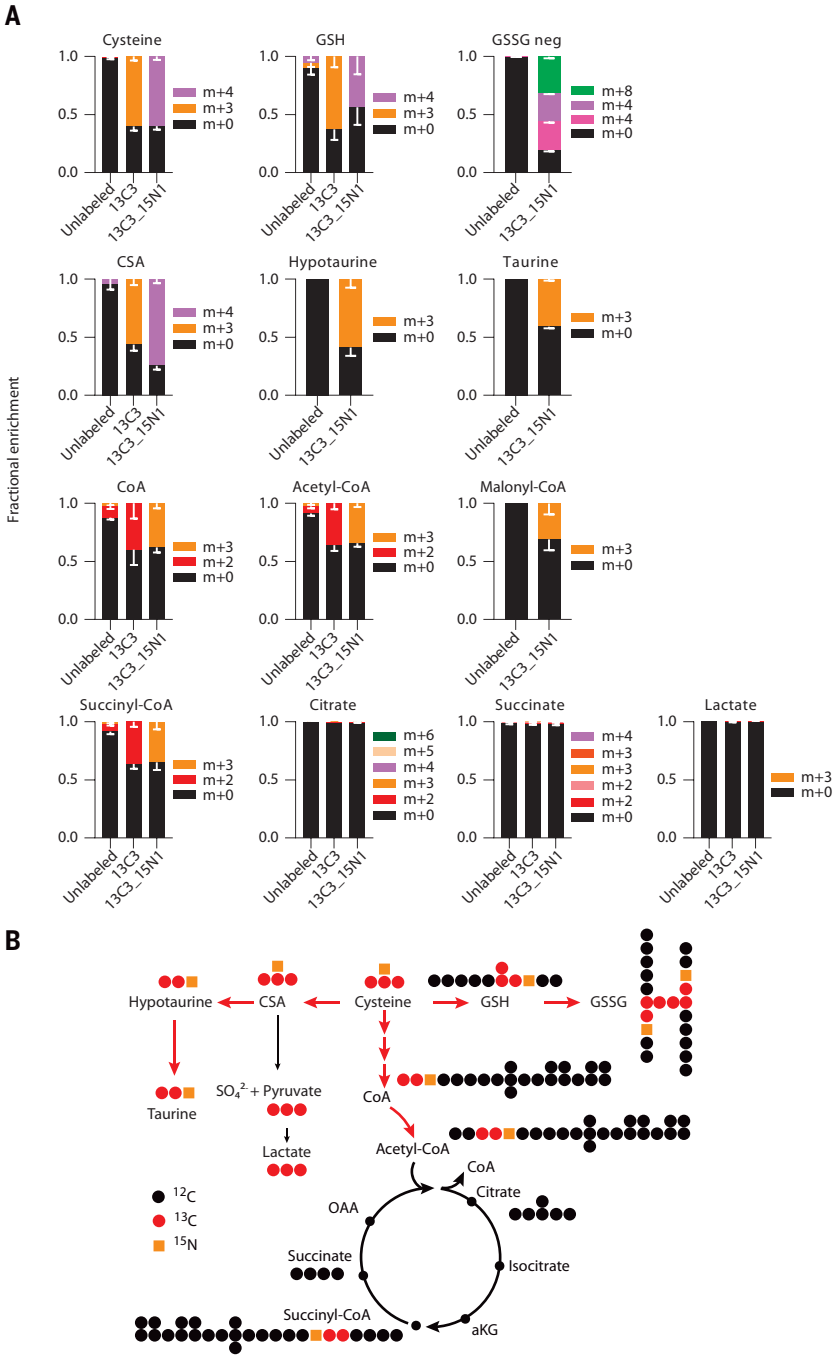

Fig. 4. Cysteine fuels de novo CoA/acetyl-CoA metabolism. (**A**) Mean fractional enrichment ± SD of U-^{13}C-cysteine (N = 10), $^{13}C_3$-$^{15}N_1$-cysteine (N = 5), or unlabeled samples (N = 10) in indicated metabolites measured by LC-MS/MS in whole larvae fast overnight with 5 mM tracer. m+n refers to the number of ^{13}C atoms (+n) added to the expected mass spectra of each measured isotopomer (m); m+0 means unlabeled. (**B**) Schematic of cysteine metabolism and labeling patterns from U-^{13}C-cysteine and $^{13}C_3$-$^{15}N_1$-cysteine tracers. Red arrows indicate main cysteine flux.

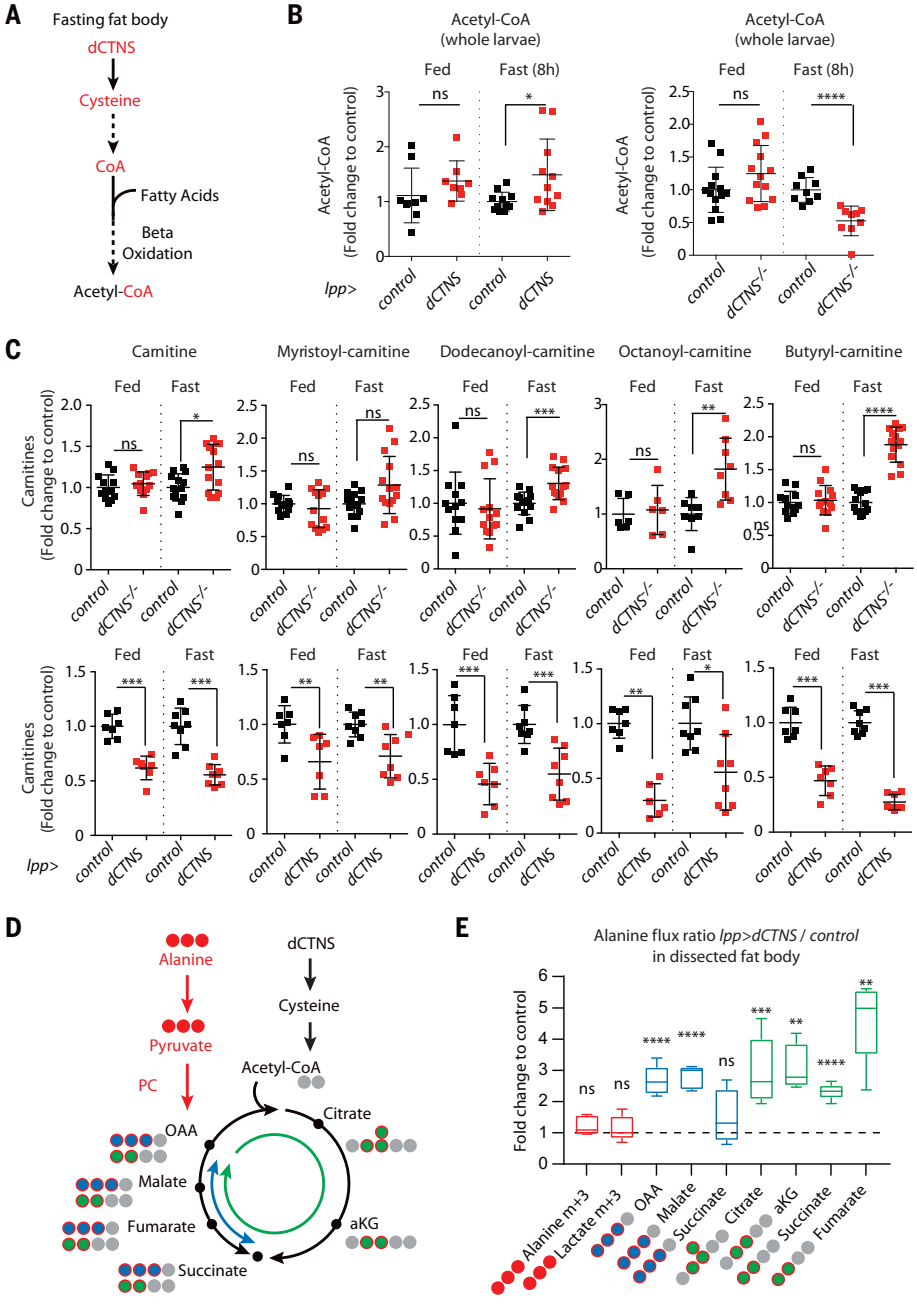

Fig. 5. Cysteine metabolism to acetyl-CoA affects the concentration of fatty acids and increases carbon flux through PC and the TCA cycle. (**A**) Schematic of acetyl-CoA synthesis during fasting. (**B** and **C**) Metabolite levels in whole third-instar larvae showing *dCTNS*$^{-/-}$ and *dCTNS* overexpression in the fat body. (**D**) Schematic of alanine carbon flux into the TCA cycle upon fasting. (**E**) Alanine flux ratio. Shown is the fold change *lpp>dCTNS*/control (*lpp>attp40*) for the indicated TCA cycle intermediates isotopomers measure by LC-MS/MS in dissected fat bodies from third-instar larvae fed a low-protein diet with 25 mM U-^{13}C-alanine for 6 hours.

B and C, and fig. S13, A and B). In addition, *dCTNS* overexpression was sufficient to deplete triglyceride stores in fed animals, whereas they slightly accumulated after depletion of *dCTNS* in the fat body upon fasting (fig. S13C). Altogether, our data suggest that during fasting, lysosomal cysteine mobilization is potentially rate limiting for de novo CoA synthesis, which in turn may promote acetyl-CoA production through β-oxidation of fatty acids remobilized from triglyceride stores. The precise contribution of acetyl moieties by fatty acids and other substrates for the synthesis of acetyl-CoA during fasting remains to be determined.

Lysosomal-derived cysteine may control TORC1 indirectly through the flow of amino acids in and out of the TCA cycle

Increased CoA synthesis from cysteine might enlarge the TCA cycle carbon pool in at least two ways: first, by providing the CoA required to accept increasing amounts of carbon from fatty acids to form acetyl-CoA, and second, by promoting anaplerosis of alternative carbon sources through the allosteric activation of PC by acetyl-CoA (*25*). To test whether increased production of acetyl-CoA supported by lysosomal cysteine efflux could increase anaplerosis, we analyzed alanine anaplerosis in the TCA cycle in animals overexpressing *dCTNS* in the fat body. We supplemented a low-protein diet with a [U-^{13}C]alanine tracer and followed the anaplerotic flux of alanine in the TCA cycle in dissected fat bodies (Fig. 5D). We used a tracer amount that had a negligible contribution to the total alanine pool and also did not affect cysteine metabolism to acetyl-CoA (fig. S14, A and B). *dCTNS* overexpression increased (by more than twofold) alanine anaplerosis as well as oxidative flux in the TCA cycle through citrate synthase (that consumes OAA and acetyl-CoA to generate citrate; Fig. 5E). We therefore propose that during fasting, cysteine recycling and metabolism to acetyl-CoA in the fat body supports anaplerosis through PC and flux through citrate synthase, thereby contributing to the accumulation of TCA cycle intermediates, in particular citrate and isocitrate.

During fasting, given the fixed and preestablished level of carbons available, increased abundance of TCA cycle intermediates may indicate the retention of anaplerotic inputs in the TCA cycle at the expense of their extraction for biosynthesis (i.e., cataplerosis). Because cataplerosis promotes amino acid synthesis (*1*), which in turn affects TORC1 signaling (*6*), we analyzed the effect of lysosomal cysteine recycling on individual amino acid pools. *dCTNS* overexpression in the fat body led to depletion of aspartate and downstream nucleotide precursors (IMP and uridine 5′-monophosphate), as well as, to a lesser extent, asparagine and glutamate (Fig. 6A and fig. S15, A and B). The abundances of aspartate and IMP were increased in fasted *dCTNS*$^{-/-}$ animals, and cysteamine treatment partially normalized their concentration (fig. S15C). Aspartate is a cataplerotic product of OAA (*1*), a process that involves glutamate oxaloacetate transaminase 2 (Got2). Cysteine metabolism may transiently trap anaplerotic carbons into the TCA cycle in fasted animals, away from their immediate extraction for biosynthesis. We analyzed whether cysteine metabolism could regulate growth and antagonize TORC1 reactivation through limiting the availability of glutamate and aspartate, because these amino acids are critical regulators of cell growth and have

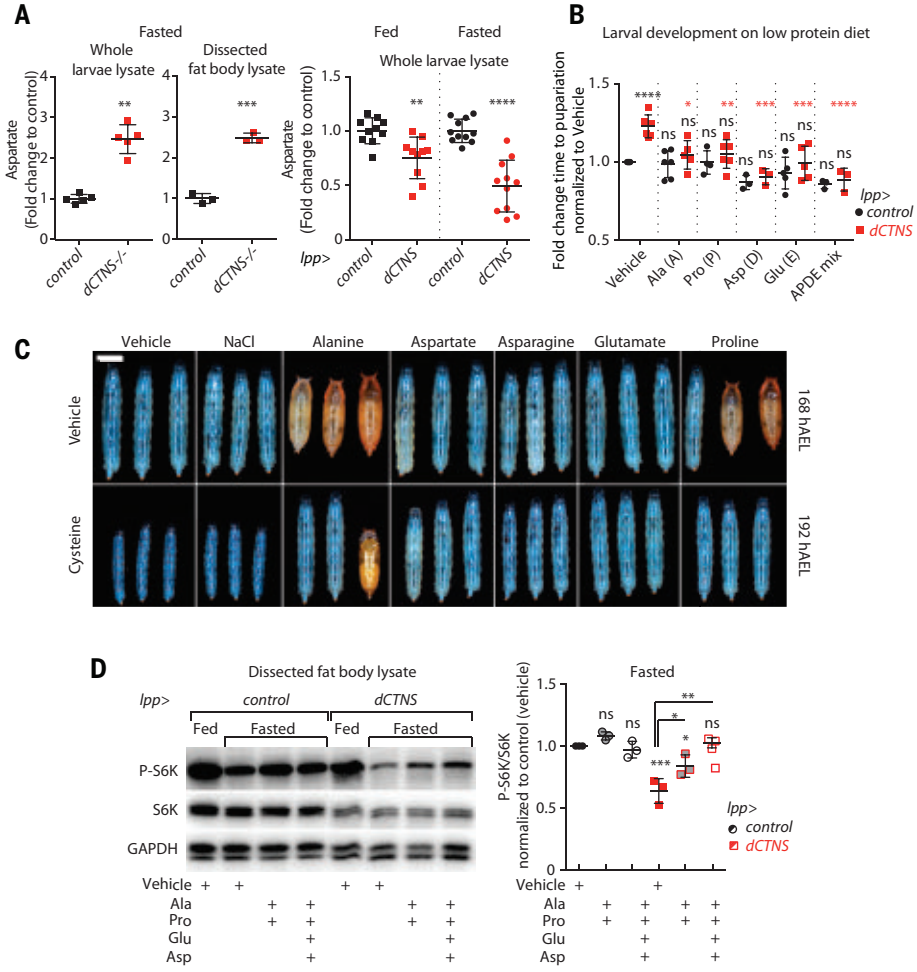

Fig. 6. Cysteine metabolism regulates TORC1 and growth through cataplerotic amino acids levels. (**A**) Relative levels of aspartate in 85-hour AEL larvae *dCTNS*$^{-/-}$ (whole larvae and fat body) and after dCTNS overexpression in the fat body. (**B**) Amino acid supplementation suppresses the developmental delay induced by *dCTNS* overexpression in the larval fat body. Shown is the fold change time to pupariation for larvae fed a low-protein diet with or without supplementation with the indicated amino acids (Ala, Pro, and Glu: 5 mM; Asp: 10 mM). Red asterisks show significance between dCTNS animals treated with vehicle versus amino acids. (**C**) Photographs of aged matched animals fed a low-protein diet with or without 5 mM cysteine with or without the indicated metabolites (25 mM each). Scale bar, 1 mm. (**D**) dCTNS-induced TORC1 inhibition is reversed by supplementation with the indicated amino acids. *P*-S6K levels in fat body from fed and fasted (6 hour) larvae of indicated genotypes. The 70- to 72-h AEL larvae were transferred to a low-protein diet with or without supplementation with the indicated amino acids (Ala and Pro: 20 mM; Asp and Glu: 10 mM). Control is GFP-i. For (A), (B), and (D), data are shown as mean ± SD. ns, $P \geq 0.05$; *$P \leq 0.05$; **$P \leq 0.01$; ***$P \leq 0.005$; ****$P \leq 0.0001$ (see the materials and methods for details).

previously been implicated in TORC1 signaling (*6*, *26*). For this analysis, we replenished aspartate and glutamate concentrations in *dCTNS*-overexpressing animals through dietary supplementation of anaplerotic amino acids. Treatments with combinations of alanine, aspartate, asparagine, glutamate, and proline [which replenishes glutamate in flies (*27*)] restored normal levels of aspartate and glutamate without compromising *dCTNS*-induced elevation of TCA intermediates (fig. S15, D and E). These treatments rescued the developmental delay induced by *dCTNS* overexpression in the fat body (Fig. 6B). Similarly, cosupplementation of cysteine with excess of single amino acids including alanine, aspartate, asparagine, glutamate, and proline each rescued cysteine-induced growth suppression upon fasting (Fig. 6C). In addition, treatments with a combination of amino acids restored TORC1 activity upon fasting after *dCTNS* overexpression in the fat body (Fig. 6D). Consistent with the importance of aspartate synthesis, clonal loss of *Got2* induced autophagy (*6*), inhibited TORC1 activity as indicated by decreased levels of phosphorylated 4E-BP, increased levels of the reporter Unk-GFP (*28*), and inhibited cell growth as shown by decreased nucleus size (fig. S14F). Thus, cysteine metabolism appears to regulate anaplerotic carbon flow in the TCA cycle and the level of cataplerotic products such as aspartate. We propose that lysosomal-derived cysteine converts the TCA cycle into a reservoir of carbons in the mitochondria while limiting their extraction for biosynthesis. This process may spare nutrients to allow animals to survive starvation while resetting TORC1 activity to a threshold that maintains minimal growth without compromising autophagy.

Discussion

Maintaining cellular homeostasis upon nutrient shortage is an important challenge for all animals. Decreased activity of TORC1 is necessary to limit translation, reduce growth rates, and promote autophagy. Conversely, minimal TORC1 activity is required to promote lysosomal biogenesis, thus maintaining autophagic degradation necessary for survival (*8*). Using *Drosophila* as an in vivo model, we found that TORC1 reactivation upon fasting integrates the biosynthesis of amino acids from anaplerotic inputs into the control of growth. The regulation of aspartate abundance appears to be critical during this process, possibly because it serves as a cataplerotic precursor for various macromolecules, including other amino acids and nucleotides, which in turn impinge on TORC1 activity (*29*). Cysteine recycling through the lysosome may fuel acetyl-CoA synthesis and prevent reactivation of TORC1 above a threshold that would compromise autophagy and survival during fasting. Reactivation of TORC1 during fasting was not passively controlled by the extent of amino acid remobilized from the lysosome. Instead, cysteine metabolism supported an increased incorporation of the carbons from these remobilized amino acids into the TCA cycle. We therefore propose that the remobilized amino acids may be transiently stored in the form of TCA cycle intermediates compartmentalized in the mitochondria, thereby restricting their accessibility. The regulation of TORC1 activity over a fasting period appears to be a combination of activating and suppressing cues that conciliate autophagy with anabolism. This process is self-regulated by autophagy, because autophagic protein degradation controls cystine availability through the lysosomal cystinosin transporter. Thus, in contrast to fed conditions, in which amino acid transporters at the plasma membrane maintain high cytosolic concentration of leucine and arginine that can directly be sensed by members of the TORC1 machinery (*3*), TORC1 reactivation in prolonged fasting is regulated indirectly by lysosome-mitochondrial cross-talk. Because cystinosin has also been shown to physically interact with several components of lysosomal TORC1 in mammalian cells (*14*), additional layers of regulation are conceivable during this process.

Multiple functions of cysteine impinge on cellular metabolism, including transfer RNA

thiolation, the generation of hydrogen sulfide, the regulation of hypoxia-inducible factor (HIF), and its antioxidant function through glutathione synthesis (*30*–*32*). Supplementation with cysteine or modified molecules such as *N*-acetyl-cysteine (NAC) can be used to efficiently buffer oxidative stress and perhaps alleviate symptoms of diseases that promote oxidative stress or glutathione deficiency, including cystinosis (*33*–*36*). Cysteine or NAC treatment extends the life span in flies, worms, and mice, and mice fed NAC show a sudden drop in body weight similar to that caused by dietary restriction (*18*, *37*). Our results indicate that cysteine may not only act through its antioxidant function but also by restricting the availability of particular amino acids and limiting mTOR activity, processes known to extend life span. Moreover, we show that CoA is a main fate of cysteine that affects oxidative metabolism in the mitochondria, which is the main source of reactive oxygen species (ROS). Thus, the antioxidant function of cysteine also might be coupled to its effects on the mitochondria to buffer ROS production.

In summary, we demonstrate that cysteine metabolism acts in a feedback loop involving de novo CoA synthesis, the TCA cycle, and amino acid metabolism to limit TORC1 reactivation upon prolonged fasting. This pathway may be particularly important for developing organisms that must maintain autophagy and balance growth and survival during periods of food shortage.

Materials and Methods

Fly stocks and maintenance

All flies were reared at 25°C and 60% humidity with a 12-hour on/off light cycle on standard laboratory food. N.P.'s standard laboratory food: 12.7 g/liter deactivated yeast, 7.3 g/liter soy flour, 53.5 g/liter cornmeal, 0.4% agar, 4.2 g/liter malt, 5.6% corn syrup, 0.3% propionic acid, and 1% Tegosept/ethanol. M.S.'s standard laboratory food: 18 g/liter deactivated yeast, 10 g/liter soy flour, 80 g/liter cornmeal, 1% agar, 40 g/liter malt, 5% corn syrup, 0.3% propionic acid, and 0.2% 4-hydroxybenzoic acid methyl ester (nipagin)/ethanol. Density was standardized for at least one generation before the experiments. For experiments, larvae were reared on freshly made food. *Lpp-gal4* was a gift from P. Léopold. *UAS-tsc1, UAS-tsc2* was a gift from C. Mirth (*38*). *yw,hs-Flp; mCherry–Atg8a; Act>CD2>GAL4, UAS–nlsGFP/TM6B* was a gift from E. Baehrecke. *hsFlp; act>CD2>Gal4, UAS nlsGFP* is a stock from N.P.'s laboratory (*39*). *yw, hsFlp, Tub-Gal4>UAS-nlsGFP/FM6;;neoFRT82B, TubGal80/TM6,Tb,Hu* was a gift from A. Bardin. *nprl2*^{1} and *mio*^{2} were a gift from M. Lilly. *hsFlp; R4-Gal4, UAS-mCherry-Atg8a; FRT82B UAS-GFP/TM6b* was a gift from G. Juhász. The following stocks were obtained from the Bloomington Drosophila Stock Center (BDSC) at Indiana University: *UAS-w*^{RNAi} (HMS00045), *UAS-w*^{RNAi} (HMS00017), *UAS-GFP*^{RNAi} (#9330) *attp40* (#36304), *attp2* (#36303), *UAS-mCherry-nls* (#38425), *UAS-Atg1*^{RNAi} (HMS02750), *UAS-Atg18a*^{RNAi} (JF02898), *UAS-TSC2*^{RNAi} (HM04083), *w*^{1118}, *UAS-dCTNS*^{RNAi} (HMS00213), *UAS-Got2*^{RNAi} (HMJ21924), *UAS-CPT1/whd*^{RNAi} (HMS00033), *UAS-Cbs*^{RNAi} (GL01309), *UAS-pdp*^{RNAi} (HMS018888), and *UAS-pcb*^{RNAi} (HMC04104). When comparing the effects of RNA interference (RNAi) knockdown or protein overexpression through induction of UAS-dsRNA or UAS-cDNA expression, *UAS-w*^{RNAi} (HMS00045), *UAS-w*^{RNAi} (HMS00017), *attp2* (#36303), and *attp40* (#36304) were used as controls for the TRIP collection (https://www.flyrnai.org/TRiP-HOME.html), and UAS-GFP RNAi for *dCTNS* overexpression. *dCTNS* knockout flies were generated with CRISPR/Cas9 technology according to (*40*). Two single guide RNAs (sgRNAs) using oligos (one after the ATG start codon in exon 3: GGTGATGTCATGGGAATCGA, and the other before the translation of the first transmembrane domain in exon 4: GGGCAGTACTCGAAATCAGT) were produced by polymerase chain reaction (PCR) and in vitro transcribed into RNA using the MEGAscript T7 Transcription Kit (Thermo Fisher Scientific). RNA was injected into *act-Cas9* flies (from F. Port and S. Bullock). F_0 flies were crossed to w;; TM3,Sb/TM6,Tb balancer flies and F_1 progenies were screened through PCR using oligos flanking the targeted genome region. Any indel difference >3 bp was visualized in 4% agarose gel in heterozygot F_1 progeny. To generate *dCTNS-mKate2* fusion allele, an *mKate2* open reading frame was inserted at the C terminus of *dCTNS* using a CRISPR/Cas9 endogenous tagging strategy with vectors kindly provided by Y. Bellaiche (Curie Institut, Paris). In brief, two 1-kb-long homology arms (HR1 and HR2) of the *dCTNS* gene flanking the sgRNA-guided Cas9 cutting site were cloned into a vector flanking the ATG/STOP-less *mKate2* allele (HR1-linker-mKate2-loxP-mini-white-loxP-linker-HR2). In addition, two vectors for the expression of sgRNA (sgRNA-1: CCACCGTGACCGATGTTCAAAAT, sgRNA-2: CCGAGCGAAGTGACGACTGAGAA) targeting the C-terminal coding region of *dCTNS* were generated. All three vectors were injected into *vas-Cas9* flies (BDSC, #55821) embryos by Bestgene. Progenies were screened for the red eyes (selection marker mini-*white*) and crossed to Cre-expressing flies to remove the mini-*white* by *loxP*/Cre excision. For overexpression of *dCTNS*, *dCTNS* cDNA was cloned into the Gateway destination vector pUASg-HA.attB (GeneBank: KC896837) according to (*41*). The plasmid was injected by Bestgene into embryos (BDSC, #24482) for ϕ31-mediated recombination at a *attP* insertion site on the second chromosome.

Fly food and starvation protocols

Heavy isotope tracers were from Cambridge Isotope Laboratories. All other amino acids and compounds used were from Sigma-Aldrich. In N.P.'s laboratory, compounds in solution were added to the following food mixture: 60 g/liter sucrose, deactivated yeast as a source of total protein (2 g/liter for low-protein diet, 4 g/liter for mild low-protein diet, 20 g/liter for fed fly food), 80 g/liter cornmeal, 0.35% agar, 0.3% propionic acid, and 1% Tegosept (100 g/liter in ethanol). Glucose tracing was done without sucrose and alanine tracing without yeast. In M.S.'s laboratory, fasting food had to be adapted to 6 g/liter of deactivated yeast to match control fast (2 g/liter) developmental rates observed in N.P.'s laboratory. For control food in the M.S. laboratory, the standard laboratory food was used (see protocol above). In fig. S4 specifically, 100% amino acid was 17 g/liter deactivated yeast. For fasting experiments, larvae were placed on paper wipes soaked in phosphate-buffered saline (PBS) in a petri dish.

Generation of clones

For autophagy experiments, clones were generated by crossing *yw, hs-flp; mCherry–Atg8a; Act>CD2>GAL4, UAS–nlsGFP/TM6B* with the indicted UAS lines. Progeny of the relevant genotype was reared at 25°C, and spontaneous clones were generated in the fat body because of the leakiness of the heat-shock flipase (*hs-flp*). For *dCTNS*$^{-/-}$ clones, autophagy was analyzed by crossing *w;;neoFRT82B, dCTNS*$^{-/-}$ to *hs-flp; R4-Gal4, UAS-mCherry-Atg8a; FRT82B UAS-GFP/TM6b*. For P-4EBP1 experiments, clones were either generated by crossing *hs-flp; act>CD2>Gal4, UAS nlsGFP* with the indicted UAS lines or, for *dCTNS*$^{-/-}$ clones, by crossing *w;;neoFRT82B, dCTNS*$^{-/-}$ to *yw, hs-flp, tub-Gal4>UAS-nlsGFP/FM6;;neoFRT82B, tubGal80/TM6,Tb,Hu*. F_1 embryos collected overnight were heat shocked for 2 hours at 37°C the following morning.

Amino acid screen

Larvae were fed a diet with reduced yeast extract and proteins (50% of normal diet), individual amino acids were systematically added to the food, and the time to pupariation was monitored as a proxy for growth rate. The following mixture was diluted 1:1 with amino acid solutions in water: 10 g/liter agar, 120 g/liter sucrose, 17 g/liter deactivated yeast extract, 80 g/liter cornmeal, 6 ml/liter propionic acid, and 20 ml/liter Tegosept. The amount of amino acids added to the food was determined based on those used in tissue culture growth supplements (see table S1) (*42*–*44*).

Food intake

Larvae were synchronized in L1 and reared on the indicated food types until the mid-second

instar stage. They were then transferred on the same food type supplemented with 0.5% weight/volume erioglaucine disodium salt (Sigma-Aldrich) for 2 hours. Samples were homogenized in 200 µl of PBS, and absorbance of the dye in the supernatant was measured at 625 nm. Results were normalized to protein content.

Developmental timing

Three-day-old crosses were used for 3- to 4-hour periods of egg collection on standard laboratory food. Newly hatched L1 larvae were collected 24 hours later for synchronized growth using the indicated diets at a density of 30 animals per vial. The time to develop was monitored by counting the number of animals that underwent pupariation every 2 hours in fed conditions or once or twice a day in starved conditions. The time at which half the animals had undergone pupariation was recorded.

Adult survival experiments

To generate age-synchronized adult flies, larvae were raised on laboratory food at low density, transferred to fresh food upon emerging as adults, and mated for 48 hours. Animals were anesthetized with low levels of CO_2, and males were sorted at a density of 10 per vial. Each condition contained eight to 10 vials. Each experiment was repeated at least three times, and the average values of each experiment were used for statistical analysis. Flies were transferred to fresh food vials three times per week, at which point deaths were scored. After 10 days, deaths were scored every day. Chemically defined (holidic) fasting medium was prepared following the protocol described in (*43*), which contains all physiologically relevant ions (including biometals) but lacks energy sources such as sugar, proteins, amino acids, lipids, and lipid-related metabolites, as well as nucleic acids and vitamins.

Growth curves and pupal weight

Synchronized, newly-hatched L1 larvae were immediately weighed or placed on the indicated food at a density of 30 to 50 animals per vial. Pools of 20 to 80 animals were weighed every 24 hours using an analytical scale (Mettler Toledo), and the weight was reported ± SEM. For pupal weight, 2-day-old pupae from vials at a density of 30 animals were weighed in batches of five to 10 pupae. The weights of different batches of larvae from the same vials were averaged and counted as $N = 1$.

Metabolite profiling

For whole-body metabolic profiling, 25 to 38 mid-second-instar or eight to 15 mid-third-instar larvae per sample were collected, snap-frozen in liquid nitrogen, and stored at −80°C in extraction buffer (four to six biological replicates/experiment). For fat body metabolic profiling, fat bodies from 35 to 40 larvae 96 hours after egg laying (AEL) were dissected in 20 µl of PBS, diluted in 300 µl of cold extraction buffer, and snap frozen. Tissues were homogenized in extraction buffer using 1 mm zirconium beads (Next Advance, ZROB10) in a Bullet Blender tissue homogenizer (model BBX24, Next Advance). Metabolites were extracted using 80% (v/v) aqueous methanol (two sequential extractions with 300 to 600 µl), and metabolites were pelleted by vacuum centrifugation. Pellets were resuspended in 20 µl of high-performance liquid chromatography (HPLC)–grade water, and metabolomics data were acquired using targeted liquid chromatography tandem mass spectrometry (LC-MS/MS). A 5500 QTRAP hybrid triple quadrupole mass spectrometer (AB/SCIEX) coupled to a Prominence UFLC HPLC system (Shimadzu) was used for steady-state analyses of the samples. Selected reaction monitoring (SRM) of 287 polar metabolites using positive/negative switching with hydrophilic interaction LC (HILIC) was performed. Peak areas from the total ion current for each metabolite SRM Q1/Q3 transition were integrated using MultiQuant version 2.1 software (AB/SCIEX). The resulting raw data from the MultiQuant software were normalized by sample weight for the whole animal. Fat body samples were normalized by the mean protein content measured from duplicate dissection for each condition. Data were analyzed using Prism informatic software. Alternatively, collected larvae were rinsed with water, 70% ethanol, and PBS to remove food and bacteria; snap-frozen in liquid nitrogen; and stored at −80°C until extraction in 50% methanol, 30% acetonitrile, and 20% water. The volume of extraction solution added was adjusted to larvae mass (40 mg/ml), samples were vortexed for 5 min at 4°C and then centrifuged at 16,000*g* for 15 min at 4°C. Supernatants were collected and analyzed by LC-MS using a QExactive Plus Orbitrap mass spectrometer equipped with an Ion Max source and a HESI II probe and coupled to a Dionex UltiMate 3000 UPLC system (Thermo Fisher Scientific, USA). An SeQuant ZIC-pHilic column (Millipore) was used for liquid chromatography separation (*45*). The aqueous mobile-phase solvent was 20 mM ammonium carbonate plus 0.1% ammonium hydroxide solution, and the organic mobile phase was acetonitrile. The metabolites were separated over a linear gradient from 80% organic to 80% aqueous for 15 min and detected across a mass range of 75 to 1000 m/z at a resolution of 35,000 (at 200 m/z) with electrospray ionization and polarity switching mode. Lock masses were used to ensure mass accuracy <5 ppm. The peak areas of different metabolites were determined using TraceFinder software (Thermo Fisher Scientific) using the exact mass of the singly charged ion and known retention time on the HPLC column. In total, each metabolic profiling experiment was performed at least two times with three to seven biological replicates per genotype.

TCA cycle isotopomer method from U-^{13}C-cysteine, $^{13}C_3$-$^{15}N_1$-cysteine, U-^{13}C-glucose, and U-^{13}C-alanine

Fed and starved mid-third-instar animals were supplemented with the indicated concentrations of U-^{13}C-cysteine, $^{13}C_3$-$^{15}N_1$-cysteine, U-^{13}C-glucose, U-^{13}C-alanine, or vehicle in the food for the indicated times. For tracing experiments on the low-protein diet (starved), animals were prestarved for 1 hour on PBS before being transferred to the relevant tracer and food. Samples were collected (at least five biological replicates for labeled conditions and at least four biological replicates for the unlabeled condition), and intracellular metabolites were extracted using 80% (v/v) aqueous methanol. Q1/Q3 SRM transitions for incorporation of ^{13}C-labeled metabolites were established for polar metabolite isotopomers, and data were acquired by LC-MS/MS. Peak areas were generated using MultiQuant version 2.1 software. Peak areas from unlabeled conditions were used for background determination in each experiment. In Fig. 5E and figs. S2A, S10, A and B, and S14, data for both labeled and unlabeled conditions were corrected for natural isotope abundance before normalization using the R package IsoCorrectoR GUI 1.9.0. In Fig. 4A, data for both labeled and unlabeled conditions were not corrected for natural isotope abundance. In Fig. 5E, $^{13}C_3$-alanine incorporation into the indicated isotopomer of TCA cycle intermediates was measured in control and lpp>dCTNS–overexpressing animals. Values were corrected for natural isotope abundance before normalization, and data present the fold change ^{13}C labeling in TCA cycle intermediates in dCTNS-overexpressing versus control animals.

Cysteine measurement (other than LC-MS/MS)

The 25 to 40 mid-second-instar animals were homogenized in cold PBS with 0.1% Triton X-100 (PBST) and centrifuged at 4°C. Cysteine measurement was performed in triplicate from the supernatant using the MicroMolar Cysteine Assay Kit (ProFoldin, CYS200) according to the manufacturer's instructions. Data were normalized to protein content.

Cystine measurements

Larvae were washed three times (in water, quickly in 70% ethanol, and finally in PBS), dried on tissue paper, and 10 larvae per sample were shock frozen in liquid nitrogen and stored at −80°C until lysis. Larvae were lysed in 80 µl of 5.2 mM N-ethylmaleimide, centrifuged for 10 min at 4°C, and 75 µl of supernatant was

deproteinized by the addition of 25 µl of 12% sulfosalicylic acid. Protein-free supernatants were kept frozen at −80°C until analysis and centrifuged at 1200*g* before use. Cystine quantification was performed using the AccQ-Tag Ultra kit (Waters) on a UPLC-xevoTQD system (Waters) according to the manufacturer's recommendations. Ten microliters of sample was mixed with 10 µl of a 30 µM internal standard solution (stable isotope of cystine), 70 µl of borate buffer, and 20 µl of derivative solution and incubated at 55°C for at least 10 min. Derivatized samples were diluted with 150 µl of ultrapurified water, and 5 µl of the final mixture was injected in the triple quadrupole mass spectrometer in positive mode. Transitions used for derivatized cystine quantification and the internal standard were 291.2>171.1 and 294.2>171.1, respectively. Cystine values were normalized by protein content using the Lowry's method on protein pellets.

Immunostaining

Fat body tissues from 68- to 85-hour AEL larvae were dissected in PBS with 2% formaldehyde at room temperature, fixed 20 to 30 min in 4% formaldehyde, washed twice for 10 min each in PBST 0.3 %, blocked for 30 min [PBST, 5% bovine serum albumin (BSA), 2% fetal bovine serum, and 0.02% NaN_3], incubated with primary antibodies in the blocking buffer overnight, and washed four times for 15 min each. Secondary antibodies diluted 1:200 or 1:500 in PBST were added for 1 hour and tissues were washed four times before mounting in Vectashield/4′,6-diamidino-2-phenylindole (DAPI). Rabbit anti–P-4EBP1 from Cell Signaling Technologies (CST 236B4, #2855) was diluted 1:500, rabbit anti-tRFP was from Evrogen (#AB233) and was used against mKate2 to stain *d*CTNS-mKate2. Purified polyclonal antibody against Mitf was generated in guinea pig by the company Eurogentec using the epitope CRRFNINDRIKELGTL. Samples were imaged using Zeiss LSM 780 and Leica TCS SP8 SMD confocal systems with a 40× water or oil-immersion objective, and images were processed with Fiji software.

Western blots

Tissues from 10 to 30 animals were dissected in CST lysis buffer (#9803) containing 2× protease inhibitor (Roche, #04693159001) and 3× phosphatase inhibitor (Roche, #04906845001), and homogenized using 1-mm zirconium beads (Next Advance, #ZROB10) in a Bullet Blender tissue homogenizer (model BBX24, Next Advance). Protein content was measured to normalize samples, 2× Laemmli sample buffer (Bio-Rad) was added and samples boiled for 6 min at 95°C. Lysates were resolved by electrophoresis (Mini-PROTEAN TGX Precast Gels, BioRad, PAGEr EX Gels, Lonza, or home-made SDS gels), proteins transferred onto polyvinylidene difluoride (PVDF) membranes (Immobilon P, Millipore), blocked in Tris-buffered saline with or without 0.1% Tween-20 buffer containing 3 to 6% BSA or 5% milk, and probed with P-S6K antibody (1:1000, CST 9209). After P-S6K was revealed, membranes were stripped for 5 to 30 min (Restore PLUS Buffer, Thermo Scientific, catalog #46430), washed, blocked in PBS Tween-20 buffer containing 5% dry milk, and probed with S6K antibody [1:10,000, a gift from A. Teleman (*46*)]. For normalization blots were probed with GADPH antibody (1:5000, GeneTex, #GTX100118). Data show representative results from at least two or three biological replicates (see quantification plots). Horseradish peroxidase (HRP)–conjugated secondary IgG antibodies (1:10000) were used together with the SuperSignal West Dura Extended Duration Substrate (Thermo Scientific, #34076) to detect the protein bands.

Statistics

Experiments are presented with whisker plots or show the mean ± SD or SEM. *P* values and significance were as follows: ns, $P \geq 0.05$; $^{*}P \leq 0.05$; $^{**}P \leq 0.01$; $^{***}P \leq 0.005$; and $^{****}P \leq 0.0001$. For the life span experiments shown in Fig. 3A, $N = 2$; for Fig. 3, C, E, and G, and fig. S11, $N \geq 3$. Significance was determined by a two-tailed *t* test (Mann-Whitney). $N = 1$ means average of eight to 10 vials per genotype and condition in one experiment. For the larval development (pupariation assay) results shown in Fig. 3B and fig. S7G, significance was determined by a two-tailed *t* test (Mann-Whitney); for Figs. 3, D and F; Fig. 6B; and fig. S12, C and E, one-way ANOVA followed by a Bonferroni's multiple-comparisons test was used. For cysteine measurements (Profoldin kit) shown in Fig. 2B, significance was determined by *t* test; for fig. S6A, one-way ANOVA followed by Dunnett's multiple-comparisons test was used; for fig. S7A, E, and F, two-tailed *t* test (Mann-Whitney) was used; and for figs. S8B and S9D, one-way ANOVA followed by a Bonferroni's multiple-comparisons test was used. For Western blots shown in Fig. 1A, the spline curve represents the trend over multiple experiments; for those shown in Fig. 1D and fig. S1A, significance was determined by two-way ANOVA followed by Sidak's multiple-comparisons test; for Fig. 2, D and F; Fig. 6D; and fig. S12B, one-way ANOVA followed by a Bonferroni's multiple-comparisons test was used. For the metabolomics shown in Fig. 1B (left plots), fig. S12D, fig. S13B, and fig. S15, C and D, significance was determined by one-way ANOVA followed by a Bonferroni's multiple comparisons test; in fig. S3A, two-way ANOVA followed by Sidak's multiple-comparisons test was used; for Fig. 1B (right plots); Fig. 2H; Fig. 5, B, C, and E; Fig. 6A; fig. S8, C and D; fig. S13, A and C; fig. S15, A, B, and E; and fig. S3B, two-tailed *t* test (Mann-Whitney) was used. For pupal weights shown in fig. S4C and food intakes shown in fig. S4D, significance was determined by unpaired two-tailed *t* test.

REFERENCES AND NOTES

1. D. A. Cappel *et al*., Pyruvate-carboxylase-mediated anaplerosis promotes antioxidant capacity by sustaining TCA cycle and redox metabolism in liver. *Cell Metab.* **29**, 1291–1305.e8 (2019). doi: 10.1016/j.cmet.2019.03.014; pmid: 31006591
2. L. R. Gray *et al*., Hepatic mitochondrial pyruvate carrier 1 is required for efficient regulation of gluconeogenesis and whole-body glucose homeostasis. *Cell Metab.* **22**, 669–681 (2015). doi: 10.1016/j.cmet.2015.07.027; pmid: 26344103
3. R. L. Wolfson, D. M. Sabatini, The dawn of the age of amino acid sensors for the mTORC1 pathway. *Cell Metab.* **26**, 301–309 (2017). doi: 10.1016/j.cmet.2017.07.001; pmid: 28768171
4. R. C. Scott, O. Schuldiner, T. P. Neufeld, Role and regulation of starvation-induced autophagy in the *Drosophila* fat body. *Dev. Cell* **7**, 167–178 (2004). doi: 10.1016/j.devcel.2004.07.009; pmid: 15296714
5. T.-C. Lin *et al*., Autophagy: Resetting glutamine-dependent metabolism and oxygen consumption. *Autophagy* **8**, 1477–1493 (2012). doi: 10.4161/auto.21228; pmid: 22906967
6. H. W. S. Tan, A. Y. L. Sim, Y. C. Long, Glutamine metabolism regulates autophagy-dependent mTORC1 reactivation during amino acid starvation. *Nat. Commun.* **8**, 338 (2017). doi: 10.1038/s41467-017-00369-y; pmid: 28835610
7. G. A. Wyant *et al*., NUFIP1 is a ribosome receptor for starvation-induced ribophagy. *Science* **360**, 751–758 (2018). doi: 10.1126/science.aar2663; pmid: 29700228
8. L. Yu *et al*., Termination of autophagy and reformation of lysosomes regulated by mTOR. *Nature* **465**, 942–946 (2010). doi: 10.1038/nature09076; pmid: 20526321
9. J. Colombani *et al*., A nutrient sensor mechanism controls *Drosophila* growth. *Cell* **114**, 739–749 (2003). doi: 10.1016/S0092-8674(03)00713-X; pmid: 14505573
10. C. Géminard, E. J. Rulifson, P. Léopold, Remote control of insulin secretion by fat cells in *Drosophila*. *Cell Metab.* **10**, 199–207 (2009). doi: 10.1016/j.cmet.2009.08.002; pmid: 19723496
11. W. Cai, Y. Wei, M. Jarnik, J. Reich, M. A. Lilly, The GATOR2 component Wdr24 regulates TORC1 activity and lysosome function. *PLOS Genet.* **12**, e1006036 (2016). doi: 10.1371/journal.pgen.1006036; pmid: 27166823
12. Y. Wei, M. A. Lilly, The TORC1 inhibitors Nprl2 and Nprl3 mediate an adaptive response to amino-acid starvation in *Drosophila*. *Cell Death Differ.* **21**, 1460–1468 (2014). doi: 10.1038/cdd.2014.63; pmid: 24786828
13. J. Onodera, Y. Ohsumi, Autophagy is required for maintenance of amino acid levels and protein synthesis under nitrogen starvation. *J. Biol. Chem.* **280**, 31582–31586 (2005). doi: 10.1074/jbc.M506736200; pmid: 16027116
14. Z. Andrzejewska *et al*., Cystinosin is a component of the vacuolar H+-ATPase-Ragulator-Rag complex controlling mammalian target of rapamycin complex 1 signaling. *J. Am. Soc. Nephrol.* **27**, 1678–1688 (2016). doi: 10.1681/ASN.2014090937; pmid: 26449607
15. B. P. Festa *et al*., Impaired autophagy bridges lysosomal storage disease and epithelial dysfunction in the kidney. *Nat. Commun.* **9**, 161 (2018). doi: 10.1038/s41467-017-02536-7; pmid: 29323117
16. M. Town *et al*., A novel gene encoding an integral membrane protein is mutated in nephropathic cystinosis. *Nat. Genet.* **18**, 319–324 (1998). doi: 10.1038/ng0498-319; pmid: 9537412
17. H. Kabil, O. Kabil, R. Banerjee, L. G. Harshman, S. D. Pletcher, Increased transsulfuration mediates longevity and dietary restriction in *Drosophila*. *Proc. Natl. Acad. Sci. U.S.A.* **108**, 16831–16836 (2011). doi: 10.1073/pnas.1102008108; pmid: 21930912
18. A. A. Parkhitko, P. Jouandin, S. E. Mohr, N. Perrimon, Methionine metabolism and methyltransferases in the regulation of aging and life span extension across species. *Aging Cell* **18**, e13034 (2019). doi: 10.1111/acel.13034; pmid: 31460700
19. R. O. Ball, G. Courtney-Martin, P. B. Pencharz, The in vivo sparing of methionine by cysteine in sulfur amino acid requirements in animal models and adult humans. *J. Nutr.* **136** (suppl.), 1682S–1693S (2006). doi: 10.1093/jn/136.6.1682S; pmid: 16702340

20. W. C. Rose, R. L. Wixom, The amino acid requirements of man. 13. The sparing effect of cystine on the methionine requirement. *J. Biol. Chem.* **216**, 763–773 (1955). doi: 10.1016/S0021-9258(19)81430-8
21. W. A. Gahl, F. Tietze, J. D. Butler, J. D. Schulman, Cysteamine depletes cystinotic leucocyte granular fractions of cystine by the mechanism of disulphide interchange. *Biochem. J.* **228**, 545–550 (1985). doi: 10.1042/bj2280545; pmid: 4026796
22. M. J. Holness, M. C. Sugden, Pyruvate dehydrogenase activities and rates of lipogenesis during the fed-to-starved transition in liver and brown adipose tissue of the rat. *Biochem. J.* **268**, 77–81 (1990). doi: 10.1042/bj2680077; pmid: 2188650
23. J. Lee, J. Choi, S. Scafidi, M. J. Wolfgang, Hepatic fatty acid oxidation restrains systemic catabolism during starvation. *Cell Rep.* **16**, 201–212 (2016). doi: 10.1016/j.celrep.2016.05.062; pmid: 27320917
24. T. C. Linn, F. H. Pettit, F. Hucho, L. J. Reed, Alpha-keto acid dehydrogenase complexes. XI. Comparative studies of regulatory properties of the pyruvate dehydrogenase complexes from kidney, heart, and liver mitochondria. *Proc. Natl. Acad. Sci. U.S.A.* **64**, 227–234 (1969). doi: 10.1073/pnas.64.1.227; pmid: 4312751
25. M. St. Maurice *et al*., Domain architecture of pyruvate carboxylase, a biotin-dependent multifunctional enzyme. *Science* **317**, 1076–1079 (2007). doi: 10.1126/science.1144504; pmid: 17717183
26. L. B. Sullivan *et al*., Aspartate is an endogenous metabolic limitation for tumour growth. *Nat. Cell Biol.* **20**, 782–788 (2018). doi: 10.1038/s41556-018-0125-0; pmid: 29941931
27. H. Li *et al*., *Drosophila* larvae synthesize the putative oncometabolite L-2-hydroxyglutarate during normal developmental growth. *Proc. Natl. Acad. Sci. U.S.A.* **114**, 1353–1358 (2017). doi: 10.1073/pnas.1614102114; pmid: 28115720
28. M. Tiebe *et al*., REPTOR and REPTOR-BP regulate organismal metabolism and transcription downstream of TORC1. *Dev. Cell* **33**, 272–284 (2015). doi: 10.1016/j.devcel.2015.03.013; pmid: 25920570
29. G. Hoxhaj *et al*., The mTORC1 signaling network senses changes in cellular purine nucleotide levels. *Cell Rep.* **21**, 1331–1346 (2017). doi: 10.1016/j.celrep.2017.10.029; pmid: 29091770
30. K. J. Briggs *et al*., Paracrine induction of HIF by glutamate in breast cancer: EglN1 senses cysteine. *Cell* **166**, 126–139 (2016). doi: 10.1016/j.cell.2016.05.042; pmid: 27368101
31. C. Hine *et al*., Endogenous hydrogen sulfide production is essential for dietary restriction benefits. *Cell* **160**, 132–144 (2015). doi: 10.1016/j.cell.2014.11.048; pmid: 25542313
32. S. Laxman *et al*., Sulfur amino acids regulate translational capacity and metabolic homeostasis through modulation of tRNA thiolation. *Cell* **154**, 416–429 (2013). doi: 10.1016/j.cell.2013.06.043; pmid: 23870129
33. M. AlMatar, T. Batool, E. A. Makky, Therapeutic potential of N-acetylcysteine for wound healing, acute bronchiolitis, and congenital heart defects. *Curr. Drug Metab.* **17**, 156–167 (2016). doi: 10.2174/1389200217666151210124713; pmid: 26651980
34. R. Bavarsad Shahripour, M. R. Harrigan, A. V. Alexandrov, N-acetylcysteine (NAC) in neurological disorders: Mechanisms of action and therapeutic opportunities. *Brain Behav.* **4**, 108–122 (2014). doi: 10.1002/brb3.208; pmid: 24683506
35. K. Q. de Andrade *et al*., Oxidative stress and inflammation in hepatic diseases: Therapeutic possibilities of N-acetylcysteine. *Int. J. Mol. Sci.* **16**, 30269–30308 (2015). doi: 10.3390/ijms161226225; pmid: 26694382
36. L. Pache de Faria Guimaraes *et al*., N-acetyl-cysteine is associated to renal function improvement in patients with nephropathic cystinosis. *Pediatr. Nephrol.* **29**, 1097–1102 (2014). pmid: 24326786
37. M. V. Shaposhnikov *et al*., Effects of N-acetyl-L-cysteine on life span, locomotor activity and stress-resistance of 3 *Drosophila* species with different life spans. *Aging (Albany NY)* **10**, 2428–2458 (2018). doi: 10.18632/aging.101561; pmid: 30243020
38. T. Koyama, C. K. Mirth, Growth-Blocking Peptides As Nutrition-Sensitive Signals for Insulin Secretion and Body Size Regulation. *PLOS Biol.* **14**, e1002392 (2016).
39. P. Karpowicz, Y. Zhang, J. B. Hogenesch, P. Emery, N. Perrimon, The circadian clock gates the intestinal stem cell regenerative state. *Cell Rep.* **3**, 996–1004 (2013).
40. A. R. Bassett, C. Tibbit, C. P. Ponting, J.-L. Liu, Highly efficient targeted mutagenesis of *Drosophila* with the CRISPR/Cas9 system. *Cell Rep.* **6**, 1178–1179 (2014).
41. J. Bischof *et al*., A versatile platform for creating a comprehensive UAS-ORFeome library in *Drosophila*. *Development* **140**, 2434–2442 (2013).
42. W. C. Lee, C. A. Micchelli, Development and characterization of a chemically defined food for *Drosophila*. *PLOS ONE* **8**, e67308 (2013).
43. M. D. Piper *et al*., A holidic medium for *Drosophila melanogaster*. *Nat. Methods* **11**, 100–105 (2014).
44. A. M. Troen *et al*., Life span modification by glucose and methionine in *Drosophila melanogaster* fed a chemically defined diet. *Age (Dordr.)* **29**, 29–39 (2007).
45. G. M. Mackay, L. Zheng, N. J. F. van den Broek, E. Gottlieb, "Analysis of cell metabolism using LC-MS and isotope tracers," in *Metabolic Analysis Using Stable Isotopes*, C. M. Metallo, Ed. (Academic, 2015), *Methods in Enzymology* series, vol. 561, pp. 171–196.
46. K. Hahn *et al*., PP2A regulatory subunit PP2A-B' counteracts S6K phosphorylation. *Cell Metab.* **11**, 438–444 (2010).

ACKNOWLEDGMENTS

We thank E. Baehrecke, C. Mirth, P. Léopold, A. Teleman, F. Wirtz-Peitz, Y. Bellaïche, I. Gaugue, S. Sanquer, A.-C. Boschat, M. A. Lilly, and the TRIP (https://www.flyrnai.org/TRiP-HOME.html), BDSC, and VDRC stock centers for providing stocks and reagents; the Microscopy Resources on the North Quad (MicRoN) core at Harvard Medical School; A. Comjean for help with the R package IsoCorrectoR GUI 1.9.0; and C. Antignac, L. C. Cantley, B. Gasnier, J. D. Rabinowitz, and D. M. Sabatini for comments on the manuscript. **Funding:** This work was supported by the Cystinosis Research Foundation (P.J., Z.M., M.S., and N.P.), the LAM Foundation (fellowship award LAM00105E01-15 to A.P.), the National Institutes of Health (grant 5P01CA120964-04 to J.M.A. and N.P. and grant R01AR057352 to N.P), the National Institutes of Health and the National Cancer Institute (grant R00-CA194314 to C.C.D.), the V Foundation for Cancer Research (V Scholar Grant 2019 V2019-009 to C.C.D), the European Research Council (ERC) under the European Horizon 2020 research and innovation program (grant 865408, to M.S.), the Deutsche Forschungsgemeinschaft Heisenberg-Programm (grant DFG SI1303/5-1, to M.S.), the Fondation Bettencourt-Schueller (Liliane Bettencourt Chair of Developmental Biology, to M.S.), and state funding by the Agence Nationale de la Recherche (ANR) under the "Investissements d'avenir" program (grant ANR-10-IAHU-01 to M.S.) and NEPHROFLY (grant ANR-14-ACHN-0013 to M.S.). N.P. is an investigator of the Howard Hughes Medical Institute. **Author contributions:** P.J., Z.M., C.C.D., M.S., and N.P. designed the experiments. P.J., Z.M., Y.-H.S., A.P., M.D., J.A., and I.N. performed the experiments. P.J., Z.M., M.S., and N.P. participated in interpretation of data. P.J. wrote the manuscript with inputs from Z.M., C.C.D., M.S., and N.P. **Competing interests:** The authors declare no competing interests. **Data and materials availability:** All data are available in the main text or the supplementary materials.

SUPPLEMENTARY MATERIALS

science.org/doi/10.1126/science.abc4203
Supplementary Text S1 and S2
Figs. S1 to S15
Tables S1
References (*47*–*50*)
MDAR Reproducibility Checklist

23 April 2020; accepted 12 January 2022
10.1126/science.abc4203

RESEARCH ARTICLE SUMMARY

BLOOD-BRAIN BARRIER

Engineered Wnt ligands enable blood-brain barrier repair in neurological disorders

Maud Martin, Simon Vermeiren, Naguissa Bostaille, Marie Eubelen, Daniel Spitzer, Marjorie Vermeersch, Caterina P. Profaci, Elisa Pozuelo, Xavier Toussay, Joanna Raman-Nair, Patricia Tebabi, Michelle America, Aurélie De Groote, Leslie E. Sanderson, Pauline Cabochette, Raoul F. V. Germano, David Torres, Sébastien Boutry, Alban de Kerchove d'Exaerde, Eric J. Bellefroid, Timothy N. Phoenix, Kavi Devraj, Baptiste Lacoste, Richard Daneman, Stefan Liebner, Benoit Vanhollebeke*

INTRODUCTION: Central nervous system (CNS) endothelial cells establish a selective filter at the interface between the blood and the brain tissue, called the blood-brain barrier (BBB). The BBB is established during early embryogenesis and maintained throughout adulthood by neurovascular communications occurring within functionally integrated neurovascular units. In numerous CNS disorders, these homeostatic neurovascular microenvironments are disrupted, and consequently, excessive infiltrations of fluids, molecules, and cells alter the neuronal milieu and worsen disease outcome. Therapeutic strategies are needed for the restoration of compromised BBB function.

RATIONALE: An appealing strategy from a therapeutic standpoint is to repair the dysfunctional BBB by using the molecules that endogenously control its formation during embryogenesis. By respecting the developmental molecular logic of the target tissue, such an approach is best positioned to achieve physiological refunctionalization. More so, by focusing on the upstream regulators of BBB development, the likelihood of correctly setting the stage for a productive repair process increases. Wnt7a/b are some of the earliest and best characterized BBB-inducing signals across vertebrates and therefore constitute a priori prime candidates as BBB-repairing agents. Nonetheless, safe therapeutic use of Wnt ligands such as Wnt7a is unlikely because of their pleiotropic Frizzled (Fz) signaling activities and the widespread expression of Fz receptors across cells and tissues. However, at the BBB, Wnt7a/b ligands signal through an atypical receptor complex containing the adhesion G protein–coupled receptor Gpr124 and the glycosylphosphatidylinositol-anchored glycoprotein Reck. We reasoned that this receptor complex, more than the Fz receptors themselves, could be exploited to achieve BBB repair with the required level of specificity.

RESULTS: Wnt ligands exhibit a conserved two-domain structure, each domain making one functionally important contact with Fz receptors. We discovered that a hemisected Wnt7a, lacking the C-terminal domain and its embedded Fz contact site, retained partial but selective activity on the Gpr124/Reck-containing receptor complexes of the BBB. This specificity provided proof-of-concept evidence that the presence of Gpr124/Reck changes the modalities of Fz-Wnt interactions, and that Wnt7a/b can be used as scaffolds to achieve Gpr124/Reck-specific agonism. Accordingly, a class of highly specific and fully active Gpr124/Reck agonists, differing from Wnt7a by only a single surface-exposed residue, was identified through large-scale mutagenesis. Mechanistically, the selectivity of the uncovered agonists resulted from their strict dependency on Reck and Gpr124 for Fz binding and activation. In contrast to the wild-type Wnt7a ligand or other canonical Wnt ligands, whose overexpression is incompatible with vertebrate development, Gpr124/Reck agonists were well tolerated in vivo, even when delivered ubiquitously during *Xenopus* or zebrafish early development, or throughout the neonatal mouse brain. Furthermore, Gpr124/Reck agonists exhibited therapeutic efficacy in mouse models of brain tumors and ischemic stroke, where long-lasting BBB normalization was achieved through a single "hit-and-run" intravenous gene delivery. By restoring endothelial Wnt signaling, Gpr124/Reck agonists normalized the BBB pleiotropically, affecting both the transcellular and paracellular permeability pathways.

CONCLUSION: This work reveals that the signaling specificity of Wnt ligands is adjustable and defines a modality to treat CNS neurological disorders by normalizing BBB function. Such BBB-focused intervention strategies have considerable potential as disease-modifying treatments or as secondary preventive agents in various CNS pathologies, including stroke, multiple sclerosis, epilepsy, and neurodegenerative disorders such as Alzheimer's disease. ■

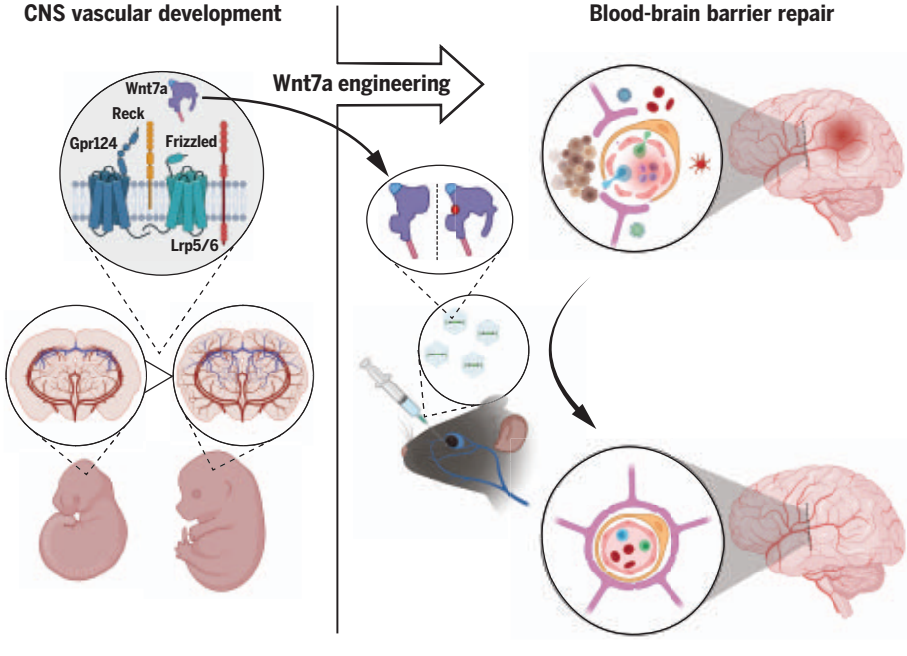

Repurposing Wnt7a ligands into BBB therapeutics. BBB dysfunction has been implicated in the etiology of a large set of CNS disorders. Wnt7a/b ligands, which dominate the neurovascular differentiation cascade during vertebrate development, are here repurposed as safe BBB therapeutics by engineering them into highly specific Gpr124/Reck agonists. [Illustration created with BioRender]

The list of author affiliations is available in the full article online.
***Corresponding author. Email: benoit.vanhollebeke@ulb.be**
Cite this article as M. Martin *et al.*, *Science* **375**, eabm4459 (2022). DOI: 10.1126/science.abm4459

READ THE FULL ARTICLE AT
https://doi.org/10.1126/science.abm4459

RESEARCH ARTICLE

BLOOD-BRAIN BARRIER

Engineered Wnt ligands enable blood-brain barrier repair in neurological disorders

Maud Martin[1], Simon Vermeiren[1], Naguissa Bostaille[1], Marie Eubelen[1], Daniel Spitzer[2], Marjorie Vermeersch[3], Caterina P. Profaci[4], Elisa Pozuelo[5], Xavier Toussay[6], Joanna Raman-Nair[6], Patricia Tebabi[1], Michelle America[1], Aurélie De Groote[5], Leslie E. Sanderson[1], Pauline Cabochette[1], Raoul F. V. Germano[1], David Torres[7], Sébastien Boutry[3], Alban de Kerchove d'Exaerde[5], Eric J. Bellefroid[8], Timothy N. Phoenix[9], Kavi Devraj[2], Baptiste Lacoste[6], Richard Daneman[4], Stefan Liebner[2], Benoit Vanhollebeke[1,10]*

The blood-brain barrier (BBB) protects the central nervous system (CNS) from harmful blood-borne factors. Although BBB dysfunction is a hallmark of several neurological disorders, therapies to restore BBB function are lacking. An attractive strategy is to repurpose developmental BBB regulators, such as Wnt7a, into BBB-protective agents. However, safe therapeutic use of Wnt ligands is complicated by their pleiotropic Frizzled signaling activities. Taking advantage of the Wnt7a/b-specific Gpr124/Reck co-receptor complex, we genetically engineered Wnt7a ligands into BBB-specific Wnt activators. In a "hit-and-run" adeno-associated virus–assisted CNS gene delivery setting, these new Gpr124/Reck-specific agonists protected BBB function, thereby mitigating glioblastoma expansion and ischemic stroke infarction. This work reveals that the signaling specificity of Wnt ligands is adjustable and defines a modality to treat CNS disorders by normalizing the BBB.

Proper function of the central nervous system (CNS) requires a tightly controlled environment that safeguards the nervous system from harmful blood-borne components and pathogens. A blood-brain barrier (BBB) enables this separation via a selectively semipermeable boundary established by CNS vascular endothelial cells (ECs) that is induced and maintained by signals derived from other cells of the neurovascular unit, most notably pericytes and astrocytes (*1*–*5*).

BBB dysfunction displays varying degrees of cerebrovascular hyperpermeability, neurovascular uncoupling, or blood flow dysregulation; it has been linked to stroke, gliomas, epilepsy, traumatic brain injury, and neurodegenerative disorders (*1*, *3*, *5*, *6*). Upon BBB breakdown, leakage of neurotoxic plasma components, infiltration of immune cells, and CNS milieu alterations contribute to neuronal demise and worsen disease outcome (*4*, *5*). Because of their therapeutic potential across a wide range of disorders, clinically approved BBB-protective strategies are needed.

Among the many pathways that control neurovascular function, endothelial Wnt/β-catenin signaling acts as a master regulator of BBB physiology. It initiates the BBB differentiation cascade at the earliest steps of CNS vascular invasion and maintains BBB function in health and disease (*7*–*14*). Hence, identifying safe modalities to enhance Wnt/β-catenin signaling, selectively at the BBB, constitutes a promising therapeutic avenue for a range of neurological disorders.

Wnt/β-catenin–dependent BBB maturation is controlled by Wnt7a/b ligands (*7*–*9*), which therefore represent potential therapeutic agents to repair the dysfunctional BBB. However, the 19 Wnt ligands, including Wnt7a/b, interact promiscuously with the 10 Frizzled (Fz) receptors, with many Wnts able to engage a single Fz receptor and vice versa (*15*). Delivering Wnt7a/b ligands in vivo is thus predicted to have multiple adverse outcomes, including altered organogenesis, stem cell expansion, and tumorigenesis (*16*). Accordingly, Wnt7a overexpression is incompatible with proper vertebrate development. When expressed in *Xenopus* or zebrafish embryos, Wnt7a causes axis duplication or posteriorization of the anterior nervous system, respectively, which are classical dysmorphic outcomes of exacerbated Wnt/β-catenin signaling (fig. S1). This promiscuous signaling mode, together with the widespread Fz expression patterns and the difficulty in producing active Wnt proteins at bulk levels, has contributed to hampering the clinical development of Wnt signaling–based therapies.

In cerebral ECs, an atypical Wnt7a/b-specific co-receptor complex activates Wnt/β-catenin signaling during brain angiogenesis and BBB regulation (*17*, *18*). This co-receptor complex contains the glycosylphosphatidylinositol-anchored glycoprotein Reck and the adhesion G protein–coupled receptor Gpr124. Wnt7a/b thus activates two distinct types of membrane receptor complexes. One has broad tissue distribution and binds nondiscriminately to Wnt7a/b and other Wnt ligands via two contact sites with Fz and a third interaction with Lrp5/6 (Fig. 1A, hereafter termed the systemic "off-target" complex). The other complex is enriched at the level of the BBB ECs and is highly specific for Wnt7a/b. In this case, Reck provides an additional contact point by binding at least in part to the divergent linker peptide of Wnt7a/b (Fig. 1A, BBB "on-target"). After physically binding to Wnt7a/b, Reck stabilizes the ligand in a signaling-competent lipophilic conformation and delivers it to Fz receptors via the transmembrane tethering function of Gpr124. Thereby, Reck and Gpr124 synergistically stimulate Wnt7a/b-specific responses by assembling higher-order Gpr124/Reck/Fz/Lrp5/6 complexes (*19*–*21*).

Discovery of highly specific Gpr124/Reck agonists

Taking advantage of the differential composition of these receptor complexes, we attempted to selectively target the BBB by engineering Wnt7a/b into Gpr124/Reck-specific agonists. To that end, we determined which Fz receptors are competent for Wnt7a/b signaling in Wnt/β-catenin–reporting super top flash (STF) HEK293(T) cells (fig. S2). Wnt7a and Wnt7b signaled preferentially through Fz5 and Fz8 in wild-type or *GPR124*$^{-/-}$;*RECK*$^{-/-}$ cells (fig. S2, A and B, and table S1). Upon Gpr124 and Reck overexpression in wild-type cells, Wnt7a/b signals were selectively and potently stimulated even in the absence of a coexpressed Fz, probably because of confounding endogenous expression of Fz (fig. S2C and table S1). In a *GPR124*$^{-/-}$;*RECK*$^{-/-}$;*FZ*$_{1\text{-}10}^{-/-}$ CRISPR/Cas9 null genetic background, Fz5 and Fz8 were confirmed as the only Wnt7a/b receptors signaling in the absence of Gpr124/Reck, whereas most Fz receptors proved competent for Gpr124/Reck-dependent signaling (fig. S3). If we assume similar expression and localization of the ectopically expressed Fz receptors, Wnt7a/b thus signal through distinct Fz receptors depending on the absence or presence of Gpr124/Reck (Fig. 1A).

[1]Laboratory of Neurovascular Signaling, Department of Molecular Biology, ULB Neuroscience Institute, Université libre de Bruxelles, Gosselies B-6041, Belgium. [2]Institute of Neurology (Edinger Institute), University Hospital, Goethe University Frankfurt, Frankfurt am Main, Germany. [3]Center for Microscopy and Molecular Imaging, Université libre de Bruxelles, Université de Mons, Gosselies B-6041, Belgium. [4]Departments of Pharmacology and Neurosciences, University of California, San Diego, La Jolla, CA, USA. [5]Laboratory of Neurophysiology, ULB Neuroscience Institute, Université libre de Bruxelles, Brussels B-1070, Belgium. [6]Ottawa Hospital Research Institute, Neuroscience Program, Department of Cellular and Molecular Medicine, University of Ottawa Brain and Mind Research Institute, Faculty of Medicine, Ottawa, Ontario, Canada. [7]Institut d'Immunologie Médicale, Université libre de Bruxelles, Gosselies, Belgium. [8]Laboratory of Developmental Genetics, ULB Neuroscience Institute, Université libre de Bruxelles, Gosselies B-6041, Belgium. [9]Division of Pharmaceutical Sciences, James L. Winkle College of Pharmacy, University of Cincinnati, Cincinnati, OH, USA. [10]Walloon Excellence in Life Sciences and Biotechnology (WELBIO), Wavre, Belgium.
*Corresponding author. Email: benoit.vanhollebeke@ulb.be

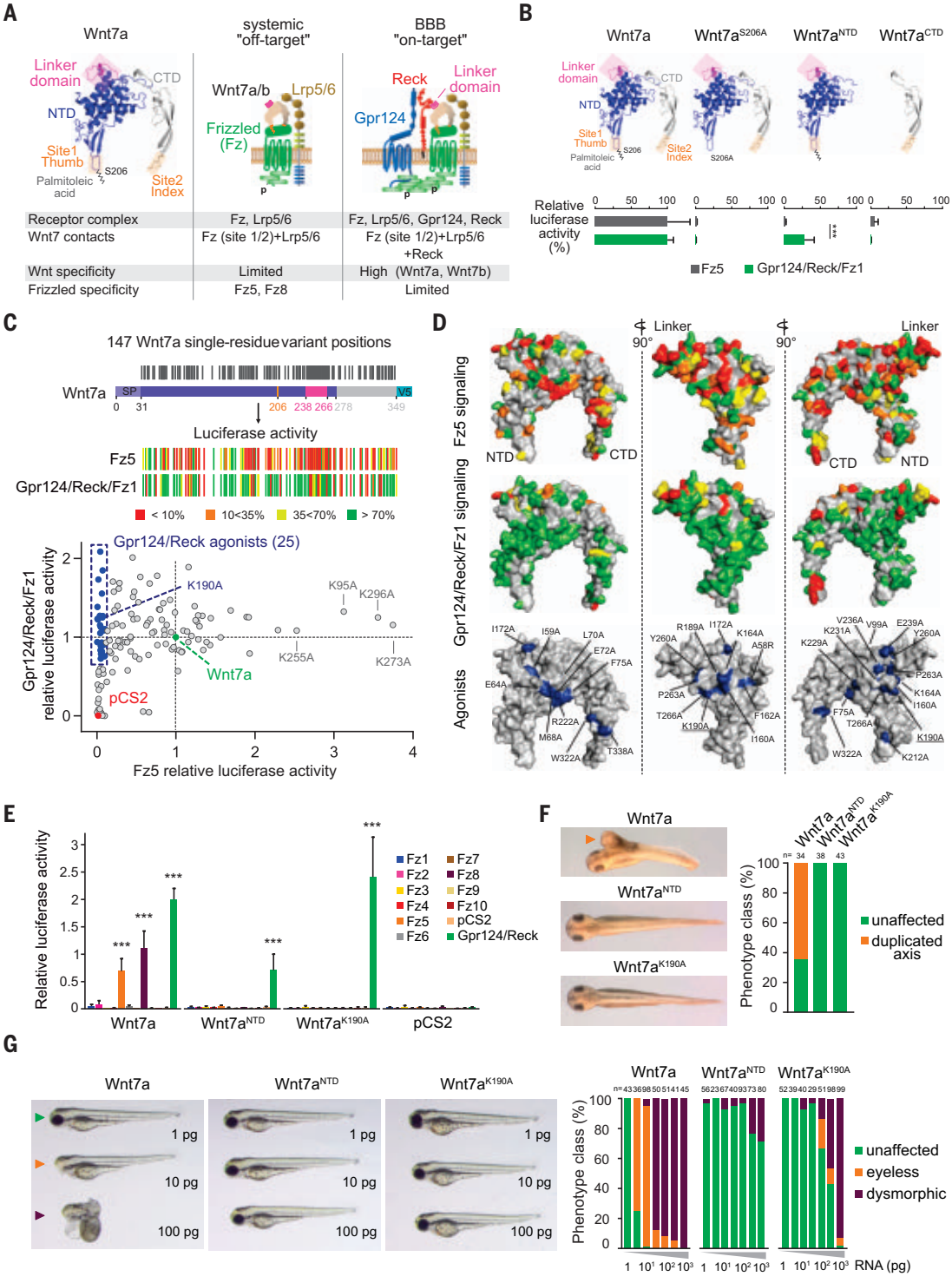

Fig. 1. Engineering Wnt7a ligands into highly specific Gpr124/Reck activators. (**A**) Backbone model of murine Wnt7a based on the crystal structure of XWnt8a (*15*) and schematics of the receptor complexes mediating Wnt7a/b/β-catenin signaling. (**B**) Relative STF (super top flash) luciferase activity of Wnt7a and its depicted variants on Fz5 or Gpr124/Reck/Fz1. (**C**) Position and color-coded Gpr124/Reck/Fz1 or Fz5 STF activities of 147 V5-tagged single-residue Wnt7a variants. Gpr124/Reck agonists (blue dots) were defined as variants with >70% Gpr124/Reck/Fz1 and <10% Fz5 activity. (**D**) Front, lateral, and back views of the Wnt7a surface model with integrated color-coded activities of all 147 single-residue variants. Agonists are in blue. (**E**) β-Catenin signaling assays using STF cells transfected with any of the 10 Fz receptors or Gpr124/Reck, together with Wnt7a, Wnt7a^{NTD}, Wnt7a^{K190A}, or the empty pCS2 vector. (**F**) Phenotypic scoring of stage 36 *Xenopus laevis* embryos injected into the ventral vegetal region of the four-cell embryo with 15 pg of the indicated mRNA. Arrowhead indicates duplicated axis. (**G**) Phenotypic scoring of 3-dpf zebrafish larvae injected at the one-cell stage with Wnt7a, Wnt7a^{NTD}, or Wnt7a^{K190A} mRNA at the indicated doses. Colored arrowheads refer to the phenotypic classes on the right. Wnt7a and variants are V5-tagged. Data are means ± SD. ***P < 0.001. Amino acid abbreviations: A, Ala; E, Glu; F, Phe; I, Ile; K, Lys; L, Leu; M, Met; P, Pro; R, Arg; T, Thr; V, Val; W, Trp; Y, Tyr.

The near-uniform competence of Fz isoforms for Gpr124/Reck-dependent Wnt7a/b signaling reveals that these ligands lose their capacity to distinguish Fz receptors when bound by Reck within the Gpr124/Reck/Fz/Lrp5/6 complex. Because Wnt ligands discriminate Fz receptors primarily via site 2 (*15*), we suspected that Wnt7a/b activity at the BBB might be dominated by site 1 of the N-terminal domain (NTD). Supporting this hypothesis, chimeric Wnt ligands composed of Wnt7a NTD fused to a C-terminal domain (CTD) derived from another Wnt were competent for Reck binding and Gpr124/Reck-dependent signaling (fig. S4) (*19*, *21*).

This suggested that in contrast to the systemic "off-target" situation, where both contact sites 1 and 2 are strictly required for Wnt signaling, Wnt7a/b-Fz interaction at site 2 might become dispensable in the context of Gpr124/Reck-stimulated signaling. Accordingly, Wnt7a^{NTD}, a hemisected Wnt7a variant, retained partial activity on Gpr124/Reck/Fz1-mediated signaling while showing no stimulation of Fz5 signaling, used as a paradigm "off-target" readout (Fig. 1B). Furthermore, mutating three of the five Wnt7a residues involved

in site 2 contacts did not affect Gpr124/Reck-mediated signaling while reducing Fz5 signaling by more than 50% (fig. S5). Both Wnt7a^{CTD} and Wnt7a^{S206A}, with impaired site 1, were fully inactive. These findings show that altering the structure of Wnt ligands can modulate their signaling specificity, and more specifically, that Wnt7a can be engineered into a Gpr124/Reck-specific ligand.

On the basis of this proof of concept, we implemented a large-scale screen for Gpr124/Reck-specific Wnt7a variants with optimal "on-target" activity because Wnt7a^{NTD} is only ~30% as active as the parental Wnt7a ligand. We generated a collection of 147 single-residue variants of V5-tagged murine Wnt7a, mostly through alanine substitutions. This collection corresponds to 46% of the residues of the secreted protein and 51% of its exposed surface. Each variant was tested for its Gpr124/Reck-dependent and -independent activity (Fig. 1, C and D, fig. S6A, and table S2). Wnt7a/Fz5 signaling appeared highly sensitive to Wnt7a mutations, with 37% of the variants exhibiting <10% activity and only 31% maintaining >70% activity. Most tested inactive variants (15/17) showed levels of extracellular accumulation similar to those of Wnt7a, ruling out improper trafficking as a leading cause for the large proportion of Fz5-inactive variants (fig. S7). In contrast to Fz5, Gpr124/Reck signaling appeared homogeneous and largely insensitive to Wnt7a variations, as 76% of the variants retained >70% activity (Fig. 1, C and D, and fig. S6A).

This led to the identification of 25 single-residue variants displaying highly specific Gpr124/Reck activity (so-called "agonists" >70% on-target, <10% off-target; Fig. 1, C and D, fig. S6B, and table S2). Wnt7a^{K190A} was selected as a single-residue Gpr124/Reck agonist prototype, optimally combining a wild type–like signal on Gpr124/Reck and undetectable "off-target" Fz5 activity.

In vitro, none of the transfected Fz receptors could be stimulated by Wnt7a^{NTD} or Wnt7a^{K190A} in the absence of Gpr124/Reck (Fig. 1E). In vivo, contrary to Wnt7a, ubiquitous expression of Wnt7a^{NTD} or Wnt7a^{K190A} after mRNA injections failed to trigger gross morphological alterations in *Xenopus* or zebrafish (Fig. 1, F and G). Although the in vivo expression level and secretion rate were not formally compared, dose response experiments in zebrafish revealed that 3 pg of Wnt7a mRNA was sufficient to trigger "off-target" signaling, whereas Wnt7a^{NTD} and Wnt7a^{K190A} were well tolerated even when expressed in a 100-fold excess (Fig. 1G). Wnt7a signaling in this setting is Gpr124-independent, as revealed by the analysis of zygotic and maternal-zygotic *gpr124^{s984}* mutants (*17*) (fig. S1C). As a control, in Gpr124/Reck-overexpressing zebrafish embryos, Wnt7a or Wnt7a^{K190A} triggered morphological alterations at low mRNA doses (fig. S8).

Gpr124/Reck agonists require Reck to bind Fz

Mechanistically, the selectivity of the uncovered agonists resulted from their incapacity to bind, and therefore activate, Fz receptors in the absence of Gpr124/Reck. Indeed, whereas Wnt7a immunolocalized to the surface of *RECK$^{-/-}$;GPR124$^{-/-}$* cells transiently transfected with Reck or Fz5, Wnt7a^{NTD} and Wnt7a^{K190A} labeled the membrane in the presence of Reck, but not Fz5 (Fig. 2, A and B). Accordingly, the agonists coimmunoprecipitated with hemagglutinin (HA)–tagged Reck as efficiently as did Wnt7a (Fig. 2C) but failed to bind HA-Fz5 in *RECK$^{-/-}$* cells unless Reck was coexpressed (Fig. 2D).

The distant position of the agonistic K190A mutation on the Wnt7a structure makes it unlikely that K190A directly affects the interaction with Fz. Instead, such a mutation could affect the biophysical properties of the ligand. Wnt ligands are indeed short-lived and rapidly lose activity by oligomerization, in a process that increases their hydrosolubility (*22*, *23*). Reck has been shown to extend the half-life of Wnt7a activity by maintaining it in a monomeric, hydrophobic state (*20*, *24*). It is thus possible that the introduction of single-residue variations into Wnt7a reduces ligand stability below a threshold required for Fz signaling, a property that the stabilizing action of Reck could counteract. In agreement with this idea, a clear correlation was seen at the single-residue level between Fz5 and Gpr124/Reck/Fz1 activities when assessed across the 147 Wnt7a variants. Variants displaying even slightly reduced activity on Gpr124/Reck (yellow, orange, or red residues in Fig. 1, C and D) were generally fully inactive in the more sensitive Fz5 setting (Fig. 2E). Conversely, preservation of at least partial Fz5 activity (orange, yellow, or green residues in Fig. 1, C and D) strongly correlated with full activity on Gpr124/Reck (Fig. 2E).

The stability of morphogens influences their range of action, with more stable ligands capable of activating more distant cells. We analyzed the capacity of Wnt7a and Wnt7a^{K190A} to activate Wnt signaling at short distances (autocrine monocultures) versus longer distances (paracrine cocultures) (Fig. 2F). Although Wnt7a exhibited partial paracrine activity, Wnt7a^{K190A} could not reach the receiving cell in an active form. The whole collection of agonists behaved similarly in this assay (fig. S9). Furthermore, combining agonistic mutations almost invariably resulted in fully inactive ligands, even when tested on Gpr124/Reck signaling in monocultures (Fig. 2G). Conversely, introducing K95A, K255A, K273A, and K296A mutations into Wnt7a^{K190A} (all of which increase Fz5 activity; Fig. 1C) was sufficient to abolish selectivity by restoring partial Fz5 signaling (Fig. 2H). Finally, mutating Lys^{190} to alternative residues (Gly, Ser, Leu, Pro, Asp, Glu, or Arg) had variable effects on signaling specificity (Fig. 2I). In sum, by recruiting Wnt7a/b into a higher-order receptor complex, Gpr124/Reck profoundly redefines the Wnt7a/b primary structure requirements for Fz signaling.

Activity of Gpr124/Reck agonists in zebrafish

To test the functionality of the agonists in vivo, we first generated a genetic deficiency model in zebrafish. Morpholino-mediated gene knockdown and in situ hybridization of the four zebrafish Wnt7a/b paralogs identified *wnt7aa* as the BBB-relevant ligand (fig. S10). We therefore generated *wnt7aa^{ulb2}*, a CRISPR/Cas9 frame-shift allele (Fig. 3A). *gpr124* mutants (*17*) and homozygous *wnt7aa^{ulb2}* mutants (*wnt7aa$^{-/-}$*) display similar cerebrovascular and dorsal root ganglia (DRG) neurogenesis defects (Fig. 3B) and lack Wnt/β-catenin reporter expression in CNS-invading vessels (Fig. 3C). In cell cultures, all tested human, mouse, and zebrafish orthologs of the Wnt7/Gpr124/Reck signaling module were functionally interchangeable (fig. S11), supporting the functional assessment of murine ligands in zebrafish.

The *wnt7aa$^{-/-}$* DRG defects could be partially corrected by injecting 100 pg of Wnt7a^{NTD} or Wnt7a^{K190A} mRNA at the one-cell stage. By contrast, Wnt7a was toxic at equivalent doses (Figs. 1G and 3D). *Wnt7aa$^{-/-}$* cerebrovascular phenotypes could not be rescued by mRNA injections, presumably as a result of the late onset of zebrafish hindbrain angiogenesis (36 hpf). Therefore, we adopted a mosaic transgenic endothelial expression strategy using a *kdrl* (*vegfr2*) promoter. In this approach, Wnt7a^{K190A} restored the formation of central arteries (CtAs) to a level comparable to Wnt7a, and these vessels expressed glucose transporter–1 (Glut1), a marker of BBB maturation (Fig. 3E). Reflecting its partial activity in vitro, Wnt7a^{NTD} was less potent.

These results, demonstrating the capacity of the agonists (in particular Wnt7a^{K190A}) to stimulate Wnt signaling at the BBB, led us to test their protective potential in a zebrafish atorvastatin (ATV)–induced hemorrhagic stroke model, reminiscent of human cerebral cavernous malformation (CCM)–like lesions (*25*). Although more than 90% of ATV-exposed wild-type larvae displayed moderate to severe intracranial (IC) hemorrhages, transgenic endothelial expression of Wnt7a^{K190A} decreased the extent of cerebrovascular ruptures, with more than half of the embryos showing no or little bleeding (Fig. 3F). ATV also caused the accumulation of intracardially injected 10-kDa dextran into the hindbrain (Fig. 3G). Wnt7a^{K190A} expression could as well counteract these more subtle ATV-induced BBB defects, as revealed by the examination of embryos expressing Wnt7a^{K190A} hemispherically (Fig. 3H).

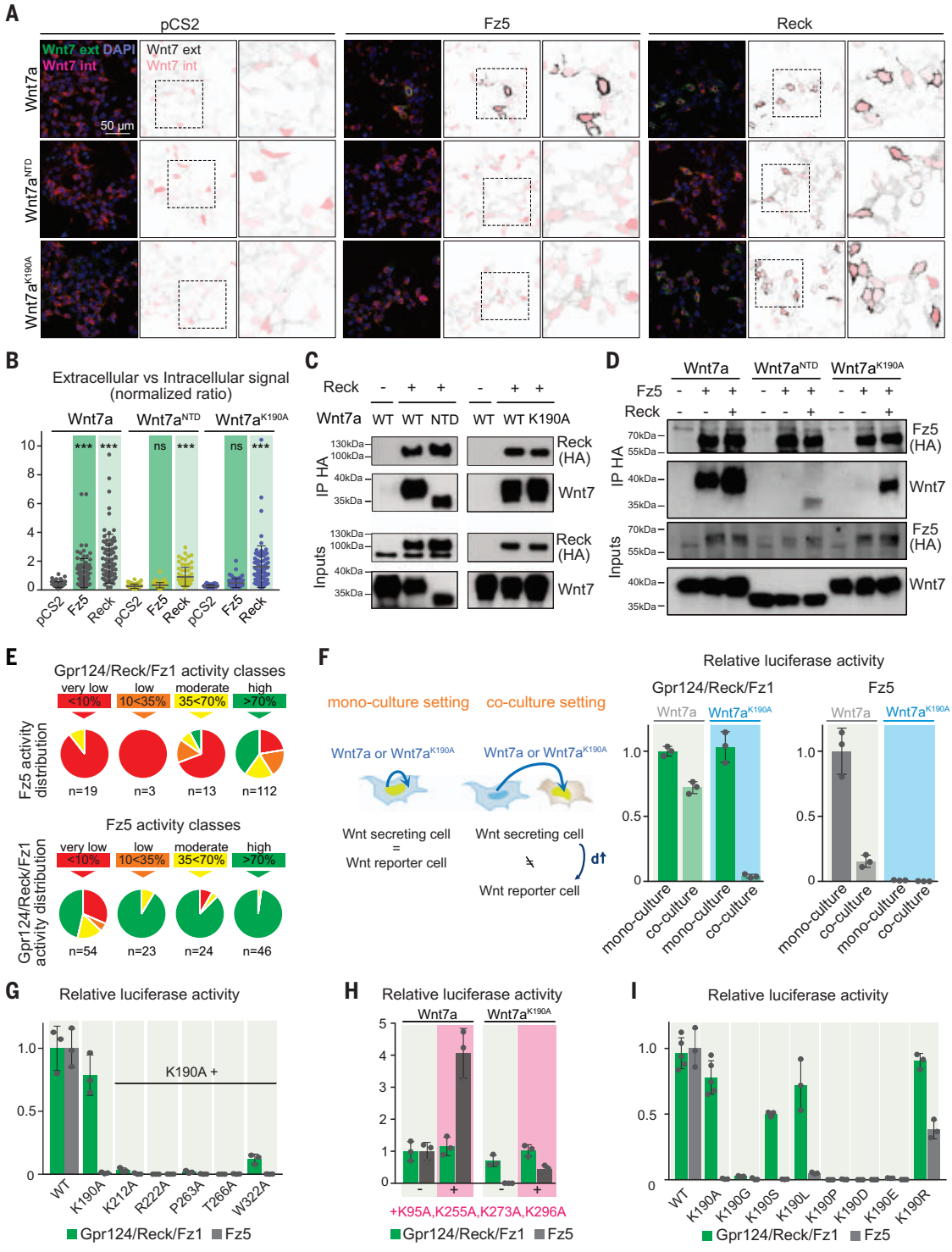

Fig. 2. Gpr124/Reck agonists are unable to bind Fz autonomously. (**A**) *GPR124*$^{-/-}$;*RECK*$^{-/-}$ HEK293 cells transiently expressing Wnt7a, Wnt7a^{NTD}, or Wnt7a^{K190A} together with Fz5, Reck, or the empty pCS2 vector were submitted to Wnt7a double immunostaining, before (Wnt7a extracellular, green/black) and after (Wnt7a intracellular, pink) cell permeabilization. (**B**) Quantification of (A), as described in the supplementary materials. (**C** and **D**) Anti-HA coimmunoprecipitation assays after membrane-impermeable cross-linking in total lysates of *RECK*$^{-/-}$ HEK293T cells expressing HA-Reck (C) or HA-Fz5 (D) together with Wnt7a, Wnt7a^{NTD}, or Wnt7a^{K190A}, with or without expression of untagged Reck (D). (**E**) Gpr124/Reck/Fz1 and Fz5 activity correlations across the Wnt7a single-residue variants collection. (**F**) Relative STF luciferase activity in the presence of Gpr124/Reck/Fz1 or Fz5 in response to Wnt7a or Wnt7a^{K190A} in autocrine monoculture or paracrine coculture variants settings. (**G** to **I**) Gpr124/Reck/Fz1 or Fz5 STF activities of Wnt7a^{K190A} with combined agonistic mutations (G), activity-increasing mutations (H), or alternative substitutions of Lys^{190} (I). Wnt7a and variants are V5-tagged. Data are means ± SD. ***P < 0.001; ns, nonsignificant.

Brainwide delivery of Gpr124/Reck agonists in mice

We next evaluated Gpr124/Reck agonists as BBB-protective agents in mammals. To deliver the agonists widely throughout the mouse CNS, we generated PHP.eB adeno-associated viruses expressing enhanced green fluorescent protein (AAV-EGFP), Wnt7a-P2A-EGFP (AAV-Wnt7a), or Wnt7a^{K190A}-P2A-EGFP (AAV-K190A) under the control of a constitutive CAG promoter. Upon intravenous injection of 4×10^{11} vg (viral genomes) in 8-week-old mice, CD31-positive brain vessels were surrounded by EGFP^{+} cells (Fig. 4A), exposing ECs to local sources of Wnt7a or Wnt7a^{K190A}. The AAV-PHP.eB capsid drives expression of the transgenes in ~25% of ECs, ~30% of astrocytes, and ~45% of NeuN^{+} neurons (fig. S12A), as reported previously (*26*). More than 95% of the desmin^{+} pericytes were negative for EGFP. Pericytes are thus, at best, marginal sources of Wnt7a in this approach (fig. S12B).

Although expressed from widely distributed cells, Wnt7a and Wnt7a^{K190A} showed a more discrete distribution, with preferential accumulation at the level of CD31-positive vessels, as well as some scattered parenchymal cells

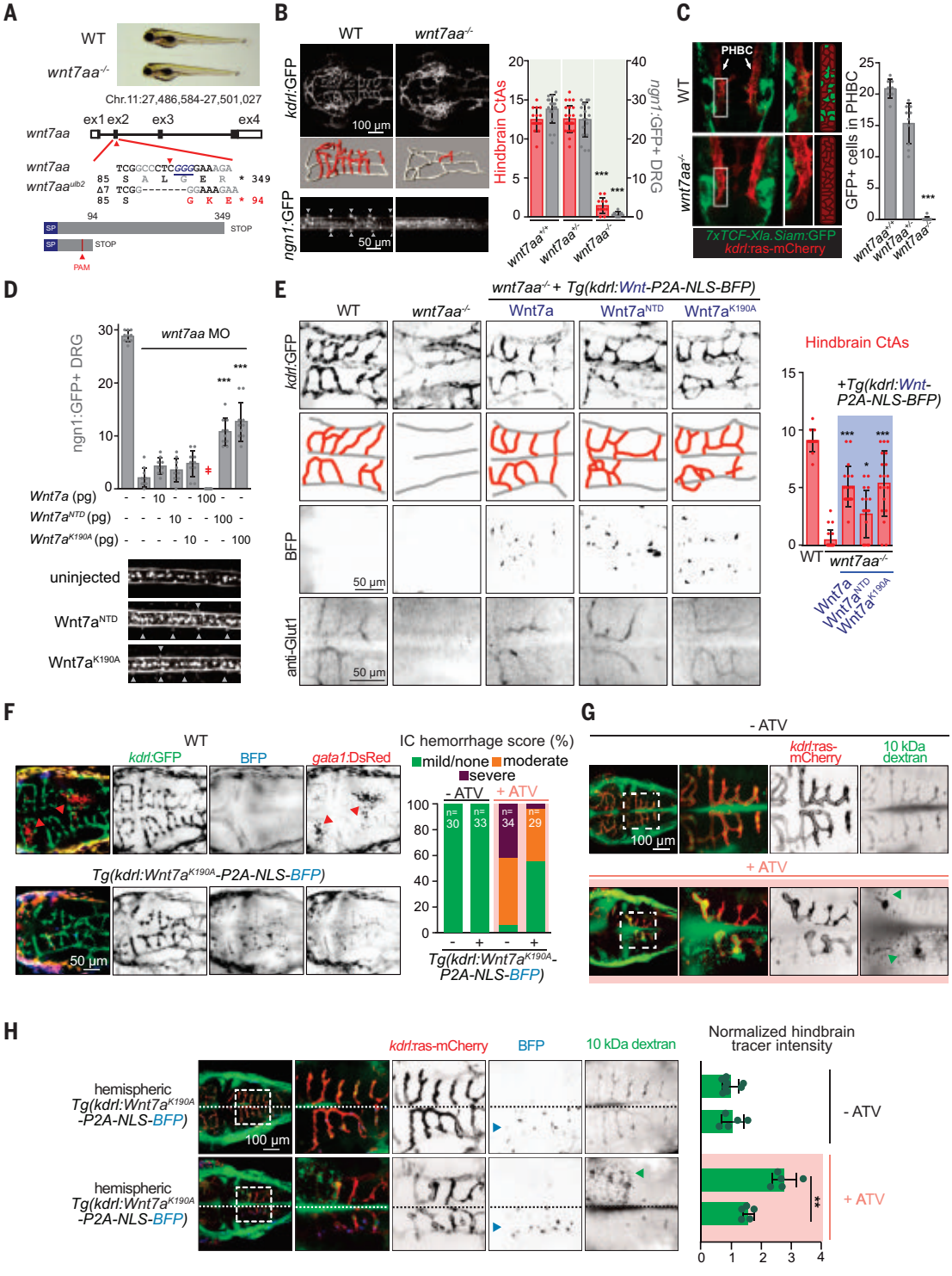

Fig. 3. Gpr124/Reck agonists stimulate brain angiogenesis, promote blood-brain barrier induction, and prevent hemorrhagic stroke in zebrafish. (**A**) Characterization of the *wnt7aa*^{ulb2} allele. PAM, protospacer adjacent motif. (**B**) 60-hpf *Tg(kdrl:GFP)* hindbrain CtAs (central arteries) and 72-hpf *Tg(neurog1:GFP)* dorsal root ganglia (DRG, gray arrowheads) in wild-type (WT) and *wnt7aa* mutant zebrafish. (**C**) 30-hpf WT and *wnt7aa* mutant *Tg(7xTCF-Xia.Siam:GFP);Tg(kdrl:ras-mCherry)* hindbrains and quantification of GFP^{+} (β-catenin signaling–positive) ECs in the perineural PHBCs (primordial hindbrain channels). (**D**) DRG in 72-hpf *wnt7aa* morphants injected at the one-cell stage with the indicated mRNAs. Injection of 100 pg of Wnt7a mRNA is developmentally toxic (‡). (**E**) 48-hpf WT and *wnt7aa*$^{-/-}$ *Tg(kdrl:GFP)* hindbrain cerebrovasculatures, with transgenic endothelial expression of Wnt7a, Wnt7a^{NTD}, or Wnt7a^{K190A}. BFP is used as a transgenesis marker; Glut1 immunostaining illustrates BBB differentiation. (**F**) Intracerebral (IC) hemorrhage score of 54 hpf *Tg(kdrl:GFP);Tg(gata1a:dsRed)* embryos treated from 34 hpf onward with 1 µM atorvastatin (ATV), with or without transgenic endothelial expression of Wnt7a^{K190A}. Red arrowheads point to extravasated erythrocytes. (**G**) BBB leakage of 10-kDa dextran upon ATV exposure. (**H**) Quantification of 10-kDa dextran tracer leakage upon ATV exposure, with or without hemispheric transgenic endothelial expression of Wnt7a^{K190A} in 54-hpf embryos. Data are means ± SD. *P < 0.05, **P < 0.01, ***P < 0.001.

(Fig. 4B, asterisks). The distribution of the ligands, and hence their potential activity, likely reflects the expression patterns of their receptors, with unbound ligands getting cleared through the glymphatic system (*27*) or other routes. Accordingly, Wnt7a exhibited a more significant nonvascular distribution (Fig. 4B, asterisks). More so, immunodetection of β-catenin activity (LacZ signal) in coronal brain sections of BAT-GAL mice (*28*) revealed that, in contrast to Wnt7a^{K190A}, Wnt7a triggered ectopic Wnt/β-catenin signaling in non-endothelial cells of the hippocampus (dentate gyrus) and the parafascicular nucleus of the thalamus at all examined time points [7, 14, and 28 days post-injection (dpi)] (Fig. 4C). These two areas are associated with Fz5 expression (*29*, *30*). Other brain regions did not exhibit increased LacZ signal (fig. S13). The BAT-GAL results were confirmed using RNAScope hybridization of the Wnt target *Axin2* (Fig. 4D and fig. S14).

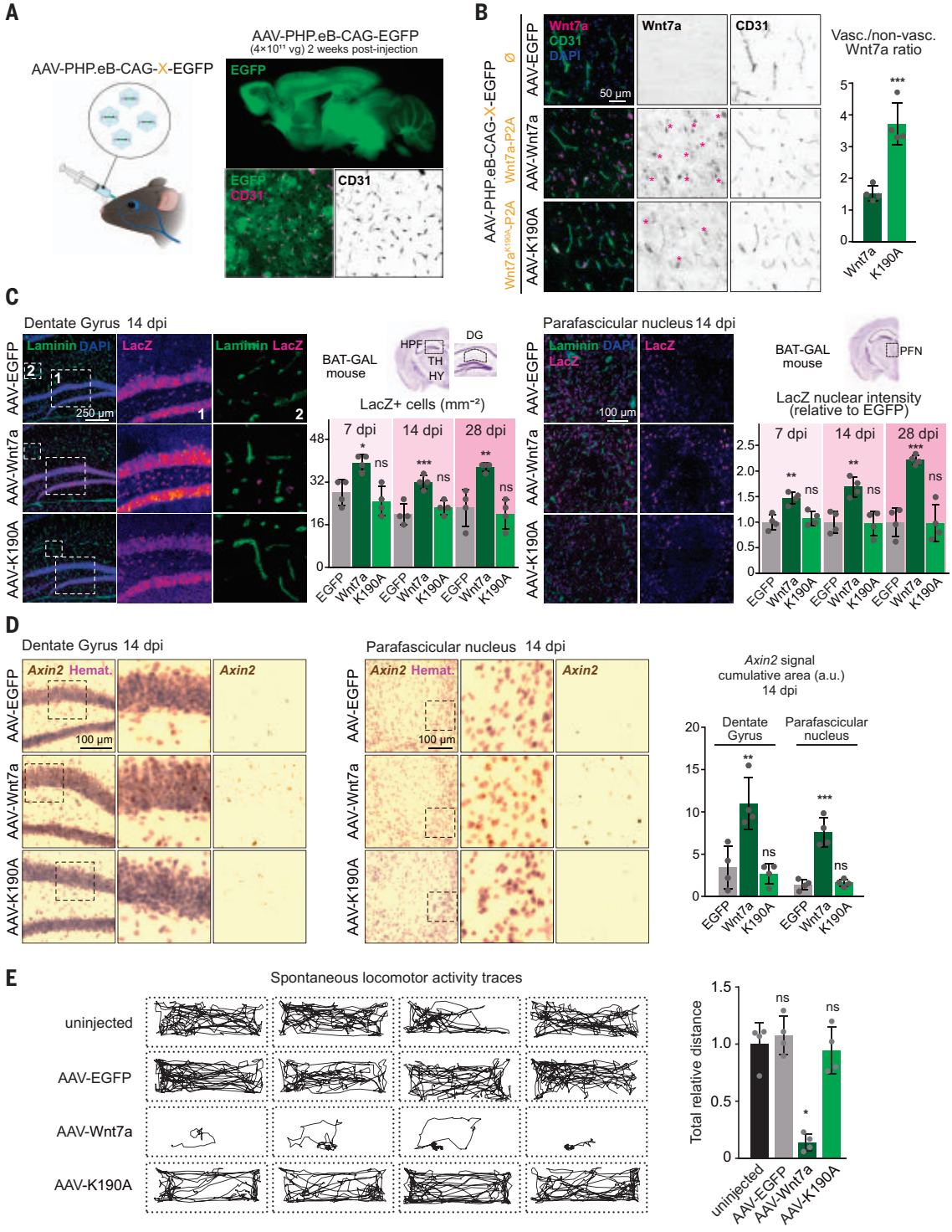

Fig. 4. Absence of ectopic Wnt activities or behavioral defects after brainwide AAV-mediated gene delivery of Gpr124/Reck agonists in mice. (**A** and **B**) Immunostaining of sagittal brain sections for EGFP and CD31 (vessels) (A) and coronal sections for Wnt7a or its variant and CD31 together with a DAPI counterstain (B), 2 weeks after intravenous injections of the indicated AAVs. (**C**) Staining of coronal sections of AAV-injected BAT-GAL mice for LacZ, laminin, and DAPI in the hippocampal area dorsal to the dentate gyrus (DG, left) and in the parafascicular nucleus area (PFN, right). Nuclear LacZ-positive cells or signal intensities were quantified at 7, 14, and 28 days post-injection (dpi). HPF, hippocampal formation; TH, thalamus; HY, hypothalamus. (**D**) RNAScope in situ hybridization of *Axin2* in coronal sections of AAV-injected WT mice. (**E**) Spontaneous open-field locomotor activity traces of postnatal day 20 (P20) mice injected retro-orbitally at P2 with 4×10^{10} vg of the indicated AAV-PHP.eB viruses. Spontaneous locomotor activity is quantified as the distance traveled for 3 min; data are means ± SD. $^{*}P < 0.05$, $^{**}P < 0.01$, $^{***}P < 0.001$.

Although the ectopic Wnt7a activities did not result in obvious behavioral defects in adult mice (fig. S15), gene delivery of Wnt7a, but not Wnt7a^{K190A} or EGFP, was detrimental to neonatal spontaneous locomotor activity (Fig. 4E). We next assessed the Wnt activity status at the target BBB endothelium by staining for lymphoid enhancer binding factor 1 (LEF1) because the low Wnt activity levels of adult BBB ECs are not detectable using BAT-GAL reporter mice (fig. S13) (*31*). AAV-based delivery of Wnt7a or Wnt7a^{K190A} did not increase LEF1 signals in healthy ECs (fig. S16).

A "hit-and-run" gene delivery of Gpr124/Reck agonists in glioblastoma multiforme

The absence of "off-target" Wnt signaling activity after widespread Wnt7a^{K190A} expression in the mouse brain prompted us to test its therapeutic potential in CNS pathologies associated with BBB dysfunction, starting with glioblastoma multiforme (GBM). GBM, the most aggressive and frequent primary brain tumor, is characterized by a dense vascular network exhibiting disrupted BBB properties, and endothelial Wnt signaling has been reported to control vascular integrity in this and other

brain tumors (*12*, *14*, *32*, *33*). Two days after orthotopic implantation of 1×10^5 GL261 tumor cells into the C57BL/6 mouse striatum, we performed a single "hit-and-run" intravenous AAV-PHP.eB gene delivery and monitored tumor volume by magnetic resonance imaging (MRI) at 21 to 24 days post-implantation (dpi) (Fig. 5A). Although control tumor expansion was highly variable, with volumes ranging from 10 to 80 mm^3, $Wnt7a^{K190A}$ expression (AAV-K190A) reduced this variability and limited tumor volume to ~20 mm^3. In particular, the proportion of larger tumors (>40 mm^3) was reduced (8% in K190A versus 33% in controls).

At 25 dpi, mice with the largest tumors started to exhibit disease symptoms, including faulty postural syndromes and abnormal gait. This time point was therefore chosen for terminal analysis and tissue harvesting. Control tumors exhibited more prominent microvascular hemorrhages (asterisks) and edema than did AAV-K190A tumors (Fig. 5B), suggesting cerebrovascular differences between the groups. Accordingly, the K190A tumor-associated vasculature showed features of vessel normalization, such as reduced $CD31^+$ vascular density (Fig. 5C), fewer large vessels (Fig. 5C), and

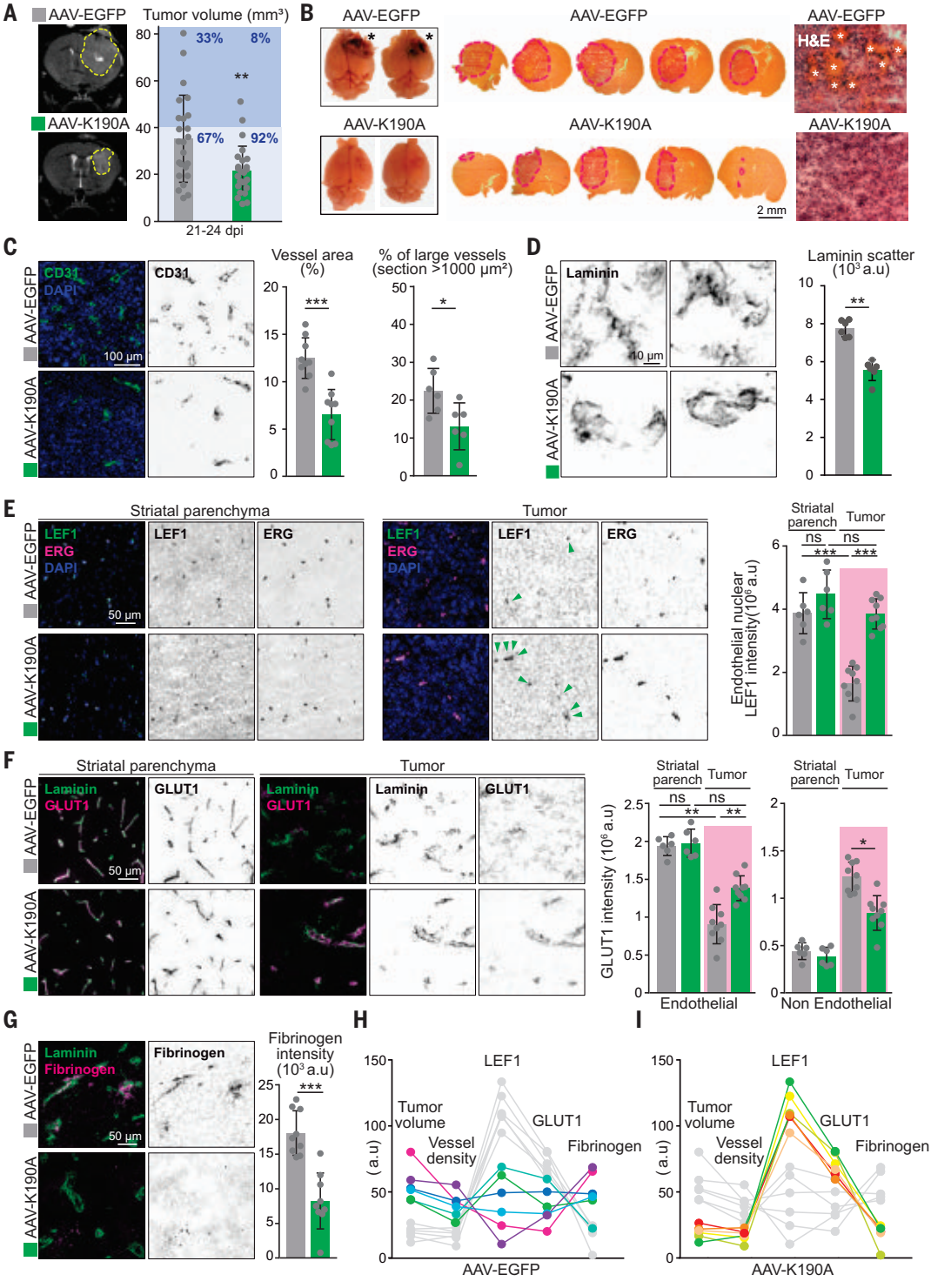

Fig. 5. A single "hit-and-run" gene delivery of Gpr124/Reck agonists achieves neurovascular-specific Wnt/β-catenin activation and vessel normalization in glioblastoma multiforme. (**A**) GL261-implanted mice, injected intravenously at 2 dpi (days post-implantation) with 4×10^{11} to 1×10^{12} vg of AAVs, were imaged by MRI to evaluate tumor volumes between 21 and 24 dpi. The dashed lines highlight the tumor margin. (**B**) At 25 dpi, mice were euthanized for brain gross morphology assessment (left) and H&E staining of serial sections (center and right). Asterisks indicate hemorrhages. (**C** to **G**) Coimmunostaining of tumor or parenchymal (parench) 25-dpi coronal sections for ECs (CD31) (C), vascular basement membranes (laminin) (D), LEF1 together with the endothelial nuclear marker ERG (E), GLUT1 together with laminin (F), or fibrinogen together with laminin (G). (**H**) Correlation between endothelial Wnt activity (LEF1) and tumor volume, vessel density, GLUT1, and fibrinogen leakage in tumors of AAV-EGFP–injected mice (colored lines). (**I**) Same as (H) in AAV-K190A–injected mice. Data are means ± SD; a.u, arbitrary units. *$P < 0.05$, **$P < 0.01$, ***$P < 0.001$.

more compact and smoother distribution of laminin (Fig. 5D). Cell densities were comparable in AAV-EGFP and AAV-K190A tumors (6425 versus 7141 cells mm^{-2}, respectively), implying that differential tumor volumes are more prominently explained by altered tumor cell proliferation than by vasogenic edema. Nuclear LEF1 staining revealed the low endothelial Wnt signaling activity typically associated with GBM vessels (Fig. 5E) (*14*). $Wnt7a^{K190A}$ restored Wnt activity in the tumor endothelium, to a level similar to the steady-state activity of nontumoral parenchymal vessels. In contrast, it did not significantly affect LEF1 levels in vessels of the contralateral hemisphere (Fig. 5E), confirming the findings in healthy mice (fig. S16). In agreement with nuclear LEF1 accumulation, BBB integrity was partially restored in tumor vessels, as revealed by increased GLUT1 immunoreactivity (Fig. 5F) and reduced fibrinogen extravasation (Fig. 5G). The restoration of GLUT1 signal in GBM vessels was accompanied by reduced tumor parenchymal GLUT1, paralleling the developmental switch of GLUT1 expression from the neuroepithelium to the vessels upon CNS vascularization (*8*, *9*).

To determine the source of $Wnt7a^{K190A}$ within the tumor microenvironment, we monitored the distribution of the coexpressed EGFP (fig. S17). Glioblastoma cells were negative, as expected from the nonreplicative nature of AAV genomes and the numerous cell divisions of these cells upon implantation. Within the tumor, 30% of $CD31^+$ endothelium was $EGFP^+$, and blood vessels accounted for ~60% of the total intratumoral $EGFP^+$ signal. In addition, the EGFP signals were particularly intense in $S100\beta^+/GFAP^-$ astrocytes of the tumor glial scar, whereas $Iba1^+$ microglia were $EGFP^-$.

These discrete $Wnt7a^{K190A}$ sources resulted in relatively uniform effects on tumor growth. By contrast, control GL261 tumors exhibited more significant heterogeneity (Fig. 5A). We reasoned that this heterogeneity could reflect differences in endothelial Wnt signaling levels. In agreement, endothelial LEF1 and GLUT1 levels in control tumors inversely correlated with vessel density, fibrinogen leakage, and tumor volume (Fig. 5H). These correlations suggest that the growth rate of GL261 tumors is at least partially determined by the level of residual Wnt signaling of its perfusing vasculature, and that AAV-delivery of $Wnt7a^{k190A}$ is sufficient to uniformly raise the signaling level to promote neurovascular normalization and tumor growth reduction (Fig. 5I).

Gpr124/Reck agonists as BBB repair agents in glioblastoma and stroke models

The variable degree of residual endothelial Wnt signaling within the wild-type GL261 tumor endothelium complicated the analysis of the mechanism underlying endothelial Wnt-induced BBB repair. Therefore, we resorted to transgenic Tet-Off GL261 cells that conditionally express the secreted Wnt inhibitor Dkk1 (dickkopf WNT signaling pathway inhibitor 1) (*12*). When exposed to doxycycline, these cells potently repress Dkk1 expression in vitro and in vivo without affecting their intrinsic in vitro growth rate (fig. S18). The characteristics of $Dkk1^+$ (–dox) GL261 tumors (Wnt inhibition) were compared with those of $Dkk1^-$ (+dox) tumors of mice injected with AAV-EGFP (control) or AAV-K190A (Wnt activation). We observed that $Dkk1^-$ cells behaved as wild-type GL261 cells, with ~95% of the AAV-K190A–treated $Dkk1^-$ tumors being smaller than 40 mm^3 at 20 to 24 dpi, and the AAV-EGFP cohort exhibiting more variable volumes (10 to 80 mm^3) (Fig. 6A). $Dkk1^+$ tumors grew even bigger, up to 160 mm^3. Endothelial Wnt activity markers (LEF1 and GLUT1) were the highest in the Wnt-stimulated $Dkk1^-$/K190A tumors and the lowest in Wnt inhibitory $Dkk1^+$ tumors, with $Dkk1^-$/EGFP tumors showing intermediate values (fig. S19, A and B). Hemorrhage (fig. S20), vascular density (fig. S19C), and fibrinogen leakage (Fig. 6B) followed the opposite trend, being gradually reduced by the stepwise increase in endothelial Wnt signaling.

Contrary to BBB restoration toward 350-kDa fibrinogen, small-molecule 557-Da sulfo-NHS-biotin leaked within all examined tumors, irrespective of their endothelial Wnt activation level. However, $Dkk1^+$ tumors exhibited slightly higher leakage values (Fig. 6C). To assess BBB repair to protein-sized tracers, we examined tumor and cortical vessels by electron microscopy after intravenous injection of 44-kDa horseradish peroxidase (HRP). In the healthy mouse cerebral cortices, HRP, revealed as an electron-dense 3,3′-diaminobenzidine reaction product, penetrated the intercellular spaces of adjacent ECs only over small distances. The signal sharply stopped at presumptive tight junctions (Fig. 6D, arrowheads), as reported previously (*34*). The electron density of the endothelial basement membranes was consequently much lower than the lumen. This spatially restricted distribution of HRP contrasted with almost all $Dkk1^+$ and most $Dkk1^-$/EGFP tumor vessels, in which the signal was observed along the entire length of the intercellular spaces. In these dysfunctional vessels, no difference was found between HRP levels within blood vessel lumens and their basement membranes. However, mice injected with AAV-K190A exhibited tumor vessels with a functional BBB phenotype. In line with the electron micrographs, claudin-5 immunostaining appeared denser in AAV-K190A tumor vessels (Fig. 6E). These findings are compatible with the hypothesis that AAV-K190A partially corrects the tight-junctional defects of glioblastoma vessels. On a cautionary note, however, we cannot formally exclude the possibility that the accumulation of HRP within the basement membranes and basolateral side of the inter-endothelial clefts results, at least in part, from HRP leaks associated with more distant hemorrhages.

The substantial intratumoral leak of HRP resulted in overall modest electron-dense contrast, making unambiguous scoring of transcytosis vesicles in glioblastoma vessels impractical. However, Mfsd2a, an endothelium-specific inhibitor of caveolae-mediated transcytosis (*34*), was increased by endothelial Wnt activation (Fig. 6F). Accordingly, caveolin-1 levels were lowered by AAV-K190A (fig. S21). The pericyte loss, typically associated with glioblastoma (*12*, *14*) and up-regulated transcytosis (*34*), could also be partially counteracted by AAV-K190A (Fig. 6G). Together, these findings show that in GL261 tumors, $Wnt7a^{K190A}$ restores endothelial Wnt signaling, reduces vascular density, and normalizes the BBB pleiotropically, thereby affecting both the transcellular and paracellular permeability routes and slowing tumor progression.

As proof of concept that the BBB-protective properties of the uncovered Gpr124/Reck agonists could have implications in CNS disorders of radically different etiology and BBB dysfunction kinetics, we turned to large-vessel and focal transient ischemic stroke models. After stroke, surgical or pharmacological recanalization therapies are crucial to promptly restore perfusion of the ischemic penumbra, a rim of cells whose survival will depend on the timing of recanalization. However, upon salutary blood flow restoration, reperfusion-associated tissue injury leads to BBB damage and contributes to worsening outcomes (*1*, *35*). To establish whether Gpr124/Reck-stimulated Wnt signaling at the BBB could mitigate the infarct size by limiting post-stroke injury, we subjected AAV-EGFP and AAV-K190A injected mice to transient middle cerebral artery occlusions (tMCAO). 2,3,5-Triphenyltetrazolium chloride (TTC) staining of whole-brain coronal sections revealed a significantly reduced infarct volume upon $Wnt7a^{K190A}$ expression (Fig. 6H). This reduction is consistent with previously reported effects of conditional endothelial β-catenin stabilization (*14*). A similar beneficial effect was observed in a transient focal endothelin-1 (ET-1) stroke model but not in a permanent photothrombotic (PT) stroke model (Fig. 6I); hence, we tentatively assign the protective effects of $Wnt7a^{K190A}$ to the post-stroke reperfusion process.

Discussion

Our study has revealed that Wnt7a ligands can be engineered into highly specific Gpr124/Reck agonists, thereby disclosing a novel class of BBB therapeutics. This level of specificity was deemed unreachable for Wnt-derived proteins by virtue of their promiscuous mode

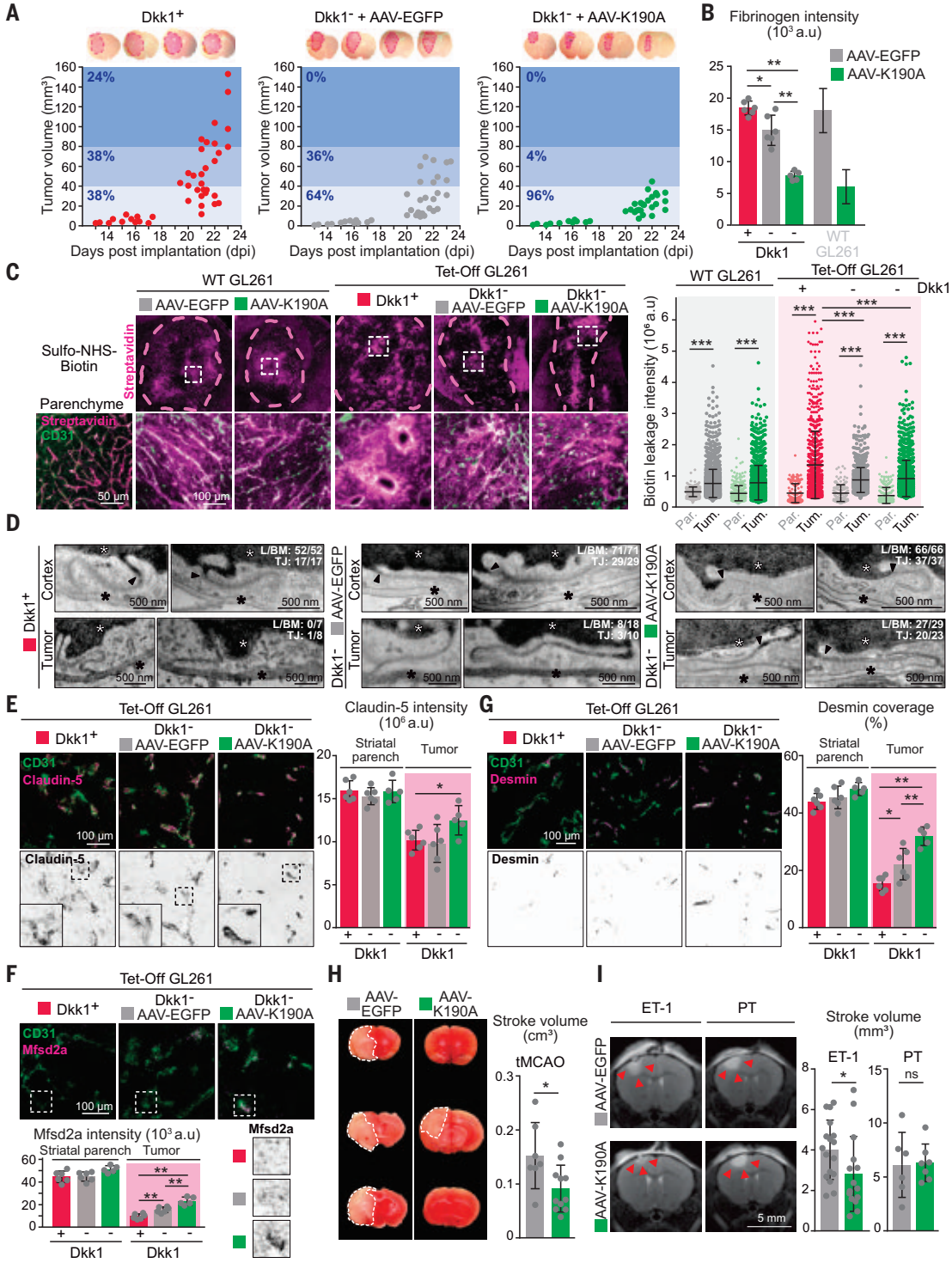

Fig. 6. Gpr124/Reck agonists as BBB repair agents in glioblastoma and stroke models. (**A**) MRI monitoring of tumor volumes after implantation of 1×10^5 Tet-Off Dkk1 GL261 cells, in the absence of doxycycline (Dkk1$^+$, –dox) or the presence of doxycycline (Dkk1$^-$, +dox). Doxycycline-exposed mice were injected intravenously with AAV-EGFP or AAV-K190A as indicated. (**B**) Quantification of fibrinogen leakage into the tumor. Data for WT GL261 are the same as in Fig. 5G. (**C**) Leakage of transcardially perfused sulfo-NHS-biotin within the tumor (Tum.) and the healthy parenchyma (Par.). The dashed lines highlight the tumor margin. (**D**) Electron micrographs of tumor and cortical sections of HRP-injected mice. White and black asterisks indicate tracer within the vessel lumen and vascular basement membrane, respectively. Proportions of vessels with high lumen–basement membrane HRP ratios (L/BM) and functional tight junctions (TJ) are indicated. Arrowheads label the tight junctions kissing points. (**E** to **G**) Coimmunostaining of CD31 together with claudin-5 (E), Mfsd2a (F), or desmin (G). (**H** and **I**) Infarct volumes of AAV-injected mice subjected to tMCAO [(H), TTC-stained sections, 24 hours after stroke], transient focal endothelin-1 stroke [(I), ET-1, MRI scans, 48 hours after stroke] or permanent bengal rose photothrombotic stroke [(I), PT, MRI scans, 48 hours after stroke]. Data are means ± SD. *P < 0.05, **P < 0.01, ***P < 0.001.

of interaction with the widely expressed Fz receptors.

In contrast to Wnt7a, the uncovered Gpr124/Reck agonists were well tolerated in vivo despite the broad expression strategies adopted in this study. In *Xenopus* and zebrafish, their ubiquitous expression during early development did not cause morphological alterations. In mice, CNS-wide expression of Gpr124/Reck agonists did not trigger ectopic Wnt activation or detectable adverse phenotypes. In addition to their strict signaling specificity, we suspect that homeostatic feedback loops maintain Wnt signaling within carefully controlled physiological activity windows. Accordingly, we detected increased endothelial Wnt signaling only in dysfunctional BBB vessels, leaving healthy parenchymal vessels unaffected.

Alternative strategies are being pursued to restore BBB function in disease, including those relying on protein C–mediated activation of endothelial PAR-1 signaling (*36*) or PDGF-C inhibition within the neurovascular unit (*37*). As a contrasting strategy to these

approaches, we here repurposed a key developmental BBB-inductive signal, acting at the top of the differentiation cascade that primes ECs for BBB development. As also reflected in this study, Wnt/β-catenin has been implicated in many aspects of BBB physiology. These include expression of tight junction proteins and solute transporters, suppression of vesicular transport, reduction of plasmalemma vesicle-associated protein (PLVAP) expression, and pericyte recruitment via control of PDGF-B secretion levels (*7*–*12*). Such a pleiotropic impact on BBB function seems well positioned to initiate a productive repair process. Despite this potential, Gpr124/Reck agonists are lipophilic, complicating their recombinant production at scale.

The therapeutic scope of Gpr124/Reck agonists is possibly large but remains to be functionally explored. Indeed, although the glioblastoma endothelium displays an aberrant Wnt expression profile (*14*), the post-stroke endothelium does not (*35*, *38*). Instead, multiple etiologically distinct disorders converge to a common diseased BBB transcriptomic signature reminiscent of peripheral endothelia (*38*). This observation suggests that reshaping the neurovascular niche by reinforcing the priming Gpr124/Reck-activating signal will likely have a broader impact than what can rationally be inferred from transcript profiling or biomarker analysis.

Our work defines a modality to treat CNS disorders by repairing the BBB. BBB-focused intervention strategies have potential as disease-modifying or secondary prevention agents in various pathologies beyond those explored in this study, including multiple sclerosis, epilepsy, and neurodegenerative disorders such as Alzheimer's disease.

Methods summary

Throughout this study, Wnt ligands and their variants were C-terminally tagged (V5 or P2A fusions). In cellular assays, ligands and co-receptor components were transiently expressed from CMV promoters. Firefly luciferase activities (derived from a genomic transgene in STF cells or ectopically expressed from the transfected M50 Super 8x TOPFlash plasmid) were normalized to Renilla luciferase activities (pTK-Renilla vector transfection). Immunodetection of extracellular and intracellular Wnt7a was performed using distinct antibodies (anti-Wnt7a and anti-V5) before and after cell permeabilization. Zebrafish and *Xenopus* were injected respectively at the 1-cell and 4-cell stage with in vitro transcribed V5-tagged Wnt7a mRNA or variants thereof. Transgenic endothelial expression in zebrafish was achieved using the Tol2 transposase system. In mice, Wnt7a or variants thereof were expressed using PHP.eB AAV particles and CAG promoters. AAVs were delivered retro-orbitally or by tail vein injections. The Dkk1 Tet-Off GL261 cells were cultured in media supplemented or not with doxycycline (1 μg/ml) for 5 days before implantation. To implant tumor cells, anesthetized mice were placed into a stereotactic device, and 2 μl of PBS containing 105 living GL261 cells were injected at 0.25 μl/min into the striatum. For Tet-Off–dependent experiments, mice were fed with control diet or diet containing doxycycline hyclate (1 g/kg) starting 2 weeks before the implantation. To evaluate BBB permeability, EZ-Link-Sulfo-NHS-Biotin was perfused intracardially and HRP was injected retro-orbitally. Electron microscopy was performed after DAB revelation of brain sections from HRP-injected mice. Transient MCAO was performed by a 1-hour occlusion of the right MCA using standardized monofilament 24 hours prior to tissue harvesting for TTC staining. PT stroke was induced by a 530-nm laser exposure of Rose Bengal–injected mice for 10 min. ET-1–induced stroke was achieved by a stereotaxic injection of 1 μl of 800 pmol ET-1 in the motor cortex. PT and ET-1 infarct volumes were monitored using magnetic resonance imaging 48 hours after stroke. Categorical phenotypic assessments were performed by researchers blind to the experimental conditions.

REFERENCES AND NOTES

1. B. Obermeier, R. Daneman, R. M. Ransohoff, Development, maintenance and disruption of the blood-brain barrier. *Nat. Med.* **19**, 1584–1596 (2013). doi: 10.1038/nm.3407; pmid: 24309662
2. B. W. Chow, C. Gu, The molecular constituents of the blood-brain barrier. *Trends Neurosci.* **38**, 598–608 (2015). doi: 10.1016/j.tins.2015.08.003; pmid: 26442694
3. Z. Zhao, A. R. Nelson, C. Betsholtz, B. V. Zlokovic, Establishment and Dysfunction of the Blood-Brain Barrier. *Cell* **163**, 1064–1078 (2015). doi: 10.1016/j.cell.2015.10.067; pmid: 26590417
4. M. D. Sweeney, Z. Zhao, A. Montagne, A. R. Nelson, B. V. Zlokovic, Blood-Brain Barrier: From Physiology to Disease and Back. *Physiol. Rev.* **99**, 21–78 (2019). doi: 10.1152/physrev.00050.2017; pmid: 30280653
5. C. P. Profaci, R. N. Munji, R. S. Pulido, R. Daneman, The blood-brain barrier in health and disease: Important unanswered questions. *J. Exp. Med.* **217**, e20190062 (2020). doi: 10.1084/jem.20190062; pmid: 32211826
6. U. Lendahl, P. Nilsson, C. Betsholtz, Emerging links between cerebrovascular and neurodegenerative diseases-a special role for pericytes. *EMBO Rep.* **20**, e48070 (2019). doi: 10.15252/embr.201948070; pmid: 31617312
7. S. Liebner *et al.*, Wnt/β-catenin signaling controls development of the blood-brain barrier. *J. Cell Biol.* **183**, 409–417 (2008). doi: 10.1083/jcb.200806024; pmid: 18955553
8. J. M. Stenman *et al.*, Canonical Wnt signaling regulates organ-specific assembly and differentiation of CNS vasculature. *Science* **322**, 1247–1250 (2008). doi: 10.1126/science.1164594; pmid: 19023080
9. R. Daneman *et al.*, Wnt/β-catenin signaling is required for CNS, but not non-CNS, angiogenesis. *Proc. Natl. Acad. Sci. U.S.A.* **106**, 641–646 (2009). doi: 10.1073/pnas.0805165106; pmid: 19129494
10. Y. Wang *et al.*, Norrin/Frizzled4 signaling in retinal vascular development and blood brain barrier plasticity. *Cell* **151**, 1332–1344 (2012). doi: 10.1016/j.cell.2012.10.042; pmid: 23217714
11. Y. Zhou *et al.*, Canonical WNT signaling components in vascular development and barrier formation. *J. Clin. Invest.* **124**, 3825–3846 (2014). doi: 10.1172/JCI76431; pmid: 25083995
12. M. Reis *et al.*, Endothelial Wnt/β-catenin signaling inhibits glioma angiogenesis and normalizes tumor blood vessels by inducing PDGF-B expression. *J. Exp. Med.* **209**, 1611–1627 (2012). doi: 10.1084/jem.20111580; pmid: 22908324
13. J. E. Lengfeld *et al.*, Endothelial Wnt/β-catenin signaling reduces immune cell infiltration in multiple sclerosis. *Proc. Natl. Acad. Sci. U.S.A.* **114**, E1168–E1177 (2017). doi: 10.1073/pnas.1609905114; pmid: 28137846
14. J. Chang *et al.*, Gpr124 is essential for blood-brain barrier integrity in central nervous system disease. *Nat. Med.* **23**, 450–460 (2017). doi: 10.1038/nm.4309; pmid: 28288111
15. C. Y. Janda, D. Waghray, A. M. Levin, C. Thomas, K. C. Garcia, Structural basis of Wnt recognition by Frizzled. *Science* **337**, 59–64 (2012). doi: 10.1126/science.1222879; pmid: 22653731
16. R. Nusse, H. Clevers, Wnt/β-Catenin Signaling, Disease, and Emerging Therapeutic Modalities. *Cell* **169**, 985–999 (2017). doi: 10.1016/j.cell.2017.05.016; pmid: 28575679
17. B. Vanhollebeke *et al.*, Tip cell-specific requirement for an atypical Gpr124- and Reck-dependent Wnt/β-catenin pathway during brain angiogenesis. *eLife* **4**, e06489 (2015). doi: 10.7554/eLife.06489; pmid: 26051822
18. C. Cho, P. M. Smallwood, J. Nathans, Reck and Gpr124 Are Essential Receptor Cofactors for Wnt7a/Wnt7b-Specific Signaling in Mammalian CNS Angiogenesis and Blood-Brain Barrier Regulation. *Neuron* **95**, 1056–1073.e5 (2017). doi: 10.1016/j.neuron.2017.07.031; pmid: 28803732
19. M. Eubelen *et al.*, A molecular mechanism for Wnt ligand-specific signaling. *Science* **361**, eaat1178 (2018). doi: 10.1126/science.aat1178; pmid: 30026314
20. M. Vallon *et al.*, A RECK-WNT7 Receptor-Ligand Interaction Enables Isoform-Specific Regulation of Wnt Bioavailability. *Cell Rep.* **25**, 339–349.e9 (2018). doi: 10.1016/j.celrep.2018.09.045; pmid: 30304675
21. C. Cho, Y. Wang, P. M. Smallwood, J. Williams, J. Nathans, Molecular determinants in Frizzled, Reck, and Wnt7a for ligand-specific signaling in neurovascular development. *eLife* **8**, e47300 (2019). doi: 10.7554/eLife.47300; pmid: 31225798
22. X. Zhang *et al.*, Tiki1 is required for head formation via Wnt cleavage-oxidation and inactivation. *Cell* **149**, 1565–1577 (2012). doi: 10.1016/j.cell.2012.04.039; pmid: 22726442
23. X. Zhang *et al.*, Notum is required for neural and head induction via Wnt deacylation, oxidation, and inactivation. *Dev. Cell* **32**, 719–730 (2015). doi: 10.1016/j.devcel.2015.014; pmid: 25771893
24. H. Li *et al.*, RECK in Neural Precursor Cells Plays a Critical Role in Mouse Forebrain Angiogenesis. *iScience* **19**, 559–571 (2019). doi: 10.1016/j.isci.2019.08.009; pmid: 31445376
25. S. Eisa-Beygi, G. Hatch, S. Noble, M. Ekker, T. W. Moon, The 3-hydroxy-3-methylglutaryl-CoA reductase (HMGCR) pathway regulates developmental cerebral-vascular stability via prenylation-dependent signalling pathway. *Dev. Biol.* **373**, 258–266 (2013). doi: 10.1016/j.ydbio.2012.11.024; pmid: 23206891
26. K. Y. Chan *et al.*, Engineered AAVs for efficient noninvasive gene delivery to the central and peripheral nervous systems. *Nat. Neurosci.* **20**, 1172–1179 (2017). doi: 10.1038/nn.4593; pmid: 28671695
27. N. A. Jessen, A. S. F. Munk, I. Lundgaard, M. Nedergaard, The Glymphatic System: A Beginner's Guide. *Neurochem. Res.* **40**, 2583–2599 (2015). doi: 10.1007/s11064-015-1581-6; pmid: 25947369
28. S. Maretto *et al.*, Mapping Wnt/β-catenin signaling during mouse development and in colorectal tumors. *Proc. Natl. Acad. Sci. U.S.A.* **100**, 3299–3304 (2003). doi: 10.1073/pnas.0434590100; pmid: 12626757
29. C. Liu, Y. Wang, P. M. Smallwood, J. Nathans, An essential role for Frizzled5 in neuronal survival in the parafascicular nucleus of the thalamus. *J. Neurosci.* **28**, 5641–5653 (2008). doi: 10.1523/JNEUROSCI.1056-08.2008; pmid: 18509025
30. M. Sahores, A. Gibb, P. C. Salinas, Frizzled-5, a receptor for the synaptic organizer Wnt7a, regulates activity-mediated synaptogenesis. *Development* **137**, 2215–2225 (2010). doi: 10.1242/dev.046722; pmid: 20530549
31. M. Corada *et al.*, Fine-Tuning of Sox17 and Canonical Wnt Coordinates the Permeability Properties of the Blood-Brain Barrier. *Circ. Res.* **124**, 511–525 (2019). doi: 10.1161/CIRCRESAHA.118.313316; pmid: 30591003
32. T. N. Phoenix *et al.*, Medulloblastoma Genotype Dictates Blood Brain Barrier Phenotype. *Cancer Cell* **29**, 508–522 (2016). doi: 10.1016/j.ccell.2016.03.002; pmid: 27050100
33. A. Griveau *et al.*, A Glial Signature and Wnt7 Signaling Regulate Glioma-Vascular Interactions and Tumor Microenvironment.

Cancer Cell **33**, 874–889.e7 (2018). doi: 10.1016/j.ccell.2018.03.020; pmid: 29681511
34. A. Ben-Zvi *et al*., Mfsd2a is critical for the formation and function of the blood-brain barrier. *Nature* **509**, 507–511 (2014). doi: 10.1038/nature13324; pmid: 24828040
35. R.-I. Kestner *et al*., Gene Expression Dynamics at the Neurovascular Unit During Early Regeneration After Cerebral Ischemia/Reperfusion Injury in Mice. *Front. Neurosci.* **14**, 280 (2020). doi: 10.3389/fnins.2020.00280; pmid: 32300291
36. J. H. Griffin, J. A. Fernández, P. D. Lyden, B. V. Zlokovic, Activated protein C promotes neuroprotection: Mechanisms and translation to the clinic. *Thromb. Res.* **141** (Suppl 2), S62–S64 (2016). doi: 10.1016/S0049-3848(16)30368-1; pmid: 27207428
37. S. A. Lewandowski, L. Fredriksson, D. A. Lawrence, U. Eriksson, Pharmacological targeting of the PDGF-CC signaling pathway for blood-brain barrier restoration in neurological disorders. *Pharmacol. Ther.* **167**, 108–119 (2016). doi: 10.1016/j.pharmthera.2016.07.016; pmid: 27524729
38. R. N. Munji *et al*., Profiling the mouse brain endothelial transcriptome in health and disease models reveals a core blood-brain barrier dysfunction module. *Nat. Neurosci.* **22**, 1892–1902 (2019). doi: 10.1038/s41593-019-0497-x; pmid: 31611708

ACKNOWLEDGMENTS

We thank C. Hénin, L. Conrard, E. Zindy, G. Oldenhove, M. Moser, F. Andris, M. I. Garcia, K. Somme, M. S. Jeffers, G. O. Cron, O. A. Stone, P. Gut, and D. Y. R. Stainier for their help, and D. L. Silver and V. Gradinaru for the anti-Mfsd2a antibodies and the PHP.eB construct (Addgene plasmid #103005), respectively. The summary page figure and the illustration of Fig. 4A were created with BioRender.com. **Funding:** M.E., and N.B. are FRIA fellows, A.D.G. is FNRS-L'Oreal fellow, and S.V. and P.C. are postdoctoral researchers of the FRS-FNRS. Work in the B.V. laboratory is supported by the FNRS (MIS F.4543.15), the Concerted Research Action, the Fondation ULB, the H2020 ITN "BtRAIN," the Queen Elisabeth Medical Foundation, the FRFS-WELBIO (CR-2017S-05R), and the ERC (CtrI-BBB 865176). Also supported by DFG grant LI 911/5-1, LI 911/7-1, the Excellence Cluster Cardio-Pulmonary Institute, the H2020 ITN "BtRAIN," the DZHK, and the LOEWE CePTER Epilepsy Research Center of the state Hesse (S.L. and K.D.) and by Heart and Stroke Foundation of Canada grant G-17-0018290, Canadian Institute of Health Research grant 388805, and New Frontiers Research Funds-Exploration grant NFRFE-2019-00641 (B.L.). A.d.K.d'E. is research director of FRS-FNRS, supported by FRS-FNRS and the Fondation Clerdent. The Center for Microscopy and Molecular Imaging is supported by the European Regional Development Fund and the Walloon Region. **Author contributions:** All authors performed research and/or analyzed data. All authors discussed results and edited the manuscript. M.M. and B.V. wrote the manuscript. B.V. supervised the study. **Competing interests:** The ULB (B.V.) has filed for patent protection for Gpr124/Reck-specific agonism. B.V. is a founder, shareholder, and consultant of NeuVasQ Biotechnologies. **Data and materials availability:** All data are available in the main text or the supplementary materials.

SUPPLEMENTARY MATERIALS

23 September 2021; accepted 14 December 2021
10.1126/science.abm4459

1848 SOCIETY
AAAS

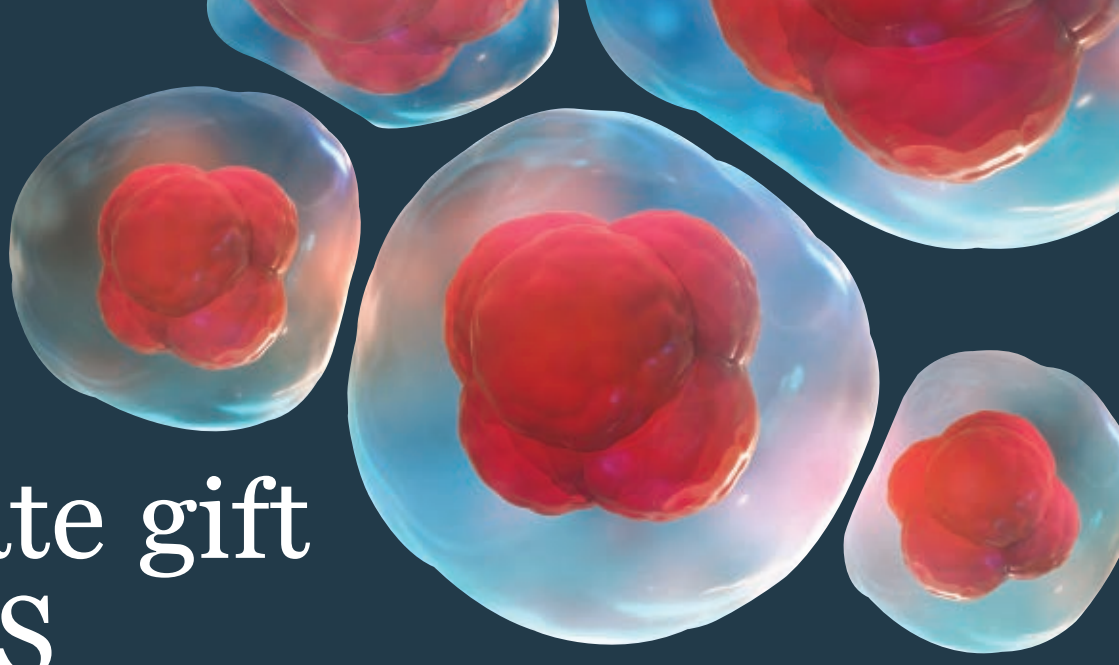

An estate gift to AAAS

Going all the way back to 1848, our founding year, the American Association for the Advancement of Science (AAAS) has been deeply committed to advancing science, engineering and innovation around the world for the benefit of all people.

Today, we are dedicated to advocating for science and scientific evidence to be fully and positively integrated into public policy and for the community to speak with one voice to advance science and engineering in the United States and around the world.

By making AAAS a beneficiary of your will, trust, retirement plan or life insurance policy, you will become a member of our 1848 Society and will help fuel our work on behalf of science and society – including publishing the world's most promising, innovative research in the *Science* family of journals and engaging in the issues that matter locally, nationally and around the world.

"As a teacher and instructor, I bear responsibility for the younger generations. If you have extra resources, concentrate them on organizations, like AAAS, that are doing work for all."

—Prof. Elisabeth Ervin-Blankenheim, 1848 Society member

If you intend to include AAAS in your estate plans, provide this information to your lawyer or financial adviser:

Legal Name: American Association for the Advancement of Science
Federal Tax ID Number: 53-0196568
Address: 1200 New York Avenue, NW, Washington, DC 20005

If you would like more information on making an estate gift to AAAS, cut out and return the form below or send an email to philanthropy@aaas.org. Additional details are also available online at **www.aaas.org/1848Society**.

AMERICAN ASSOCIATION FOR THE ADVANCEMENT OF SCIENCE

cut here

Yes, I would like more information about joining the AAAS 1848 Society.

1848 SOCIETY
AAAS

PLEASE CONTACT ME AT:

Name: _____

Address: _____

City: _____ State: _____ Zip code: _____ Country: _____

Email: _____ Phone: _____

RETURN THIS FORM TO:
AAAS Office of Philanthropy and Strategic Partnerships • 1200 New York Avenue, NW • Washington, DC 20005 USA

RESEARCH ARTICLE SUMMARY

STRUCTURAL BIOLOGY

Structures from intact myofibrils reveal mechanism of thin filament regulation through nebulin

Zhexin Wang†, Michael Grange†, Sabrina Pospich, Thorsten Wagner, Ay Lin Kho, Mathias Gautel, Stefan Raunser*

INTRODUCTION: Muscles underpin movement and heart function. Contraction and relaxation of muscles relies on the sliding between two types of filaments—the thin filament [made up of mainly filamentous actin (F-actin), tropomyosin, and troponin] and the thick myosin filament. Additionally, several other proteins are involved in the contraction mechanism, and their mutational malfunction can lead to debilitating and even life-threatening diseases. One such component in skeletal muscle, nebulin, binds to the thin filaments and stabilizes them. It is also responsible for maintaining the length of thin filaments and is involved in regulating myosin binding. Nebulin consists mainly of tandem repeats with different sequences but a conserved SDxxYK motif. Mutations in the nebulin gene are closely linked to a group of muscle diseases called nemaline myopathies.

RATIONALE: The mechanism underlying nebulin stabilization and the regulation of thin filaments remains nebulous because of missing structural information about the protein. It has been challenging to characterize isolated nebulin because of its enormous size and elongated and flexible nature. To investigate the structure of nebulin in its native environment, we prepared myofibrils from skeletal and cardiac muscle using focused ion beam milling and imaged them using cryo–electron tomography (cryo-ET). With subtomogram averaging, we obtained structures of cardiac and skeletal thin filaments. Because nebulin is only present in skeletal but not cardiac muscle, comparing the thin filament structures allowed us to unambiguously identify and characterize nebulin in the native muscle.

RESULTS: We resolved nebulin bound to the thin filament within myofibrils isolated from the mouse psoas muscle at near-atomic resolution. In skeletal muscle, two elongated nebulin molecules bind along one actin filament. The structure reveals a 1:1 binding stoichiometry between nebulin repeats and actin subunits. Each nebulin repeat consists of two helices separated by a kink and followed by a loop region. Different nebulin repeats located at different positions along the filament have the same physical length despite their slightly varying sizes, which supports the role of nebulin as a "molecular ruler." A nebulin repeat interacts with all three neighboring actin subunits though the SDxxYK motif and other conserved charged residues. This explains how nebulin stabilizes the thin filament. Additionally, the position of nebulin on the filament demonstrates that it does not interact with tropomyosin or myosin but likely with a troponin T (TnT) linker. Our reconstruction of myosin shows that the myosin double head exhibits inherent variability within a sarcomere and that nebulin does not alter actin-myosin interactions directly. Therefore, we propose that the myosin-binding regulatory role of nebulin is through its potential interactions with TnT. Nebulin is likely to interact with the TnT linker on two sites, which feature a WLKGIGW motif and a ExxK motif.

CONCLUSION: Our results show that nebulin is an integral component of the thin filament in skeletal muscle. The interactions between nebulin and other thin filament components set the molecular basis for its functions in thin filament stabilization, length control, and myosin-binding regulation. Our structure of nebulin enables the development of experimental models that further help to reveal how mutations responsible for nemaline myopathies affect nebulin's function in the sarcomere. The in situ structures of nebulin and myosin illustrated differences from in vitro characterizations and provided structural details relevant in a biology context. Our approach—using focused ion beam milling and cryo-ET to study the proteins of muscles at high resolution—paves the way for studying other muscle components in the future to understand muscle diseases at the molecular level. ■

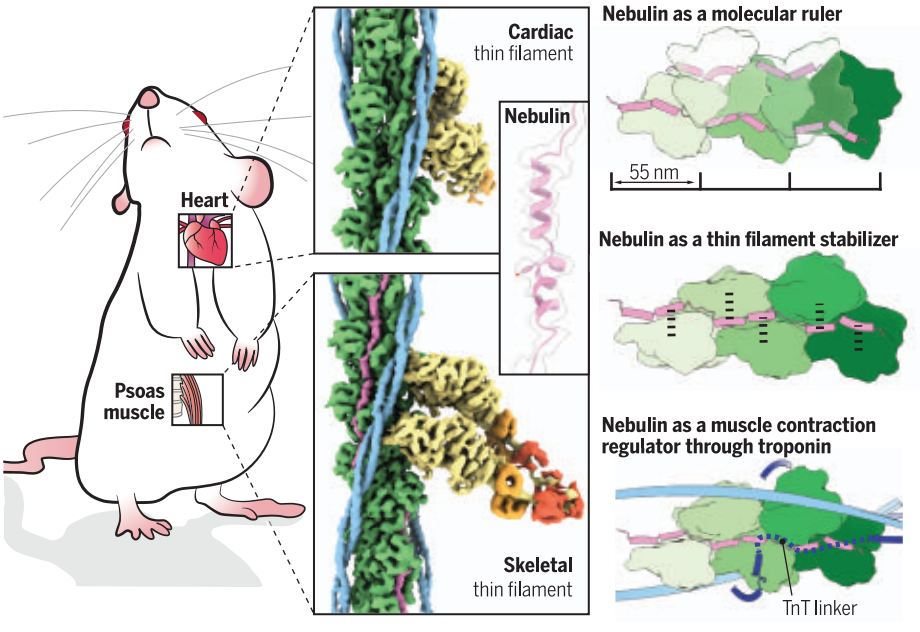

In situ structure of nebulin on the thin filament from mouse skeletal muscle. Nebulin, resolved at a resolution of 4.5 Å, was identified by comparing cardiac and skeletal thin filament structures. The structure of nebulin reveals the mechanism underlying its function to maintain the length and stability of the thin filament and to regulate muscle contraction. Actin, nebulin, tropomyosin, TnT, myosin heavy chain, myosin essential light chain, and myosin regulatory light chain are colored in green, magenta, light blue, dark blue, yellow, orange, and red, respectively.

The list of author affiliations is available in the full article online.
*Corresponding author. Email: stefan.raunser@mpi-dortmund.mpg.de
†These authors contributed equally to this work.
Cite this article as Z. Wang *et al.*, *Science* 375, eabn1934 (2022). DOI: 10.1126/science.abn1934

READ THE FULL ARTICLE AT
https://doi.org/10.1126/science.abn1934

RESEARCH ARTICLE

STRUCTURAL BIOLOGY

Structures from intact myofibrils reveal mechanism of thin filament regulation through nebulin

Zhexin Wang[1]†, Michael Grange[1]†‡, Sabrina Pospich[1], Thorsten Wagner[1], Ay Lin Kho[2], Mathias Gautel[2], Stefan Raunser[1]*

In skeletal muscle, nebulin stabilizes and regulates the length of thin filaments, but the underlying mechanism remains nebulous. In this work, we used cryo–electron tomography and subtomogram averaging to reveal structures of native nebulin bound to thin filaments within intact sarcomeres. This in situ reconstruction provided high-resolution details of the interaction between nebulin and actin, demonstrating the stabilizing role of nebulin. Myosin bound to the thin filaments exhibited different conformations of the neck domain, highlighting its inherent structural variability in muscle. Unexpectedly, nebulin did not interact with myosin or tropomyosin, but it did interact with a troponin T linker through two potential binding motifs on nebulin, explaining its regulatory role. Our structures support the role of nebulin as a thin filament "molecular ruler" and provide a molecular basis for studying nemaline myopathies.

Nebulin is a major structural protein of skeletal sarcomeres and is essential for proper assembly and contraction of skeletal muscle (*1*). A sarcomere is composed of thin filaments made up of mainly filamentous actin (F-actin), tropomyosin, and troponin- and myosin-containing thick filaments. Thin and thick filaments are organized into morphologically distinct zones. The Z-disc and M-band mark the boundary and center of a sarcomere, respectively. Proximal to the Z-disc is the I-band, which contains only thin filaments. Between the M-band and the I-band, myosin cross-bridges are formed between thin and thick filaments in the A-band (fig. S1A) (*2*). A single nebulin molecule (with a molecular weight of >700 kDa) has been proposed to bind along the entire thin filament from the Z-disc to near the M-band (*3*, *4*), maintaining the stability of thin filaments (*5*). Mutations in its encoding gene, *NEB*, are a major cause of a class of skeletal muscle disorders called nemaline myopathies that present with a range of pathological symptoms, such as hypotonia, muscle weakness, and, in some cases, respiratory failure leading to death (*6*–*8*). Despite the critical role of nebulin in skeletal muscle, nebulin is only minimally expressed in cardiac muscle (*9*), where instead nebulette, a short homolog of nebulin, is present but only close to the Z-disc. The absence of nebulin results in a broader range of thin filament lengths (*10*) in cardiomyocytes that possibly enables greater tunability of activation (*11*).

Nebulin primarily consists of 22 to 28 tandem super repeats. Each super repeat consists of seven simple repeats, each made up of 31 to 38 amino acid residues, featuring a conserved sequence motif SDxxYK (*12*, *13*). The N and C termini of nebulin associate with the capping proteins on the two ends of the thin filaments, tropomodulin (toward the M-band) (*14*) and CapZ (at the Z-disc) (*15*), respectively. Nebulin is thus hypothesized to regulate thin filament length as a molecular ruler, albeit with the exact mechanism still unknown (*5*, *16*–*19*). Genetic ablation of nebulin in mice is lethal and results in sarcomeres with loss of their length regulation (*20*, *21*).

It has been suggested that, based on the modular sequence of nebulin, each simple repeat would bind to one actin subunit, and every seventh repeat—i.e., a super repeat—would interact with the tropomyosin-troponin regulatory complex (*12*). However, structural details of these interactions and native nebulin are lacking. It therefore remains unclear how nebulin stabilizes or regulates thin filaments. The enormous size of nebulin combined with its elongated and flexible nature has prevented the use of in vitro reconstituted systems of nebulin and thin filaments that would resemble the native state in a sarcomere. Recombinant nebulin fragments bind to and bundle F-actin (*22*), which precludes a reconstitution approach for electron-microscopical structural biology. Here, we imaged nebulin directly inside mature mouse skeletal sarcomeres from isolated myofibrils using cryo–focused ion beam (cryo-FIB) milling and cryo–electron tomography (cryo-ET).

[1]Department of Structural Biochemistry, Max Planck Institute of Molecular Physiology, 44227 Dortmund, Germany.
[2]Randall Centre for Cell and Molecular Biophysics, School of Basic and Medical Biosciences, Kings College London BHF Centre of Research Excellence, Guy's Campus, London SE1 1UL, UK.
*Corresponding author. Email: stefan.raunser@mpi-dortmund.mpg.de
†These authors contributed equally to this work. ‡Present address: Structural Biology, The Rosalind Franklin Institute, Harwell Science and Innovation Campus, Didcot OX11 0FA, UK.

In situ position of nebulin on thin filaments

We determined the structure of the core of the thin filament from intact myofibrils isolated from the mouse psoas muscle to 4.5-Å resolution and with actomyosin resolved to 6.6-Å resolution (figs. S1 and S2). In the core of the thin filament, two extra continuous densities were visible alongside the actin filament (Fig. 1, A to C). The elongated structure predicted for nebulin (*23*) suggested that this density might be natively organized nebulin bound to the thin filament. To verify this putative identification, we determined the in situ actomyosin structure in the A-band from cardiac muscle (fig. S3, A and B). Nebulin is barely expressed and is only present in small subpopulations of myofibrils in cardiac muscle. The averaged reconstruction of the cardiac thin filament, determined to an overall resolution of 7.7 Å with the core of the thin filament resolved to 6.3 Å, depicts similar organizations of actin, myosin, and tropomyosin. Notably, the extra density observed in skeletal actomyosin was missing (Fig. 1E), consistent with this density corresponding to averaged segments of nebulin.

Nebulin was observed in the grooves between the two strands of the actin filament, in accordance with their helical turn (Fig. 1A). Nebulin occupies a site that is known to be bound by actin-stabilizing compounds, such as phalloidin and jasplakinolide (*24*) (fig. S4). This may explain why excessive phalloidin can unzip nebulin from thin filaments (*25*) and may also suggest a similar mechanism of F-actin stabilization. Like phalloidin, nebulin binding to F-actin did not alter the helical arrangement of F-actin or the conformation of the actin subunits (Fig. 2, A and B). A single actin filament was decorated by two nebulin molecules on the opposite sides (Fig. 1B). To ascertain the molecular organization of nebulin in different regions of a sarcomere, we also determined the structure of the thin filament in the skeletal muscle I-band to a resolution of 7.4 Å (fig. S3, C and D). Nebulin appeared in the I-band at the same position on the thin filament as was observed within the A-band (Fig. 1D), which indicates that nebulin spans most of the thin filament (*18*, *26*). This suggests that nebulin maintains a structural role within the sarcomere. Notably, the position of nebulin bound to actin from native skeletal muscle is different from the three putative sites previously proposed on the outer surface of the actin filament based on reconstituted actin-nebulin fragment complexes (*27*). The observed differences could represent the limitations of the use of in vitro fragments of nebulin or suggest different interaction patterns during sarcomerogenesis.

The position of nebulin implies that it does not interact with tropomyosin (Fig. 1B). The subdomains 3 and 4 (SD3 and SD4) of

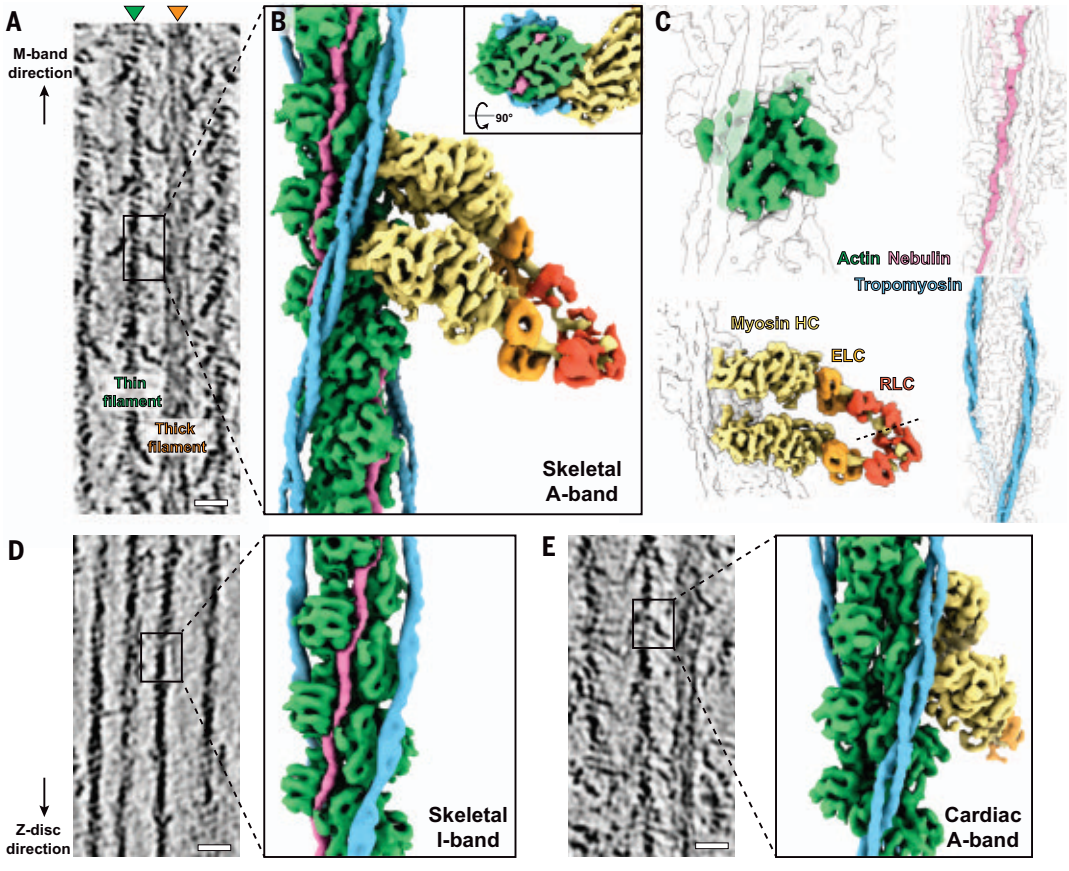

Fig. 1. Thin filament structures in striated muscle sarcomeres. (**A**) Tomographic slice of skeletal sarcomere A-band depicting adjacent thin and thick filaments. (**B**) Actomyosin structure from the skeletal sarcomere A-band consisting of actin (green), myosin [heavy chain (HC), yellow; essential light chain (ELC), orange; RLC, red], tropomyosin (blue), and nebulin (magenta). Myosin is a composite map including light chains from different averaged structures (see figs. S1 and S5). (Inset) Cross-sectional view of the structure. (**C**) Different components of a thin filament and their positions highlighted within the structure. The dotted line highlights the interface between the two RLCs of the trailing and leading myosin head. (**D**) Tomographic slice of a skeletal sarcomere I-band (left) and structure of the thin filament (right). (**E**) Tomographic slice of a cardiac sarcomere A-band (left) and structure of actomyosin, including a pair of myosin double heads (right). All tomographic slices are 7-nm thick. Scale bars, 20 nm.

adjacent actin monomers physically separate nebulin from tropomyosin, regardless of the tropomyosin state at different Ca^{2+} concentrations (*28*) (Fig. 2, C to F). This is contradictory to previous results from in vitro experiments (*29*). The discrepancy between our in situ structures and in vitro assays again demonstrates that nebulin may have different properties when purified compared with its properties in its native state in a sarcomere. Purified large fragments of nebulin are extremely insoluble when expressed (*22*, *30*, *31*). Both rotary-shadowed images of nebulin (*31*) and the structure of nebulin predicted by the machine learning–based software AlphaFold (*32*) suggest nonfilamentous structures. These visualizations clearly deviate from the elongated shape of nebulin when bound to actin filaments. Our approach of investigating nebulin inside sarcomeres therefore provides in situ structural information about nebulin interactions with the thin filament that are not accessible by sequence-based structure-prediction programs or from isolated proteins. Furthermore, during sarcomerogenesis, nebulin integration into the thin filament is likely to require cellular cofactors to prevent the formation of aggregates or large globular structures.

Myosin double head does not interact with nebulin and has high variability

Nebulin has been shown to regulate the actin-myosin cross-bridge cycle. It can increase thin filament activation, promote myosin binding, and thereby improve the efficiency of contraction (*33*–*35*). In vitro studies have suggested a direct interaction between a nebulin fragment and myosin (*36*, *37*). In our rigor-state sarcomere structures, two myosin heads from a single myosin molecule are bound to the thin filament in most cross-bridges, forming a double head. However, the myosin heads do not interact with nebulin (Fig. 1A), and nebulin does not alter the interactions between actin and myosin (fig. S5B).

Having a better-resolved structure available (~9 Å in the neck domain), we were able to accurately fit the lever arms and light chains of myosin based on their secondary structure elements (fig. S5, D to F), completing the model of the entire myosin double head (Fig. 3A and fig. S5). Notably, the angles of the kinks in the lever arm helix are different between the two heads (Fig. 3A). Especially, the kink between the two regulatory light chain (RLC) lobes differs considerably in the two heads, resulting in the clamp-like arrangement of the neck domains (Fig. 3B). The RLC-RLC interface resembles that of the RLCs of the free and blocked head in an interacting-head-motif (IHM) of an inactive myosin (*38*, *39*), but with a rotation of ~20° (Fig. 3C). Although the motor domains are similarly arranged in the cardiac muscle (fig. S6A), our 12-Å reconstruction of the neck domain clearly demonstrates that the interface between the two RLCs is different compared with the skeletal counterpart, resulting in a subtle difference in the arrangement of the two neck domains (fig. S6B). Thus, our structures of myosin in the on state in skeletal and cardiac muscles and previous structures of myosin in the off state (*38*, *39*) imply natural variabilities within RLCs and at the RLC-RLC interface that allow a dynamic cooperation between the two myosin heads.

We noticed that 18% of the skeletal double heads had a different conformation in which both neck domains are bent by ~20° perpendicular to the direction of the myosin power stroke (Fig. 3, D and E, and fig. S7A). This different structural arrangement increases the range within which myosin can bind to the thin filament by ~5 nm without interfering with force transmission during the power stroke (Fig. 3F). Thus, the bending contributes additional adaptability on top of that provided

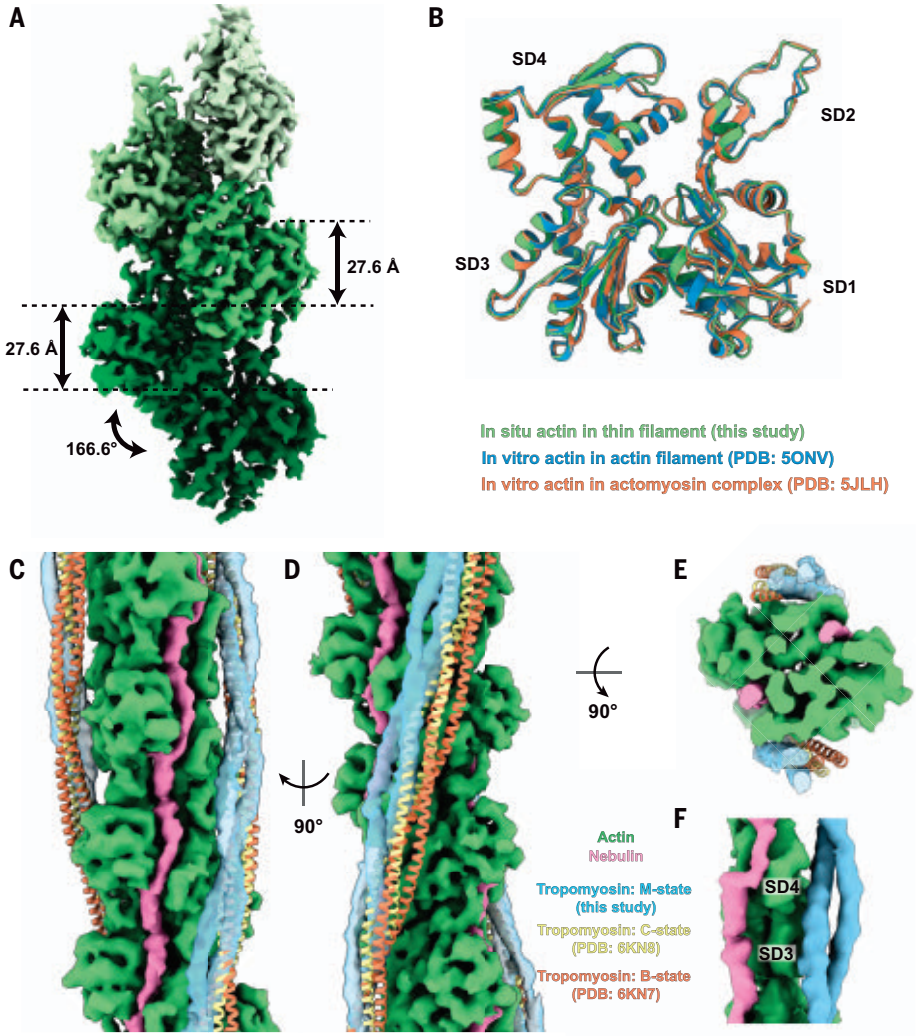

Fig. 2. Actin in a thin filament and different tropomyosin states on a thin filament. (**A**) Helical parameters of F-actin determined within a thin filament in a sarcomere. (**B**) Comparison of the structures of the actin subunit from different filamentous structures. (**C** to **E**) Different views depicting a thin filament, including nebulin and different states of tropomyosin. (**F**) Zoom-in view of nebulin, tropomyosin, and actin depicting the physical separation between nebulin and tropomyosin by the SD3 and SD4 of actin subunits.

by the flexibility of the S2 domain for cross-bridge formation between actin and myosin filaments (Fig. 3G). The myosin arm can thereby hold on tightly to a thin filament but, at the same time, have enough freedom to cooperate the mismatch between helical pitches of thick and thin filaments and account for local deformation of the sarcomere. In fact, the double heads with bent-neck domains are randomly distributed in the A-band of the sarcomere (fig. S7, B to D), ensuring efficient binding of myosin during contraction.

Nebulin structure and localization of residues

Although nebulin consists of repetitive simple repeats, each simple repeat has different sequences, with a few conserved charged residues and a putative actin-binding SDxxYK motif (Fig. 4, A and H, and fig. S8A). Owing to the nature of subtomogram averaging, the obtained electron microscopy (EM) density map of nebulin is an averaged density of all repeats in the A-band. Taking advantage of the 4.5-Å map, where bulky side chains are typically resolved (fig. S2), we were able to build an atomic model for actin and refine a polyalanine nebulin model into its density (table S1). Using a published convention (*12*), we defined the start of a simple repeat at two residues preceding a conserved aspartic acid, resulting in the SDxxYK motif residing at positions 18 to 23.

The model of nebulin consists of a repetitive structure of two α helices (H1 and H2), with a short kink of 46° in between, followed by a loop region spanning around SD1 of actin (Fig. 4, C to F). As validation, and to map the sequence to our structural model, we predicted the average secondary structure to highlight structured and unstructured regions from the sequences of nebulin simple repeats (fig. S8B and Materials and methods). The prediction implied that each nebulin simple repeat should form a long helix, with a drop in probability in the middle of this helix (Fig. 4G). By matching the predicted start of the helix in the sequence with the start of H1 in the structure, the predicted end of the helix matched the end of H2, and the dip in probability matched the position of the kink in our model (Fig. 4, F and G). Based on this registry, a noticeable bulky side-chain density aligned with position 22, corresponding to a fully conserved tyrosine residue. We attributed this density to the phenyl group of this tyrosine (Fig. 4F and fig. S2D). This observation further validates the sequence-structure mapping. As such, H1 starts at position 5, which is often occupied by a proline (Fig. 4, F to H). The SDxxYK motif, where the exon boundaries are, is located at the beginning of H2, among which the serine is positioned at the kink between H1 and H2. This registry allowed us to assign the location of other conserved residues and further investigate their roles in the interactions between nebulin and the thin filament.

Nebulin as a molecular ruler of the thin filament

A molecular ruler for the actin filament should coordinate two main functions: capping of the barbed and pointed end of the filament at a defined distance and being in close association with actin subunits along the filament length. Although the general concept of nebulin as a molecular ruler is supported by its size being proportional to the length of the thin filament in different muscle fibers (*16*, *40*), it has been speculated that the interaction of nebulin with the thin filament differs at the N and C termini (*14*, *15*). Because we averaged over all nebulin repeats, our study does not give insights into the ends of nebulin. However, the structures of the native thin filaments clearly depict a 1:1 stoichiometry between nebulin repeats and actin subunits in both the A-band and I-band (Fig. 1D and Fig. 4D). Furthermore, unlike previously suggested (*23*), the repeats are distinct structural units rather than part of a contiguous α helix. Thus, each nebulin repeat likely denotes the gradation of a ruler in measuring the number of actin subunits.

Although most nebulin simple repeats contain 35 amino acids (as is modeled above), some repeats can be as short as 31 amino acids or as long as 38 amino acids (fig. S8C). Different sizes of nebulin repeats typically correspond to different positions in a super repeat (Fig. 4B). The predicted secondary structure implies that, in the shorter repeats, the helix ends earlier than in an average-length repeat and, in the longer repeats, the loop is longer

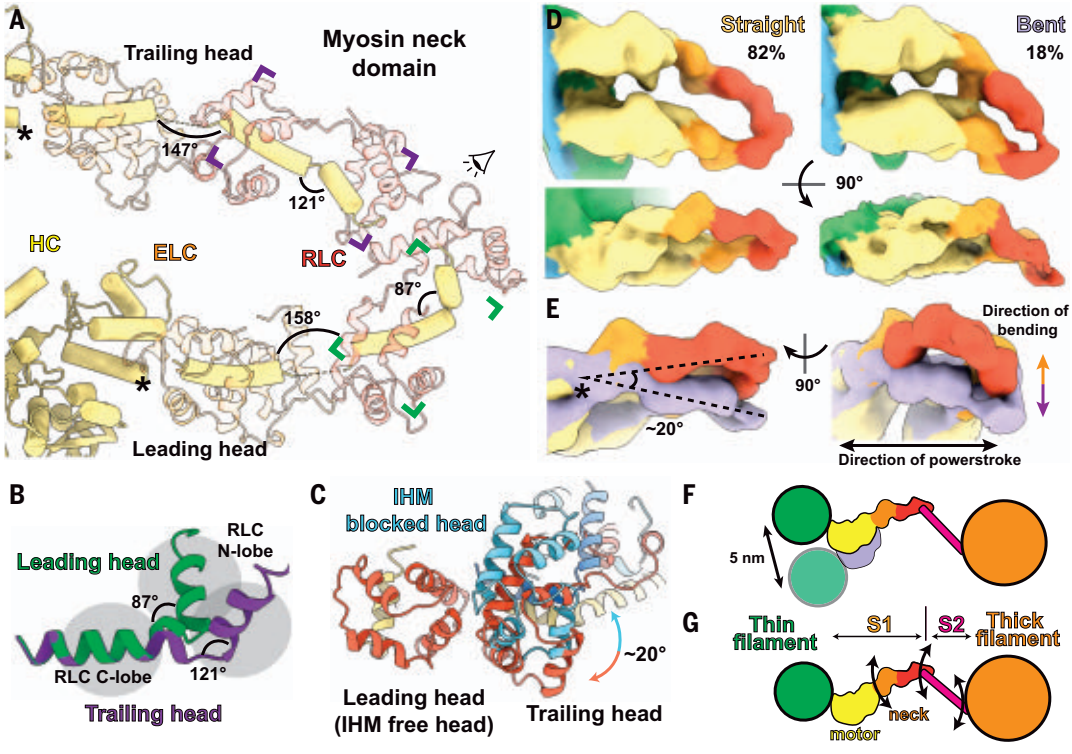

Fig. 3. Structural variability within the in situ myosin double head in skeletal muscle. (**A**) The lever arms of the trailing and leading myosin heads form kinked helices (yellow). Different angles at the kinks between the two heads are labeled. ELCs and RLCs are shown as transparent models. (**B**) Different conformations of the lever arm at the RLC-binding regions of the trailing head (purple) and the leading head (green). (**C**) View from the eye symbol in (A) showing the interface between the RLCs from the trailing and leading head (red for RLC, yellow for lever arm helices) compared with the interface of the blocked head (aligned to the leading head) and the free head in the IHM (blue for RLC, dark blue for lever arm helices). (**D**) Two different conformations, straight and bent forms, of myosin double heads determined by 3D classification. HC, ELC, and RLC regions are colored in yellow, orange, and red, respectively. (**E**) Comparison between the straight (orange) and bent (purple) double-head conformations. The origin of bending is marked by an asterisk, as also indicated in (A). (**F**) Schematic drawing describing the increased range of thin filament positions that can be bound by myosin heads because of the bending of the double heads. (**G**) Schematic drawing depicting the three flexible junctions in a myosin head.

(fig. S8D). Although we did not observe separate classes within our cryo-ET data for these repeats owing to their low abundancy, it is noticeable that the density corresponding to H2 and the first half of the loop has lower occupancy compared with that of H1 (fig. S8E). This suggests that in the shorter nebulin repeats, part of H2 is extruded into the loop along segments of actin to compensate for fewer amino acids, whereas in the longer nebulin repeats, the extra amino acids reside flexibly in the loop (fig. S8F). This ensures that in all regions of the sarcomere, nebulin repeats have the same physical length to span an actin subunit to maintain a 1:1 binding stoichiometry, which is one of the main functions of a molecular ruler.

Interactions between nebulin and the thin filament

On the basis of our model, we were able to show that the interactions between actin and nebulin are mediated by residues throughout one nebulin simple repeat and three adjacent actin subunits (Fig. 5A). In the SDxxYK motif, Y22 forms a potential cation-pi interaction with K68 on SD1 of one actin subunit (N) (Fig. 5C). S18 likely forms a hydrogen bond with E276 on SD3 of the laterally adjacent actin subunit on the other strand (N+1). D19 and K23 interact with residues on SD1 and SD2 of actin subunit N through electrostatic attractions. Additionally, other highly conserved charged residues outside the SDxxYK motif are also involved in the interactions between actin and nebulin. D3, K11, and K30 can form electrostatic interactions with SD1 of actin subunit N+2, SD4 of actin subunit N+1, and SD1 of actin subunit N, respectively (Fig. 5C). Every nebulin repeat interacts with all three neighboring actin subunits (Fig. 5A), which prevents them from depolymerizing and confers rigidity and mechanical stability to the thin filament.

An intramolecular interaction occurs between positions 15 and 21 on nebulin at the position of the kink between H1 and H2 (Fig. 5, A and B). Although both positions can accommodate either positively or negatively charged residues, they appear to be often complementary to each other among all repeat sequences (fig. S9, A to C). Their interaction is also supported by weak side-chain densities in our averaged reconstruction (fig. S9D). This intramolecular interaction stabilizes the kink conformation of the two helices, which is necessary for positioning charged residues near actin.

Nebulin simple repeats share a higher sequence similarity with the repeats that are six repeats apart, forming a seven-repeat super repeat pattern (Fig. 4B). This modular structure suggests an interaction with the troponin-tropomyosin regulatory complex, which also has a 1:7 stoichiometry ratio to actin. The physical separation of nebulin and tropomyosin by actin has ruled out their interaction. The core of troponin, including troponin C (TnC), troponin I (TnI), and most of troponin T (TnT), is also located away from nebulin (Fig. 6A). However, a linker region in TnT between R134 and R179 is likely to be the binding partner of nebulin (Fig. 6C). It was hypothesized to cross the groove between two actin strands (*41*). Although nebulin and this TnT linker could not be resolved in a structure of the thin filament containing troponin determined from our data (fig. S10), previous structures of troponin with actin reported from cardiac thin filaments (*42*, *43*) show that this TnT linker is localized close to the region where nebulin resides in our structure. Despite the lack of a structural model for the linker owing to its flexibility, superimposing previous EM densities for TnT with our structural model of actin and nebulin suggests the location of two contact sites between TnT and nebulin (Fig. 6, A and B). One site is located at the end of H2 (Fig. 6, A to C, site I). This site is consistent with the position of a WLKGIGW motif in nebulin, which has previously been proposed to be the tropomyosin-troponin binding motif at the

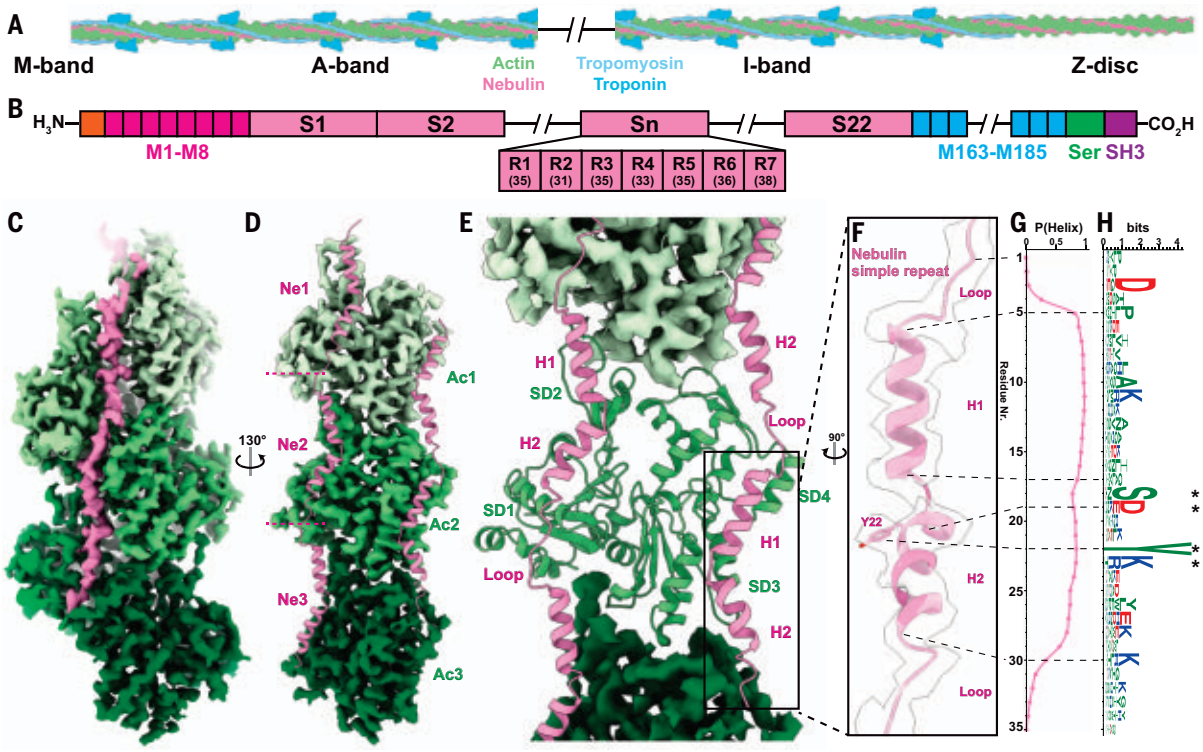

Fig. 4. Nebulin structure and its binding to the actin filament. (**A**) Schematic drawing of the nebulin-bound thin filament. (**B**) Modular organization of the primary sequence of nebulin demonstrating its super repeats and simple repeats. Nebulin contains an N-terminal sequence (orange), repeats 1 to 8 (M1 to M8; bright magenta), a super repeat region (magenta), repeats 163 to 185 (M163 to M185; blue), a serine-rich region (Ser; green), and a C-terminal Src homology-3 domain (SH3; purple). The number below each simple repeat indicates its most common size in number of amino acids. (**C**) Subtomogram-averaged structure of the actin filament in complex with nebulin (magenta) at a resolution of 4.5 Å. Different actin subunits are colored in different shades of green with darker green toward the barbed end. (**D**) Rotated view of (C) highlighting both nebulin (Ne) molecules (shown as structural models of three and two simple repeats) on the actin (Ac) filament. Only one strand of the actin filament is shown. Nebulin simple repeats are labeled on one strand to show 1:1 stoichiometry with actin subunits. (**E**) Structural model of one actin subunit and two nebulin molecules. One nebulin binds along actin subdomains 1 and 2 (SD1 and SD2), and the other binds along actin SD3 and SD4. The averaged cryo-ET map of the neighboring actin subunits is shown. (**F**) Zoom-in view of one nebulin simple repeat. The side chain of residue Y22 is highlighted. (**G**) Averaged predicted score for an α helix at each residue position of a simple repeat. (**H**) Graphical representation of sequence alignment of all simple repeats (M1 to M163). A larger amino acid symbol corresponds to a greater occurrence at a certain position. Positive, negative, and neutral residues are colored in blue, red, and green, respectively. Dotted lines map the sequence to the structural model in (F) and (G). Asterisks mark the conserved SDxxYK motif.

end of repeat 3 (*12*). The other site is located downstream of the first site at the start of H1, indicating another potential troponin-binding motif, ExxK, at the beginning of repeat 4 (Fig. 6, A to C, site II). The TnT linker region contains a hydrophobic C terminus and a highly charged N terminus matching the orientation of the two binding sites, which suggests that the WLKGIGW motif and the ExxK motif interact with TnT through hydrophobic and electrostatic interactions, respectively (Fig. 6D).

Although missense mutations have not been localized to this linker, TnT is the only troponin component where mutations can lead to nemaline myopathy (*7*). For example, Amish nemaline myopathy, a severe type, is caused by a *TNNT1* (slow muscle troponin) truncation (*44*), and a splicing variant of *TNNT3* (fast muscle troponin) can also lead to nemaline myopathy (*45*). This is in agreement with our proposed interactions between nebulin and TnT. On the basis of our observation that nebulin does not interact with myosin or tropomyosin, the role nebulin plays in regulating myosin binding is likely to be a downstream effect of its interaction with the TnT linker. This interaction in skeletal muscle may rigidify the linker and thereby help to maintain efficient calcium regulation and subsequent binding of myosin. It can also increase the cooperativity in calcium regulation across the two actin strands, which has been recently observed in cardiac muscle (*43*).

Human nebulin and insights into nemaline myopathy

Nebulin in mice shares >90% sequence similarity with human nebulin (*46*). Key residues involved in the interactions between nebulin and the thin filament are conserved among repeats of mouse and human nebulin (fig. S11). Our structural model of nebulin derived from mice is therefore also applicable to humans and enables the understanding of the mechanism underlying the pathogenicity caused by recessive mutations in the *NEB* gene, which is the major cause of nemaline myopathies (*7*). Nemaline myopathy mutations are usually compound heterozygous, in some cases with one truncating and one missense variant (*7*). Two missense *NEB* mutations, S6366→I (S6366I) and T7382P, have been identified as founder mutations in the Finnish population (*47*). The locations of the two sites on a simple repeat correspond to S18 and T14 (fig. S9E). A mutation of S18 into a hydrophobic isoleucine would disrupt its potential hydrogen bond with actin (Fig. 5C and fig. S9F). A mutation of T14 to proline, despite not being at a conserved residue position, can lead to the disruption of H1 helical secondary structure and thus alter the local conformation

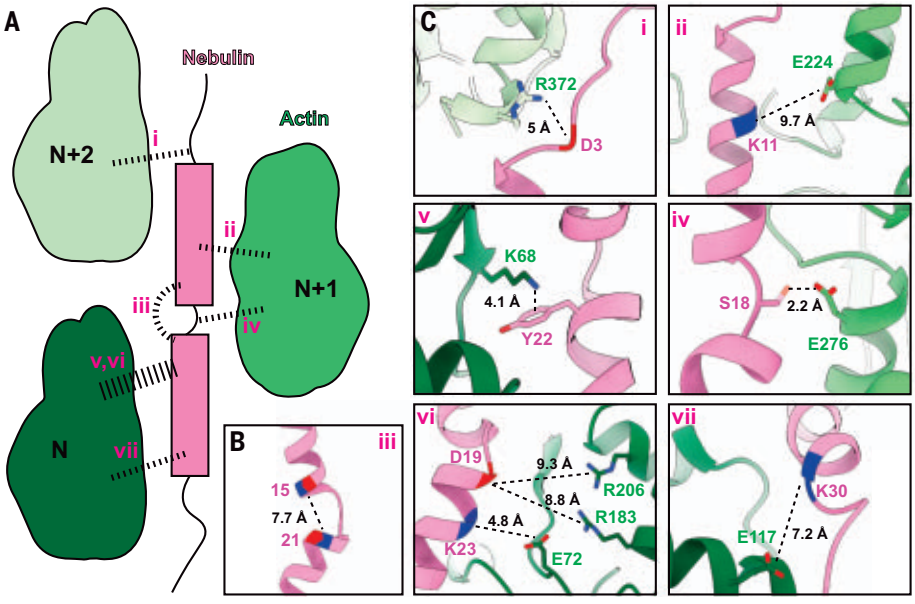

Fig. 5. Interactions between nebulin and actin. (**A**) Schematic depiction of interactions between nebulin (magenta) and three adjacent actin (green) subunits. Interactions are marked as dotted lines and labeled as i to vii. (**B**) Intranebulin interactions [iii in (A)] between residues with complementary charges at positions 15 and 21. (**C**) Details of interactions i, ii, and iv to vii in (A). Distances were measured between actin residues and the Cβ of the polyalanine model of nebulin where the side chain is not resolved. A potential side-chain conformation of S18 is shown for visualization, although it was not determined from the map. Single-letter abbreviations for the amino acid residues are as follows: A, Ala; C, Cys; D, Asp; E, Glu; F, Phe; G, Gly; H, His; I, Ile; K, Lys; L, Leu; M, Met; N, Asn; P, Pro; Q, Gln; R, Arg; S, Ser; T, Thr; V, Val; W, Trp; and Y, Tyr.

of nebulin and interfere with actin binding (fig. S9F).

Our structural model of actin and nebulin maps residues crucial to maintaining the interactions between nebulin and the thin filament. When also applied to clinical genetics, this information should help to determine additional pathogenic interfaces of nebulin variants. This is especially crucial when considering missense variants, where pathogenicity is often difficult to determine (*47*), and will thus aid the early diagnosis of nemaline myopathies and genetic counseling of variant carriers.

Conclusions

Our structural reconstruction of nebulin within a native skeletal sarcomere provides the basis of interaction between nebulin and thin filaments. Our structures determined across several tissue types and regions enable a comparative analysis of nebulin in its native context. This analysis reveals the mechanism underlying the roles nebulin plays in regulating thin filament length, as a thin filament stabilizer, and in regulating myosin binding through its interaction with TnT. Our approach using cryo-FIB milling and cryo-ET provides a high-resolution structural approach within an isolated tissue. Our findings highlight different conformations of myosin and illustrate similarities and differences from in vitro structures. Together with a recent study reporting the high-resolution structure of bacterial ribosomes (*48*), our structures showcase the full potential of in situ structural biology using cryo-ET. In the context of the sarcomere, where several flexible proteins—such as titin and myosin-binding protein-C—are present and still lack structural visualization, our approach is a general tool for structural analysis where other methods are limited. Determining the structure of these key players in the context of native sarcomeres will enable better modeling of skeletal muscle in the future, directly affecting the understanding of disease. The structure of nebulin presented here is one such case, where the molecular interactions described might help to establish a foundation for future developments of the treatment of nemaline myopathies.

Materials and methods

Myofibril isolation

Skeletal myofibrils were prepared from prestretched BALB/c mouse psoas muscle fiber bundles, as described previously (*2*).

Cardiac myofibrils were prepared from left ventricular strips prestretched overnight to a sarcomere length of ~2 μm in rigor buffer [20 mM HEPES pH 7, 140 mM KCl, 2 mM $MgCl_2$, 2 mM EGTA, 1 mM dithiothreitol (DTT), Roche complete protease inhibitor] at 4°C. Left ventricles were cut into ~1-mm pieces using scalpel blades and homogenized first in rigor buffer with complete protease inhibitors, then resuspended and homogenized three to four times in rigor buffer containing 1% (v/v) Triton X-100 essentially as described (*49*). Dissociation into myofibril bundles containing three to five myofibrils was monitored by microscopy. The concentration of myofibrils was adjusted with complete rigor buffer to ~5 mg ml^{-1}, using an extinction coefficient of myofibrils in 1% (w/v) warm SDS solution of ~0.7 ml $mg^{-1}cm^{-1}$. Both cardiac myofibrils and skeletal myofibrils were prepared from 3-month female BALB/c mice, and myofibrils from both tissues were prepared from the same animal for each biological replicate.

Vitrification of myofibrils and cryo-FIB milling

Myofibrils were frozen on grids by plunge-freezing using a Vitrobot. Generally, 2 μl of myofibril suspension was applied onto the glow-discharged carbon side of Quantifoil R 1.2/1.3 Cu 200 grids. After a 60-s incubation at 13°C, the grids were blotted from the opposite side of the carbon layer for 15 s before plunging into liquid ethane. For the dataset aimed at determining the I-band thin filament structure, myofibrils were frozen on Quantifoil R 1/4 Au 200 grids with SiO_2 film after a longer blotting time of 20 s. Frozen grids were clipped into cryo-FIB–specific AutoGrids with marks for grid orientation and a cut-out for low-angle FIB milling.

Clipped grids were transferred into an Aquilos cryo-FIB/scanning electron microscopy (SEM) dual-beam microscope (Thermo Fisher). Cryo-FIB milling was performed as previously described (*2*). Briefly, the grids were first sputter-coated with platinum and then coated with metalloorganic platinum through a gas-injection system. The myofibrils were thinned into lamellae in a four-step milling process with an ion beam of decreasing current from 0.5 μA to 50 nA. For the dataset of I-band thin filaments, AutoTEM (TEM, transmission electron microscopy) was used to automatically produce lamellae with thicknesses of 50 to 200 nm. During auto-milling, an anticontamination shield replacing the original shutter was inserted to minimize contamination from water deposition (*50*).

Cryo-ET data acquisition

Grids containing milled lamellae were transferred through a low-humidity glovebox (*50*), to avoid contamination, into a Titan Krios (Thermo Fisher) transmission electron microscope equipped with a K2 Summit or K3 camera (Gatan) and an energy filter. Projection images were acquired using SerialEM software (*51*). Overview images of myofibrils in lamellae were acquired at 6300× or 8400× nominal magnification to identify locations for high-magnification tilt series acquisition and serve as reference images for batch tomography data

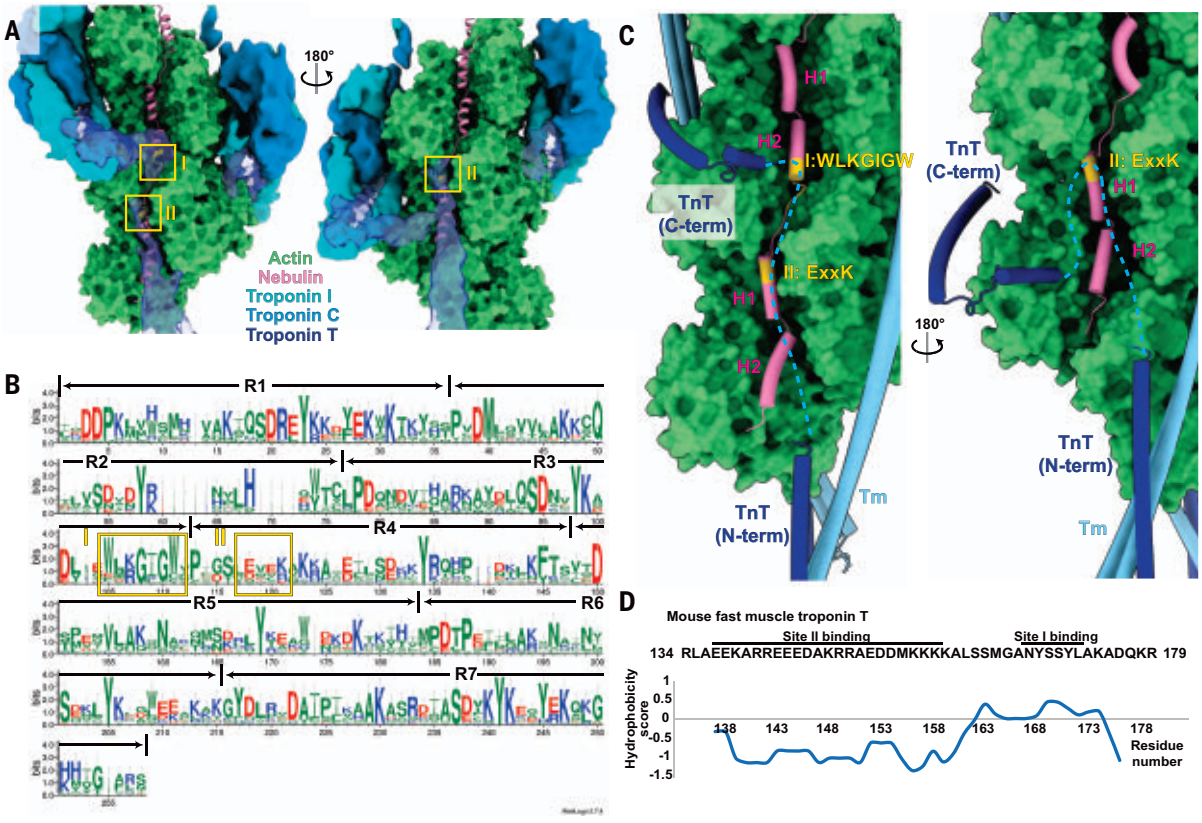

Fig. 6. Potential interactions between nebulin and TnT. (**A**) The actin-nebulin complex superimposed with the cryo–electron microscopy (cryo-EM) densities of the troponin complex (EMD-0729). Two contact sites between nebulin and TnT are marked in yellow as I and II. (**B**) Graphical representation of the sequence alignment of all nebulin super repeats (each super repeat contains the simple repeats R1 to R7). A larger amino acid symbol corresponds to a greater occurrence at a certain position. The troponin binding sites I and II are marked corresponding to the WLKGIGW and ExxK motifs, respectively. (**C**) Two different TnT models (dark blue) that bind to opposite sides of the actin filament (PDB: 6KN8) are shown. The linker region between R134 and R179 (corresponding to R151 and S198 in the original model) is missing in the structural model. Possible shapes of the TnT linkers are marked as cyan dotted lines based on weak EM densities (EMD-0729). Potential TnT binding sites on nebulin are highlighted in yellow. Tropomyosin (Tm) is shown in light blue. (**D**) Hydrophobicity of the linker in mouse fast muscle TnT (*TNNT3*). Potential regions that can bind to sites I and II are marked.

acquisition. Tilt series of the skeletal A-band dataset were acquired at 81,000× nominal magnification {pixel size, 1.73 Å; calibrated based on an averaged reconstruction and a crystal structure of myosin [Protein Data Bank (PDB) ID: 3I5G] (*52*)} with the K2 Summit camera. Tilt series of the cardiac A-band dataset and the skeletal I-band dataset were acquired with the K3 camera, at 42,000× (pixel size, 2.23Å) or 81,000× (pixel size, 1.18 Å) nominal magnification, respectively. A dose-symmetric tilting scheme (*53*) was used during acquisition with a tilt range of −54° to 54° relative to the lamella plane at 3° increments. A total dose of 130 to 150 $e^{-}/Å^{2}$ was applied to the sample.

Tomogram reconstruction and automatic filament picking

Individual tilt movies acquired from the microscope were motion corrected (*54*) and combined into stacks for a given tomogram with matched angles using a custom script for subsequent tomogram reconstruction. The combined stacks were then aligned, contrast transfer function (CTF) corrected through strip-based phase flipping, and reconstructed using IMOD (*55*). In total, three datasets were collected: skeletal (psoas) A-band (171 tomograms), cardiac A-band (24 tomograms), and skeletal I-band (115 tomograms). Tomograms containing the wrong field of view, incompletely vitrified ice, or lacking visible inherent sarcomere features as a result of the lamella being too thick (>150 nm) were discarded. Eventually, 48, 24, and 47 tomograms were selected from the skeletal A-band, cardiac A-band, and skeletal I-band datasets, respectively, for further processing.

Automated picking of the mouse psoas A-band

The picking of thin filaments within the mouse psoas A-band was performed as previously outlined (*2*). Briefly, tomograms were reoriented so that the thin and thick filaments of the sarcomere lay along the *Y* axis of the volume and such that XY slices contained the central section of the thin and thick filaments. After applying an equatorial filter as a Fourier mask, thin filaments were recognized and traced from the XZ slices by the TrackMate plugin (*56*) in Fiji (*57*, *58*). In total, 183,260 segments of the thin filaments (subtomograms) were picked from 48 tomograms with an intersegment distance of 62 Å. The distance was determined to accommodate two adjacent actin subunits on one strand for further averaging of myosin double head structure.

Automated picking of the mouse cardiac A-band

The picking of the mouse cardiac A-band thin filament used a similar approach as described above for skeletal A-band, with the following changes: After the rotation of the tomograms, from the XZ slices, positions of the thin filaments were determined using crYOLO (*59*) instead of TrackMate. Manual picking of thin filaments from 28 XZ slices from six tomograms were used for initial training in crYOLO. The positions for thin filament in all tomograms were then picked and traced by crYOLO. In total, 202,864 segments of the thin filaments were picked from 24 tomograms with an intersegment distance of 65 Å.

Automated picking of the mouse psoas I-band

The picking of the mouse psoas I-band was performed using the latest development version of crYOLO (1.8.0b33) to pick directly on XY slices without any prerotation of tomograms. Tomograms were reconstructed using the program Warp after alignment in IMOD, at a down-sampled scale of 8×. Thin filaments were manually picked on 21 XY slices from four tomograms. These picked positions were then used to train a model in crYOLO, which was used to pick all tomograms. The picked positions were then traced through different XY planes in three dimensions. In total, 84,937 segments of I-band thin filaments were picked from 47 tomograms with an intersegment distance of 38 Å.

Subtomogram averaging

Skeletal A-band thin filament

Subtomogram averaging of the skeletal A-band thin filaments first followed a previously published approach (*2*). Briefly, the determined positions for filaments within the tomograms were used to extract subtomograms in RELION (*60*) using a box size of 200 voxels (346 Å), which were then projected (central 100 slices) and sorted into good and bad particle classes through two-dimensional (2D) classification in ISAC (*61*). Good particles were then subjected to 3D refinement using a cylindrical reference in RELION, achieving a global resolution (0.143 criterion) of 8.8 Å.

To increase resolution, the particles were then subjected to further refinement in the program M (*62*). Tilt movies and image stacks were motion corrected and CTF-estimated within Warp (*63*) and new tomograms were reconstructed. The original particle position information obtained from the final step of refinement in RELION was then transformed to match the output geometry of tomograms from Warp. The new particles were extracted in Warp for subsequent averaging in RELION using a 2× down sampling. After 3D refinement in RELION, the structure of the thin filament was determined to 7.8 Å (fig. S1). The final half maps and alignment parameters were subjected to M for refinement. The strategy for refinement in M followed previously published regimens (*62*). After this refinement, the structure reached a global resolution of 6.7 Å. The core of the thin filament, including actin and nebulin, was masked and reached a resolution of 4.5 Å (figs. S1 and S2), which was used for model building of actin and nebulin.

Skeletal A-band actomyosin and myosin neck domain

To resolve the actomyosin structure, including thin filaments and a bound myosin double head, a 3D classification approach similar to the one previously published (*2*) was used. After the refinement in M, subtomograms were re-extracted and classified in RELION. Classes were translated and rotated to a common double-head configuration and re-refined in M. The final reconstruction at a resolution of 6.6 Å was used for model building of the myosin heavy chain. To increase the resolution of the myosin neck domains [predominantly the essential light chain (ELC) and RLC], the subtomograms were first recentered toward the ELC and re-refined in RELION with a mask containing only myosin. This resulted in an ELC-centered myosin double-head structure with a resolution of 8.9 Å (fig. S1). Afterward, the subtomograms were further recentered toward the RLC and re-refined with a smaller mask containing ELCs and RLCs to reconstruct a structure of RLC-centered myosin double head with a resolution of 9 Å. The ELC- and RLC-centered myosin double-head maps were used for rigid-body docking of the ELC and RLC models, respectively.

Cardiac A-band thin filament, actomyosin, and myosin neck domain

Subtomogram averaging of the cardiac A-band thin filament followed the same strategy as that for the A-band of skeletal muscle and resulted in a structure of thin filament resolved to a global resolution of 8 Å, with the core of the thin filament (actin) resolved to 6.3 Å (fig. S3, A and B). Structures of cardiac actomyosin and myosin neck domain were determined using the same classification and recentering approach as that used for for skeletal structures, resulting in resolutions of 7.7 and 12 Å, respectively.

Skeletal I-band thin filament

Subtomogram averaging of the skeletal I-band thin filament excluding troponin was performed largely as described for the A-band structures, except for using helical symmetry (twist −167.4°, rise 28.8 Å) during the initial refinement in RELION to reduce alignment error as a result of the missing wedge artifacts. The final structure of the I-band thin filament was determined to a global resolution of 9.4 Å, with the core (actin and nebulin) resolved to 7.4 Å (fig. S3, C and D). Subtomogram averaging of the thin filament including troponin was performed as previously described (*2*). A total of 2030 manually picked subtomograms were used for averaging using a cylinder-like reference generated from averaging all particles without alignment.

Model building of actin, nebulin, and myosin heavy chain

To reduce the risk of overrefinement and account for the heterogeneous resolution of our structures, several density maps—which were masked to different areas, filtered to nominal or local resolution as determined by SPHIRE (*64*), and sharpened using various B-factors—were used for model building. In addition, density modified maps were calculated from half maps providing the reported nominal resolution (*65*).

An initial model for actin was generated by homology modeling using Modeller (*66*) in Chimera based on a previous atomic model [PDB: 5JLH (*67*), chain A] and a sequence alignment from Clustal Ω. The unresolved N terminus of actin (amino acids 1 to 6) was removed and Mg^{2+}–adenosine 5′-diphosphate (ADP) was added from PDB 5LJH. HIS 73 was replaced by HIC (4-methyl-histidine) and regularized in Coot (*68*). A pentameric composite model was assembled by rigid-body fitting in Chimera including an initial model of nebulin (see below). Model building was performed in ISOLDE (*69*) in ChimeraX (*70*). A total of four density maps were loaded (filtered to nominal resolution and sharpened with B-factors −70 and −150, filtered to local resolution and sharpened to B-factor −100, and the density-modified map). Only the central actin chain and residues in close contact were included in the simulation and rebuilt. Unresolved side chains are in the most likely positions. After a first pass through the complete molecule, Ramachandran and rotamer issues were addressed locally. Based on the refined central chain, the composite actin-nebulin pentamer was updated. Hydrogens were removed, and the resulting model was real-space refined against the map filtered to nominal resolution in Phenix (*71*). To avoid large deviations from the input model, the ISOLDE model was used as a reference, while local grid search, rotamer, and Ramachandran restraints were deactivated. The actin model was further improved by a second round of model building in ISOLDE.

Modeling of nebulin was performed in analogy. An initial polyalanine model for nebulin was built manually in Coot based on the density of the central repeat (4.5-Å resolution). To cover the connection between two nebulin repeats, a peptide of 56 amino acids (instead of 35 amino acids) was initially built. The density corresponding to residue 22 was consistent with a consensus tyrosine residue, so tyrosine was used instead of alanine. A segmented postprocessed map (filtered to nominal resolution and sharpened with B-factor −70) was loaded for further modeling in ISOLDE. Secondary structure and rotamer restraints were applied where appropriate. Based on the resulting model, a continuous model of nebulin was created by first cutting the model to 35 amino acids and rigid-body fitting into the density. The termini of three consecutive nebulin chains were then manually connected. To address geometry issues caused by the connection, the combined nebulin chain was real-space refined in Phenix against the segmented

map and subjected to another round of refinement in ISOLDE.

Refined models of actin and nebulin were finally combined into one pentameric model. Minor adjustments to the orientation of side chains were done in Coot where necessary. The composite model was real-space refined against the 4.5-Å-resolution map filtered to local resolution (B-factor −100) in Phenix using the same settings as before.

An initial model of the actin-nebulin-tropomyosin-myosin (actomyosin) complex was assembled from the refined actin-nebulin model, a homology model of myosin (*52*) (PDB: 3I5G, chain A), and a polyalanine model of tropomyosin (*67*) (PDB: 5JLH, chains J and K) using rigid-body fitting. Only the heavy chain of myosin (up to residue 788) was modeled. After the addition of hydrogens, the central myosin chain was refined in ISOLDE using four segmented density maps of actomyosin, as described for actin. All applicable secondary structure restraints and many rotamer restraints were applied. Manual building was started from the acto-myosin interface, as it is best resolved. Unresolved residues including loop 1 (amino acids 207 to 215), loop 2 (626 to 643), and the N terminus (1 to 11) were removed. After deletion of hydrogens, the resulting atomic model was real-space refined in Phenix and further improved by a second round of refinement in ISOLDE. The refined atomic model of the central myosin chain was finally used to assemble an updated composite model of the actomyosin complex. This model was subjected to a final round of real-space refinement in Phenix against a 6.6-Å-resolution density map filtered to nominal resolution (B-factor −75) using the same settings as before, but with both Ramachandran and Rotamer restraints applied.

Because the resolution was not sufficient to reliably model Mg^{2+} ions, they were replaced with the ones from PDB 5JLH by superposition of actin subunits. The final atomic models of actin-nebulin and actomyosin complexes were assessed by Molprobity (*72*) and EMRinger (*73*) statistics (table S1).

Rigid-body docking of myosin light chains

Because the density for the C terminus of the myosin heavy chain lever arm as well as the ELC and RLC is of insufficient quality for reliable model building with refinement, rigid-body docking of previously published structural models (*52*) (PDB: 3I5G) was performed. First, the ELC model together with the ELC-binding lever arm helix (amino acids 785 to 802 in PDB 3I5G) were docked into both myosin ELC densities in the ELC-centered myosin double-head map (8.9 Å, B-factor −500) in Chimera. Then, the RLC model together with RLC-binding HC helices (amino acids 809 to 839) were docked into the RLC density of the leading myosin head in the RLC-centered myosin double-head map (9 Å, B-factor −300). For the RLC of the trailing head, the C-lobe of RLC (together with HC helix amino acids 809 to 824) and the N-lobe of RLC (together with HC helix amino acids 826 to 839) were docked separately into a segmented map of trailing myosin RLC (fig. S5). The maps of actomyosin, ELC-centered myosin double head, and RLC-centered myosin double head were aligned in Chimera to unify the coordinate system of all models. In the end, a final homology model was calculated on the basis of these initial models and the sequences of mouse myosin heavy chain and light chains from mouse fast muscles using SWISS-MODEL (*74*). To compare the difference of the RLC-RLC interface between active and inactive myosin, this model was compared with previous structures of myosin IHM (*38*) (PDB: 6XE9) through aligning the leading head RLC from our model to the free head RLC from IHM in Chimera.

Sequence analysis of nebulin and TnT

Because a defined boundary on the nebulin sequence between the A-band and I-band is not present, the nebulin sequence of M1 to M8 and the entire super repeat region (Fig. 4A) from a mouse (Uniprot: E9Q1W3) was considered as the A-band nebulin sequence and divided into 176 simple repeats (M1 to M162) through placing the SDxxYK motif at positions 18 to 23. Multiple sequence alignment was performed using ClustalW (*75*) with gaps disabled (fig. S8A) and visualized in WebLogo (*76*). Secondary structure of each simple repeat was predicted using RaptorX-Property (*77*). Probability values for there being an α helix at each residue position were averaged and used for Fig. 4 and fig. S8. To estimate relationship between the charge of the amino acid at position 15 and 21 a Bayesian multinominal regression was performed. For both positions and for each of the 176 sequences, the amino acid type was assigned a number, representing one of four categories: 1 (positive), 2 (negative), 3 (hydrophobic), or 4 (other). With this, the categorical variables $y_{i,j}^{15}$ and $y_{i,j}^{21}$ were constructed, representing the category i at positions 15 and 21 for sequence j, respectively. The hierarchical Bayesian model was then modeled in the following way and fitted with Stan (*78*)

$$\begin{aligned} a_i &\sim \text{normal}(0,1) \\ \beta_i &\sim \text{normal}(-0.3,1.5) \\ y_{i,j}^{21} &= \text{softmax}\left(\alpha_i + \sum_{k=1}^{4}\beta_k x_{i,j}^{15}\right) \\ p_{i,j}^{15} &= \text{cat}\left(y_{i,j}^{21}\right) \end{aligned}$$

Here, a_i is the intercept, β_i is the regression coefficients, and $p_{i,j}^{15}$ is the probability of seeing category i in sequence j. The variable $x_{i,j}^{15}$ is an indicator variable, which is 1 when sequence j at position 15 is of class i. The priors for a_i and β_i were chosen in a way so that the prior predictive distribution of $p_{i,j}^{15}$ has a mean probability for each class of 0.18. After fitting, 1000 samples were drawn from the posterior distribution for each possible state of category of amino acid 21 (fig. S9B).

TnT linker sequence was from mouse fast skeletal muscle TnT (UniProt: Q9QZ47-1) after sequence alignment with the sequence of the missing segment of TnT (R151 to S198) in PDB: 6KN8 (*34*). The hydrophobicity score (Fig. 6D) was calculated through ProtScale (*79*), using the scale from Abraham and Leo (*80*).

REFERENCES AND NOTES

1. M. Yuen, C. A. C. Ottenheijm, Nebulin: Big protein with big responsibilities. *J. Muscle Res. Cell Motil.* **41**, 103–124 (2020). doi: 10.1007/s10974-019-09565-3; pmid: 31982973
2. Z. Wang *et al.*, The molecular basis for sarcomere organization in vertebrate skeletal muscle. *Cell* **184**, 2135–2150.e13 (2021). doi: 10.1016/j.cell.2021.02.047; pmid: 33765442
3. K. Wang, C. L. Williamson, Identification of an N2 line protein of striated muscle. *Proc. Natl. Acad. Sci. U.S.A.* **77**, 3254–3258 (1980). doi: 10.1073/pnas.77.6.3254; pmid: 6997874
4. K. Wang, J. Wright, Architecture of the sarcomere matrix of skeletal muscle: Immunoelectron microscopic evidence that suggests a set of parallel inextensible nebulin filaments anchored at the Z line. *J. Cell Biol.* **107**, 2199–2212 (1988). doi: 10.1083/jcb.107.6.2199; pmid: 3058720
5. C. T. Pappas, P. A. Krieg, C. C. Gregorio, Nebulin regulates actin filament lengths by a stabilization mechanism. *J. Cell Biol.* **189**, 859–870 (2010). doi: 10.1083/jcb.201001043; pmid: 20498015
6. N. B. Romero, S. A. Sandaradura, N. F. Clarke, Recent advances in nemaline myopathy. *Curr. Opin. Neurol.* **26**, 519–526 (2013). doi: 10.1097/WCO.0b013e328364d681; pmid: 23995272
7. C. A. Sewry, J. M. Laitila, C. Wallgren-Pettersson, Nemaline myopathies: A current view. *J. Muscle Res. Cell Motil.* **40**, 111–126 (2019). doi: 10.1007/s10974-019-09519-9; pmid: 31228046
8. M. M. Ryan *et al.*, Nemaline myopathy: A clinical study of 143 cases. *Ann. Neurol.* **50**, 312–320 (2001). doi: 10.1002/ana.1080; pmid: 11558787
9. C. L. Moncman, K. Wang, Nebulette: A 107 kD nebulin-like protein in cardiac muscle. *Cell Motil. Cytoskeleton* **32**, 205–225 (1995). doi: 10.1002/cm.970320305; pmid: 8581976
10. T. Burgoyne, F. Muhamad, P. K. Luther, Visualization of cardiac muscle thin filaments and measurement of their lengths by electron tomography. *Cardiovasc. Res.* **77**, 707–712 (2008). doi: 10.1093/cvr/cvm117; pmid: 18178575
11. J. Kolb *et al.*, Thin filament length in the cardiac sarcomere varies with sarcomere length but is independent of titin and nebulin. *J. Mol. Cell. Cardiol.* **97**, 286–294 (2016). doi: 10.1016/j.yjmcc.2016.04.013; pmid: 27139341
12. S. Labeit, B. Kolmerer, The complete primary structure of human nebulin and its correlation to muscle structure. *J. Mol. Biol.* **248**, 308–315 (1995). doi: 10.1016/S0022-2836(95)80052-2; pmid: 7739042
13. K. Donner, M. Sandbacka, V. L. Lehtokari, C. Wallgren-Pettersson, K. Pelin, Complete genomic structure of the human nebulin gene and identification of alternatively spliced transcripts. *Eur. J. Hum. Genet.* **12**, 744–751 (2004). doi: 10.1038/sj.ejhg.5201242; pmid: 15266303
14. A. S. McElhinny, B. Kolmerer, V. M. Fowler, S. Labeit, C. C. Gregorio, The N-terminal end of nebulin interacts with tropomodulin at the pointed ends of the thin filaments. *J. Biol. Chem.* **276**, 583–592 (2001). doi: 10.1074/jbc.M005693200; pmid: 11016930
15. C. T. Pappas, N. Bhattacharya, J. A. Cooper, C. C. Gregorio, Nebulin interacts with CapZ and regulates thin filament architecture within the Z-disc. *Mol. Biol. Cell* **19**, 1837–1847 (2008). doi: 10.1091/mbc.e07-07-0690; pmid: 18272787
16. S. Labeit *et al.*, Evidence that nebulin is a protein-ruler in muscle thin filaments. *FEBS Lett.* **282**, 313–316 (1991). doi: 10.1016/0014-5793(91)80503-U; pmid: 2037050
17. D. S. Gokhin *et al.*, Thin-filament length correlates with fiber type in human skeletal muscle. *Am. J. Physiol. Cell Physiol.*

302, C555–C565 (2012). doi: 10.1152/ajpcell.00299.2011; pmid: 22075691
18. B. Kiss *et al*., Nebulin and Lmod2 are critical for specifying thin-filament length in skeletal muscle. *Sci. Adv.* **6**, eabc1992 (2020). doi: 10.1126/sciadv.abc1992; pmid: 33177085
19. V. M. Fowler, C. R. McKeown, R. S. Fischer, Nebulin: Does it measure up as a ruler? *Curr. Biol.* **16**, R18–R20 (2006). doi: 10.1016/j.cub.2005.12.003; pmid: 16401411
20. C. C. Witt *et al*., Nebulin regulates thin filament length, contractility, and Z-disk structure *in vivo*. *EMBO J.* **25**, 3843–3855 (2006). doi: 10.1038/sj.emboj.7601242; pmid: 16902413
21. M. L. Bang *et al*., Nebulin-deficient mice exhibit shorter thin filament lengths and reduced contractile function in skeletal muscle. *J. Cell Biol.* **173**, 905–916 (2006). doi: 10.1083/jcb.200603119; pmid: 16769824
22. S. M. Gonsior, M. Gautel, H. Hinssen, A six-module human nebulin fragment bundles actin filaments and induces actin polymerization. *J. Muscle Res. Cell Motil.* **19**, 225–235 (1998). doi: 10.1023/A:1005372915268; pmid: 9583363
23. M. Pfuhl, S. J. Winder, A. Pastore, Nebulin, a helical actin binding protein. *EMBO J.* **13**, 1782–1789 (1994). doi: 10.1002/j.1460-2075.1994.tb06446.x; pmid: 8168478
24. S. Pospich, F. Merino, S. Raunser, Structural Effects and Functional Implications of Phalloidin and Jasplakinolide Binding to Actin Filaments. *Structure* **28**, 437–449.e5 (2020). doi: 10.1016/j.str.2020.01.014; pmid: 32084355
25. X. Ao, S. S. Lehrer, Phalloidin unzips nebulin from thin filaments in skeletal myofibrils. *J. Cell Sci.* **108**, 3397–3403 (1995). doi: 10.1242/jcs.108.11.3397; pmid: 8586652
26. A. Castillo, R. Nowak, K. P. Littlefield, V. M. Fowler, R. S. Littlefield, A nebulin ruler does not dictate thin filament lengths. *Biophys. J.* **96**, 1856–1865 (2009). doi: 10.1016/j.bpj.2008.10.053; pmid: 19254544
27. N. Lukoyanova *et al*., Each actin subunit has three nebulin binding sites: Implications for steric blocking. *Curr. Biol.* **12**, 383–388 (2002). doi: 10.1016/S0960-9822(02)00678-4; pmid: 11882289
28. K. J. V. Poole *et al*., A comparison of muscle thin filament models obtained from electron microscopy reconstructions and low-angle X-ray fibre diagrams from non-overlap muscle. *J. Struct. Biol.* **155**, 273–284 (2006). doi: 10.1016/j.jsb.2006.02.020; pmid: 16793285
29. M. Marttila *et al*., Nebulin interactions with actin and tropomyosin are altered by disease-causing mutations. *Skelet. Muscle* **4**, 15 (2014). doi: 10.1186/2044-5040-4-15; pmid: 25110572
30. J. Q. Zhang, A. Weisberg, R. Horowits, Expression and purification of large nebulin fragments and their interaction with actin. *Biophys. J.* **74**, 349–359 (1998). doi: 10.1016/S0006-3495(98)77792-6; pmid: 9449335
31. R. Chitose *et al*., Isolation of nebulin from rabbit skeletal muscle and its interaction with actin. *J. Biomed. Biotechnol.* **2010**, 108495 (2010). doi: 10.1155/2010/108495; pmid: 20467585
32. J. Jumper *et al*., Highly accurate protein structure prediction with AlphaFold. *Nature* **596**, 583–589 (2021). doi: 10.1038/s41586-021-03819-2; pmid: 34265844
33. M.-L. Bang *et al*., Nebulin plays a direct role in promoting strong actin-myosin interactions. *FASEB J.* **23**, 4117–4125 (2009). doi: 10.1096/fj.09-137729; pmid: 19679637
34. M. Chandra *et al*., Nebulin alters cross-bridge cycling kinetics and increases thin filament activation: A novel mechanism for increasing tension and reducing tension cost. *J. Biol. Chem.* **284**, 30889–30896 (2009). doi: 10.1074/jbc.M109.049718; pmid: 19736309
35. B. Kiss *et al*., Nebulin stiffens the thin filament and augments cross-bridge interaction in skeletal muscle. *Proc. Natl. Acad. Sci. U.S.A.* **115**, 10369–10374 (2018). doi: 10.1073/pnas.1804726115; pmid: 30249654
36. J. P. Jin, K. Wang, Cloning, expression, and protein interaction of human nebulin fragments composed of varying numbers of sequence modules. *J. Biol. Chem.* **266**, 21215–21223 (1991). doi: 10.1016/S0021-9258(18)54843-2; pmid: 1682316
37. D. D. Root, K. Wang, Calmodulin-sensitive interaction of human nebulin fragments with actin and myosin. *Biochemistry* **33**, 12581–12591 (1994). doi: 10.1021/bi00208a008; pmid: 7918483
38. S. Yang *et al*., Cryo-EM structure of the inhibited (10S) form of myosin II. *Nature* **588**, 521–525 (2020). doi: 10.1038/s41586-020-3007-0; pmid: 33268893
39. C. A. Scarff *et al*., Structure of the shutdown state of myosin-2. *Nature* **588**, 515–520 (2020). doi: 10.1038/s41586-020-2990-5; pmid: 33268888
40. M. Kruger, J. Wright, K. Wang, Nebulin as a length regulator of thin filaments of vertebrate skeletal muscles: Correlation of thin filament length, nebulin size, and epitope profile. *J. Cell Biol.* **115**, 97–107 (1991). doi: 10.1083/jcb.115.1.97; pmid: 1717482
41. E. P. Manning, J. C. Tardiff, S. D. Schwartz, A model of calcium activation of the cardiac thin filament. *Biochemistry* **50**, 7405–7413 (2011). doi: 10.1021/bi200506k; pmid: 21797264
42. Y. Yamada, K. Namba, T. Fujii, Cardiac muscle thin filament structures reveal calcium regulatory mechanism. *Nat. Commun.* **11**, 153 (2020). doi: 10.1038/s41467-019-14008-1; pmid: 31919429
43. C. M. Risi *et al*., The structure of the native cardiac thin filament at systolic Ca^{2+} levels. *Proc. Natl. Acad. Sci. U.S.A.* **118**, e2024288118 (2021). doi: 10.1073/pnas.2024288118; pmid: 33753506
44. J. J. Johnston *et al*., A novel nemaline myopathy in the Amish caused by a mutation in troponin T1. *Am. J. Hum. Genet.* **67**, 814–821 (2000). doi: 10.1086/303089; pmid: 10952871
45. S. A. Sandaradura *et al*., Nemaline myopathy and distal arthrogryposis associated with an autosomal recessive *TNNT3* splice variant. *Hum. Mutat.* **39**, 383–388 (2018). doi: 10.1002/humu.23385; pmid: 29266598
46. S. T. Kazmierski *et al*., The complete mouse nebulin gene sequence and the identification of cardiac nebulin. *J. Mol. Biol.* **328**, 835–846 (2003). doi: 10.1016/S0022-2836(03)00348-6; pmid: 12729758
47. V. L. Lehtokari *et al*., Mutation update: The spectra of nebulin variants and associated myopathies. *Hum. Mutat.* **35**, 1418–1426 (2014). doi: 10.1002/humu.22693; pmid: 25205138
48. F. J. O'Reilly *et al*., In-cell architecture of an actively transcribing-translating expressome. *Science* **369**, 554–557 (2020). doi: 10.1126/science.abb3758; pmid: 32732422
49. R. J. Solaro, D. C. Pang, F. N. Briggs, The purification of cardiac myofibrils with Triton X-100. *Biochim. Biophys. Acta Bioenerg.* **245**, 259–262 (1971). doi: 10.1016/0005-2728(71)90033-8; pmid: 4332100
50. S. Tacke *et al*., A streamlined workflow for automated cryo focused ion beam milling. *J. Struct. Biol.* **213**, 107743 (2021). doi: 10.1016/j.jsb.2021.107743; pmid: 33971286
51. D. N. Mastronarde, Automated electron microscope tomography using robust prediction of specimen movements. *J. Struct. Biol.* **152**, 36–51 (2005). doi: 10.1016/j.jsb.2005.07.007; pmid: 16182563
52. Y. Yang *et al*., Rigor-like structures from muscle myosins reveal key mechanical elements in the transduction pathways of this allosteric motor. *Structure* **15**, 553–564 (2007). doi: 10.1016/j.str.2007.03.010; pmid: 17502101
53. W. J. H. Hagen, W. Wan, J. A. G. Briggs, Implementation of a cryo-electron tomography tilt-scheme optimized for high resolution subtomogram averaging. *J. Struct. Biol.* **197**, 191–198 (2017). doi: 10.1016/j.jsb.2016.06.007; pmid: 27313000
54. S. Q. Zheng *et al*., MotionCor2: Anisotropic correction of beam-induced motion for improved cryo-electron microscopy. *Nat. Methods* **14**, 331–332 (2017). doi: 10.1038/nmeth.4193; pmid: 28250466
55. J. R. Kremer, D. N. Mastronarde, J. R. McIntosh, Computer visualization of three-dimensional image data using IMOD. *J. Struct. Biol.* **116**, 71–76 (1996). doi: 10.1006/jsbi.1996.0013; pmid: 8742726
56. J. Y. Tinevez *et al*., TrackMate: An open and extensible platform for single-particle tracking. *Methods* **115**, 80–90 (2017). doi: 10.1016/j.ymeth.2016.09.016; pmid: 27713081
57. J. Schindelin *et al*., Fiji: An open-source platform for biological-image analysis. *Nat. Methods* **9**, 676–682 (2012). doi: 10.1038/nmeth.2019; pmid: 22743772
58. C. A. Schneider, W. S. Rasband, K. W. Eliceiri, NIH Image to ImageJ: 25 years of image analysis. *Nat. Methods* **9**, 671–675 (2012). doi: 10.1038/nmeth.2089; pmid: 22930834
59. T. Wagner *et al*., SPHIRE-crYOLO is a fast and accurate fully automated particle picker for cryo-EM. *Commun. Biol.* **2**, 218 (2019). doi: 10.1038/s42003-019-0437-z; pmid: 31240256
60. T. A. M. Bharat, S. H. W. Scheres, Resolving macromolecular structures from electron cryo-tomography data using subtomogram averaging in RELION. *Nat. Protoc.* **11**, 2054–2065 (2016). doi: 10.1038/nprot.2016.124; pmid: 27685097
61. Z. Yang, J. Fang, J. Chittuluru, F. J. Asturias, P. A. Penczek, Iterative stable alignment and clustering of 2D transmission electron microscope images. *Structure* **20**, 237–247 (2012). doi: 10.1016/j.str.2011.12.007; pmid: 22325773
62. D. Tegunov, L. Xue, C. Dienemann, P. Cramer, J. Mahamid, Multi-particle cryo-EM refinement with M visualizes ribosome-antibiotic complex at 3.5 Å in cells. *Nat. Methods* **18**, 186–193 (2021). doi: 10.1038/s41592-020-01054-7; pmid: 33542511
63. D. Tegunov, P. Cramer, Real-time cryo-electron microscopy data preprocessing with Warp. *Nat. Methods* **16**, 1146–1152 (2019). doi: 10.1038/s41592-019-0580-y; pmid: 31591575
64. T. Moriya *et al*., High-resolution single particle analysis from electron cryo-microscopy images using SPHIRE. *J. Vis. Exp.* **123**, e55448 (2017). doi: 10.3791/55448; pmid: 28570515
65. T. C. Terwilliger, S. J. Ludtke, R. J. Read, P. D. Adams, P. V. Afonine, Improvement of cryo-EM maps by density modification. *Nat. Methods* **17**, 923–927 (2020). doi: 10.1038/s41592-020-0914-9; pmid: 32807957
66. N. Eswar, D. Eramian, B. Webb, M.-Y. Shen, A. Sali, in *Structural Proteomics: High-Throughput Methods*, B. Kobe, M. Guss, T. Huber, Eds., vol. 426 of *Methods in Molecular Biology* (Humana Press, 2008), pp. 145–159. doi: 10.1007/978-1-60327-058-8_8
67. J. von der Ecken, S. M. Heissler, S. Pathan-Chhatbar, D. J. Manstein, S. Raunser, Cryo-EM structure of a human cytoplasmic actomyosin complex at near-atomic resolution. *Nature* **534**, 724–728 (2016). doi: 10.1038/nature18295; pmid: 27324845
68. P. Emsley, B. Lohkamp, W. G. Scott, K. Cowtan, Features and development of *Coot*. *Acta Cryst.* **D66**, 486–501 (2010). doi: 10.1107/S0907444910007493; pmid: 20383002
69. T. I. Croll, *ISOLDE*: A physically realistic environment for model building into low-resolution electron-density maps. *Acta Cryst.* **D74**, 519–530 (2018). doi: 10.1107/S2059798318002425; pmid: 29872003
70. T. D. Goddard *et al*., UCSF ChimeraX: Meeting modern challenges in visualization and analysis. *Protein Sci.* **27**, 14–25 (2018). doi: 10.1002/pro.3235; pmid: 28710774
71. P. V. Afonine *et al*., New tools for the analysis and validation of cryo-EM maps and atomic models. *Acta Cryst.* **D74**, 814–840 (2018). doi: 10.1107/S2059798318009324; pmid: 30198894
72. V. B. Chen *et al*., *MolProbity*: All-atom structure validation for macromolecular crystallography. *Acta Cryst.* **D66**, 12–21 (2010). doi: 10.1107/S0907444909042073; pmid: 20057044
73. B. A. Barad *et al*., EMRinger: Side chain–directed model and map validation for 3D cryo-electron microscopy. *Nat. Methods* **12**, 943–946 (2015). doi: 10.1038/nmeth.3541; pmid: 26280328
74. A. Waterhouse *et al*., SWISS-MODEL: Homology modelling of protein structures and complexes. *Nucleic Acids Res.* **46**, W296–W303 (2018). doi: 10.1093/nar/gky427; pmid: 29788355
75. M. A. Larkin *et al*., Clustal W and Clustal X version 2.0. *Bioinformatics* **23**, 2947–2948 (2007). doi: 10.1093/bioinformatics/btm404; pmid: 17846036
76. G. E. Crooks, G. Hon, J. M. Chandonia, S. E. Brenner, WebLogo: A sequence logo generator. *Genome Res.* **14**, 1188–1190 (2004). doi: 10.1101/gr.849004; pmid: 15173120
77. S. Wang, W. Li, S. Liu, J. Xu, RaptorX-Property: A web server for protein structure property prediction. *Nucleic Acids Res.* **44**, W430–W435 (2016). doi: 10.1093/nar/gkw306; pmid: 27112573
78. Stan Development Team, Stan Modeling Language Users Guide and Reference Manual, version 2.27 (2019); https://mc-stan.org.
79. E. Gasteiger, C. Hoogland, A. Gattiker, S. Duvaud, M. R. Wilkins, R. D. Appel, A. Bairoch, in *The Proteomics Protocols Handbook*, J. M. Walker, Ed. (Humana Press, 2005), pp. 571–607. doi: 10.1385/1-59259-890-0:571
80. D. J. Abraham, A. J. Leo, Extension of the fragment method to calculate amino acid zwitterion and side chain partition coefficients. *Proteins* **2**, 130–152 (1987). doi: 10.1002/prot.340020207; pmid: 3447171

ACKNOWLEDGMENTS

We thank S. Tacke for hardware optimization for cryo-FIB milling. We are grateful to O. Hofnagel and D. Prumbaum for EM support and B. Brandmeier for technical support. We thank S. Biswas for support in manual particle selection. **Funding:** This work was supported by funds from the Max Planck Society (to S.R.), the Wellcome Trust (Collaborative Award in Sciences 201543/Z/16/Z to S.R. and M.Ga.), the European Research Council under the European Union's Horizon 2020 Programme (ERC-2019-SyG, grant no. 856118 to S.R. and M.Ga.), and the Medical Research Council (MR/R003106/1 to M.Ga. and A.L.K.). M.Gr. was supported by an EMBO Long-Term Fellowship. M.Ga. holds the BHF Chair of Molecular Cardiology. **Author contributions:** S.R. designed and supervised the project. A.L.K. and M.Ga. developed methods and isolated mouse myofibrils. Z.W. performed cryo-FIB milling and collected cryo-ET data. M.Gr. optimized cryo-ET data acquisition. Z.W. and M.Gr. performed subtomogram averaging.

T.W. implemented automatic filament picking and tools for data conversion and statistical analysis. S.P. built atomic models for actin, nebulin, and myosin motor domain. Z.W. performed rigid-body fitting of myosin neck domain models. Z.W. prepared figures with the assistance of M.Gr. Z.W., M.Gr., M.Ga., and S.R. wrote the manuscript. All authors reviewed the results and commented on the manuscript. **Competing interests:** The authors declare no competing interests. **Data and materials availability:** Cryo-ET structures are deposited in the Electron Microscopy Data Bank under accession numbers EMD-13990 (skeletal A-band actin-nebulin), EMD-13991 (skeletal actomyosin), EMD-13992 (skeletal ELC-centered myosin), EMD-13993 (skeletal RLC-centered myosin), EMD-13994 (skeletal I-band actin-nebulin), EMD-13995 (cardiac actin), EMD-13996 (cardiac actomyosin), and EMD-13997 (cardiac myosin neck domain). Representative tomograms are deposited under accession numbers EMD-13998 (skeletal A-band), EMD-13999 (skeletal I-band), and EMD-14000 (cardiac A-band). The atomic models are deposited in the Protein Data Bank under accession numbers 7QIM (skeletal actin-nebulin), 7QIN (skeletal actomyosin), and 7QIO (skeletal myosin neck domain). Other structures and EM density maps used in this study are available under PDB 3I5G, 6KN8, and 6XE9 and EMD-0729.

SUPPLEMENTARY MATERIALS

science.org/doi/10.1126/science.abn1934
Figs. S1 to S11
Table S1
MDAR Reproducibility Checklist
Movies S1 to S4

9 November 2021; accepted 12 January 2022
10.1126/science.abn1934

Your Legacy to Science

AN ESTATE GIFT TO THE
AMERICAN ASSOCIATION FOR THE ADVANCEMENT OF SCIENCE



Since 1848, our founding year, the American Association for the Advancement of Science (AAAS) has been deeply committed to advancing science, engineering and innovation around the world for the benefit of all people.

By making AAAS a beneficiary of your will, trust, retirement plan or life insurance policy, you become a member of our 1848 Society, joining Thomas Edison, Alexander Graham Bell and the many distinguished individuals whose vision led to the creation of AAAS and our world-renowned journal, *Science*, so many years ago.

Unlike many of its peers, *Science* is not for-profit. Your estate gift would provide long-term financial stability and durable annual income that will support operations and competitive innovation for years to come. **This support is vital.**

"As a teacher and instructor, I bear responsibility for the younger generations. If you have extra resources, concentrate them on organizations, like AAAS, that are doing work for all."

—Prof. Elisabeth Ervin-Blankenheim, 1848 Society member

If you intend to include AAAS in your estate plans, provide this information to your lawyer or financial adviser:

Legal Name: American Association for the Advancement of Science
Federal Tax ID Number: 53-0196568
Address: 1200 New York Avenue, NW, Washington, DC 20005

If you would like more information on making an estate gift to AAAS, cut out and return the form below or send an email to philanthropy@aaas.org. Additional details are also available online at **www.aaas.org/1848Society**.

1848 SOCIETY
AAAS

cut here

Yes, I would like more information about joining the AAAS 1848 Society.

PLEASE CONTACT ME AT:

Name: _____

Address: _____

City: _____ State: _____ Zip code: _____ Country: _____

Email: _____ Phone: _____

RETURN THIS FORM TO:
AAAS Office of Philanthropy and Strategic Partnerships • 1200 New York Avenue, NW • Washington, DC 20005 USA

RESEARCH ARTICLES

BATTERIES

Self-assembled monolayers direct a LiF-rich interphase toward long-life lithium metal batteries

Yujing Liu[1]†, Xinyong Tao[1]*†, Yao Wang[1]†, Chi Jiang[1], Cong Ma[1], Ouwei Sheng[1], Gongxun Lu[1], Xiong Wen (David) Lou[2]*

High–energy density lithium (Li) metal batteries (LMBs) are promising for energy storage applications but suffer from uncontrollable electrolyte degradation and the consequently formed unstable solid-electrolyte interphase (SEI). In this study, we designed self-assembled monolayers (SAMs) with high-density and long-range–ordered polar carboxyl groups linked to an aluminum oxide–coated separator to provide strong dipole moments, thus offering excess electrons to accelerate the degradation dynamics of carbon-fluorine bond cleavage in Li bis(trifluoromethanesulfonyl)imide. Hence, an SEI with enriched lithium fluoride (LiF) nanocrystals is generated, facilitating rapid Li^+ transfer and suppressing dendritic Li growth. In particular, the SAMs endow the full cells with substantially enhanced cyclability under high cathode loading, limited Li excess, and lean electrolyte conditions. As such, our work extends the long-established SAMs technology into a platform to control electrolyte degradation and SEI formation toward LMBs with ultralong life spans.

Lithium (Li) metal is designated as a promising anode material for next-generation Li-based batteries because of its high specific capacity (3860 mA·hour g^{-1}) and low redox potential (−3.04 V versus the standard hydrogen electrode) (*1*, *2*). However, the practical application of Li anodes is limited by dendritic Li growth (*3*, *4*), leading to safety concerns and fast capacity fading of Li metal batteries (LMBs) (*5*, *6*). Among the efforts to inhibit the formation of Li dendrites, modification or rebuilding of the solid-electrolyte interphase (SEI) might be the most crucial (*7*, *8*) because the SEI, which is spontaneously derived from the reaction between chemically active Li metal and the electrolyte, is responsible for Li^+ transport and mechanical accommodation of rapid Li growth (*9*, *10*). Functional fluorinated electrolyte constituents—such as Li bis(trifluoromethanesulfonyl)imide (LiTFSI) (*11*), Li bis(fluorosulfonyl)imide (*12*), 1,2-difluorobenzene (*13*), and fluoroethylene carbonate (*14*)—have been designed to perform interface engineering to regulate the nanostructure and chemical composition of the SEI. The developed SEIs generated by these strategies are all proven to involve the specific constituent of lithium fluoride (LiF), which has high interfacial energy, high chemical stability, and a low Li^+ diffusion barrier (*15*, *16*). Generally, LiF is believed to be the decomposition product of F-containing electrolyte ingredients and contributes to boosting the cycle life of LMBs. Therefore, precisely controlling the electrolyte decomposition, particularly the C–F dissociation chemistry, to construct a LiF-rich SEI is a logically viable but still challenging method.

To regulate the electrolyte degradation process, it is desirable to seek a strategy to implement control of the redox state of the electrolyte, focusing on the electronic properties of the anode interface related to the loss or gain of electrons. As a reference, polar groups (e.g., the carboxyl group) can promote the cleavage of fluorinated bonds by changing the kinetics of electron transfer (*17*). Thus, how the degradation kinetics of fluorinated constituents transform when these disordered and dispersed functional groups become ordered and close-packed is of interest. Self-assembled monolayers (SAMs) have been extensively studied to construct surfaces with highly oriented molecules and ordered terminal groups and thus provide a convenient, flexible, and universal platform through which to tailor the interfacial properties of metals, metal oxides, and semiconductors (*18*, *19*). As a specific feature, long-range–ordered SAMs can regulate or even determine the distribution of surface dipoles relative to the molecular electronic structure and the orientation of terminal groups (*20*–*22*). Thus, the SAM-induced dipole moment may influence the kinetics of electron transfer and change the electrochemical redox dynamics of electrolytes to regulate the nanostructure of the SEI. As such, SAMs can possibly control the decomposition of fluorinated ingredients contained in electrolytes through ordering of the terminal groups that determine the surface electronic properties.

[1]College of Materials Science and Engineering, Zhejiang University of Technology, Hangzhou 310014, People's Republic of China. [2]School of Chemical and Biomedical Engineering, Nanyang Technological University, 62 Nanyang Drive, Singapore 637459, Singapore.
*Corresponding author. Email: tao@zjut.edu.cn (X.T.); xwlou@ntu.edu.sg (X.W.L.)
†These authors contributed equally to this work.

In this study, we fabricated SAMs onto an aluminum oxide (Al_2O_3)–coated polypropylene separator [Al_2O_3-$OOC(CH_2)_2X$] and employed various terminal functional groups (X = NH_2, COOH) to guide the smooth deposition of Li metal. The simulation predicts that ordered polar groups, particularly the carboxyl group, expedite the decomposition of C–F bonds involving the excess electrons induced by surface dipoles (Fig. 1A). The proposed mechanism is supported by atomic visualization and spectral interpretation, in which many LiF nanocrystals are identified in the SEI. Through the generation of a LiF-rich SEI, half cells and full cells both exhibit greatly improved cycling stability.

SAM fabrication and structural examination

An organic molecule [$NH_2(CH_2)_2COOH$ or $HOOC(CH_2)_2COOH$] with a consistent chain length is selected to establish SAMs on the surface of an Al_2O_3-coated separator (figs. S1 and S2) through a facile soaking method. The formation of SAMs originates from the specific binding between the carboxyl group and the hydroxyl-containing Al_2O_3 surface (*23*). To verify that SAMs are successfully constructed on the Al_2O_3 surface, atomic force microscopy (AFM) is used to examine the morphological evolution. In particular, the molecules are densely packed like a full monolayer with ~20-Å topographic features after modifying the Al_2O_3 matrix (Fig. 1, B to D), indicative of SAM establishment on Al_2O_3 as Al_2O_3-$OOC(CH_2)_2NH_2$ and Al_2O_3-$OOC(CH_2)_2COOH$. In addition, the full x-ray photoelectron spectroscopy (XPS) spectra show that the C content is higher in both Al_2O_3-$OOC(CH_2)_2NH_2$ (23.95%) and Al_2O_3-$OOC(CH_2)_2COOH$ (23.70%) than in bare Al_2O_3 (18.41%) (Fig. 1E). More specifically, the peaks at 284.8, 286.2, and 288.6 eV in the C 1s region are assigned to C–C, C–O, and C=O, respectively, and the peaks at 530.8 and 532.1 eV in the O 1s region belong to Al–O–Al and Al–O–C, respectively (fig. S3). The peak intensities (and hence contents) of C=O and Al–O–C in SAM-grafted Al_2O_3 (Al_2O_3-SAMs) are increased compared with those of pristine Al_2O_3 (fig. S4). In addition, the Fourier transform infrared (FTIR) spectra of Al_2O_3-SAMs exhibit the typical signals of C=O (1730 cm^{-1}), N–H (1583 cm^{-1}), and C–O (1168 cm^{-1}) (*24*, *25*), which belong to the terminal groups of the SAMs (Fig. 1F and fig. S5). In particular, two notable peaks at ~1638 and ~1443 cm^{-1} appear in Al_2O_3-SAMs, representing asymmetric and symmetric bonding modes of the essential (bidentate) interaction between the headgroup carboxylate and the Al_2O_3 surface, respectively (Fig. 1F and fig. S5) (*23*). Furthermore, the water wetting experiment demonstrates an apparently increased contact angle that can be attributed to the highly ordered

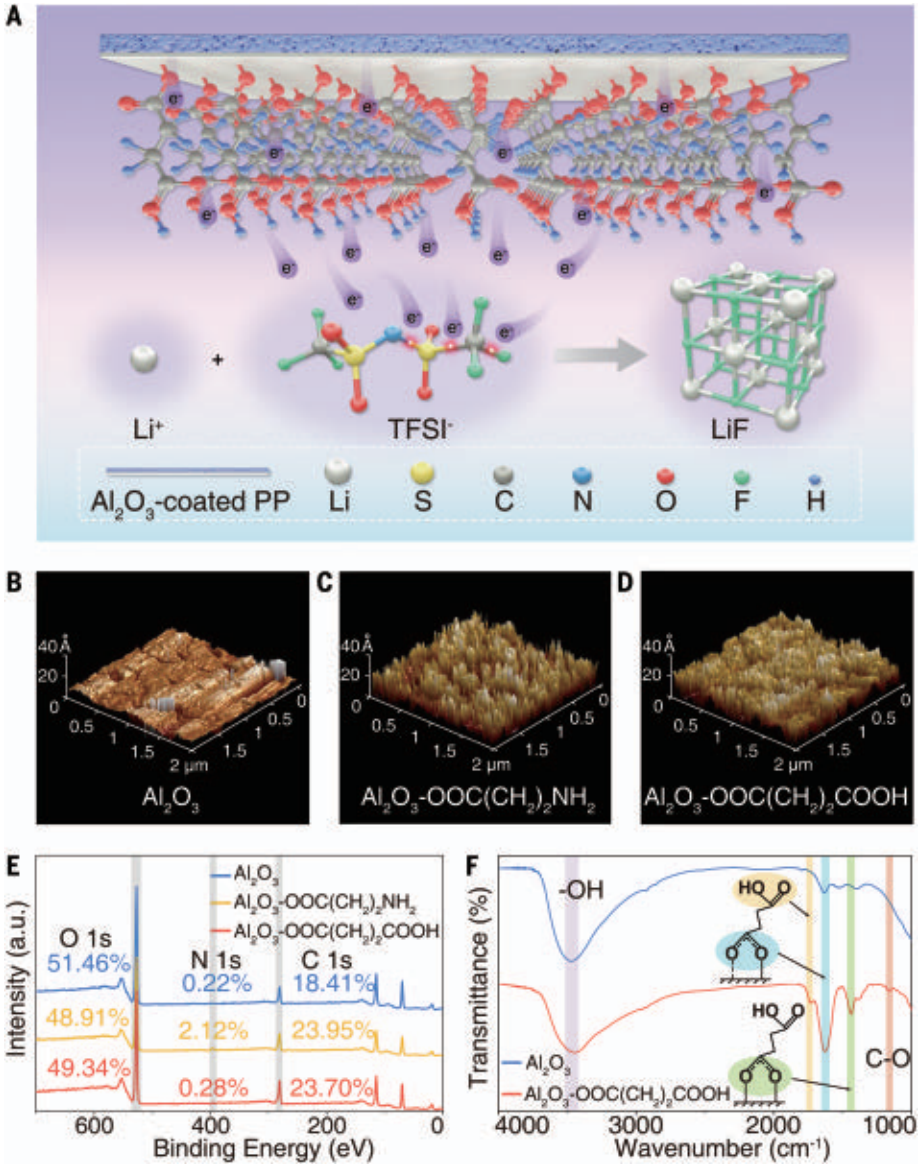

Fig. 1. Schematic illustration of SAMs in LMBs and characterization of Al_2O_3-SAMs. (**A**) SAMs with carboxyl terminal groups accelerate the reduction of LiTFSI through dipole moment–directed electron provision and thus generate a LiF-rich SEI. PP, polypropylene. (**B** to **D**) AFM images showing the topographic features of (B) Al_2O_3, (C) Al_2O_3-$OOC(CH_2)_2NH_2$, and (D) Al_2O_3-$OOC(CH_2)_2COOH$. (**E**) XPS full-scan survey spectra of Al_2O_3, Al_2O_3-$OOC(CH_2)_2NH_2$, and Al_2O_3-$OOC(CH_2)_2COOH$. a.u., arbitrary units. (**F**) FTIR spectra of Al_2O_3 and Al_2O_3-$OOC(CH_2)_2COOH$.

alignment of SAMs (fig. S6). These results all indicate that the specific molecules are successfully grafted onto the surface of the Al_2O_3-coated separator to generate SAMs with ordered terminal groups.

Li plating and stripping behaviors with SAMs

To confirm the effect of SAMs on Li deposition, electrochemical Li plating and stripping experiments are carried out using typical coin cells of bare Li and Cu coupled with an Al_2O_3-SAMs separator. The results are plotted as coulombic efficiency (CE) versus cycle number of cells at different current densities with the same plating capacity of 1 mA·hour cm^{-2} (Fig. 2A). Specifically, the cells equipped with Al_2O_3-$OOC(CH_2)_2COOH$ and Al_2O_3-$OOC(CH_2)_2NH_2$ exhibit stable CEs of ~97.7 and ~95.3%, respectively, over 300 cycles under a current density of 1 mA cm^{-2}. By contrast, the cell with bare Al_2O_3 shows inferior cycle life, and the CE fades to 74.2% after 220 cycles. More specifically, the cell with Al_2O_3-$OOC(CH_2)_2COOH$ is stable with the overpotential of only ~15 mV (Fig. 2B). When the current density is increased to 2 and 3 mA cm^{-2}, the cells using Al_2O_3-$OOC(CH_2)_2COOH$ also deliver more stable electrochemical cycling and still maintain high CEs of 99.2% (2 mA cm^{-2}) over 300 cycles and 99.4% (3 mA cm^{-2}) over 150 cycles, and the cells using Al_2O_3-$OOC(CH_2)_2NH_2$ have CEs of 93.6% (2 mA cm^{-2}) after 200 cycles and 93.5% (3 mA cm^{-2}) after 150 cycles. By contrast, the cells with Al_2O_3 exhibit rather unsatisfactory cycling stability, showing CEs of 82.4% (2 mA cm^{-2}) at the 200th cycle and 70.9% (3 mA cm^{-2}) at the 150th cycle (Fig. 2A). As a comparison, the individual $HOOC(CH_2)_2COOH$ or $HOOC(CH_2)_2NH_2$ molecules are directly added into the electrolyte as additives, and these dispersed molecules fail to form SAMs because of the weak solvent polarity of the ether-based electrolyte (figs. S7 and S8). The CE of the cells using both individual additives is apparently lower than that of the cell with ordered SAMs (fig. S9). We also find that the typical FTIR signals representing the interactions between the head group of SAMs and the Al_2O_3 substrate remain evident after 5 or even 100 cycles, indicating that the structure of SAMs does not change substantially during long-term battery cycling (figs. S10 and S11).

The morphologies of Li deposits are examined through scanning electron microscopy. Li deposition onto the bare Cu electrode results in uneven striped Li with obvious cracks and voids after 10 and 50 cycles, whereas Li deposited in the presence of SAMs exhibits a smooth morphology (figs. S12 and S13). The morphology of the Li deposited with

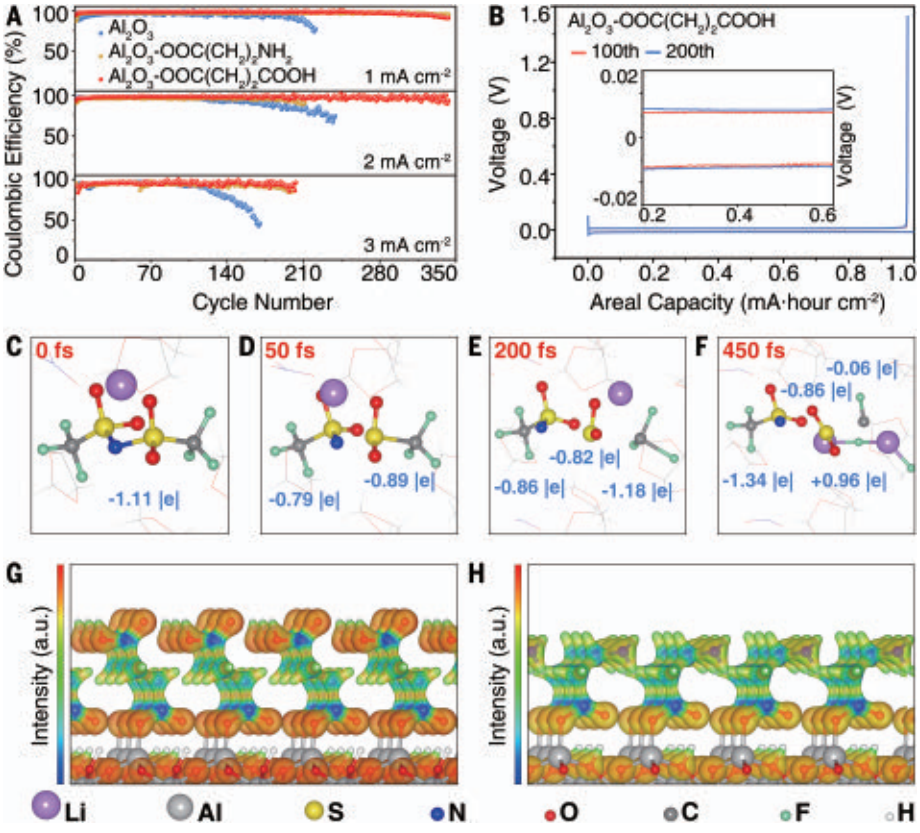

Fig. 2. Electrochemical performances of Li–Cu half cells and simulations of the degradation mechanism of LiTFSI. (**A**) CE comparison of the anodes in three cells equipped with Al_2O_3, Al_2O_3-$OOC(CH_2)_2NH_2$, and Al_2O_3-$OOC(CH_2)_2COOH$ at current densities of 1, 2, and 3 mA cm^{-2} with an areal capacity of 1 mA·hour cm^{-2}. (**B**) Voltage profiles of the cell equipped with Al_2O_3-$OOC(CH_2)_2COOH$ at 1 mA cm^{-2} of the 100th and 200th cycles. (**C** to **F**) Snapshots of AIMD simulations with instantaneous Bader charges (the unit of charge is |*e*|) illustrating the degradation dynamics: (C) 0 fs, (D) 50 fs, (E) 200 fs, and (F) 450 fs. (**G** and **H**) Electrostatic potential plotted on the isosurface of $\rho = 0.2|e|$ $bohr^{-3}$ (ρ, charge density) of oriented (G) Al_2O_3-$OOC(CH_2)_2COOH$ and (H) Al_2O_3-$OOC(CH_2)_2NH_2$.

Al_2O_3-$OOC(CH_2)_2COOH$ remains uniform, whereas the morphology of the Li deposited with Al_2O_3 becomes irregularly dendritic with locally aggregated sediments after 200 cycles (fig. S14). In addition, the thickness of deposits is related to the generated inactive Li debris termed "dead Li." After 50 cycles, the thickness of the deposit with Al_2O_3-$OOC(CH_2)_2COOH$ is found to be ~36 μm, smaller than those with Al_2O_3-$OOC(CH_2)_2NH_2$ (44 μm) and Al_2O_3 (69 μm), indicating that Al_2O_3-$OOC(CH_2)_2COOH$ can reduce the amount of dead Li (fig. S15). Therefore, SAMs with ordered terminal groups, especially Al_2O_3-$OOC(CH_2)_2COOH$, are demonstrated to greatly improve the CE and extend the cycle life of half cells.

Simulation of functional mechanism of SAMs

Density functional theory (DFT) and ab initio molecular dynamics (AIMD) calculations are carried out to explore the relationship between the oriented functional groups of SAMs and the electrochemical process. First, we illustrate the lowest unoccupied molecular orbital (LUMO) and highest occupied molecular orbital (HOMO) energy levels of related molecules (fig. S16), which are associated with the electrolyte reaction activity in terms of frontier molecular orbital theory (*26*). Our calculations show that apart from the low-concentration $LiNO_3$, LiTFSI has the lowest LUMO energy level (−1.03 eV) and can therefore be easily reduced (i.e., accept electrons) during the battery cycling operation.

We construct four configurations based on the corresponding experimental conditions (see the supplementary materials for methodological details) to capture the thermodynamic behavior of LiTFSI. During the AIMD equilibration process up to 12 ps, the formation of LiF is observed only in the case of oriented carboxyl groups (fig. S17). To reveal the LiF formation mechanism, we trace all LiTFSI decomposition steps through the AIMD simulation time (Fig. 2, C to F). The Bader charge analysis reveals that ~−1|*e*| charge is transferred from the carboxyl group to the $TFSI^-$ anion at 50 fs, leading to cleavage of the N–S bond, as described in reaction Eq. 1 (*27*)

$$N(SO_2CF_3)_2^- + e^- \rightarrow NSO_2CF_3^- + SO_2CF_3^- \quad (1)$$

Subsequently, the CF_3^- group is removed from the $SO_2CF_3^-$ fragment at 200 fs, owing to the acquisition of one electron (e^-). This CF_3^- group is further decomposed into CF and F^- at 450 fs, eventually resulting in LiF formation. These reactions can be described as follows

$$SO_2CF_3^- + e^- \rightarrow SO_2^- + CF_3^- \quad (2)$$

$$CF_3^- + e^- \rightarrow CF + 2F^- \quad (3)$$

$$F^- + Li^+ \rightarrow LiF \quad (4)$$

This LiTFSI decomposition mechanism is in good agreement with previous simulation results (*28*, *29*). We attempt to understand the role that high-density and highly ordered functional groups play in this process. Electrostatic potential and differential charge density calculations show that the directed polar functional groups attract electrons from the Al_2O_3 substrate to the electrolyte (Fig. 2, G and H). The red electrostatic potential isosurface indicates electrophilicity, and the blue isosurface represents nucleophilicity (*30*). The dipole moment induced by carboxyl groups (higher molecular polarity compared with amino groups) facilitates transfer of more electrons from the Al_2O_3 slab to the electrolyte environment than that induced by amino groups (smaller molecular polarity) (*31*). Furthermore, the differential charge density between Al_2O_3 and functional groups shows more obvious charge transfer from Al_2O_3 to carboxyl groups compared with pristine Al_2O_3 or amino groups (fig. S18), consistent with our electrostatic potential calculation results. In addition to the effect of induced dipole moment, the dipole-dipole interaction between free ether-based solvent molecules and carboxyl group–terminated SAMs that can mitigate solvent decomposition is also taken into consideration (*32*). Detailed DFT calculations show that such interaction may not be suitable for the low-polarity ether-based electrolyte used here (fig. S19). In short, the ordered orientation of the polar functional groups on the Al_2O_3 surface enables the same dipole direction, which attracts electrons from Al_2O_3 to the electrolyte environment. These excess electrons thus facilitate the decomposition of LiTFSI into F^- species, finally forming LiF.

Characterization of the LiF-enriched SEI

In view of the simulated predictions of SAM-induced LiTFSI decomposition, we perform cyclic voltammetry (CV) analysis to examine

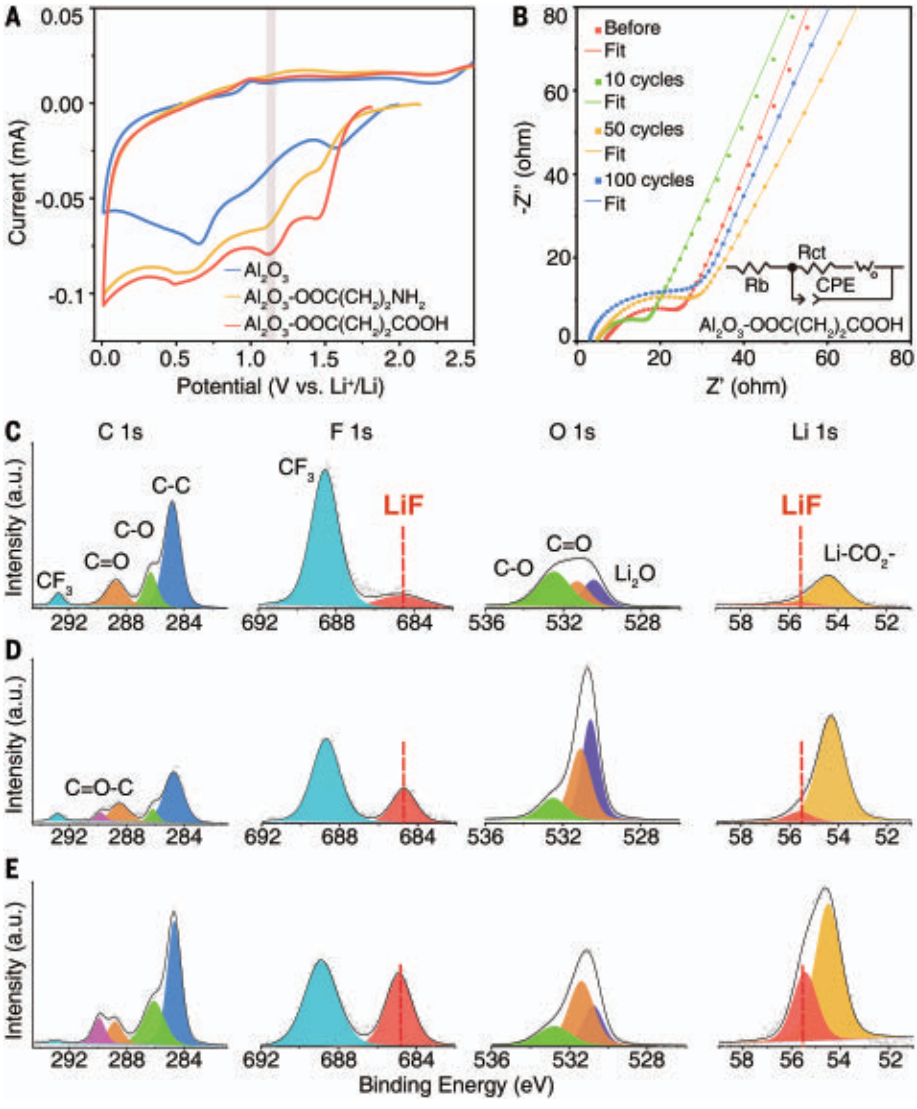

Fig. 3. Analysis of the interfacial stability and SEI chemical composition. (**A**) First-cycle CV curves of cells equipped with Al_2O_3, Al_2O_3-$OOC(CH_2)_2NH_2$, and Al_2O_3-$OOC(CH_2)_2COOH$. (**B**) Electrochemical impedance spectroscopy spectra of the cell equipped with Al_2O_3-$OOC(CH_2)_2COOH$ before cycling and after 10, 50, and 100 cycles. Z′, real part of complex impedance; Z″, imaginary part of complex impedance; Rct, charge-transfer resistance; Rb, bulk resistance; W_o, Warburg impedance; CPE, constant phase element. (**C** to **E**) XPS spectra of the SEIs in cells with (C) Al_2O_3, (D) Al_2O_3-$OOC(CH_2)_2NH_2$, and (E) Al_2O_3-$OOC(CH_2)_2COOH$.

the redox reactions of the electrolyte system. The CV curve of the cell with pristine Al_2O_3 shows two cathodic peaks at ~1.56 and ~0.65 V corresponding to reduction of $LiNO_3$ and solvent, respectively (*33*). In addition to these two peaks, one pronounced cathodic peak at ~1.11 V is observed in the CV curves of cells with Al_2O_3-SAMs, which is assigned to the reduction of $TFSI^-$ (Fig. 3A) (*34*). This peak of $TFSI^-$ reduction attenuates greatly in the subsequent cycles (fig. S20). The CV results demonstrate that SAMs facilitate the preferential reduction of LiTFSI. Impedance tests are also performed on the cells before cycling and after 10, 50, and 100 cycles. The impedance of the cell employing Al_2O_3-$OOC(CH_2)_2COOH$ remains relatively stable after 100 cycles (Fig. 3B). By contrast, both cells with Al_2O_3 and Al_2O_3-$OOC(CH_2)_2NH_2$ experience more substantial impedance increase (fig. S21 and table S1). The impedance evaluations show that Al_2O_3-$OOC(CH_2)_2COOH$ can deliver optimum efficiency in enhancing interfacial stability.

We next investigate the chemical composition of the SEI by applying XPS on the Li deposits after the first discharge (Fig. 3, C to E). In the C 1s spectra, the peaks assigned to C–C, C–O, C=O, C=O–C, and CF_3 originate from the decomposition of the electrolyte. In the F 1s spectra, there are two peaks of LiF and CF_3 species at 684.8 and 688.6 eV, respectively (*35*). A high percentage of LiF (6.9%) is detected on the surface of Li deposited in the presence of Al_2O_3-$OOC(CH_2)_2COOH$. In comparison, the percentages of LiF are only 4.2 and 3.8% in the cells equipped with Al_2O_3-$OOC(CH_2)_2NH_2$ and Al_2O_3, respectively. If $HOOC(CH_2)_2COOH$ molecules are added to the electrolyte as an additive instead of forming ordered SAMs, the Li deposit has only 4.2% LiF (fig. S22). In addition, the XPS depth profiles of the Li deposited with Al_2O_3-$OOC(CH_2)_2COOH$ show that LiF appears on the SEI surface and its content ratio gradually increases up to the surface of the Li metal anode (fig. S23). The results indicate that the LiF generated by SAMs can efficiently passivate the reactive surfaces to reduce the initial side reaction and can improve Li^+ diffusion throughout the SEI (*36*). Moreover, as the temperature is increased, the degradation kinetics may accelerate to facilitate LiF formation (fig. S24).

In our recent studies, we have investigated the SEI in Li metal anodes at subangstrom resolution using cryo–transmission electron microscopy (cryo-TEM) (*28*, *37*–*39*). In this study, we employ the same technique to directly visualize the nanostructure of the SEI. Metallic Li is deposited on a Cu grid with a capacity of 1 mA·hour cm^{-2} at a current density of 1 mA cm^{-2} for cryo-TEM observation. In the presence of SAMs, the deposited Li appears homogeneous with spherical morphologies (Fig. 4A and fig. S25). Various Li deposits are visualized by the cryo–scanning transmission electron microscopy (cryo-STEM), and the corresponding distributions and amounts of typical elements—such as C, O, and F—in the SEI are analyzed (Fig. 4, B and C, and figs. S25 to S28). Usually, the content of F in the SEI induced by Al_2O_3-$OOC(CH_2)_2COOH$ is much higher than those induced by Al_2O_3-$OOC(CH_2)_2NH_2$ and pristine Al_2O_3 (Fig. 4D). However, the SEI generated by the dispersed $HOOC(CH_2)_2COOH$ additive without forming ordered SAMs contains a relatively low amount of F (fig. S29). Therefore, we have obtained high-resolution TEM (HRTEM) images of the specific F-enriched SEI nanostructure generated by Al_2O_3-$OOC(CH_2)_2COOH$. The SEI exhibits a classical mosaic structure that consists of an amorphous phase and embedded Li, Li_2O, LiOH, and LiF nanocrystals (Fig. 4E). The crystalline phases of Li, LiOH, and Li_2O are confirmed by matching the long-range–ordered lattices with their known lattice planes (Fig. 4, F to H) (*39*). Specifically, the calibrated interplanar spacing of 2.48 Å well matches the (110) plane of metallic Li (Fig. 4F). More notably, LiF nanoparticles with lattice corresponding to the (111) plane can be clearly detected in the SEI (Fig. 4I and fig. S30). In summary, both the XPS and cryo-TEM results confirm the distribution and enrichment of LiF nanocrystals in the Al_2O_3-$OOC(CH_2)_2COOH$-induced SEI, consistent with the simulated prediction.

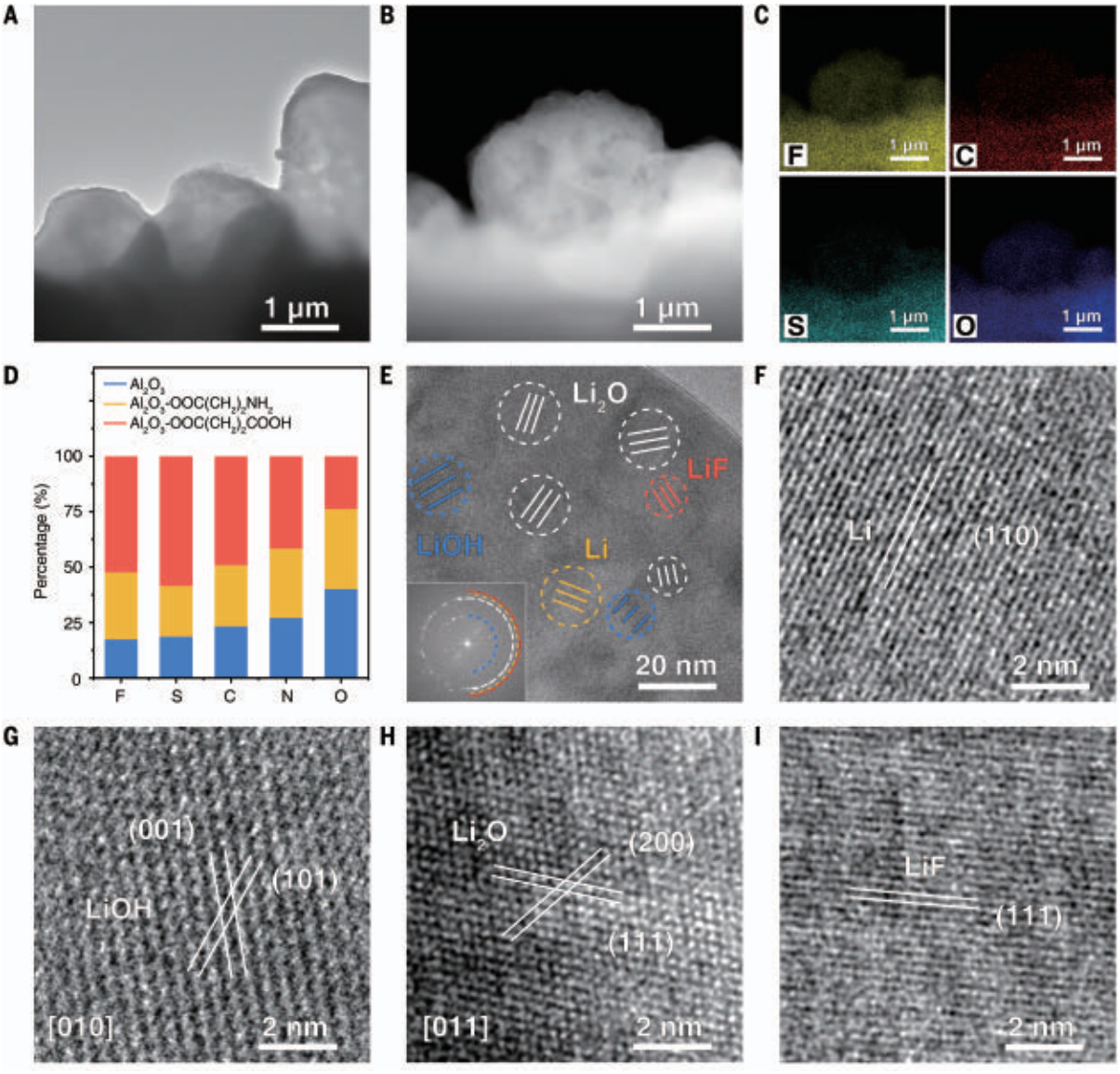

Fig. 4. Cryo-TEM visualization of the Li deposits and SEI nanostructures. (**A**) Morphology of Li plated on a Cu grid in the presence of Al_2O_3-OOC$(CH_2)_2$COOH. (**B**) Cryo-STEM image of Li deposit in the presence of Al_2O_3-OOC$(CH_2)_2$COOH and (**C**) corresponding elemental distributions of C, O, F, and S. (**D**) Elemental mass ratios of the SEIs formed in three cells equipped with Al_2O_3, Al_2O_3-OOC$(CH_2)_2NH_2$, and Al_2O_3-OOC$(CH_2)_2$COOH. (**E**) Enlarged TEM image of the Li/Al_2O_3-OOC$(CH_2)_2$COOH interface, where the typical mosaic SEI structure and the incorporated crystalline regions are shown. (Inset) Corresponding fast Fourier transform with yellow circle indexed to LiF, 2.32 Å (PDF#45-1460); red circle indexed to Li, 2.48 Å (PDF#15-0401); white circle indexed to Li_2O, 2.66 Å (PDF#32-0564); and blue circle indexed to LiOH, 4.35 Å (PDF#32-0564). (**F** to **I**) HRTEM images of (F) Li, (G) LiOH, (H) Li_2O, and (I) LiF nanocrystals with long-range–ordered lattices.

Performance of cells containing SAMs under stringent conditions

Reversible Li plating and stripping are evaluated by testing symmetric cells. The symmetric cell with carboxyl group–terminated SAMs (SAMsC) exhibits steady cyclability over 1000 cycles for more than 2500 hours, with a small overpotential of 40 mV (Fig. 5A). By contrast, the symmetric cell with Al_2O_3 exhibits a much larger overpotential (75 mV for 700 hours), with greatly reduced cycle life. Even when the current density and areal capacity are increased to 5 mA cm^{-2} and 5 mA·hour cm^{-2}, respectively, the symmetric cell with SAMsC can still be steadily cycled over 600 hours (Fig. 5B). For the full cell tests, coin cells with a $LiFePO_4$ (LFP) cathode and a Li anode (Li foil or Li-deposited Cu) are evaluated at a current density of 1 C in a LiTFSI-containing ether electrolyte in the presence of SAMsC and amino group–terminated SAMs (SAMsA). The Li//SAMsC//LFP cell can be cycled steadily over 1000 cycles, with a capacity retention of 92.8% (fig. S31). Notably, the full cell of Li//SAMsC//LFP under a low capacity ratio of the negative electrode to the positive electrode (N/P ratio of ~3) can still exhibit an enhanced life span over 450 cycles, with a capacity retention above 80% and an average CE above 99.9% (Fig. 5C), indicative of a promising strategy to boost high–energy density LMBs (table S2). Even if the ratio of electrolyte weight to cathode capacity is further decreased to below 5 g A^{-1}·$hour^{-1}$ with lean electrolyte conditions (15 μl), the full cell of Li//SAMsC//LFP shows marked cycling stability, with little capacity loss over 270 cycles (fig. S32). The Li//SAMsC//LFP full cell also delivers higher discharge specific capacities (163 to 137 mA·hour g^{-1}) at current densities ranging from 0.2 to 3 C (Fig. 5, D and E) than the Li//LFP and Li//SAMsA//LFP cells. After the current density is reduced back to 0.5 C,

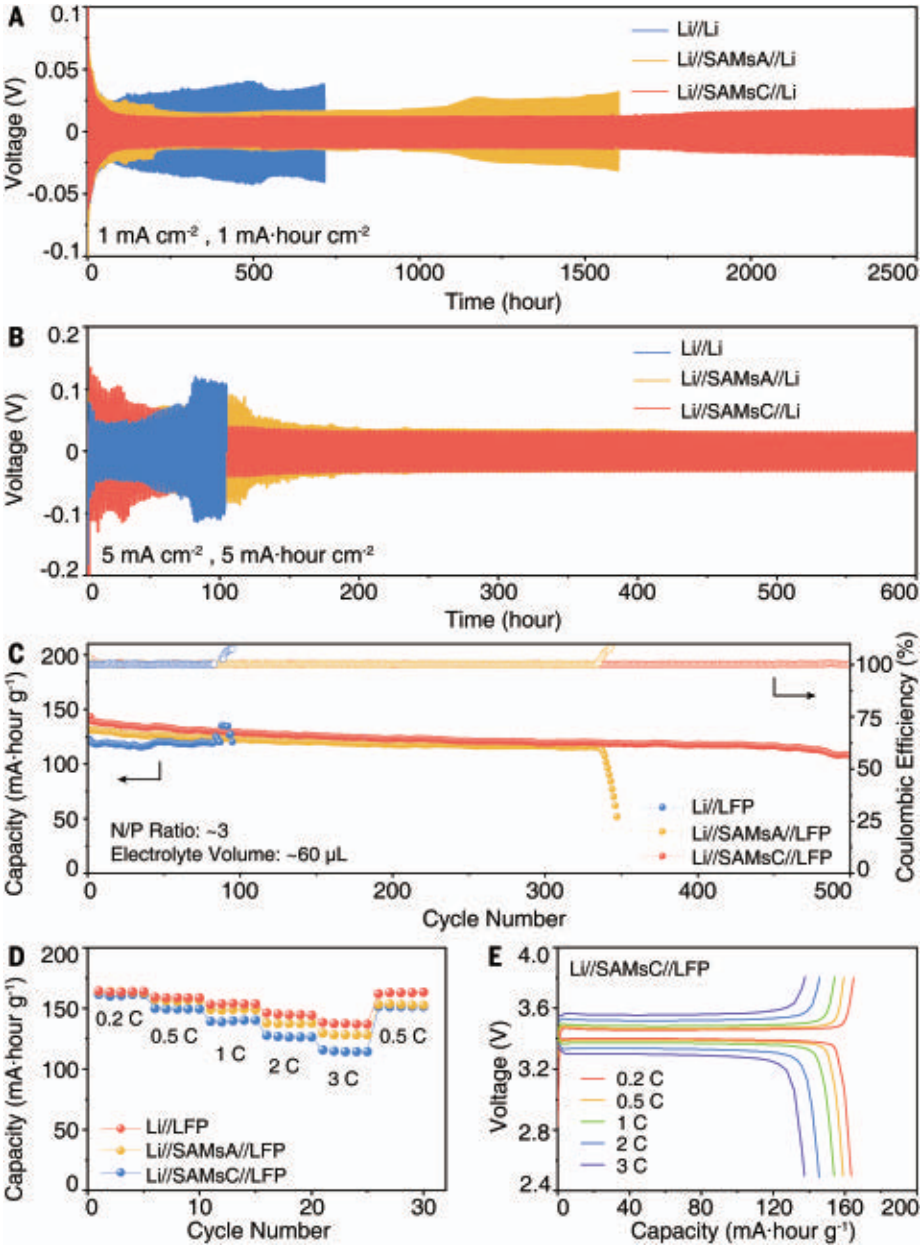

Fig. 5. Electrochemical performance of symmetric half cells and full cells equipped with SAMs. (**A** and **B**) Galvanostatic discharge and charge voltage curves of the symmetric coin cells at (A) 1 mA cm^{-2} with an areal capacity of 1 mA·hour cm^{-2} and at (B) 5 mA cm^{-2} with an areal capacity of 5 mA·hour cm^{-2}. (**C**) Long-term cycling performance of the batteries using a Li-deposited Cu anode (10 mA·hour cm^{-2}), a LFP cathode (3.2 mA·hour cm^{-2}), and a LiTFSI-containing ether-based electrolyte (60 µl) at a current density of 1 C (1 C = 170 mA g^{-1}). (**D**) Rate performance of Li//LFP, Li//SAMsA//LFP, and Li//SAMsC//LFP full cells with a N/P ratio of 3.5. (**E**) Discharge and charge voltage profiles of a Li//SAMsC//LFP full cell at different current densities.

the reversible capacity of Li//SAMsC//LFP recovers to 163 mA·hour g^{-1}, indicating excellent rate performance (Fig. 5D). In addition, SAMs can be employed to boost the performance of cells with highly concentrated electrolytes (HCEs). The SAMsC-based full cell with a higher concentration of LiTFSI generates more LiF in the SEI, thus rendering a prolonged life span of the battery under the HCE condition (fig. S33). Using another typical unstable cathode, the Li//SAMsC//$LiNi_{0.8}Co_{0.1}Mn_{0.1}O_2$ (NCM811) full cell also has enhanced cyclability (fig. S34) and rate performance (fig. S35). The potential practical application of SAMs is further demonstrated in pouch cells. The pristine Li//LFP pouch cell with a N/P ratio of ~5 manifests rapid capacity decay toward battery failure, whereas the Li//SAMsC//LFP pouch cell exhibits much better cycling stability, with an extended cycle life under similar conditions (fig. S36). The improved cycle life proves the substantial advantages of the LiF-rich SEI originating from the surface dipole–directed degradation of Li salts.

With the use of a SAM-grafted separator, we have demonstrated a strategy to regulate electrolyte degradation for constructing stable LMBs. Comprehensive simulations and characterizations reveal the critical role of ordered polar carboxyl groups in promoting the cleavage of C–F bonds to generate a LiF-rich SEI involving dipole moment–induced excess electrons. The LiF-enriched SEI is beneficial for stabilizing the Li/electrolyte interface, thus substantially inhibiting the formation of Li dendrites and boosting the life span of the Li anode. This long-established SAMs technique based on surface chemistry provides a solution to uncontrollable electrolyte degradation and SEI formation in batteries. With SAM-grafted separators, full cells of LMBs exhibit enhanced cyclability even under stringent conditions. This facile strategy can potentially be extended to other electrode systems by tailoring the molecular structures of SAMs to build better energy devices.

REFERENCES AND NOTES

1. J. Liu *et al.*, *Nat. Energy* **4**, 180–186 (2019).
2. X. B. Cheng, R. Zhang, C. Z. Zhao, Q. Zhang, *Chem. Rev.* **117**, 10403–10473 (2017).
3. L. Li *et al.*, *Science* **359**, 1513–1516 (2018).
4. D. C. Lin, Y. Y. Liu, Y. Cui, *Nat. Nanotechnol.* **12**, 194–206 (2017).
5. C. B. Jin *et al.*, *Nat. Energy* **6**, 378–387 (2021).
6. C. Fang *et al.*, *Nature* **572**, 511–515 (2019).
7. Z. W. Zhang *et al.*, *Science* **375**, 66–70 (2022).
8. Y. Gao *et al.*, *Nat. Energy* **5**, 534–542 (2020).
9. P. C. Zou *et al.*, *Chem. Rev.* **121**, 5986–6056 (2021).
10. Y. Z. Li *et al.*, *Science* **358**, 506–510 (2017).
11. J. Alvarado *et al.*, *Energy Environ. Sci.* **12**, 780–794 (2019).
12. M. Q. Wang *et al.*, *J. Phys. Chem. C* **122**, 9825–9834 (2018).
13. D. J. Yoo, S. Yang, K. J. Kim, J. W. Choi, *Angew. Chem. Int. Ed.* **59**, 14869–14876 (2020).
14. X. Q. Zhang, X. B. Cheng, X. Chen, C. Yan, Q. Zhang, *Adv. Funct. Mater.* **27**, 1605989 (2017).
15. X. L. Fan *et al.*, *Sci. Adv.* **4**, eaau9245 (2018).
16. M. Chen *et al.*, *Adv. Funct. Mater.* **31**, 2102228 (2021).
17. M. Mitsuya, *Langmuir* **10**, 1635–1637 (1994).
18. J. C. Love, L. A. Estroff, J. K. Kriebel, R. G. Nuzzo, G. M. Whitesides, *Chem. Rev.* **105**, 1103–1169 (2005).
19. R. W. Yi, Y. Y. Mao, Y. B. Shen, L. W. Chen, *J. Am. Chem. Soc.* **143**, 12897–12912 (2021).
20. S. Duhm *et al.*, *Nat. Mater.* **7**, 326–332 (2008).
21. T. Morita, S. Kimura, *J. Am. Chem. Soc.* **125**, 8732–8733 (2003).
22. L. J. Zuo *et al.*, *J. Am. Chem. Soc.* **137**, 2674–2679 (2015).
23. M. S. Lim *et al.*, *Langmuir* **23**, 2444–2452 (2007).
24. C. F. Li *et al.*, *Nat. Commun.* **10**, 1363 (2019).
25. D. C. Lin *et al.*, *Nat. Nanotechnol.* **11**, 626–632 (2016).
26. Z. X. Wang *et al.*, *Adv. Energy Mater.* **10**, 1903843 (2020).
27. H. Yildirim, J. B. Haskins, C. W. Bauschlicher Jr., J. W. Lawson, *J. Phys. Chem. C* **121**, 28214–28234 (2017).
28. O. W. Sheng *et al.*, *Adv. Mater.* **32**, 2000223 (2020).
29. L. E. Camacho-Forero, P. B. Balbuena, *Phys. Chem. Chem. Phys.* **19**, 30861–30873 (2017).
30. P. Politzer, J. S. Murray, in *Chemical Reactivity Theory*, vol. 17 (CRC, 2009), pp. 243–254.
31. R. A. Lewis *et al.*, *Proc. Natl. Acad. Sci. U.S.A.* **78**, 4579–4583 (1981).
32. J. Bae *et al.*, *Energy Environ. Sci.* **12**, 3319–3327 (2019).

33. H. P. Wu, Y. Cao, L. X. Geng, C. Wang, *Chem. Mater.* **29**, 3572–3579 (2017).
34. B. Tong *et al.*, *J. Power Sources* **400**, 225–231 (2018).
35. S. F. Liu *et al.*, *Adv. Mater.* **31**, 1806470 (2019).
36. J. H. Zheng *et al.*, *J. Mater. Chem. A* **9**, 10251–10259 (2021).
37. H. D. Yuan *et al.*, *Sci. Adv.* **6**, eaaz3112 (2020).
38. Y. J. Liu *et al.*, *Acc. Chem. Res.* **54**, 2088–2099 (2021).
39. Z. J. Ju *et al.*, *Nat. Commun.* **11**, 488 (2020).

ACKNOWLEDGMENTS

Funding: The authors acknowledge financial support by the National Natural Science Foundation of China (grants 51722210, 51972285, U21A20174, and 52102314), the Natural Science Foundation of Zhejiang Province (grants LD18E020003 and LQ20E030012), and the Leading Innovative and Entrepreneur Team Introduction Program of Zhejiang (2020R01002). **Author contributions:** Y.L., X.T., Y.W., and X.W.L. conceived the idea and co-wrote the manuscript. Y.L., C.J., and C.M. designed and performed the experiments and analyzed the data. O.S. contributed to interpreting the mechanism. G.L. assisted in TEM characterizations for materials. All authors discussed the results. **Competing interests:** The authors declare no competing interests. **Data and materials availability:** All data needed to evaluate the conclusions in the paper are present in the paper and/or the supplementary materials.

SUPPLEMENTARY MATERIALS

science.org/doi/10.1126/science.abn1818
Materials and Methods
Figs. S1 to S36
Tables S1 and S2
References (*40*–*60*)

9 November 2021; accepted 20 January 2022
10.1126/science.abn1818

ELECTROCHEMISTRY

Modular terpene synthesis enabled by mild electrochemical couplings

Stephen J. Harwood[1]†, Maximilian D. Palkowitz[1]†, Cara N. Gannett[2], Paulo Perez[3], Zhen Yao[4], Lijie Sun[4], Héctor D. Abruña[2]*, Scott L. Anderson[3]*, Phil S. Baran[1]*

The synthesis of terpenes is a large field of research that is woven deeply into the history of chemistry. Terpene biosynthesis is a case study of how the logic of a modular design can lead to diverse structures with unparalleled efficiency. This work leverages modern nickel-catalyzed electrochemical sp^2–sp^3 decarboxylative coupling reactions, enabled by silver nanoparticle–modified electrodes, to intuitively assemble terpene natural products and complex polyenes by using simple modular building blocks. The step change in efficiency of this approach is exemplified through the scalable preparation of 13 complex terpenes, which minimized protecting group manipulations, functional group interconversions, and redox fluctuations. The mechanistic aspects of the essential functionalized electrodes are studied in depth through a variety of spectroscopic and analytical techniques.

The study of terpene synthesis holds a special place in the annals of organic synthesis, with the formalization of the stereoelectronic effect, conformational analysis, rules for pericyclic reactions, and even retrosynthetic analysis stemming from this field (*1*). Beyond synthesis, the pivotal role that terpenes play in nature and medicine has inspired practitioners from a wide spectrum of the scientific community (*2*, *3*). As medicines, they exhibit broad activity ranging from modulation of human physiology (e.g., steroid hormones, cannabinoids) to amelioration of disease (e.g., Taxol, artemisinin) (*2*). Terpenes also pervade the fine chemicals industry and are found in commercial fragrances and food additives (*4*). Not surprisingly, this class of natural isolates has inspired numerous total syntheses, a legendary example being Johnson's synthesis of progesterone in 1971 (Fig. 1A) (*5*). As one of the first biomimetic terpene syntheses, it validated the Stork-Eschenmoser hypothesis by stitching together the polycyclic steroid core through a bold cation-olefin cyclization (*6*). This tactic subsequently shaped the landscape of future chemical approaches to such molecules through its ability to generate polycyclic ring systems and multiple stereocenters from prochiral alkenes. Polyene cyclization is still an active area of research in the modern era, as evidenced by the steady development of new polycyclization reactions and enantioselective variants (*7*). Although the power of cation-olefin cyclization is undisputed, the construction of polyunsaturated precursors remains oddly challenging. Retrosynthetic strategies to forge such entities are still plagued with a nonintuitive logic where building blocks used do not clearly map onto the product into which they are ultimately incorporated. Specifically, these approaches are nonmodular and individually target each polyolefin cyclization precursor synthesized. Furthermore, they often lack complete control of olefin geometry (a critical feature controlling the resulting sp^3 stereochemistry) and require multiple functional group interconversions (FGIs) (*8*). The current barrier to rapid, modular, and controlled polyene construction therefore limits the effectiveness of what is arguably one of the most powerful complexity-inducing chemical transformations known. Meanwhile, steady advancement in the development of methodology for creating sp^2–sp^3 linkages has pointed toward a simpler approach to polyene synthesis (Fig. 1B) (*9*, *10*). The cyclase phase of natural terpene assembly points to inherent advantages of a modular approach, as a simple building block like isopentenyl pyrophosphate (IPP) can be intuitively mapped onto the final polyene product (*11*). The goal of this study was to mimic this strategy for modular terpene synthesis by focusing on disconnecting sp^2–sp^3 bonds directly to arrive at simple carboxylic acid precursors (Fig. 1C). By combining the knowledge of decarboxylative C–C bond formation and electrochemical cross-electrophile coupling with a new application of in situ electrode functionalization, we show how halo-acid modules can be iteratively coupled, resulting in more logical retrosynthetic analyses that reduce step counts and reliance on pyrophoric reagents while removing nonideal manipulations (*12*, *13*). The scalable access to 13 terpene natural products exemplifies the strategic power of this logic. Furthermore, the mechanistic interplay between the Ag-embedded heterogeneous interface and the homogenous Ni catalyst exemplifies the untapped potential of functionalized electrodes in synthetic organic electrochemistry.

Reaction development

The execution of the plan outlined above would require a departure from many of the (alkenyl)-sp^2–sp^3 disconnection strategies previously used that combine alkyl organometallic reagents or boronates with vinyl halides (Fig. 1B) (*9*, *10*). The functional group compatibility needed (tolerating free carboxylic acids, for example) and a desire to minimize functional group interconversions (e.g., R–X to R–BR_2) were vividly illustrated in our initial forays (Fig. 2). Here we enlisted the recently disclosed decarboxylative alkenylation with organozincs (prepared through lithium halogen exchange) (*14*). In the coupling with redox-active ester (RAE) **2**, more than three equivalents (equiv.) of **1** and six equiv. of *t*-BuLi under cryogenic conditions were required to generate the organometallic. Deprotection and oxidation of the resulting product ***3*** set the stage for the ensuing coupling. Although conceptually attractive, this approach fell short of the modular and mild aspirations of the initial plan (see supplementary materials for

[1]Department of Chemistry, Scripps Research, La Jolla, CA 92037, USA. [2]Department of Chemistry and Chemical Biology, Baker Laboratory, Cornell University, Ithaca, NY 14853, USA. [3]Department of Chemistry, University of Utah, Salt Lake City, UT 84112, USA. [4]Asymchem Life Sciences (Tianjin) Co., Ltd., TEDA Tianjin, 300457, P.R. China.
***Corresponding author. Email: hda1@cornell.edu (H.D.A.); anderson@chem.utah.edu (S.L.A.); pbaran@scripps.edu (P.S.B.)**
†These authors contributed equally to this work.

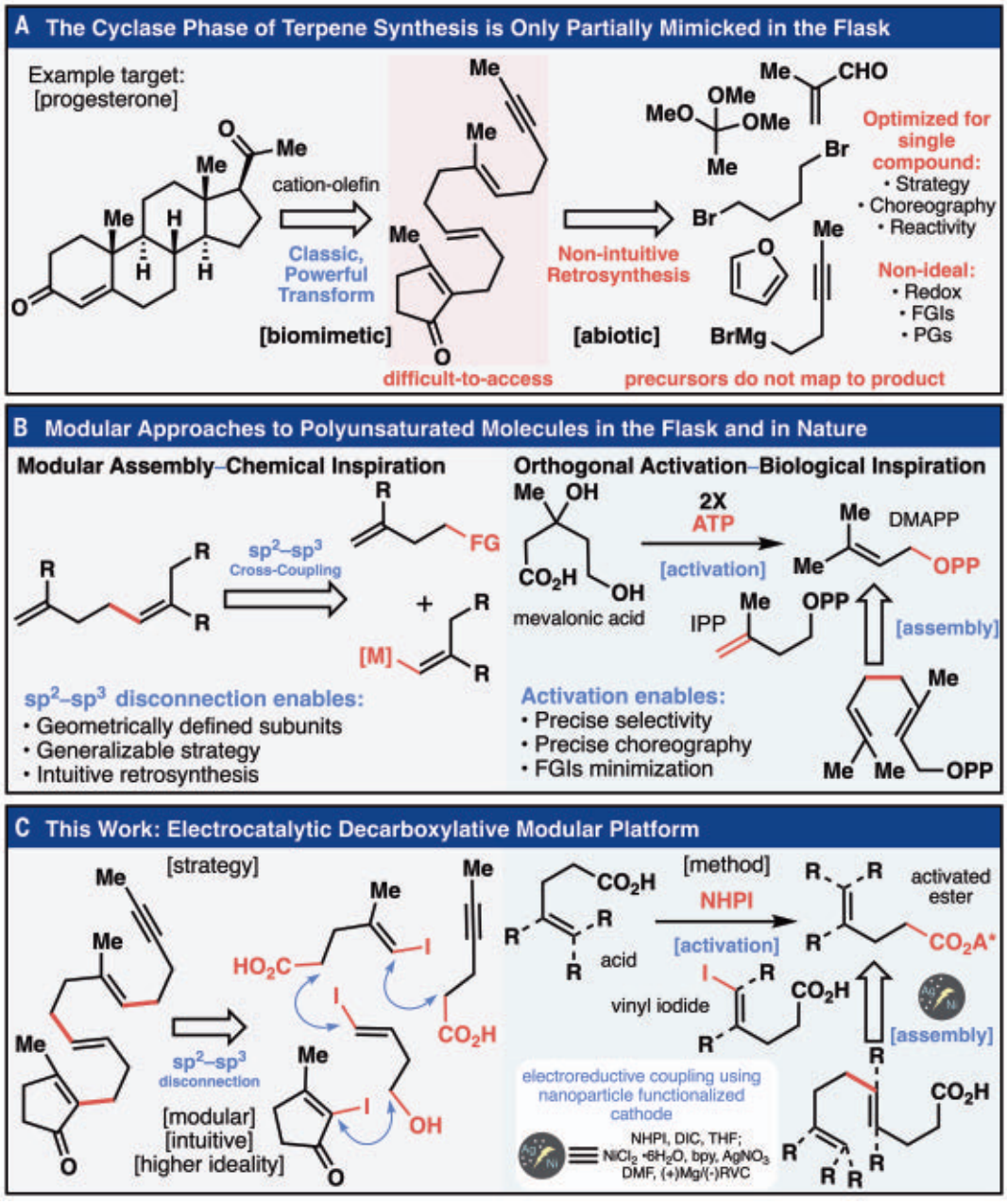

Fig. 1. The synthesis of polyene cyclization precursors remains a challenge to chemists. Taking inspiration from chemical and natural precedent, this work developed a modular platform constructing sp^2–sp^3 bonds using an electrochemical reaction and functionalized electrodes. (**A**) Retrosynthetic analysis of Johnson's classic total synthesis of progesterone. (**B**) The advantages of a prototypical sp^2–sp^3 disconnection and the biosynthesis of geraniol pyrophosphate. Adenosine triphosphate (ATP) activation of an alcohol generates the reactive chemical feedstocks necessary for terpene synthesis. (**C**) Combining the advantages of the sp^2–sp^3 disconnection and the modular and selective activation characteristics of the biosynthesis required development of a mild reaction using nickel electrocatalysis and Ag-nanoparticle functionalized electrodes. DMAPP, dimethylallyl pyrophosphate; OPP, O-pyrophosphate; NHPI, N-hydroxyphthalimide; DIC, N,N′-diisopropylcarbodiimide; DMF, N,N-dimethylformamide.

discussion). The seminal work of Périchon and Nédélec on electrochemical reductive cross-coupling was inspirational, as it demonstrated the coupling of vinyl halides with electronically biased alkyl halides in a simple undivided cell (*15*). Additionally, reports adapting this reactivity to aryl-alkyl cross-coupling using alkyl RAEs as alternatives to alkyl halides have emerged (*16*). Inspired by these precedents, initial conditions were developed that enabled a more functional group–tolerant reductive coupling of pregenerated RAEs with vinyl iodides. Unfortunately, after initial optimization efforts (tables S31 to 36), the use of free acid **5** in this milder coupling only provided trace quantities of **6** with an in situ protocol for the conversion of **4** to the corresponding RAE. An extensive series of optimization experiments were performed in the hope of overcoming this apparently intractable problem. Many of the traditional experimental variables associated with the optimization of electrochemical reactions such as electrolyte and electrode were reevaluated to no avail. Modification of the properties of the Ni-based electrocatalytic system were also re-explored by screening ligands, Ni sources, and other metals known to promote reductive coupling. Finally, given the heterogeneous nature of electrochemistry, efforts to modify the surface of the electrode were pursued because the deposition of metals onto electrode materials has been used to improve the performance of reductive electrochemical transformations (*17*). Two metals that are known to readily and reproducibly plate onto carbon electrodes, Cu and Ag, were explored, with the latter providing a substantial increase in reaction efficiency and functional group compatibility (*18*). Thus, addition of 0.30 equiv. $AgNO_3$ relative to the RAE starting material to the standard reductive coupling conditions [$NiCl_2$•$6H_2O$ (10 mol %), 2,2′-bpy (10 mol %), *N*,*N*′-dimethylformamide (DMF), room temperature (r.t.)] resulted in 50%

isolated yield of **6**. The precise nature of this electrode modification was studied in detail (see below) and supported the notion that Ag-based nanoparticles were present and responsible, at least in part, for this enhanced outcome. Before applying these newly developed conditions, a number of control studies were undertaken, as illustrated at the bottom of Fig. 2. Using coupling partners **5** and **7** as model substrates that give measurable yields without $AgNO_3$, several experiments confirmed that the Ag ion was the essential additive (entries 1 to 4). Entries 5 to 7 corroborate the role of Ag-based nanoparticles, as the use of pure Ag electrodes or Ag-plated electrodes did not work well, whereas Ag-nanoparticles, deposited on RVC (reticulated vitreous carbon) electrodes, could be recycled without the need for added Ag. Finally, the critical role of electrochemistry in this process was confirmed (entries 8 to 11) by running the reaction in the absence of current or by employing stoichiometric chemical (Mg) reductants, although addition of Ag to those nonelectrochemical processes did lead to notable improvements. Previously developed $C(sp^3)$-$C(sp^2)$ decarboxylative cross-coupling conditions were unamenable to the desired decarboxylative alkenylation with electrophiles such as **7** (see table S44) (*19*–*21*). In the final optimized manifestation, a free carboxylic acid (1.0 equiv.) could be converted to the NHPI-RAE (*N*,*N*′-diisopropylcarbodiimide, *N*-hydroxyphthalimide, 1 to 3 hours) in a minimal amount of tetrahydrofuran (THF) (maximum 1 mmol/0.75 ml of THF) followed by direct addition of vinyl iodide (1.5 equiv.) and Ni catalyst in DMF (0.07 to 0.25M); the solution was then added to a commercial electrochemical cell fitted with a sacrificial Mg anode and RVC cathode containing $AgNO_3$ (0.3 equiv.). Then, the reaction was electrolyzed (~2.5 F/mol, 2.5 hours) at ambient temperature.

Application to total and formal syntheses

With a viable method in hand for chemoselective and modular C–C coupling, execution of the blueprint outlined in Fig. 1 could be explored. Rather than pursue a tabular listing of coupling partners to illustrate functional group tolerance and geometric control (all stereoretentive), the value of the methodology was exemplified through the total or formal synthesis of 13 terpene natural products (Fig. 3). A range of functional groups is tolerated, including epoxides, alkynes, alcohols, free carboxylic acids on the vinyl iodide, esters, ethers, ketones, enones, aldehydes, electron-rich (hetero)aromatics, β-keto esters, and skipped dienes. The simplification enabled by this method is apparent in three polyene cyclization precursors prepared en route to complex terpene natural products: progesterone (**8**), celastrol (**9**), and isosteviol (**10**).

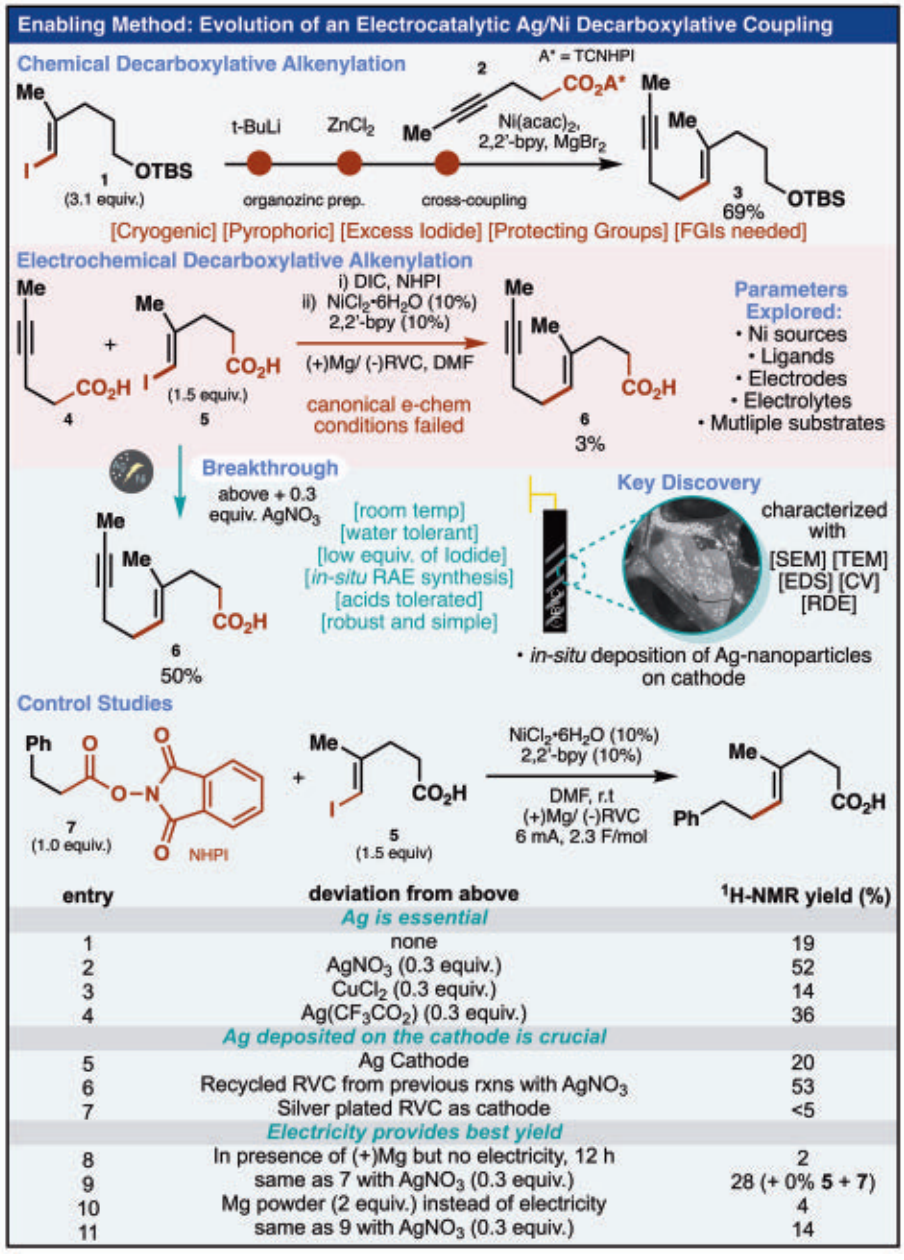

entry	deviation from above	^{1}H-NMR yield (%)
	Ag is essential	
1	none	19
2	$AgNO_3$ (0.3 equiv.)	52
3	$CuCl_2$ (0.3 equiv.)	14
4	$Ag(CF_3CO_2)$ (0.3 equiv.)	36
	Ag deposited on the cathode is crucial	
5	Ag Cathode	20
6	Recycled RVC from previous rxns with $AgNO_3$	53
7	Silver plated RVC as cathode	<5
	Electricity provides best yield	
8	In presence of (+)Mg but no electricity, 12 h	2
9	same as 7 with $AgNO_3$ (0.3 equiv.)	28 (+ 0% **5** + **7**)
10	Mg powder (2 equiv.) instead of electricity	4
11	same as 9 with $AgNO_3$ (0.3 equiv.)	14

Fig. 2. The discovery and optimization of the electrocatalytic methodology is described. The published decarboxylative alkenylation is a prototypical example of literature methods to construct sp^2–sp^3 bonds requiring harsh reagents, cryogenic temperatures, protecting groups, and functional group interconversions (FGIs). Initial electrochemical conditions were insufficient to accomplish the envisioned plan to cross-couple in situ–activated acids and halo-acid modules. The addition of $AgNO_3$ (0.3 equiv.) to the reaction was a breakthrough. Control experimentation suggests that nanosilver on the cathode is responsible for the improved yield and that electrochemistry offers a distinct advantage over other systems. OTBS, tert-butyldimethylsilyl ether.

A protecting group free synthesis of progesterone precursor **8** begins with the electrochemical cross-coupling of two simple acids **4** (in situ activated) and **5** (prepared in two steps via carboiodination and oxidation). The product acid **6** was next in situ activated and coupled to a vinyl iodide bearing a free alcohol (**11**). Alcohol **12** was converted to the bromide (**13**) via Appel conditions and coupled to 2-iodo-3-methylcyclopentenone using an electrochemical reaction inspired by Hansen's electrochemical conditions (see tables S3 to S6) to deliver the desired polyene endpoint (**8**) directly (*22*). By contrast, similar reported couplings have employed Suzuki conditions, which required three steps to prepare a suitable

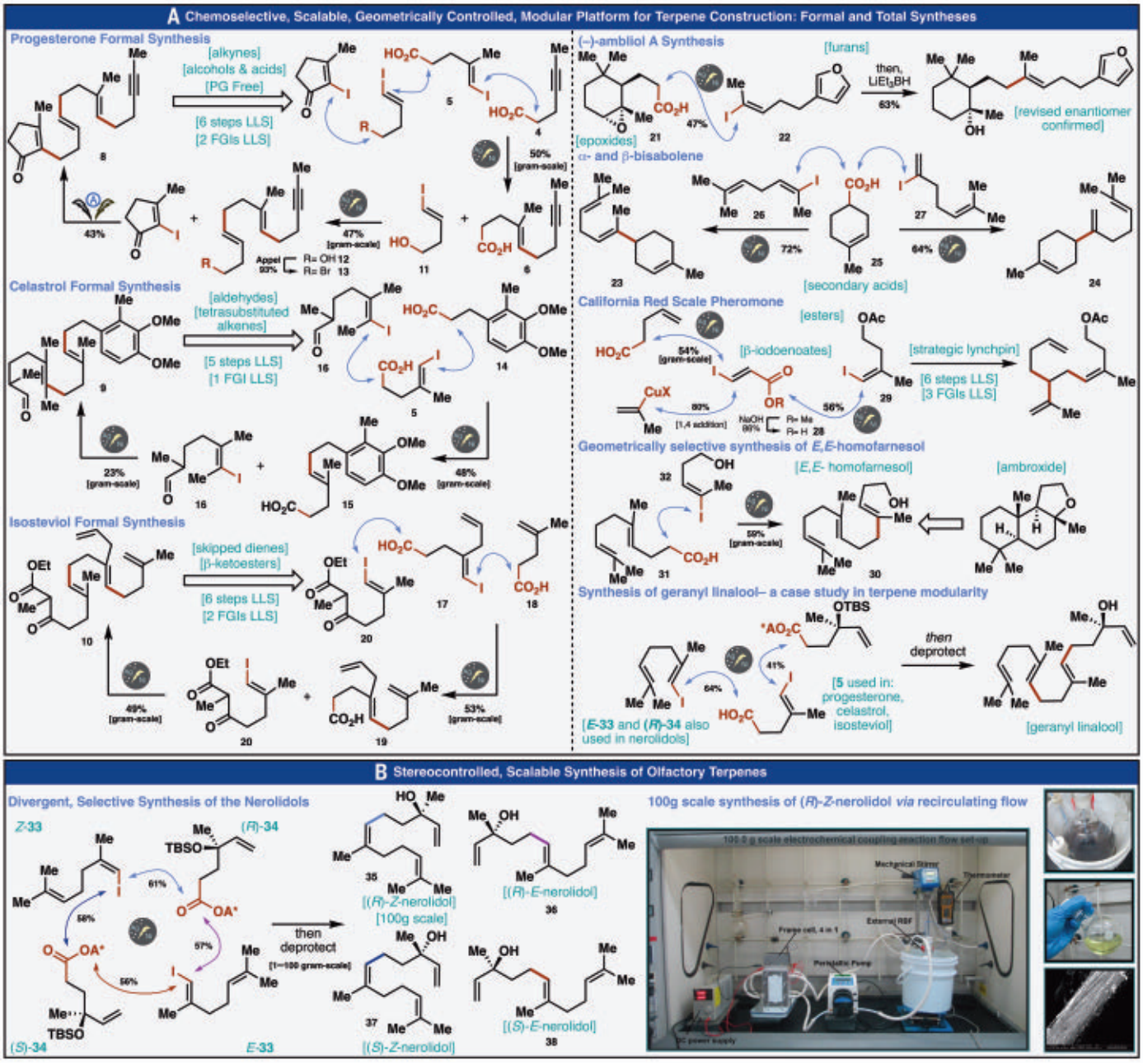

Fig. 3. The utility and scalability of the developed electrocatalytic methodology is showcased through the formal or total synthesis of 13 natural products. (**A**) Three polyene cyclization precursors and five natural products are synthesized through iterative electrochemical cross-electrophile couplings showing a functional group tolerance inclusive of alkynes, alcohols, acids, esters, ketones, enones, aldehydes, ethers, epoxides, electron-rich heteroaromatics, and skipped dienes. (**B**) A unified and scalable synthesis of the four nerolidol isomers is described. A recirculating flow system was used to conduct a 100-g-scale electrochemical cross-coupling. The large image showcases the complete flow system consisting of a frame cell, power source, peristaltic pump, round bottom flask reservoir, and a mechanical stirrer. On right: (top) reaction reservoir, (middle) pure product after column chromatography, (bottom) SEM image of the Ag-nanoparticle–embedded carbon felt cathode after reaction.

trifluoroborate-containing coupling partner (*23*). This modular and intuitive approach takes place in six steps (longest linear sequence, LLS) relying on a single FGI and oxidation step without resorting to any protecting groups. By contrast, Johnson's synthesis of progesterone arrived at the target polyene in eight steps (LLS) with two FGIs and two protecting group (PG)–related steps (*5*). In 2016, Dudley and co-workers published a 10-step total synthesis of progesterone that also prepares polyene **8** in six steps LLS with one FGI and one oxidation (*23*).

Siegel's elegant approach to **9** leveraged a distinctive polyene cyclization precursor bearing a tetra-substituted alkene and an electron rich arene (*24*). Cleverly, inherent symmetry was exploited to arrive at the polyene in nine steps, with one FGI and one oxidation. The use of a Horner-Wadsworth-Emmons (HWE) reaction led to a 6:1 mixture of *E*/*Z* isomers, highlighting the challenges associated with

approaches that construct polyolefin cyclization precursors through Wittig-like transforms. By contrast, the modular assembly approach breaks bonds adjacent to the olefins and programs the alkene geometry at the outset. The synthesis commences with in situ activation of acid **14** and electrochemical coupling with the same vinyl iodide **5** used in the synthesis of **8**. The product acid **15** was subsequently activated and coupled with tetra-substituted vinyl iodide **16** bearing a reactive aldehyde to complete the formal synthesis endpoint of celastrol (**9**) in five steps.

Snider's impressive synthesis of isosteviol relied on pioneering oxidative radical cascade methodology from polyene **10**—prepared in ten steps (LLS) with two FGIs and three redox manipulations (*25*). Our initial attempts using more traditional organometallic cross-coupling chemistry (Fig. 2) yielded no success in the first coupling (fig. S9). Using vinyl organolithium reagents led to a retro-lithium ene reaction to expel allyl lithium, and treating the allyl vinyl iodide **17** with organometallic reagents led to recovery of vinyl iodide. The only conditions identified capable of forging the desired bond between the acid **18** and skipped diene **17** were the developed electrochemical conditions, which gratifyingly gave the desired product acid **19** in 53% isolated yield on gram scale. The resulting acid **19** was activated and coupled to vinyl iodide **20** bearing the reactive β-ketoester functionality (a testament to the functional group compatibility of the developed conditions), providing more than a gram of polyene **10** in six steps LLS.

To further test the capabilities of the developed methodology, a broad range of terpenes was targeted. The diterpene, ambliol A, first isolated from the marine sponge *Dysidea amblia* by Faulkner in 1981 off the Pacific coast (La Jolla), was chosen as an attractive target to synthesize for its antibiotic activity and distinctive functionality (*26*, *27*). Only recently (2015) was an enantioselective synthesis of (+)-ambliol A accomplished by Serra and Lissoni using an enzymatic resolution in 16 steps LLS (*28*). That synthesis led to a revision of the original enantiomeric assignment. By contrast, a convergent synthesis of (−)-ambliol A utilizing the developed electrochemical conditions was achieved in just five steps LLS by coupling the enantiopure epoxy-acid **21** (confirmed via x-ray crystallography; fig. S112) with furan **22** in 47% yield followed by reductive epoxide opening ($LiEt_3BH$), thus unambiguously confirming its stereochemical revision and enabling the first synthetic access to the natural enantiomer.

The sesquiterpenes (*E*)-α- and β-bisabolenes (**23** and **24**), which function in nature as pheromone molecules for a number of insects, were an opportunity to test the electrochemical cross-coupling on secondary acids (*29*). Targeting the central sp^2–sp^3 junction for disconnection, syntheses of **23** and **24** diverged from secondary acid **25** and enlisted vinyl iodide **26** or **27** to furnish **23** and **24** in 72 and 64% yield, respectively. The more stabilized secondary radical generated from the acid coupled efficiently under the standard reaction conditions, providing access to both natural products in three steps LLS.

The California red scale sex pheromone, produced by an invasive citrus pest, was originally identified in 1977 by Gieselmann and coworkers and is used by the females to attract males (*30*). Its synthesis has applications in the agricultural industry as a replacement for virgin female traps in monitoring the pest's population. Strategically, a synthesis was envisioned that leveraged a β-iodo-enoate as a linchpin fragment capable of forging three key C–C bonds off the central two-carbon linker. This concept was realized by first cross-coupling 4-pentenoic acid with methyl (*E*)-3-iodoacrylate in 54% yield, followed by a conjugate addition and saponification in 80 and 86% yield, respectively, to provide acid **28**. The synthesis could be completed by coupling **28** and acetate **29**; however, upon generation of the primary radical under the reaction conditions, it underwent a 5-exo-trig cyclization before cross-coupling of the vinyl iodide could take place. This problem was obviated by increasing the nickel catalyst loading to 40 mol % to provide California red scale pheromone in 56% yield and six steps LLS (*31*).

The importance of the homologated terpene (*E,E*)-homofarnesol (**30**) stems from its use as a cyclization precursor to the vital terpene Ambrox (ambroxide)—a molecule with a storied history dating back to the 15th century (*32*). Many of the reported syntheses of **30** rely on [2,3] rearrangements of the nerolidols that lead to mixtures of *E*/*Z* isomers which, if not carefully separated, give complex mixtures of cyclization products that harm its fragrant properties (*33*). By contrast, acid **31** (readily prepared from geranyl bromide and diethyl malonate) was in situ activated and coupled with vinyl iodide **32** bearing a free alcohol to arrive directly at (*E,E*)-homofarnesol (>4 g prepared in a single pass).

The diterpene geranyl linalool was synthesized through two sequential cross-couplings of common fragments: one of which was employed in the synthesis of progesterone and celastrol and the other two of which were used to access nerolidols (Fig. 3B). This mix-and-match strategy for opportunistically accessing naturally occurring terpenes highlights the advantage of using the modular logic also employed in the biosynthetic cyclase phase.

Notwithstanding the value of the disclosed methods to the academic pursuit of complex terpene total synthesis, nowhere is the study and utilization of linear terpenes more apparent than in the fragrance and flavor industry (>$30-billion-dollar per annum) (*4*). Given the sensitivity of human olfactory receptors, single terpene isomers of high purity are desired to ensure precise flavor and fragrance profiles because small changes in structure can create very different properties (*34*, *35*). One class of terpene targets, nerolidol, seemed particularly relevant in this context. A unified, controllable synthesis of the linear terpenes (*E*)- and (*Z*)-nerolidol, produced naturally as a mixture of four isomers derived from nerol and geraniol, has remained an unanswered synthetic challenge for over four decades. Whereas their synthesis and separation have been explored, preparative methods of separation or synthesis are expensive and laborious (*36*). Indeed, the extreme price disparity between the racemic mixture of isomers (~$0.09/g, Sigma-Aldrich), and the geometrically pure racemate (*trans:* $610/g, Sigma-Aldrich; *cis*: $343 to $2460/g, various suppliers) is cost-prohibitive, and the enantiopure natural products are not commercially available. Despite the difficulty in purification, nerolidol is estimated to be used per annum in quantities ranging from 10 to 100 metric tons and appears in products like shampoos, perfumes, and detergents and as a flavor additive (*37*). The need for a selective and programmable synthesis of these four isomers stems from their differing fragrance profiles.

To synthesize (*E*)- and (*Z*)- nerolidols, we imagined that these isomers could arise from two geometrically differentiated vinyl iodides (***E*-33** and ***Z*-33**, respectively) and enantiomeric RAEs derived from (*R*)- and (*S*)-linalool, respectively (***R*-34, *S*-34**). A simple mix-and-match union of the modules resulted in the controlled synthesis of **35**–**38** in 44 to 60% yield after deprotection. As a proof of concept for the scalability of the method, **35** was arbitrarily chosen, and the electrochemical coupling was performed on 100-g scale (at Asymchem; see inset photos). Of note, analysis of the electrodes in this large-scale flow run confirmed that Ag nanoparticles were present at a surface coverage of Ag analogous to small-scale reactions requiring only 0.07 equiv. of Ag (see figs. S47 and S48).

Mechanistic studies

Although the observations from the above syntheses suggested that the homogeneous Ni catalysis behaved according to literature precedent for radical cross-coupling (*31*), the impact of electrode surface functionalization on this methodology warranted further study, as existing $C(sp^3)$-$C(sp^2)$ decarboxylative coupling conditions failed to match the efficiency of the developed protocol (Fig. 4 and table S44). An induction period was observed that corresponded in duration to the amount of

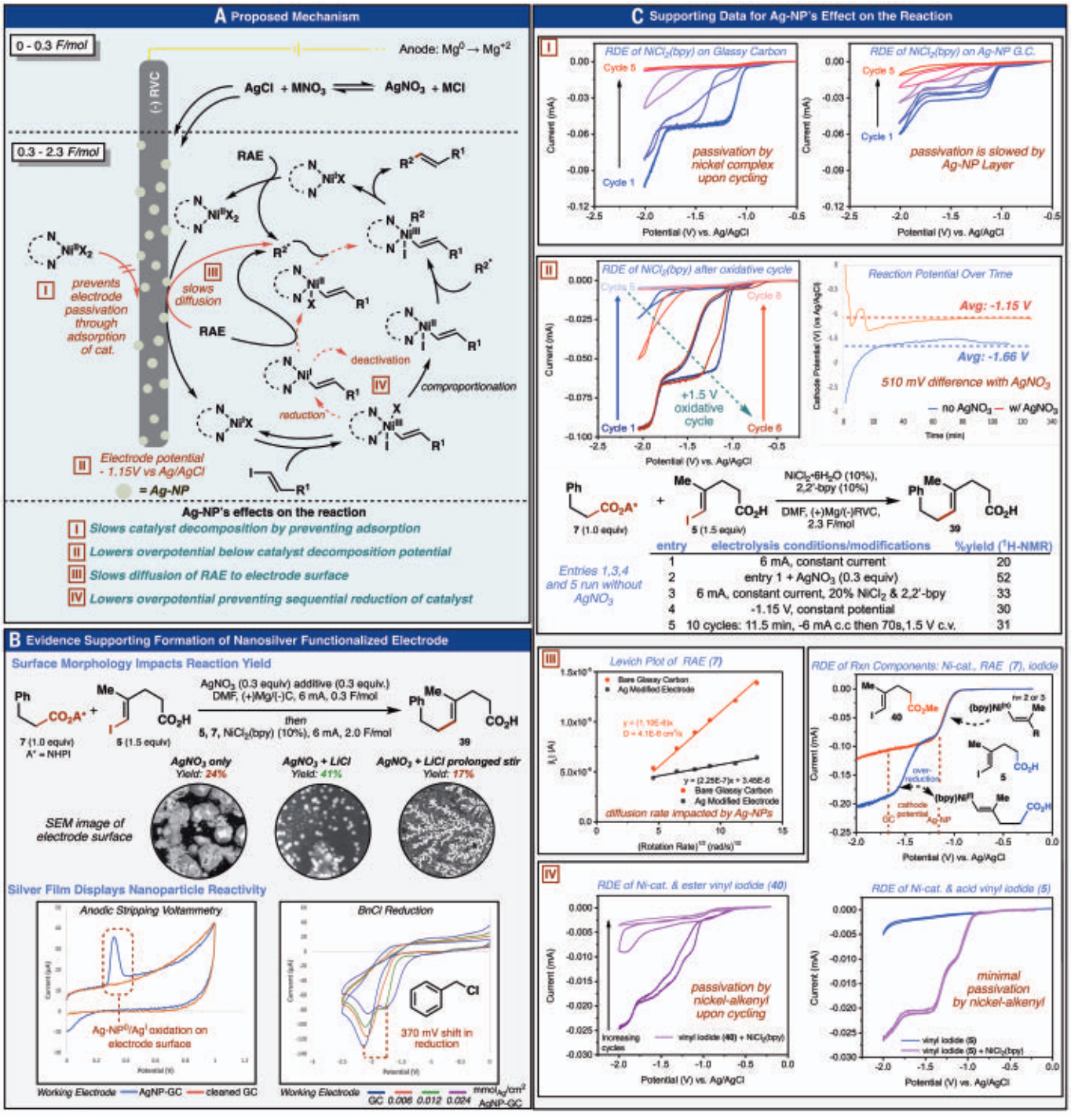

Fig. 4. The presence of silver nanoparticles on the electrode surface is confirmed and the specific roles of the silver nanoparticle layer are posited. (**A**). A mechanism is proposed, with Roman numerals indicating points of interaction with the Ag-nanoparticle layer. The silver layer slows catalyst decomposition (I), decreases overpotential so that the electrode potential falls below the decomposition potential (II), limits diffusion and mass transport of the RAE to the electrode surface (III), and prevents sequential reduction of the catalyst (IV). (**B**) Control studies and SEM and TEM imaging identify that the reaction conditions produce Ag-nanoparticles on the electrode surface, a halide source is required, and photodecomposition of the silver-halide solution before electrolysis prevents nanoparticulate formation and diminishes the reaction yield. (**C**) Rotating disk electrode (RDE) voltammetry provides supporting evidence for the differences between the Ag-nanoparticle functionalized and unfunctionalized glassy carbon electrodes. (I) RDE voltammetric profiles (at 1600 rpm) of the Ni(bpy) catalyst at bare and Ag-NP–modified glassy carbon electrodes. (II) Regeneration of activity, time evolution of cathode potential, and product yields under various electrolysis conditions. (III) Levich plots (I versus $\omega^{-1/2}$) for $NiCl_2$(bpy) catalyst and RAE **7**. [IV] RDE voltammetric profiles of vinyl iodides **5** (right) and **40** (left) at bare glassy carbon electrodes exhibiting EC_{cat} kinetics (note the two reduction waves). RDE voltammetric profile of reaction components (top) (1 mM $NiCl_2$(bpy), 10 mM RAE **7**, 15 mM vinyl iodide (**40,** red trace; **5**, blue trace). Second reduction wave at present −1.48 V versus Ag/AgCl with **5**, but not with **40.**

$AgNO_3$ added, suggesting that silver reduction preceded the cross-coupling reaction (figs. S19 and S20). Despite the use of nanoparticulate silver in heterogeneous catalysis, we have not found prior examples in which it supports and/or improves homogeneous catalysis in organic synthesis (*38*). By contrast, the field of electroanalytical sensors routinely uses electrode functionalization to engender selectivity for a specific analyte, even in the presence of species with nearly identical reduction potentials on unmodified electrode surfaces (*39*, *40*). This selectivity arises from the ability of the Ag nanoparticles to lower the overpotential (*41*) required to reduce or oxidize an analyte of interest (*42*). Additionally, selectivity can manifest as a change in the reduction potential (potential shift to less driving potentials of the voltametric wave) through metal particle–analyte interactions (*43*–*47*). Many analyte-specific sensors have been developed by using Ag-nanoparticle–decorated electrodes (*43*–*46*). Preparations of Ag-modified electrodes for sensor applications include drop casting a suspension of preformed Ag nanoparticles onto a surface and drying, or cathodic reduction of a solution of silver(I), with the latter being markedly similar to the procedure used in this developed cross-coupling reaction (*48*). To better understand the interplay between the electrode surface modification by silver and homogeneous nickel catalysis, we conducted several experiments.

First, modified electrode surfaces were characterized by scanning electron microscopy (SEM) imaging, transmission electron microscopy (TEM), and energy-dispersive x-ray spectroscopy (EDS) (Fig. 4B). When $AgNO_3$ alone was electrodeposited before the start of the reaction, the glassy carbon electrodes were coated with a gray film. The use of these modified electrodes yielded only 24% of product **39** between RAE **7** and vinyl iodide **5**. SEM imaging showed that although large silver crystals formed (1 to 5 μm in diameter), there were very small amounts of nanoparticulate silver on the electrode surface. However, addition of LiCl to this prereaction electrodeposition produced electrodes with improved reaction performance [41% NMR (nuclear magnetic resonance) yield]. SEM and TEM analyses of these electrode surfaces revealed the presence of nanoparticulate silver in sizes ranging from 10 to 100 nm in diameter (figs. S36 to S40). Control studies verified the need for a halide source, but LiCl was not required in the coupling reactions because $NiCl_2$ could serve as the halide donor in the preparative reactions. The reaction of $AgNO_3$ and halides in solution produces photosensitive silver halide salts that readily decompose. Electrodes modified with a $AgNO_3$ and LiCl solution that had been allowed to stir for several minutes before electrolysis were evaluated in the coupling reaction. In such cases, only a 17% yield of **39** was obtained, and very little nanoparticulate silver was observed in microscopic characterization (figs. S44 and S45). Collectively, these results suggest that nanoparticulate silver electrodeposited before the cross-coupling reaction is present and responsible, at least in part, for the improved performance.

To compare reactivity of these nanoparticle-coated electrodes in the cross-coupling with known reactivity of similarly functionalized electrodes, we also functionalized glassy carbon disk electrodes. Nanoparticle deposition on this disk electrode was validated by anodic stripping voltammetry (Fig. 4B) and by SEM and TEM imaging (figs. S51 and S52) (*43*). The reduction potential of benzyl chloride is known to shift 500 mV more positive on a silver-nanoparticle–decorated electrode, and such behavior was observed on our nanoparticle-coated disk (*46*). Cyclic voltametric studies of reductively labile components of the cross coupling, $NiCl_2$(bpy) and RAE **7**, revealed no appreciable differences in the onset of reduction of these two species at the functionalized electrode in comparison to glassy carbon surfaces (figs. S55 to S76).

The kinetic behavior of the modified electrode was then studied by rotating disk electrode (RDE) voltammetry (*49*). In the case of $NiCl_2$(bpy), a diminished current response in consecutive cycles at an unmodified glassy carbon RDE was observed. The decrease in the current with cycling is mitigated if the potential range is limited to a smaller (less negative) reductive window (lower potential cutoff of −1.6 V versus Ag/AgCl, fig. S83). Additionally, when the same measurements were performed with the silver-nanoparticle–modified RDE, the peak current response of the Ni(II)/Ni(0) redox couple was slightly lower and its current also decreased with continuous cycling, but at a notably slower rate (Fig. 4, C-I). The initial current response could be restored to the glassy carbon electrode by a potential excursion to +1.5 V versus Ag/AgCl, indicating that passivation is likely occurring through overreduction and deposition of the catalyst on the electrode surface. Supporting this hypothesis, the cathode potential (at constant current) of the reaction revealed a notable difference between the reactions with and without $AgNO_3$. The potential of the reaction in the presence of $AgNO_3$ ($E_{cathode}$ = −1.15 V versus Ag/AgCl) was 510 mV more positive than the reaction without silver ($E_{cathode}$ = −1.66 V versus Ag/AgCl). This shift in potential (effectively a lower overpotential) could prevent the overreduction of the catalyst, which we believe to be responsible for the passivation of the electrode. To test this hypothesis (Fig. 4C-II), we ran the reaction with doubled catalyst loading [$NiCl_2$•$6H_2O$ (20 mol %), 2,2′-bpy (20 mol %], which resulted in a modest 13% increase in yield in the absence of the silver salt. Next, the cross-coupling reaction was run at a constant potential of −1.15 V versus Ag/AgCl with standard catalyst loading without a silver salt. These conditions resulted in a 10% increase in the yield of **39**. Furthermore, a reaction conducted with intermittent potential excursions to +1.5 V (70 s at +1.5 V versus Ag/AgCl for every 11.5 min of −6 mA) resulted in an 11% increase in the yield of **39**, consistent with the results of the RDE experiments and further providing evidence for catalyst overreduction, and electrode passivation, at more forcing potentials—a deleterious process partially obviated by the silver layer.

A comparison of the Levich (I vs $\omega^{-1/2}$) analysis (Fig. 4C-III) of the catalyst and the RAE **7** showed that diffusion of $NiCl_2$(bpy) was not noticeably affected by the silver nanoparticle layer (the calculated diffusion coefficient decreased by a factor of 2) (*45*). However, **7** showed a notable change in its diffusion behavior on the silver nanoparticle–functionalized RDE. Although at slow rates of rotation, the currents at the bare and Ag-modified electrodes were comparable, at faster rates of rotations there was a clear divergence. Moreover, upon extrapolation to zero rotation, the intercept is clearly nonzero, suggesting possible adsorptive effects. To investigate if the reduction is occurring at the Ag nanoparticles or at the surface of the carbon electrode, we compared the cyclic voltammograms of the RAE and the Ni catalyst at a Ag electrode and a glassy carbon electrode to that of a Ag nanoparticle–modified glassy carbon electrode (fig. S93). The Ag-modified electrode exhibited the same features as the glassy carbon electrode, though not those of the Ag electrode, suggesting that most of the reductive events likely occur at the glassy carbon surface and require the redox-active species to diffuse through the Ag nanoparticle (NP) film to be reduced. Taken collectively with the results of reaction progress over time (figs. S19 and S20), these results suggest that a decrease in direct reduction of RAE at the cathode is likely responsible, at least in part, for the improved reaction yield.

Investigations of the vinyl iodides **5** and **40** revealed that although direct reduction does not occur, differences in behavior exist between these two model vinyl iodides when $NiCl_2$(bpy) and RAE are present (Fig. 4C-IV). When RDE voltammetry was conducted with $NiCl_2$(bpy) and **40**, a catalytic current response was observed at the Ni(0)/Ni(II) redox couple (resulting from the oxidative addition of the vinyl iodide) consistent with EC_{cat} kinetics (where E represents an electron transfer and C_{cat} represents a subsequent chemical step that regenerates the initial electroactive species) and the previously mentioned electrode passivation. Furthermore, in the presence of RAE **7**, this passivation behavior disappeared

when using the methyl ester vinyl iodide **40**. Use of halo-acid **5** in these measurements generated a catalytic current without much electrode passivation even in the absence of RAE. Unexpectedly, after addition of RAE **7** to halo-acid **5** and $NiCl_2$(bpy), the second reduction wave was still observed at −1.48 V versus Ag/AgCl. We propose that this wave is the electrochemical reduction of a nickel (II/III) alkenyl to a nickel (I) alkenyl intermediate (*46*, *47*). This profound difference in behavior when using halo-acid **5** instead of methyl ester **40** has important implications for the detrimental behavior of carboxylic acids on reaction yield in the absence of $AgNO_3$. Recent evidence has emerged suggesting the deactivation of nickel (I) intermediates through dimerization or aggregation (*48*). One can also imagine how this reduced species could accelerate the consumption of RAE in the homogeneous environment (*49*). Comparing the onset of these two reduction waves to the cathode potential of the reaction without $AgNO_3$ ($E_{cathode}$ = −1.66 V versus Ag/AgCl) and with $AgNO_3$ ($E_{cathode}$ = −1.15 V versus Ag/AgCl) is particularly informative. This finding implied that the Ag-NP layer decreases overpotential to the point immediately before the second reduction wave, whereas with the use of bare glassy carbon electrodes, more reducing potentials beyond the second wave under standard reaction conditions (constant current) are applied.

In summary, it appears that the silver-NP layer on the electrode has several effects on the reaction components. First, the silver-NP layer lowers the overpotential preventing catalyst overreduction and electrode passivation. Second, the lower overpotential also inhibits the formation of Ni(I)-alkenyl intermediates, which appear to form even in the presence of RAEs when using vinyl iodides bearing carboxylic acids. Third, this layer slows mass transport and reduction of RAEs at the electrode surface likely from complications arising with adsorptive behavior, whereas diffusion of the catalyst is slightly affected. Though no singular result explains the role of the silver-NP layer, we hypothesize that the overall benefit observed is likely the result of the findings discussed above working in concert. Further interdisciplinary studies between synthetic, electroanalytical, and materials specialists will likely provide deeper insights into this discovery.

Outlook

This study of terpene synthesis has provided an efficient platform for the modular construction of polyunsaturated molecules with precise geometrical control (*50*). Its implementation required methodological advancement, thereby revealing a relationship between productive catalysis and materials science. Electrochemistry offers chemists enabling opportunities through variables that are specifically available to it. Electrode modification offers new possibilities for synthetic chemists to optimize difficult reactions—analytical chemists and physical chemists have long embraced this concept to overcome their own chemical challenges. The potential of these parameters to enable useful chemical reactivity is an attractive area for further study.

REFERENCES AND NOTES

1. K. C. Nicolaou, E. J. Sorensen, *Classics in Total Synthesis: Targets, Strategies, Methods* (VCH, 1996). pp. xxiii–798.
2. D. Cox-Georgian, N. Ramadoss, C. Dona, C. Basu, "Therapeutic and Medicinal Uses of Terpenes" in *Medicinal Plants*, N. Joshee, S. Dhekney, P. Parajuli, Eds. (Springer, 2019), pp. 333–359 (2019).
3. D. J. Jansen, R. A. Shenvi, *Future Med. Chem.* **6**, 1127–1148 (2014).
4. S. Serra, in *Studies in Natural Products Chemistry*, R. Atta ur, Ed. (Elsevier, 2015), vol. 46, pp. 201–226.
5. W. S. Johnson, M. B. Gravestock, B. E. McCarry, *J. Am. Chem. Soc.* **93**, 4332–4334 (1971).
6. R. A. Yoder, J. N. Johnston, *Chem. Rev.* **105**, 4730–4756 (2005).
7. C. N. Ungarean, E. H. Southgate, D. Sarlah, *Org. Biomol. Chem.* **14**, 5454–5467 (2016).
8. C. Thirsk, A. Whiting, *J. Chem. Soc. Perkin Trans.* **1**, 999–1023 (2002).
9. E. Negishi, G. Wang, H. Rao, Z. Xu, *J. Org. Chem.* **75**, 3151–3182 (2010).
10. J. Li, A. S. Grillo, M. D. Burke, *Acc. Chem. Res.* **48**, 2297–2307 (2015).
11. P. M. Dewick, "The mevalonate and methylerythritol phosphate pathways: Terpenoids and steroids" in *Medicinal Natural Products. A Biosynthetic Approach* (Wiley, ed. 2, 2002), pp. 167–289.
12. J. M. Smith, S. J. Harwood, P. S. Baran, *Acc. Chem. Res.* **51**, 1807–1817 (2018).
13. D. S. Peters *et al*., *Acc. Chem. Res.* **54**, 605–617 (2021).
14. J. T. Edwards *et al*., *Nature* **545**, 213–218 (2017).
15. C. Cannes, S. Condon, M. Durandetti, J. Périchon, J. Y. Nédélec, *J. Org. Chem.* **65**, 4575–4583 (2000).
16. L. F. T. Novaes *et al*., *Chem. Soc. Rev.* **50**, 7941–8002 (2021).
17. T. Wirtanen, T. Prenzel, J.-P. Tessonnier, S. R. Waldvogel, *Chem. Rev.* **121**, 10241–10270 (2021).
18. J. M. Campelo, D. Luna, R. Luque, J. M. Marinas, A. A. Romero, *ChemSusChem* **2**, 18–45 (2009).
19. K. M. M. Huihui *et al*., *J. Am. Chem. Soc.* **138**, 5016–5019 (2016).
20. T. Koyanagi *et al*., *Org. Lett.* **21**, 816–820 (2019).
21. H. Li *et al*., *Org. Lett.* **20**, 1338–1341 (2018).
22. R. J. Perkins, D. J. Pedro, E. C. Hansen, *Org. Lett.* **19**, 3755–3758 (2017).
23. R. Slegeris, G. B. Dudley, *Tetrahedron* **72**, 3666–3672 (2016).
24. A. M. Camelio, T. C. Johnson, D. Siegel, *J. Am. Chem. Soc.* **137**, 11864–11867 (2015).
25. B. B. Snider, J. Y. Kiselgof, B. M. Foxman, *J. Org. Chem.* **63**, 7945–7952 (1998).
26. R. P. Walker, D. J. Faulkner, *J. Org. Chem.* **46**, 1098–1102 (1981).
27. J. E. Thompson, R. P. Walker, D. J. Faulkner, *Mar. Biol.* **88**, 11–21 (1985).
28. S. Serra, V. Lissoni, *Eur. J. Org. Chem.* **2015**, 2226–2234 (2015).
29. R. H. Scheffrahn, L. K. Gaston, J. J. Sims, M. K. Rust, *J. Chem. Ecol.* **9**, 1293–1305 (1983).
30. W. L. Roelofs *et al*., *Nature* **267**, 698–699 (1977).
31. D. J. Weix, *Acc. Chem. Res.* **48**, 1767–1775 (2015).
32. C. Brito, V. L. Jordão, G. J. Pierce, *J. Mar. Biol. Assoc. U. K.* **96**, 585–596 (2016).
33. A. F. Barrero, J. Altarejos, E. J. Alvarez-Manzaneda, J. M. Ramos, S. Salido, *J. Org. Chem.* **61**, 2215–2218 (1996).
34. V. Schubert, A. Dietrich, T. Ulrich, A. Mosandl, *Z. Naturforsch. C J. Biosci.* **47**, 304–307 (1992).
35. G. Ben Salha, M. Abderrabba, J. Labidi, *Rev. Chem. Eng.* **37**, 433–447 (2021).
36. W.-K. Chan, L. T. Tan, K.-G. Chan, L.-H. Lee, B.-H. Goh, *Molecules* **21**, 529 (2016).
37. D. McGinty, C. S. Letizia, A. M. Api, *Food Chem. Toxicol.* **48** (Suppl 3), S43–S45 (2010).
38. X.-Y. Dong, Z.-W. Gao, K.-F. Yang, W.-Q. Zhang, L.-W. Xu, *Catal. Sci. Technol.* **5**, 2554–2574 (2015).
39. R. R. Chillawar, K. K. Tadi, R. V. Motghare, *J. Anal. Chem.* **70**, 399–418 (2015).
40. J.-M. Zen, A. Senthil Kumar, D.-M. Tsai, *Electroanalysis* **15**, 1073–1087 (2003).
41. J. E. Nutting, J. B. Gerken, A. G. Stamoulis, D. L. Bruns, S. S. Stahl, *J. Org. Chem.* **86**, 15875–15885 (2021).
42. X. Luo, A. Morrin, A. J. Killard, M. R. Smyth, *Electroanalysis* **18**, 319–326 (2006).
43. C. M. Welch, C. E. Banks, A. O. Simm, R. G. Compton, *Anal. Bioanal. Chem.* **382**, 12–21 (2005).
44. C. M. Fox, C. B. Breslin, *J. Appl. Electrochem.* **50**, 125–138 (2020).
45. C. Karuppiah *et al*., *RSC Advances* **5**, 31139–31146 (2015).
46. A. A. Isse, S. Gottardello, C. Maccato, A. Gennaro, *Electrochem. Commun.* **8**, 1707–1712 (2006).
47. X. Ren, X. Meng, D. Chen, F. Tang, J. Jiao, *Biosens. Bioelectron.* **21**, 433–437 (2005).
48. M. A. Bhosale, B. M. Bhanage, *Curr. Org. Chem.* **19**, 708–727 (2015).
49. R. G. Compton *et al*., *Proc. R. Soc. Lond. A* **418**, 113–154 (1988).
50. J. Gu *et al*., *ChemRxiv. Cambridge: Cambridge Open Engage* doi: 10.26434/chemrxiv-2021-kn6tl (2021).

ACKNOWLEDGMENTS

We thank D.-H. H. and L.P. for assistance with NMR spectroscopy; J. Chen, B. Sanchez, and E. Sturgell (Scripps Automated Synthesis Facility) for assistance with high-performance liquid chromatography, high-resolution mass spectrometry, and liquid chromatography–mass spectrometry and A. Rheingold, M. Gembicky, and E. Samolova (University of California, San Diego) for assistance with x-ray crystallography. We are grateful to University of Utah shared facilities of the Micron Technology Foundation Inc. We thank J. Vantourout, Y. Kawamata, S. Gnaim, Y. Y. See, J. Edwards, K. McClymont, C. Bi, and B. Smith for insightful discussions; K. X. Rodriguez, J. Gu, A. L. Rerick, and C. R. Pitts, for their use of this chemistry in other systems; and K. Eberle, G. Laudadio, A. Garrido-Castro, and M. Condakes for assistance in the preparation of the manuscript. **Funding:** Financial support for this work was provided by the NIH (MIRA GM-118176), NSF Center for Synthetic Organic Electrochemistry (CHE-2002158), and the Microscopy Suite sponsored by the College of Engineering, Health Sciences Center, Office of the Vice President for Research, the Utah Science Technology and Research (USTAR) initiative of the State of Utah and, in part, by the MRSEC Program of the NSF under Award no. DMR-1121252. S.J.H. thanks the Fletcher-Jones Foundation for fellowship funding. M.D.P. thanks Richard and Nicola Lerner for the Endowed Fellowship. **Author contributions:** S.J.H. and P.S.B. conceived of the work. S.J.H., M.D.P., C.N.G., P.P., H.D.A., S.L.A., and P.S.B. designed the experiments. S.J.H., M.D.P., C.N.G., and P.P. ran the experiments. S.J.H., M.D.P., C.N.G., P.P., H.D.A., S.L.A., and P.S.B. analyzed the data. Z.Y. and L.S. conducted the flow-reactor scale-up. S.J.H., M.D.P., and P.S.B. wrote the manuscript. C.N.G., P.P., H.D.A., and S.L.A. provided revisions. **Competing interests:** The authors declare no competing interests. **Data and materials availability:** Experimental and analytical procedures and full spectral data are available in the supplementary materials. X-ray data and models are available at the Cambridge Crystallographic Data Centre under accession numbers CCDC-2033224 (**S12**) and CCDC-2109535 ($NiCl_3(PtBu_3)$ • $HPtBu_3$).

SUPPLEMENTARY MATERIALS

science.org/doi/10.1126/science.abn1395
Materials and Methods
Figs. S1 to S114
Tables S1 to S62
References (*51–102*)

5 November 2021; accepted 18 January 2022
10.1126/science.abn1395

RIVER ECOLOGY

Reducing adverse impacts of Amazon hydropower expansion

Alexander S. Flecker[1]*, Qinru Shi[2], Rafael M. Almeida[1,3]†, Héctor Angarita[4,5,6], Jonathan M. Gomes-Selman[7], Roosevelt García-Villacorta[1,8], Suresh A. Sethi[3], Steven A. Thomas[9], N. LeRoy Poff[10,11], Bruce R. Forsberg[12,13], Sebastian A. Heilpern[3,14], Stephen K. Hamilton[15,16], Jorge D. Abad[17]‡, Elizabeth P. Anderson[18], Nathan Barros[19], Isabel Carolina Bernal[20], Richard Bernstein[2,21], Carlos M. Cañas[22]§, Olivier Dangles[23], Andrea C. Encalada[24], Ayan S. Fleischmann[25]¶, Michael Goulding[26], Jonathan Higgins[27], Céline Jézéquel[28], Erin I. Larson[1,29], Peter B. McIntyre[3], John M. Melack[30], Mariana Montoya[22], Thierry Oberdorff[28], Rodrigo Paiva[25], Guillaume Perez[2], Brendan H. Rappazzo[2,21], Scott Steinschneider[31], Sandra Torres[32,33], Mariana Varese[22], M. Todd Walter[31], Xiaojian Wu[2]#, Yexiang Xue[2,21,34], Xavier E. Zapata-Ríos[32,33], Carla P. Gomes[2,21]*

Proposed hydropower dams at more than 350 sites throughout the Amazon require strategic evaluation of trade-offs between the numerous ecosystem services provided by Earth's largest and most biodiverse river basin. These services are spatially variable, hence collective impacts of newly built dams depend strongly on their configuration. We use multiobjective optimization to identify portfolios of sites that simultaneously minimize impacts on river flow, river connectivity, sediment transport, fish diversity, and greenhouse gas emissions while achieving energy production goals. We find that uncoordinated, dam-by-dam hydropower expansion has resulted in forgone ecosystem service benefits. Minimizing further damage from hydropower development requires considering diverse environmental impacts across the entire basin, as well as cooperation among Amazonian nations. Our findings offer a transferable model for the evaluation of hydropower expansion in transboundary basins.

Hydropower is a leading component of current and future renewable energy portfolios in many countries worldwide. Whereas the construction of new large hydropower projects has abated in much of Western Europe and North America (*1*), where coordinated dam removals are being considered (*2*–*4*), construction of large dams is booming in many countries with emerging economies (*5*, *6*). As plans for hydropower expansion ramp up for the world's few remaining unregulated and unfragmented river basins (*7*), tools for strategic dam planning are urgently needed to help minimize total environmental impacts at the basin scale, including transboundary river basins (*8*, *9*). Computational breakthroughs offer opportunities to guide dam site selection on the basis of trade-offs among many different criteria across multiple spatial scales and complex political landscapes (*10*).

From a socioenvironmental perspective, hydropower proliferation is an especially acute issue in tropical river basins such as the Amazon (*11*–*13*). Currently, at least 158 dams with individual installed capacities of >1 MW are operating or under construction in the five nations that constitute >90% of the Amazon basin, and another 351 dams are proposed (Fig. 1). The distribution of existing and potential hydropower is uneven among the major subbasins of the Amazon; most of the proposed sites are in either the Tapajós subbasin draining the Brazilian shield in the east (144 proposed dams) or the Marañón subbasin draining the Andes (62 proposed dams) (table S1). Relative to existing projects, many proposed Amazonian dams will be bigger and installed on larger rivers (Fig. 1B), leading to more-expansive river valley inundation and greater potential for socioenvironmental disruptions (*14*, *15*). Although integrated environmental assessments with site-specific environmental variables have been used in some Amazonian countries, particularly Brazil (*16*), these approaches rarely consider effects at the whole-basin scale, especially when rivers cross international boundaries. The variety of project sizes, combined with spatially heterogeneous river characteristics and transboundary resources, necessitates better understanding of the trade-offs between hydropower capacity and ecosystem services among different portfolios of future dams throughout the entire Amazon River network.

A multiobjective optimization framework

We developed a multiobjective optimization framework (*17*) to evaluate the trade-offs at large basin-wide scales between hydropower capacity and a set of five environmental criteria that encompass core river ecosystem services (or disservices)—river flow regulation, river connectivity, sediment transport, fish diversity, and greenhouse gas emissions—emerging from placement of dams across the entire river network. We constrained our analysis to these five environmental criteria because they could be estimated at each existing and proposed dam locality across the Amazon basin. These criteria also reflect fundamental riverine processes that underlie many benefits that ~30 million rural and urban people in the Amazon rely upon for their livelihoods, which are intimately linked to rivers and their floodplains. The natural flow regime of an undammed river fundamentally shapes riverine biodiversity and ecosystem function by mediating the timing and duration of sediment and dissolved nutrient transport,

[1]Department of Ecology and Evolutionary Biology, Cornell University, Ithaca, NY 14853, USA. [2]Institute for Computational Sustainability, Cornell University, Ithaca, NY 14853, USA. [3]Department of Natural Resources and the Environment, Cornell University, Ithaca, NY 14853, USA. [4]Northern Andes and South Central America Conservation Program, The Nature Conservancy, Bogotá 110231, Colombia. [5]Stockholm Environment Institute Latin America, Bogotá 110231, Colombia. [6]Department of Biology, Stanford University, Palo Alto, CA 94305, USA. [7]Department of Computer Science, Stanford University, Palo Alto, CA 94305, USA. [8]Centro Peruano para la Biodiversidad y Conservación, Iquitos 16001, Perú. [9]School of Natural Resources, University of Nebraska, Lincoln, NE 68583, USA. [10]Department of Biology, Colorado State University, Fort Collins, CO 80523, USA. [11]Institute for Applied Ecology, University of Canberra, Bruce, ACT 2617, Australia. [12]National Institute of Amazonian Research, Manaus 69060-001, Brazil. [13]Vermont Department of Environmental Conservation, Montpelier, VT 05620, USA. [14]Department of Ecology, Evolution and Environmental Biology, Columbia University, New York, NY 10027, USA. [15]W.K. Kellogg Biological Station and Department of Integrative Biology, Michigan State University, Hickory Corners, MI 49060, USA. [16]Cary Institute of Ecosystem Studies, Millbrook, NY 12545, USA. [17]Centro de Investigación y Tecnología del Agua, Universidad de Ingeniería y Tecnología, Lima 15063, Peru. [18]Department of Earth and Environment and Institute of Environment, Florida International University, Miami, FL 33199, USA. [19]Department of Biology, Federal University of Juiz de Fora, Juiz de Fora 36036-900, Brazil. [20]Departamento de Geología, Escuela Politecnica Nacional, Quito 170525, Ecuador. [21]Department of Computer Science, Cornell University, Ithaca, NY 14853, USA. [22]Wildlife Conservation Society Peru, Lima 15048, Peru. [23]Centre d'Ecologie Fonctionnelle et Evolutive, Université de Montpellier, UMR 5175, CNRS, Université Paul Valéry Montpellier, EPHE, IRD, F-34293 Montpellier, France. [24]Laboratorio de Ecología Acuática, Instituto BIOSFERA, Universidad San Francisco de Quito, Quito 170150, Ecuador. [25]Institute of Hydraulic Research, Federal University of Rio Grande do Sul, Porto Alegre 91501-970, Brazil. [26]Wildlife Conservation Society, New York, NY 10460, USA. [27]The Nature Conservancy, Arlington, VA 22203 USA. [28]UMR EDB (Laboratoire Évolution et Diversité Biologique), CNRS 5174, IRD253, UPS, F-31062 Toulouse, France. [29]Institute for Culture and Environment, Alaska Pacific University, Anchorage, AK 99508, USA. [30]Bren School of Environmental Science and Management, University of California at Santa Barbara, Santa Barbara, CA 93106, USA. [31]Department of Biological and Environmental Engineering, Cornell University, Ithaca, NY 14853, USA. [32]Departamento de Ingeniería Civil y Ambiental, Escuela Politécnica Nacional, Quito 170143, Ecuador. [33]Centro de Investigaciones y Estudios en Recursos Hídricos, Escuela Politécnica Nacional, Quito 170143, Ecuador. [34]Department of Computer Science, Purdue University, West Lafayette, IN 47907, USA.
*Corresponding author. Email: asf3@cornell.edu (A.S.Flec.); gomes@cs.cornell.edu (C.P.G.)
†Present address: School of Earth, Environmental, and Marine Sciences, The University of Texas Rio Grande Valley, Edinburg, TX 78539, USA.
‡Present address: Research, Education and Development, RED YAKU, Lima 15084, Peru.
§Present address: National Ecological Observatory Network, Domain 03, Battelle, Gainesville, FL 32609, USA.
¶Present address: Mamirauá Institute for Sustainable Development, Tefé 69553-225, Brazil.
#Present address: Meta, Menlo Park, CA 94025, USA.

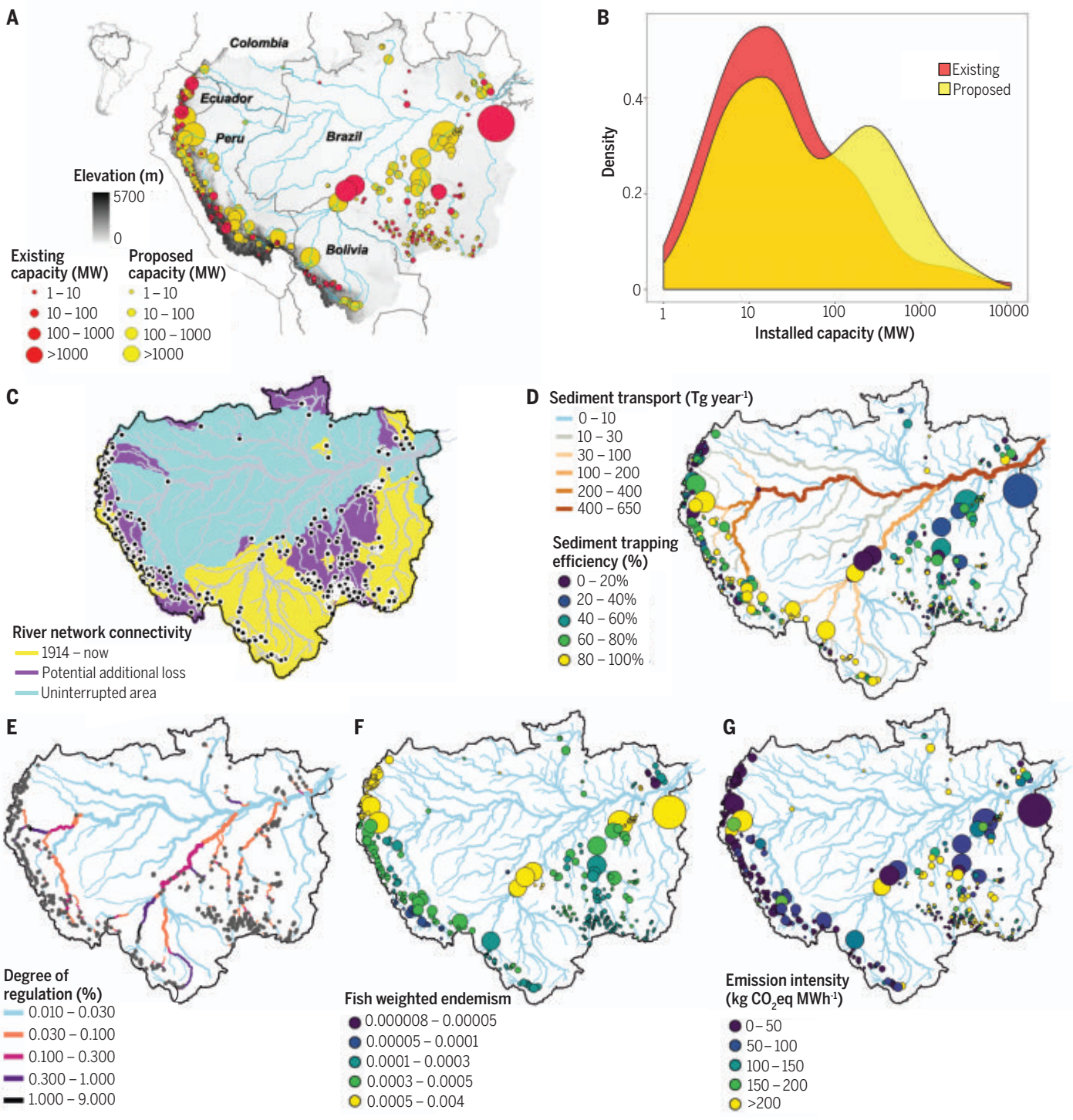

Fig. 1. Expansion of Amazon hydropower and comparative impacts for different environmental criteria. (**A**) Spatial distribution of 158 existing hydropower dams in the Amazon basin and 351 additional proposed dams. (**B**) Comparison of frequency distributions of existing and proposed dams as a function of installed capacity shows that dams are getting larger in the Amazon, with more projects proposed on large tributaries. The magnitude of impacts varies for different environmental criteria in different parts of the basin, as illustrated in the subsequent figure panels. (**C**) Existing dams have disconnected large fractions of the Amazon (yellow areas), as indicated by a river network connectivity index (RCI_D). Building all proposed dams would further disrupt Amazon basin connectivity (purple areas), with only about half of the basin remaining unfragmented (cyan areas). (**D**) Many dams with high sediment trapping efficiencies are proposed in sediment-rich river reaches in the western Amazon. (**E**) Cumulative degree of regulation, estimated as the percent annual flow that is withheld by upstream reservoirs with full buildout of all existing and proposed dams, can be manifested as alterations in the temporal dynamics of flow regimes and river-floodplain hydrological exchanges across the river network. (**F**) Some dams are located in subbasins that are fish diversity hotspots, as indicated by weighted endemism, which incorporates both fish species richness and endemism. (**G**) Estimated greenhouse gas emissions per unit of electricity generated at Amazon dams vary by more than two orders of magnitude. CO_2eq, carbon dioxide equivalent.

floodplain inundation, and habitat availability (*18*). Hydrologic connectivity of habitats via natural flows is vital for sustaining these riverine processes at river-basin scales (*7*). Dams interrupt these processes and associated ecosystem services by changing the magnitude and timing of water flux and can reduce the downstream delivery of suspended sediments. River sediments are critically important for building floodplains, which are nursery grounds of many food fishes and are used by people engaged in flood-recession agriculture (*19*, *20*). Moreover, river sediments carry nutrients essential for the productivity of floodplain agriculture and river fisheries (*21*). Additionally, dams fragment river systems by blocking the movement of migratory fishes that are the mainstay of Amazon fisheries, which provide important sources of nutrition and livelihoods to local inhabitants (*22*–*24*). River connectivity loss also interferes with traditional riverboat transport of people and goods on which riverside communities rely. Further, reservoirs created by dams generate greenhouse gas emissions, an ecosystem disservice in that minimizing carbon intensity is one of the central considerations of energy planning (*25*). While hydropower is often viewed as a less carbon intensive energy source, some reservoirs emit as much greenhouse gases as the equivalent energy generation from fossil fuels (*14*, *26*).

Our approach determines the Pareto-optimal frontier, which represents a set of solutions (i.e., portfolios composed of different configurations of dams) that minimize negative effects across environmental objectives for any given level of aggregate hydropower yield. This optimization problem is computationally intensive because it requires accounting for 2^{509} (~10^{153}) possible combinations of the 509 current and proposed dams in the Amazon basin. To overcome this challenge, we developed a fully polynomial-time approximation algorithm based on dynamic programming that, unlike previous heuristic approaches, can quickly approximate the Pareto frontier for multiple environmental criteria simultaneously and with guarantees of theoretical optimality (*27*–*29*). Given the vast number of Pareto-optimal solutions and the limitations of human cognition to visualize high-dimensional spaces such as a six-dimensional Pareto frontier, we developed an interactive graphical user interface (GUI) to navigate the high-dimensional solution space for Amazon dams (see materials and methods section 2.5 in the supplementary materials) (*30*).

Optimization across all dam sites to achieve current levels of hydropower production shows that the historical lack of strategic basin-wide planning has produced a configuration of dams that is far from optimal from an environmental perspective. We calculated the chronology of ecosystem impacts during the historical expansion of hydropower dams throughout the Amazon basin (which measures >6.3 million km^2) and compared the actual trajectory of environmental degradation under historical energy development against the original Pareto frontier, which we define as the hypothetical Pareto frontier for all existing and proposed dam sites. The difference between the historical trajectory and the original Pareto frontier represents the forgone ecosystem benefits of basin-wide planning, which were computed separately for each environmental criterion. Criteria such as river connectivity, based on a dendritic river connectivity index (RCI_P) that quantifies drainage network fragmentation, have changed drastically from the initial historic pre-dam baseline (Fig. 2A). River connectivity throughout the Amazon remained relatively intact until recently, with a loss of <10% between 1914 (when the first dam was built in the basin) and 2012. However, the blockage of major tributaries by construction of two large dams on the Madeira River (Santo Antônio and Jirau, completed in 2012 and 2013, respectively) and the Belo Monte dam on the Xingu River (completed in 2016) has led to abrupt and steep declines in river connectivity. These three recent projects, among the largest in the world, have increased fragmentation of the Amazon River network by nearly 40% in the past decade alone. Comparing the existing and baseline Pareto frontiers illustrates that other dam configurations could have delivered equivalent amounts of hydropower capacity as exists today in the Amazon, with relatively little loss in connectivity (Fig. 2A). Indeed, coordinated planning could have produced up to four times as much hydropower without exceeding the current level of connectivity loss. Loss of network connectivity is the most conspicuous case of forgone benefits; the impact of historical dam construction on flow regulation and other criteria falls much closer to the original Pareto frontier for achieving current hydropower production (Fig. 2), demonstrating the heterogeneous impacts of dam development among different ecosystem services.

The enormous differences in environmental impact per unit of electricity production illustrated by our Pareto frontier analyses underscore the need for strategic, basin-wide planning of any future hydropower expansion based on many criteria. Both computational challenges and data limitations have constrained previous

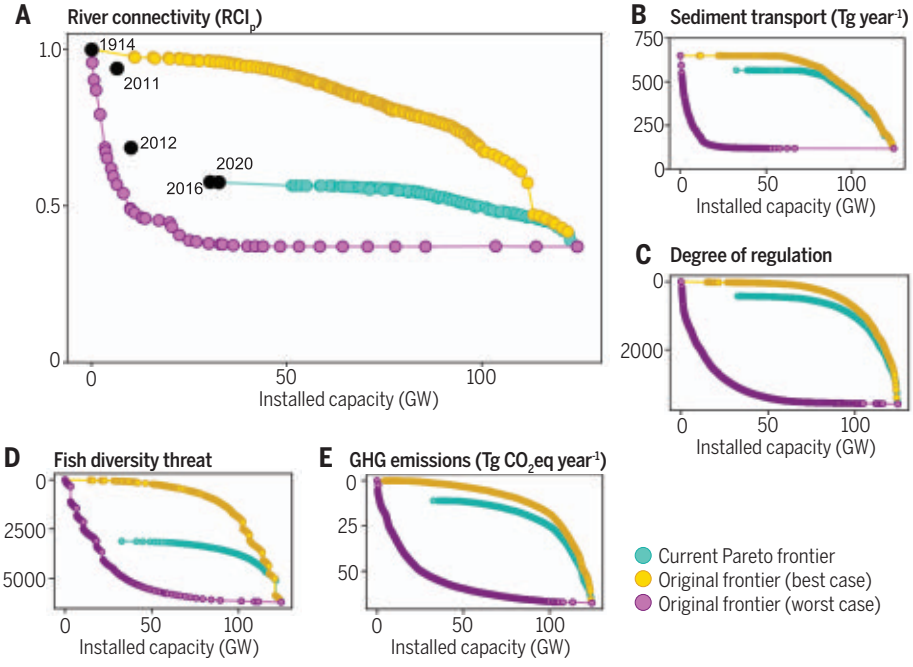

Fig. 2. Forgone environmental and energy benefits of uncoordinated dam planning in the Amazon. Pareto-optimal solutions for Amazon hydropower development based on electricity generation and different environmental criteria. For each environmental criterion (**A** to **E**), the plots show the original best-case scenario that could have been achieved with optimal planning from the commencement of dam building in the Amazon (yellow) compared with the original worst-case scenario (purple) for hydropower placement; black filled circles show the chronological trajectory of existing dams, whereas the cyan line shows the current possible best-case scenario for optimal hydropower placement moving forward from current conditions in 2020 for proposed dams considering (A) river connectivity, (B) sediment transport, (C) cumulative downstream flow alteration estimated using a degree of regulation index (values are the sum of degree of regulation for each dam portfolio), (D) fish diversity threat score, and (E) greenhouse gas emissions from reservoirs.

basin-wide hydropower planning to include only one or a few environmental objectives at a time (*14*, *31*–*34*). Yet rivers provide suites of ecosystem services that are potentially affected by damming, and jointly considering multiple criteria can substantially alter optimization outcomes. In contrast to two-dimensional Pareto frontiers exploring trade-offs between only energy production and connectivity (Fig. 3A), simultaneous consideration of additional criteria (sediment delivery, degree of regulation, fish diversity, greenhouse gas emissions) results in large changes in the identity and frequency of particular dams occurring within optimal dam portfolios. These changes in optimization outcomes ensue because trade-offs emerge among river ecosystem services (Fig. 3A). For example, optimal solutions for river connectivity include many high-elevation dams at sites farthest away from the mouth of the Amazon; consequently, dams in the high Andes are often included in Pareto-optimal solutions when optimizing only for river connectivity (Fig. 3B). Conversely, Andean-sourced rivers produce most of the nutrient-rich sediment in the Amazon River that sustains productivity and structures the geomorphology of the floodplains (Fig. 1D); accordingly, dams in Andean-sourced rivers interrupt sediment transport more substantially and are therefore rarely included in Pareto-optimal solutions for sediments alone (Fig. 3B). Thus, replacing one environmental criterion with another can greatly modify the frequency with which some dams are Pareto optimal (Fig. 3A). Notably, ~60% of proposed Amazon dams always appear in Pareto-optimal solutions for certain environmental criteria while never appearing in optimal solutions for others (Fig. 3B). Owing to this large incongruence among objectives, optimizing dam planning for a single environmental criterion inevitably results in suboptimal performance for other environmental criteria (Fig. 3C). This case is clearly illustrated when comparing the sediment transport outcomes optimized for river connectivity against those attained when optimized directly for sediments. For example, the 80 GW dam portfolio planned optimally for river connectivity would trap a far larger proportion of sediments basin-wide than the 80 GW dam portfolio planned optimally for sediments (Fig. 3C).

Basin-wide planning outcomes

As more environmental criteria are evaluated simultaneously, we observe further complexity in optimization outcomes. Consequently, when all five of our environmental criteria are considered in a six-dimensional Pareto frontier, few dams remain that are frequently Pareto optimal (Fig. 3A) (*30*). In addition, a diversity of trade-off outcomes among environmental criteria are revealed by the six-dimensional Pareto frontier (Fig. 3D) (*30*). For example, our algorithm identifies ~30 optimal solutions for a hydropower target of 80 GW, but these equivalently optimal dam portfolios can result in vastly dissimilar environmental performance for different individual criteria (Fig. 3D). Given the sharp trade-offs among environmental objectives that become evident with multiobjective optimization, certain criteria may be given more weight depending on the values of society and decision-makers. Regardless, basin-wide strategic planning needs to consider suites of multiple criteria simultaneously, recognizing that the chosen set of criteria can alter our perception of "high-impact" versus "low-impact" dams.

Yet another challenge in strategic hydropower planning is its dependence on the spatial scale of analyses. To quantify the importance of spatial scale, we conducted a set of analyses at subbasin, regional, and whole-basin scales. We ranked all proposed dams according to the frequency with which these projects appear in at least 50% of Pareto-optimal solutions, with higher frequencies indicating less detrimental environmental outcomes in aggregate. For example, when Pareto-optimal solutions are evaluated for sediment transport at the western Amazon scale (Marañón, Napo, and Ucayali subbasins), ~32% of proposed dams (36 of 114 dams) appear in at least half of the Pareto-optimal portfolios (Fig. 4). In contrast, when optimizing for sediment transport at the scale of the entire Amazon basin, fewer than 20% (21 of 114) of these same dams appear in at least half of the Pareto-optimal portfolios (Fig. 4). Moreover, while ~48% of the proposed Tapajós River dams (70 of 144 dams) appear in at least half of the Pareto-optimal portfolios at the Tapajós optimization scale, nearly all of these same dams (142 of 144) are included at the whole-basin scale. The clear-water Tapajós River originates in Precambrian shields in the eastern Amazon and is characteristically sediment poor, whereas western Amazon rivers drain geologically younger terrains in the Andes and are notoriously sediment rich (*21*, *35*). Consequently, Tapajós dams fare better when optimizing for sediment at larger spatial scales that include consideration of dams in sediment-rich rivers. These findings build on previous efforts showing that Amazon subbasins differ in their vulnerabilities to dams on the basis of different hydrophysical features and biotic diversity (*12*, *36*) and bolster the notion that planners and decision-makers need to consider how spatial scale influences their perceptions of better solutions with respect to different environmental criteria.

Our results illustrate how strategic, basin-wide planning enhances the probability of selecting dam configurations with less destructive, aggregate environmental outcomes. In practice, however, hydropower planning generally occurs at the national scale, even though electricity may be exported across borders, for example from the Andean Amazonian countries to Brazil. We assessed the potential of international cooperation to improve environmental outcomes by comparing basin-wide Pareto frontiers with those based on country-level optimal planning for each of our five environmental criteria. Clear opportunities exist for reducing environmental costs through international cooperation (Fig. 5). For example, developing 50% of the proposed hydropower potential optimally on a country scale but without international coordination would result in trapping substantially more sediments on a basin-wide scale (Fig. 5A). For all Amazonian countries, optimal planning at the country scale yields suboptimal environmental outcomes at the whole-basin scale for at least one of our five environmental criteria (Fig. 5B). Further, dam sites that are disfavored in a country-scale analysis can be strongly favored in Amazon-wide optimization. This disparity in site prioritization between different scales is especially notable for proposed dams in Ecuador. Because almost all Ecuadorian dams are run-of-river projects located in the Andes at mid to high elevations in the far western Amazon basin, they would fragment comparatively short river segments (*22*), yield relatively small greenhouse gas emissions (*14*), and are often situated in montane zones beyond the distributional limits of diverse Amazon fish assemblages. However, our analyses only consider environmental criteria and do not include other factors such as seismic risk and long energy transmission distances that could make dams in Ecuador much less satisfactory when a broader suite of planning objectives is considered.

Conclusion and prospects

Enhanced computational capabilities are unlocking the potential for strategic, basin-wide planning to guide dam site selection during hydropower expansion. Our quantitative analysis shows how, in the absence of basin-wide integrated environmental assessments, historical dam-by-dam decision-making has resulted in large forgone ecosystem benefits (Fig. 2). The comparison of the original Pareto frontier for all existing and proposed dams with historical patterns of hydropower development underscores the adverse consequences of uncoordinated planning in the Amazon. On the basis of these findings, we highlight four key principles for reducing the environmental costs of hydropower expansion.

First, multiobjective optimization provides an effective first filter to identify dams that would be particularly detrimental and can be a valuable step for strategic and integrated environmental assessments (*16*, *37*). However, a notable limitation has been the inability to apply strategic environmental assessments to all hydropower potential across large areas

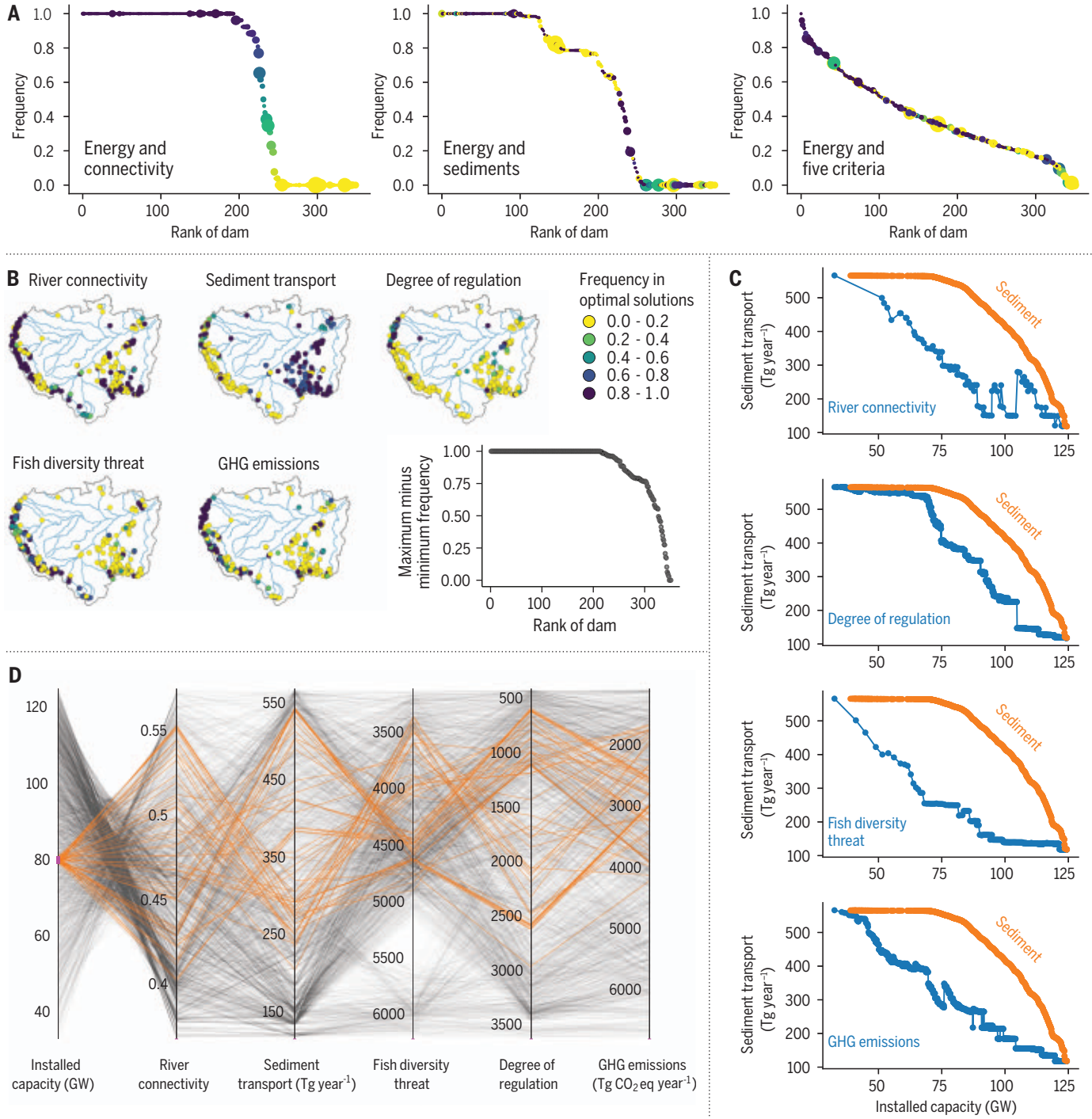

Fig. 3. The importance of choice of criteria for strategic hydropower planning. (**A**) Rank frequency plots showing the frequency with which each of the 351 proposed Amazon dams appears in optimal solutions for trade-off analyses between energy and river network connectivity, sediment transport, and all five environmental criteria considered simultaneously; dams in the middle and right-hand plots are colored according to their frequency in optimal solutions (purple, high frequency; yellow, low frequency) compared with when only energy and connectivity are analyzed (left-hand plot), and dot sizes are proportional to installed capacity. Note that as more objectives are considered, fewer dams are in Pareto-optimal solutions owing to trade-offs among criteria. (**B**) Maps showing the frequency with which each dam appears in optimal solutions for each environmental criterion when criteria are optimized individually; the bottom-right plot shows the difference between the maximum and minimum frequencies in optimal solutions among the five criteria for each dam, with the 351 dams ranked from highest to lowest values. (**C**) Basin-wide sediment transport outcomes of Amazon dam portfolios planned optimally to minimize sediment retention in comparison to sediment outcomes attained when optimizing individually for each of the other four criteria (river connectivity, degree of regulation, fish diversity, and greenhouse gases). (**D**) Parallel coordinate plot with solutions that are Pareto-optimal for all criteria simultaneously. Each coordinate corresponds to a criterion, and each line connecting different values along the coordinates corresponds to a single Pareto-optimal solution; all optimal solutions for 80 ± 0.5 GW are highlighted in orange. GHG, greenhouse gas emissions.

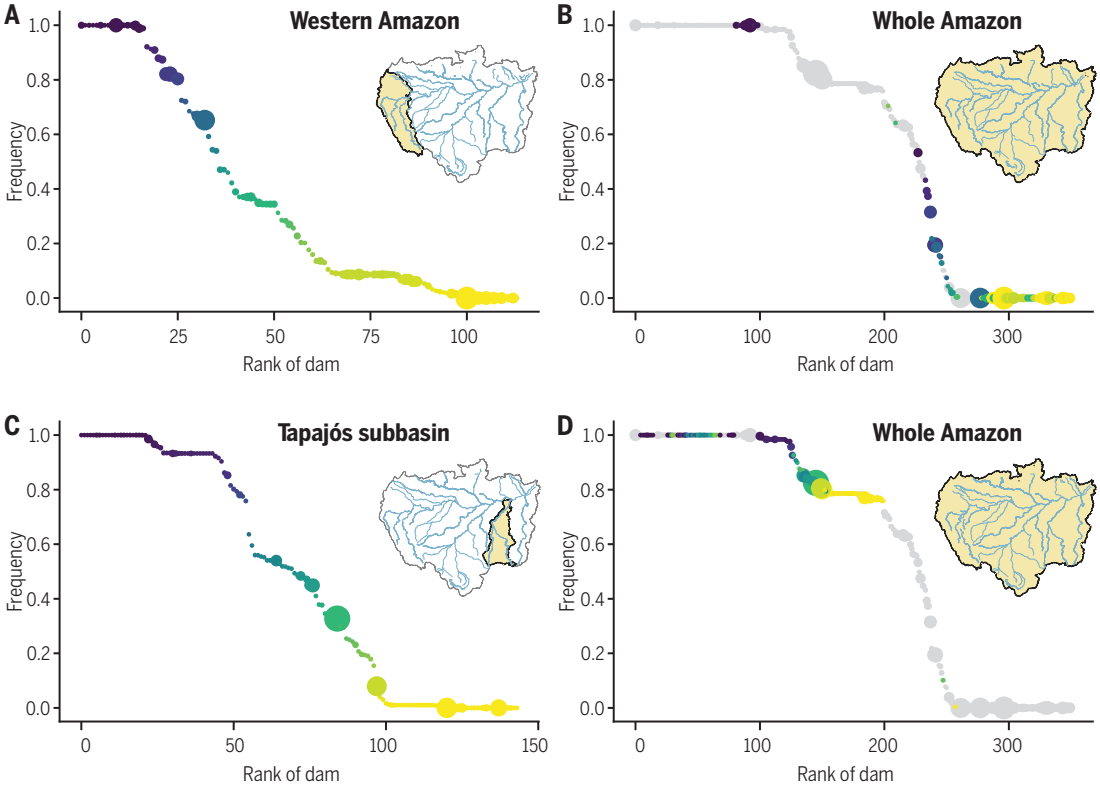

Fig. 4. The importance of spatial scale for strategic hydropower planning. Rank frequency plots showing the frequency with which each of the 351 proposed Amazon dams appears in optimal solutions for trade-off analyses between energy generation and sediment transport. (**A**) Rank frequency plot showing the frequency with which proposed dams in three western Amazon subbasins (Marañón, Napo, and Ucayali rivers) are in configurations along the Pareto-optimal frontier. (**B**) Frequency with which the same proposed western Amazon dams are in optimal solutions when analyzed at the scale of the entire Amazon basin; dams are colored according to their frequency in optimal solutions at the western Amazon scale (purple, high frequency; yellow, low frequency). (**C** and **D**) Same as (A) and (B), but for the Tapajós subbasin. Note the contrasting effects of increasing spatial scale of analysis for western Amazon subbasins with high sediment loads as opposed to the Tapajós subbasin with little sediment load. Dot sizes are proportional to installed capacity.

(*16*), and here we provide advanced computational methods for basin-wide assessment at the scale of the world's largest river network. Traditionally, energy and economics drive the selection of hydropower projects, with environmental impacts assessed subsequently during the licensing process for select individual dams. By identifying projects that approach the worst-case development trajectory, our analysis can screen out proposed dams with highly adverse environmental risks. In addition to foreseeable environmental consequences, these same high-impact projects often carry large social and economic risks, increase investment uncertainty, and contribute to considerable cost overruns and substantial time delays (*38*), highlighting the utility of effective first filters. Environmental impacts are often viewed as economically expensive roadblocks to energy development; instead, by marshaling extensive environmental data as part of a first filter, our approach can serve the mutual benefits of avoiding far-reaching and costly socioenvironmental impacts in the context of meeting broader energy goals, thereby helping inform more-sustainable solutions (*39*).

Second, simultaneous consideration of multiple criteria is critical for identifying the least detrimental projects (Fig. 3). The importance of evaluating trade-offs involving multiple criteria has long been recognized in the context of sustainable development goals and the management of ecosystem services (*40*, *41*). However, previous quantitative approaches could not scale up to handle a large number of criteria at the scale of the entire Amazon with optimality guarantees; here we quantify the marked disparities in seemingly optimal portfolios that ensue as more criteria are considered. As a broader suite of criteria are evaluated, increasingly complex trade-offs among criteria sharply curtail the number of dams consistently identified as low impact. Although we focused on five heuristically valuable environmental criteria, we recognize that additional objectives (political, economic, social, environmental) need to be included for overall strategic hydropower development planning (*8*, *37*). Optimizing variables that integrate a set of related services into bundles (*7*, *12*, *36*) may also be effective in advancing strategic hydropower planning and minimizing challenges associated with complex trade-offs among criteria. Further considering uncertainties in river basin planning—such as climate change, disruptions in governance, and adoption of alternative energy sources including wind and solar (*42*–*46*)—will be critical before embracing hydropower expansion in the Amazon, because these are likely to shape trade-offs among criteria. In addition, site-scale optimization of operations can partly mitigate some of the adverse effects of poor dam placement (*47*). Currently, it is not possible to include operations at a basin-wide scale, because few details are known for most Amazon dams that have not yet reached an advance planning stage; changes in operational rules made during the licensing process further compound this limitation. As more data become available for inclusion in our computationally efficient approach, more-informed strategic hydropower planning will lead to better outcomes for nature and people.

Third, in large and complex river systems, basin-wide analysis is essential for minimizing forgone benefits. Optimization of dam site selection at national, subbasin, and whole-basin scales often yields conflicting results for particular projects because the pool of candidate dams increases with area, and the perspective of the magnitude of impacts in any region can be modified by changing geographical scale (Figs. 4 and 5). This creates risk of uninformed decision-making, as seemingly low-impact dams based on optimization at the subbasin or country level can in reality be highly problematic when assessed at a whole-basin scale. Yet, whole-basin planning requires new tools and perspectives and is especially complicated when rivers cross political boundaries. Our use of artificial intelligence with optimality guarantees to consider the impacts of all

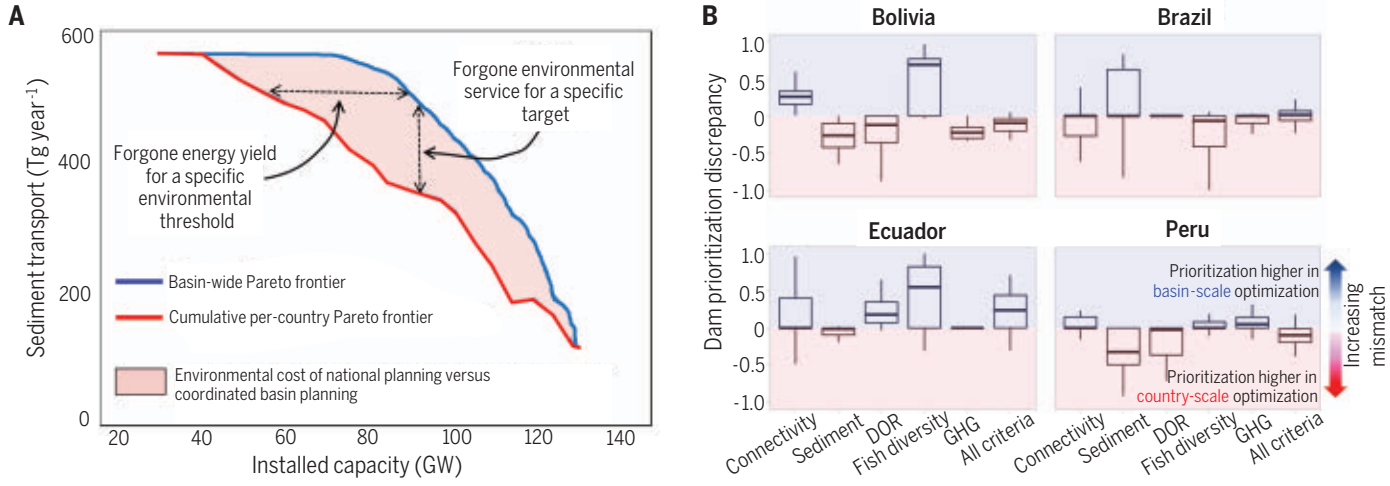

Fig. 5. International cooperation among Amazonian countries can lead to more-efficient strategic hydropower planning outcomes. (**A**) Pareto frontiers for cumulative country-level (red line) and basin-wide (blue line) optimizations for sediment transport. For country-level analyses, each country contributes an equivalent proportion of its own proposed hydropower potential toward meeting basin-wide energy generation targets. The difference between basin-wide and country-level lines illustrates the environmental and hydropower costs of the lack of basin-wide strategic planning. (**B**) Disparities in the frequency with which individual dams appear in optimal solutions when planning occurs at the basin-wide scale versus the country scale for each criterion and all criteria simultaneously. Box and whisker plots are shown for five environmental criteria run for four Amazonian countries (Bolivia, Brazil, Ecuador, and Peru) that make up >90% of the area of the Amazon basin. Values near zero indicate concordance between country-scale and whole-Amazon assessment of dam prioritization. Dams that are often included in basin-wide planning but that are rarely included in country-level planning (positive values) and vice versa (negative values) indicate a potential mismatch between countries' hydropower dam selection priorities and those that are preferable for minimizing basin-wide ecosystem service impacts. Mismatches in dam priorities across scales also vary depending on the criteria used for multiobjective optimization, indicating that coordination on the selection of planning criteria is also an important feature of cooperative pan-Amazon dam planning. DOR, degree of regulation. The horizontal lines inside the box and whisker plots indicate the median, and the boundaries indicate the 25th and 75th percentiles. For improved visualization, outliers are not shown.

possible dam portfolios is complementary to other approaches for assessing regional-scale impacts of Amazon dams that identify subbasins and geological-physiographic domains where environmental consequences are likely to be most acute (*12*). Although we stress the importance of system-scale risk screening, this does not preclude the essential role of local stakeholder interests in guiding dam siting, once the potentially most detrimental projects are removed from consideration.

Finally, international cooperation is paramount for reducing adverse impacts of hydropower expansion in transboundary basins (Fig. 5). Without a basin-wide approach to planning, and requisite decision-support tools, a sustainable path for energy development in the Amazon will remain elusive. Coordinated planning moving forward is challenging and requires mechanisms for cooperative agreements and their enforcement. For example, the Amazon Cooperation Treaty Organization has existed for nearly two decades as a forum for cooperation and dialog among Amazonian countries to promote sustainable development (*48*), but this transboundary policy instrument has yet to be adequately leveraged to enhance the scale and caliber of integrated environmental assessments of Amazon hydropower (*12*). The Leticia Pact, signed in 2019, provides a fresh opportunity for a whole-basin approach to guide cooperation among Amazonian countries through mutual agreements regarding sustainable Amazon development (*49*). An encouraging step is the recent launch of the Amazon Regional Observatory as a platform for sharing information pertinent to environmental resource management and biodiversity conservation (*50*), which should provide additional data needed for whole-basin planning. Moreover, Brazil has begun to deploy integrated environmental assessment at subbasin scales, and the existence of such regulatory frameworks could provide a blueprint for upscaling to more extensive planning (*16*). In addition to improved policy mechanisms and greater data availability, breakthroughs in computer science will lead to more opportunities to develop novel decision-support tools for building more-sustainable integrated energy systems (*10*). The data and tools produced by this study can provide unbiased input to such policy instruments, assuming political leaders and financial institutions are committed to collective benefits of basin-wide strategic planning for hydropower expansion in transboundary river basins.

REFERENCES AND NOTES

1. J. E. O'Connor, J. J. Duda, G. E. Grant, *Science* **348**, 496–497 (2015).
2. M. J. Kuby, W. F. Fagan, C. S. ReVelle, W. L. Graf, *Adv. Water Resour.* **28**, 845–855 (2005).
3. T. M. Neeson *et al.*, *Proc. Natl. Acad. Sci. U.S.A.* **112**, 6236–6241 (2015).
4. S. G. Roy *et al.*, *Proc. Natl. Acad. Sci. U.S.A.* **115**, 12069–12074 (2018).
5. K. O. Winemiller *et al.*, *Science* **351**, 128–129 (2016).
6. C. Zarfl, A. Lumsdon, J. Berlekamp, L. Tydecks, K. Tockner, *Aquat. Sci.* **77**, 161–170 (2014).
7. G. Grill *et al.*, *Nature* **569**, 215–221 (2019).
8. E. F. Moran, M. C. Lopez, N. Moore, N. Müller, D. W. Hyndman, *Proc. Natl. Acad. Sci. U.S.A.* **115**, 11891–11898 (2018).
9. J. Opperman *et al.*, *Connected and Flowing: A Renewable Future for Rivers, Climate and People* (WWF and The Nature Conservancy, 2019).
10. C. Gomes *et al.*, *Commun. ACM* **62**, 56–65 (2019).
11. L. Castello, M. N. Macedo, *Global Change Biol.* **22**, 990–1007 (2016).
12. E. M. Latrubesse *et al.*, *Nature* **546**, 363–369 (2017).
13. J. G. Tundisi, J. Goldemberg, T. Matsumura-Tundisi, A. C. F. Saraiva, *Energy Policy* **74**, 703–708 (2014).
14. R. M. Almeida *et al.*, *Nat. Commun.* **10**, 4281 (2019).
15. H. I. Jager, R. A. Efroymson, J. J. Opperman, M. R. Kelly, *Renew. Sustain. Energy Rev.* **45**, 808–816 (2015).
16. F. Fortes Westin, M. A. Santos, I. Duran Martins, *Renew. Sustain. Energy Rev.* **37**, 750–761 (2014).
17. See supplementary materials.
18. N. L. Poff *et al.*, *Bioscience* **47**, 769–784 (1997).
19. O. T. Coomes, M. Lapointe, M. Templeton, G. List, *J. Hydrol.* **539**, 214–222 (2016).
20. M. E. McClain, R. J. Naiman, *Bioscience* **58**, 325–338 (2008).
21. B. R. Forsberg *et al.*, *PLOS ONE* **12**, e0182254 (2017).
22. E. P. Anderson *et al.*, *Sci. Adv.* **4**, eaao1642 (2018).
23. S. A. Heilpern *et al.*, *Sci. Adv.* **7**, eabf9967 (2021).
24. A. J. Lynch *et al.*, *Environ. Rev.* **24**, 115–121 (2016).
25. International Energy Agency, *World Energy Outlook 2020* (International Energy Agency, 2020); https://www.iea.org/reports/world-energy-outlook-2020.

26. F. A. M. de Faria, P. Jaramillo, H. O. Sawakuchi, J. E. Richey, N. Barros, *Environ. Res. Lett.* **10**, 124019 (2015).
27. J. M. Gomes-Selman *et al.*, *Lect. Notes Comput. Sci.* **10848**, 263–279 (2018).
28. Q. Shi *et al.*, "Efficiently optimizing for dendritic connectivity on tree-structured networks in a multi-objective framework," *Proceedings of the 1st ACM SIGCAS Conference on Computing and Sustainable Societies*, article 26 (2018).
29. X. Wu *et al.*, *Proc. Conf. AAAI Artif. Intell.* **32**, 849–858 (2018).
30. Amazon EcoVistas: Visualization of the Ecosystem Services Pareto Frontier for Proposed Amazon Hydropower Development; https://www.cs.cornell.edu/gomes/udiscoverit/amazon-ecovistas/.
31. T. B. A. Couto, M. L. Messager, J. D. Olden, *Nat. Sustain.* **4**, 409–416 (2021).
32. R. J. P. Schmitt, S. Bizzi, A. Castelletti, G. M. Kondolf, *Nat. Sustain.* **1**, 96–104 (2018).
33. R. J. P. Schmitt, S. Bizzi, A. Castelletti, J. J. Opperman, G. M. Kondolf, *Sci. Adv.* **5**, eaaw2175 (2019).
34. G. Ziv, E. Baran, S. Nam, I. Rodríguez-Iturbe, S. A. Levin, *Proc. Natl. Acad. Sci. U.S.A.* **109**, 5609–5614 (2012).
35. J. A. Constantine, T. Dunne, J. Ahmed, C. Legleiter, E. D. Lazarus, *Nat. Geosci.* **7**, 899–903 (2014).
36. E. M. Latrubesse *et al.*, *Aquat. Conserv.* **31**, 1136–1149 (2021).
37. S. Athayde *et al.*, *Curr. Opin. Environ. Sustain.* **37**, 50–69 (2019).
38. J. Opperman *et al.*, "The power of rivers—A business case: How system-scale planning and management of hydropower can yield economic, financial and environmental benefits" (The Nature Conservancy, 2017).
39. N. L. Poff *et al.*, *Nat. Clim. Chang.* **6**, 25–34 (2016).
40. K. Böck, R. Polt, L. Schülting, in *Riverine Ecosystem Management: Science for Governing Towards a Sustainable Future*, S. Schmutz, J. Sendzimir, Eds. (Aquatic Ecology Series, Springer International Publishing, Cham, 2018), pp. 413–433.
41. S. R. Carpenter *et al.*, *Proc. Natl. Acad. Sci. U.S.A.* **106**, 1305–1312 (2009).
42. R. M. Almeida *et al.*, *Glob. Environ. Change* **71**, 102383 (2021).
43. M. E. Arias *et al.*, *Nat. Sustain.* **3**, 430–436 (2020).
44. F. A. M. de Faria, P. Jaramillo, *Energy Sustain. Dev.* **41**, 24–35 (2017).
45. R. J. P. Schmitt, N. Kittner, G. M. Kondolf, D. M. Kammen, *Environ. Res. Lett.* **16**, 054054 (2021).
46. K. Siala, A. K. Chowdhury, T. D. Dang, S. Galelli, *Nat. Commun.* **12**, 4159 (2021).
47. T. B. Wild, P. M. Reed, D. P. Loucks, M. Mallen-Cooper, E. D. Jensen, *J. Water Resour. Plan. Manage.* **145**, 05018019 (2019).
48. M. A. Tigre, *Regional Cooperation in Amazonia: A Comparative Environmental Law Analysis* (Brill Nijhoff, 2017).
49. P. R. Prist *et al.*, *Science* **366**, 699–700 (2019).
50. Amazon Regional Observatory, https://oraotca.org/en/.

ACKNOWLEDGMENTS

This work was carried out by our Amazon Dams Computational Sustainability Working Group based at Cornell University. The contribution of X.W. was completed while at Cornell University. We thank the Cornell Atkinson Center for Sustainability; the Universidad de Ingeniería y Tecnología (UTEC) in Lima, Peru; and Florida International University for hosting working group meetings to develop the project framework. The Amazon Fish Project (www.amazon-fish.com/) provided data for fish diversity threat analyses. We acknowledge the inspirational ideas of our late colleagues Greg Poe and Javier Maldonado-Ocampo, who were instrumental in the conceptualization of this work. **Funding:** This work was funded by an NSF Expeditions in Computing award (CCF-1522054) to C.P.G. and a Cornell University Atkinson Academic Venture Fund award to A.S.Flec., C.P.G., and S.S. Computations were performed using the AI for Discovery Avatar (AIDA) computer cluster funded by an Army Research Office (ARO), Defense University Research Instrumentation Program (DURIP) award (W911NF-17-1-0187) to C.P.G. **Author contributions:** Conceptualization: All authors contributed to conceptualization through active participation in working group meetings. R.G.-V., Q.S., R.M.A., B.R.F., E.P.A., and A.S.Flec. compiled and curated the hydropower dam dataset. Hydrological and sediment flux analyses were developed by H.A., A.S.Flei., R.P., B.R.F., Q.S., S.S., N.L.P., S.A.T., S.K.H., R.M.A., R.G.-V., J.D.A., I.C.B., X.E.Z.-R., S.T., and M.T.W. and were conducted by H.A., Q.S., and A.S.Flei. Dendritic connectivity was analyzed by Q.S. and R.G.-V., with assistance from S.A.S., E.P.A., C.M.C., and M.G. Fish diversity threat analyses were conducted by Q.S., E.I.L., and C.J., with assistance from E.P.A., C.M.C., A.C.E., J.H., M.G., O.D., M.M., and M.V., using Amazon fish data provided by T.O. Greenhouse gas emissions were analyzed by R.M.A., S.A.S., and N.B. with input from B.R.F., S.K.H., and J.M.M. Computational analyses were developed and performed by C.P.G., J.M.G.-S., Q.S., X.W., Y.X., and G.P. The interactive visual supplement [Amazon EcoVistas (*30*)] was developed by R.B. and B.H.R. with input from C.P.G., Q.S., R.M.A., and S.A.H. Visualizations were made by Q.S., R.M.A., R.B., and B.H.R., with substantial contributions from S.A.T. and S.A.H. Funding for our Amazon Dams Computational Sustainability Working Group was acquired by C.P.G. and A.S.Flec. The manuscript was drafted by A.S.F., R.M.A., S.A.H., B.R.F., Q.S., and C.P.G. in close collaboration with S.A.S., S.A.T., N.L.P., S.K.H., J.H., P.B.M., M.G., J.M.M., and A.S.Flei. All authors reviewed the manuscript. **Competing interests:** The authors declare that they have no competing interests. **Data and materials availability:** The Pareto optimization code is available on eCommons and can be downloaded from the following persistent URL: https://doi.org/10.7298/qh5x-6f22. The Amazon EcoVistas tutorial and visualization of the Pareto frontier are available at www.cs.cornell.edu/gomes/udiscoverit/amazon-ecovistas/. All data needed to evaluate the conclusions in the paper are present in the paper and the supplementary materials. For convenience, the data, code, GitHub, and tutorial can also be accessed through a single webpage: www.cs.cornell.edu/gomes/udiscoverit/?tag=hydro.

SUPPLEMENTARY MATERIALS

science.org/doi/10.1126/science.abj4017
Materials and Methods
Figs. S1 to S6
Tables S1 to S3
References (*51*–*98*)
MDAR Reproducibility Checklist
Data S1 and S2

11 May 2021; accepted 16 December 2021
10.1126/science.abj4017

REPORTS

CORONAVIRUS

SARS-CoV-2 Omicron variant: Antibody evasion and cryo-EM structure of spike protein–ACE2 complex

Dhiraj Mannar[1]†, James W. Saville[1]†, Xing Zhu[1]†, Shanti S. Srivastava[1], Alison M. Berezuk[1], Katharine S. Tuttle[1], Ana Citlali Marquez[2], Inna Sekirov[2,3], Sriram Subramaniam[1,4]*

The newly reported Omicron variant is poised to replace Delta as the most prevalent severe acute respiratory syndrome coronavirus 2 (SARS-CoV-2) variant across the world. Cryo–electron microscopy (cryo-EM) structural analysis of the Omicron variant spike protein in complex with human angiotensin-converting enzyme 2 (ACE2) reveals new salt bridges and hydrogen bonds formed by mutated residues arginine-493, serine-496, and arginine-498 in the receptor binding domain with ACE2. These interactions appear to compensate for other Omicron mutations such as the substitution of asparagine for lysine at position 417 (K417N) that are known to reduce ACE2 binding affinity, resulting in similar biochemical ACE2 binding affinities for the Delta and Omicron variants. Neutralization assays show that pseudoviruses that display the Omicron spike protein exhibit increased antibody evasion. The increase in antibody evasion and the retention of strong interactions at the ACE2 interface thus represent important molecular features that likely contribute to the rapid spread of the Omicron variant.

The Omicron (B.1.1.529) variant of severe acute respiratory syndrome coronavirus 2 (SARS-CoV-2), first reported in November 2021, was quickly identified as a variant of concern with the potential to spread rapidly across the world. This concern is heightened because the Omicron variant is now circulating even among doubly vaccinated individuals. SARS-CoV-2 relies on a trimeric spike protein for host cell entry via recognition of the angiotensin-converting enzyme 2 (ACE2) receptor. The Omicron variant spike protein has 37 mutations, as compared to 12 mutations in the Gamma variant spike protein, which was previously the variant with the greatest number of spike protein mutations (*1*). Understanding the consequences of these mutations for ACE2 receptor binding and neutralizing antibody evasion is important in guiding the development of effective therapeutics to limit the spread of the Omicron variant and related variants.

The spike protein comprises two domains: the S1 domain, which contains the receptor binding domain (RBD), and the S2 domain, which is responsible for membrane fusion. The Omicron variant has 37 mutations (Fig. 1A) in the spike protein relative to the initial Wuhan-Hu-1 strain, with 15 of them present in the RBD

[1]Department of Biochemistry and Molecular Biology, University of British Columbia, Vancouver, BC, Canada. [2]BC Center for Disease Control Public Health Laboratory, Vancouver, BC, Canada. [3]Department of Pathology and Laboratory Medicine, University of British Columbia, Vancouver, BC, Canada. [4]Gandeeva Therapeutics, Inc., Vancouver, BC, Canada.
***Corresponding author. Email: sriram.subramaniam@ubc.ca**
†These authors contributed equally to this work.

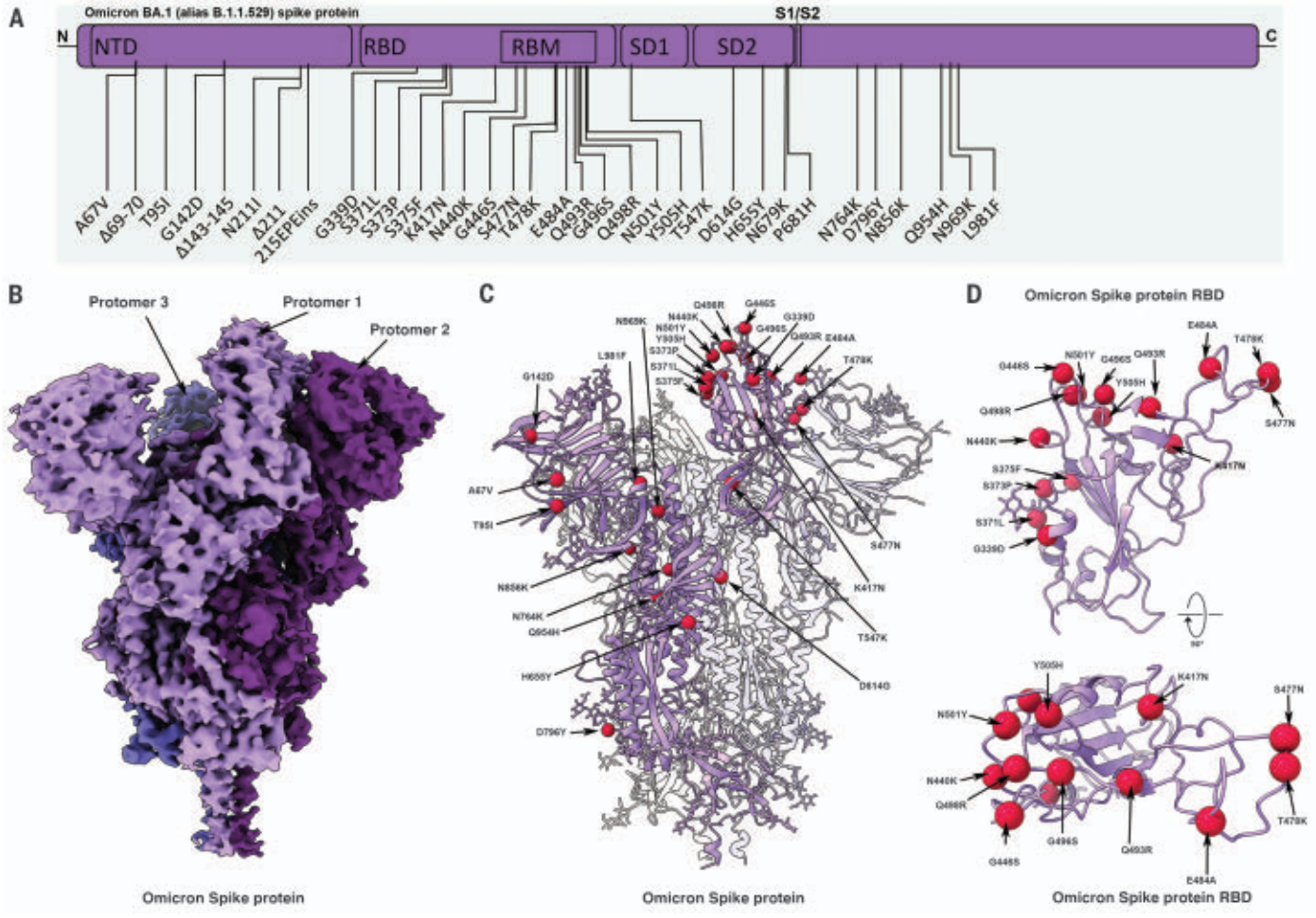

Fig. 1. Cryo-EM structure of the Omicron spike protein. (**A**) A schematic diagram illustrating the domain arrangement of the spike protein. Mutations present in the Omicron variant spike protein are labeled. RBM, receptor binding motif. (**B**) Cryo-EM map of the Omicron spike protein at 2.79-Å resolution. Protomers are colored in different shades of purple. (**C**) Cryo-EM structure of Omicron spike protein indicating the locations of modeled mutations on one protomer. (**D**) The Omicron spike protein RBD shown in two orthogonal orientations with Cα positions of the mutated residues shown as red spheres. Single-letter abbreviations for the amino acid residues are as follows: A, Ala; C, Cys; D, Asp; E, Glu; F, Phe; G, Gly; H, His; I, Ile; K, Lys; L, Leu; M, Met; N, Asn; P, Pro; Q, Gln; R, Arg; S, Ser; T, Thr; V, Val; W, Trp; and Y, Tyr.

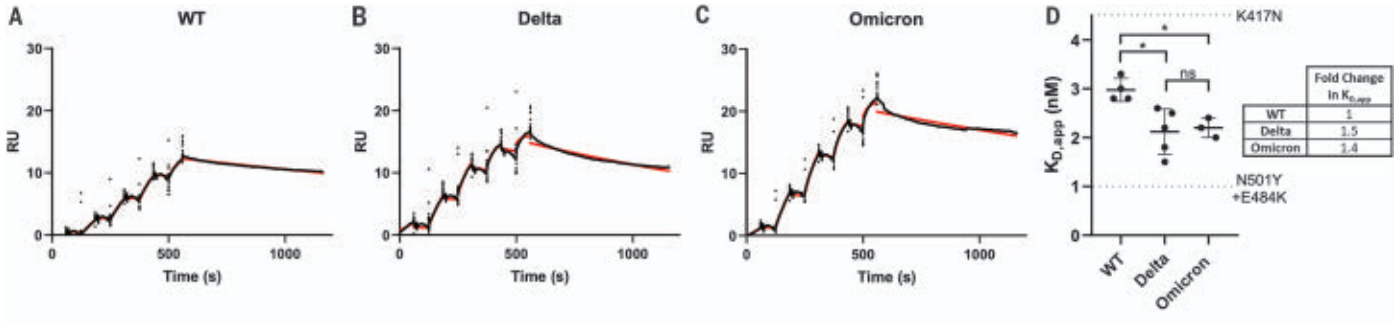

Fig. 2. SPR analysis of the wild-type, Delta, and Omicron spike protein affinities for human ACE2. (**A** to **C**) Representative traces of single-cycle kinetic analyses of spike protein–ACE2 binding. The raw data (black) is fit (red) to a model using a 1:1 binding stoichiometry from which apparent dissociation constants were derived. The curves were obtained by injecting 6.25, 31.25, 62.5, 125, and 250 nM of each spike protein in successive cycles. RU, response units; WT, wild type. (**D**) Quantitation of apparent dissociation constants ($K_{D,app}$) for the wild-type, Delta, and Omicron spike protein–ACE2 interactions. The standard deviation obtained from at least three technical replicates is shown. Horizontal dotted lines are plotted for mutants carrying only K417N (top) or N501Y and E484K (Glu^{484}→Lys; bottom) mutations to demonstrate the range of this assay (see fig. S2 for binding data). A Tukey's multiple comparisons test was performed on the wild-type, Delta, and Omicron binding affinities (*$P \leq 0.05$; ns, not significant). A table highlighting the fold changes in $K_{D,app}$ for the Delta and Omicron spike protein–ACE2 interactions relative to wild type is shown.

(*1*). The RBD mediates attachment to human cells through the ACE2 receptor and is the primary target of neutralizing antibodies (*2*, *3*). The Delta variant, which was the predominant SARS-CoV-2 lineage until the emergence of Omicron, has seven mutations in the spike protein relative to the Wuhan-Hu-1 strain, with two mutations falling within its RBD. Of the Delta spike protein mutations, two [T478K (Thr^{478}→Lys) in the RBD and D614G (Asp^{614}→Gly) at the C terminus of S1] are shared with the Omicron strain. Analysis of the sequence of the Omicron genome suggests that it is not derived from any of the variants circulating at present and may have a different origin (*4*).

Cryo–electron microscopy (cryo-EM) structural analysis of the Omicron spike protein ectodomain shows that the overall organization of the trimer is similar to that observed for the ancestral strain (*5*–*7*) and all earlier variants (*8*–*10*) (Fig. 1B and table S1). The RBD in one of the protomers (protomer 1) is well-resolved and is in the "down" position, whereas the other two RBDs are less well-resolved because they are flexible relative to the rest of the spike protein polypeptide. Similarly, the amino terminal domain (NTD) is poorly resolved, reflecting the dynamic and flexible nature of this domain. The mutations in the Omicron variant spike protein are distributed both on the surface and the interior of the spike protein (Fig. 1C), including the NTD and RBD regions. The mutations in the RBD are predominantly distributed on one face of the domain (Fig. 1D), which spans regions that bind ACE2 as well as those that form epitopes for numerous neutralizing antibodies (*11*).

The Omicron variant shares RBD mutations with previous variants of concern [K417N (Lys^{417}→Asn), T478K, and N501Y (Asn^{501}→Tyr)]. The N501Y and K417N mutations impart increased and decreased ACE2 binding affinities, respectively (*8*, *12*–*16*). These mutational effects preserve the same general impact on ACE2 affinity when present in isolation or in combination with other RBD mutations (*12*). However, the Omicron RBD contains additional mutations, most of which have been shown to decrease receptor binding in a high-throughput assay (table S2) (*17*), with the exception of G339D (Gly^{339}→Asp), N440K (Asn^{440}→Lys), S447N (Ser^{447}→Asn), and Q498R (Gln^{498}→Arg) (*17*, *18*). To measure the impact of Omicron spike protein mutations on human ACE2 binding affinity, we performed surface plasmon resonance (SPR) studies and compared the resulting apparent binding affinities ($K_{D,app}$) to wild-type and Delta spike proteins (Fig. 2). "Wild type" is used in this work to refer to the ancestral Wuhan-Hu-1 strain with the addition of the D614G mutation. Although the Omicron spike protein exhibits a measurable increase in apparent affinity for ACE2 relative to the wild-type spike protein [in agreement with a recent preprint (*19*)], the apparent ACE2 affinity is similar for both the Delta and Omicron variants (Fig. 2D). Despite harboring several RBD mutations that decrease ACE2 binding (fig. S2) (*12*, *16*, *17*), the preservation of overall ACE2 binding affinity for the Omicron spike protein suggests there are compensatory mutations that restore higher affinity for ACE2. Such mutational effects should be possible to visualize

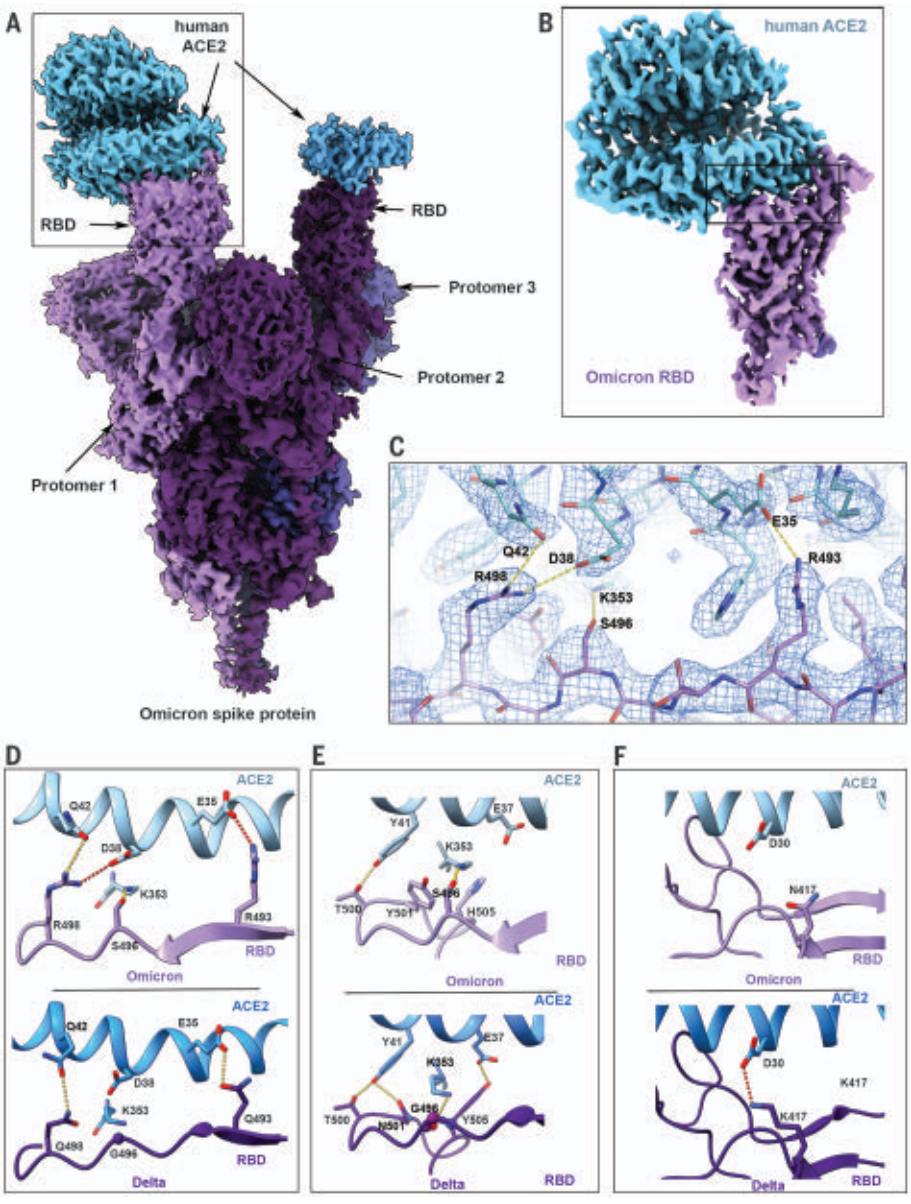

Fig. 3. Cryo-EM structure of the Omicron spike protein–ACE2 complex. (**A**) Cryo-EM map of the Omicron spike protein in complex with human ACE2 at 2.45-Å resolution after global refinement. The three protomers are colored in different shades of purple, and the density for bound ACE2 is colored in blue. (**B**) Cryo-EM map of the Omicron spike protein RBD in complex with ACE2 at 2.66-Å resolution after focused refinement. The boxed area indicates the region highlighted in (C). (**C**) Cryo-EM density mesh at the Omicron spike protein RBD–ACE2 interface, with fitted atomic model. Yellow and red dashed lines represent new hydrogen bonds and ionic interactions, respectively. (**D** to **F**) Comparison of the RBD-ACE2 interface between the Omicron (top) and Delta (bottom) variants. Compared with the Delta variant, new interactions are formed as a result of the mutations Q493R, G496S, and Q498R (D) and local structural changes owing to the N501Y and Y505H (Tyr^{505}→His) mutations (E) present in the Omicron variant. The salt bridge between Delta RBD K417 and ACE2 D30 that is present in the Delta variant spike protein but lost in the Omicron variant is highlighted in (F). Yellow and red dashed lines represent hydrogen bonds and ionic interactions, respectively.

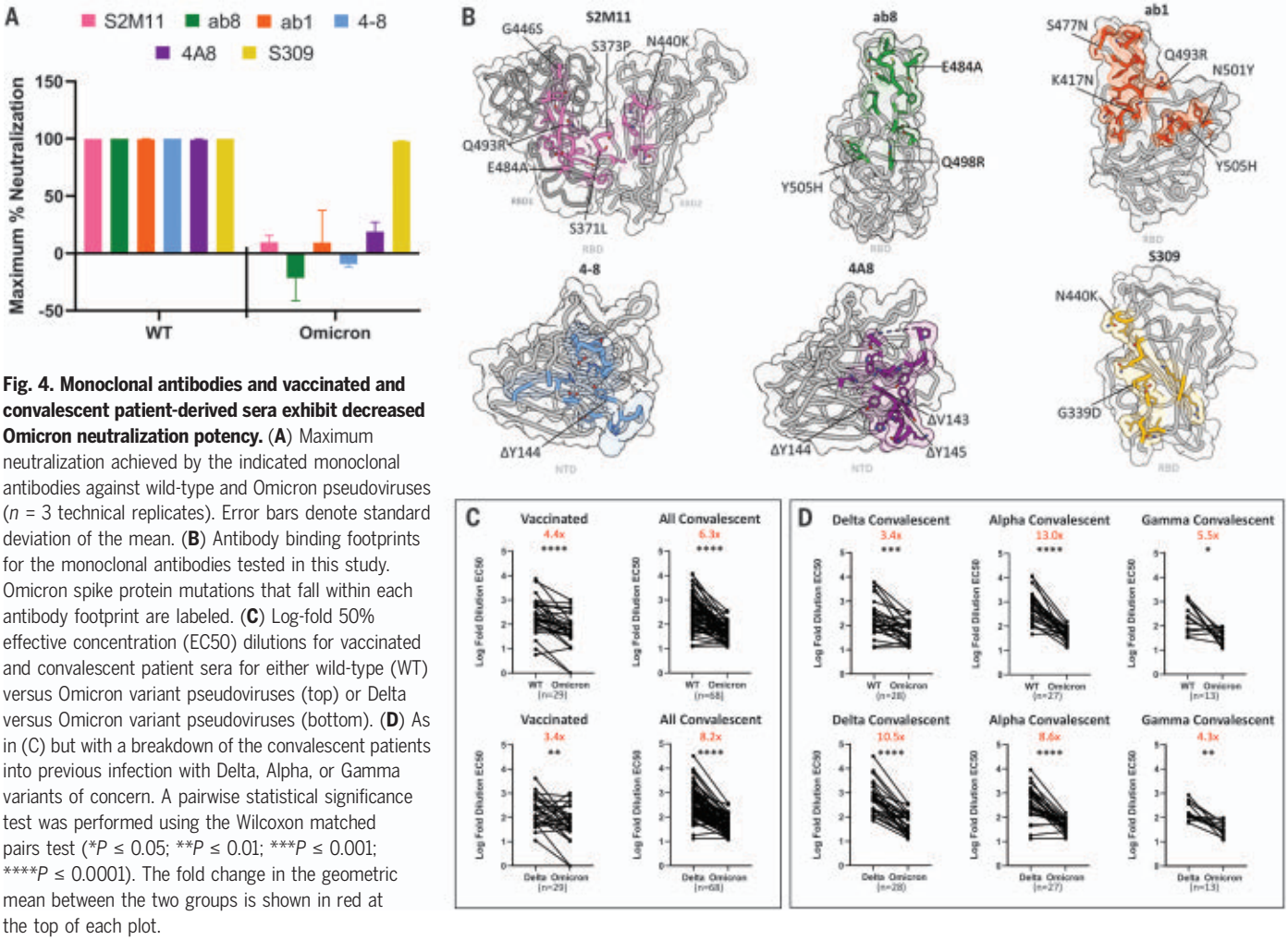

Fig. 4. Monoclonal antibodies and vaccinated and convalescent patient-derived sera exhibit decreased Omicron neutralization potency. (**A**) Maximum neutralization achieved by the indicated monoclonal antibodies against wild-type and Omicron pseudoviruses (n = 3 technical replicates). Error bars denote standard deviation of the mean. (**B**) Antibody binding footprints for the monoclonal antibodies tested in this study. Omicron spike protein mutations that fall within each antibody footprint are labeled. (**C**) Log-fold 50% effective concentration (EC50) dilutions for vaccinated and convalescent patient sera for either wild-type (WT) versus Omicron variant pseudoviruses (top) or Delta versus Omicron variant pseudoviruses (bottom). (**D**) As in (C) but with a breakdown of the convalescent patients into previous infection with Delta, Alpha, or Gamma variants of concern. A pairwise statistical significance test was performed using the Wilcoxon matched pairs test (*$P \leq 0.05$; **$P \leq 0.01$; ***$P \leq 0.001$; ****$P \leq 0.0001$). The fold change in the geometric mean between the two groups is shown in red at the top of each plot.

in a high-resolution structure of the spike protein–ACE2 complex.

Cryo-EM structural analysis of the human ACE2–Omicron spike protein complex shows strong density for ACE2 bound to the RBD of one of the protomers in the "up" position (Fig. 3A and table S1). Weaker density is observed for a second bound ACE2, suggesting partial occupancy of a second RBD under our experimental conditions. We focus on the structure of the ACE2–spike protein interface in the most strongly bound ACE2 molecule. Focused refinement of the RBD-ACE2 region resulted in a density map with a resolution of 2.66 Å at the spike protein–ACE2 interface (Fig. 3B), allowing the visualization of side chains involved in the interface (Fig. 3C). In Fig. 3, D to F, we compare the key interactions at this interface in the Omicron variant with corresponding interactions that we have recently reported for the Delta variant (*20*). In the Delta variant–ACE2 complex, there are hydrogen bonds formed by residues Q493 and Q498 on the spike protein with residues E35 (E, Glu) and Q42, respectively, on ACE2 (Fig. 3D). In the Omicron variant, three mutations are observed in this stretch: Q493R (Gln^{493}→Arg), G496S (Gly^{496}→Ser), and Q498R. Residue R493 replaces the hydrogen bond to ACE2 residue E35 with a new salt bridge, whereas residue R498 forms a new salt bridge with ACE2 residue D38 while maintaining a hydrogen bond interaction with ACE2 residue Q42. RBD residue S496 adds a new interaction at the interface by forming a hydrogen bond with ACE2 residue K353 (Fig. 3D). Additionally, the mutated residue Y501 in the Omicron RBD makes π-stacking interactions with Y41 in ACE2, as previously seen in the Alpha (B.1.1.7), Beta (B.1.351), and Gamma (P.1) variants (*8*, *12*), whereas mutated residue H505 (H, His) is not hydrogen-bonded to E37 in ACE2, in contrast to what we reported previously for the Y505 residue (Fig. 3E) (*20*).

These new interactions are offset by the loss of a key salt bridge between spike protein residue K417 and ACE2 residue D30 that is present in the Delta variant (Fig. 3F). In isolation, the K417N mutant displays reduced ACE2 binding affinity (*12*, *16*), but our findings suggest that the new mutations in the Omicron interface have a compensatory effect on the strength of ACE2 binding, providing an explanation for the similar ACE2 binding affinities that are observed (Fig. 2).

We next investigated the effects of Omicron mutations on neutralization by (i) a selection of monoclonal antibodies, (ii) sera obtained from 30 doubly vaccinated individuals with no prior history of COVID-19 infection, and (iii) sera obtained from a set of 68 unvaccinated convalescent patients who recovered from infection with either the Alpha, Gamma, or Delta variants. (A summary of patient demographics is in table S3.) We performed neutralization experiments using pseudoviruses that incorporate the wild-type, Delta variant, or Omicron variant spike proteins and compared the ability of these pseudovirions to evade antibodies. We compare evasion relative to the Delta variant, given that the Omicron variant is rapidly supplanting the Delta variant

in global prevalence, and to wild-type SARS-CoV-2, given that most SARS-CoV-2 vaccine immunogens at this time are based on this sequence (*21*).

We used a panel of neutralizing monoclonal antibodies that include four RBD-directed antibodies [ab1, ab8, S309, and S2M11; (*22*–*25*)] and two NTD-directed antibodies [4-8 and 4A8; (*26*, *27*)] to investigate the impact of Omicron RBD and NTD mutations on monoclonal antibody escape. In contrast to wild-type SARS-CoV-2 and the Alpha (B.1.1.7), Gamma (P.1), Kappa (B.1.617.1), and Delta (B.1.617.2) variants, the Omicron variant could not be completely neutralized at maximum concentrations of five of the six antibodies tested (Fig. 4A and fig. S4) (*20*, *28*). The loss of neutralizing activity for both the NTD-directed antibodies (4-8 and 4A8) against Omicron is likely due to the Δ144-145 deletion, which falls within the footprint of both of these antibodies (Fig. 4B). The escape from RBD-directed antibodies S2M11, ab8, and ab1 is likely due to the numerous Omicron mutations that lie within their respective footprints (Fig. 4B). By contrast, S309 (an antibody undergoing evaluation in clinical trials for treating patients with COVID-19) was able to fully neutralize the Omicron variant, consistent with previous reports that show retained neutralization capacity of S309 despite a mild decrease in potency (*19*, *29*–*31*). The unusually high number of mutations in the Omicron variant spike protein thus appear to confer broad antibody escape relative to previously emerged variants of SARS-CoV-2, consistent with emerging reports (*19*).

Sera obtained from patients not exposed to SARS-CoV-2 (prepandemic) showed negligible neutralization activity against wild-type SARS-CoV-2 and both the Delta and Omicron variants (fig. S5). Sera from either vaccinated or convalescent patients exhibited potent neutralization of wild-type pseudoviruses (figs. S6 to S9); sera from convalescent patients displayed, on average, a 6.3× decrease in ability to neutralize the Omicron variant relative to wild type (Fig. 4C, top). Sera from the vaccinated cohort also displayed reduced neutralization ability (4.4× decrease on average) with a wider variation driven by some individuals that showed greater loss of neutralization ability against Omicron. The comparison of change in neutralization potential between the Delta and Omicron variants is perhaps more relevant given the previous worldwide dominance of the Delta variant. Sera from convalescent patients shows an even greater drop in neutralization potency relative to the Delta variant (8.2× decrease), whereas the vaccinated group also shows reduction in potency, although to a lesser extent (3.4× decrease) (Fig. 4C, bottom).

A finer analysis of the unvaccinated convalescent cohort stratified into those who recovered from infection with either the Delta, Alpha, or Gamma variants (Fig. 4D) highlights the reduction in neutralization potency against the Omicron variant relative to the Delta variant in all populations, with especially notable drops for patients who recovered from infection with the earlier Alpha and Delta variants. The findings we report here are consistent with several other recent reports (*19*, *32*–*34*) that support the finding that the Omicron variant is more resistant to neutralization dependent on prior infection with an earlier variant or vaccination than any other variant of concern that has emerged over the course of the COVID-19 pandemic.

The large number of mutations on the surface of the spike protein, including the immunodominant RBD (Fig. 1), would be expected to help the virus escape antibodies elicited by vaccination or prior infection. It is interesting that the Omicron variant evolved to retain its ability to bind ACE2 efficiently despite these extensive mutations. The cryo-EM structure of the spike protein–ACE2 complex provides a structural rationale for how this is achieved: Interactions involving the new mutations in the Omicron variant at residues 493, 496, 498, and 501 appear to restore ACE2 binding efficiency that would be lost as a result of other mutations such as K417N. The Omicron variant thus appears to have evolved to selectively balance an increase in escape from neutralization with its ability to interact efficiently with ACE2. The increase in antibody evasion and the retention of strong interactions at the ACE2 interface are thus factors that likely contribute to the increase in transmissibility of the Omicron variant.

REFERENCES AND NOTES

1. S. Elbe, G. Buckland-Merrett, *Glob. Chall.* **1**, 33–46 (2017).
2. M. Hoffmann *et al*., *Cell* **181**, 271–280.e8 (2020).
3. L. Piccoli *et al*., *Cell* **183**, 1024–1042.e21 (2020).
4. C. Wei *et al*., *J. Genet. Genomics* 10.1016/j.jgg.2021.12.003 (2021).
5. A. C. Walls *et al*., *Cell* **181**, 281–292.e6 (2020).
6. D. Wrapp *et al*., *Science* **367**, 1260–1263 (2020).
7. J. Zhang *et al*., *Science* **372**, 525–530 (2021).
8. X. Zhu *et al*., *PLOS Biol.* **19**, e3001237 (2021).
9. J. Zhang *et al*., *Science* **374**, 1353–1360 (2021).
10. S. M.-C. Gobeil *et al*., *Science* **373**, eabi6226 (2021).
11. K. M. Hastie *et al*., *Science* **374**, 472–478 (2021).
12. D. Mannar *et al*., *Cell Rep.* **37**, 110156 (2021).
13. M. I. Barton *et al*., *eLife* **10**, e70658 (2021).
14. H. Liu *et al*., *Cell Res.* **31**, 720–722 (2021).
15. F. Tian *et al*., *eLife* **10**, e69091 (2021).
16. C. Laffeber, K. de Koning, R. Kanaar, J. H. G. Lebbink, *J. Mol. Biol.* **433**, 167058 (2021).
17. T. N. Starr *et al*., *Cell* **182**, 1295–1310.e20 (2020).
18. J. Zahradník *et al*., *Nat. Microbiol.* **6**, 1188–1198 (2021).
19. E. Cameroni *et al*., *Nature* 10.1038/s41586-021-04386-2 (2021).
20. J. W. Saville *et al*., bioRxiv 2021.2009.2002.458774 [Preprint] (2021); https://doi.org/10.1101/2021.09.02.458774.
21. F. Krammer, *Nature* **586**, 516–527 (2020).
22. W. Li *et al*., *Proc. Natl. Acad. Sci. U.S.A.* **117**, 29832–29838 (2020).
23. W. Li *et al*., *Cell* **183**, 429–441.e16 (2020).
24. M. A. Tortorici *et al*., *Science* **370**, 950–957 (2020).
25. D. Pinto *et al*., *Nature* **583**, 290–295 (2020).
26. L. Liu *et al*., *Nature* **584**, 450–456 (2020).
27. X. Chi *et al*., *Science* **369**, 650–655 (2020).
28. D. Mannar *et al*., bioRxiv 2021.12.17.473178 [Preprint] (2021); https://doi.org/10.1101/2021.12.17.473178.
29. L. VanBlargan *et al*., bioRxiv 2021.2012.2015.472828 [Preprint] (2021); https://doi.org/10.1101/2021.12.15.472828.
30. A. Cathcart *et al*., bioRxiv 2021.03.09.434607 [Preprint] (2021); https://doi.org/10.1101/2021.03.09.434607.
31. M. McCallum *et al*., bioRxiv 2021.2012.2028.474380 [Preprint] (2021); https://doi.org/10.1101/2021.12.28.474380.
32. D. Planas *et al*., *Nature* 10.1038/s41586-021-04389-z (2021).
33. A. Rössler, L. Riepler, D. Bante, D. v. Laer, J. Kimpel, medRxiv 2021.2012.2008.21267491 [Preprint] (2021); https://doi.org/10.1101/2021.12.08.21267491.
34. L. Liu *et al*., *Nature* 10.1038/s41586-021-04388-0 (2021).

ACKNOWLEDGMENTS

We thank K. Leopold (University of British Columbia) and C. Leung (Gandeeva Therapeutics, Inc.) for assistance with the SPR experiments and for helpful discussions. **Funding:** This work was supported by awards to S.S. from a Canada Excellence Research Chair Award; the VGH Foundation; Genome BC, Canada; and the Tai Hung Fai Charitable Foundation. D.M. is supported by a CIHR Frederick Banting and Charles Best Canada Graduate Scholarship Master's Award (CGS-M). J.W.S. is supported by a CIHR Frederick Banting and Charles Best Canada Graduate Scholarships Doctoral Award (CGS D) and a University of British Columbia President's Academic Excellence Initiative PhD Award. **Author contributions:** This work was the result of a concerted team effort from all individuals listed as authors. J.W.S. and D.M. carried out expression and purification of the Omicron spike protein and antibodies. D.M. performed the SPR binding analyses. D.M. and J.W.S. performed the pseudovirus neutralization experiments. I.S. and A.C.M. provided the vaccine-induced patient-derived sera samples and aided the interpretation of the patient data. A.M.B., S.S.S., and K.S.T. carried out experimental aspects of EM, including specimen preparation and data collection. X.Z. carried out computational aspects of image processing and structure determination. X.Z., S.S.S., D.M., J.W.S., and S.S. interpreted and analyzed the cryo-EM structures, binding analyses, and patient neutralization data and composed the manuscript with input from the rest of the authors. S.S. provided overall supervision for the project. **Competing interests:** All authors except for S.S. declare no competing interests. S.S. is the Founder and CEO of Gandeeva Therapeutics, Inc. **Data and materials availability:** All newly created materials described in this manuscript will be available from the corresponding author upon reasonable request. Cryo-EM reconstructions and atomic models generated during this study are available at the Protein Data Bank (PDB) and lectron Microscopy Data Bank (EMBD) databases under the following accession codes: unbound Omicron spike protein trimer (PDB ID 7T9J, EMD-25759), global ACE2-bound Omicron spike protein trimer (PDB ID 7T9K, EMD-25760), and focus-refinement of the ACE2-RBD interface for the ACE2-bound Omicron spike protein trimer (PDB ID 7T9L, EMD-25761). This work is licensed under a Creative Commons Attribution 4.0 International (CC BY 4.0) license, which permits unrestricted use, distribution, and reproduction in any medium, provided the original work is properly cited. To view a copy of this license, visit https://creativecommons.org/licenses/by/4.0/. This license does not apply to figures/photos/artwork or other content included in the article that is credited to a third party; obtain authorization from the rights holder before using such material.

SUPPLEMENTARY MATERIALS

science.org/doi/10.1126/science.abn7760
Materials and Methods
Figs. S1 to S9
Tables S1 to S3
References (*35*–*39*)
MDAR Reproducibility Checklist

19 December 2021; accepted 18 January 2022
Published online 20 January 2022
10.1126/science.abn7760

CULTURAL HERITAGE

Forgotten books: The application of unseen species models to the survival of culture

Mike Kestemont[1]*†, Folgert Karsdorp[2]†, Elisabeth de Bruijn[1,3], Matthew Driscoll[4], Katarzyna A. Kapitan[5,6,7,8,9], Pádraig Ó Macháin[10], Daniel Sawyer[11], Remco Sleiderink[1], Anne Chao[12]

The study of ancient cultures is hindered by the incomplete survival of material artifacts, so we commonly underestimate the diversity of cultural production in historic societies. To correct this survivorship bias, we applied unseen species models from ecology to gauge the loss of narratives from medieval Europe, such as the romances about King Arthur. The estimates obtained are compatible with the scant historic evidence. In addition to events such as library fires, we identified the original evenness of cultural populations as an overlooked factor in these assemblages' stability in the face of immaterial loss. We link the elevated evenness in island literatures to analogous accounts of ecological and cultural diversity in insular communities. These analyses call for a wider application of these methods across the heritage sciences.

Historical studies of human culture are hindered by the fact that they must work with incomplete samples of material artifacts (books, paintings, statues, etc.) that still survive (*1*, *2*) but do not necessarily represent the original population faithfully. Because of this survivorship bias, we risk underestimating the diversity of the cultural production of past societies. In response to this risk, we turn to bias correction methods from ecology. For monitoring species richness reliably, ecologists use statistical models that account for the unseen species in samples (*3*). This is necessitated by the common underdetection of species that are difficult to observe during bioregistration campaigns, creating a detection bias that must be accounted for quantitatively. Following recent studies (*4*, *5*) pointing to parallels between cultural and ecological diversity, we show that unseen species models can be applied to manuscripts preserving medieval literature. This enables us to estimate the size of the original population of works and documents and, in turn, the losses that these cultural domains sustained. We offer a large-scale estimate of the (im)material loss of narrative fiction from medieval Europe. This endeavor resonates with a broader interest in the persistence of cultural information in human societies, particularly in the domain of cultural evolution (*5*–*9*).

Narrative fiction was a mainstay of medieval culture (~600 to 1450 CE). The courtly chivalric romances concerning King Arthur

[1]University of Antwerp, Antwerp, Belgium. [2]KNAW Meertens Institute, Amsterdam, the Netherlands. [3]Ruhr-Universität Bochum, Bochum, Germany. [4]Arnamagnæan Institute, University of Copenhagen, Copenhagen, Denmark. [5]Linacre College, University of Oxford, Oxford, UK. [6]Department of Nordic Studies and Linguistics, University of Copenhagen, Copenhagen, Denmark. [7]Vigdís Finnbogadóttir Institute of Foreign Languages, University of Iceland, Reykjavík, Iceland. [8]The National Museum of Iceland, Reykjavík, Iceland. [9]The Museum of National History, Frederiksborg Castle, Hillerød, Denmark. [10]University College Cork, Cork, Ireland. [11]Merton College, University of Oxford, Oxford, UK. [12]Institute of Statistics, National Tsing Hua University, Hsin-Chu, Taiwan.
***Corresponding author. Email: mike.kestemont@uantwerp.be**
†These authors contributed equally to this work.

Fig. 1. Narrative fiction survives in a diverse range of medieval text carriers. (**A**) Fragment of *Strengleikar* repurposed to stiffen a bishop's miter (Copenhagen, Denmark, Arnamagnæanske Samling, AM 666 b 4to; used with permission). (**B**) Intact, lavishly illustrated codex (*Wigalois*; Leiden, University Library, Ltk. 537, f. 72v, CC-BY). (**C**) Fragment (binding waste) of an unidentified Dutch romance (KU Leuven Libraries, Special Collections, manuscript no. 1488; public domain).

and the Knights of the Round Table, for example, have had a long-lasting impact. Before movable-type printing in Europe (~1450 CE), handwritten documents (manuscripts) were used for the sustainable storage of text (*10*). In some places, such as Ireland and Iceland, manuscript circulation continued in this role into the modern era. Works of narrative fiction circulated through manually produced copies that survive as unique material artifacts, typically in the form of parchment or, later, paper codices (*11*). Thus, multiple parallel witnesses of the same medieval work could circulate. Today, manuscripts constitute the main evidence regarding medieval narrative fiction. Textual witnesses have been subject to various processes of decay and destruction (e.g., library fires) (*1*, *2*, *11*, *12*). Texts may survive in intact codices (Fig. 1B), but many of those works that survive at all now only exist in manuscripts that are fragmentary, lacking leaves or bearing damage from tearing, insects, overuse, etc. Because of parchment's durability, books were often recycled for more everyday practical uses (Fig. 1A) such as small boxes or used as tailors' measures or even packing material for meat. Additionally, strips of parchment were frequently used by binders to strengthen book spines (Fig. 1C).

The (material) loss of documents can entail the (immaterial) loss of works: A work becomes "lost" when none of the copies that once preserved it is known to have survived (*13*). A theoretical distinction must be made between documents that have been destroyed and those that have not been recovered yet, for example, because of inadequate cataloging; sources in the latter category might still reemerge. Different survival scenarios are represented in Fig. 2. We adopt a distinction between the (nonmaterial) work as listed in preexisting scholarly repertories and the (material) documents in which these works are attested (*14*). Although medieval narratives also circulated orally, the present analysis is necessarily limited to written production.

The survival rates for medieval documents are traditionally estimated based on medieval library catalogs: If the listed specimens can still be identified, then the calculation of the survival rates of these books is straightforward (*1*). Authoritative studies have suggested (for the Holy Roman Empire) an overall survival rate of ~7% for general purpose manuscripts, which must be adjusted upward to ~20% for higher-end codices (*1*, *11*, *15*). Such estimates are nevertheless problematic because they depend on a small sample of catalogs from protected collection environments, with catalogers frequently omitting lower-end documents (*15*). A prior attempt (*16*) to apply methods from survival studies to this problem met with criticism because the figures obtained did not fit with other historical evidence (*17*, *18*). Regarding the loss of works, there has been little quantitative work (*19*). Conventional approaches rely on allusions to lost works, for example, in library catalogs (*13*), but many lost works will not have been mentioned. Egghe and Proot

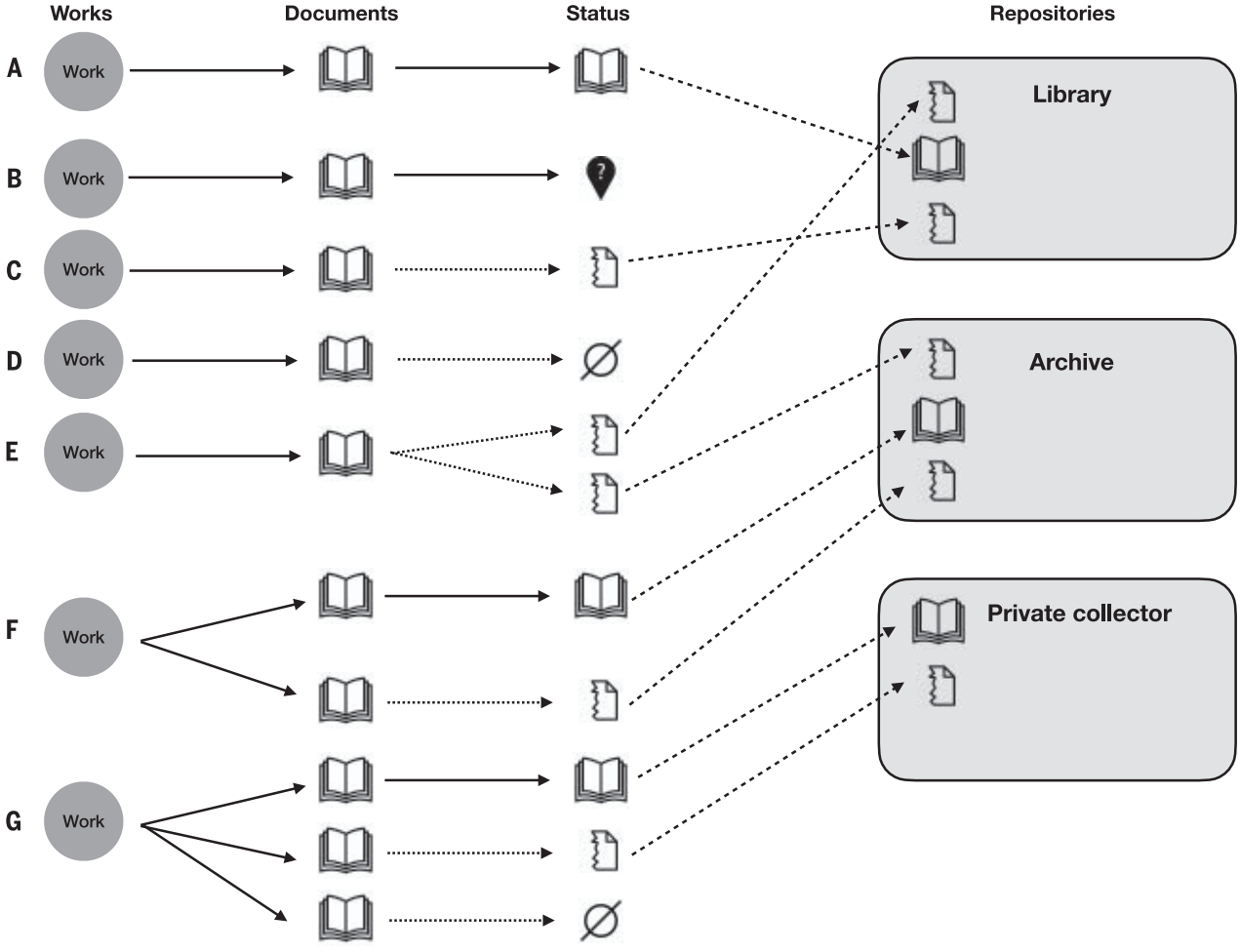

Fig. 2. Schematic representation of example survival scenarios for medieval literature. Individual works were copied into one [(**A**) to (**E**)] or more [(**F**) and (**G**)] documents, the survival status of which varies from intact codices (A) to fragments [(C) and (E)] residing in repositories such as libraries, archives, or private collections. Lost documents can be fully (D) or partly (G) destroyed or may not have been recovered yet (B). For lost works [(B) and (D)], none of the original documents has been recovered.

published a pioneering estimator for the loss of multicopy printed works (*20*), which was later identified as an unseen species model. Their approach, however, requires an estimate of the print runs of hand-pressed books, which does not suit manuscripts.

We build on the information-theoretic analogy that medieval works can be treated as distinct species in ecology, and that the number of extant documents for each work can be regarded as analogous to the number of sightings for an individual species in a sample. Thus, if we treat the available count information for medieval literature as "abundance data" (*3*), then one can apply unseen species models to estimate the number of lost works in a corpus or assemblage. We collected count data for surviving medieval heroic and chivalric fiction in six European vernaculars (*21*): three insular (Irish, Icelandic, and English) and three continental (Dutch, French, and German). For all works, we have listed the number of handwritten medieval documents in which they survive (Table 1). Next, we applied nonparametric methods to estimate the original richness of these traditions. For a given assemblage, let $(X_1, X_2, \ldots, X_{S_{obs}})$ represent the abundance-based frequencies for S_{obs} unique works that were observed in n documents.

Chao1 is a method to estimate a lower bound on $\hat{f}_0$, or the number of undetected species in an assemblage, based on the number of singletons (f_1, species sighted only once) and doubletons (f_2, species sighted exactly twice) in a sample of n individuals. The original number of works ($\hat{S}$) can then be estimated as $S_{obs} + \hat{f}_0$ (*22*). Chao1 is not specific to ecology and has been derived under a very general model; it can be applied as a universally valid lower-bound richness estimator to any hyperdiverse, undersampled collection of types, such as stone tools, coins, or even words (*23*). Therefore, this estimator is even more widely applicable in the heritage sciences than shown here (*24*). In this framework, the survival ratio for the works can be quantified as the sample completeness or $S_{obs}/\hat{S}$: the ratio of the number of unique observed works (S_{obs}) over the estimated true species abundance $\hat{S}$ (*25*). Species richness is an intuitive measure to quantify species diversity, but there are alternative measures, such as the Shannon or Simpson diversity (both put less weight on rare species). The Hill number profile (*26*) allows us to compare a sample's diversity across various values of q, a scalar corresponding to different diversity measures at specific points (e.g., $q = 0$ for richness, $q = 1$ for Shannon, $q = 2$ for Simpson). Hill numbers are now the diversity measure of choice in ecology for quantifying species diversity and decomposition (*25*).

We also use an extension of Chao1 (*27*) that estimates the minimum number m of additional observations that are required to observe each of the $\hat{f}_0$ species at least once. This number will approximate the number of lost documents in an assemblage, so that we can estimate the original population size as $n + m$. Chao1 and the minimum sampling extension were derived as a lower bound, which implies that the estimates of the survival ratios below, strictly speaking, offer an upper bound on the loss of works and documents, and it is possible that even more literature was lost. Nevertheless, Chao1 works satisfactorily as a nearly unbiased point estimator when the abundances of rare species are nearly homogeneous or singletons and undetected species have approximately the same mean abundances (*23*). Because Chao1 is nonparametric, the lower bound is valid for any distribution of entities among types and it should be robust to differences in survival across document types (*15*).

Finally, we analyzed the evenness in these assemblages or the extent of equity among species abundances (*28*). A community's evenness will affect its stability in the face of external forcing, in particular its ability to withstand the impact of diversity-threatening events such as wildfires (*29*). Given two equal-sized assemblages, the more even assemblage will be more resistant to the loss of works through document losses. Below, we chart evenness profiles for one class (E_3) of evenness measures. These curves can be connected to the slope of a Hill number profile; their steepness enables the intuitive comparison of the (un)evenness in the works' abundances for the reconstructed assemblages (*21*).

The results for the union of the corpora (Table 1 and table S2) suggest an overall survival ratio with a 68.3% confidence interval (CI) of 63.2 to 73.5% for works and a 9.0% CI of 7.5 to 10.7% for documents. The species accumulation curve (Fig. 3B) indicates at which rate we might still be discovering new works in the future by sighting more documents (*3*). Figure 3A shows the empirical and estimated Hill number profiles. At $q = 0$, the curves indicate the absolute size of our current underestimation of the original diversity in the

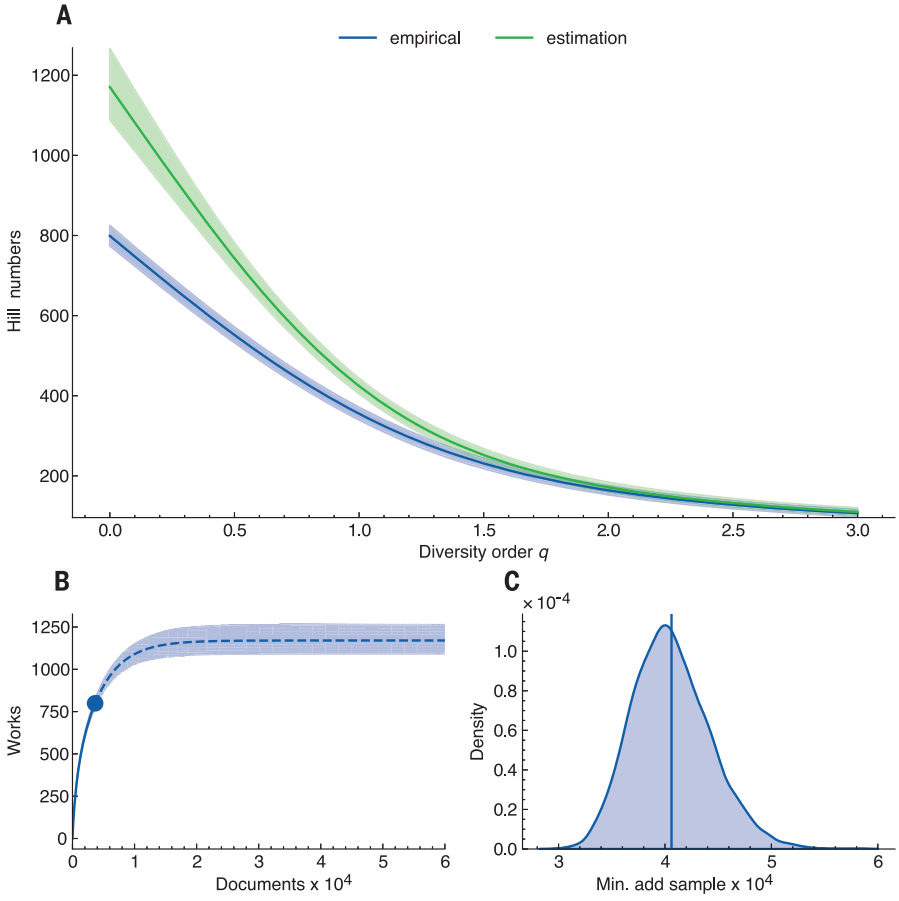

Fig. 3. Estimates for the union of the six assemblages. (**A**) Hill number curves (for $0 \le q \le 3$), empirical and estimated, showing the absolute underestimation of the original diversity of works. (**B**) Species accumulation curve plotting the number of works as a function of the number of documents. The filled circle shows the observable data, the solid line the rarefaction for sample sizes $<n$, and the dashed line the extrapolation to sample sizes $>n$. (**C**) Kernel-density plot for the estimated number of documents.

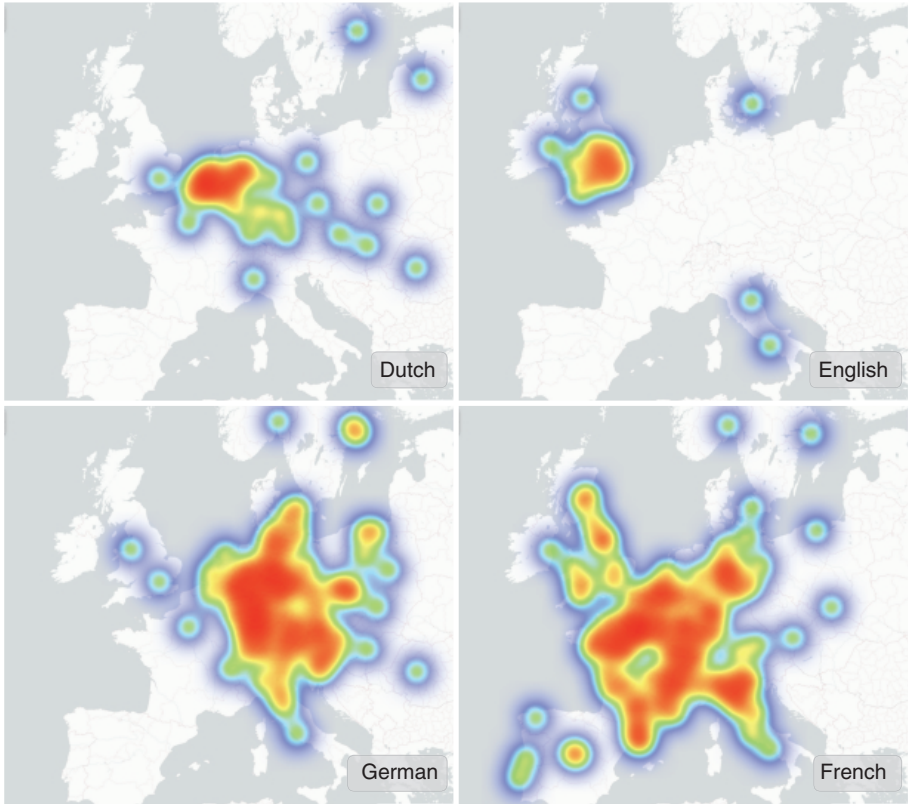

Fig. 4. Heatmap of the geolocations of the repositories where documents are kept for four vernaculars. Figure was made with Leaflet version 1.7.1 software.

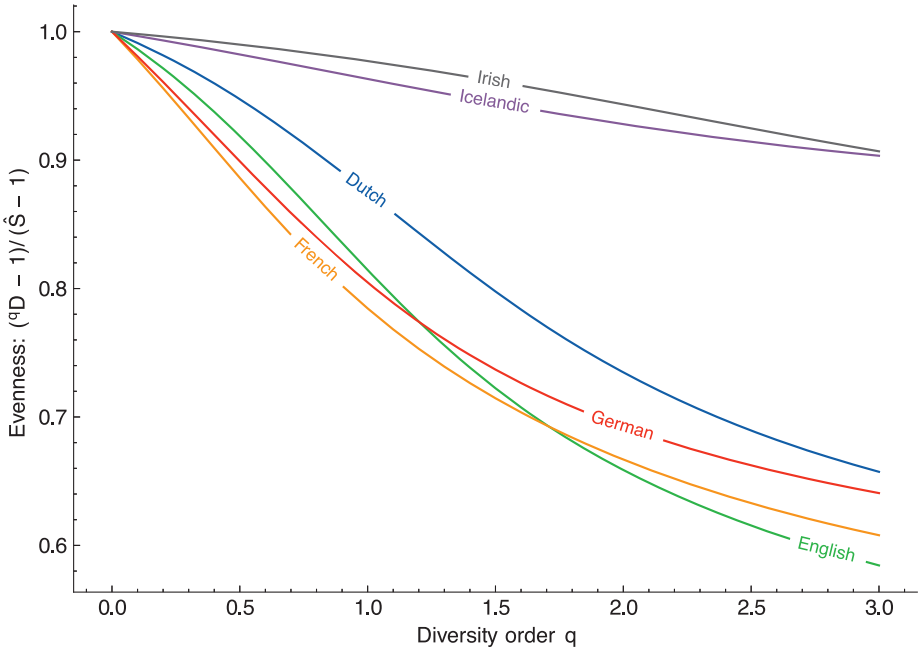

Fig. 5. Normalized evenness profiles (E_3) for the six individual vernaculars, plotting ^qE as a function of order $0 \le q \le 3$. The values on the *y*-axis reflect the estimated evenness in the reconstructed assemblages.

combined assemblage of chivalric and heroic narratives from the medieval period. Of the original ~1170 works that once would have existed, 799 would survive today. Likewise, the 3648 documents that are still observable constitute a sample from a population that originally would have counted ~40,614 specimens (Fig. 3C).

We observed considerable intervernacular variation (Table 1), ranging from the relatively poorly surviving English works (38.6%) to the relatively intact German tradition (79.0%). Dutch and French have a substantially lower survival factor than German, whereas two of the insular assemblages, Icelandic and Irish, have sustained similar losses to German, with point estimates of 77.3 and 81.0% and 16.9 and 19.2% for the survival of works and documents, respectively (*12*). It is puzzling that Old and Middle English documents did not travel far during their postmedieval afterlives (Fig. 4), yet other literatures survive in a wide manuscript diaspora. The survival estimates for works and documents yield similar rankings

Table 1. Point estimates of survival ratios in six traditions. For works using Chao1 (i.e., sample completeness at $q = 0$) and documents (ms) using the minimum sampling extension, including the number of works (S_{obs}), documents (n), singletons (f_1), and doubletons (f_2).

Language	f_1	f_2	S_{obs}	n	Chao1	ms
Dutch	45	13	75	167	0.492	0.075
English	42	8	69	176	0.386	0.049
French	90	21	222	1473	0.535	0.054
German	36	19	128	1088	0.790	0.145
Icelandic	44	28	117	295	0.773	0.169
Irish	69	54	188	449	0.810	0.192
Total	326	143	799	3648	0.683	0.090

(Table 1). In the supplementary materials, we compare Chao1 with three other estimators with similar results (fig. S1). Figure 5 shows the (estimated) evenness profiles and offers further insight into the distributional properties characterizing the assemblages. The profiles (fig. S2) for additional evenness classes ($E_1 - E_5$) yield consistent findings. Here, too, we note the atypical nature of Icelandic and Irish: Compared with the highly uneven distribution of French, for example, these two insular literatures feature a much more even distribution of documents over works.

Regarding documents, our results confirm the severity of the losses, with survival ratio estimates ranging from 4.9% (English) to 19.2% (Irish). This corroborates previous estimates from book history, positing an overall survival factor of 7%, i.e., slightly lower than our point estimate for the union (9.0% CI = 7.5 to 10.7%). Contrary to previous analyses (*16*, *17*), these results are therefore compatible with evidence from book history. It remains to be seen whether these estimates will scale to other cultural domains, but this analysis reveals important relative differences in the persistence of medieval heroic and chivalric narrative across Europe. Some of these differences have not been observed before and challenge existing assumptions. For example, our results suggest that Irish and Icelandic literature has been preserved comparatively well compared with some of the more canonical mainland literatures (*12*).

In ecology, island ecosystems stand out; despite being comparatively species-poor for their land surface, they feature a higher endemic species richness compared with mainland regions (*30*). Additionally, insular assemblages demonstrate a higher species evenness because of the lack of predators and other factors. A parallel emerges with some of the cultural diversity profiles for island regions reconstructed here: If land-isolated areas preserve biological heritage more effectively, then the same might hold true for cultural heritage. Previous discussions about the survival of historic literature have focused on factors such as library fires or collectors' interests (*1*). We have identified an additional key aspect that is typically overlooked: the evenness with which documents were originally distributed over works fundamentally affected an assemblage's stability (*29*). Medieval French literature, for instance, was sizable, but its long tail of low-abundance works rendered it more susceptible to immaterial loss. Thus, whereas the loss figures for Icelandic and Irish are considerable, their distributional characteristics seem to have made them more resistant to post-medieval losses.

Which societies produce a highly even cultural output to safeguard the retention of their diversity? The role of demography, especially population size, has been hotly debated in cultural evolution (*6*, *7*, *31*). Smaller, isolated social groups can be more susceptible to the random loss of cultural traits because of stochastic drift (*6*), although these communities can adopt fitness-improving behavior to guard against such information loss. The topology of social networks seems crucial: A low network degree (or interconnectedness between individuals) can counter the impact of drift and promote the retention of cultural complexity (*32*). For the remote island of Rapa Nui, for example, a model-based account showed how structural constraints in social interactions might have stimulated the retention of diversity (*8*). We have extended these simulations (*21*) to show that a lower network degree, under neutral models of transmission, invariably leads to a more evenly distributed cultural production (fig. S3).

REFERENCES AND NOTES

1. E. Buringh, *Medieval Manuscript Production in the Latin West, Explorations with a Global Database* (Brill, 2011).
2. F. Bruni, A. Pettegree, *Lost Books: Reconstructing the Print World of Pre-Industrial Europe* (Brill, 2016).
3. N. J. Gotelli, R. K. Colwell, in *Biological Diversity: Frontiers in Measurement and Assessment*, A. E. Magurran, B. J. McGill, Eds. (Oxford University Press, 2011), pp. 39–54.
4. L. J. Gorenflo, S. Romaine, R. A. Mittermeier, K. Walker-Painemilla, *Proc. Natl. Acad. Sci. U.S.A.* **109**, 8032–8037 (2012).
5. H. Zhang, R. Mace, *Evol. Hum. Sci.* **3**, e30 (2021).
6. J. Henrich, *Am. Antiq.* **69**, 197–214 (2004).
7. J. Henrich *et al.*, *Proc. Natl. Acad. Sci. U.S.A.* **113**, E6724–E6725 (2016).
8. C. P. Lipo, R. J. DiNapoli, M. E. Madsen, T. L. Hunt, *PLOS ONE* **16**, e0250690 (2021).
9. A. Acerbi, J. Kendal, J. J. Tehrani, *Evol. Hum. Behav.* **38**, 474–480 (2017).
10. E. Kwakkel, *Books Before Print* (Arc Humanities Press, 2018).
11. U. Neddermeyer, *Von der Handschrift zum gedruckten Buch. Schriftlichkeit und Leseinteresse im Mittelalter und in der frühen Neuzeit. Quantitative und qualitative Aspekte* (Harrassowitz, 1998).
12. D. Ó Corráin, *Peritia* **22–23**, 191–223 (2011–2012).
13. R. Wilson, *The Lost Literature of Medieval England* (Methuen, ed. 2, 1970).
14. P. Eggert, *The Work and the Reader in Literary Studies: Scholarly Editing and Book History* (Cambridge Univ. Press, 2019).
15. H. Wijsman, *Luxury Bound. Illustrated Manuscript Production and Noble and Princely Book Ownership in the Burgundian Netherlands (1400-1550)* (Brepols, 2010).
16. J. L. Cisne, *Science* **307**, 1305–1307 (2005).
17. G. Declercq, *Science* **310**, 1618 (2005).
18. N. D. Pyenson, L. Pyenson, *Science* **309**, 698–701 (2005).
19. M. S. Cuthbert, *Musica Disciplina* **54**, 39–74 (2009).
20. L. Egghe, G. Proot, *J. Informetrics* **1**, 257–268 (2007).
21. Materials and methods are available as supplementary materials.
22. A. Chao, *Scand. J. Stat.* **11**, 265–270 (1984).
23. A. Chao, C. H. Chiu, in *Methods and Applications of Statistics in the Atmospheric and Earth Sciences*, N. Balakrishnan, Ed. (Wiley, 2012), pp. 76–111.
24. M. I. Eren, A. Chao, W.-H. Hwang, R. K. Colwell, *PLOS ONE* **7**, e34179 (2012).
25. A. Chao *et al.*, *Ecol. Res.* **35**, 292–314 (2020).
26. M. O. Hill, *Ecology* **54**, 427–432 (1973).
27. A. Chao, R. K. Colwell, C.-W. Lin, N. J. Gotelli, *Ecology* **90**, 1125–1133 (2009).
28. A. Chao, C. Ricotta, *Ecology* **100**, e02852 (2019).
29. I. Donohue *et al.*, *Ecol. Lett.* **19**, 1172–1185 (2016).
30. R. J. Whittaker, J. M. Fernández-Palacios, *Island Biogeography: Ecology, Evolution, and Conservation* (Oxford Univ. Press, 2006).
31. A. Acerbi, R. A. Bentley, *Evol. Hum. Behav.* **35**, 228–236 (2014).
32. M. Cantor *et al.*, *Proc. Biol. Sci.* **288**, 20203107 (2021).

ACKNOWLEDGMENTS

We thank D. Schoenaers, G. Henley, J.-B. Camps, B. Bastert, D. Könitz, and J. Deploige for their help, as well as the five anonymous referees. **Funding:** E.D.B. was supported by a postdoctoral fellowship from FWO Flanders; K.A.K. was supported by the Carlsberg Foundation (Visiting Fellowship CF20-225 and H. M. Queen Margrethe II Distinguished Research Fellowship CF18-500). **Author contributions:** Conceptualization: M.K., F.K., E.D.B., M.D., K.A.K., P.O.M., D.S., R.S., A.C.; Data curation: M.K., F.K., E.D.B., M.D., K.A.K., P.O.M., D.S., R.S., A.C.; Formal analysis: M.K., F.K.; Investigation: M.K., F.K., E.D.B., M.D., K.A.K., P.O.M., D.S., R.S., A.C.; Methodology: M.K., F.K., A.C.; Software: M.K., F.K.; Validation: M.K., F.K., E.D.B., M.D., K.A.K., P.O.M., D.S., R.S., A.C.; Visualization: M.K., F.K.; Writing – original draft: M.K., F.K., E.D.B., M.D., K.A.K., P.O.M., D.S., R.S., A.C.; Writing – review and editing: M.K., F.K., E.D.B., M.D., K.A.K., P.O.M., D.S., R.S., A.C. **Competing interests:** The authors declare no competing interests. **Data and materials availability:** Data and code have been deposited to an open access repository (33). This paper is released with a Python software package (Copia, available from PyPI), all under a CC-BY-SA license, to replicate our findings and stimulate the adoption of this approach in other domains.

SUPPLEMENTARY MATERIALS

science.org/doi/10.1126/science.abl7655
Materials and Methods
Supplementary Text
Figs. S1 to S3
Tables S1 and S2
References (*33*–*99*)

4 August 2021; accepted 18 November 2021
10.1126/science.abl7655

BIOMECHANICS

Biomimetic fracture model of lizard tail autotomy

Navajit S Baban[1], Ajymurat Orozaliev[1], Sebastian Kirchhof[2], Christopher J Stubbs[3], Yong-Ak Song[1,4,5]*

Lizard tail autotomy is an antipredator strategy consisting of sturdy attachment at regular times but quick detachment during need. We propose a biomimetic fracture model of lizard tail autotomy using multiscale hierarchical structures. The structures consist of uniformly distributed micropillars with nanoporous tops, which recapitulate the high-density mushroom-shaped microstructures found on the lizard tail's muscle fracture plane. The biomimetic experiments showed adhesion enhancement when combining nanoporous interfacial surfaces with flexible micropillars in tensile and peel modes. The fracture modeling identified micro- and nanostructure-based toughening mechanisms as the critical factor. Under wet conditions, capillarity-assisted energy dissipation pertaining to liquid-filled microgaps and nanopores further increased the adhesion performance. This research presents insights on lizard tail autotomy and provides new biomimetic ideas to solve adhesion problems.

For millions of years, the constant struggle for survival has driven lizards to evolve a defense mechanism known as tail or caudal autotomy (*1*, *2*). This autotomy has a seemingly paradoxical nature: sturdy attachment at normal times but quick detachment during need. As an explanation of tail autotomy, previous studies have reported the segmented anatomy of the lizard tail with functional fracture planes (*3*, *4*) in skeletal muscles throughout the postpygal vertebrae (for details, see supplementary text 1). The fracture planes consist of the bulged-out distal ends of muscle fibers arranged as highly dense, mushroom-shaped micropillars (separated by connective tissue) (*3*, *4*) with a role in autotomy that is still not understood quantitatively.

From an engineering perspective, a typical fracture plane would make the tail overly vulnerable to fracture, even in situations that are not life threatening. In reality, the tail remains sturdily and faithfully connected to the body part, quickly detaching only when the lizard wills it. Simplistic fracture models of lizard tail autotomy cannot resolve the tail's attachment's seemingly paradoxical nature. A proteomic study (*3*) on the fluid that was released after Tokay gecko tail autotomy revealed an absence of any protein-breaking chemicals, thus suggesting a mechanical fracture problem. To understand the biophysics of lizard tail autotomy, we analyzed the fracture plane connections of three different lizard species: *Hemidactylus flaviviridis* (Gekkonidae), *Cyrtopodion scabrum* (Gekkonidae), and *Acanthodactylus schmidti* (Lacertidae).

Fig. 1A shows the autotomy location in the *H. flaviviridis* individual's tail and illustrates the segmented nature of the tail connected

[1]Division of Engineering, New York University Abu Dhabi, Abu Dhabi, United Arab Emirates. [2]Division of Science, New York University Abu Dhabi, Abu Dhabi, United Arab Emirates. [3]Gildart Haase School of Computer Sciences and Engineering, Fairleigh Dickinson University, Teaneck, NJ 07666, USA. [4]Department of Chemical and Biomolecular Engineering, Tandon School of Engineering, New York University, New York, NY 11201, USA. [5]Department of Biomedical Engineering, Tandon School of Engineering, New York University, New York, NY 11201, USA.
*Corresponding author. Email: rafael.song@nyu.edu

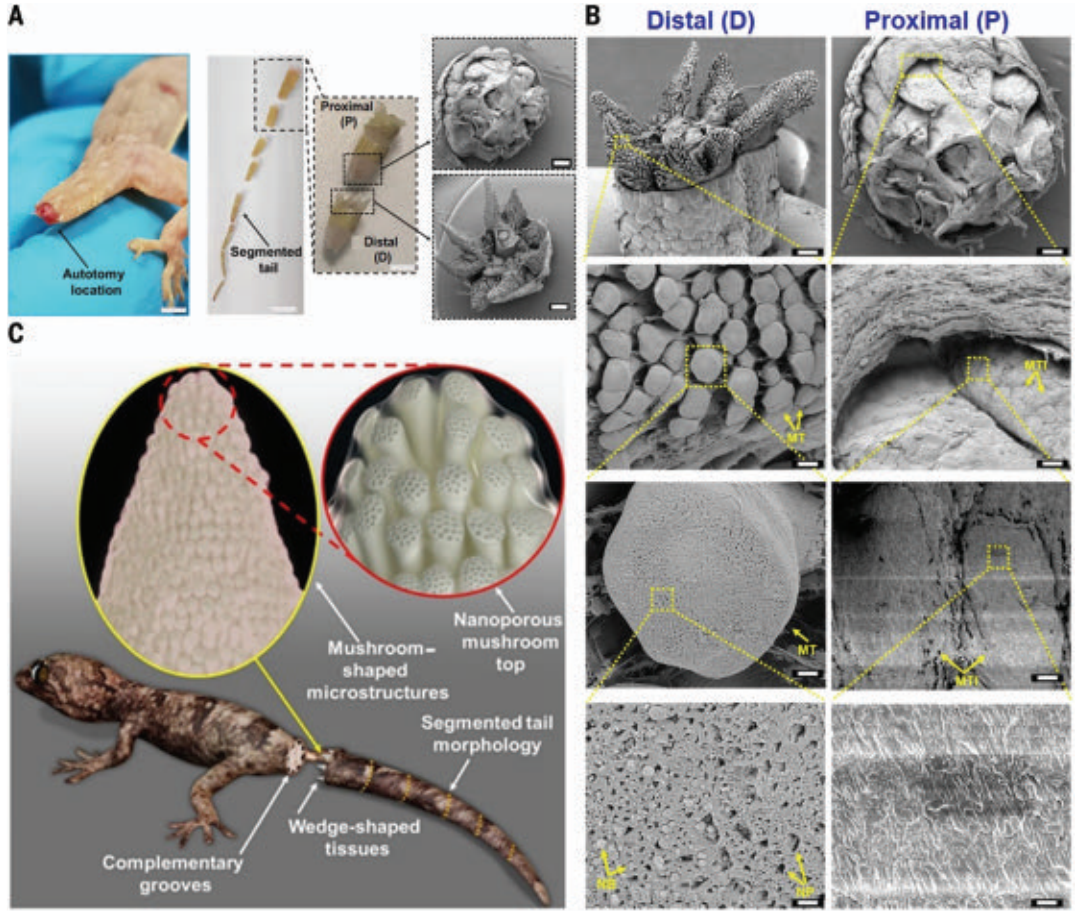

Fig. 1. Scanning electron microscope (SEM) image of the autotomized interface of an *H. flaviviridis* tail. (**A**) Autotomized tail location (scale bar, 1.5 cm). Segmented tail morphology (scale bar, 1 cm) shows region P, representing the proximal part of the tail, and region D, representing the distal part (scale bar, 0.5 cm), in a plug-and-socket type assembly (scale bar, 1 mm). (**B**) SEM of the distal (D) part showing the wedge-shaped tissues with highly dense mushroom-shaped microstructures (scale bar, 1 mm). The enlarged portion shows the mushroom-shaped micropillared arrangement (scale bar, 100 μm) with the single mushroom top indicated as MT (scale bar, 10 μm) containing the nanopores (NP) and nanobeads (NB) (scale bar, 1 μm). SEM of region P (scale bar, 1 mm) shows the corresponding MT imprints indicated as MTI (scale bar, 100 μm). The single MTI (scale bar, 10 μm) shows a planar topology (scale bar, 1 μm). (**C**) Hypothesized model of the lizard tail interface between two complementary segments before fracture, consisting of micropillared nanoporous top connections at the wedge-shaped tissue faces.

through a "plug-and-socket" sort assembly. The distal part contains eight (two ventral, four lateral, and two dorsal) circumferentially arranged wedge-shaped muscle bundles, whereas the proximal part encloses the corresponding complementary grooves or pockets lined with layers of connective tissue (myosepta). Fig. 1B shows the high-density mushroom-shaped micropillars (muscle fibers with dilated termini) on the wedge-shaped muscle bundle and the complementary pockets where the wedges remained inserted before fracture. Microcomputer tomography of the fractured tail (*H. flaviviridis* individual) showed fragmented intravertebral fracture planes located in close proximity to the wedge-shaped muscle fracture planes (see supplementary text 2). The enlarged portions within Fig. 1B show the associated mushroom top with dense nanopores and scanty nanobeads constituting the interface. The magnified view of the complementary pockets shows the planar mushroom top imprints in the myoseptum resulting from its surface contact–based attachment with the mushroom top in vivo. These surface imprints implied that the mushroom tops were not penetrating the proximal part, as would be the case for stronger tail attachment. Instead, the lizard has adopted a different strategy for tail attachment at the interface composed of the surface contact–based attachment with microscale and nanoscale discontinuities. Thus, we hypothesize a model of how the distal tail section could have been attached to the proximal one before fracture, in which mushroom-shaped microstructures contact the opposite surface with their nanoporous tops, as schematically illustrated in Fig. 1C.

These multiscale hierarchical features correlated with design strategies extensively found in nature (for examples, see supplementary text 3) that imply toughening mechanisms associated with micro- and nanoscale structural features. The high-speed video analysis showed that the tail's bending actuated the fracture (movies S3 and S4 and supplementary text 4). By contrast, the tensile stretching of the tail showed no fracture at all (Fig. 2). Moreover, on the basis of the *H. flaviviridis* specimens analyzed (n = 7), it was also confirmed that the tail should be grasped at least a short distance distal to the autotomy plane. This would provide a sufficient pivot length about which the muscles can favorably act. For *A. schmidti*, the shorter pivot distance required more force to induce the fracture (movie S5 and S6).

To support our hypothesis, we built a biomimetic model using polydimethylsiloxane micropillars with nanoporous tops in two different height ranges: 1.75 to 30 μm as low-aspect-ratio micropillars and 30 to 100 μm as high-aspect-ratio micropillars (Fig. 3, A and B). For both the low- and high-aspect-ratio micropillars, the results in Fig. 3, C to H and I to N (summarized in table S1), show that adhesion energy and peak force significantly decreased in peel mode (see experimental details in supplementary text 5), demonstrating the fracture's mode-dependent vulnerability. The difference in mode-dependent results can be explained by the equal load sharing of the micropillars (*5*), which was quantified by comparing the associated characteristic stress decay lengths (*6*, *7*). We recorded a 17-fold difference between the modes (see the "Equal load sharing calculation" section in supplementary text 5). The mode-dependent findings correlated with the experimental results of the high-speed video analysis showing a facile fracture in the bending mode.

Within each mode, a significant increase in adhesion energy and peak force was obtained at nanoporous top surfaces, thus validating the role of micropillared nanoporous interface in improving the adhesion performance. The combined use of micropillared interface with nanoporous top showed a significant adhesion enhancement for both low-aspect ratio micropillars (maximally, 7.9-fold in the tensile mode and 4.5-fold in the peel mode) and high-aspect ratio micropillars (maximally, 14.8-fold in the tensile mode and 14-fold in the peel mode) compared with the plain unstructured interface. The enhancement effect of the nanoporous interface can specifically be filtered out by comparing the plain top and nanoporous top pillars' results, in which a significant adhesion increment was recorded for both the low-aspect-ratio micropillar (4.8-fold in the tensile mode and 2.5-fold in the peel mode) and the high-aspect-ratio micropillar (1.4-fold in the tensile mode and 2.1-fold in the peel mode).

The hierarchical toughening can be explained as follows. First, the nanoporous-assisted contact on top of the micropillars exerts a crack-arresting effect that can be explained by the crack initiation at multiple discontinuities plus the coplanar Cook-Gordon mechanism (*7*, *8*) that imparted repulsive stress interactions between the vicinal coplanar cracks (*8*, *9*) during propagation. This greatly contributed toward the intrinsic (*10*) fracture toughening mechanism at the interface. Furthermore, multiple nanolevel discontinuity-associated intermittent crack propagations induced a coplanar Lake-Thomas (*8*) effect that dissipated energy similar to bond rupturing in soft elastomer chains. Second, the phenomenon of flaw insensitiveness (*5*) caused by micropillar-based contact-splitting phenomena also contributed to the increasing adhesion through extrinsic (*10*) toughening in tandem with the nanopore-induced intrinsic toughening. Last, as the micropillars' height increased, a considerably large amount of strain energy was absorbed by the flexible micropillars, improving the extrinsic toughening further (see the "Flaw insensitivity" and "Effect of micropillar height" sections in supplementary text 5). For the high-aspect-ratio micropillars, the 100-μm-high micropillars that closely resembled the mushroom-like microstructures in terms of their aspect ratio showed the highest adhesion energy and peak forces.

We also evaluated the effect of strain rate, prestress, and wet conditions (see supplementary text 6) and found improvement in adhesion performance in all cases. The adhesion performance improvement in wet conditions was attributed to the combined effect of microscale and nanoscale liquid bridges (*11*) in dissipating elastic energy, plus the spatially varying

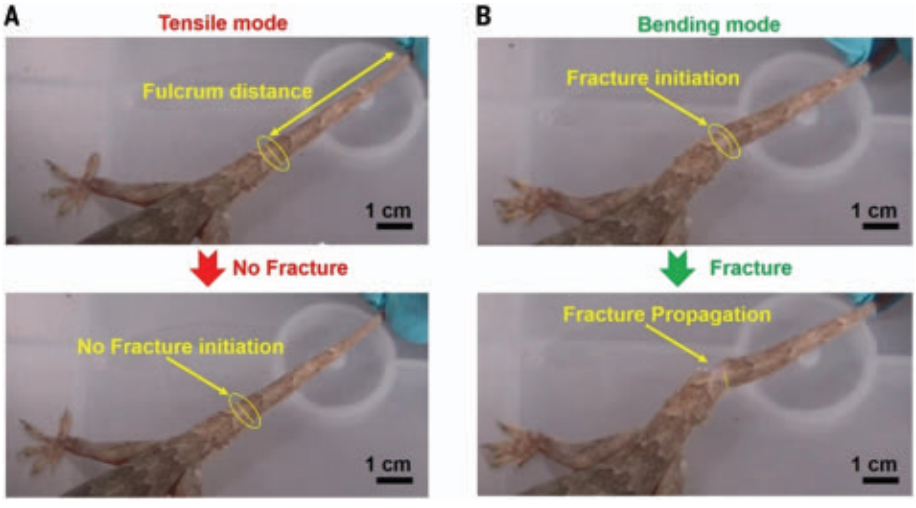

Fig. 2. High-speed analysis of tail autotomy. (**A**) Tensile mode, in which the tail was in the fully stretched condition with the fulcrum distance between the fracture plane and the grasp point. No fracture initiation was observed for the tensile stretching mode. (**B**) Bending mode, in which the tail was in the fully stretched condition showing fracture initiation. Catastrophic fracture propagation was observed after the fracture initiation in the bending mode.

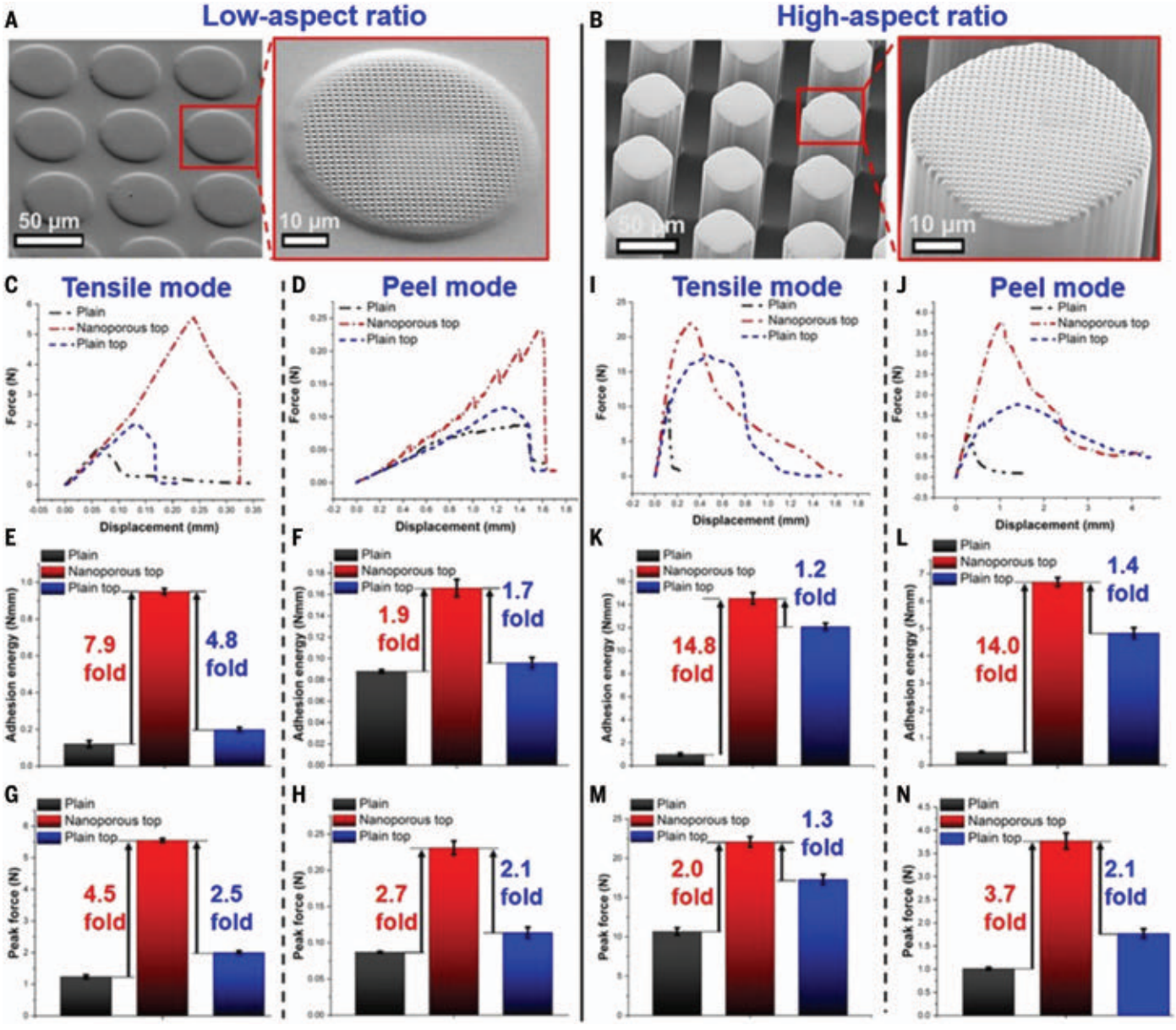

Fig. 3. Adhesion test results using a biomimetic model. (**A**) Low-aspect-ratio nanoporous top micropillars (50 μm in diameter, 1.75 μm in height). (**B**) High-aspect-ratio nanoporous top micropillars (50 μm in diameter, 100 μm in height). (**C** to **H**) Results for the low-aspect-ratio micropillars. Shown are force-displacement curves [(C) and (D)], adhesion energy results [(E) and (F)], and peak force results [(G) and (H)]. (**I** to **N**) Results for the high-aspect-ratio micropillars. Shown are force-displacement curves of the fracture tests [(I) and (J)], adhesion energy results [(K) and (L)], and peak force results [(M) and (N)]. The sample number was $n = 10$ for each case. The error bars represent SD. Each difference in the figure was significant with a P value < 0.05.

modulus during contact separation (*12*). Regarding the prestress condition at the interface before fracture, we found a notable effect of the prestress in restricting the fracture initiation and propagation. On the basis of this finding, we hypothesize that relieving the prestress by the skeletal muscle fibers' contraction (*4*) would provide favorable autotomy conditions.

To analyze and compare the toughening mechanism at the nanoscale and microscale levels, we also performed cohesive zone modeling and submodeling (*7*). The contour plots in Fig. 4 show the repulsive (*9*) stress interaction between the primary and the secondary crack, which was generated because of the subsequent nanopore-induced discontinuity (supplementary text 7). The plain top micropillar interface in Fig. 4, A and B, showed a single crack front with a larger crack tip stress singularity zone compared with the nanoporous top in both the tensile mode (Fig. 4, C and E) and the peel mode (Fig. 4, D and F). The stresses were distributed through nanolevel discontinuities, indicating intermittent crack propagation [as described in the coplanar version of the Lake-Thomas effect (*8*)], with considerably less crack tip singularity. Fig. 4, G and H, compare the strain energy dissipation or release rate and contact opening between the nanoporous and plain top pillar interface. A decrease in the strain energy release rate was found between the concerned interfaces (54 and 48% for the tensile and peel modes, respectively). Similarly, a decrease in the contact opening was found between the concerned interfaces (19 and 39% for the tensile and peel modes, respectively), illustrating the nanoporous interface's intrinsic toughening effect.

Our studies based on two species of the Gekkonidae and one species of the Lacertidae lizard family revealed an essential role of the highly dense mushroom-shaped micropillars

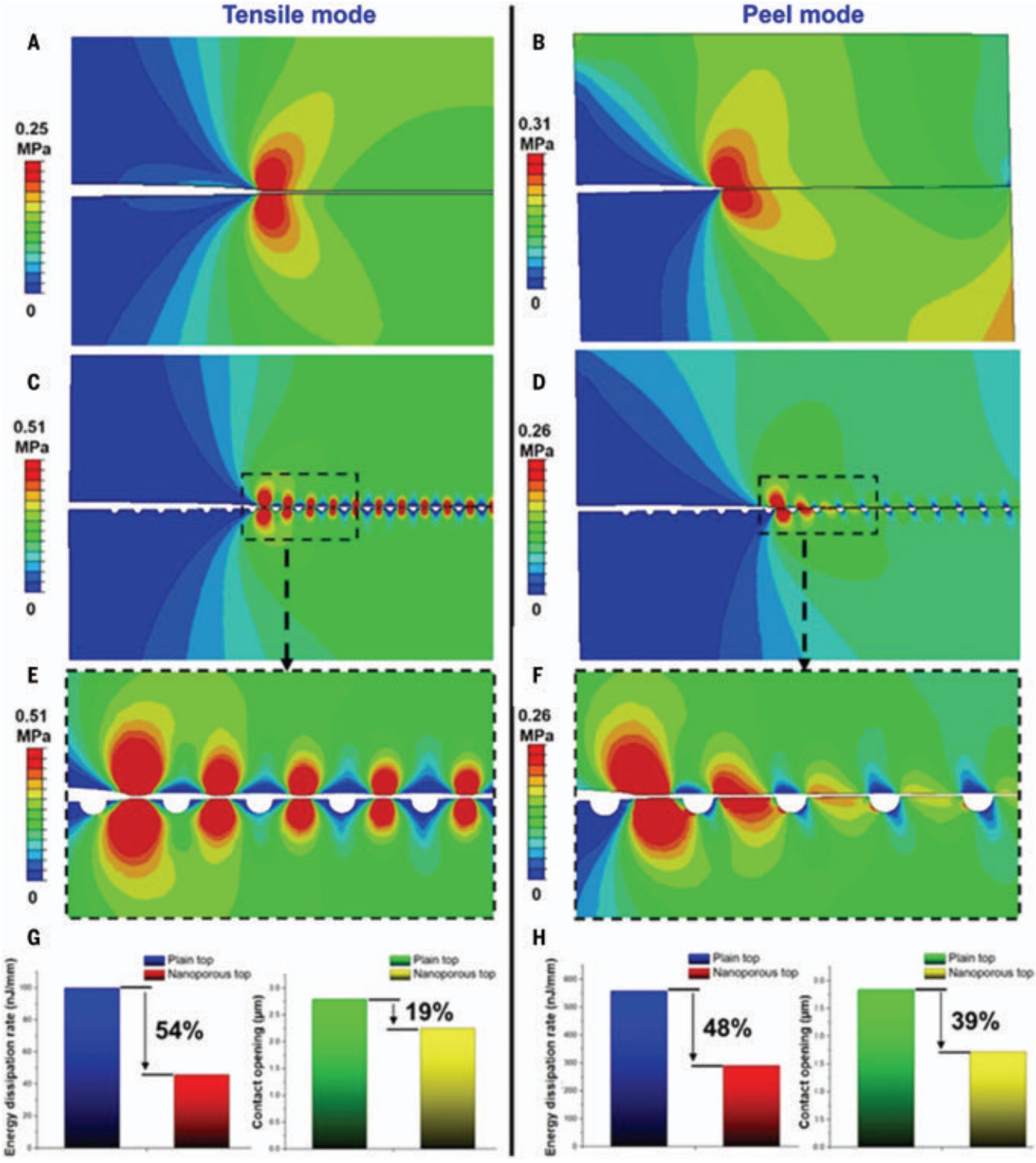

Fig. 4. Computational fracture modeling of a plain top versus nanoporous micropillar interface. (**A** to **D**) Maximum principal stress contour plots for the plain top micropillar (1.75 μm in height) in the tensile mode (A) and in the peel mode (B) and for the nanoporous top micropillar in the tensile mode (C) and in the peel mode (D). (**E** and **F**) Stress field interaction as a result of the coplanar Cook-Gordon mechanism in the tensile mode (E) and in the peel mode (F). (**G** and **H**) Strain energy dissipation rate and contact opening comparison in the tensile mode (G) and in the peel mode (H).

with nanoporous top surfaces in tail autotomy. These micropillars and nanopores establish interfacial connections along the tail fracture planes that are exposed to higher vulnerability in bending mode than in tensile mode. However, within each mode, the connections showed toughening mechanisms with nanoporous top micropillars that helped the tail avoid undue breakage. The intrinsic toughening mechanisms were composed of nanolevel crack discontinuities that assisted the coplanar version of the Cook-Gordon mechanism and the Lake-Thomas effect. Furthermore, the increased height of micropillars, as well as the flaw insensitivity caused by microlevel discontinuities, contributed

to the extrinsic toughening mechanisms. In wet conditions, microscale and nanoscale liquid bridges facilitated capillary-assisted and suction-based energy dissipation. This, along with the toughening mechanisms associated with direct solid-solid contact, improved the adhesion performance. Using this multiscale interfacial strategy, the lizard carefully balances attachment and detachment, achieving the "just right" connection in its tail that is neither too weak nor too strong for its best chance of survival.

REFERENCES AND NOTES

1. E. N. N. Arnold, *J. Nat. Hist.* **18**, 127–169 (1984).
2. P. W. Bateman, P. A. Fleming, *J. Zool.* **277**, 1–14 (2009).
3. K. W. Sanggaard *et al.*, *PLOS ONE* **7**, e51803 (2012).
4. T. H. Araújo, F. P. de Faria, E. Katchburian, E. F. Haapalainen, *Acta Zool.* **91**, 440–446 (2010).
5. A. Jagota, C. Y. Hui, *Mater. Sci. Eng. Rep.* **72**, 253–292 (2011).
6. D. A. Dillard, B. Mukherjee, P. Karnal, R. C. Batra, J. Frechette, *Soft Matter* **14**, 3669–3683 (2018).
7. N. S. Baban, A. Orozaliev, C. J. Stubbs, Y. A. Song, *Phys. Rev. E* **102**, 012801 (2020).
8. J. Y. Chung, M. K. Chaudhury, *J. R. Soc. Interface* **2**, 55–61 (2005).
9. J. C. Hill *et al.*, *Int. J. Fract.* **119**, 365–386 (2003).
10. R. O. Ritchie, *Nat. Mater.* **10**, 817–822 (2011).
11. Q. Liu *et al.*, *ACS Appl. Mater. Interfaces* **12**, 19116–19122 (2020).
12. A. Ghatak, *Phys. Rev. E Stat. Nonlin. Soft Matter Phys.* **89**, 032407 (2014).

ACKNOWLEDGMENTS

We thank A. Bauer for helpful discussions on the biology of tail autotomy; P. Salmon from Bruker Belgium for CT scanning the lizard tail; the NYU Abu Dhabi graduate office for providing N.S.B. with a Global Ph.D. Fellowship; and the NYU Abu Dhabi Core Technology Platform, especially R. Pasricha and J. Weston, for providing us access and help with the SEM study. **Funding:** This work was supported by an annual research grant provided by NYU Abu Dhabi. **Author contribution:** N.S.B. conducted SEM analysis, high-speed videography and analysis, biomimetic sample preparation, characterization and results analysis, and finite element simulations. A.O. fabricated masters for the biomimetic model. S.K. was in charge of lizard biology and evolution and assisted in capturing, identifying, and performing high-speed videography of autotomy. C.J.S assisted and checked finite element simulations. Y.A.S planned, guided, and coordinated the project. All authors contributed to the writing of the manuscript. **Competing interests:** The authors declare no competing interests. S.K is also affiliated with the Museum für Naturkunde Berlin, Leibniz Institute for Evolution and Biodiversity Science, Berlin (Germany) as a guest researcher, but this affiliation has no competing interests for the current paper. **Data and materials availability:** All data and materials are available in the main manuscript or the supplementary materials.

SUPPLEMENTARY MATERIALS

science.org/doi/10.1126/science.abh1614
Materials and Methods
Supplementary Text 1 to 7
Figs. S1 to S32
Tables S1 to S4
References (*13*–*31*)
Movies S1 to S12

Accepted 20 December 2021

21 February 2021; resubmitted 5 November 2021
Accepted 20 December 2021
10.1126/science.abh1614

2D MATERIALS

Isospin magnetism and spin-polarized superconductivity in Bernal bilayer graphene

Haoxin Zhou[1]†, Ludwig Holleis[1], Yu Saito[1], Liam Cohen[1], William Huynh[1], Caitlin L. Patterson[1], Fangyuan Yang[1], Takashi Taniguchi[2], Kenji Watanabe[3], Andrea F. Young[1]*

In conventional superconductors, Cooper pairing occurs between electrons of opposite spin. We observe spin-polarized superconductivity in Bernal bilayer graphene when doped to a saddle-point van Hove singularity generated by a large applied perpendicular electric field. We observe a cascade of electrostatic gate-tuned transitions between electronic phases distinguished by their polarization within the isospin space defined by the combination of the spin and momentum-space valley degrees of freedom. Although all of these phases are metallic at zero magnetic field, we observe a transition to a superconducting state at finite magnetic field $B_{\parallel} \approx 150$ milliteslas applied parallel to the two-dimensional sheet. Superconductivity occurs near a symmetry-breaking transition and exists exclusively above the $B_{\parallel}$ limit expected of a paramagnetic superconductor with the observed transition critical temperature $T_C \approx 30$ millikelvins, consistent with a spin-triplet order parameter.

Spin-triplet superconductors are rare in nature. This scarcity is traceable, at least in part, to the inapplicability of Anderson's theorem (*1*), which renders conventional superconductors immune to disorder. Realizing spin-triplet superconductivity therefore places stringent bounds on materials' quality. Experimentally, one of the most notable manifestations of triplet superconductivity is resilience to applied magnetic fields, which may exceed the limit set by comparing the Zeeman energy with the superconducting gap (*2*, *3*). Prominent examples of candidate spin-triplet superconductors observed to violate this limit include uranium-based compounds (*4*), such as URhGe (*5*) and UTe_2 (*6*). Recently, graphene-based, two-dimensional materials have emerged as a platform for superconductivity (*7*–*11*). In particular, two varieties of graphene trilayer—one rotationally faulted (*12*) and one in a metastable rhombohedral stacking order (*11*)—have shown superconducting states that persist above the paramagnetic limit (*2*, *3*), suggestive of a spin-triplet order parameter. However, neither of these materials represents a structural ground state. Rotationally faulted structures are generally unstable, which limits sample uniformity and, consequently, reproducibility (*13*). Rhombohedral stacking orders, meanwhile, are only metastable, which allows uniform structures to be produced, but at great cost in the practical yield of working devices. These drawbacks hamper efforts to systematically vary experimental parameters and to build more-complex devices making use of the array of gate-tuned phases available in these materials.

Here, we report magnetic field–induced superconductivity in Bernal bilayer graphene (BBG); the crystal structure is shown in Fig. 1A. Bilayer graphene has been the subject of hundreds of experimental studies since its original experimental description in 2006 (*14*). However, prior explorations of electron correlation physics have focused on instabilities of the parabolic band touching that occurs in the absence of an applied displacement field (*15*–*18*). When a perpendicular electric displacement field (D) is applied, the parabolic band touching is replaced by a bandgap (Fig. 1B), with van Hove singularities characterized by divergent single-particle density of states appearing near the band edge. Energy bands and associated single-particle density of states calculated within a four-band tight-binding model (*19*) are plotted in Fig. 1, B and C. Figure 1D shows the calculated density of states and select Fermi contours at an interlayer potential difference of 50 meV, corresponding (*20*) to $D \approx 0.5$ V nm^{-1}. A van Hove singularity occurs at a carrier density of $n_e \approx -0.5 \times 10^{12}$ cm^{-2}, where three low-density Fermi pockets merge into an annulus. Our choice of tight-binding parameters, derived from numerical band structure modeling (*19*), has not been quantitatively benchmarked to experiment in the regime of interest. However, the existence of a saddle-point van Hove singularity in this approximate density regime is expected to be generic.

The electronic structure of BBG resembles that of rhombohedral graphite multilayers (*21*, *22*). However, BBG is considerably easier to manufacture owing to its structural stability. Our devices consist of a BBG channel encapsulated in single-crystal hexagonal boron

[1]Department of Physics, University of California at Santa Barbara, Santa Barbara, CA 93106, USA. [2]International Center for Materials Nanoarchitectonics, National Institute for Materials Science, 1-1 Namiki, Tsukuba 305-0044, Japan. [3]Research Center for Functional Materials, National Institute for Materials Science, 1-1 Namiki, Tsukuba 305-0044, Japan.
***Corresponding author. Email: andrea@physics.ucsb.edu**
†Present address: Department of Applied Physics and Material Science, California Institute of Technology, Pasadena, CA 91125, USA.

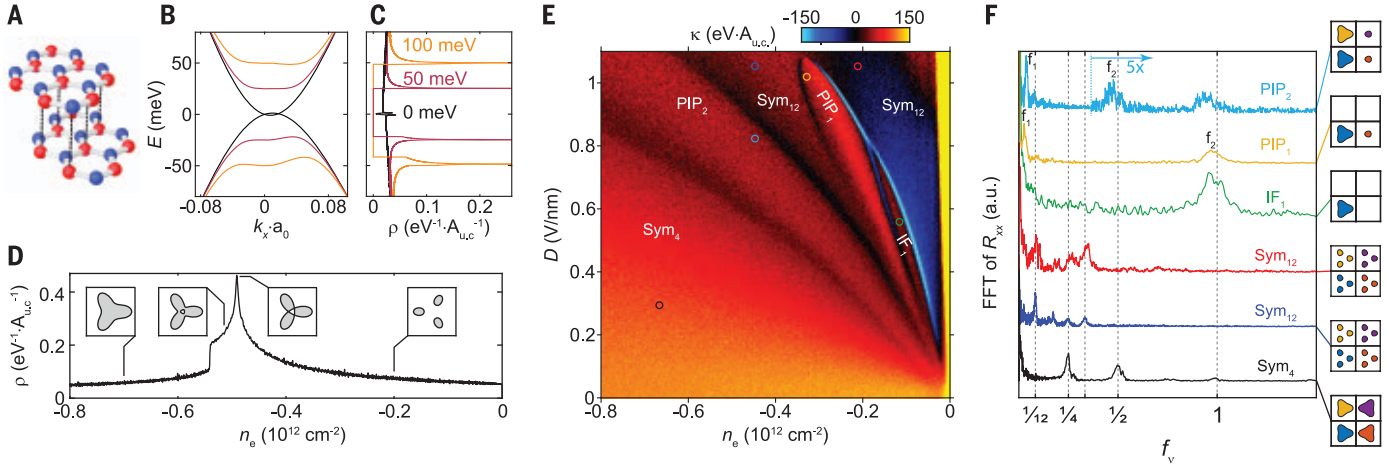

Fig. 1. Broken isospin symmetry phases in BBG. (**A**) Lattice structure of BBG. (**B**) Band structure calculated within a tight-binding model (*11*) near the Brillouin zone corner. a_0 = 2.46 Å is the graphene lattice constant. (**C**) Noninteracting density of states, ρ, at 10 mK. Different curves are calculated for varying interlayer potential differences, as marked. $A_{u.c.} \approx 5.24$ Å^2 is the graphene unit cell area. (**D**) ρ as a function of carrier density calculated (*11*) for fixed interlayer potential difference of 50 mV and temperature of 10 mK. (Insets) Fermi contours at the indicated values of n_e, plotted on the interval $(-0.06, 0.06)a_0^{-1}$ for both k_x and k_y. (**E**) Experimentally determined inverse compressibility at zero magnetic field. (**F**) Fast Fourier transform (FFT) of $R_{xx}(1/B_\perp)$ measured at the (n_e, D) points indicated by the colored symbols in (E). The x axis is the frequency normalized to n_e. Peaks reflect fractional areas of the Fermi sea enclosed by a phase-coherent orbit. For each trace, we show a schematic of the spin-dependent Fermi surfaces in the two valleys inspired by a rigid-band Stoner model of the type considered in (*12*). Here, each quadrant depicts the Fermi surface for a particular spin and valley isospin flavor. a.u., arbitrary units.

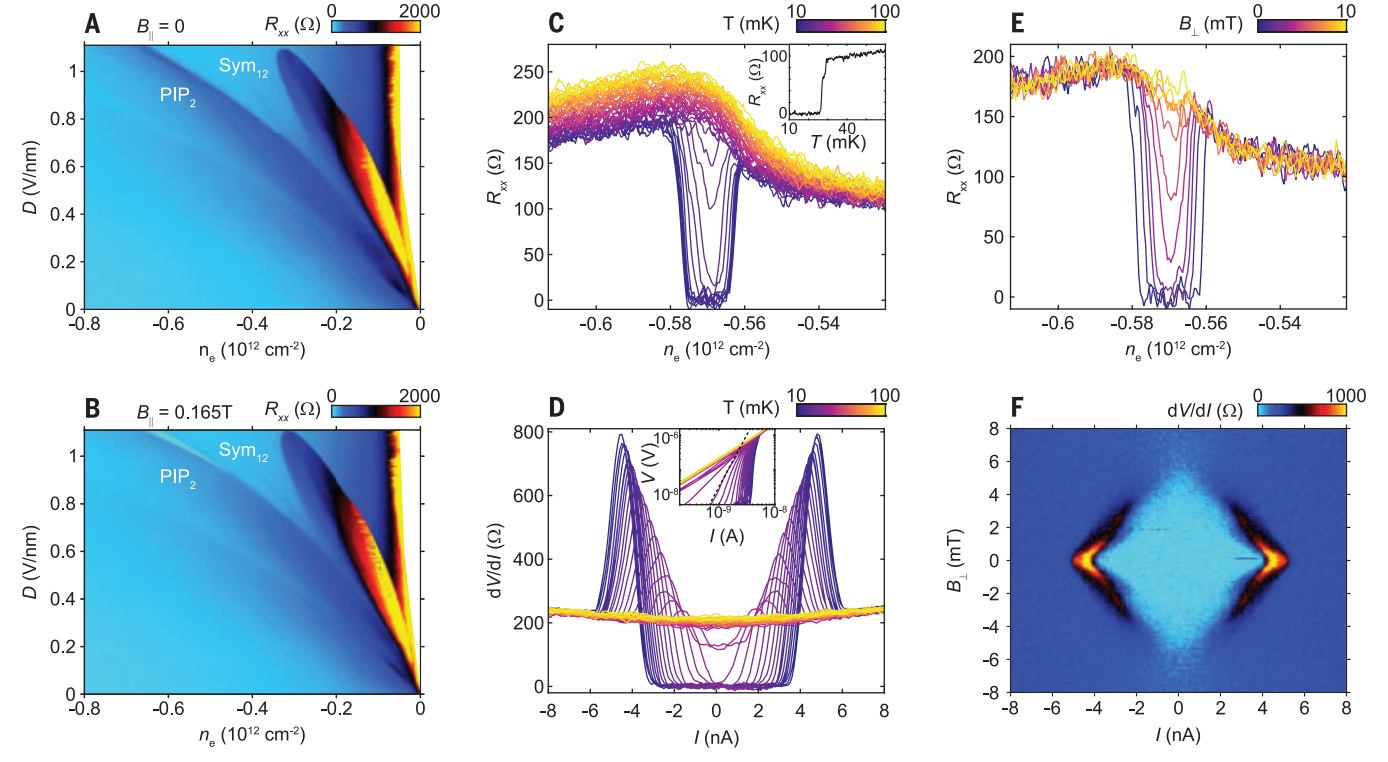

Fig. 2. Magnetic field–induced superconductivity. (**A**) R_{xx} measured at fixed $B_\parallel$ = 0 at a nominal temperature of 10 mK. (**B**) Same as (A) but measured at $B_\parallel$ = 165 mT. Zero resistance renders as bright cyan in a sash between the Sym$_{12}$ and PIP$_2$ states for $D \gtrsim 1$. (**C**) n_e dependence of R_{xx} measured at fixed D = 1.02 V nm^{-1} and $B_\parallel$ = 165 mT and variable temperatures. (Inset) $R(T)$ measured at $n_e = -0.57 \times 10^{12}$ cm^{-2} and D = 1.02 V nm^{-1}. (**D**) Nonlinear transport in the superconducting state measured at $n_e = -0.57 \times 10^{12}$ cm^{-2}, D = 1.02 V nm^{-1}, and $B_\parallel$ =165 mT. (Inset) $V(I)$ plotted on a log scale. Dotted line corresponds to $V \propto I^3$, from which we determine T_{BKT} = 26 mK. (**E**) n_e dependence of R_{xx} measured at fixed D = 1.02 V nm^{-1} and $B_\parallel$ = 165 mT, for variable $B_\perp$. (**F**) $B_\perp$-dependent nonlinear transport for fixed $n_e = -0.57 \times 10^{12}$ cm^{-2}, D = 1.02 V nm^{-1}, and $B_\parallel$ =165 mT.

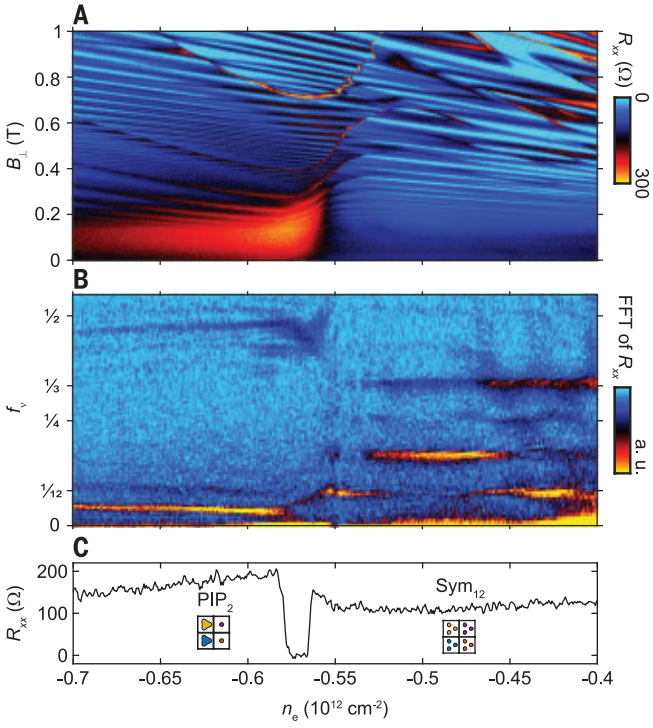

Fig. 3. Fermiology of the superconducting state. (**A**) $B_\perp$ dependence of R_{xx} at fixed D = 1.02 V nm^{-1} and $B_\parallel$ =165 mT in the n_e range near the superconducting phase. (**B**) Fourier transform of $R_{xx}(1/B)$, calculated from the data in (A). Only data within 0.1 T < B < 0.4 T are used to calculate the result. Data are plotted as a function of f_v, as in Fig. 1. In the color bar, cyan and yellow represent small and large FFT amplitudes, respectively. (**C**) R_{xx} versus n_e at $B_\perp$ = 0 and $B_\parallel$ = 165 mT.

nitride gate dielectrics in which the charge carrier density n_e and electrical displacement field D are controlled by single-crystal graphite top and bottom gates (*23*) (fig. S1). We report data from two devices that show nearly identical behavior. Data shown in the main text are from device A, and data from device B are shown in fig. S11 (*24*).

Figure 1E shows inverse electronic compressibility $\kappa = \partial\mu/\partial n_e$ (*23*, *25*) measured for small-hole doping. A series of transitions are visible as dips in the inverse compressibility, accompanied by concomitant sharp changes in the electrical resistivity (see fig. S2 for additional data). High-resolution quantum oscillation data as a function of the perpendicular magnetic field $B_\perp$ show that these features are associated with changes in the Fermi surface topology linked to breaking of the spin and valley symmetries. Figure 1F shows the Fourier transform of the magnetoresistance (see fig. S3 for additional data), $R(1/B_\perp)$ (where $B_\perp$ is the out-of-plane magnetic field), measured at different (n_e, D) points indicated in Fig. 1E. Fourier transforms are plotted as a function of the oscillation frequency normalized to the total carrier density, which we denote as f_v. f_v corresponds to the fraction of the Luttinger volume encircled by the phase coherent orbit that generates a given oscillation peak. To determine Luttinger volume, we use the geometric capacitance per unit area of the top and bottom gates (c_t and c_b) and the spectroscopically determined (*16*) bandgap of bilayer graphene (Δ) to calculate the carrier density n_e. Accounting for the finite bandgap, the system will be doped with holes when $\frac{c_t v_t + c_b v_b}{c_t + c_b} < -\frac{\Delta}{4e}$ (where v_b and v_t are the bottom and top gate voltages and e is the elementary charge). Then, $n_e = c_t v_t + c_b v_b + \frac{(c_t + c_b)\Delta}{4e}$. At large negative n_e, a prominent peak is visible at f_v = 0.25, along with associated harmonics. This is consistent with four identical Fermi surfaces, each enclosing one quarter of the Luttinger volume, as expected for a state that preserves the four-fold combined spin and valley degeneracy of the honeycomb lattice (see bottom right of Fig. 1F for a schematic depiction, with spin and valley flavors rendered in different colors). We refer to this symmetric phase as Sym$_4$. At low densities and high D, by contrast, the strongest peak occurs at $f_v = {}^1/_{12}$. This is again consistent with intact isospin symmetry but in the regime of density where trigonal warping produces three Fermi pockets within a single isospin flavor. This phase is referred to as Sym$_{12}$. In the single-particle picture, Sym$_{12}$ and Sym$_4$ are the phases that straddle the van Hove singularity (Fig. 1D).

We also identify regions with lowered degeneracy. The first, which appears at low density, is characterized by a broad peak at f_v = 1 and corresponds to a quarter metal with a single, fully isospin-polarized Fermi surface (we denote this isospin ferromagnet IF$_1$). Adjoining IF$_1$ is a phase with a strong peak at $f_v = f_1$ that is slightly smaller than 1, and another peak at $f_v = f_2$ that is close to 0. We associate this signature with a partially isospin-polarized phase featuring a large Fermi surface of one isospin flavor and smaller Fermi surfaces in a second, and we refer to it as PIP$_1$. For this phase, $f_1 + f_2 \neq 1$, which suggests that there may be multiple small Fermi pockets per isospin. An additional phase appears as a sash at densities intermediate between Sym$_4$ and Sym$_{12}$. This phase shows two prominent peaks at $f_v = f_1$ and at $f_v = f_2$, such that $f_1 + f_2$ = 0.5. We call this phase PIP$_2$ and associate it with the existence of a single Fermi surface in each of two majority and two minority isospin flavors. Possible Fermi surface topologies for the observed phases are depicted in Fig. 1F for the case where spin and valley remain good quantum numbers. Notably, these schematic depictions do not allow for the possibility of intervalley coherence, which is theoretically possible but cannot be unambiguously determined from the quantum oscillation data alone.

The symmetry-breaking transitions move to higher $|n_e|$ with increasing $|D|$, as expected from a Stoner picture given that increasing $|D|$ enhances the size of the van Hove singularity, favoring isospin symmetry-breaking states at higher carrier concentration (*26*). This behavior resembles that observed in rhombohedral trilayer graphene (RTG) (*27*), but the observed phases differ between the two systems. First, the critical temperature (T_C) of the isospin symmetry-breaking phases is found to be ~1 K (fig. S10), lower than that in RTG. Additionally, in BBG we find no signatures of the annular Fermi sea that hosts superconductivity in RTG. BBG also does not appear to host the spin-polarized, half-metal state found in RTG. Finally, the quarter metal state IF$_1$ occupies only a very small domain in the parameter space. These differences may be tied to subtle differences in the underlying band wave functions in these two systems. Further differentiating BBG and RTG, electrical resistivity remains finite at all densities at B = 0 in BBG (Fig. 2A).

Most unusually, superconductivity emerges with the application of a finite magnetic field. Figure 2B shows the resistivity, measured at a nominal temperature of 10 mK and $B_\parallel$ = 165 mT applied in the plane of the sample. A zero-resistance state appears at large D at the apparent transition between the PIP$_2$ and Sym$_{12}$ states (similar data are obtained for D < 0; fig. S4). Figure 2, C and D, shows the temperature-dependent linear and nonlinear resistivity within this zero-resistance state. We define T_{BKT} = 26 mK (where BKT indicates the Berezinskii-Kosterlitz-Thouless theory) from the temperature where the voltage $V \propto I^3$. The critical temperature is not found to decrease appreciably with applied $B_\parallel$ over the accessible range (see fig. S5 for additional data). For the observed T_C, the maximum critical field for a paramagnetic superconductor is expected at $B_\parallel \approx 1.23\frac{k_B T_C}{\mu_B} \approx 40$ mT (where k_B is the Boltzmann constant and μ_B is the Bohr magneton). The entire range of the observed superconductivity, from its onset until the

maximum field of our experimental setup, is thus well in excess of this limit.

We conclude that the Zeeman effect is not pair breaking for the superconductor, consistent with a spin-triplet order parameter. The negligible strength of spin-orbit coupling in graphene plays a key role in drawing this conclusion. In transition metal dichalcogenides 2H-NbSe2 (*28*) and 2H-MoS2 (*29*), for example, similarly large violations of the paramagnetic limit are also observed but are not thought to imply spin-triplet order parameters. Instead, those observations were interpreted in terms of Ising superconductivity (*30*), where the strong spin orbit coupling locks the spins perpendicular to the sample plane, rendering them immune to magnetic fields smaller than the spin-orbit coupling strength λ_{SO}. For a similar mechanism to apply in graphene would require $\lambda_{SO} \gg 100$ μeV, the largest Zeeman energy reached in our experiment. This is much larger than expected from previous theoretical and experimental literature (*31*, *32*). In many spin-triplet superconductors, nonmagnetic impurities play the role of magnetic impurities in conventional superconductors. To assess whether such exotic superconducting order is plausible, we estimate the disorder strength parameterized by the ratio $d = \xi/\ell_{mf}$ (*33*) of the superconducting coherence length ξ and the electronic mean free path in the normal state ℓ_{mf}. ξ may be estimated from the upper critical field at base temperature of $B_{c\perp} \approx 5$ mT (Fig. 2, E and F) from the relation (*34*) $\xi = \sqrt{\Phi_0/(2\pi B_{c\perp})} \approx 250$ nm (where Φ_0 is the superconducting magnetic flux quantum). This value is comparable to that of RTG (*11*) and is much longer than that in moiré graphene multilayers (*7*, *12*).

We may estimate ℓ_{mf} from the magnetic field where quantum oscillations are first observed. This corresponds to $\ell_{mf} \approx 2\pi k_F \ell_B^2$, the circumference of a cyclotron orbit (*35*) (where ℓ_B is the magnetic length and k_F is the Fermi wave vector). Figure 3 shows quantum oscillation data in the vicinity of the superconducting state. At $n_e \approx -0.57 \times 10^{12}$ cm^{-2}, on the cusp of the superconducting state, two oscillation frequencies are observed. Taking the higher $f_\nu \lesssim 1/2$, we estimate $k_F = \sqrt{2\pi f_\nu |n_e|} = 0.13$nm^{-1}. In this regime, the onset field is found to be ≈140 mT (fig. S6), giving $\ell_{mf} \approx 5$ μm. This estimate is comparable to device dimensions (*36*), so we conclude that $d < 0.05$, placing superconductivity deep in the clean limit. Exotic superconducting order parameters are thus not ruled out by disorder considerations.

BBG and RTG share the same crystal symmetries, differing only in quantitative details. It is likely then that, just as for RTG, the bare fact that superconductivity occurs at a magnetic transition in BBG can be explained by both conventional electron-phonon as well as electronically mediated attraction (*37*–*46*). We therefore turn our attention to previously unrecognized constraints offered by BBG on theories of the superconducting state that seek to capture the qualitative details of the phase diagram.

In contrast to superconductors in RTG, the fermiology indicates that the superconducting state in BBG emerges from a partially isospin-polarized normal state with both majority and minority Fermi surfaces. In the domain of the superconducting state, both a high-frequency and a low-frequency oscillation are evident (Fig. 3, A and B, and additional data in fig. S7), evolving continuously from the peaks in the PIP_2 phase. The normal state has a somewhat distinct fermiology from that of the PIP_2 state observed at higher $|n_e|$, with the two phases showing contrasting n_e dependence of both the low- and high-frequency oscillations. In the PIP_2 state, df_ν/dn_e is negative for the low-f_ν oscillation and positive for the high-f_ν oscillation, with these trends reversing abruptly at the boundary of the superconducting state. Notably, the low-frequency peak in the superconducting regime continuously interpolates

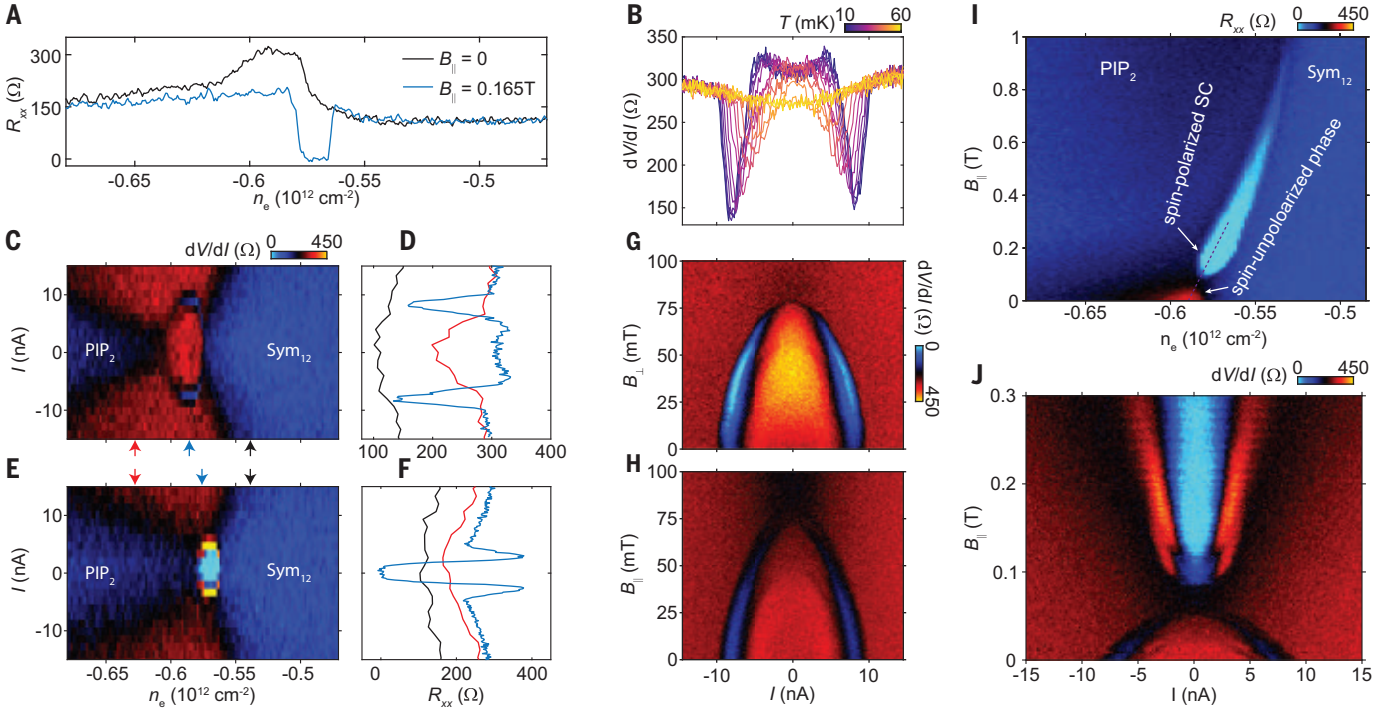

Fig. 4. Magnetic field–induced phase transitions. (**A**) n_e-dependent resistivity measured at $D = 1.02$ V nm^{-1} and $B_\parallel = 0.165$ T (blue) or zero magnetic field (black). (**B**) Nonlinear resistivity at $n_e = -0.59 \times 10^{12}$ cm^{-2}, $D = 1.02$ V nm^{-1}, and zero magnetic field for variable T. (**C**) n_e-dependent nonlinear dV/dI measured at $D = 1.02$ V nm^{-1} and zero magnetic field. (**D**) dV/dI as a function of I measured at n_e values indicated by arrows in (C). (**E**) Same as (C), but with $B_\parallel = 0.165$ T. (**F**) Same as (D), but with $B_\parallel = 0.165$ T. (**G**) dV/dI as a function of $B_\perp$ at $n_e = -0.59 \times 10^{12}$ cm^{-2}, $D = 1.02$ V nm^{-1}, and $B_\parallel = 0$. (**H**) Same as (G), but as a function of $B_\parallel$ with $B_\perp = 0$. (**I**) $B_\parallel$ dependence of linear response resistivity measured at $D = 1.02$ V nm^{-1} and $B_\perp = 0$. SC, superconductivity. (**J**) dV/dI measured along the trajectory shown by the dashed line in (I).

between the area of the small Fermi surface in the PIP_2 state at high $|n_e|$ and the area of a single Fermi pocket of the Sym_{12} state, suggestive of a continuous transition between the two. This picture implicitly requires substantial reconstruction of the Fermi surfaces relative to the single-particle band structure through either intervalley coherence or the development of nematic order. Alternatively, the superconductor may arise from a partially isospin-polarized phase that is distinct from the PIP_2 phase, existing between the PIP_2 and Sym_{12} phases and breaking a different set of spin, valley, or lattice symmetries.

Comparing transport measurements at zero and finite $B_\parallel$ (Fig. 4A) provides additional information. In the absence of a field, the Sym_{12} and PIP_2 states are separated by a resistance maximum (Fig. 4A), where the resistivity shows strong nonlinearity. Specifically, the resistance is constant up to a sharply defined threshold in the applied current, where it abruptly changes to a reduced value (Fig. 4B and fig. S11). This behavior is reminiscent of phenomena observed in charge density wave compounds associated with electric field–induced depinning (*47*). Both resistance peak and nonlinearity are low-temperature phenomena, appearing only below $T \approx 50$ mK, as shown in Fig. 4B and fig. S10. Like superconductivity at finite $B_\parallel$ (Fig. 4, E and F), at $B = 0$, the threshold current reaches a maximum between the Sym_{12} and PIP_2 states (Fig. 4, C and D). We conclude that the observed nonlinear transport is the signature of a $B = 0$, low-temperature ground state distinct from the neighboring PIP_2 phase.

The threshold observed at $B = 0$ is continuously suppressed by applied magnetic fields (Fig. 4, G and H) independent of the field direction and disappears completely for $|B| > 75$ mT (fig. S9). This suggests that the zero-field phase is spin unpolarized and that the suppression of the nonlinearity is driven by a spin polarization transition. As shown in Fig. 4I, the boundary between the PIP_2 and Sym_{12} phases shifts to lower $|n_e|$ with increasing $B_\parallel$. Tracing the nonlinear transport along the boundary between the Sym_{12} and PIP_2 phases (Fig. 4J) reveals that the suppression of the resistive state coincides precisely with the onset of superconductivity. We conclude that the observed superconductivity arises as soon as the Zeeman energy is sufficient to spin polarize the electron system, destroying the $B = 0$ phase and turning on the superconducting ground state.

The current results introduce substantial constraints to any universal theory of superconductivity in graphene systems—assuming such a theory exists. In particular, the difference in Fermi surface topology between the BBG, RTG, and moiré systems in their respective superconducting regimes suggests that Fermi surface details are not central to the superconducting mechanism. By contrast, proximity to an isospin ordered phase is a generic feature of both moiré and crystalline graphene superconductors, suggestive of a fluctuation-mediated or other purely repulsive mechanism.

However, our experiments do not yet rule out a phonon-mediated mechanism, where generic pairing only leads to observable superconducting T_C in a narrow density range and for a specific underlying isospin ordered phase. With respect to resolving the mechanism of superconductivity, the greatest effect of the current work to be practical, the stability of BBG allows exceptionally high-quality systems to be made with high yield and reproducibility. This should allow probes of the pairing symmetry, such as phase-sensitive measurements in hybrid superconducting rings (*48*), which may directly prove or disprove the spin-triplet nature inferred in this work. Moreover, van Hove singularities of the type explored here and in RTGs are generic to all graphene multilayers, so we expect field effect–controlled superconductivity to be a widespread phenomenon in graphene allotropes with sufficiently low disorder.

REFERENCES AND NOTES

1. P. W. Anderson, *J. Phys. Chem. Solids* **11**, 26–30 (1959).
2. A. M. Clogston, *Phys. Rev. Lett.* **9**, 266–267 (1962).
3. B. S. Chandrasekhar, *Appl. Phys. Lett.* **1**, 7–8 (1962).
4. D. Aoki, K. Ishida, J. Flouquet, *J. Phys. Soc. Jpn.* **88**, 022001 (2019).
5. F. Lévy, I. Sheikin, B. Grenier, A. D. Huxley, *Science* **309**, 1343–1346 (2005).
6. S. Ran *et al*., *Science* **365**, 684–687 (2019).
7. Y. Cao *et al*., *Nature* **556**, 43–50 (2018).
8. M. Yankowitz *et al*., *Nature* **557**, 404–408 (2018).
9. Z. Hao *et al*., *Science* **371**, 1133–1138 (2021).
10. J. M. Park, Y. Cao, K. Watanabe, T. Taniguchi, P. Jarillo-Herrero, *Nature* **590**, 249–255 (2021).
11. H. Zhou, T. Xie, T. Taniguchi, K. Watanabe, A. F. Young, *Nature* **598**, 434–438 (2021).
12. Y. Cao, J. M. Park, K. Watanabe, T. Taniguchi, P. Jarillo-Herrero, *Nature* **595**, 526–531 (2021).
13. L. Balents, C. R. Dean, D. K. Efetov, A. F. Young, *Nat. Phys.* **16**, 725–733 (2020).
14. K. S. Novoselov *et al*., *Nat. Phys.* **2**, 177–180 (2006).
15. R. T. Weitz, M. T. Allen, B. E. Feldman, J. Martin, A. Yacoby, *Science* **330**, 812–816 (2010).
16. A. S. Mayorov *et al*., *Science* **333**, 860–863 (2011).
17. W. Bao *et al*., *Proc. Natl. Acad. Sci. U.S.A.* **109**, 10802–10805 (2012).
18. F. Freitag, J. Trbovic, M. Weiss, C. Schönenberger, *Phys. Rev. Lett.* **108**, 076602 (2012).
19. J. Jung, A. H. MacDonald, *Phys. Rev. B* **89**, 035405 (2014).
20. Y. Zhang *et al*., *Nature* **459**, 820–823 (2009).
21. M. Koshino, E. McCann, *Phys. Rev. B* **80**, 165409 (2009).
22. F. Zhang, B. Sahu, H. Min, A. H. MacDonald, *Phys. Rev. B* **82**, 035409 (2010).
23. A. A. Zibrov *et al*., *Nature* **549**, 360–364 (2017).
24. See the supplementary materials.
25. J. P. Eisenstein, L. N. Pfeiffer, K. W. West, *Phys. Rev. B* **50**, 1760–1778 (1994).
26. E. V. Castro, N. M. R. Peres, T. Stauber, N. A. P. Silva, *Phys. Rev. Lett.* **100**, 186803 (2008).
27. H. Zhou *et al*., *Nature* **598**, 429–433 (2021).
28. X. Xi *et al*., *Nat. Phys.* **12**, 139–143 (2016).
29. J. M. Lu *et al*., *Science* **350**, 1353–1357 (2015).
30. D. Zhang, J. Falson, *Nanotechnology* **32**, 502003 (2021).
31. H. Min *et al*., *Phys. Rev. B* **74**, 165310 (2006).
32. J. Sichau *et al*., *Phys. Rev. Lett.* **122**, 046403 (2019).
33. A. A. Abrikosov, L. P. Gor'kov, *Zhur. Eksptl'. i Teoret. Fiz.* **39**, 4097498 (1960).
34. M. Tinkham, *Introduction to Superconductivity* (McGraw-Hill, ed. 2, 1975).
35. M. G. Vavilov, I. L. Aleiner, *Phys. Rev. B* **69**, 035303 (2004).
36. L. Wang *et al*., *Science* **342**, 614–617 (2013).
37. O. Vafek, J. M. Murray, V. Cvetkovic, *Phys. Rev. Lett.* **112**, 147002 (2014).
38. T. Löthman, A. M. Black-Schaffer, *Phys. Rev. B* **96**, 064505 (2017).
39. R. Ojajärvi, T. Hyart, M. A. Silaev, T. T. Heikkilä, *Phys. Rev. B* **98**, 054515 (2018).
40. A. Ghazaryan, T. Holder, M. Serbyn, E. Berg, *Phys. Rev. Lett.* **127**, 247001 (2021).
41. S. Chatterjee, T. Wang, E. Berg, M. P. Zaletel, Inter-valley coherent order and isospin fluctuation mediated superconductivity in rhombohedral trilayer graphene. arXiv:2109.00002 [cond-mat.supr-con] (2021).
42. Z. Dong, L. Levitov, Superconductivity in the vicinity of an isospin-polarized state in a cubic Dirac band. arXiv:2109.01133 [cond-mat.supr-con] (2021).
43. T. Cea, P. A. Pantaleón, V. T. Phong, F. Guinea, Superconductivity from Repulsive Interactions in Rhombohedral Trilayer Graphene: A Kohn-Luttinger-Like Mechanism. arXiv:2109.04345 [cond-mat.mes-hall] (2021).
44. A. Szabo, B. Roy, Parent (half)metal and emergent superconductivity in rhombohedral trilayer graphene. arXiv:2109.04466 [cond-mat.str-el] (2021).
45. Y.-Z. You, A. Vishwanath, Kohn-Luttinger Superconductivity and Inter-Valley Coherence in Rhombohedral Trilayer Graphene. arXiv:2109.04669 [cond-mat.str-el] (2021).
46. Y.-Z. Chou, F. Wu, J. D. Sau, S. Das Sarma, *Phys. Rev. Lett.* **127**, 187001 (2021).
47. R. M. Fleming, C. C. Grimes, *Phys. Rev. Lett.* **42**, 1423–1426 (1979).
48. C. C. Tsuei, J. R. Kirtley, *Rev. Mod. Phys.* **72**, 969–1016 (2000).
49. H. Zhou *et al*., Isospin magnetism and spin-polarized superconductivity in Bernal bilayer graphene, *Dryad* (2021); https://doi.org/10.25349/D9G892.

ACKNOWLEDGMENTS

The authors acknowledge discussions with E. Berg, S. Das Sarma, Y.-Z. Chou, A. Ghazaryan, L. Levitov, A. Macdonald, M. Serbyn, C. Varma, and M. Zaletel. **Funding:** This project was primarily funded by the Department of Energy under DE-SC0020043. Support to purchase the cryogen-free dilution refrigerator was provided by the Army Research Office under award W911NF-17-1-0323. A.F.Y. acknowledges the support of the Gordon and Betty Moore Foundation under award GBMF9471 and the Packard Foundation under award 2016-65145 for general group activities. K.W. and T.T. acknowledge support from the Elemental Strategy Initiative conducted by the MEXT, Japan (grant no. JPMXP0112101001), and JSPS KAKENHI (grant nos. 19H05790, 20H00354, and 21H05233). **Author contributions:** H.Z. and L.H. fabricated the devices. H.Z., L.H., Y.S., W.H., C.L.P., and F.Y. performed the measurements. H.Z., L.H., Y.S., W.H., C.L.P., F.Y., and A.F.Y. analyzed the data. L.C. assembled the cryogenic instrumentation. T.T. and K.W. grew the hexagonal boron nitride crystals. H.Z. and A.F.Y. conceived the experiment and wrote the paper. **Competing interests:** The authors declare no competing interests. **Data and materials availability:** All data shown in the main text and the supplementary materials are available in the Dryad data repository (*49*).

SUPPLEMENTARY MATERIALS

science.org/doi/10.1126/science.abm8386
Materials and Methods
Figs. S1 to S11
References (*50*–*52*)

18 October 2021; accepted 4 January 2022
Published online 13 January 2022
10.1126/science.abm8386

ECOTOXICOLOGY

Demographic implications of lead poisoning for eagles across North America

Vincent A. Slabe[1,2]*, James T. Anderson[3], Brian A. Millsap[4], Jeffrey L. Cooper[5], Alan R. Harmata[6], Marco Restani[7], Ross H. Crandall[8], Barbara Bodenstein[9], Peter H. Bloom[10], Travis Booms[11], John Buchweitz[12], Renee Culver[13], Kim Dickerson[14], Robert Domenech[15], Ernesto Dominguez-Villegas[16], Daniel Driscoll[17], Brian W. Smith[18], Michael J. Lockhart[19], David McRuer[16,20], Tricia A. Miller[21], Patricia A. Ortiz[22], Krysta Rogers[23], Matt Schwarz[24], Natalie Turley[25], Brian Woodbridge[26], Myra E. Finkelstein[27], Christian A. Triana[27], Christopher R. DeSorbo[28], Todd E. Katzner[22]

Lead poisoning occurs worldwide in populations of predatory birds, but exposure rates and population impacts are known only from regional studies. We evaluated the lead exposure of 1210 bald and golden eagles from 38 US states across North America, including 620 live eagles. We detected unexpectedly high frequencies of lead poisoning of eagles, both chronic (46 to 47% of bald and golden eagles, as measured in bone) and acute (27 to 33% of bald eagles and 7 to 35% of golden eagles, as measured in liver, blood, and feathers). Frequency of lead poisoning was influenced by age and, for bald eagles, by region and season. Continent-wide demographic modeling suggests that poisoning at this level suppresses population growth rates for bald eagles by 3.8% (95% confidence interval: 2.5%, 5.4%) and for golden eagles by 0.8% (0.7%, 0.9%). Lead poisoning is an underappreciated but important constraint on continent-wide populations of these iconic protected species.

Lead, the most abundant nonessential heavy metal in Earth's crust, is also one of the most common environmental toxicants released by human activity (*1*, *2*). Although clinically relevant exposure to anthropogenically released lead has been documented for multiple wildlife taxa (*2*), the population-wide demographic effects of this exposure are, for nearly all species, completely unknown. Bald eagles (*Haliaeetus leucocephalus*) and golden eagles (*Aquila chrysaetos*) are iconic apex predators widely distributed across North America (*3*, *4*). Both species have been the subject of large-scale conservation actions epitomized by efforts within the US and globally (*3*, *4*). Despite these efforts, there is evidence of widespread and localized hotspots of acute lead exposure for both species (*5*–*7*). However, there is no understanding of large-scale spatial and temporal patterns of lead exposure, nor of the demographic consequences of lead-induced mortality for these species (*8*).

We quantified the lead exposure of 1210 bald and golden eagles sampled over the annual cycle and across North America from 2010 to 2018 (Fig. 1A). We used multiple lines of evidence from blood of live eagles (n = 237 bald, 383 golden) and from bone, liver, and feathers of dead eagles (n = 343 bald, 270 golden, of which 21 bald and 2 golden were sampled both ante- and postmortem) to test hypotheses about (i) the spatial, temporal, and demographic extent of lead exposure across the continent, and (ii) the degree to which lead exposure influences the trajectory of populations of these two species in North America.

Chronic poisoning suggests repeated exposure to lead over the long term and, in vertebrate species, can be measured in bone (*9*). Inductively coupled plasma mass spectrometry indicated that of 448 dead birds, 47% of bald eagles and 46% of golden eagles had bone lead concentrations above thresholds for chronic poisoning (i.e., above thresholds used by veterinary pathologists as indicative of a "clinical poisoning"; threshold >10 μg/g for femur, n = 226 bald, 222 golden; Fig. 1B and table S1) (*10*).

We detected age-related variation in the frequency of chronic poisoning as indicated by femur lead concentrations of both bald and golden eagles, but regional differences only for bald eagles (Fig. 2, fig. S1, and tables S1, S5, and S6). For both species, adults were more frequently chronically poisoned than subadults (bald, P = 0.02; golden, P < 0.01) and juveniles (bald, P < 0.01; golden, P < 0.01). Bald eagles in the Central Flyway exhibited higher rates of chronic lead poisoning than did those in the Atlantic (P < 0.01) and Pacific Flyways (P < 0.01).

Acute lead poisoning suggests a short-term high-exposure event and is best measured in blood, liver, or feather tissue [i.e., poisoning defined as above a threshold of >40 μg/dl wet weight for blood, >20 μg/g dry weight for liver, >2.1 μg/g dry weight for feathers (*9*–*11*)]. Of 620 live birds, 28% of bald eagles and 9% of golden eagles had blood lead concentrations indicative of acute poisoning (n = 237 bald, 383 golden; Fig. 1C and table S2). Similarly, 27% of dead bald eagles and 7% of dead golden eagles had liver lead concentrations indicative of acute poisoning (n = 271 bald, 163 golden; Fig. 1D and table S3). Feather lead concentrations can be used to identify acute poisoning events during the time period of feather growth (*11*). Lead profiles for feathers with ≥4 weeks of growth revealed that 35% of dead golden eagles (one feather sampled from each of n = 23 birds) and 33% of dead bald eagles (one feather sampled from each of n = 3 birds) experienced at least one acute lead poisoning event during the growth of that individual feather (Fig. 1E and table S4).

We detected age-related, seasonal, and regional differences in frequency of acute poisoning of bald eagles but not golden eagles (Fig. 2, figs. S1 and S2, and tables S2, S3, S5, and S6). Liver lead concentrations suggested that adult bald eagles were more frequently poisoned than were juveniles (P = 0.03). Likewise, blood lead concentrations indicated that acute poisoning of bald eagles was less common in summer than in fall (P = 0.02) or winter (P < 0.01). Blood lead concentrations also showed that bald eagles in the Central Flyway exhibited a higher rate of lead poisoning than did those in the Atlantic (P = 0.03) and Mississippi Flyways (P = 0.01).

Veterinary pathologists use thresholds of lead concentrations in the liver of dead birds, along with other postmortem findings, to

[1]Division of Forestry and Natural Resources, West Virginia University, Morgantown, WV, USA. [2]Conservation Science Global, Bozeman, MT, USA. [3]James C. Kennedy Waterfowl and Wetlands Conservation Center, Clemson University, Georgetown, SC, USA. [4]Division of Migratory Bird Management, US Fish & Wildlife Service, Washington, DC, USA. [5]Virginia Department of Wildlife Resources, Richmond, VA, USA. [6]Ecology Department, Montana State University, Bozeman, MT, USA. [7]NorthWestern Energy, Butte, MT, USA. [8]Craighead Beringia South, Kelly, WY, USA. [9]US Geological Survey, National Wildlife Health Center, Madison, WI, USA. [10]Bloom Research Inc., Santa Ana, CA, USA. [11]Alaska Department of Fish and Game, Fairbanks, AK, USA. [12]Department of Pathobiology and Diagnostic Investigation, Michigan State University, East Lansing, MI, USA. [13]NextEra Energy Resources, Juno Beach, FL, USA. [14]US Fish & Wildlife Service, Cheyenne, WY, USA. [15]Raptor View Research Institute, Missoula, MT, USA. [16]Wildlife Center of Virginia, Waynesboro, VA, USA. [17]American Eagle Research Institute, Apache Junction, AZ, USA. [18]US Fish & Wildlife Service, Denver, CO, USA. [19]Wildlands Photography and Bio-consulting, Littleton, CO, USA. [20]Parks Canada, Gatineau, Quebec, Canada. [21]Conservation Science Global, Cape May, NJ, USA. [22]US Geological Survey, Forest and Rangeland Ecosystem Science Center, Boise, ID, USA. [23]Wildlife Investigations Laboratory, California Department of Fish and Wildlife, Rancho Cordova, CA, USA. [24]US Fish & Wildlife Service, Pierre, SD, USA. [25]Idaho Power Company, Boise, ID, USA. [26]US Fish & Wildlife Service, Yreka, CA, USA. [27]Microbiology and Environmental Toxicology Department, University of California, Santa Cruz, CA, USA. [28]Biodiversity Research Institute, Portland, ME, USA.
*Corresponding author. Email: vince.slabe@consciglobal.org

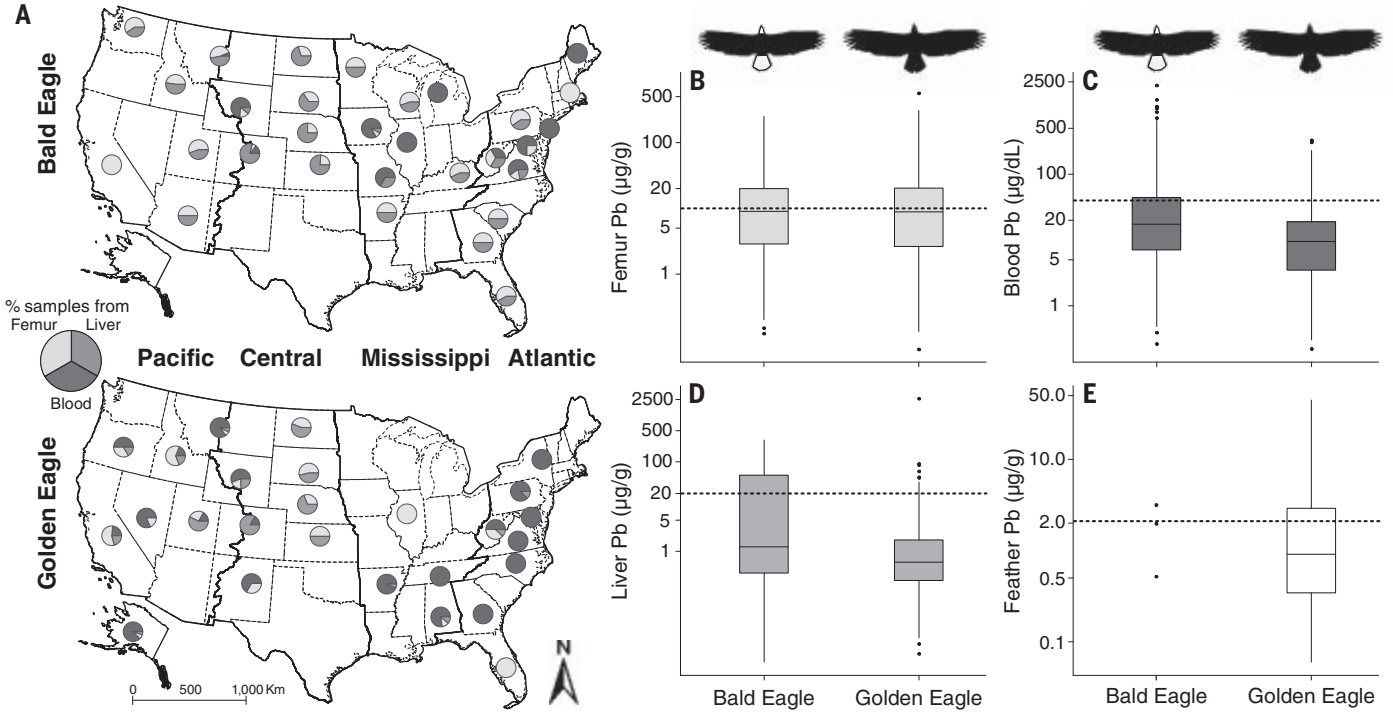

Fig. 1. Origins and lead concentrations of eagles used to interpret demographic effects of lead poisoning. (**A**) Collection locations (by state and US Fish & Wildlife Service–designated flyway) for eagle blood (bald, 237; golden, 383) taken from live birds, and eagle liver (bald, 271; golden, 163) and femur (bald, 226; golden, 222) from dead birds. (**B** to **D**) Censored boxplots (*16*) of lead concentrations in femur (dry weight) (B), blood (wet weight) (C), and liver (dry weight) (D), all shown on a log scale. (**E**) Peak feather (dry weight) lead concentration measured across ≥4 weeks of growth. Feather samples were collected from birds in six US states (see supplementary materials for details). Dotted horizontal lines on boxplots represent thresholds designating clinical poisoning (*9*–*11*, *17*).

determine cause of death (*9*). Measurements of blood lead concentrations from live birds are generally considered a good indicator of recent acute-exposure events, but because the birds are released back into the wild with unknown survival outcomes, there is no empirically defined blood lead concentration threshold associated with death (*6*, *9*). Our analyses suggest that liver lead concentrations above the thresholds used to define severe clinical poisoning occur in 4.9% of dead golden eagles and 25.8% of dead bald eagles. (If liver lead concentrations are above that threshold, then lead poisoning is generally determined to be the cause of death; this threshold is substantially higher and more conservative than the clinical poisoning threshold described above.) Hypothetical matrix population models built for both species suggest that if liver lead concentrations above that conservative threshold always result in death, then the continent-wide population growth rates of these species are being suppressed, for bald eagles by 3.8% (95% confidence interval: 2.5%, 5.4%) and for golden eagles by 0.8% (0.7%, 0.9%; tables S7 and S8), with probable long-term impacts to the population (Fig. 3). If only 75% of birds with liver lead concentrations above that threshold die, then there is a smaller but still demographically relevant suppression of population growth rates (fig. S3).

Acute poisoning of both species was generally higher in winter months, when bald and golden eagles commonly scavenge (*3*–*5*). Elevated lead concentrations in predatory and scavenging birds are usually caused by primary lead poisoning, most frequently direct ingestion of lead fragments from ammunition (*2*, *12*, *13*). Use of lead in ammunition during hunting seasons corresponds directly, both spatially and temporally, with the feeding ecology of facultative scavengers such as bald and golden eagles (*5*, *14*), a problem that has been studied extensively (*5*, *14*, *15*). Our data show a continent-wide temporal correspondence between acute lead poisoning of eagles and the use of lead ammunition.

Our large-scale data set hints at drivers of spatial and subcontinental trends in the frequency of lead poisoning of eagles that would be impossible to detect in local studies. For example, the high frequency of acute lead poisoning we detected for bald eagles in the Central Flyway could be influenced in part by differential timing of sampling (i.e., if more samples were taken in winter in that flyway than in other flyways). However, such an argument would not hold for the similar spatial patterns in chronic poisoning. Therefore, a more plausible explanation for these two patterns together lies in the potential for unexplained differential scavenging rates of bald eagles in the different flyways.

The age-related patterns we found in lead poisoning in the bones of bald and golden eagles reflect the accumulation of lead in scavenging birds as they age. Metallic lead is ingested, corroded by digestive acidity, incorporated into the bloodstream, absorbed by soft-tissue organs such as liver, and ultimately stored in the skeletal system (*6*, *9*). Thus, the age-related patterns we document show that across North America, eagles are repeatedly exposed to lead that builds up in their bodies as they age, creating an underappreciated demographic constraint for North American eagles.

Of the two eagle species, acute poisoning was more common for bald eagles. Although we did not test hypotheses to explain this, our data suggest that despite the rapidly increasing numbers of this species, their continent-wide populations are still vulnerable to negative demographic consequences associated with lead poisoning.

Demographic modeling of these populations implicates lead poisoning in suppression of growth rates of 0.8 to 3.8% per year, with

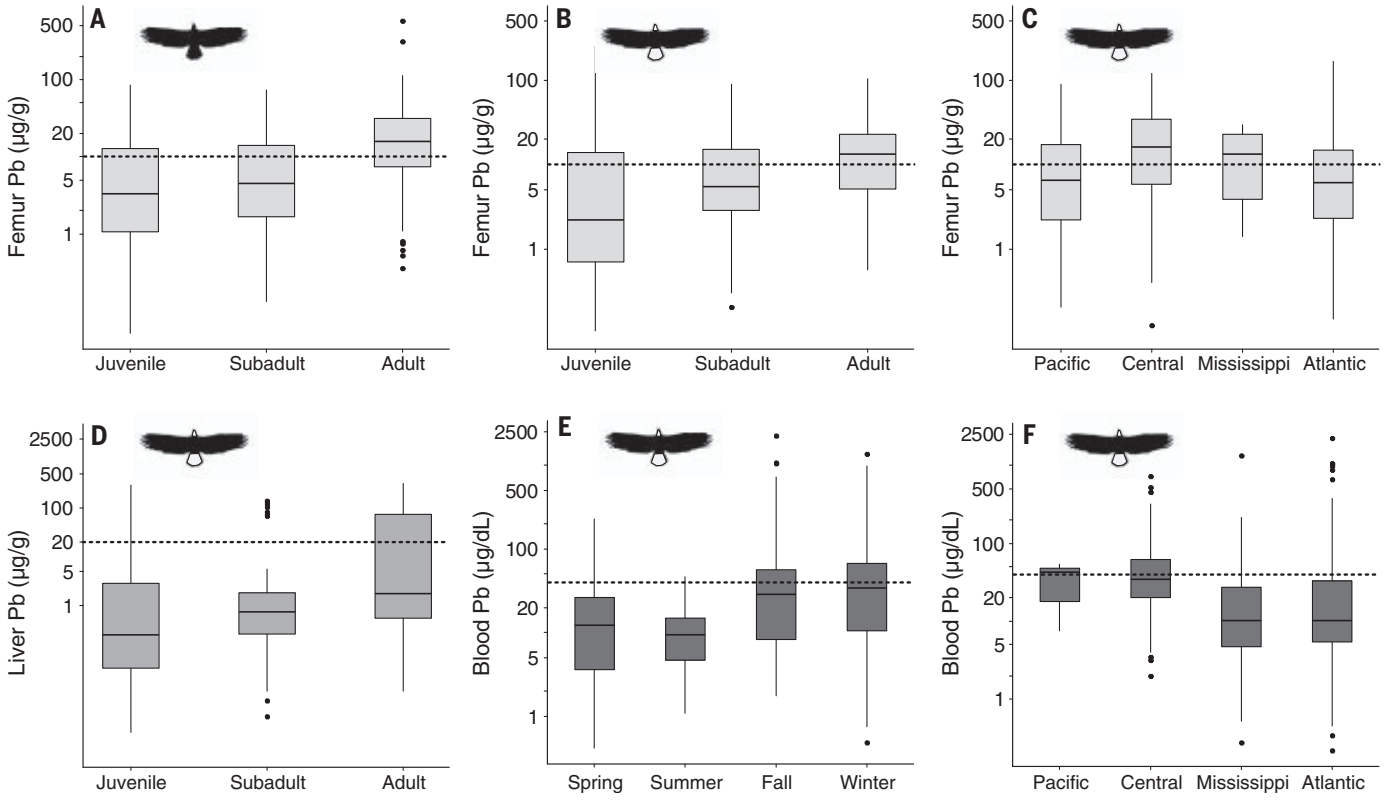

Fig. 2. Lead concentrations in femur, liver, and blood of bald and golden eagles, grouped by age, flyway, and season. (**A**) Censored boxplots of lead concentrations in golden eagle femur (dry weight), sorted by age. (**B** and **C**) Same as (A) for bald eagle femur lead concentrations, sorted by age (B) and by flyway (C). (**D** to **F**) Bald eagle lead concentrations in liver (dry weight) sorted by age (D), in blood (wet weight) sorted by season (E), and in blood, sorted by flyway (F). Boxplots are presented on a log scale; sample sizes are in tables S1 to S3. Dotted horizontal lines on boxplots represent thresholds for clinical poisoning (*9*, *10*, *17*).

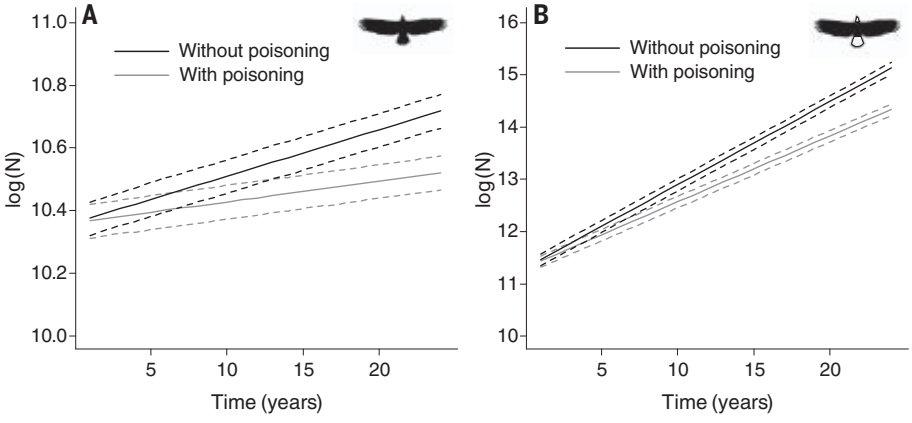

Fig. 3. Deterministic projections for populations of golden and bald eagles with and without effects to growth rates of lead poisoning. (**A**) Hypothetical matrix model projections for populations of golden eagles in scenarios without lead poisoning (upper black line) and with lead poisoning (lower gray line) at levels documented in this study. Solid lines are median estimates; dotted lines are 95% confidence intervals. (**B**) Same as (A) for bald eagles. The model assumes 100% mortality of individuals with liver lead concentrations above the threshold for severe clinical poisoning [33 µg/g dry weight (*15*)]. To isolate the effect of lead-caused mortality on eagle populations, these plots incorporate variation in lambda but no stochastic variation in population size.

consequences over the long term for populations of both species. Such a finding highlights the spatial and temporal extents to which lead poisoning affects populations of bald and golden eagles across North America. Our data identify directions for future conservation action supporting populations of these iconic species.

REFERENCES AND NOTES

1. J. Liang, J. Mao, *Environ. Sci. Pollut. Res. Int.* **22**, 7129–7138 (2015).
2. D. Avery, in *Ingestion of Lead from Spent Ammunition: Implications for Wildlife and Humans* (Peregrine Fund, 2009; www.peregrinefund.org/Lead_conference/PDF/0115 Avery.pdf.
3. D. A. Buehler, Bald Eagle (*Haliaeetus leucocephalus*) (Birds of the World, 2020); https://birdsoftheworld.org/bow/species/baleag/cur/introduction.
4. T. E. Katzner *et al*., Golden Eagle (*Aquila chrysaetos*) (Birds of the World, 2020); https://birdsoftheworld.org/bow/species/goleag/cur/introduction.
5. V. A. Slabe *et al*., *Environ. Toxicol. Chem.* **39**, 882–892 (2020).
6. J. C. Franson, R. E. Russell, *Ecotoxicology* **23**, 1722–1731 (2014).
7. A. R. Harmata, M. Restani, *J. Wildl. Dis.* **49**, 114–124 (2013).
8. W. G. Hunt *et al*., *PLOS ONE* **12**, e0172232 (2017).
9. J. C. Franson, D. Pain, in *Environmental Contaminants in Biota* (CRC Press, 2011), pp. 563–593.
10. P. A. Martin, D. Campbell, K. Hughes, T. McDaniel, *Sci. Total Environ.* **391**, 96–103 (2008).
11. M. E. Finkelstein *et al*., *Environ. Sci. Technol.* **44**, 2639–2647 (2010).
12. N. H. Golden, S. E. Warner, M. J. Coffey, *Rev. Environ. Contam. Toxicol.* **237**, 123–191 (2016).
13. L. K. Manning *et al*., *Vet. Pathol.* **56**, 289–299 (2019).
14. M. Nadjafzadeh, H. Hofer, O. Krone, *J. Wildl. Manage.* **77**, 48–57 (2013).
15. L. Cruz-Martinez, P. T. Redig, J. Deen, *Hum. Wildl. Interact.* **6**, 94–104 (2012).
16. D. Helsel, *Statistics for Censored Environmental Data Using Minitab and R* (Wiley, 2011).
17. J. A. Fallon, P. Redig, T. A. Miller, M. Lanzone, T. Katzner, *Wildl. Soc. Bull.* **41**, 205–211 (2017).

ACKNOWLEDGMENTS

People who helped with data collection, analysis, and reviews are noted in the supplementary materials. Any use of trade, firm, or product names is for descriptive purposes only and does not imply endorsement by the US government. The findings and conclusions in this article are those of the authors and do not necessarily represent the views of the US Fish & Wildlife Service. **Funding:** Supported by Virginia Federal Aid in Wildlife Restoration grant 2013-14308, USFWS contract F13PX02485, the American Eagle Foundation, and NSF grant OIA-1458952 and USDA McIntire Stennis grant WVA00812 (J.T.A.). Feather analyses were funded by the Horne Family Foundation, William P. Wharton Trust. **Author contributions:** T.E.K., V.A.S., J.T.A., and B.A.M. designed the study, V.A.S. and T.E.K. organized sample collection conducted by all authors, P.A.O. maintained and managed the sample archive and laboratory results, V.A.S. led analysis of the data with support from T.E.K. and the other authors, V.A.S. and T.E.K. led writing of the manuscript, M.E.F. and C.A.T. conducted feather lead analysis, J.B. coordinated analyses of other tissue types, and all authors contributed to manuscript revisions. **Competing interests:** All authors declare no competing interests. **Data and materials availability:** Data underpinning this research are available at https://doi.org/10.5066/P9BXIY3B. All (other) data needed to evaluate the conclusions in the paper are present in the paper or the supplementary materials.

SUPPLEMENTARY MATERIALS

science.org/doi/10.1126/science.abj3068
Materials and Methods
Tables S1 to S8
Figs. S1 to S3
References (*18*–*36*)

4 May 2021; accepted 11 January 2022
10.1126/science.abj3068

CORONAVIRUS

SARS-CoV-2 Beta variant infection elicits potent lineage-specific and cross-reactive antibodies

S. Momsen Reincke[1,2,3]*†, Meng Yuan[4]†, Hans-Christian Kornau[2,5]†, Victor M. Corman[6,7,8]†, Scott van Hoof[1,2,3], Elisa Sánchez-Sendin[1,2,3], Melanie Ramberger[2,3], Wenli Yu[4], Yuanzi Hua[4], Henry Tien[4], Marie Luisa Schmidt[6,7], Tatjana Schwarz[6,7], Lara Maria Jeworowski[6,7], Sarah E. Brandl[1,2,3], Helle Foverskov Rasmussen[1,2,3], Marie A. Homeyer[1,2,3], Laura Stöffler[1,2,3], Martin Barner[3], Désirée Kunkel[9], Shufan Huo[1], Johannes Horler[1,2,3], Niels von Wardenburg[1,2,3], Inge Kroidl[10,11], Tabea M. Eser[10,11], Andreas Wieser[10,11], Christof Geldmacher[10,11], Michael Hoelscher[10,11], Hannes Gänzer[12], Günter Weiss[13], Dietmar Schmitz[2,5], Christian Drosten[6,7], Harald Prüss[1,2,3]*‡, Ian A. Wilson[4,14]*‡, Jakob Kreye[1,2,3,15]*‡

Severe acute respiratory syndrome coronavirus 2 (SARS-CoV-2) Beta variant of concern (VOC) resists neutralization by major classes of antibodies from COVID-19 patients and vaccinated individuals. In this study, serum of Beta-infected patients revealed reduced cross-neutralization of wild-type virus. From these patients, we isolated Beta-specific and cross-reactive receptor-binding domain (RBD) antibodies. The Beta-specificity results from recruitment of VOC-specific clonotypes and accommodation of mutations present in Beta and Omicron into a major antibody class that is normally sensitive to these mutations. The Beta-elicited cross-reactive antibodies share genetic and structural features with wild type–elicited antibodies, including a public VH1-58 clonotype that targets the RBD ridge. These findings advance our understanding of the antibody response to SARS-CoV-2 shaped by antigenic drift, with implications for design of next-generation vaccines and therapeutics.

In the course of the COVID-19 pandemic, multiple severe acute respiratory syndrome coronavirus 2 (SARS-CoV-2) lineages have emerged, including lineages defined as variants of concern (VOCs), such as Alpha (also known as lineage B.1.1.7), Beta (B.1.351), Gamma (P.1), Delta (B.1.617.2), and recently, Omicron (B.1.1.529). VOCs are associated with increased transmissibility, virulence, or resistance to neutralization by sera from vaccinated and convalescent individuals who were infected with the original strain (*1*–*7*). These distinct lineages carry a variety of mutations in the spike protein, several of which are within the receptor-binding domain (RBD), especially at residues K417, L452, T478, E484, and N501. Some mutations such as N501Y are associated with enhanced binding to angiotensin-converting enzyme 2 (ACE2), largely driving the global spread of VOCs that incorporate these mutations (*2*). (Single-letter abbreviations for the amino acid residues are as follows: A, Ala; C, Cys; D, Asp; E, Glu; F, Phe; G, Gly; H, His; I, Ile; K, Lys; L, Leu; M, Met; N, Asn; P, Pro; Q, Gln; R, Arg; S, Ser; T, Thr; V, Val; W, Trp; and Y, Tyr. In the mutants, other amino acids were substituted at certain locations; for example, N501Y indicates that asparagine at position 501 was replaced by tyrosine.)

However, with increasing immunity either through natural infection or vaccination, antibody escape will become more relevant in emerging VOCs. Many studies have investigated RBD antibodies in COVID-19 patients before identification of SARS-CoV-2 variants, and we refer to these as wild-type antibodies. Wild-type RBD antibodies revealed a preferential response toward distinct epitopes, with enriched recruitment of particular antibody germline genes, where the most prominent were VH3-*53* and closely related VH3-*66*, as well as VH1-2 (*8*, *9*). Structural and functional classification of wild-type RBD monoclonal antibodies (mAbs) has demonstrated that mAbs from these three enriched germline genes form two major classes of receptor-binding site (RBS) mAbs whose binding and neutralizing activity depends on either K417 or E484 (*9*, *10*). Mutations at these key residues (K417N and E484K) together with N501Y are hallmarks of Beta (*2*) and largely account for the reduced neutralizing activity of sera from vaccinated and convalescent individuals against this VOC (*1*–*6*, *11*, *12*). Of the first four VOCs (Alpha through Delta), Beta shows the highest resistance to neutralization by wild-type–elicited sera (*12*), suggesting conspicuous differences in its antigenicity (*13*). First reports indicate that Omicron, which shares K417N and N501Y with Beta and carries a different mutation at the third key residue (E484A) as well as 34 further spike mutations, shows even higher resistance to neutralization by wild-type–elicited sera (*14*). Although mutations at position K417 and E484 influence the antigenicity of the RBD, little is known about the antibody response elicited by Beta infection. For example,

[1]Department of Neurology and Experimental Neurology, Charité–Universitätsmedizin Berlin, corporate member of Freie Universität Berlin and Humboldt-Universität zu Berlin, Berlin, Germany. [2]German Center for Neurodegenerative Diseases (DZNE) Berlin, Berlin, Germany. [3]Helmholtz Innovation Lab BaoBab (Brain Antibody-omics and B-cell Lab), Berlin, Germany. [4]Department of Integrative Structural and Computational Biology, The Scripps Research Institute, La Jolla, CA 92037, USA. [5]Neuroscience Research Center (NWFZ), Cluster NeuroCure, Charité–Universitätsmedizin Berlin, corporate member of Freie Universität Berlin and Humboldt-Universität zu Berlin, Berlin, Germany. [6]Institute of Virology, Charité–Universitätsmedizin Berlin, corporate member of Freie Universität Berlin and Humboldt-Universität zu Berlin, Berlin, Germany. [7]German Centre for Infection Research (DZIF), Berlin, Germany. [8]Labor Berlin–Charité Vivantes GmbH, Berlin. [9]Flow and Mass Cytometry Core Facility, Berlin Institute of Health at Charité–Universitätsmedizin Berlin, Berlin, Germany. [10]Division of Infectious Diseases and Tropical Medicine, Medical Center of the University of Munich (LMU), Germany. [11]German Center for Infection Research (DZIF), partner site Munich, Germany. [12]Department of Internal Medicine, BKH Schwaz, Schwaz, Austria. [13]Department of Internal Medicine II, Medical University of Innsbruck, Innsbruck, Austria. [14]The Skaggs Institute for Chemical Biology, The Scripps Research Institute, La Jolla, CA 92037, USA. [15]Department of Pediatric Neurology, Charité–Universitätsmedizin Berlin, corporate member of Freie Universität Berlin and Humboldt-Universität zu Berlin, Berlin, Germany.
***Corresponding author. Email: momsen.reincke@charite.de (S.M.R.); harald.pruess@charite.de (H.P.); wilson@scripps.edu (I.A.W.); jakob.kreye@charite.de (J.K.)**
†These authors contributed equally to this work.
‡These authors contributed equally to this work.

it is unknown whether antibodies targeting the RBD Beta share the preferential recruitment of particular germline genes with wild-type antibodies, or whether VOC-defining mutations K417N and E484K could be accommodated in the canonical binding modes of public VH3-53/VH3-66 antibody classes. Thus, we set out to explore genetic, functional, and structural features of the antibody response against RBD in Beta-infected individuals.

We identified 40 individuals infected with SARS-CoV-2 Beta from three metropolitan areas in Germany and Austria (table S1) and collected serum at 38.6 ± 19.2 days after their first positive SARS-CoV-2 reverse transcription polymerase chain reaction (RT-PCR) test. The patients' immunoglobulin G (IgG) bound to wild-type nucleocapsid protein, wild-type spike, or both proteins in 37 of 40 patients, and with stronger reactivity to RBD Beta than to wild-type RBD (fig. S1A). The patients' sera also inhibited ACE2 binding to RBD Beta to a greater extent than to wild-type RBD (fig. S1B and table S1). Reactivity to wild-type spike S1 was confirmed in an additional commercially available enzyme-linked immunosorbent assay (ELISA); however, only 23 of 40 samples tested positive, according to the manufacturer's cutoff (fig. S1, C and D). In a plaque reduction neutralization test (PRNT), 37 of 40 sera neutralized an authentic SARS-CoV-2 Beta isolate with a half-maximal inhibitory concentration (IC_{50}) at 1:20 dilution or greater (Fig. 1A). By contrast, only 11 of 40 sera neutralized wild-type virus (Fig. 1B). The neutralizing activity against the two isolates was modestly correlated (fig. S1E), with a ~20-fold reduction of neutralizing activity against wild-type virus compared with Beta (Fig. 1C and fig. S1F). A converse effect has been reported after immune responses against wild-type RBD in convalescent and vaccinated individuals (*2*), in which neutralization of SARS-CoV-2 Beta was ~8- to ~14-fold reduced compared with wild-type virus (*1*–*6*). No positive correlation was found between neutralizing antibodies against Beta and the time point of sample collection relative to first positive PCR test (fig. S1G). Neutralizing antibodies against Beta modestly correlated with age (fig. S1H), but no statistically significant gender difference was observed (fig. S1I). Collectively, these data show that sera from Beta-infected patients exhibit reduced cross-reactivity to wild-type SARS-CoV-2, therefore affecting diagnostic antibody testing when using wild-type antigens and adding complexity to the concept of defining a threshold for protective antibody titers.

To investigate the effect of this difference in reactivity between RBD Beta and wild-type RBD at the level of mAbs elicited by SARS-CoV-2 Beta infection, we isolated $CD19^+CD27^+$ memory B cells from the peripheral blood of 12 donors in our cohort by means of fluorescence activated cell sorting using a recombinant RBD Beta probe (fig. S2, A and B). Using single-cell Ig gene sequencing (*15*, *16*), we derived 289 pairs of functional heavy (IGH) and light (IGL) chain sequences from IgG mAbs (table S2). Sequence analysis showed enrichment of certain genes compared with mAbs derived from healthy, noninfected individuals—including VH1-58, VH3-30, VH4-39, and VH3-53—illustrating a preferential recruitment of certain VH genes (Fig. 2A), VH-JH gene combinations (fig. S3A), and variable light chain genes (fig. S3B). For some genes such as VH1-58 and VH3-53, enrichment has previously been identified in CoV-AbDab, a database of published SARS-CoV-2 mAbs (*9*, *17*). We confirmed this finding for all human wild-type RBD mAbs in CoV-AbDab (Fig. 2A). Consistent with reports from wild-type SARS-CoV-2 infections (*18*–*20*), the somatic hypermutation (SHM) count was generally low in mAbs of our cohort (fig. S3C). Together, these findings argue for conservation of certain antibody sequence features between antibody responses in different donors and between antibody responses elicited against Beta and wild-type virus. Hence, we compared antibody sequences after Beta infection with all previously published wild-type RBD mAbs and identified several clonotypes shared between both datasets (Fig. 2B), some of which were present in multiple patients of our study (Fig. 2C). Thus, a subset of the antibodies to RBD Beta and wild-type RBD converge upon recruitment of specific germline genes.

However, other gene enrichments found in our study, such as VH4-39, have not been identified within the CoV-AbDab mAbs (Fig. 2A) (*9*), exemplifying concurrent divergence in the antibody response to the different RBDs. VH1-2, one of the most common genes contributing to the RBD antibody response to wild-type SARS-CoV-2, was strongly reduced in our dataset (Fig. 2A and table S2), which is consistent with the dependence of VH1-2 mAbs on E484 (*9*). VH3-53/VH3-66 antibodies bind to wild-type RBD in two canonical binding modes, which involve residues K417 and E484, respectively; binding and neutralization of these antibodies are strongly affected by the K417N and E484K mutations in RBD Beta (*9*, *21*). We therefore hypothesized a similarly reduced recruitment of VH3-53/VH3-66 mAbs after Beta infection. Unexpectedly, we identified 15 VH3-53/VH3-66 mAbs, albeit at a reduced frequency compared with that of the CoV-AbDab dataset (4.7 versus 19.4%), but still at an increased frequency compared with that of healthy donors (Fig. 2A), thus indicating either a noncanonical binding mode or accommodation of these mutations into the known binding modes.

To determine the binding properties of antibodies elicited by SARS-CoV-2 Beta, we selected representative mAbs for expression (table S2). We identified 81 mAbs with strong binding to RBD Beta (table S3). Of those, 44 revealed comparable binding to wild-type RBD and were considered cross-reactive mAbs, whereas 37 mAbs did not bind wild-type RBD and were considered Beta-specific. There were no differences in V gene SHMs, CDR H3/L3 hydrophobicity, and ACE2-binding inhibition between Beta-specific and cross-reactive antibodies (fig. S4, A to C), but the cross-reactive antibodies had a slightly shorter CDR H3/L3 and lower isoelectric point of their CDR H3 (fig. S4, D and E). The neutralization potencies were similar between Beta-specific and cross-reactive mAbs (fig. S4F). All Beta-specific VH3-30 mAbs paired

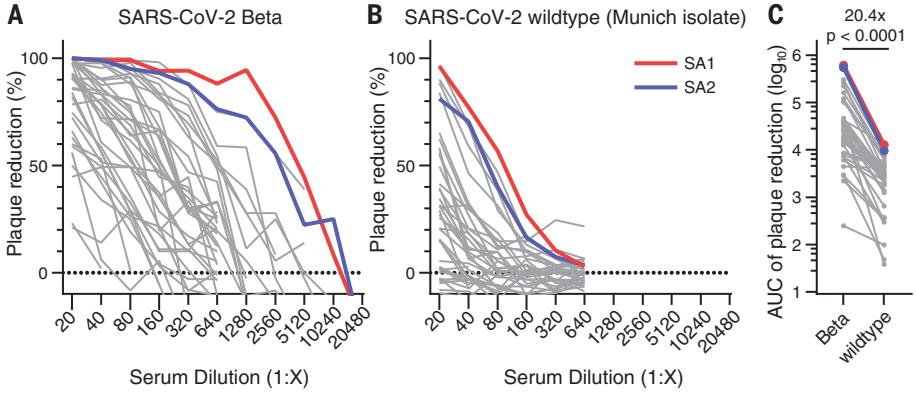

Fig. 1. Authentic virus neutralization of sera from individuals after infection with SARS-CoV-2 Beta. (**A** and **B**) Neutralizing activity of sera of patients infected with SARS-CoV-2 Beta variant was measured by using a plaque-reduction neutralization assay with the indicated authentic virus. Results are given as reduction of plaque number at indicated serum dilutions. Patients SA1 and SA2 mounted the strongest antibody response, which are highlighted in red and blue, respectively. Means of duplicate measurements are shown. Values below zero indicate no plaque reduction. (**C**) Change in neutralization activity against SARS-CoV-2 Beta and wild-type SARS-CoV-2 based on area-under-the-curve (AUC) calculations from authentic virus PRNT curves [shown in (A) and (B)]. Mean fold change is indicated above the *P* value. Statistical analysis was performed by using a Wilcoxon matched-pairs signed-rank test with two-tailed *P* value.

with JH6 (fig. S4G), whereas all cross-reactive VH3-30 mAbs paired with JH4 (fig. S4H). Competition experiments showed that many of the strongly neutralizing Beta-elicited mAbs compete for RBD binding (fig. S4I), indicating that they target similar epitopes.

Next, we aimed to determine the residues that define the binding selectivity for the 37 RBD Beta-specific mAbs and performed ELISAs with single-mutant constructs of RBD Beta and wild-type RBD. For all three Beta-defining RBD mutations (K417N, E484K, and N501Y), we identified mAbs with RBD binding that depended on a single residue. The Beta-specificity of the other mAbs was dependent on multiple residues (Fig. 3A). RBD Beta–specific mAbs were encoded by diverse VH genes (Fig. 3A and table S2), and 26 of the RBD Beta-specific mAbs (70.3%) neutralized the authentic SARS-CoV-2 Beta isolate (Fig. 3A). All nine Beta-specific VH4-39 mAbs from three different patients were Y501-dependent, comprising 81.8% of all Y501-dependent mAbs. This finding suggests a common binding mode of these clonally unrelated mAbs that depends on Y501—which is a residue present in RBD Beta, Alpha, Gamma, and Omicron but not Delta—and may explain the frequent use of VH4-39 in mAbs to RBD Beta (Fig. 2A). VH4-39 Y501–dependent mAbs revealed few SHMs in VH genes but no uniform pattern in other sequence features (fig. S5A). Although all VH4-39 RBD Beta-specific mAbs bind to a Y501-dependent epitope, their neutralization activity showed noticeable differences (IC_{50} ranging from 5.2 to 947 ng/ml) (fig. S5B). Surface plasmon resonance measurements of these mAbs to RBD Beta revealed equilibrium dissociation constants (K_D) between 3.39 and 80.4 nM (fig. S5C) with correlation to their PRNT-derived IC_{50} values (fig. S5D), providing an explanation for the variability in neutralizing activity within VH4-39 Y501-dependent mAbs.

Furthermore, we identified three VH3-53/VH3-66 mAbs with RBD Beta specificity that all showed neutralizing activity. To determine whether this RBD Beta specificity results from a noncanonical binding mode or accommodation of Beta-defining mutations in one of the two main VH3-53/VH3-66 mAb binding modes, we determined a crystal structure of VH3-53 antibody CS23 in complex with RBD Beta. VH3-53/VH3-66 mAbs with short CDRs H3 (<15 amino acids) target the RBS of wild-type RBD through a canonical mode (*10*, *22*–*25*) that is highly sensitive to the K417N mutation (*9*). CS23 contains a CDR H3 with only 10 amino acids and is specific to N417 RBDs, including RBD Beta (Fig. 3A). However, CS23 binds to RBD Beta in the canonical mode, with a nearly identical approach angle compared with that of a representative wild-type VH3-53 antibody CC12.3 (Fig. 3B) (*24*). We previously showed that the CDR H1 ^{33}NY^{34} and H2 ^{53}SGGS^{56} motifs of VH3-53/VH3-66 mAbs are critical for RBD recognition (*24*). We found that CS23 retains these motifs and that they interact with the RBD in the same way (Fig. 3, C and D). Residues in CDR H3 usually interact with K417 and thus confer specificity to the wild-type RBD (*9*). For example, variable region of immunoglobulin heavy chain (V_H) D97 of CC12.1 forms a salt bridge with the outward-facing RBD-K417, whereas V_H F99 and V_H G97 of CC12.3 interact with K417 through cation-π and hydrogen bonds (H-bonds), respectively (Fig. 3, E and F). Instead, in RBD Beta, the shorter N417 flips inward and H-bonds with RBD-E406 and Q409 (Fig. 4G). V_H M98 occupies the vacated space and interacts with RBD-Y453, L455, and variable region of immunoglobulin light chain (V_L) W91 in a hydrophobic pocket. Modeling shows that K417 would be unfavorable for RBD binding to CS23 (fig. S6A). CDR H3 contains a V_H ^{96}TAMA^{99} sequence that forms an ST motif that stabilizes CDR H3 and the orientation of M98. The first serine (S) or threonine (T) residue in a four- or five-residue ST motif makes two internal H-bonds from the side-chain oxygen of residue *i* to the main-chain NH of residue *i* + 2 or *i* + 3, and between the main-chain

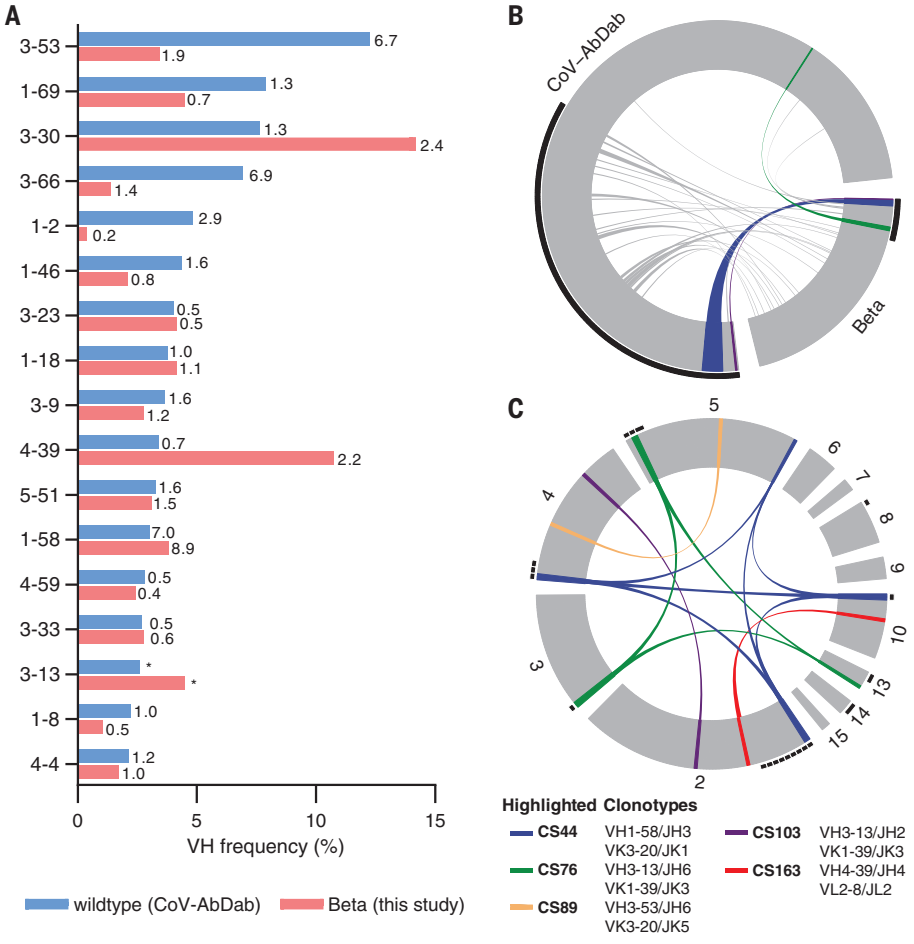

Fig. 2. Germline gene usage and clonotype analysis of Beta-elicited antibodies. (**A**) VH gene usage of 289 RBD Beta IgG mAbs from this study (red) is compared with 1037 wild-type RBD mAbs from 96 previously published studies (blue, CoV-AbDab) (*17*). Frequencies of mAbs encoded by each VH gene are shown as bars. Enrichment of indicated VH genes is compared with that of healthy individuals (*31*), with fold-enrichment shown as number next to bars. VH gene frequencies that were not reported in healthy individuals (*31*) are indicated with an asterisk. Only VH genes with a frequency of at least 2% in CoV-AbDab are shown, and VH genes are ordered by frequency in CoV-AbDab. (**B**) Circos plot shows the relationship between 289 IgG mAbs from this study (Beta) and 1037 previously published human mAbs reactive to wild-type RBD (CoV-AbDab) from 96 studies (*17*). Interconnecting lines display clonotypes shared between both datasets, as defined by the usage of the same V and J gene on both Ig heavy and light chain. Thin black lines at the outer circle border indicate expanded clonotypes within the respective data set. (**C**) Circos plot displaying the 289 IgG mAbs from this study grouped per patient. Interconnecting colored lines indicate clonotypes found in more than one patient. Small black at the outer circle border indicate clonally expanded clones within one patient. In (B) and (C), colored interconnecting lines depict clonotypes found in more than one patient of our cohort.

oxygen of residue i and the main-chain NH of residue $i + 3$ or $i + 4$. In this case, the T96 side-chain H-bonds with the main-chain NH of M98, and the T96 main-chain oxygen H-bonds with the main-chain NH of A99 (fig. S6A).

This V_H ^{96}TxMx^{99} motif is different from all known CDR H3 of VH3-53/VH3-66 antibodies to RBD (*17*) and explains the newly acquired specificity of this VH3-53 antibody for an RBD with N417. Previously, wild-type VH3-53 antibody COVOX-222 was shown to cross-react with RBD Beta despite interacting with K417 and N501, but nevertheless binds the RBD in the canonical mode; in this case, a rare SHM V_L S30P mutation accommodated Y501 (fig. S6, B and C) (*1*). Likewise, for CS23, the CDR L1 ^{30}SK^{31} dipeptide is mutated to ^{30}GQ^{31} and accommodates Y501 in Beta (fig. S6D). Another VH3-53 antibody from our cohort, CS82, is highly cross-reactive and binds SARS-CoV (Fig. 4A), which was not known for any previous VH3-53 antibodies. CS82 competes with CR3022, which binds to a lateral face of the RBD outside the RBS (fig. S6E) and might suggest a possible alternative binding mode or orientation compared with the two previously identified binding modes of wild-type VH3-53 antibodies that are usually sensitive either to K417N or to E484K (*23*, *24*). Collectively, VH3-53/VH3-66 mAbs contribute to the immune response to RBD Beta with mAbs that accommodate Beta-specific mutations in canonical modes and by mAbs that may bind in alternative binding modes.

We next aimed to characterize the functional breadth of the cross-reactive mAbs. Twenty of the 44 cross-reactive mAbs (45.5%) neutralized authentic SARS-CoV-2 Beta isolate (Fig. 4A). To investigate their cross-reactivity against further RBD variants, we performed ELISAs with RBD constructs of VOCs Alpha through Delta and SARS-CoV. Whereas only two mAbs (10%) strongly detected SARS-CoV RBD, the majority of cross-reactive antibodies bound the RBD of Alpha, Gamma, and Delta (Fig. 4A). In PRNT assays with further authentic virus isolates, 15 (75%) Beta-neutralizing cross-reactive mAbs also neutralized wild-type virus, and 14 (70%) neutralized a Delta virus isolate, which of the VOCs was the most antigenically distinct from the others at the time of testing (Fig. 4A). Six cross-neutralizing antibodies were encoded by VH1-58 (Fig. 4A). VH1-58 is the most enriched germline VH gene in RBD antibodies in both Beta and wild-type infection (Fig. 2A) (*26*). VH1-58 RBD antibodies almost exclusively pair with JH3 (fig. S3A). This VH1-58/JH3/VK3-20/JK1 clonotype has been described in individuals infected with wild-type virus (*20*, *26*) and found in several patients within our cohort (Fig. 2C and table S6), representing 2.4% of all Beta-elicited IgG mAbs analyzed in this study (table S2).

To elucidate the structural basis of this public broadly reactive clonotype, we determined

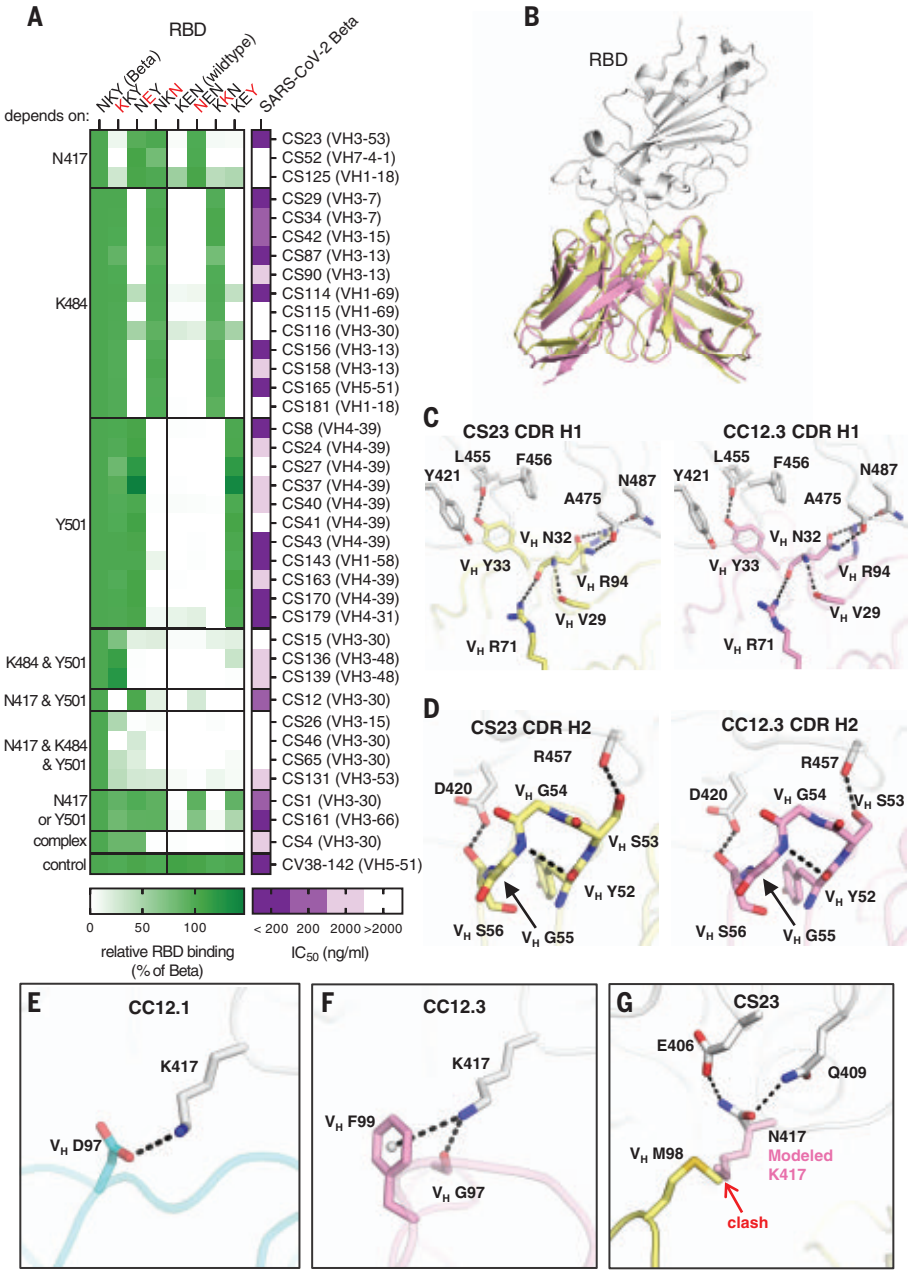

Fig. 3. Binding, neutralization, and structures of Beta-specific antibodies. (**A**) Neutralization of indicated Beta-specific mAbs against authentic Beta virus is shown in purple. Binding to single-point mutant RBD constructs with the indicated amino-acid residues at positions 417, 484, and 501 is shown in green, normalized to RBD Beta. (**B** to **G**) Structural comparison of VH3-53 mAbs between Beta-specific CS23 and wild-type–specific CC12.1 and CC12.3. (B) CC12.3 and CS23 adopt the same binding mode. The crystal structure of CC12.3 (pink) in complex with wild-type RBD was superimposed onto CS23 (yellow) in complex with RBD Beta. Only the variable domains of the antibodies are shown for clarity. A small local conformational difference was observed between CS23-bound RBD Beta and CC12.3-bound wild-type RBD (191 Cα, root mean square deviation = 0.8 Å). [(C) and (D)] Comparison of the (C) CDR H1 ("NY" motif) and (D) CDR H2 ("SGGS" motif) between CS23 and CC12.3. [(E) to (G)] Structures of CDR H3 of (E) CC12.1, (F) CC12.3, and (G) CS23. A modeled side chain of K417 is shown as transparent pink sticks, which would be unfavorable for binding to CS23, where V_H M98 occupies this pocket. Structures of CC12.1 (PDB 6XC3, cyan), CC12.3 (PDB 6XC4, pink), and CS23 (this study, yellow) are used throughout this figure, and the RBD is shown in white. Hydrogen bonds, salt bridges, or cation-π bonds are represented with black dashed lines.

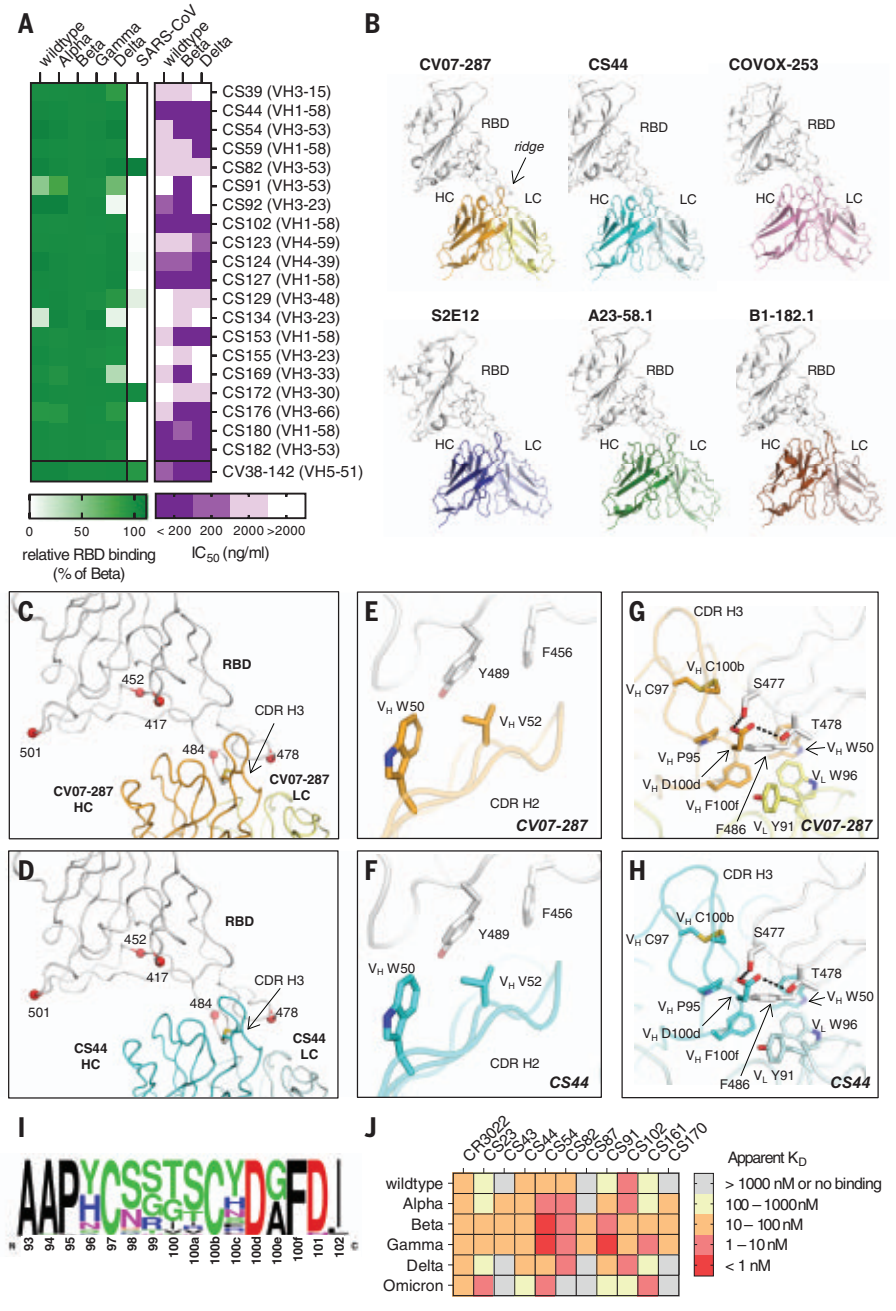

Fig. 4. Characterization of cross-reactive mAbs and crystal structures of CV07-287 and CS44. (**A**) Neutralization of cross-reactive antibodies against authentic Beta, Delta, and wild-type virus is shown in purple. Binding to the indicated RBD constructs is shown in green, normalized to RBD Beta. (**B**) VH1-58 antibodies target SARS-CoV-2 RBD through the same binding mode. Crystal structures of CV07-287 in complex with wild-type RBD and CS44 in complex with RBD Beta are shown. COVA1-16 Fab that was used in the crystallization to form the crystal lattice is not shown for clarity. Structures of VH1-58 antibodies from other studies are shown for comparison, including COVOX-253 (PDB 7BEN), S2E12 (PDB 7K45), A23-58.1 (PDB 7LRT), and B1-182.1 (PDB 7MM0). All structures are shown in the same orientation, with the constant domains of the Fab omitted for clarity. The location of the ridge region of the RBD is indicated at top right. (**C** and **D**) Mutated residues in VOCs B.1.1.7 (Alpha), B.1.351 (Beta), B.1.617.2 (Delta), and P.1 (Gamma) variants are represented by red spheres. All of these residues are distant from VH1-58 antibodies (C) CV07-287 and (D) CS44, except for T478. The disulfide bond in each CDR H3 is shown as sticks. (**E** to **H**) Detailed interactions between the RBD and [(E) and (G)] CV07-287 and [(F) and (H)] CS44, respectively. RBDs are shown in white, with heavy and light chains of CV07-287 in orange and yellow, and those of CS44 in cyan and light cyan, respectively. Interactions of CDR H2 are shown in (E) and (F), and those of CDR H3 are in (G) and (H). Hydrogen bonds are represented with black dashed lines. (**I**) Sequence logo of CDR H3 of VH1-58/VK3-20 antibodies. CDR H3 sequences of VH1-58/VK3-20 antibodies from COVID-19 patients (*17*) were aligned and analyzed with WebLogo. (**J**) Affinity of indicated Beta-elicited mAbs to RBD of indicated VOCs was determined by means of biolayer interferometry.

crystal structures of CS44 and CV07-287, a mAb of the same clonotype that was isolated from a wild-type–infected individual (*19*), in complex with RBD Beta and wild-type RBD, respectively (Fig. 4B). We compared the structures of CS44 and CV07-287 with other published VH1-58 antibodies including COVOX-253 (*27*), S2E12 (*28*), A23-58.1, and B1-182.1 (*26*). These antibodies all target the RBD in the same binding mode (Fig. 4B), which suggests that this public clonotype is structurally conserved. The dominant interaction of VH1-58 antibodies is with the RBD ridge region (residues 471 to 491), which accounts for ~75% of the entire epitope surface. Most of the VOC mutations occur outside of the ridge region (for example, residues 417, 452, and 501) and are distant from the binding sites of VH1-58 antibodies CV07-287 and CS44 (Fig. 4, C and D). T478 interacts with VH1-58 antibodies, but mutation to a lysine can be accommodated (Fig. 4A) (*26*). V_H W50 and Y52 in CDR H2 provide hydrophobic interactions with the RBD (Fig. 4, E and F). CDR H3 also forms extensive interactions with the RBD (Fig. 4, G and H). The CDR H3 sequences of 38 antibodies that belong to this clonotype (Fig. 4I) (*17*) are highly conserved, and all contain a disulfide bond between V_H C97 and C100b, with four relatively small residues (G, S, and T) in between (Fig. 4, I, G, and H). V_H D100d is also conserved (Fig. 4I), forming H-bonds with S477 and T478 (Fig. 4, G and H). In addition, the conserved V_H P95 and F100f (Fig. 4I) stack with RBD-F486 together with V_H W50, V_L Y91, and V_L W96 (Fig. 4, G and H). Although E484 is often an important residue for antibody binding on the ridge region, here it is 5 Å distant from the antibodies, and mutations at this site have not been reported as being sensitive for VH1-58 antibodies.

Thousands of anti-SARS-CoV-2 mAbs were isolated before the VOCs started to emerge (*17*), many of which are highly potent but with varying sensitivity to VOCs. We characterized

the antibody response to the RBD after SARS-CoV-2 Beta infection to provide insights into diverging and converging features of antibodies elicited by this lineage compared with wild-type–elicited antibodies. Recently, the highly mutated Omicron variant has further increased the complexity of SARS-CoV-2 cross-variant immunity and resembles Beta as an antigenically distant VOC. On the basis of their shared RBD mutations, we hypothesized that some Beta-elicited mAbs also bind Omicron. Accordingly, VH3-53 mAb CS23, which binds the shared mutated residues N417 and Y501, showed comparable binding to Omicron and Beta (Fig. 4J). By contrast, Y501-dependent VH4-39 antibodies CS43 and CS170 did not bind to Omicron, suggesting that other mutations in Omicron impede binding of this clonotype. Similarly, VH1-58 mAbs CS44 and CS102 also showed a drastic reduction in affinity to Omicron (Fig. 4J), suggesting that Omicron may not be efficiently neutralized by this public clonotype that exhibits ultrahigh potency and high resistance to VOCs Alpha, Beta, Gamma, and Delta (*26*). These findings emphasize the antigenic complexity and high temporal dynamics that define antibody immunity against SARS-CoV-2 in the context of ongoing antigenic drift and provide insights for next-generation vaccine design and antibody therapeutics. For example, simultaneous or sequential immunization with vaccines based on diverse RBD sequences could be evaluated for superiority in induction of cross-variant immunity. Although large-scale production of novel vaccine candidates based on the Omicron sequence have been initiated, those based on the Beta sequence already show promising cross-variant antibody titers in preclinical studies (*29*, *30*), which led to the subsequent initiation of a phase II/III clinical trial. These clinical trials should be complemented by studies of the immune response against recent and future SARS-CoV-2 variants, including Delta and Omicron, which are currently dominating global infections.

REFERENCES AND NOTES

1. W. Dejnirattisai *et al*., *Cell* **184**, 2939–2954.e9 (2021).
2. P. Wang *et al*., *Nature* **593**, 130–135 (2021).
3. M. Hoffmann *et al*., *Cell* **184**, 2384–2393.e12 (2021).
4. M. Hoffmann *et al*., *Cell Rep.* **36**, 109415 (2021).
5. D. Planas *et al*., *Nat. Med.* **27**, 917–924 (2021).
6. D. Zhou *et al*., *Cell* **184**, 2348–2361.e6 (2021).
7. M. Widera *et al*., *J. Infect. Dis.* **224**, 1109–1114 (2021).
8. M. Rapp *et al*., *Cell Rep.* **35**, 108950 (2021).
9. M. Yuan *et al*., *Science* **373**, 818–823 (2021).
10. C. O. Barnes *et al*., *Nature* **588**, 682–687 (2020).
11. D. Geers *et al*., *Sci. Immunol.* **6**, eabj1750 (2021).
12. C. Lucas *et al*., *Nature* **600**, 523–529 (2021).
13. M. Cevik, N. D. Grubaugh, A. Iwasaki, P. Openshaw, *Cell* **184**, 5077–5081 (2021).
14. E. Cameroni *et al*., *Nature* 10.1038/s41586-021-04386-2 (2021).
15. J. Kreye *et al*., *Brain* **139**, 2641–2652 (2016).
16. T. Tiller *et al*., *J. Immunol. Methods* **329**, 112–124 (2008).
17. M. I. J. Raybould, A. Kovaltsuk, C. Marks, C. M. Deane, *Bioinformatics* **37**, 734–735 (2021).
18. C. Kreer *et al*., *Cell* **182**, 1663–1673 (2020).
19. J. Kreye *et al*., *Cell* **183**, 1058–1069.e19 (2020).
20. D. F. Robbiani *et al*., *Nature* **584**, 437–442 (2020).
21. Z. Wang *et al*., *Nature* **592**, 616–622 (2021).
22. C. O. Barnes *et al*., *Cell* **182**, 828–842.e16 (2020).
23. N. C. Wu *et al*., *Cell Rep.* **33**, 108274 (2020).
24. M. Yuan *et al*., *Science* **369**, 1119–1123 (2020).
25. M. Yuan, H. Liu, N. C. Wu, I. A. Wilson, *Biochem. Biophys. Res. Commun.* **538**, 192–203 (2021).
26. L. Wang *et al*., *Science* **373**, eabh1766 (2021).
27. W. Dejnirattisai *et al*., *Cell* **184**, 2183–2200.e22 (2021).
28. M. A. Tortorici *et al*., *Science* **370**, 950–957 (2020).
29. A. J. Spencer *et al*., *bioRxiv* 447308 [Preprint] (2021).
30. B. Ying *et al*., *Sci. Transl. Med.* 10.1126/scitranslmed.abm3302 (2021).
31. S. D. Boyd *et al*., *J. Immunol.* **184**, 6986–6992 (2010).

ACKNOWLEDGMENTS

We thank all study participants who devoted samples and time to our research; K. Stahlberg and M. Zuo for patient recruitment; S. Bandura, M. Sillmann, D. Brandl, P. Tscheak, and S. Engl for excellent technical assistance; and M. A. Müller and D. Niemeyer for support with BSL3 work. We acknowledge BIAFFIN GmbH & Co. KG (Kassel, Germany) for performance of SPR measurements and the Flow and Mass Cytometry Core Facility at Charité–Universitätsmedizin Berlin for support with single-cell sorting. We thank R. Stanfield for assistance in data collection, F. Zhao for assistance in the biolayer interferometry binding assay, and the staff of Advanced Light Source beamline 5.0.1 and Stanford Synchrotron Radiation Laboratory (SSRL) beamline 12-1 for assistance. SARS-CoV-2 RBD variants antigens for sera testing were kindly provided by InVivo BioTech Services GmbH (Hennigsdorf, Germany) to the Seramun Diagnostica GmbH (Heidesee, Germany). S.M.R. and J.K. are participants in the BIH-Charité Junior Clinician Scientist Program, and V.M.C is supported by Berlin Institute of Health (BIH) Charité Clinician Scientist program, both funded by Charité–Universitätsmedizin Berlin and the Berlin Institute of Health. **Funding:** This work was supported by the Bill and Melinda Gates Foundation INV-004923 (I.A.W.); the Bavarian State Ministry of Science and the Arts; University Hospital; Ludwig-Maximilians-Universität Munich; German Ministry for Education and Research (project 01KI20271, M.H.; Connect-Generate 01GM1908D, H.P.); the Helmholtz Association (ExNet-0009-Phase2-3, D.S.; HIL-A03, H.P.); the German Research Foundation (DFG) (FOR3004 SYNABS, PR1274/3-1, and PR1274/5-1, H.P.); and the Austrian Science Fund (FWF J4157-B30, M.R.). Parts of the work were funded by the European Union's Horizon 2020 research and innovation program through project RECOVER (GA101003589) to C.D.; the German Ministry of Research through the projects VARIPath (01KI2021) to V.M.C and NaFoUniMedCovid19–COVIM, FKZ: 01KX2021 to C.D. and V.M.C. This research used resources of the Advanced Light Source, which is a US Department of Energy (DOE) Office of Science User Facility under contract DE-AC02-05CH11231. Use of the SSRL, SLAC National Accelerator Laboratory, is supported by the DOE, Office of Science, Office of Basic Energy Sciences under contract DE-AC02–76SF00515. The SSRL Structural Molecular Biology Program is supported by the DOE Office of Biological and Environmental Research and by the National Institutes of Health, National Institute of General Medical Sciences (including P41GM103393). **Author contributions:** Conceptualization: S.M.R., M.Y., H.-C.K., V.M.C., H.P., I.A.W., and J.K. Patient recruitment and sample preparation: S.M.R., M.R., M.A.H., I.K., T.M.E., C.G., A.W., M.H., H.G., G.W., S.H., H.P., and J.K. Antibody production: S.M.R., S.v.H., E.S.-S., M.R., S.E.B., H.F.R., M.A.H., L.S., D.K., N.v.W., and J.K. Antibody reactivity testing: H.-C.K. Serological assays and neutralization testing: V.M.C., M.L.S., T.S., L.M.J., and C.D. Protein production and crystallography: M.Y., W.Y., Y.H., and H.T. Software: M.B., J.H., and S.M.R. Resources: V.M.C., M.H., G.W., D.S., C.D., H.P., and I.A.W. Writing, original draft: S.M.R., M.Y., H.-C.K., H.P., I.A.W., and J.K. Writing, review and editing: all authors. Supervision: S.M.R., M.Y., H.-C.K., V.M.C., H.P., I.A.W., and J.K. **Competing interests:** The German Center for Neurodegenerative Diseases (DZNE) and Charité-Universitätsmedizin Berlin have filed a patent application (application no. PCT/EP2021/064352) on antibodies for the treatment of SARS-CoV-2 infection described in an earlier publication, on which S.M.R., H.-C.K., V.M.C., E.S.-S., H.P., and J.K. are named as inventors. V.M.C. is named together with Euroimmun GmbH on a patent application filed recently regarding the diagnostic of SARS-CoV-2 by antibody testing. **Data and materials availability:** X-ray coordinates and structure factors are deposited at the RCSB Protein Data Bank under accession codes 7S5P, 7S5Q, and 7S5R. The amino acid sequences of the antibodies described in this study can be found in table S3. Nucleotide sequences have been deposited to GenBank (accession nos. OM457661 to OM457822). All requests for materials including antibodies, viruses, plasmids, and proteins generated in this study should be directed to the corresponding authors. Materials will be made available for noncommercial usage.

SUPPLEMENTARY MATERIALS

science.org/doi/10.1126/science.abm5835
Materials and Methods
Figs. S1 to S6
Tables S1 to S6
References (*32*–*45*)

29 September 2021; accepted 18 January 2022
Published online 25 January 2022
10.1126/science.abm5835

innovative health initiative

INNOVATIVE HEALTH INITIATIVE (IHI) EXECUTIVE DIRECTOR

WHO WE ARE
IHI is a €2.4 billion research and innovation partnership between the European Union and Europe's health-related industries.

WHAT WE'RE LOOKING FOR
An outstanding and dynamic professional with top leadership, communication and people skills, and a deep understanding of health research and innovation.

A mediator with experience in collaboration between different stakeholders in health.

An experienced manager of research funds.

As part of the EU strategic engagement for gender equality, we encourage applications from female candidates.

WHAT WE OFFER
The opportunity to lead and shape an exciting new research programme, in collaboration with leaders from the public and private sectors and the IHI staff.

LOCATION: Brussels, Belgium

DEADLINE: 12:00 (noon) CET on 28 February 2022
More information: **https://ec.europa.eu/dgs/human-resources/seniormanagementvacancies/**

Who's the top employer for 2021?

Science Careers' annual survey reveals the top companies in biotech & pharma voted on by *Science* readers.

Read the article and employer profiles at sciencecareers.org/topemployers

Science 2021 TOP EMPLOYER

Science Careers helps you advance your career. Learn how!

- Register for a free online account on **ScienceCareers.org**.
- Search hundreds of job postings and find your perfect job.
- Sign up to receive e-mail alerts about job postings that match your criteria.
- Upload your resume into our database and connect with employers.
- Watch one of our many webinars on different career topics such as job searching, networking, and more.
- Download our career booklets, including Career Basics, Careers Beyond the Bench, and Developing Your Skills.
- Complete an interactive, personalized career plan at "my IDP."
- Visit our Employer Profiles to learn more about prospective employers.
- Read relevant career advice articles from our library of thousands.

Visit **ScienceCareers.org** today — all resources are free

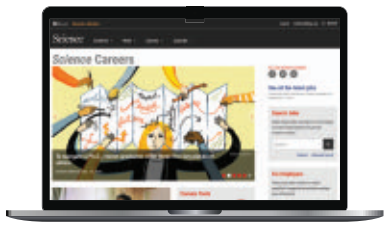

SCIENCECAREERS.ORG

ScienceCareers
FROM THE JOURNAL SCIENCE AAAS

National Institute on Aging

ASSOCIATE DIRECTOR FOR SCIENTIFIC STRATEGY, INNOVATION, AND MANAGEMENT

The National Institute on Aging (NIA), a component of the National Institutes of Health (NIH) and the Department of Health and Human Services (DHHS), is seeking candidates for the **Associate Director for Scientific Strategy, Innovation, and Management, Office of the Director**. The role is categorized into four functional areas: scientific strategic planning; science management; science innovation; and inter-agency collaboration and liaison. The ideal candidate has expertise in aging research, science policy, clinical research management and evaluation. Additional, the candidate has an M.D., Ph.D., or equivalent degree in a field relevant to one or more scientific areas of aging research. The position requires superior executive leadership and communication skills to effectively brief NIA, NIH, HHS, and Congressional staff on high-level research accomplishments in both Alzheimer's Disease/Alzheimer's and Related Dementias (AD/ADRD) as well as aging research in general, including gaps in scientific knowledge and access to needed services. Candidates must possess recognized research management and leadership abilities.

Applications will be accepted for 60 days starting **January 26th, 2022**. Applicants must submit a current curriculum vitae, bibliography, and full contact details for three references. Applicants are asked to prepare two statements: a vision statement and a statement that addresses the specific qualification requirements (limit both statements to two pages each). Send application package to **NIAJobs@mail.nih.gov**.

Information about the NIA or this position please visit: **www.nia.nih.gov** or contact Jessica Moreno with questions at **morenojs@mail.nih.gov**.

DHHS and NIH are Equal Opportunity Employers

South Carolina

TENURE-TRACK ASSISTANT PROFESSOR

The NIH Center for Dietary Supplements and Inflammation (CDSI) at the University of South Carolina (UofSC) invites applications for two tenure-track **ASSISTANT PROFESSOR** positions with research expertise in Inflammation. The phase-2 Center of Biomedical Research Excellence (COBRE) will provide NIH research support and mentoring to junior faculty who have not received NIH R01 or similar grants as a PI, to become successful independent investigators.

More information is available at:
https://sc.edu/study/colleges_schools/medicine/centers_and_institutes_new/ce nter_for_dietary_supplements_and_inflam mation/index.php

Candidates must have a PhD or equivalent, and at least 3 years of postdoctoral research experience. Competitive salary and startup funds are available. Please submit CV and a statement of research and teaching interests with names of 3 references online at **https://uscjobs.sc.edu/postings/93433**. The search will start immediately and will continue until the position is filled.

The University of South Carolina does not discriminate in educational or employment opportunities on the basis of race, sex, gender, gender identity, transgender status, age, color, religion, national origin, disability, sexual orientation, genetics, protected veteran status, pregnancy, childbirth or related medical conditions.

EPFL Empa

Faculty Position in Environmental Sensing Technologies

Joint Appointment between the Swiss Federal Laboratories for Materials Science and Technology (Empa) and the Ecole polytechnique fédérale de Lausanne (EPFL)

EPFL's School of Architecture, Civil and Environmental Engineering (ENAC) and the Swiss Federal Laboratories for Materials Science and Technology (Empa) invite applications for a tenured (Associate or Full) Professor in the Institute of Environmental Engineering. The appointee will participate in Empa's Functional Materials Department, and contribute to research and teaching activities within the EPFL Institute of Environmental Engineering.

The Institute of Environmental Engineering (IIE) in ENAC carries out basic and translational research spanning fundamental understanding of environmental systems and their resilience to design of adaption strategies. It covers a diverse portfolio in research, teaching and innovative technology development across transversal themes: understanding and adapting to climate change, distributed and dynamic environmental sensing, resource quality and its effects on ecosystem health, and human-environment interactions.

Empa's Functional Materials Department develops in highly interdisciplinary teams sustainable material and technology solutions for a climate-neutral society, as well as novel soft robotic systems for infrastructure maintenance and environmental monitoring.

The joint Empa/EPFL professor in Environmental Sensing Technologies will have acknowledged strengths in research and innovation related to sensing of relevant variables in water, soil or the atmosphere, as well as leveraging the resulting data for improved environmental sustainability and adaptation. We welcome a range of applications, from environmental specialists who leverage sensing technologies to mobile sensing specialists with interests in environmental questions. Areas of interest within these domains include, but are not limited to:

- Distributed and local sensing of (new) environmental variables via novel methodologies/technologies
- Multi-environment sensing of spatially and/or temporally varying phenomena using mobile platforms
- Integration of sensing with localization, estimation and optimization across multiple scales and terrains (air/soil/water)
- Unconventional sensing (e.g., combining living organisms and mechatronics)

The Empa/EPFL professor will lead an internationally recognized research program that leverages the opportunities offered by Empa and EPFL in cross-institutional, complementary research groups. The appointee will promote excellence in research and in undergraduate and graduate level teaching.

EPFL is a growing and well-funded institution with excellent experimental and computational infrastructure. Teaching and research at EPFL covers essentially the entire palette of engineering and science, and offers a fertile environment for research collaboration between different disciplines. Empa conducts cutting-edge research for the benefit of industry and the well-being of society. The EPFL and Empa environments are multilingual and multicultural, with English serving as a common interface.

The following documents are requested in PDF format: cover letter including a statement of motivation, curriculum vitae, publications list, concise statements of research and teaching interests, as well as the contact information of at least five references who are ready to supply their letter upon request.

To apply, please follow the application procedure at:
https://facultyrecruiting.epfl.ch/position/35848192

Formal evaluation of the applications will begin on **1 April 2022** and the search will continue until the position is filled.

Further enquiries should be made to:
Prof. Athanasios Nenes
Chair of the Search Committee
E-mail: SearchEnvSensingTech@epfl.ch

Additional information on Empa:
Dr. Tanja Zimmerman (tanja.zimmermann@empa.ch)
Head of Department Functional Materials

Additional information on Empa and EPFL: https://empa.ch, https://www.epfl.ch

EPFL and Empa are equal opportunity and family friendly employers. We are committed to increasing the diversity of their faculty, and strongly encourage women to apply.

By **Erika Moore**

The debt trap

As I sat in the financial aid office, the seat was cold and the chill seeped into my body. I was about to sign away another $20,000 in student loans to continue my education at one of the best universities in the United States. I didn't want to sign; I had never seen $20,000 in my life. But I had already come so far—I was in my third year of college—and I didn't see any other choice. Looking back, though, I wish I'd thought more about the implications of my financial decisions. My debt nearly kept me from pursuing graduate school and becoming the scientist I am today.

When I got accepted, I had three siblings already in college, and like many Black families, we didn't have inherited family wealth to dip into to finance our education. My parents had always made it clear that the cost of my schooling was my responsibility.

So I applied for student loans. I had a scholarship that covered two-thirds of my tuition. But I needed money for the remainder, as well as for books, housing, and food. I hadn't thought through those costs before I started, and it was daunting when they started to add up. I worked at the student center and tried to live frugally, tracking my expenses and eating for free whenever possible. But by the end of my degree, the loans had snowballed.

"My debt nearly kept me from pursuing graduate school."

As graduation neared, I returned to the financial aid office and learned just how big the snowball had gotten: I owed $65,000. I had been preparing to apply to graduate school to study biomedical engineering. But after seeing how much I owed, I wondered whether that was even an option.

I could defer my student loan payments while in graduate school. But when I examined the details, I discovered my debt would continue to collect interest at a rate of 6%. That meant if I didn't make any payments during a 5-year Ph.D. program, I would owe $88,354 instead of $65,000. Was my graduate education worth adding more than $23,000 in interest on my loans?

Friends were signing job offers and making plans to pay off their loans, which made me wonder whether that was the path I should take. Weighing my options left me feeling overwhelmed. I didn't want to ignore my debt problem. But I also didn't want to put off attaining my Ph.D.

I knew it would be challenging to make student loan payments while living off a graduate student stipend. But I applied for graduate school anyway and gave it a try. I earned roughly $33,000 per year, and I supplemented that income by working as a dog walker, a house sitter, and a babysitter. I took a job in campus housing, which allowed me to live rent free. I also continued to live frugally.

Hustling from the lab to a dog-sitting gig and back was not an easy task. I had to manage my calendar carefully. But it was worth it: I was able to pay off all my student loans by the time I graduated. I also secured an offer for a faculty job before graduating—which was a relief because by now, I had educated myself on finances. I knew it was important to start making retirement contributions as early as possible in life. And I wasn't sure I wanted to spend years as a postdoc making barely more than what I earned as a Ph.D. student.

Looking back, I wish I'd had more training in financial literacy during high school and college. Had I been more aware, I might have taken a different path. For instance, I could have reduced the cost of my education by going to a lower priced community college for the first 2 years. Or I could have applied for scholarships more aggressively.

Now that I'm a faculty member, I've made it a priority to pass what I've learned about finances on to students I teach and mentor. I worry, in particular, about those who are members of historically excluded groups because they are more likely to graduate with debt. I tell them to apply for as many scholarships as possible, to pay attention to the details in each loan, and to keep track of their expenses.

Seeing them pay off their loans and make decisions that are financially informed fills my heart with joy. I don't want them to have to question their career aspirations the way I did. I want them to pursue the path that's best for them, with a clear understanding of how it will impact their finances. ■

Erika Moore is an assistant professor at the University of Florida. Her nonprofit, Moore Wealth Inc., teaches financial literacy and awards scholarships to students in need.

ILLUSTRATION: ROBERT NEUBECKER

NOMIS & Science
YOUNG EXPLORER AWARD 2022

Research at the intersection of the social and life sciences

Unconventional. Interdisciplinary. Bold.

The **NOMIS & *Science* Young Explorer Award** recognizes and rewards early-career M.D., Ph.D., or M.D./Ph.D. scientists that perform research at the intersection of the social and life sciences. Essays written by these bold researchers on their recent work are judged for clarity, scientific quality, creativity, and demonstration of cross-disciplinary approaches to address fundamental questions.

A cash prize of up to 15 000 USD will be awarded to essay winners, and their engaging essays will be published in ***Science***. Winners will also be invited to share their work and forward-looking perspective with leading scientists in their respective fields at an award ceremony as well as a meeting of the NOMIS Board of Directors to consider future funding.

Apply by May 15, 2022

at www.science.org/nomis

NOMIS FOUNDATION
Creating the Spark

Science
AAAS